

POLISH SOCIETY OF THEORETICAL AND APPLIED MECHANICS

**JOURNAL OF THEORETICAL
AND APPLIED MECHANICS**

No. 4 • Vol 54

Quarterly

WARSAW, OCTOBER 2016

JOURNAL OF THEORETICAL AND APPLIED MECHANICS

(until 1997 Mechanika Teoretyczna i Stosowana, ISSN 0079-3701)

Beginning with Vol 45, No. 1, 2007, *Journal of Theoretical and Applied Mechanics* (JTAM) has been selected for coverage in Thomson Reuters products and custom information services. Now it is indexed and abstracted in the following:

- **Science Citation Index Expanded** (also known as SciSearch®)
- **Journal Citation Reports/Science Edition**

Advisory Board

MICHAŁ KLEIBER (Poland) – Chairman

JORGE A.C. AMBROSIO (Portugal) * ANGEL BALTOV (Bulgaria) * ROMESH C. BATRA (USA) *
ALAIN COMBESURE (France) * JÜRI ENGELBRECHT (Estonia) * WITOLD GUTKOWSKI (Poland) *
JÓZEF KUBIK (Poland) * GERARD A. MAUGIN (France) * ZENON MRÓZ (Poland) *
RYSZARD PARKITNY (Poland) * EUGENIUSZ ŚWITOŃSKI (Poland) * HISAAKI TOBUSHI (Japan) *
DIETER WEICHERT (Germany) * JOSE E. WESFREID (France) * JÓZEF WOJNAROWSKI (Poland) *
JOSEPH ZARKA (France) * VLADIMIR ZEMAN (Czech Republic)

Editorial Board

WŁODZIMIERZ KURNIK – Editor-in-Chief,

PIOTR CUPIAŁ, KRZYSZTOF DEMS, KURT FRISCHMUTH (Germany), PIOTR KOWALCZYK,
ZBIGNIEW KOWALEWSKI, TOMASZ KRZYŻYŃSKI, TOMASZ ŁODYGOWSKI, EWA MAJCHRZAK,
WIESŁAW NAGÓRKO, JANUSZ NARKIEWICZ, BŁAŻEJ SKOCZEŃ, ANDRZEJ STYCZEK,
ANDRZEJ TYLIKOWSKI, UTZ VON WAGNER (Germany), JERZY WARMIŃSKI,
ELŻBIETA WILANOWSKA – Secretary, PIOTR PRZYBYŁOWICZ – Language Editor,
EWA KOISAR – Technical Editor



Articles in JTAM are published under Creative Commons Attribution – Non-commercial 3.0. Unported License <http://creativecommons.org/licenses/by-nc/3.0/legalcode>. By submitting an article for publication, the authors consent to the grant of the said license.



The journal content is indexed in Similarity Check, the Crossref initiative to prevent plagiarism.

* * * * *

Editorial Office

Al. Armii Ludowej 16, room 650

00-637 Warszawa, Poland

phone (+48 22) 825 7180, (+48) 664 099 345, e-mail: biuro@ptmts.org.pl

www.ptmts.org.pl/jtam.html

* * * * *



Publication supported by Ministry of Science and Higher Education of Poland

(Journal of Theoretical and Applied Mechanics: 1) digitalizacja publikacji i monografii naukowych w celu zapewnienia i utrzymania otwartego dostępu do nich przez sieć Internet, 2) stworzenie anglojęzycznych wersji wydawanych publikacji, 3) wdrożenie procedur zabezpieczających oryginalność publikacji naukowych oraz zastosowane techniki zabezpieczeń – są finansowane w ramach umowy 734/P-DUN/2016 ze środków Ministra Nauki i Szkolnictwa Wyższego przeznaczonych na działalność upowszechniającą naukę)

SDRE APPLIED TO POSITION AND VIBRATION CONTROL OF A ROBOT MANIPULATOR WITH A FLEXIBLE LINK

JEFERSON JOSÉ DE LIMA, ANGELO MARCELO TUSSET, FREDERIC CONRAD JANZEN,
VINCIUS PICCIRILLO, CLAUDINOR BITENCOURT NASCIMENTO

*UTFPR, Ponta Grossa, PR, Brazil; email: jefersonjl82@gmail.com; tuset@utfpr.edu.br; fcjanzen@utfpr.edu.br;
piccirillo@utfpr.edu.br; claudinor@utfpr.edu.br*

JOSÉ MANOEL BALTHAZAR

UNESP, Bauru, SP, Brazil; email: jmbaltha@gmail.com

REYOLANDO MANOEL LOPES REBELLO DA FONSECA BRASIL

UFABC, Santo Andre, SP, Brazil; email: reyolando.brasil@ufabc.edu.br

This paper presents position and vibration control of a flexible robot composed of two rigid and one flexible links. Position is controlled by the current applied to the DC motor armature. To control vibrations of the flexible structure, Shape Memory Alloys (SMA) are used. Due to phase transformations, the SMA can change its stiffness through temperature variation, considering and taking advantage of this characteristic the vibration control is done. Control is achieved via the State Dependent Ricatti Equations (SDRE) technique, which uses sub-optimal control and system local stability search. The simulation results show the feasibility of the proposed control for the considered system.

Keywords: SDRE control, flexible robotic arm, SMA, active vibration control

1. Introduction

In the last decades, several researches on robotic manipulators with flexible links have come to attention due to their many advantages over rigid manipulators (Kalyoncu, 2008).

Shawky *et al.* (2013) remarked that flexible manipulator systems offer several advantages in contrast to the traditional rigid manipulator. The advantages include faster response, lower energy consumption, relatively smaller actuators and less overall mass and, in general, smaller final cost. Due to its flexible nature, control of these flexible systems takes into account both rigid body and elastic degrees of freedom. It is important to recognize the flexible nature of the manipulator and construct a mathematical model for the system that accounts for the interactions between the actuators and payload.

According to Banks *et al.* (1996) and Gabbert and Schulz (1996), it is necessary to improve robotic manipulators including the use of smart materials to assist control by changing the structural behavior.

There are several studies suggesting solutions to the problem of handlers with flexible elements such as (Sawada *et al.*, 2004), which have been exploited for the purposes of efficiency and flexibility of a handler in microgravity environment. In Inifene (2007), the dynamics of a flexible link and a comparative study of some implemented control is shown. (Heidari *et al.*, 2013) proposes a nonlinear finite element modeling of flexibility of handlers. In Grandinetti *et al.* (2012), a three-degree-of-freedom cylindrical manipulator system with a flexible link on its tip is studied and experimentally implemented, and the active vibration control is analyzed. In Halim *et al.* (2014), the use of a decentralized vibration control scheme for suppressing vibration of a multi-link flexible robotic manipulator using embedded smart piezoelectric transducers is

investigated. In Pereira *et al.* (2012), an adaptive control applied to single link-flexible manipulators, utilizing a feedback controller of the joint angle to guarantee trajectory tracking of the joint angle with an adaptive input shaper updated by algebraic non-asymptotic identification is proposed.

Bottega *et al.* (2009) proposed a tracking control model for a flexible link robotic manipulator using simultaneously motor torques and piezoelectric actuators. Molter *et al.* (2010) used SDRE control technique design for flexible manipulators using piezoelectric actuators. In Shawky *et al.* (2013), the tip position of a one-link flexible manipulator was modeled and controlled. The control strategy was based on the SDRE control design method in the context of application to robotics. The experimental results revealed that the nonlinear SDRE controller was near optimal and robust, and its performance compared favorably to the conventional PD controller strategy.

This work proposes the control of a robotic manipulator for aerospace applications. It is composed of two rigid links modeled as proposed by Korayem *et al.* (2011), and one flexible link modeled as proposed by Janzen *et al.* (2014). The gravity effects are not considered, similar to the proposal presented by Sawada *et al.* (2004). In order to reduce vibrations of the flexible manipulator, it is proposed to use SMAs. Shape Memory Alloys (SMAs) are a group of metallic materials with the ability to return to a previously defined shape or size, after deformation, by applying a specific temperature. This effect occurs due to the shift in the materials crystalline structure between two different phases, called martensite and austenite (Piccirillo *et al.*, 2008, 2009). When SMAs are heated, they present changes in crystal structure. These changes generate large forces that can be used in actuator systems (Ge *et al.*, 2013). In this way, SMAs can be used in many application areas, like robotics, since they allow for a lighter weight manipulator and longer links, which are important for aerospace applications.

The proposed feedback control system is designed to take the system into a desired coordinate. The feedback control is obtained using SDRE. The SDRE control choice is because the control computer algorithm is simple and highly effective for nonlinear feedback control. It has been successfully used in robotic manipulators (Innocenti *et al.*, 2000; Xin *et al.*, 2001; Korayem *et al.*, 2010; Nekoo, 2013; Korayem and Nekoo, 2014, 2015a), and in robotic manipulators with a flexible joint or/and with flexible link (Korayem *et al.* 2011; Fenili and Balthazar, 2011; Shawky *et al.*, 2013; Lima *et al.*, 2014; Korayem and Nekoo, 2015b).

The paper is organized as follows. Section 2 provides the dynamic model for a two rigid and a flexible link manipulator. Section 3 presents the SDRE control project considering both control of just positioning, without vibration control of the flexible link, as in the case of vibration control of the flexible link by temperature variation (SMAs). Concluding remarks are given in Section 4.

2. Mathematical model

The adopted manipulator model consists of two rigid links and the third flexible one. The DC motors and joints of the robotic manipulator are presented in Fig. 1, and the transmission motor torque to the manipulator is given by Eq. (2.6),

The governing equations of motions are obtained through Lagrangian formalism. To derive the equations of motion of the manipulator, one needs the kinetic energy \mathfrak{S} and the potential energy Γ in the Lagrangian function L

$$L = \mathfrak{S} - \Gamma \quad (2.1)$$

Next, one must apply the equations of Euler-Lagrange (Lima *et al.*, 2014)

$$\frac{d}{dt} \left(\frac{\partial L}{\partial \dot{\theta}_i} \right) - \frac{\partial L}{\partial \theta_i} = \tau_i \quad (2.2)$$

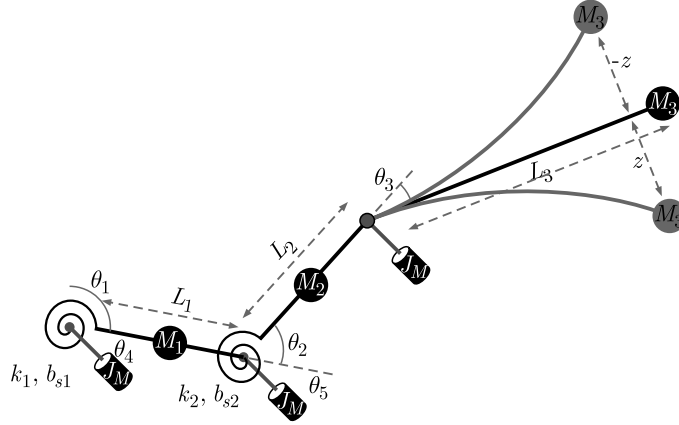


Fig. 1. Schematic of the manipulator model, where $\theta_{1,2,3}$ are the joint angles of each link, $\theta_{4,5}$ are the corresponding motor angles for the link, b_s is the damping constant, k is the spring constant, and the variable z is the displacement of the beam end

The right hand side of Eq. (2.2) are non-conservative forces. Thus, we obtain Eq. (2.3), the equations of motion of the link (Korayem *et al.*, 2011; Lima *et al.*, 2014)

$$\mathbf{M}(\boldsymbol{\theta})\ddot{\boldsymbol{\theta}} = -\mathbf{C}(\boldsymbol{\theta}, \dot{\boldsymbol{\theta}}) - \mathbf{F}(\dot{\boldsymbol{\theta}}) + \boldsymbol{\tau} \quad (2.3)$$

where $\mathbf{M}(\boldsymbol{\theta})$ is the inertia matrix, $\ddot{\boldsymbol{\theta}}$ represents the acceleration of the i -th link, $\mathbf{C}(\boldsymbol{\theta}, \dot{\boldsymbol{\theta}})$ are the centrifugal and Coriolis forces, $\mathbf{F}(\dot{\boldsymbol{\theta}})$ describes friction between the joint and the link and $\boldsymbol{\tau}$ is the torque effect on the rotors.

The system matrices $\mathbf{C}(\boldsymbol{\theta}, \dot{\boldsymbol{\theta}})$ and $\mathbf{F}(\dot{\boldsymbol{\theta}})$ are presented by

$$\mathbf{C}(\boldsymbol{\theta}, \dot{\boldsymbol{\theta}}) = \begin{bmatrix} v_{11} & v_{12} & v_{13} \\ v_{21} & v_{22} & v_{23} \\ v_{31} & v_{32} & v_{33} \end{bmatrix} \begin{bmatrix} \dot{\theta}_1 \\ \dot{\theta}_2 \\ \dot{\theta}_{M3} \end{bmatrix} \quad \mathbf{F}(\dot{\boldsymbol{\theta}}) = \begin{bmatrix} k_a \dot{\theta}_1 \\ k_a \dot{\theta}_2 \\ b_v \dot{\theta}_{M3} \end{bmatrix} \quad (2.4)$$

where $\mathbf{v}_{3 \times 3}$ are the variables of centrifugal/coriolis forces.

The equations that define the dynamics of the DC motor, are obtained by Eq. (2.1) and Eq. (2.2), and represented by

$$\ddot{\theta}_{M_i} = \frac{b_v \dot{\theta}_{M_i} - k_t i_i + \tau_s}{J} \quad i_i = \frac{-R_M i_i - k_b \dot{\theta}_{M_i} + V_i}{L_m} \quad (2.5)$$

where $\ddot{\theta}_{M_i}$ is the acceleration and $\dot{\theta}_{M_i}$ the velocity of DC motor, i_i is the current, V_i is the voltage applied in the DC motor armature, R_M , k_b and L_m are the resistance of the armature, the electromotive force constant and the inductance of the armature of the motor, respectively.

For the coupling of the equations, we replace $\tau_i = \tau_{s_i}$ in Eqs. (2.3), (2.4) and (2.5)₁, thus considering the characteristic of the proposed model flexible joints, according to (Lima *et al.*, 2014)

$$\boldsymbol{\tau}_s = \begin{bmatrix} b_s(\dot{\theta}_{M_1} - \dot{\theta}_1) + k(\theta_{M_1} - \theta_1) \\ b_s(\dot{\theta}_{M_2} - \dot{\theta}_2) + k(\theta_{M_2} - \theta_2) \\ k i_3 \end{bmatrix} \quad (2.6)$$

The dynamics of the system with a flexible beam coupled to the shaft of the DC motor is given by (Janzen *et al.*, 2014)

$$\begin{aligned} i &= \frac{-R_M i - k_b \dot{\theta} + V}{L_M} & \dot{\theta}_v &= \frac{-b_v \dot{\theta} + k_t i - C(\boldsymbol{\theta}, \dot{\boldsymbol{\theta}}) + EI \phi_0'' z}{J_v} \\ \ddot{z} &= -\mu \dot{z} - w^2 z - \alpha_v \ddot{\theta} + \dot{\theta}^2 z \end{aligned} \quad (2.7)$$

where E is Young's modulus and I is the moment of inertia of the cross section of the beam, z is the displacement for the first mode of vibration of the beam and ϕ_0'' is the constant of the beam vibration modes for the first mode, obtained by applying the assumed mode method (Fenili and Balthazar, 2011). Thus, the proposed system is represented by Eq. (2.3) coupled with Eq. (2.7), in the state space of the variables, represented by

$$\begin{aligned}
\dot{x}_1 &= x_2 \\
\dot{x}_2 &= p_{11}(-kx_1 + kx_3 + b_s x_4) + p_{12}(-kx_6 + kx_8 + b_s x_9) - p_{13}(EI\phi_0'' x_{14}) \\
&\quad + \varphi_{11}x_2 + \varphi_{12}x_6 + \varphi_{13}x_{11} \\
\dot{x}_3 &= x_4 \\
\dot{x}_4 &= \frac{k}{J_m}x_1 + \frac{b_s}{J_m}x_2 - \frac{k}{J_m}x_3 - \frac{b_s + b_v}{J_m}x_4 + \frac{k_t}{J_m}x_5 \\
\dot{x}_5 &= -\frac{k_b}{L_m}x_4 - \frac{R_m}{L_m}x_5 \\
\dot{x}_6 &= x_7 \\
\dot{x}_7 &= p_{21}(-kx_1 + kx_3 + b_s x_4) + p_{22}(-kx_6 + kx_8 + b_s x_9) - p_{23}(EI\phi_0'' x_{14}) \\
&\quad + \varphi_{21}x_2 + \varphi_{22}x_6 + \varphi_{23}x_{11} \\
\dot{x}_8 &= x_9 \\
\dot{x}_9 &= \frac{k}{J_m}x_6 + \frac{b_s}{J_m}x_7 - \frac{k}{J_m}x_8 - \frac{b_s + b_v}{J_m}x_9 + \frac{k_t}{J_m}x_{10} \\
\dot{x}_{10} &= -\frac{k_b}{L_m}x_9 - \frac{R_m}{L_m}x_{10} \\
\dot{x}_{11} &= x_{12} \\
\dot{x}_{12} &= p_{31}(-kx_1 + kx_3 + b_s x_4) + p_{32}(-kx_6 + kx_8 + b_s x_9) - p_{33}(EI\phi_0'' x_{14}) \\
&\quad + \varphi_{31}x_2 + \varphi_{32}x_6 + \varphi_{33}x_{11} \\
\dot{x}_{13} &= -\frac{k_b}{L_m}x_{14} - \frac{R_m}{L_m}x_{15} \\
\dot{x}_{14} &= x_{15} \\
\dot{x}_{15} &= -\alpha_v \varphi_{31}x_{12} - \alpha_v + (\omega^2 + \alpha_v(p_{33}(EI\phi_0'' + x_{12}^2)))x_{14} - \mu x_{15}
\end{aligned} \tag{2.8}$$

where $x_1 = \theta_1$, $x_2 = \dot{\theta}_1$, $x_3 = \theta_{M_1}$, $x_4 = \dot{\theta}_{M_1}$, $x_5 = i_1$, $x_6 = \theta_2$, $x_7 = \dot{\theta}_2$, $x_8 = \theta_{M_2}$, $x_9 = \dot{\theta}_{M_2}$, $x_{10} = i_2$, $x_{11} = \theta_{M_3}$, $x_{12} = \dot{\theta}_{M_3}$, $x_{13} = i_3$, $x_{14} = z$, $x_{15} = \dot{z}$ and φ_{nm} are the nonlinear elements.

The index n indicates the equation of the system $\dot{\theta}_n$ it belongs to, and m is the corresponding coefficient of velocity $\dot{\theta}_m$. We can see the elements of φ_{nm} below

$$\begin{aligned}
\varphi_{11} &= p_{11}(-k_a - v_{11} - b_s) - p_{12}v_{21} - p_{13}v_{31} \\
\varphi_{12} &= -p_{11}v_{12} + p_{12}(-v_{22} - k_a - b_s) - p_{13}v_{32} \\
\varphi_{13} &= -p_{11}v_{13} - p_{12}v_{23} + p_{13}(-v_{33} - b_v) \\
\varphi_{21} &= p_{21}(-k_a - v_{11} - b_s) - p_{22}v_{21} - p_{23}v_{31} \\
\varphi_{22} &= -p_{21}v_{12} + p_{12}(-v_{22} - k_a - b_s) - p_{23}v_{32} \\
\varphi_{23} &= -p_{21}v_{13} - p_{12}v_{23} + p_{23}(-v_{33} - b_v) \\
\varphi_{31} &= p_{31}(-k_a - v_{11} - b_s) - p_{32}v_{21} - p_{33}v_{31} \\
\varphi_{32} &= -p_{31}v_{12} + p_{32}(-v_{22} - k_a - b_s) - p_{33}v_{32} \\
\varphi_{33} &= -p_{31}v_{13} - p_{32}v_{23} + p_{33}(-v_{33} - b_v)
\end{aligned} \tag{2.9}$$

and

$$\mathbf{p}_{3 \times 3} = \mathbf{M}(\boldsymbol{\theta})^{-1} \tag{2.10}$$

3. Proposed control

Consider system (2.8) in the form

$$\dot{\mathbf{x}} = \mathbf{A}(\mathbf{x})\mathbf{x} + \mathbf{B}\mathbf{u} \quad (3.1)$$

where $\mathbf{x} \in \mathfrak{R}^n$ is the state vector, $\mathbf{A}(\mathbf{x}) \in \mathfrak{R}^{n \times n}$ is the state-dependent matrix, $\mathbf{B} \in \mathfrak{R}^{n \times m}$ is the control matrix and \mathbf{u} is a feedback control vector.

The proposed control \mathbf{u} can be determined using SDRE control (Balthazar *et al.*, 2014). The methodology used in SDRE control makes the synthesis of LQR control gains varying in time (Mracek and Cloutier, 1998). The quadratic cost function for the regulator problem is given by

$$J = \frac{1}{2} \int_{t_0}^{\infty} [\mathbf{e}^T \mathbf{Q} \mathbf{e} + \mathbf{u}^T \mathbf{R} \mathbf{u}] dt \quad (3.2)$$

where $\mathbf{Q} \in \mathfrak{R}^{n \times n}$ and $\mathbf{R} \in \mathfrak{R}^{m \times m}$ are positive definite matrices, and

$$\mathbf{e} = \begin{bmatrix} x_1 - x_1^* & 0 & 0 & 0 & 0 & x_2 - x_2^* & 0 & 0 & 0 & 0 & x_3 - x_3^* & 0 & 0 & 0 & 0 \end{bmatrix}^T \quad (3.3)$$

where \mathbf{x} are the system state variables, and x^* is the desired state.

Assuming full state feedback, the control law is given by

$$\mathbf{u} = -\mathbf{R}^{-1} \mathbf{B}^T \mathbf{P} \mathbf{e} \quad (3.4)$$

The State-Dependent-Riccati equation to obtain \mathbf{P} is given by

$$\mathbf{P}(\mathbf{x})\mathbf{A}(\mathbf{x}) + \mathbf{A}(\mathbf{x})^T \mathbf{P}(\mathbf{x}) - \mathbf{P}(\mathbf{x})\mathbf{B}\mathbf{R}^{-1} \mathbf{B}^T \mathbf{P}(\mathbf{x}) + \mathbf{Q} = \mathbf{0} \quad (3.5)$$

In numerical simulations, we consider two situations. First, we consider control of the handler via DC motors at the joints without control of vibrations of the flexible beam. Next, we consider control of the vibration of the flexible beam. It is assumed throughout this paper that the parameters considered are presented in Table 1.

Table 1. Parameters for simulation

$L_1 = 0.5 \text{ m}$	$L_2 = 0.5 \text{ m}$	$L_3 = 1.2 \text{ m}$
$M_1 = 1 \text{ kg}$	$M_2 = 1 \text{ kg}$	$M_3 = 1.318 \cdot 10^{-4} \text{ kg}$
$k_{t1} = 0.08 \text{ Nm/A}$	$k_{t2} = 0.08 \text{ Nm/A}$	$k_{t3} = 0.058 \text{ Nm/A}$
$k_{b1} = 0.008 \text{ V/rpm}$	$k_{b2} = 0.008 \text{ V/rpm}$	$k_{b3} = 0.008 \text{ V/rpm}$
$b_{v1} = 0.2 \text{ Nms/rad}$	$b_{v2} = 0.2 \text{ Nms/rad}$	$b_{v3} = 4.62 \text{ Nms/rad}$
$R_{m1} = 1.7 \Omega$	$R_{m2} = 1.7 \Omega$	$R_{m3} = 1.914 \Omega$
$L_{m1} = 0.003 \text{ H}$	$L_{m2} = 0.003 \text{ H}$	$L_{m3} = 3.4 \cdot 10^{-3} \text{ H}$
$E = 0.7 \cdot 10^{11} \text{ N/m}^2$	$I_m = 6.54 \cdot 10^{-5} \text{ kg/m}^2$	$I_e = 6.54 \cdot 10^{-7} \text{ kg/m}^2$
$I = 1.56 \cdot 10^{-13} \text{ m}^4$	$\mu = 0.1$	$\phi_0'' = 4.898 \text{ m}$
$\alpha_v = 0.821$	$w = 11.3097 \text{ rad/s}$	

The initial values for \mathbf{x} are given by: $x_1(0) = \pi$, $x_2(0) = 0$, $x_3(0) = \pi$, $x_4(0) = 0$, $x_5(0) = 0$, $x_6(0) = 0.6981$, $x_7(0) = 0$, $x_8(0) = 0.6981$, $x_9(0) = 0$, $x_{10}(0) = 0$, $x_{11}(0) = 0.5236$, $x_{12}(0) = 0$, $x_{13}(0) = 0$, $x_{14}(0) = 0$ and $x_{15}(0) = 0$.

The desired state is: $x_1^* = 2.0944$, $x_2^* = 0$, $x_3^* = x_3$, $x_4^* = x_4$, $x_5^* = x_5$, $x_6^* = -0.6981$, $x_7^* = 0$, $x_8^* = x_8$, $x_9^* = x_9$, $x_{10}^* = x_{10}$, $x_{11}^* = -0.5236$, $x_{12}^* = 0$, $x_{13}^* = x_{13}$, $x_{13}(0) = 0$, $x_{14}^* = 0$ and $x_{15}^* = 0$.

3.1. Position control for DC motor (control I)

Consider the case in which the control \mathbf{u} is applied only to position control of θ_1 , θ_2 and θ_{M3} , and flexible link vibrations are not controlled directly. Thus, we define \mathbf{Q} , $\mathbf{R} = \mathbf{R}_1$ and consider $\mathbf{u} = [u_1 \ u_2 \ u_3]^T$, $\mathbf{A} = [\mathbf{A}_1 \ \mathbf{A}_2]$, $\mathbf{B} = \mathbf{B}_1$, where the control signal (u_1 , u_2 and u_3) represents the voltage applied to the motor terminals (matrices \mathbf{Q} , \mathbf{R}_1 , \mathbf{A}_1 , \mathbf{A}_2 and \mathbf{B}_1 in Appendix). In Figs. 2a,b,c, we can observe the position error of the manipulator (θ_1 , θ_2 and θ_{M3}), considering only position control of the link by the motor current. In Fig. 2d, we can observe vibrations at the tip of the flexible link (z).

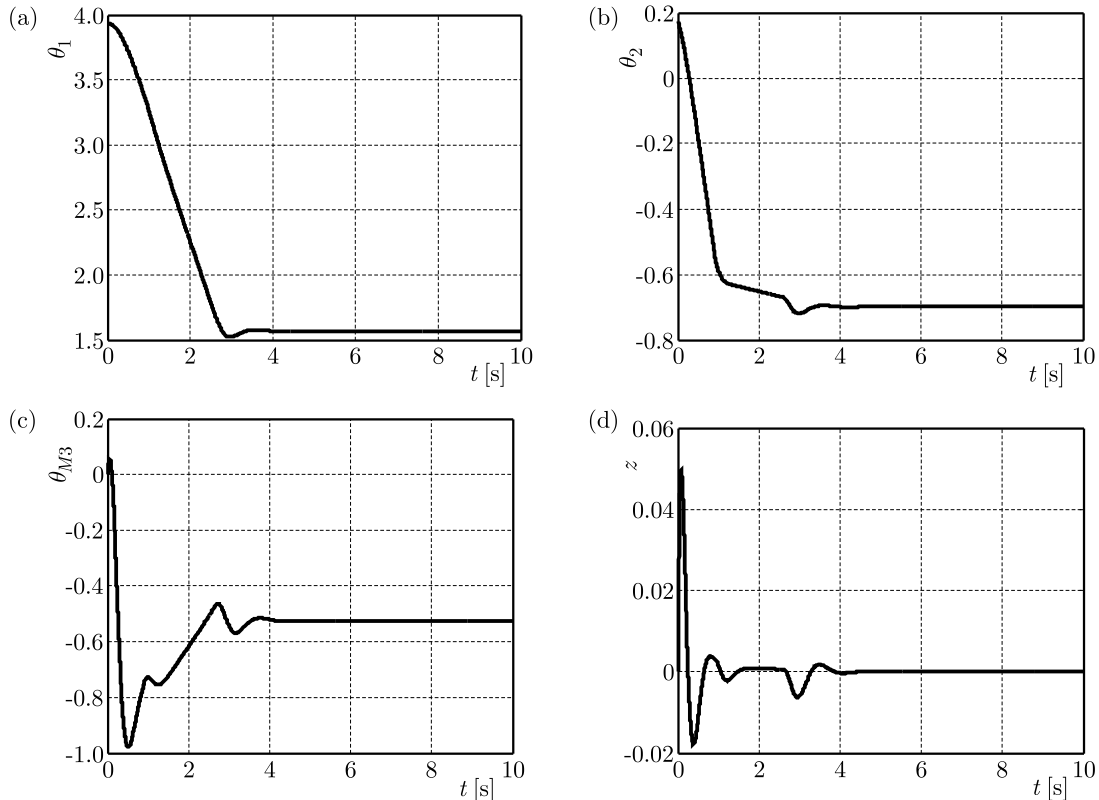


Fig. 2. (a) Positioning θ_1 , (b) positioning θ_2 , (c) positioning motor θ_{M3} , (d) displacement of the beam z

Although the system controlled by the motors can position the links at the desired points, we observe oscillations in the positioning (Fig. 2a,b,c) caused by vibrations of the flexible link (Fig. 2d).

3.2. Position control for DC motor and beam deflection control (control II)

In the adopted second strategy we control θ_1 , θ_2 and θ_{M3} and control the flexible link vibrations using SMAs fixed to the link. SMAs capacity to change their physical properties with temperature variation allows for their use as means to vibration suppression of the flexible link.

Falk (1980, 1993) proposed the SMA mathematical model used in this paper. It is based on the Devonshire theory that considers free energy in a polynomial form. This model does not consider internal variables and potential dissipation to describe the pseudo-elasticity and the shape memory effect. The Falk model considers only the temperature T and the deformation (ε) (Janzen *et al.*, 2014).

The SMA polynomial model was chosen due to its capacity to represent qualitatively the pseudo-elasticity and shape memory effects of the SMA structure. The Helmholtz free energy ψ

was chosen so there are minimum and maximum points that represent the stability and instability of the SMA phases. The potential of free energy can be described by

$$\rho\psi(\varepsilon, T) = \frac{1}{2}q(T - T_M)\varepsilon^2 - \frac{1}{4}b\varepsilon^4 + \frac{b^2\varepsilon^6}{24q(T_A - T_M)} \quad (3.6)$$

The variables T_A and T_M are temperatures in which the austenitic and martensitic phases are stable, q and b are positive constants. A constitutive equation can be written as (Savi *et al.*, 2002)

$$\sigma = q(T - T_M)\varepsilon - \frac{1}{4}b\varepsilon^3 + \frac{b^2\varepsilon^5}{4q(T_A - T_M)} \quad (3.7)$$

where $b = 1.868 \cdot 10^7$ MPa, $q = 523.29$ MPa/K, $T_M = 364.3$ K and $T_M = 288$ K for (Cu-Zn-Al-Ni).

The SMA element can be coupled to the beam-like structure as a stiffness component which can be described by

$$k(x, T) = \bar{q}(T - T_M)x - \bar{b}x^3 + \bar{e}x^5 \quad (3.8)$$

where

$$\bar{q} = \frac{qA_r}{L} \quad \bar{b} = \frac{bA_r}{L^3} \quad \bar{e} = \frac{eA_r}{L^5}$$

Considering the case in which the objective is to position the beam-like link and reducing its oscillations, we define \mathbf{Q} , $\mathbf{R} = \mathbf{R}_2$ and consider $\mathbf{u}_f = [u_1 \ u_2 \ u_3 \ u_4]^T$, $\mathbf{A} = [\mathbf{A}_1 \ \mathbf{A}_3]$ and $\mathbf{B} = \mathbf{B}_2$ (matrices \mathbf{Q} , \mathbf{R}_2 , \mathbf{A}_1 , \mathbf{A}_3 and \mathbf{B}_2 in Appendix). And considering: $\bar{q} = 1.56987$, $\bar{b} = 114367.348$ and $\bar{e} = 7232491.36$ (Janzen *et al.*, 2014).

The control signal (u_1 , u_2 and u_3) represents the voltage applied to the motor terminals, and (u_4) represents the temperature variation of the SMA given by

$$u_4 = \Delta T = T - T_M \quad (3.9)$$

In Figs. 3a,b and 3c, we can observe the manipulator position error (θ_1 , θ_2 and θ_{M3}) considering the positioning control of links through the motors, and the vibration control of flexible link through the use of SMA in Fig. 3d (z).

As we can see in Fig. 3, the addition of SMA reduces vibrations of the flexible link, therefore reducing oscillations (θ_{M3}). Thus, we avoid inversion of the torques of the motors, which caused the oscillations seen in Fig. 2.

In Fig 4a, we can observe the temperature variation of the SMA to control the vibration of the flexible link (ΔT), and in Fig. 4b we present the comparative results between the two control strategies proposed.

First, the structure is fully austenite, and it can be seen from Fig. 4 that no phase transformation occurs in the alloy, namely, the SMA remains in the austenite phase ($T_A \geq 364.3$ K). This variation of the parameter ΔT acts on the beam rigidity (Eq. (3.8)) and reduces the amplitude of displacement of the flexible link as can be observed in Fig. 4b.

It is also possible to observe that ΔT remained at a constant value of $\Delta T = 77$ K for $t > 0.029$ s, due to the need of keeping the SMA in the austenite phase, enables control of the stiffness according to equation (3.8).

By applying DC control motors and using flexible SMA one observes a smoother response for all angles θ_1 , θ_2 and θ_{M3} and a smaller amplitude of oscillation z .

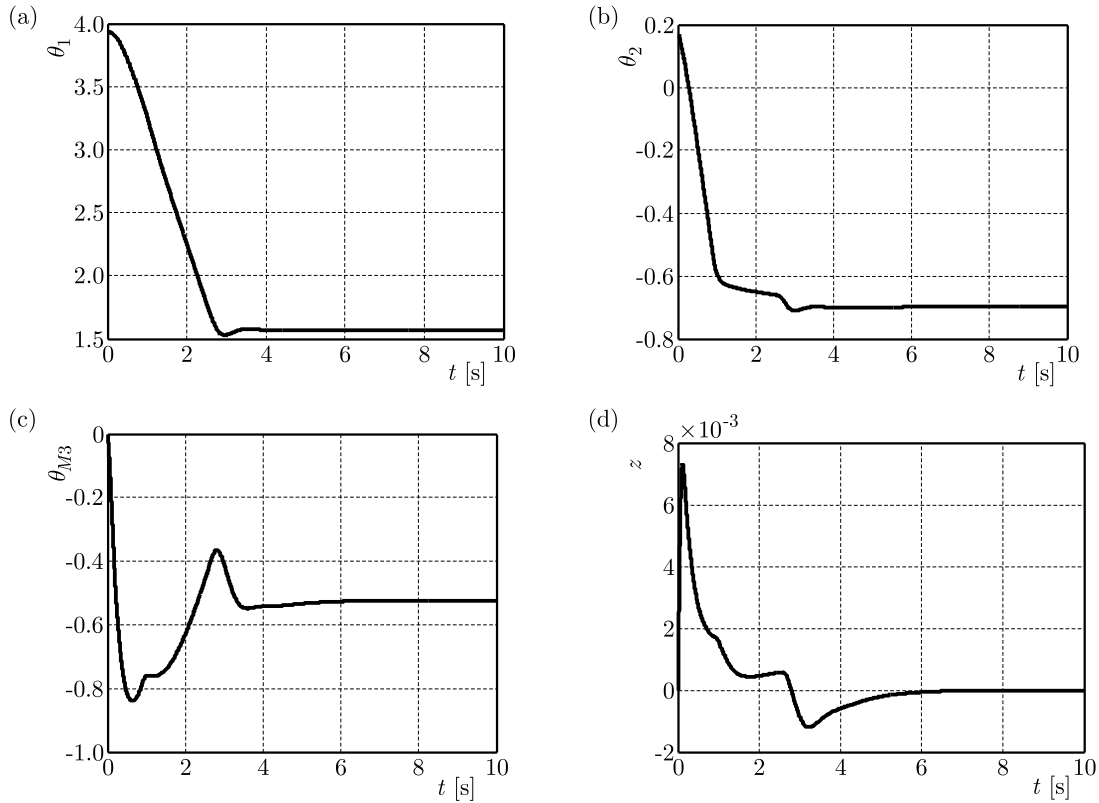


Fig. 3. (a) Positioning θ_1 , (b) positioning θ_2 , (c) positioning motor θ_{M3} , (d) displacement of the beam z

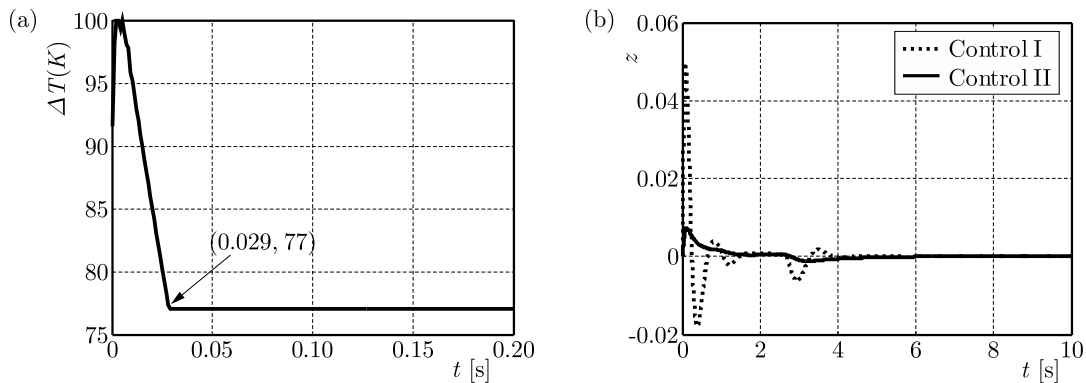


Fig. 4. (a) Temperature variation in SMA ($u_4 = T - 288 = \Delta T$), (b) displacement of the beam z

4. Conclusion

We can observe in the simulations results that vibration control of the flexible link allows for a more efficient control than the control provided by the motors only. This demonstrates the importance of controlling vibrations of the flexible link. By using the polynomial model of SMA it is possible to estimate the temperature variation in the SMA to attenuate vibrations of the flexible link. The temperature variation of the SMA causes changes in their physical characteristics, allowing for its use as a way to reduce vibrations of the flexible beam. The numerical results show that the proposed control strategy using SMA in vibration control of the flexible links is a good alternative to constructing lighter handlers with longer links, such as those applied in aerospace activities.

Acknowledgements

The authors would like to acknowledge Conselho Nacional de Desenvolvimento Científico e Tecnológico – CNPQ grant: 484729/2013-6 and grant: 447539/2014-0, for the financial support.

Appendix

$$\mathbf{A}_1 = \begin{bmatrix} 0 & 1 & 0 & 0 & 0 & 0 & 0 & 0 & 0 & 0 \\ -p_{11}k & \varphi_{11} & p_{11}k & p_{11}b_s & 0 & -p_{12}k & \varphi_{12} & p_{12}k & p_{12}b_s & 0 \\ 0 & 0 & 0 & 1 & 0 & 0 & 0 & 0 & 0 & 0 \\ \frac{k}{J_m} & \frac{b_s}{J_m} & -\frac{k}{J_m} & -\frac{b_s+b_v}{J_m} & \frac{k_t}{J_m} & 0 & 0 & 0 & 0 & 0 \\ 0 & 0 & 0 & 0 & 0 & 0 & 1 & 0 & 0 & 0 \\ 0 & 0 & 0 & -\frac{k_b}{L_m} & -\frac{R_m}{L_m} & 0 & 0 & 0 & 0 & 0 \\ -p_{21}k & \varphi_{21} & p_{21}k & p_{21}b_s & 0 & -p_{22}k & \varphi_{22} & p_{22}k & p_{22}b_s & 0 \\ 0 & 0 & 0 & 0 & 0 & 0 & 0 & 0 & 1 & 0 \\ 0 & 0 & 0 & 0 & 0 & \frac{k}{J_m} & \frac{b_s}{J_m} & -\frac{k}{J_m} & -\frac{b_s+b_v}{J_m} & \frac{k_t}{J_m} \\ 0 & 0 & 0 & 0 & 0 & 0 & 0 & 0 & -\frac{k_b}{L_m} & -\frac{R_m}{L_m} \\ 0 & 0 & 0 & 0 & 0 & 0 & 0 & 0 & 0 & 0 \\ -p_{31}k & \varphi_{31} & p_{31}k & p_{31}b_s & 0 & -p_{32}k & \varphi_{32} & p_{32}k & p_{32}b_s & 0 \\ 0 & 0 & 0 & 0 & 0 & 0 & 0 & 0 & 0 & 0 \\ 0 & 0 & 0 & 0 & 0 & 0 & 0 & 0 & 0 & 0 \\ 0 & 0 & 0 & 0 & 0 & 0 & 0 & 0 & 0 & 0 \end{bmatrix}$$

$$\mathbf{B}_1^T = \begin{bmatrix} 0 & 0 & 0 & \frac{1}{L_M} & 0 & 0 & 0 & 0 & 0 & 0 & 0 & 0 & 0 & 0 \\ 0 & 0 & 0 & 0 & 0 & 0 & 0 & 0 & \frac{1}{L_M} & 0 & 0 & 0 & 0 & 0 \\ 0 & 0 & 0 & 0 & 0 & 0 & 0 & 0 & 0 & 0 & \frac{1}{L_M} & 0 & 0 & 0 \end{bmatrix}$$

$$\mathbf{Q}_{15 \times 15} = \{q_{ij}\} \quad q_{ij} = \begin{cases} 0 & \text{if } i \neq j \\ 1 & \text{if } i = 2, 3, 4, 5, 7, 8, 9, 10, 12, 13, 15 \\ 100 & \text{if } i = 1, 6, 11, 14 \end{cases}$$

$$\mathbf{R}_1 = \begin{bmatrix} 0.1 & 0 & 0 \\ 0 & 0.1 & 0 \\ 0 & 0 & 0.1 \end{bmatrix} \quad \mathbf{R}_2 = \begin{bmatrix} 0.1 & 0 & 0 & 0 \\ 0 & 0.1 & 0 & 0 \\ 0 & 0 & 0.1 & 0 \\ 0 & 0 & 0 & 0.1 \end{bmatrix}$$

$$\mathbf{A}_2 = \begin{bmatrix} 0 & 0 & 0 & 0 & 0 \\ 0 & \varphi_{13} & p_{13}k_t & -p_{13}EI\phi_0'' & 0 \\ 0 & 0 & 0 & 0 & 0 \\ 0 & 0 & 0 & 0 & 0 \\ 0 & 0 & 0 & 0 & 0 \\ 0 & 0 & 0 & 0 & 0 \\ 0 & \varphi_{23} & p_{23}k_t & -p_{23}EI\phi_0'' & 0 \\ 0 & 0 & 0 & 0 & 0 \\ 0 & 0 & 0 & 0 & 0 \\ 0 & 0 & 0 & 0 & 0 \\ 0 & 0 & 0 & 0 & 0 \\ 0 & \varphi_{33} & p_{33}k_t & -p_{33}EI\phi_0'' & 0 \\ 0 & -\frac{k_b}{L_M} & -\frac{R_M}{L_M} & 0 & 0 \\ 0 & 0 & 0 & 0 & 1 \\ 0 & -\alpha_v\varphi_{33} & \alpha_v p_{33}k_t & w^2 + \alpha_v p_{33}EI\phi_0'' + x_{12}^2 & \mu \end{bmatrix}$$

$$\mathbf{B}_2 = \begin{bmatrix} 0 & 0 & 0 & 0 \\ 0 & 0 & 0 & 0 \\ 0 & 0 & 0 & 0 \\ \frac{1}{L_M} & 0 & 0 & 0 \\ 0 & 0 & 0 & 0 \\ 0 & 0 & 0 & 0 \\ 0 & 0 & 0 & 0 \\ 0 & 0 & 0 & 0 \\ 0 & \frac{1}{L_M} & 0 & 0 \\ 0 & 0 & 0 & 0 \\ 0 & 0 & 0 & 0 \\ 0 & 0 & \frac{1}{L_M} & 0 \\ 0 & 0 & 0 & 0 \\ 0 & 0 & 0 & -\bar{q}x_{14} \end{bmatrix}$$

$$\mathbf{A}_3 = \begin{bmatrix} 0 & 0 & 0 & 0 & 0 \\ 0 & \varphi_{13} & p_{13}k_t & -p_{13}EI\phi_0'' & 0 \\ 0 & 0 & 0 & 0 & 0 \\ 0 & 0 & 0 & 0 & 0 \\ 0 & 0 & 0 & 0 & 0 \\ 0 & 0 & 0 & 0 & 0 \\ 0 & \varphi_{23} & p_{23}k_t & -p_{23}EI\phi_0'' & 0 \\ 0 & 0 & 0 & 0 & 0 \\ 0 & 0 & 0 & 0 & 0 \\ 0 & 0 & 0 & 0 & 0 \\ 0 & 0 & 0 & 0 & 0 \\ 0 & \varphi_{33} & p_{33}k_t & -p_{33}EI\phi_0'' & 0 \\ 0 & -\frac{k_b}{L_M} & -\frac{R_M}{L_M} & 0 & 0 \\ 0 & 0 & 0 & 0 & 1 \\ 0 & -\alpha_v\varphi_{33} & \alpha_v p_{33}k_t & w^2 + \alpha_v p_{33}EI\phi_0'' + x_{12}^2 - x_{14}^2(\bar{b} - \bar{e}x_{14}^2) & \mu \end{bmatrix}$$

References

1. BALTHAZAR J.M., BASSINELLO D.G., TUSSET A.M., BUENO A.M., PONTES B.R., 2014, Nonlinear control in an electromechanical transducer with chaotic behavior, *Meccanica*, **49**, 8, 1859-1867, doi: 10.1007/s11012-014-9910-4
2. BANKS H.T., SMITH R.C., WANG Y., 1996, *Smart Material Structures: Modeling, Estimation and Control*, John Wiley & Sons, Paris
3. BOTTEGA V., PERGHER R., FONSECA J.S.O., 2009, Simultaneous control and piezoelectric insert optimization for manipulators with flexible link, *Journal of the Brazilian Society of Mechanical Sciences and Engineering*, **31**, 2, 105-116, doi: 10.1590/S1678-58782009000200003
4. FALK F., 1980, Model free energy, mechanics, and thermodynamics of shape memory alloys, *Acta Metallurgica*, **28**, 12, 1773-1780, doi: 10.1016/0001-6160(80)90030-9
5. FALK F., 1983, One dimensional model of shape memory alloys, *Archives of Mechanics*, **35**, 1, 63-84.
6. FENILI A., BALTHAZAR J.M., 2011, The rigid-flexible nonlinear robotic manipulator: modeling and control, *Communications in Nonlinear Science and Numerical Simulation*, **16**, 5, 2332-2341, doi: 10.1016/j.cnsns.2010.04.057

7. GABBERT U., SCHULZ I., 1996, Optimal placement of piezoelectric actuators in vibration control of adaptative structures, *Proceedings of ASME International Mechanical Engineering Congress and Exposition*, 271-277
8. GE S.S., TEE K.P., VAHHI I.E., TAY F.E.H., 2006, Tracking and vibration control of flexible robots using shape memory alloys, *IEEE/ASME Transactions on Mechatronics*, **11**, 690-698, doi: 10.1109/TMECH.2006.886242
9. GRANDINETTI F.J., SOARES A.M.S., LAMAS W.Q., GOES L.C.S., 2012, Notes on vibration control of a micro/macromanipulator mounted on a flexible structure, *Proceedings of the Institution of Mechanical Engineers, Part K: Journal of Multi-body Dynamics March*, **226**, 1, 72-82, doi: 10.1177/1464419311424090
10. HALIM D., LUO X., TRIVAILO P.M., 2014, Decentralized vibration control of a multi-link-flexible robotic manipulator using smart piezoelectric transducers, *Acta Astronautica*, **104**, 186-196, doi: 10.1016/j.actaastro.2014.07.016
11. HEIDARI H.R., KORAYEM M.H., HAGHPANAHI M., BATLLE V.F., 2013, Optimal trajectory planning for flexible link manipulators with large deflection using a new displacements approach, *Journal of Intelligent and Robotic Systems*, **72**, 3/4, 287-300, doi: 10.1007/s10846-012-9807-1
12. INNOCENTI M., BARALLI F., SALOTTI F., CAITI A., 2000, Manipulator path control using SDRE, *American Control Conference*, **5**, 3348-3352, doi: 10.1109/ACC.2000.879186
13. JANZEN F.C., TUSSET A.M., PICCIRILLO V., BALTHAZAR J.M., SILVEIRA M., PONTES JUNIOR B.R., 2014, Control of slewing motions of flexible structures using shape memory alloy actuators, *Proceedings of ASME International Mechanical Engineering Congress and Exposition*, 1-7
14. JNIFENE A., 2007, Active vibration control of flexible structures using delayed position feedback, *Systems and Control Letters*, **56**, 3, 215-222, doi: 10.1016/j.sysconle.2006.10.005
15. KALYONCU M., 2008, Mathematical modelling and dynamic response of a multistraight-line path tracing flexible robot manipulator with rotating-prismatic joint, *Applied Mathematical Modelling*, **32**, 1087-1098, doi: 10.1016/j.apm.2012.10.042
16. KORAYEM M.H., IRANI M., NEKOO S.R., 2010, Analysis of manipulators using SDRE: a closed loop nonlinear optimal control approach, *Scientia Iranica, Transaction B: Mechanical Engineering*, **17**, 6, 456-467
17. KORAYEM M., IRANI M., NEKOO S.R., 2011, Load maximization of flexible joint mechanical manipulator using nonlinear optimal controller, *Acta Astronautica*, **69**, 7, 458-469, doi: 10.1016/j.actaastro.2011.05.023
18. KORAYEM M.H., NEKOO S.R., 2014, Nonlinear optimal control via finite time horizon state-dependent Riccati equation, *International Conference on Robotics and Mechatronics*, 878-883, doi: 10.1109/ICRoM.2014.6991015
19. KORAYEM M.H., NEKOO S.R., 2015a, State-dependent differential Riccati equation to track control of time-varying systems with state and control nonlinearities, *ISA Transactions*, **57**, 117-135, doi: 10.1016/j.isatra.2015.02.008
20. KORAYEM M.H., NEKOO S.R., 2015b, Finite-time state-dependent Riccati equation for time-varying nonaffine systems: rigid and flexible joint manipulator control, *ISA Transactions*, **54**, 125-144, doi:10.1016/j.isatra.2014.06.006
21. LIMA J.J., TUSSET A.M., JANZEN F.C., PICCIRILLO V., NASCIMENTO C.B., BALTHAZAR J.M., BRASIL M.R.L.F., 2014, Nonlinear state estimation and control applied to a manipulator robotic including drive motor, *Mathematics in Engineering, Science and Aerospace: the Transdisciplinary International Journal*, **5**, 413-425
22. MRACEK P.C., CLOUTIER J.R., 1998, Control designs for the nonlinear benchmark problem via the state-dependent Riccati equation method, *International Journal of Robust and Nonlinear Control*, **8**, 401-433

23. MOLTER A., SILVEIRA O.A.A., FONSECA J.S.O., BOTTEGA V., 2010, Simultaneous piezoelectric actuator and sensor placement optimization and control design of manipulators with flexible links using SDRE method, *Mathematical Problems in Engineering*, 1-23, doi: 10.1155/2010/362437
24. NEKOO S.R., 2013, Nonlinear closed loop optimal control: a modified state-dependent Riccati equation, *ISA Transactions*, **52**, 2, 285-290, doi:10.1016/j.isatra.2012.10.005
25. PEREIRA E., TRAPERIO J.R., DIAZ I.M., FELIU V., 2012, Adaptive input shaping for single-link flexible manipulators using an algebraic identification, *Control Engineering Practice*, **20**, 138-147, doi: 10.1016/j.conengprac.2011.10.004
26. PICCIRILLO V., BALTHAZAR J.M., PONTES JR. B.R., FELIX J.L.P., 2008, On a nonlinear and chaotic non-ideal vibrating system with Shape Memory Alloy (SMA), *Journal of Theoretical and Applied Mechanics (Poland)*, **46**, 597-620
27. PICCIRILLO V., BALTHAZAR J.M., PONTES JR. B.R., FELIX J.L.P., 2009, Chaos control of a nonlinear oscillator with shape memory alloy using an optimal linear control. Part II: Non-ideal energy source, *Nonlinear Dynamics*, **56**, 3, 243-253, doi: 10.1007/s11071-008-9396-5
28. SAVI M.A., PACHECO P.M.C.L., BRAGA A.M.B., 2002, Chaos in a shape memory two-bars truss, *International Journal of Non-Linear Mechanics*, **37**, 1387-1395
29. SAWADA H., UI K., MORI M., YAMAMOTO H., HAYASHI R., MATUNAGA S., OHKAMI Y., 2004, Micro-gravity experiment of a space robotic arm using parabolic flight, *Advanced Robotics*, **18**, 3, 247-267, doi: 10.1163/156855304322972431
30. SHAWKY A., ZYDEK D., ELHALWAGY Y.Z., ORDYS A., 2013, Modeling and nonlinear control of a flexible-link manipulator, *Applied Mathematical Modelling*, **37**, 9591-9602, doi: 10.1016/j.apm.2013.05.003
31. XIN M., BALAKRISHNAN S.N., HUANG Z., 2001, Robust state dependent Riccati equation based robot manipulator control, *International Conference on Control Applications*, **3**, 369-374, doi: 10.1109/CCA.2001.973893

Manuscript received February 4, 2015; accepted for print December 7, 2015

DUCTILE FRACTURE CRITERION FOR SPECIMENS WITH NOTCHES MADE OF ALUMINIUM ALLOY EN-AW 2024

ŁUKASZ DERPEŃSKI, ANDRZEJ SEWERYN

*Białystok University of Technology, Faculty of Mechanical Engineering, Poland
e-mail: l.derpeński@pb.edu.pl; a.seweryn@pb.edu.pl*

The paper presents the experimental verification of the most frequently used ductile fracture criteria based on authors own experimental results and numerical calculations. Attention is drawn to the large discrepancy of results of fracture prediction and experimental data for six considered criteria. Based on own results, a new ductile fracture criterion for notched specimens is proposed. In the criterion, it is assumed that fracture initiation occurs when the maximum normal stress reaches a critical value depending on the maximum value of plastic shear strain.

Keywords: numerical analysis, fracture of specimen with notches, ductile fracture criterion

1. Introduction

Exploration of the phenomena associated with ductile fracture of materials continues over 50 years. Attempts to describe ductile failure are carried out at two scales. The microscopic, where fracture is a result of complex physical processes (Thomason, 1990; Öchsner *et al.*, 2001; Bandsta and Koss, 2004), and the macroscopic where fracture is assumed to be caused by state variables which are components of the stress and strain tensor and their variation during load (Bao, 2001, 2005). Starting from the work by McClintock (1968), continuously more and more new fracture criteria are created showing how important the problem is. Yanshan *et al.* (2012) proposed a new ductile fracture criterion to model fracture behavior of sheet metals for nucleation, growth and shear coalescence of voids during plastic deformation. Komori (2005) showed the effect of various ductile fracture criteria on crack initiation and propagation during shearing and tensile tests. Yanshan and Hoon (2013) presented evaluation of ductile fracture criteria in a general three-dimensional stress state of stress triaxiality, the Lode parameter and the equivalent plastic strain to fracture. Ma *et al.* (2015) presented damage evaluation in tube spinnability test using ductile fracture criteria.

This study aims to select appropriate ductile fracture criteria (DFCs) in terms of damage limits which have been obtained by mechanical tests, to accurately predict the forming limit and damage evolution in the tube spinability test. Chena *et al.* (2015) calculated the sheet metal forming limit prediction based on the general plastic work criterion and some ductile fracture criteria. There is a continuing need to develop new and verify the existing criteria. Most of them are due to the used material parameters and components of the stress or strain tensor which is very complicated and often difficult to verify. Therefore, it is necessary to create a fracture criterion, which is sufficiently simple and not containing many difficult to determine parameters in order to predict fracture of material. Based on the authors' own research results (Derpeński, Seweryn, 2011, Derpeński, Seweryn, 2013), verification of selected ductile fracture criteria and formulation of authors' own stress fracture criterion, in which the critical stress value depends on the value of the maximum plastic shear strain, is presented.

2. Experimental tests

The main stage of experimental tests is the analysis of fracture in specimens with circumferential notches (Fig. 1) whose dimensions have been selected so that different states of stress could be obtained in the plane of notch symmetry (Derpeński and Seweryn, 2011). The dimensions of the specimens selected for the analysis are listed in Table 1.

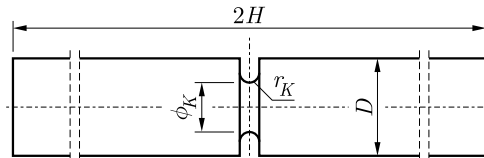


Fig. 1. A cylindrical notched specimen with radius r_k and diameter ϕ_k

Table 1. Dimensions of specimens for experimental tests

Shape	r_k [mm]	ϕ_k [mm]	$2H$ [mm]	D [mm]
I	0.3; 0.5; 1.0; 2.0; 4.0; 8.0; 15; 30	8.0	120	10
II	0.3; 0.5; 1.0; 2.0; 4.0; 8.0; 15; 30	7.0		
III	0.3; 0.5; 1.0; 2.0; 4.0; 8.0; 15; 30	6.0		

r_k – notch radius; ϕ_k – specimen diameter at the root of the notch;
 $2H$ – height of the specimen; D – diameter of the specimen

The specimens have been extended by applying forced displacement controlled by means of an extensometer with its measurement base of 25 mm (Fig. 2).

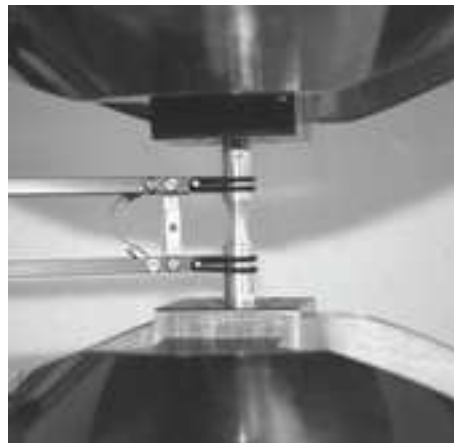


Fig. 2. Round notched specimen with an axial extensometer

As a result of the conducted tests, the authors recorded the relations between the tensile force and the elongation of the measurement base ($l_0 = 25$ mm) for each notch, particularly the maximum (critical) displacement of the measurement base u_c and the critical force F_c causing fracture initiation in the specimen. The moment of fracture initiation indicates a significant decrease in the force value in the force-displacement graph. Table 2 and 3 present the results of tests on specimens with notches in different shapes as well as the averaged values of four specimens: the maximum displacement \bar{u}_c and the critical force \bar{F}_c .

Figure 3 presents the dependence of the constant diameter at the root of the notch ϕ_k . The curves shown in the graphs are the average values of four repetitions conducted for each type of the specimen.

Table 2. Results of fracture tests on notched specimens

No. of spec.	r_k [mm]	ϕ_k [mm]	u_c [mm]				\bar{u}_c [mm]	F_c [kN]				\bar{F}_c [kN]
1	0.3	6	0.246	0.234	0.268	0.248	0.249	19.18	19.31	19.23	18.81	19.13
2		7	0.396	0.384	0.372	0.384	0.384	23.42	23.84	23.54	23.30	23.52
3		8	0.588	0.552	0.566	0.618	0.581	26.00	26.48	27.04	27.08	26.65
4	0.5	6	0.350	0.340	0.342	0.350	0.345	19.89	19.56	20.06	19.82	19.83
5		7	0.424	0.476	0.468	0.456	0.456	23.61	23.71	23.64	23.91	23.72
6		8	0.742	0.750	0.698	0.718	0.726	27.49	27.15	27.47	27.92	27.51
7	1.0	6	0.492	0.466	0.492	0.498	0.483	19.72	19.38	20.00	19.72	19.70
8		7	0.600	0.652	0.632	0.676	0.640	23.61	23.79	23.82	25.17	24.10
9		8	1.006	1.200	1.018	1.058	1.071	28.46	28.94	28.42	28.72	28.63
10	2.0	6	0.676	0.666	0.668	0.658	0.667	18.06	18.08	18.42	18.30	18.22
11		7	0.980	1.084	1.016	1.016	1.024	24.03	24.06	24.29	24.11	24.12
12		8	1.712	1.692	1.552	1.564	1.630	29.55	29.39	29.67	29.26	29.47
13	4.0	6	0.700	0.756	0.714	0.754	0.731	16.29	16.46	15.97	16.37	16.27
14		7	1.144	1.088	1.068	1.112	1.103	22.71	22.27	21.68	22.37	22.26
15		8	2.044	1.980	2.036	1.924	1.996	28.02	29.00	28.58	28.46	28.51
16	8.0	6	1.092	1.142	1.094	1.108	1.109	15.18	15.35	15.37	14.78	15.17
17		7	1.280	1.212	1.220	1.196	1.227	20.33	20.36	20.51	19.30	20.13
18		8	2.032	2.108	2.056	2.048	2.061	27.19	27.46	27.20	27.34	27.30
19	15.0	6	1.572	1.600	1.552	1.572	1.574	14.59	14.39	14.78	14.12	14.47
20		7	1.780	1.705	1.625	1.705	1.705	19.911	19.64	19.30	19.61	19.61
21		8	2.125	2.140	2.155	2.145	2.141	25.90	25.65	26.30	25.94	25.95
22	30.0	6	2.160	2.104	2.076	2.072	2.103	13.64	13.76	13.72	13.67	13.70
23		7	2.295	2.305	2.265	2.295	2.290	19.25	19.28	19.23	19.25	19.25
24		8	2.632	2.605	2.623	2.620	2.620	25.26	25.03	25.04	25.21	25.14

Additionally, the linear strain at the notch root for whole specimens at the fracture initiation moment (Bringdman, 1964) has been calculated.

Table 3. Values of linear strain at the fracture initiation moment

r_k	0.3			0.5			1			2		
d_0	6	7	8	6	7	8	6	7	8	6	7	8
d_f	5.312	6.084	7.042	5.306	6.236	7.139	5.382	6.325	7.199	5.519	6.286	7.131
ε_f	0.244	0.280	0.255	0.246	0.231	0.228	0.217	0.203	0.211	0.167	0.215	0.230
r_k	4			8			15			30		
d_0	6	7	8	6	7	8	6	7	8	6	7	8
d_f	5.657	6.487	7.199	5.604	6.580	7.437	5.598	6.548	7.464	5.566	6.501	7.433
ε_f	0.118	0.152	0.211	0.137	0.124	0.146	0.139	0.133	0.139	0.150	0.148	0.147

The authors paid special attention to the influence of radius r_k and diameter ϕ_k at the root of the notch on the course of F - u graph as well as values of u_c and F_c . The critical displacement u_c increases along with an increase in the radius r_k , and the course of F - u relation becomes less dramatic. In most cases, an increase in the radius r_k resulted in a decrease in the critical force F_c . An increase in the diameter ϕ_k at the root of the notch, with a constant radius r_k , increased the loading which resulted in the appearance of plastic strain in the specimen and also increased the critical force F_c as well as critical displacement of the measurement base u_c .

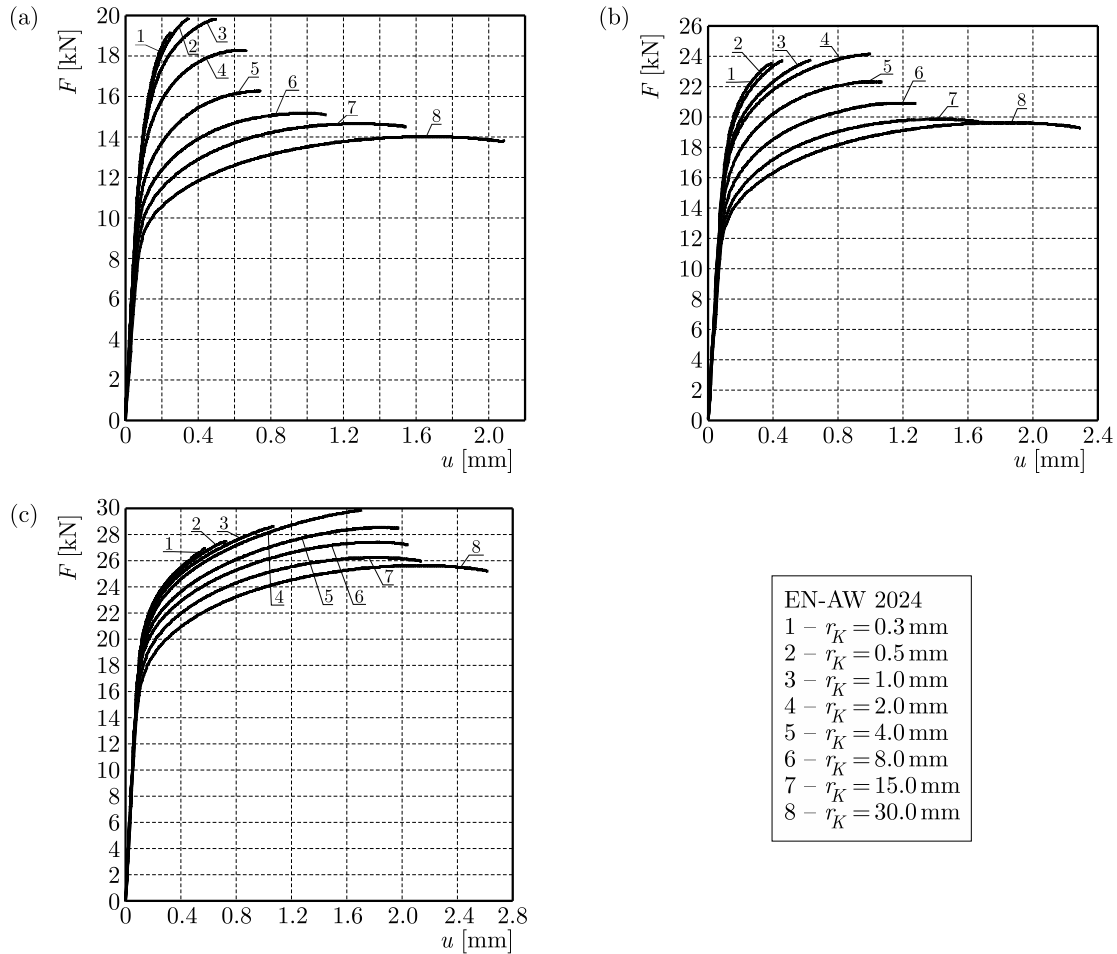


Fig. 3. Comparison of the force-displacement dependence in the notched specimen: (a) $\phi_k = 6$ mm, (b) $\phi_k = 7$ mm, (c) $\phi_k = 8$ mm

3. Numerical research

The stress and strain distribution in the specimens with notches made of aluminum alloy EN-AW 2024 have been defined according to MSC.MARC software (Derpeński and Seweryn, 2013). The calculations allowed for the axial as well as notch symmetry. Four-nodal isoparametric finite elements have been applied. Geometric and material non-linearity has been taken into consideration. For all the samples undertaken, in the plane symmetry of notches, the same division of finished elements has been used.

For all specimens, in the surface of notch symmetry, identical finite elements have been applied. The following boundary conditions are applied in calculations (Fig. 5): the axial symmetry of the geometric model ($u_r = 0$ on the specimen axis), notch symmetry ($u_z = 0$ on the surface of the notch symmetry). The load of the numerical calculation has been realized with the help of the set displacement u_c of the measurement base, which have been calculated for each specimen type directly as a result of the experiment.

In order to describe the dependence between the stress σ_{zz} and the axial strain ε_{zz} in the specimens, an elastic and plastic material model with isotropic hardening has been applied. The Huber-von Mises plasticity yield criterion has been applied. The curve of material hardening has been approximated with a broken line (straight segments). The shape of the hardening curve up to necking has been determined directly from the experiment. The remaining curve range has been defined with a repeated numerical calculations, taking the necking effect into consideration

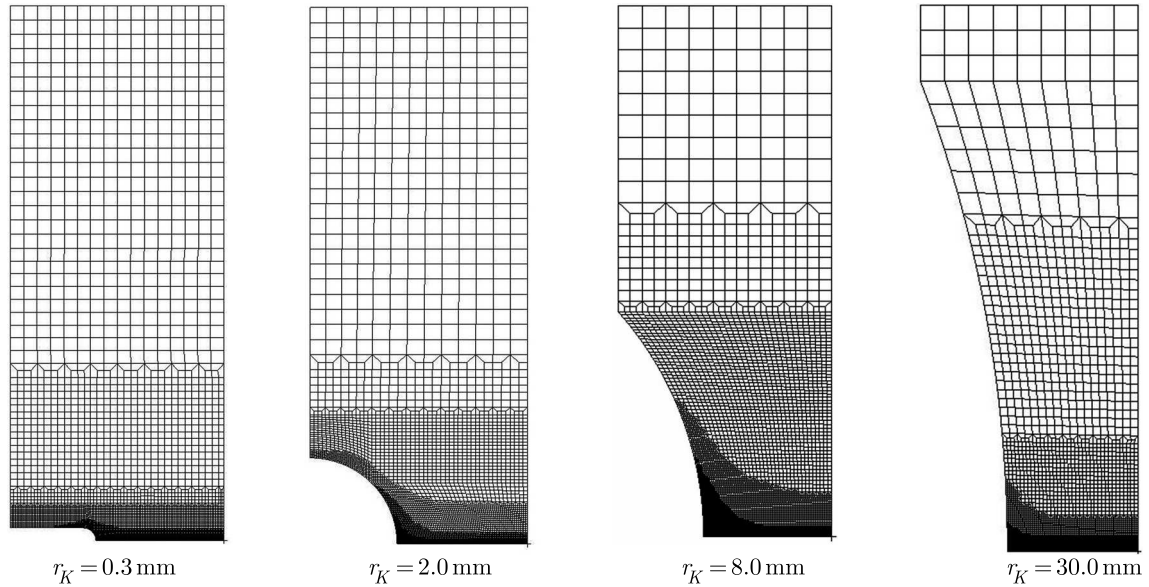


Fig. 4. Finite element mesh for specimens with diameter $\phi_k = 6$ mm

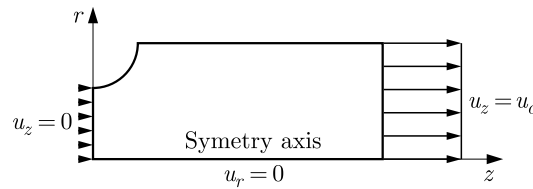


Fig. 5. Boundary conditions and loads used in numerical calculation

up to the moment when the shape of the curve force-displacement ($F-u$) from the numerical calculations was close to the value of the curve force-displacement from experimental research. Figure 6 shows the actual hardening curves $\sigma-\varepsilon$ received in the complete range for aluminum alloys.

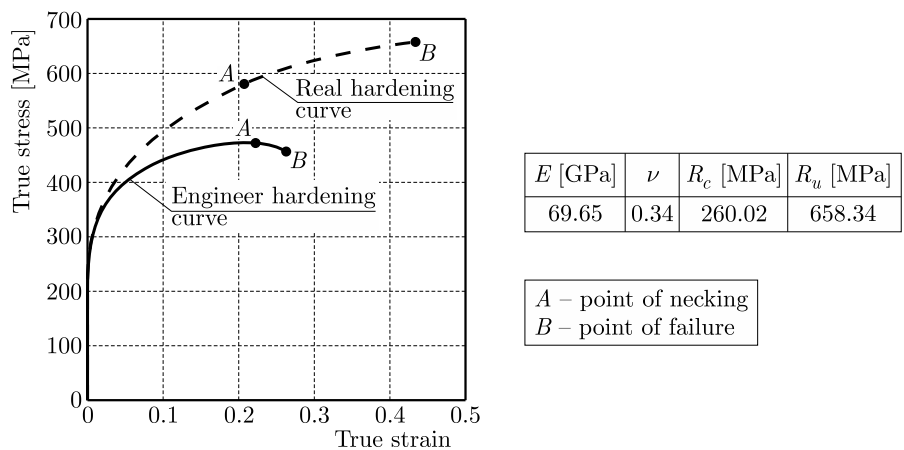


Fig. 6. Stress-strain curve for aluminum alloy EN-AW 2024

Based on numerical results (Derpeński and Seweryn, 2013), it is found that the distribution of σ_1 depends on the size of r_k . For notches with larger radii ($r_k \geq 2$ mm), these values are located on the axis of the specimen. In the case of notches with smaller radii ($r_k < 2$ mm), the maximum value of σ_1 is found near to the notch root.

It should be noted that in the case of specimens with $r_k = 0.3$ and $r_k = 0.5$ mm, the plasticization has not taken place in the entire cross-section of the symmetry plane of the notch. In specimens with $r_k = 1$ and $r_k = 2$ mm, at the moment of fracture initiation, complete plasticization the cross-section in the plane symmetry of the specimen occurred. Although, the difference in values of stresses at the notch root and at the axis are very wide. Almost equal plasticization takes place in the whole cross-section at the remaining specimens with notches ($r_k = 4, 8, 15, 30$ mm). From the experimental research (Derpeński and Seweryn, 2011), it is known that the surface of the fracture depends on the notch radius, and partially or fully cover with the plane of symmetry of the notch. Therefore, the distributions of stress and strain fields are subjected to detailed analysis in the plane of symmetry of the notch where the fracture initiates. Figures 7-9 present selected distributions: stress and plastic strain tensor components, the maximal plastic transverse strain at the critical load. The values of r (distance from the axis of specimen) are normalized by ϕ_k . In Table 4 for EN-AW 2024 aluminum alloy, values of the stress and plastic strain tensor components at the notch root and at the point of the maximum normal stress at the moment of fracture initiation are given.

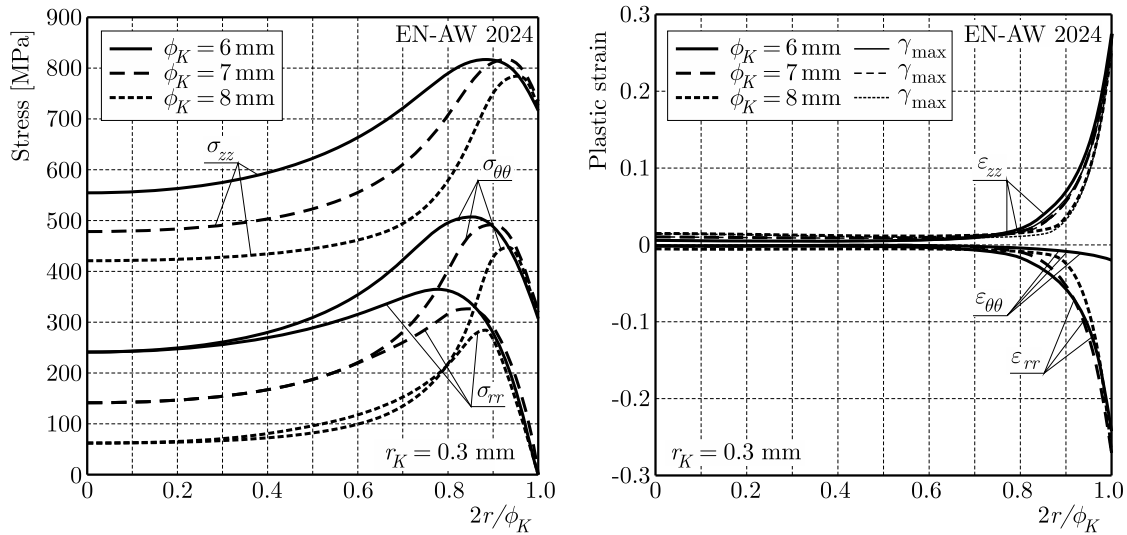


Fig. 7. The distribution of stress and plastic strains in the symmetry plane of the notch at the moment of fracture initiation ($r_k = 0.3$ mm, aluminum alloy EN-AW 2024)

4. Verification of the ductile fracture criterion

In the literature, there are many papers on ductile fracture criteria for elements with notches. Among them, a certain group stands out, e.g., papers by Wierzbicki *et al.* (2005), Venugopal *et al.* (2003), Ozturk and Lee (2004), Han and Kim (2003) developed on the basis of the results of experimental research and numerical calculations and, most often, used in engineering practice. These criteria are described with the help of the scalar function

$$\int_0^{\varepsilon_f} f(\boldsymbol{\sigma}) d\varepsilon_{eq} = C \quad (4.1)$$

where ε_{eq} is the equivalence strain, ε_f – equivalence strain at the moment of fracture initiation, $\boldsymbol{\sigma}$ – stress tensor, C – material constant. The stress function $f(\boldsymbol{\sigma})$ is proposed as various interdependencies between the components of the stress tensor, hydrostatic stress, maximum and equivalence stress. The constant C plays a role similar to the damage state variable in the

Table 4. Stress and plastic strain tensor components in tensile specimens with notches at the moment of fracture initiation (aluminum alloy EN-AW 2024)

r_k [mm]	ϕ_k [mm]	Plastic strain								Stress [MPa]					
		ε_{rr}		$\varepsilon_{\theta\theta}$		ε_{zz}		γ_{max}		σ_{rr}		$\sigma_{\theta\theta}$		σ_{zz}	
0.3	6	-0.232	-0.048	-0.019	-0.008	0.251	0.056	0.242	0.052	1.05	302.96	304.56	500.01	713.70	816.73
	7	-0.267	-0.083	-0.020	-0.011	0.287	0.093	0.277	0.088	1.23	241.35	319.49	477.04	731.62	817.56
	8	-0.243	-0.075	-0.019	-0.012	0.262	0.087	0.252	0.081	1.29	220.31	315.06	445.79	720.85	785.79
0.5	6	-0.234	-0.064	-0.034	-0.016	0.268	0.080	0.251	0.072	0.74	268.24	269.98	438.59	714.84	811.63
	7	-0.220	-0.075	-0.026	-0.015	0.246	0.090	0.233	0.083	0.73	209.95	283.75	412.59	706.51	774.73
	8	-0.217	-0.093	-0.025	-0.017	0.241	0.110	0.229	0.101	0.65	158.57	287.12	379.04	704.24	750.66
1.0	6	-0.207	-0.061	-0.063	-0.034	0.271	0.095	0.239	0.078	0.38	279.20	185.96	362.62	693.01	810.76
	7	-0.193	-0.089	-0.044	-0.029	0.237	0.118	0.215	0.103	0.41	156.37	223.43	316.36	686.92	740.30
	8	-0.201	-0.108	-0.041	-0.037	0.241	0.139	0.221	0.123	0.31	110.82	236.53	296.48	692.51	721.86
2.0	6	-0.159	-0.062	-0.093	-0.062	0.252	0.124	0.206	0.093	1.25	339.74	82.49	339.88	645.60	863.13
	7	-0.205	-0.074	-0.092	-0.057	0.296	0.131	0.250	0.103	1.28	229.82	121.83	272.44	682.28	780.55
	8	-0.219	-0.122	-0.081	-0.061	0.300	0.183	0.259	0.152	1.19	106.17	153.59	215.63	694.81	724.91
4.0	6	-0.112	-0.096	-0.103	-0.096	0.215	0.192	0.163	0.144	0.97	255.75	6.92	255.82	591.30	831.11
	7	-0.145	-0.085	-0.108	-0.085	0.253	0.169	0.199	0.127	0.57	255.53	30.01	255.63	621.95	816.13
	8	-0.201	-0.089	-0.125	-0.886	0.327	0.177	0.264	0.133	0.34	233.01	41.23	233.01	656.60	799.06
8.0	6	-0.130	-0.133	-0.115	-0.133	0.245	0.267	0.187	0.200	0.31	192.84	-30.48	192.84	587.27	806.14
	7	-0.118	-0.120	-0.122	-0.120	0.240	0.241	0.181	0.181	0.48	201.69	-24.64	201.69	588.07	802.43
	8	-0.139	-0.125	-0.155	-0.125	0.294	0.251	0.224	0.188	0.41	216.98	-24.50	216.97	613.47	822.75
15.0	6	-0.132	-0.164	-0.155	-0.164	0.287	0.328	0.221	0.246	0.61	161.42	-53.85	161.42	594.40	797.46
	7	-0.127	-0.155	-0.148	-0.155	0.275	0.310	0.211	0.232	0.36	164.63	-46.63	164.58	592.92	795.86
	8	-0.132	-0.147	-0.145	-0.147	0.277	0.294	0.211	0.221	0.45	170.65	-47.75	170.64	593.20	796.51
30.0	6	-0.143	-0.181	-0.169	-0.181	0.312	0.362	0.241	0.272	0.10	138.06	-73.36	138.19	592.25	783.08
	7	-0.141	-0.178	-0.167	-0.178	0.308	0.357	0.237	0.268	0.20	143.42	-70.21	143.09	592.87	786.91
	8	-0.140	-0.175	-0.164	-0.175	0.304	0.350	0.234	0.263	0.09	147.06	-67.80	147.05	593.10	789.14

white box – at the notch root, grey box – at the point of maximum normal stress

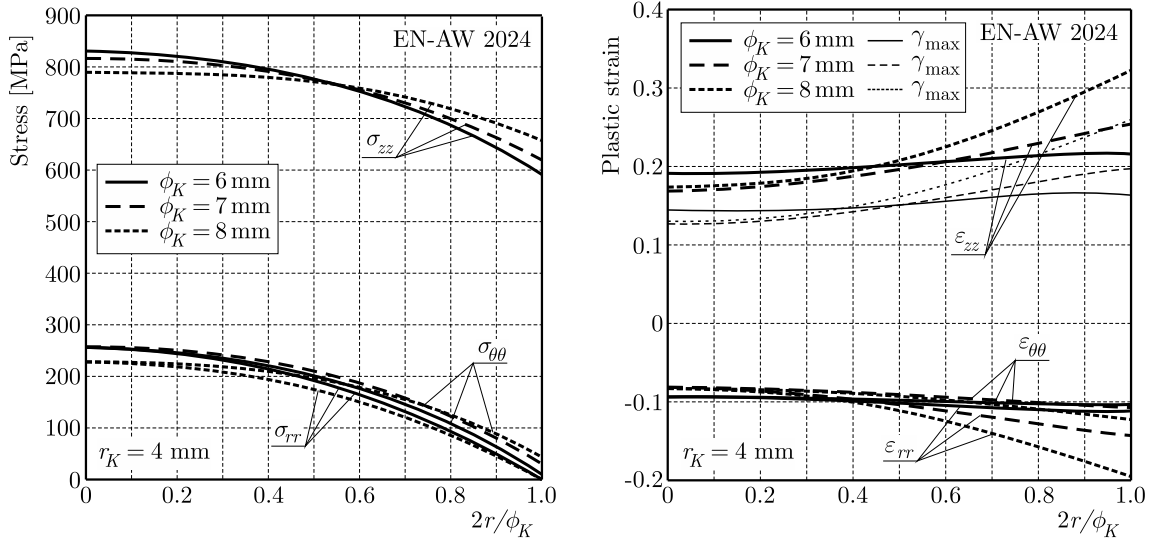


Fig. 8. The distribution of stress and plastic strains in the symmetry plane of the notch at the moment of fracture initiation ($r_k = 4$ mm, aluminum alloy EN-AW 2024)

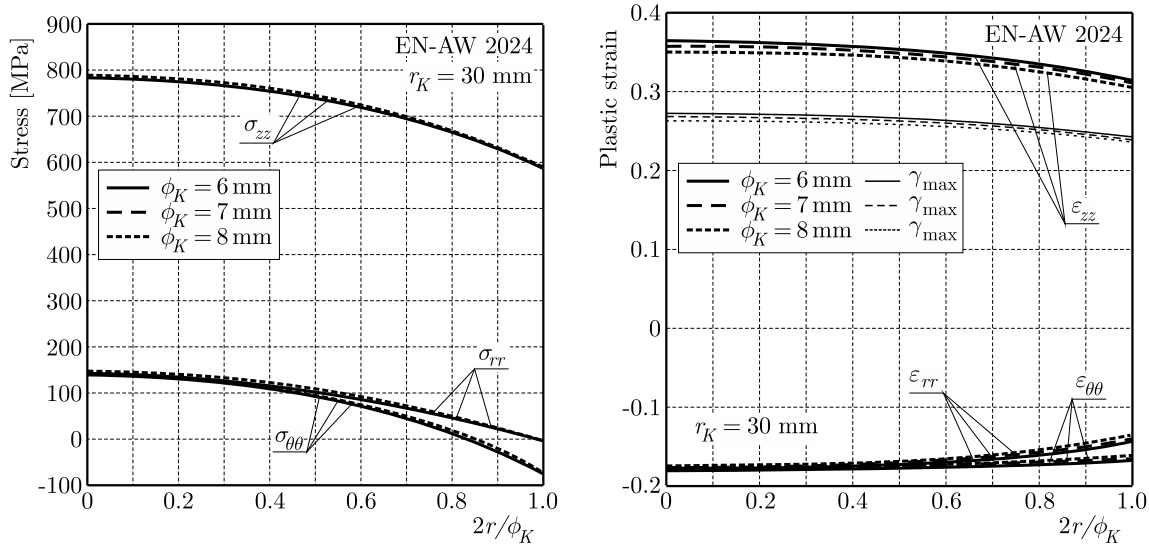


Fig. 9. The distribution of stress and plastic strains in the symmetry plane of the notch at the moment of fracture initiation ($r_k = 30$ mm, aluminum alloy EN-AW 2024)

damage mechanics. Our own results from experimental tests (Derpeński and Seweryn, 2011) and numerical calculations of stress and strain fields (Derpeński and Seweryn, 2013) are used for the verification. The most popular criteria (Derpeński and Seweryn, 2008) do not include the material constant in the integrand function. The verification provides the following ductile fracture criteria:

— Cockroft-Latham (1968)

$$\int_0^{\varepsilon_f} \sigma_{max} d\varepsilon_{eq} = C \quad (4.2)$$

— hydrostatic stress (McClintock, 1968)

$$\int_0^{\varepsilon_f} \frac{\sigma_H}{\sigma_{eq}} d\varepsilon_{eq} = C \quad (4.3)$$

— Oh *et al.* (1979)

$$\int_0^{\varepsilon_f} \frac{\sigma_{max}}{\sigma_{eq}} d\varepsilon_{eq} = C \quad (4.4)$$

— Brozzo *et al.* (1972)

$$\int_0^{\varepsilon_f} \frac{2\sigma_{max}}{3(\sigma_{max} - \sigma_H)} d\varepsilon_{eq} = C \quad (4.5)$$

— Rice-Tracey (1969)

$$\int_0^{\varepsilon_f} \exp\left(\frac{3}{2} \frac{\sigma_H}{\sigma_{eq}}\right) d\varepsilon_{eq} = C \quad (4.6)$$

— Le Roy *et al.* (1981)

$$\int_0^{\varepsilon_f} (\sigma_{max} - \sigma_H) d\varepsilon_{eq} = C \quad (4.7)$$

where σ_{eq} is the equivalence stress (in the Huber-von Mises sense), σ_{max} – maximum normal stress, σ_H – hydrostatic stress, ε_{eq} – equivalence strains (in the Huber-von Mises sense).

Authors' own numerical calculations (Derpeński and Seweryn, 2013) show that at the moment of the critical load, the maximum equivalence strain ε_f and maximum stress σ_{max} , depending on the shape of the notch, appear in two places:

- ε_f – at the axis of the specimen ($r_k = 8, 15, 30$ mm) and at the notch root ($r_k = 0.3, 0.5, 1, 2, 4$ mm),
- σ_{max} – near the notch root ($r_k = 0.3, 0.5, 1$ mm) and at the axis of the specimen ($r_k = 2, 4, 8, 15, 30$ mm).

Therefore, numerical calculations for these six criteria have been performed at the point where the maximum stress values σ_{max} appeared (in the plane of notch symmetry) and at the notch root. The values of function $f(\boldsymbol{\sigma})$ and equivalent strain for increasing displacement of the measurement base Δu have been calculated. Then, on the basis on each criterion, the value of C coefficient has been calculated. As a result, two values of C coefficient for the assumed material, and type of the notch (at the notch root and at the point of maximal normal stress) have been obtained. The calculation results for the aluminum alloy EN AW 2024 are shown graphically in Fig. 10.

For each of the selected criteria (for specimens with different values of the notch radius r_k and the diameter at the notch root ϕ_k), the average value of the critical coefficient C and the relative standard deviation s/\overline{C} for these results have been determined. They are presented in Table 5.

The verification of ductile fracture criteria known from the literature shows large discrepancy between the results of the calculations and experimental data, namely:

- Standard deviation s , in reference to the average critical value of coefficient \overline{C} , ranges from 10% to 17%;
- The maximum error for prediction of the fracture of specimens with notches fluctuates from 18% to 43%;

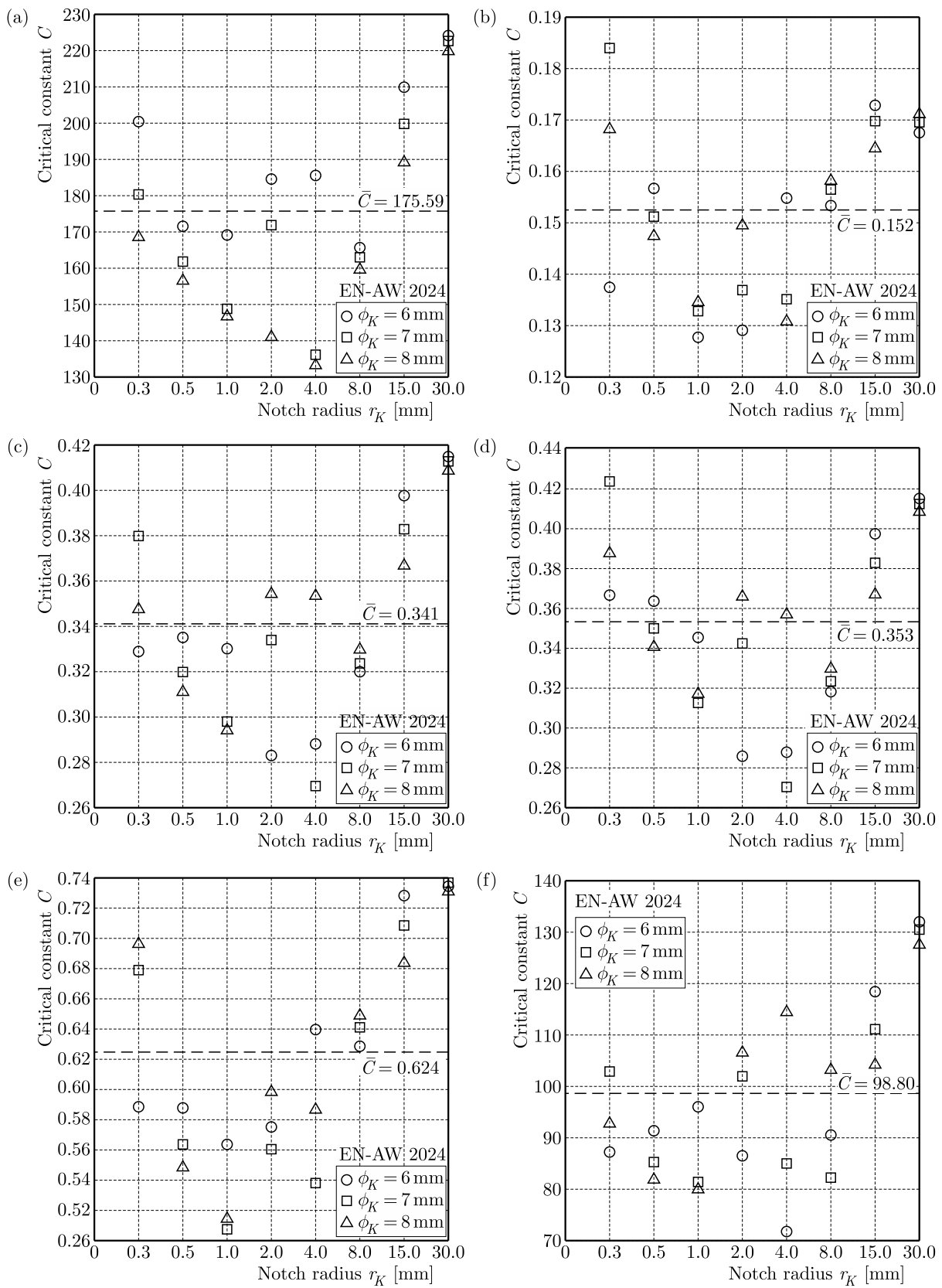


Fig. 10. Results obtained from: Cockcroft-Latham (a), McClintock (b), Oh *et al.* (c), Brozzo *et al.* (d), Rice-Tracey (e), LeRoy *et al.* (f) criterion

Table 5. Critical values of coefficient C

Criterion	EN-AW 2024			
	C	s/C	$1 - (C_{min}/C)$	$(C_{max}/C) - 1$
Cockroft-Latham, Eq. (4.2)	175.59	0.153	0.236	0.276
McClintock, Eq. (4.3)	0.152	0.105	0.434	0.191
Oh <i>et al.</i> , Eq. (4.4)	0.341	0.123	0.211	0.214
Brozzo <i>et al.</i> , Eq. (4.5)	0.353	0.122	0.357	0.184
Rice-Tracey, Eq. (4.6)	0.624	0.119	0.178	0.178
LeRoy <i>et al.</i> , Eq. (4.7)	98.80	0.172	0.182	0.340

C_{min} – minimum value of coefficient C

C_{max} – maximum value of coefficient C

\bar{C} – average value of coefficient C

s – standard deviation

- With the two parameters defining the shape of the notch in the specimen, the notch radius r_k has larger influence on the dispersion of critical values of the coefficient C than the diameter at the notch root ϕ_k .

Therefore, the use of these ductile fracture criteria in practical engineering calculations requires extreme caution and should be limited to special cases documented experimentally.

5. New ductile fracture criteria for specimens with notches

The experimental verification of the selected ductile fracture criteria shows that they are not very precise in predicting fracture of aluminum alloys in which there are stress concentrators in form of notches of different shape. Therefore, the authors' own experimental research results and numerical modelling have been used to develop a new fracture criterion.

In the case when the fracture initiation occurs at the axis of symmetry of the specimen (specimens with notch radii $r_k > 2$ mm), the fracture plane is perpendicular to the direction of loading. In this plane, large normal stress values appear, which determine the fracture. In the proposed fracture criteria for specimens with notches, it is assumed that the fracture initiation appears when normal stress in this physical plane reaches critical values, depending on the isotropic damage state variable ω due to plastic flow of the material, namely

$$\max_{(x_0)} \sigma_{max} = \sigma_c(1 - \omega) \quad (5.1)$$

where σ_c is the critical stress for an undamaged material, \mathbf{x}_0 – position vector which determines location of the fracture initiation.

The isotropic damage state variable ω in the proposed criterion, in the case of monotonic loads, depends on the value of the maximum plastic shear strain γ_{max}^p

$$\omega = \frac{|\gamma_{max}^p|}{\gamma_c^p} \quad (5.2)$$

where γ_c^p is the critical plastic shear strain.

Figure 11 shows a comparison of the critical stress σ_{max} in function of the maximum plastic shear strain $|\gamma_{max}^p|$ obtained on the basis of dependences (5.1) and (5.2) and experimental research. Into consideration are only taken the specimens with notches for which σ_{max} and $|\gamma_{max}^p|$ occur on the axis of symmetry of the specimen. These are the specimens with dimensions:

- $r_k = 2$ mm; $\phi_k = 6$ mm

- $r_k = 4, 8, 15, 30$ mm; $\phi_k = 6, 7, 8$ mm
- without notch (smooth).

In the case of the examined aluminum alloy, the following critical values have been determined: $\sigma_c = 876.5$ MPa, $\gamma_c^p = 2.42$.

In figures below, the following indicators of points obtained from the experimental research and numerical analysis are used: the first number shows r_k , and the second (after the dash) shows ϕ_k . In the figures, the places of points outermost from the line defining the proposed ductile fracture criterion are marked by the dashed line.

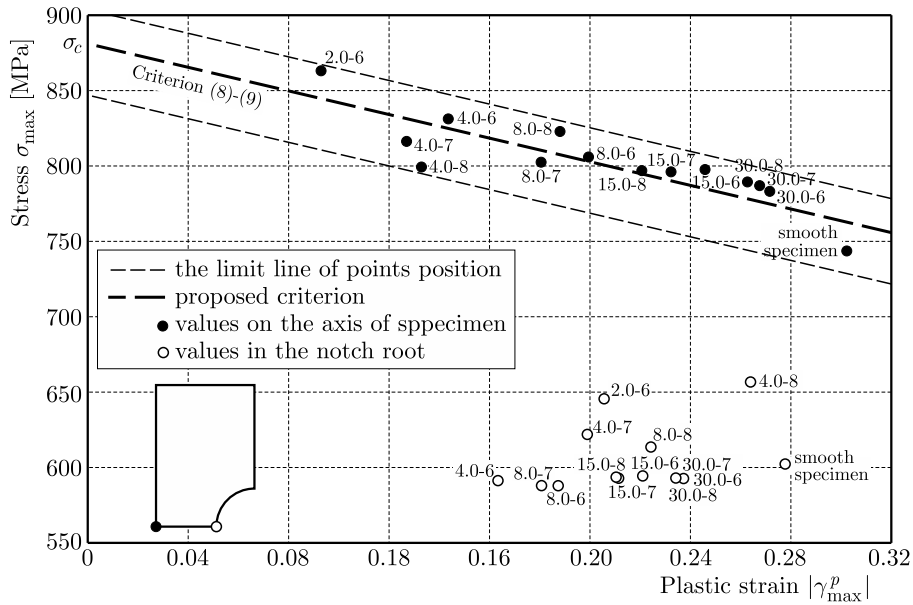


Fig. 11. Dependence of the critical normal stress on the maximum plastic shear strain. Fracture at the axis of the specimen

Another situation is faced in the case of specimens with small radii of notches. It is important to investigate two potential places for fracture initiation:

- the notch root, where the maximum plastic transverse strain appears,
- the point at a certain distance from the notch root, where there is maximum normal stress value.

In both cases, the fracture plane is perpendicular in the direction of the load and is covered by the plane of symmetry of the notch. Figure 12 shows the normal stress σ_{max} and the maximal plastic shear strains γ_{max}^p in both the above-mentioned points for the specimens with small notch radii. It is important to note that all values lie significantly below the line marking fracture condition (5.1) and (5.2) (Fig. 11). It can therefore be concluded that the state of damage inside the material is different than in a thin layer near the free surface. It is assumed that the machining process, which has been used for blanking the notches, has made the initial damage to the material. In the course, for example, of machining in the vicinity of the tool tip, a plastic zone through which the fracture surface passes (separation surface of a material) occurs. In this zone, large plastic strains appear, similar to those in the plastic zone ahead the crack tip. The part of this zone remains during the machining, hence also, in some thin layer in the vicinity of the free surface the plastic strain remains, and so the associated to them preliminary damage of the material. This is also why, in the case of the free surface, it is necessary to modify formula (5.2) in the following way

$$\omega = \frac{|\gamma_{max}^p|}{\gamma_c^p} + \omega_0 \quad (5.3)$$

where ω_0 is the preliminary damage of the material on the free surface resulting from the manufacturing process.

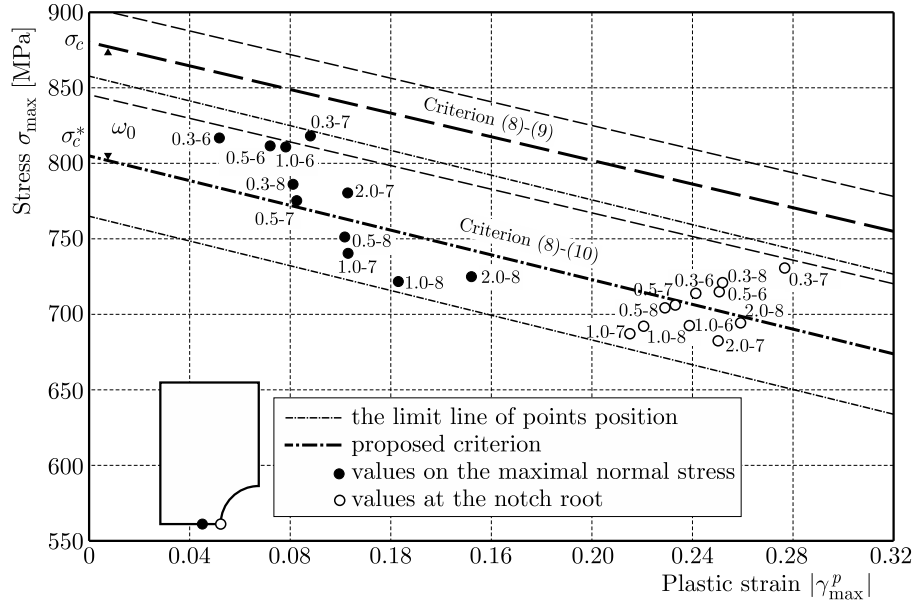


Fig. 12. Dependence of the critical normal stress on the maximum plastic shear strain (fracture in the vicinity of the notch root)

Taking into consideration the material damage ω_0 on the surface of the notch, one can predict the fracture of the specimens with notches with a small radius ($r_k \leq 2$ mm). It is necessary to take into account much larger values for plastic strains (as well as the maximum plastic shear strains γ_{max}^p) for those specimens at the notch root. It can be therefore assumed that the fracture initiation in the specimens with small radii of the notch r_k appears at the notch root. Figure 12 shows that the points obtained from the experimental research and numerical analysis for the values of stress and strain at the notch root are close to fracture condition (5.1) and (5.2). For these points, the value of the preliminary material damage $\omega_0 = 0.087$ has been obtained.

The fracture condition on the surface of the notch is fulfilled for all specimens with notches, in which the maximum normal stress and plastic shear strain (at the moment of fracture initiation) are not located on the axis of symmetry. The same situation we have in the case of notches with the following parameters: $r_k = 0.3$ mm; $\phi_k = 6, 7, 8$ mm; $r_k = 0.5$ mm; $\phi_k = 6, 7, 8$ mm; $r_k = 1$ mm; $\phi_k = 6, 7, 8$ mm; $r_k = 2$ mm; $\phi_k = 7, 8$ mm.

6. Conclusion

On the basis of the earlier experimental research conducted on specimens with notches made of aluminum alloys EN-AW 2024, it follows that the normal stress vector component on the critical plane determines the fracture. This plane, in the case of tensile specimens with notches, is perpendicular to the load direction. It is assumed that the value of the critical normal stress depends on the maximal plastic shear strains, assuming that the accumulated damage (and material weakening) occurs faster on the free surface than on the inside of the material. Through the assumptions made, the formula of the proposed fracture criterion is characterized by a simple relationship. It is also important to note that a better correlation of the results of calculations on the basis of the proposed criterion with the experimental research has been obtained than in the case of the verification criteria found in the literature. The mean error for

fracture prediction of the specimens with notches has been found 1.6%, whereas the maximum error of the modeling 4.6%

Acknowledgement

This work has been financially supported by National Science Centre (Poland) under the project DEC-2011/03/B/ST8/06456.

References

1. BANDSTA J.P., KOSS D.A., 2004, A simulation of growth and coalescence of void during ductile fracture, *Materials Science and Engineering*, **387**, 399-403
2. BAO Y., 2001, *Comparative Study on Various Fracture Criteria. Part II: Finite Element Analysis*, Cambridge, MIT.P.40
3. BAO Y., 2005, Dependence of ductile crack formation in tensile tests on stress triaxiality, stress and strain ratios, *Engineering Fracture Mechanics*, **72**, 505-522
4. BRINGDMAN P.W., 1964, *Studies in Large Plastic Flow and Fracture with Special Emphasis on the Effects of Hydrostatic Pressure*, Harvard University Press, Cambridge
5. BROZZO P., DE LUCA B., RENDINA R., 1972, A new method for the prediction of formability in metal sheets, *Proceedings of the Seventh Biennial Conference on Sheet Metal Forming and Formability – International Deep Drawing Research Group*, 44
6. CHENA J., ZHOUB X., CHEN J., 2015, Sheet metal forming limit prediction based on plastic deformation energy, *Journal of Materials Processing Technology*, 315-322
7. COCKROFT M.G., LATHAM M.G., 1968, Ductility and the workability of metals, *Journal of the Institute of Metals*, **98**, 33-41
8. DERPEŃSKI Ł., SEWERYN A., 2008, Verification of selected fracture criteria of elements with notches (in Polish), *XXII Symposium Fatigue and Fracture Mechanic*
9. DERPEŃSKI Ł., SEWERYN A., 2011, Experimental research into fracture of EN-AW 2024 and EN-AW 2007 aluminum alloy specimens with notches subjected to tension, *Experimental Mechanics*, **51**, 1075-1094
10. DERPEŃSKI Ł., SEWERYN A., 2013, Numerical, Analysis of the Strain and Stress State in Cylindrical Notched Tensile Specimens, *Materials Science*, 49, 252-256
11. HAN H.N., KIM K.H., 2003, A ductile fracture criterion in sheet metal forming process, *Journal of Materials Processing Technology*, **142**, 231-238
12. KOMORI K., 2005, Ductile fracture criteria for simulating shear by node separation method, *Theoretical and Applied Fracture Mechanics*, **43**, 101-114
13. LE ROY G., EMBURY J. D., EDWARD G., ASHBY M.F., 1981, A model of ductile fracture based on the nucleation and growth of voids, *Acta Metallurgica*, **29**, 1509-1522
14. MA H., XU W., JIN B.C., SHAN D., NUTT S.R., 2015, Damage evaluation in tube spinnability test with ductile fracture criteria, *International Journal of Mechanical Sciences*, **100**, 99-111
15. MCCLINTOCK F.A., 1968, A criterion for ductile fracture by the growth of holes, *Journal of Applied Mechanics*, **35**, 353-371
16. ÖCHSNER A., GEGNER J., WINTER W., KUH H. G., 2001, Experimental and numerical investigations of ductile damage in aluminum alloy, *Materials Science and Engineering*, **A318**, 328-333
17. OH S.I., CHEN C.C., KOBAYASHI S., 1979, Ductile fracture in axisymmetric extrusion and drawing, *Journal of Engineering for Industry, Transactions of the ASME*, **101**
18. OZTURK F., LEE D., 2004, Analysis of forming limits using ductile fracture criteria, *Journal of Materials Processing Technology*, **147**, 397-404

19. RICE J.R., TRACEY D.M., 1969, On the ductile enlargement of voids in triaxial stress fields, *Journal of the Mechanics and Physics of Solids*, **17**, 201-217
20. THOMASON P.F., 1990, *Ductile Fracture of Metals*, NY, Pergamon Press
21. VENUGOPAL R., RAMAKRISHNAN N., KRISHNA KUMAR R., 2003, A comparative evaluation of the theoretical failure criteria for workability in cold forging, *Journal of Materials Processing Technology*, **142**, 29-42
22. YANSHAN L., HOON H., 2013, Evaluation of ductile fracture criteria in a general three-dimensional stress state considering the stress triaxiality and the Lode parameter, *Acta Mechanica Sinica*, **26**, 6
23. YANSHAN L., HOON H., SUNGJUN L., KEUNHWAN P., 2012, New ductile fracture criterion for prediction of fracture forming limit diagrams of sheet metals, *International Journal of Solids and Structures*, **49**, 3605-3615
24. WIERZBICKI T., BAO Y., LEE Y.W., BAI Y., 2005, Calibration and evaluation of fracture models, *International Journal of Mechanical Sciences at Science*, **47**, 719-743

Manuscript received July 17, 2015; accepted for print December 29, 2015

NONLINEAR VIBRATIONS OF PERIODIC BEAMS

ŁUKASZ DOMAGALSKI, JAROSŁAW JĘDRYSIAK

Lodz University of Technology, Department of Structural Mechanics, Łódź, Poland

e-mail: lukasz.domagalski@p.lodz.pl; jarek@p.lodz.pl

Geometrically nonlinear vibrations of beams with properties periodically varying along the axis are investigated. The tolerance method of averaging differential operators with highly oscillating coefficients is applied to obtain governing equations with constant coefficients. The proposed model describes dynamics of the beam with the effect of microstructure size. In an example, an analysis of undamped forced nonlinear vibrations of the periodic beam is shown. Moreover, the results obtained for undamped free vibrations of periodic beams by the tolerance model are justified by those results from the finite element method. These results can be used as a benchmark in similar problems.

Keywords: nonlinear vibrations, periodic beams, tolerance modelling

1. Introduction

The paper concerns with geometrically nonlinear vibrations of beams with geometric and material properties periodically varying along the x -axis. Moreover, such beams can interact with a periodically inhomogeneous viscoelastic subsoil. A fragment of such a beam is shown in Fig. 1.

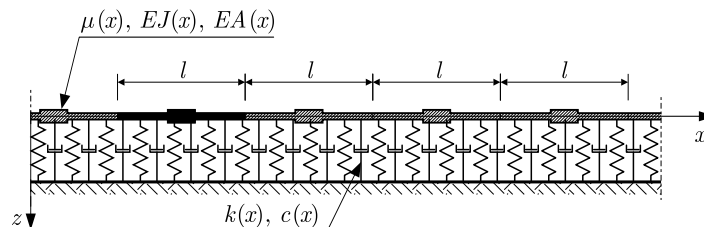


Fig. 1. A fragment of a periodic beam

Equations of motion of such structures have usually highly oscillating, periodic, non-continuous functional coefficients. For this reason, emphasis is placed on the formulation of continuous models of the considered structures. In the proposed method of modelling, this is performed by substituting the original equations with an effective model with constant coefficients. This makes it possible to avoid full discretization of the problem.

Structures with physical properties regularly arranged in the body domain are commonly found in nature and are widely used in engineering. The continuous interest in such objects is due to their specific properties. Properly designed composite structures are characterized by, among others, favourable ratio of stiffness to weight. This, due to the trends in modern technology for the design of lightweight, high-strength structures, indicates actuality of the problem. In particular, periodic structures exhibit some interesting and desirable dynamic properties, namely, they may serve as filters for some specific vibration frequency bands, cf. Banakh and Kempner (2010). Analysis of the so-called locally resonant beams were published in numerous papers, e.g. by Olhoff *et al.* (2012), where the optimization of beam geometry in order to obtain the maximum width of the frequency band-gap leads to a periodic structure.

Direct numerical modelling of structures of this kind, such as finite element discretization, is one of the possible ways of analysis the considered problems. The computational cost of the parametric analysis within the discretization approach is, however, proportional to the variation range of the parameters under consideration. Thus, it is advisable to strive to formulate alternative continuous models in order to reduce the computational cost.

Among the analytical methods applied in stationary problems of periodic structures, the most widespread are those based on the rigorous mathematical theory of asymptotic homogenization of differential operators. In this approach, the actual periodic structure is modelled as a homogeneous anisotropic structure with some effective properties. The above-mentioned effective properties are obtained through analysis of the so-called periodicity cell problem. The fundamentals of this theory are described by Bensoussan *et al.* (1978), Sanchez-Palencia (1980), Bakhvalov and Panasenko (1984), Jikov *et al.* (1994), Lewiński and Telega (2000), Krysko *et al.* (2008). Some various works are devoted to derivation of micro-periodic beam equilibrium equations in the frame of homogenization theory, wherein the starting point of analysis are three-dimensional elasticity theory equations, see Kolpakov (1991, 1995, 1998, 1999), Syerko *et al.* (2013). Certain analytical approaches and the finite element method are also used to evaluate strength and buckling of sandwich beams having corrugated cores, e.g. by Magnucki *et al.* (2013).

The literature on the problems of linear vibrations of periodic beams is extensive. In most of the research papers, attention is focused on local resonance properties of such structures. The two-scale asymptotic expansions are applied by He *et al.* (2013) in analysis of beams with periodically variable stiffness. A common approach making use of the theory of Floquet-Bloch waves in the analysis. This was applied in the analysis of the Timoshenko (Chen and Wang, 2013) and Euler-Bernoulli (Chen, 2013) beam vibrations. The problem of wave propagation in a periodic elastically supported beam was considered by Yu *et al.* (2012) using the transfer matrix method. The direct approach with use of the Heaviside step function in the case of the forced oscillation of the plate band on a periodic elastic substrate was applied by Sylvia and Hull (2013), where the investigations were brought to a one-dimensional problem.

Description of dynamic problems within geometrically linear theories imposes severe restrictions on deformations, limiting the displacements order to the smallest dimension of the structural element considered. Since the considered structures are slender at the macro level, this limitation makes it impossible to correctly analyze the whole spectrum of their applicability. In addition, some physical phenomena that occur in vibrations of nonlinear systems which have a significant impact on motion characteristics are impossible to investigate in terms of linearized theories. Nonlinear vibrations of homogeneous nano-beams cooperating with a homogeneous visco-elastic substrate were considered by Wang and Li (2014), vibrations of the sandwich beams by Krysko *et al.* (2008). The paper by Awrejcewicz *et al.* (2011) contains comparison of nonlinear vibration models of the Euler-Bernoulli beam derived through FEM discretization and the finite differences method. Despite the large number of studies dealing with non-linear vibrations (e.g. Sedighi *et al.*, 2013; Hryniewicz and Koziół, 2013), the majority of publications relates to systems with a relatively small number of degrees of freedom.

In this contribution, in order to replace differential equations with highly oscillating coefficients by equations with constant coefficients, the tolerance modelling, see Woźniak and Wierzbicki (2000), Woźniak *et al.* (2008, 2010) is applied. This approach was introduced for the purpose of analysis of various thermomechanical problems of periodic elastic composites in a series of papers, e.g. for thin periodic plates on a foundation by Jędrzyiak (1999), for micro-periodic beams under moving load by Mazur-Śniady and Śniady (2001), for periodic beams for plates with the microstructure size of an order of the plate thickness – for periodic thin by Mazur-Śniady *et al.* (2004), for periodic medium-thickness by Baron (2006), for thin functionally graded by Jędrzyiak (2013), for multiperiodic fibre reinforced composites by Jędrzyiak and

Woźniak (2006), for periodic shells by Tomczyk (2007), for functionally graded plates by Wierowski (2012). This technique was also used in vibration analysis of periodic beams within the linear theory by Mazur-Śniady (1993), where the equations of motion and their generalization by including the influence of the axial force, elastic subsoil and viscous damping were derived. The books by Woźniak and Wierzbicki (2000), Woźniak *et al.* (2008, 2010) contain the fundamentals of this theory and numerous examples of application.

The main aim of this note is to derive averaged governing equations of the nonlinear tolerance model of dynamics of periodic beams on a viscoelastic foundation and show a certain application of this model to a special problem. Moreover, some justifications of the results by the proposed model are presented by the results obtained from the finite element method for a benchmark problem of free vibrations of a linear periodic beam.

2. Formulation of the problem

The object under consideration is a linearly elastic prismatic beam, bilaterally interacting with a periodic viscoelastic foundation. Let $Oxyz$ be an orthogonal Cartesian coordinate system in which the Ox axis coincides with the axis of the beam, the cross section of the beam is symmetric with respect to the plane of the load Oxz , the load acts in the direction of the axis Oz . The problem can be treated as one-dimensional, so that we define the region occupied by the beam as $\Omega \equiv [0, L]$, where L stands for the beam length.

The beam is assumed to be made of many repetitive small elements, called periodicity cells, defined as $\Delta \equiv [-l/2, l/2]$, where $l \ll L$ is length of the cell and named the microstructure parameter.

Our considerations are based on the Rayleigh theory of beams with von Kármán type non-linearity. Since we are interested in the transverse vibrations only, the effect of axial inertia is neglected in further considerations. Let $\partial^k = \partial^k / \partial x^k$ be the k -th derivative of a function with respect to the x coordinate, overdot stands for the derivative with respect to time. Let $w = w(x, t)$ be the transverse deflection, $u_0 = u_0(x, t)$ longitudinal displacement, $EA = E(x)A(x)$ and $E(x)J = EJ(x)$ tensile and flexural stiffness, $k = k(x)$ and $c = c(x)$ – elasticity and damping coefficients of the foundation, $\mu = \mu(x)$ and $\vartheta = \vartheta(x)$ mass and rotational moment of inertia per unit length and $q = q(x, t)$ – transverse load. The strain and kinetic energy density per unit length of the beam are

$$\mathcal{W} = \frac{1}{2}EA\left(\partial u_0 + \frac{1}{2}\partial w\partial w\right)^2 + \frac{1}{2}EJ(\partial^2 w)^2 \quad \mathcal{K} = \frac{1}{2}\mu\dot{w}\dot{w} + \frac{1}{2}\vartheta\partial\dot{w}\partial\dot{w} \quad (2.1)$$

For the subsoil, we apply the Kelvin-Voight model, so that the dissipative force is assumed in the form

$$p = p(x, t) = c(x)\dot{w}(x, t) \quad (2.2)$$

The equations of motion can be obtain from the extended (Woźniak *et al.*, 2010) principle of stationary action $\mathcal{A} = \mathcal{A}(u_0, w)$ formulated as

$$\begin{aligned} \delta\mathcal{A} = \delta \int_0^1 \int_0^L \mathcal{L} \, dx \, dt = \int_0^1 \int_0^L \delta\mathcal{L} \, dx \, dt = \int_0^1 \int_0^L & \left[\left(\frac{\partial\mathcal{L}}{\partial u_0} - \partial \frac{\partial\mathcal{L}}{\partial(\partial u_0)} \right) \delta u_0 \right. \\ & \left. + \left(\frac{\partial\mathcal{L}}{\partial w} - \partial \frac{\partial\mathcal{L}}{\partial(\partial w)} + \partial^2 \frac{\partial\mathcal{L}}{\partial(\partial^2 w)} - \frac{d}{dt} \frac{\partial\mathcal{L}}{\partial\dot{w}} + \frac{d}{dt} \partial \frac{\partial\mathcal{L}}{\partial(\partial\dot{w})} \right) \delta w \right] \, dx \, dt = 0 \end{aligned} \quad (2.3)$$

where the Lagrangian is

$$\begin{aligned} \mathcal{L}(x, t, w, \dot{w}, \partial w, \partial^2 w, \partial u_0) &= \mathcal{W} - \mathcal{K} + pw + \frac{1}{2}kww - qw \\ &= \frac{1}{2}EA\left(\partial u_0 + \frac{1}{2}\partial w\partial w\right)^2 + \frac{1}{2}\partial^2 w EJ\partial^2 w - \frac{1}{2}\mu\dot{w}\dot{w} - \frac{1}{2}\vartheta\partial\dot{w}\partial\dot{w} + pw + \frac{1}{2}kww - qw \end{aligned} \quad (2.4)$$

The system of nonlinear coupled differential equations for the longitudinal displacements u_0 and the transverse deflection w resulting from (2.3) can be written as

$$\begin{aligned} \partial\left[EA\left(\partial u_0 + \frac{1}{2}\partial w\partial w\right)\right] &= 0 \\ \mu\ddot{w} - \partial(\vartheta\partial\dot{w}) + c\dot{w} + kw + \partial^2(EJ\partial^2 w) - \partial\left[EA\left(\partial u_0 + \frac{1}{2}\partial w\partial w\right)\partial w\right] &= q \end{aligned} \quad (2.5)$$

The coefficients EA , EJ , k , μ , ϑ , c are highly oscillating, often non-continuous functions of the x -coordinate. The main aim of this note is to derive an approximately equivalent model, which describes geometrically nonlinear vibrations of periodic beams bilaterally interacting with a periodic viscoelastic foundation, taking into account the effect of microstructure size.

3. Introductory concepts and basic assumptions of the tolerance modelling

The averaged equations of periodic beams with large deflections are derived using the concepts and assumptions of the tolerance modelling technique, see Woźniak *et al.* (2010). The fundamental concepts are: the tolerance system, averaging operation and certain classes of functions such as the tolerance-periodic (TP), slowly-varying (SV), highly oscillating (HO) and fluctuation shape (FS) functions. The tolerance parameter, associated with the tolerance relation, is denoted by d , $0 < d \ll 1$. The highest order of function derivative that can be included into a certain function class is denoted by α .

Let $\Delta(x) = x + \Delta$, $\Omega_\Delta = \{x \in \Omega : \Delta(x) \subset \Omega\}$ be a cell with its center at $x \in \Omega_\Delta$. The averaging operator for an arbitrary integrable function f is defined by

$$\langle f \rangle(x) = l^{-1} \int_{\Delta(x)} f(y) dy \quad x \in \Omega_\Delta \quad y \in \Delta(x) \quad (3.1)$$

It can be shown (Woźniak *et al.*, 2010) that for a periodic function f of x , its average is constant.

The first of the basic assumptions is the micro-macro decomposition of the unknown transverse deflection and longitudinal displacement

$$\begin{aligned} w(x, t) &= W(x, t) + h^A(x)V^A(x, t) \\ A = 1, \dots, N \quad W(\cdot, t), V^A(\cdot, t) &\in SV_d^2(\Omega, \Delta) \quad h^A(\cdot) \in FS_d^2(\Omega, \Delta) \end{aligned} \quad (3.2)$$

and

$$\begin{aligned} u_0(x, t) &= U(x, t) + g^K(x)T^K(x, t) \\ K = 1, \dots, M \quad U(\cdot, t), T^K(\cdot, t) &\in SV_d^1(\Omega, \Delta) \quad g^K(\cdot) \in FS_d^1(\Omega, \Delta) \end{aligned} \quad (3.3)$$

Here and hereafter, the summation convention holds.

The new basic kinematic unknowns $W(\cdot)$ and $U(\cdot)$ are called the transverse and the axial macrodisplacements, respectively; $V^A(\cdot)$ and $T^K(\cdot)$ are additional kinematic unknowns, called the fluctuation amplitudes. The unknown functions are assumed to be slowly-varying. The highly oscillating fluctuation shape functions h^A and g^K are postulated *a priori* in every problem

under consideration and are assumed to describe unknown fields oscillations caused by structure inhomogeneity. These functions have to satisfy the following conditions

$$\begin{aligned} \langle \mu h^A \rangle &= 0 & \langle \mu g^K \rangle &= 0 \langle \mu h^A h^B \rangle = 0 \quad \text{for } A \neq B \\ \langle \mu g^K g^L \rangle &= 0 \quad \text{for } K \neq L & \partial^m h^A &\in O(l^{2-m}) \\ \partial^n g^K &\in O(l^{1-m}) & A, B &= 1, \dots, N & K, L &= 1, \dots, M \end{aligned} \tag{3.4}$$

The second assumption is the tolerance averaging approximation

$$\begin{aligned} \langle f \rangle(x) &= \langle f_x \rangle(x) + O(d) & \langle f \partial^\alpha (\phi^A \Psi) \rangle(x) &= \langle f \partial^\alpha \phi^A \rangle(x) \Psi(x) + O(d) \\ \langle f \Psi \rangle(x) &= \langle f \rangle(x) \Psi(x) + O(d) & \langle f \partial(\gamma^K \Xi) \rangle(x) &= \langle f \partial \gamma^K \rangle(x) \Xi(x) + O(d) \\ \langle f \Xi \rangle(x) &= \langle f \rangle(x) \Xi(x) + O(d) & f &\in TP_d^\alpha(\Omega, \Delta) & \Psi &\in SV_d^2(\Omega, \Delta) \\ \phi^A &\in FS_d^2(\Omega, \Delta) & \Xi &\in SV_d^1(\Omega, \Delta) & \gamma^K &\in FS_d^1(\Omega, \Delta) \\ x \in \Omega & & \alpha &= 1, 2 & A &= 1, \dots, N & K &= 1, \dots, M & 0 < d \ll 1 \end{aligned} \tag{3.5}$$

in which the terms of the order of the tolerance parameter $O(d)$ are assumed to be negligibly small.

4. The governing equations of the proposed models

4.1. The equations of the tolerance model

After substitution of micro-macro decompositions (3.2) and (3.3) into Lagrangian (2.4), the next step of modelling is averaging (3.1) over an arbitrary periodicity cell with approximations (3.5).

The averaged action functional has the following form

$$\delta \mathcal{A}_h = \delta \int_0^1 \int_0^L \langle \mathcal{L}_h \rangle dx dt = \int_0^1 \int_0^L \delta \langle \mathcal{L}_h \rangle dx dt = 0 \tag{4.1}$$

where the averaged Lagrangian is formulated as follows

$$\begin{aligned} \langle \mathcal{L}_h \rangle &= \frac{1}{2} D \partial^2 W \partial^2 W + D^A \partial^2 W V^A + (P - Q)W + \frac{1}{2} K W W + \frac{1}{2} B (\partial U + \frac{1}{2} \partial W \partial W)^2 \\ &+ l^2 (P^A - Q^A + K^A W + \frac{1}{2} l^2 K^{AB} V^B) V^A - \frac{1}{2} M \dot{W} \dot{W} - \frac{1}{2} J \partial \dot{W} \partial \dot{W} \\ &- (l^2 M^A \dot{W} + l J^A \partial \dot{W}) \dot{V}^A + [B^K (\partial U + \frac{1}{2} \partial W \partial W) + \frac{1}{2} B^{KL} T^L] T^K \\ &- \frac{1}{2} l^2 (l^2 M^{AB} + J^{AB}) \dot{V}^B \dot{V}^A + l [B^A (\partial U + \frac{1}{2} \partial W \partial W) + B^{AK} T^K] V^A \partial W \\ &+ \frac{1}{2} l^2 [B^{AB} (\partial U + \frac{3}{2} \partial W \partial W) + B^{ABK} T^K] V^B V^A \\ &+ \frac{1}{2} l^3 (B^{ABC} \partial W + \frac{1}{4} l B^{ABCD} V^D) V^A V^B V^C + \frac{1}{2} D^{AB} V^A V^B \end{aligned} \tag{4.2}$$

Under essential boundary conditions it leads to a system of Euler-Lagrange equations

$$\begin{aligned} \frac{\partial \langle \mathcal{L}_h \rangle}{\partial U} - \partial \frac{\partial \langle \mathcal{L}_h \rangle}{\partial (\partial U)} &= 0 \\ \frac{\partial \langle \mathcal{L}_h \rangle}{\partial W} - \partial \frac{\partial \langle \mathcal{L}_h \rangle}{\partial (\partial W)} + \partial^2 \frac{\partial \langle \mathcal{L}_h \rangle}{\partial (\partial^2 W)} - \frac{d}{dt} \frac{\partial \langle \mathcal{L}_h \rangle}{\partial (\dot{W})} + \frac{d}{dt} \left(\partial \frac{\partial \langle \mathcal{L}_h \rangle}{\partial (\partial \dot{W})} \right) &= 0 \\ \frac{\partial \langle \mathcal{L}_h \rangle}{\partial T^K} = 0 & \quad \frac{\partial \langle \mathcal{L}_h \rangle}{\partial V^A} - \frac{d}{dt} \frac{\partial \langle \mathcal{L}_h \rangle}{\partial (\dot{V}^A)} = 0 \end{aligned} \tag{4.3}$$

After some manipulations, we arrive at the following system of equations

$$\begin{aligned}
& \partial(B\partial U + B^K T^K) + \partial\left(\frac{1}{2}B\partial W\partial W + lB^A V^A \partial W + \frac{1}{2}l^2 B^{AB} V^B V^A\right) = 0 \\
& D\partial^4 W + D^A \partial^2 V^A + KW + l^2 K^A V^A + C\dot{W} + M\ddot{W} - J\partial^2 \ddot{W} \\
& \quad + l^2 C^A \dot{W}^A + l^2 M^A \ddot{V}^A - lJ^A \partial \ddot{V}^A - Q \\
& \quad - \partial\left[\left(B\left(\partial U + \frac{1}{2}\partial W\partial W\right) + B^K T^K + lB^A V^A \partial W + \frac{1}{2}l^2 B^{AB} V^B V^A\right)\partial W\right] \\
& \quad - \partial\left[lB^{AK} V^A T^K + \left(\partial U + \frac{1}{2}\partial W\partial W\right)lB^A V^A + l^2 B^{AB} \partial W V^B V^A\right. \\
& \quad \left. + \frac{1}{2}l^3 B^{ABC} V^A V^B V^C\right] = 0 \\
& (D^{AB} + l^4 K^{AB})V^B + l^4 C^{AB} \dot{W}^B + l^2(l^2 M^{AB} + J^{AB})\ddot{V}^B + D^A \partial^2 W + l^2 K^A W \\
& \quad + l(lM^A \ddot{W} + J^A \partial \ddot{W}) + l^2 C^A \dot{W} - l^2 Q^A + l\left[B^A\left(\partial U + \frac{1}{2}\partial W\partial W\right) + B^{AK} T^K\right]\partial W \\
& \quad + l^2\left(B^{AB} \partial U + \frac{3}{2}B^{AB} \partial W\partial W + B^{ABK} T^K + \frac{3}{2}lB^{ABC} V^C \partial W\right. \\
& \quad \left. + \frac{1}{2}l^2 B^{ABCD} V^C V^D\right)V^B = 0 \\
& B^{KL} T^L + B^K \partial U + \frac{1}{2}B^K \partial W\partial W + lB^{AK} V^A \partial W + \frac{1}{2}l^2 B^{ABK} V^B V^A = 0
\end{aligned} \tag{4.4}$$

with constant coefficients related to the beam properties

$$\begin{aligned}
\langle EA \rangle &\equiv B & \langle EA \partial h^A \rangle &\equiv lB^A & \langle \mu \rangle &\equiv M \\
\langle EA \partial g^K \rangle &\equiv B^K & \langle EA \partial h^A \partial g^K \rangle &\equiv lB^{AK} & \langle \mu h^A \rangle &\equiv l^2 M^A \\
\langle EA \partial g^K \partial g^L \rangle &\equiv B^{KL} & \langle EA \partial h^A \partial h^B \partial g^K \rangle &\equiv l^2 B^{ABK} & \langle \mu h^A h^B \rangle &\equiv l^4 M^{AB} \\
\langle EJ \rangle &\equiv D & \langle EA \partial h^A \partial h^B \rangle &\equiv l^2 B^{AB} & \langle \vartheta \rangle &\equiv J \\
\langle EJ \partial^2 h^A \rangle &\equiv D^A & \langle EA \partial h^A \partial h^B \partial h^C \rangle &\equiv l^3 B^{ABC} & \langle \vartheta \partial h^A \rangle &\equiv lJ^A \\
\langle EJ \partial^2 h^B \partial^2 h^A \rangle &\equiv D^{AB} & \langle EA \partial h^A \partial h^B \partial h^C \partial h^D \rangle &\equiv l^4 B^{ABCD} & \langle \vartheta \partial h^A \partial h^B \rangle &\equiv l^2 J^{AB}
\end{aligned} \tag{4.5}$$

to the subsoil properties and to the transverse load

$$\begin{aligned}
\langle c \rangle &\equiv C & \langle k \rangle &\equiv K & \langle q \rangle &\equiv Q \\
\langle ch^A \rangle &\equiv l^2 C^A & \langle kh^A \rangle &\equiv l^2 K^A & \langle qh^A \rangle &\equiv l^2 Q^A \\
\langle ch^A h^B \rangle &\equiv l^4 C^{AB} & \langle kh^A h^B \rangle &\equiv l^4 K^{AB}
\end{aligned} \tag{4.6}$$

It is a system of $2 + N + M$ differential equations for the macrodisplacements $U(\cdot)$, $W(\cdot)$ and for the fluctuation amplitudes of the axial displacement $T^K(\cdot)$ and of the deflection $V^A(\cdot)$. The coefficients of these equations are constant, some of them depend on the size l of the periodicity cell.

Equations(4.4) can be simplified to the following form

$$\begin{aligned}
& D\partial^4 W + D^A \partial^2 V^A + KW + l^2 K^A V^A - \underline{\overline{N}}\partial^2 W - l\tilde{N}^A \partial V^A \\
& \quad + C\dot{W} + M\ddot{W} - J\partial^2 \ddot{W} + l^2 C^A \dot{W}^A + l^2 M^A \ddot{V}^A - lJ^A \partial \ddot{V}^A - Q = 0 \\
& (D^{AB} + l^4 K^{AB})V^B + l^4 C^{AB} \dot{W}^B + l^2(l^2 M^{AB} + J^{AB})\ddot{V}^B + \underline{l\tilde{N}^A \partial W + l^2 \tilde{N}^{AB} V^B} \\
& \quad + D^A \partial^2 W + l^2 K^A W + l(lM^A \ddot{W} + J^A \partial \ddot{W}) + l^2 C^A \dot{W} - l^2 Q^A = 0
\end{aligned} \tag{4.7}$$

The nonlinear terms (underlined) involve the axial force

$$N = EA\varepsilon_0 = EA\left(\partial u_0 + \frac{1}{2}\partial w\partial w\right) \tag{4.8}$$

averaged with the certain gradients of the fluctuation shape function as weights

$$\begin{aligned} \begin{Bmatrix} \bar{N} \\ l\tilde{N}^A \\ l^2\tilde{N}^{AB} \end{Bmatrix} &= \begin{Bmatrix} \langle N \rangle \\ \langle N\partial h^A \rangle \\ \langle N\partial h^A\partial h^B \rangle \end{Bmatrix} \\ &= \begin{bmatrix} \bar{B}_0 & l\bar{B}_0^C & l^2\bar{B}_0^{CD} \\ l\bar{B}_0^A & l^2\tilde{B}_0^{AC} & l^3\bar{B}_0^{ACD} \\ l^2\bar{B}_0^{AB} & l^3\bar{B}_0^{ABC} & l^4\bar{B}_0^{ABCD} \end{bmatrix} \left(\frac{1}{L} \int_0^L \begin{Bmatrix} \frac{1}{2}\partial W\partial W \\ V^C\partial W \\ \frac{1}{2}V^CV^D \end{Bmatrix} dx + \begin{Bmatrix} \delta_0 \\ 0 \\ 0 \end{Bmatrix} \right) \end{aligned} \tag{4.9}$$

where

$$\delta_0 = L^{-1} \int_0^L \partial U \, dx = L^{-1}[U(L) - U(0)] \tag{4.10}$$

stands for the relative elongation of the beam axis. The coefficients of (4.9) are

$$\begin{aligned} \bar{B}_0 &= B - B^L(B^{-1})^{LK}B^K & \tilde{B}_0^{AB} &= B^{AB} - B^{AK}(B^{-1})^{LK}B^{LB} \\ \bar{B}_0^A &= B^A - B^{AL}(B^{-1})^{LK}B^K & \bar{B}_0^{ABC} &= B^{ABC} - B^{ABL}(B^{-1})^{LK}B^{KC} \\ \bar{B}_0^{AB} &= B^{AB} - B^{ABL}(B^{-1})^{LK}B^K & \bar{B}_0^{ABCD} &= B^{ABCD} - B^{ABK}(B^{-1})^{KL}B^{LCD} \end{aligned} \tag{4.11}$$

It can be seen that the axial displacement can be eliminated in a way common in the conventional Euler-Bernoulli or Timoshenko theories of uniform beams.

4.2. The equations of the tolerance-asymptotic model

Neglecting in equations (4.4) or (4.7) the terms with the microstructure parameter l and introducing the effective bending stiffness of the beam

$$D_0 \equiv D - D^A(D^{-1})^{AB}D^B \tag{4.12}$$

we arrive at the equations

$$\begin{aligned} \bar{B}_0\partial\left(\partial U + \frac{1}{2}\partial W\partial W\right) &= 0 \\ M\ddot{W} - J\partial^2\ddot{W} + C\dot{W} + KW + \bar{D}_0\partial^4W - \bar{B}_0\left(\partial U + \frac{1}{2}\partial W\partial W\right)\partial^2W &= Q \end{aligned} \tag{4.13}$$

The above equations do not describe the effect of the cell size on the behaviour of periodic beams under consideration. Hence, the asymptotic model makes it possible to analyse vibrations on the macrolevel only. In the framework of this approximation, certain higher eigenfrequencies and eigenforms of vibrations cannot be obtained.

5. Examples of application

Let us consider a hinged-hinged beam with immovable ends. The beam has a constant cross section and is provided by a system of periodically distributed system of concentrated masses M_1, M_2 with rotational inertia I_1, I_2 , as it is shown in Fig. 2.

A single cell is shown in Fig. 3. The mass distribution in a periodicity cell is given by

$$\begin{aligned} \mu(y) &= \mu_0 + M_1\delta(y) + M_2\delta\left(y + \frac{l}{2}\right) \\ \vartheta(y) &= \vartheta_0 + I_1\delta(y) + I_2\delta\left(y + \frac{l}{2}\right) \quad y \in (x) \end{aligned} \tag{5.1}$$

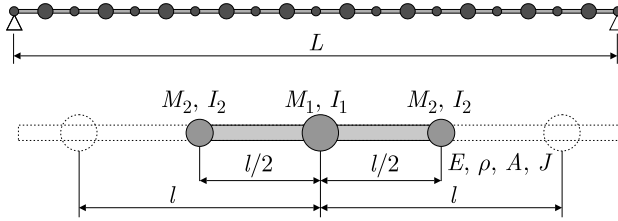


Fig. 2. The considered beam and its fragment

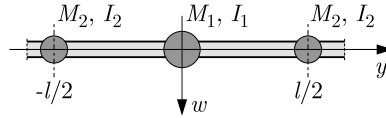


Fig. 3. A single periodicity cell

In this Section, the free undamped and forced vibrations will be analyzed. In the case of forced vibrations, we assume that the transverse load is given by

$$q(x, t) = q_0 \sin\left(\frac{\pi x}{L}\right) \cos(\Omega t) \tag{5.2}$$

6. The method of solution

6.1. Fluctuation shape functions

The fundamental assumption of the tolerance approach is the macro-micro decomposition (3.2), (3.3) of the unknown displacements. It can be seen that the fluctuation shape functions (FSF) play a crucial role in the analysis. As it has been mentioned, these functions represent the oscillations of displacements in a periodicity cell. The common practise is to use approximate functions, usually the sine and cosine that are infinitely differentiable. Another way is to utilize the periodic eigenproblem solutions of a periodicity cell, which can be obtained through numerical analysis.

Here, this is done through both the above mentioned ways. For the symmetric periodicity cell (Fig. 3), two transverse and one longitudinal approximate modes of cell vibrations are considered

$$\begin{aligned} h^1(y) &= l^2 \left[\cos\left(\frac{2A\pi y}{l}\right) + c \right] & h^2(y) &= l^2 \sin\left(\frac{2A\pi y}{l}\right) \\ g^1(y) &= l \left[\cos\left(\frac{2K\pi y}{l}\right) + c \right] & c &= \frac{M_2 - M_1}{\mu_0 l + M_1 + M_2} \end{aligned} \tag{6.1}$$

The constant c is calculated from condition (3.4)₁.

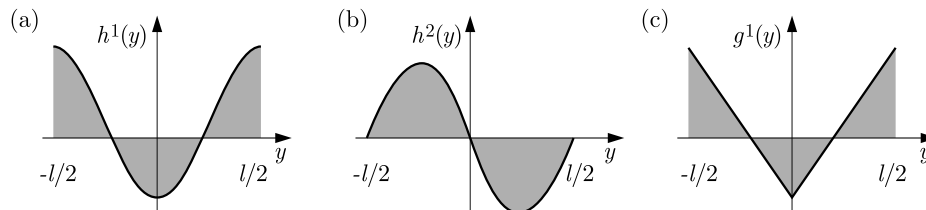


Fig. 4. FE-based fluctuation shape functions: transverse (a), (b), and longitudinal (c) modes of the periodicity cell vibrations

The refined fluctuation shape functions (Fig. 4) are obtained from a finite element analysis of the cell. The calculations are performed in the environment of Maple. The periodicity cell is divided into two elements, and the periodic boundary conditions are assumed.

Since the fluctuation shape functions satisfy the orthogonality conditions, there is possibility to obtain cell vibrations mode shapes taking more approximate FSFs and observing the convergence of total oscillation on a periodicity cell. In the case of the finite element based cell solution, a similar strategy can be adopted.

6.2. Solutions of the tolerance model

The solutions of the tolerance model equations, as well as the loads, are assumed in the form of truncated Fourier series

$$\begin{cases} W(x, t) \\ V^A(x, t) \end{cases} = \sum_{m=1}^n \begin{cases} w_m(t) \\ v_m^A(t) \end{cases} X_m(x) \tag{6.2}$$

$$\begin{cases} Q(x, t) \\ Q^A(x, t) \end{cases} = \sum_{m=1}^n \begin{cases} q_m(t) \\ q_m^A(t) \end{cases} X_m(x) \quad A = 1, \dots, N$$

For the hinged-hinged boundary conditions, the linear natural vibration modes are

$$X_m(x) = \sin(\xi_m)x \quad \xi_m = \frac{m\pi}{L} \tag{6.3}$$

Application of the Galerkin method leads to a system of $m \times (1 + N)$ ordinary differential equations

$$\mathbf{K}\mathbf{y} + \mathbf{M}\ddot{\mathbf{y}} = \mathbf{q} \quad \mathbf{K} = \mathbf{K}_0 + \mathbf{K}_{NL}(\mathbf{y}) \tag{6.4}$$

where

$$\mathbf{y} = \mathbf{y}(t) = \left\{ w_1(t) \quad w_2(t) \quad \dots \quad v_1^1(t) \quad v_2^1(t) \quad \dots \quad v_1^2(t) \quad v_2^2(t) \quad \dots \right\}^T \tag{6.5}$$

The linear natural frequencies and mode shapes are sought for as solutions to the linearized eigenproblem

$$|\mathbf{K}_0 - \omega^2\mathbf{M}| = 0 \tag{6.6}$$

In the case of free and forced nonlinear vibrations, equations (6.4) can be converted into a system of the first order ordinary differential equations

$$\ddot{\mathbf{y}} = \mathbf{M}^{-1}(\mathbf{q} - \mathbf{K}\mathbf{y}) \quad \Leftrightarrow \quad \begin{cases} \dot{\mathbf{y}} = \mathbf{v} \\ \dot{\mathbf{v}} = \mathbf{M}^{-1}(\mathbf{q} - \mathbf{K}\mathbf{y}) \end{cases} \tag{6.7}$$

and solved by forward numerical integration. The calculations have been performed in Maple, using own procedure based on the Runge-Kutta-Fehlberg (RKF45) method.

7. Computational results

The length of the beam is $L = 1.0$ m, Young’s modulus $E = 205$ GPa, mass density $\rho = 7850$ kg/m³. The other dimensionless parameters are as follows

$$\begin{aligned} \frac{b}{h} = 5 & \quad \frac{h}{l} = 0.1 & \quad \frac{l}{L} = 0.1 & \quad \frac{M_1}{\rho Al} = 5.1 \\ \frac{M_2}{M_1} = 0.5 & \quad \sqrt{\frac{I_1}{M_1 l^2}} = 10 & \quad \frac{I_2}{I_1} = 0.5 & \end{aligned} \tag{7.1}$$

Let us introduce a dimensionless central macrodeflection, deflection fluctuation and load amplitude

$$w = \frac{W_{center}}{h} \quad v = \frac{V_{center}}{h} \quad p = \frac{1}{h} \frac{q_0 L^4}{\pi^2 E J} \quad (7.2)$$

In the forced vibrations analysis, the load frequency is 5/4 times the lowest free undamped frequency of the beam

$$\Omega = \frac{5}{4} \omega_1 \quad (7.3)$$

7.1. Free undamped vibrations

We restrict ourselves to considering only the first two ($m = 2$) terms of Fourier series (6.2) and two FSFs ($N = 2$) so that the model has $m(1 + N) = 6$ degrees of freedom.

In order to validate the results, a finite element method procedure for beam dynamics analysis has been written in Maple. The Rayleigh beam elements with Hermitian polynomials and consistent mass matrix have been applied.

The results of comparative analysis of calculations obtained for the finite element (40 elements) model and the tolerance model, using the approximate (trigonometric) and refined (finite element based) fluctuation shape functions (FSF), are shown in Table 1 (linear eigenfrequencies) and Fig. 5 (linear eigenvectors).

Table 1. Comparison of linear eigenfrequencies of the considered beam

Mode	Finite element	Tolerance model			
		approximate FSFs		FE-based FSFs	
	ω_{FE} [rad/s]	ω_{TA} [rad/s]	Δ [%]	ω_{TA} [rad/s]	Δ [%]
1. w_1	15.861	15.876	0.094	15.872	0.071
2. w_2	32.884	33.050	0.505	33.041	0.477
3. v_2^2	223.491	239.454	7.143	212.200	5.052
4. v_1^2	224.244	246.109	9.751	224.088	0.069
5. v_2^1	14855.007	15129.460	1.848	15034.591	1.209
6. v_1^1	14989.493	15129.460	0.934	15034.591	0.301

Figure 6 presents the total central deflection versus the quotient of nonlinear frequency to linear frequency of free macro- and micro-vibrations (backbone curves) corresponding to the first macro-mode and symmetric cell vibrations ($m = 1$, $N = 1$). Parameters (7.1) are kept constant except the dimensionless microstructure parameter $\lambda = l/L$ that is equal to 1/10, 1/12 or 1/15.

Studying the forced vibrations, the first 200 load periods are considered. The bifurcation diagram of the total dimensionless deflection w at $x = 0.5L$ versus the dimensionless load amplitude is shown in Fig. 7. Figure 8 presents a close-up of the bifurcation diagram of deflection together with the diagram of its velocity dw/dt .

8. Discussion of results

From the results of linear free vibrations analysis, it can be seen that the finite element based fluctuation shape functions indicate a better performance than the first-term trigonometric ones, although the significant differences appear only for the antisymmetric mode shapes of the periodicity cell. This applies both to the frequencies (Table 1) and the mode shapes (Fig. 5). It should be noted that approximation of the lowest order possible is applied in the numerical

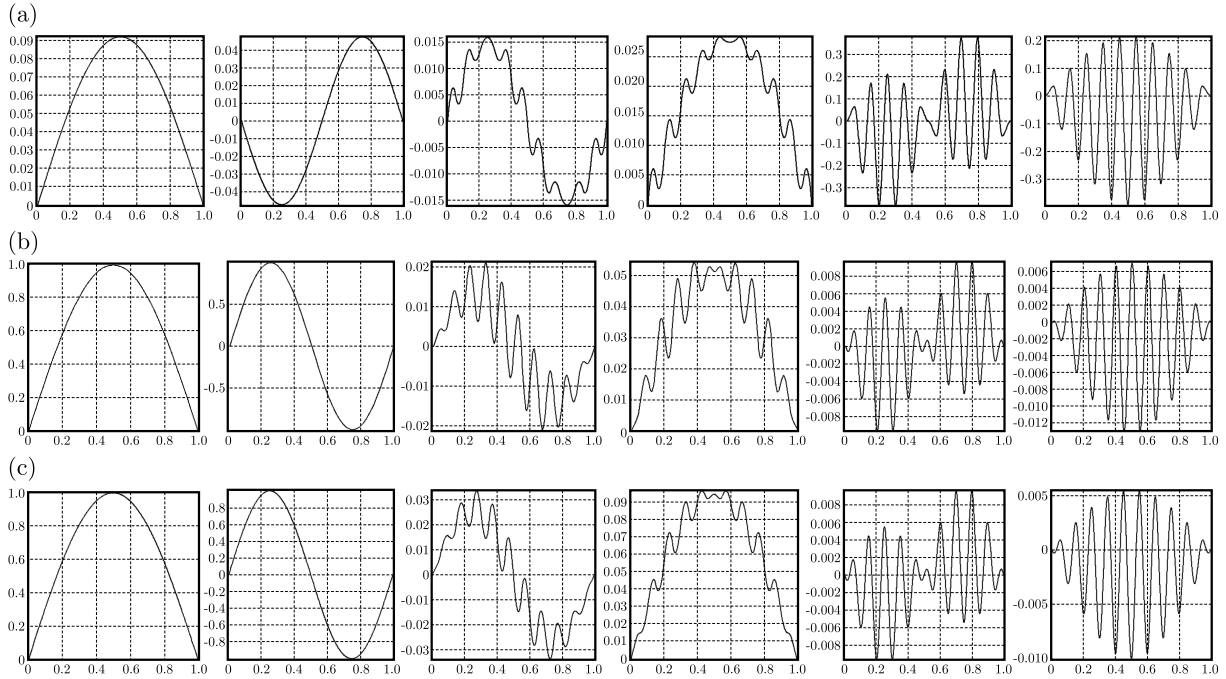


Fig. 5. Comparison of linear eigenforms of the considered beam: (a) finite element model, (b) tolerance model with trigonometric FSFs, (c) tolerance model with FE-based FSFs

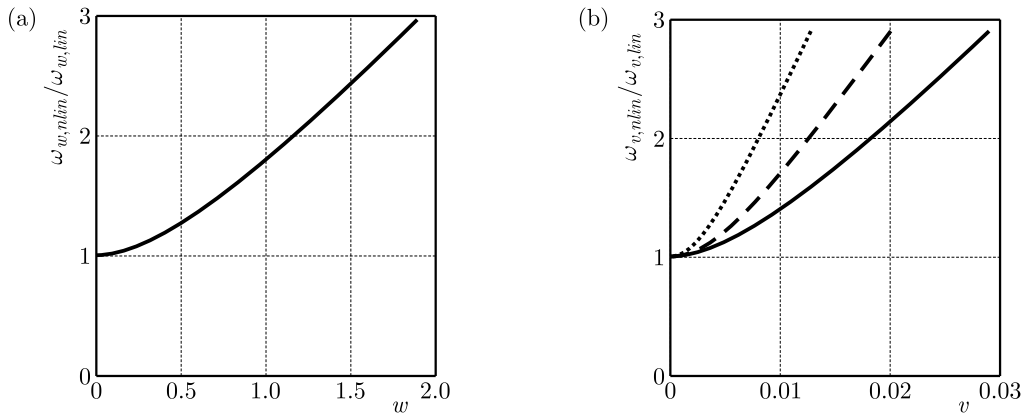


Fig. 6. Backbone curves for dimensionless macrodeflection (a) and fluctuation (b) at $x = 0.5L$ for $\lambda = 1/10$ (solid line), $\lambda = 1/12$ (dashed line), $\lambda = 1/15$ (dotted line)

analysis on the macro- and microlevel. As it is mentioned above, these results can be improved through a more accurate analysis of the cell problem.

When it comes to nonlinear free vibrations the backbone curves presented in Fig. 6 indicate that the lower order (macro-) nonlinear vibrations frequency is practically not affected by the periodicity cell length, while the higher order frequency is much more sensitive to its variation. It is caused by the fact that in the geometrically nonlinear formulation the strain terms that include the displacement fluctuations are dependent on the microstructure parameter l , what does not take place in the linear model.

Studying the results of the forced vibrations case (Figs. 7 and 8), the most characteristic feature is that the bifurcation diagram is very scattered, although there are many narrow periodic windows. This is due to the fact that free vibrations are not damped, so they do not fade with time. For the values of p higher than ~ 3 , it can be seen that the envelope of the diagram suddenly loses its regularity and becomes jagged, which may indicate irregular vibrations. This requires a more detailed analysis.

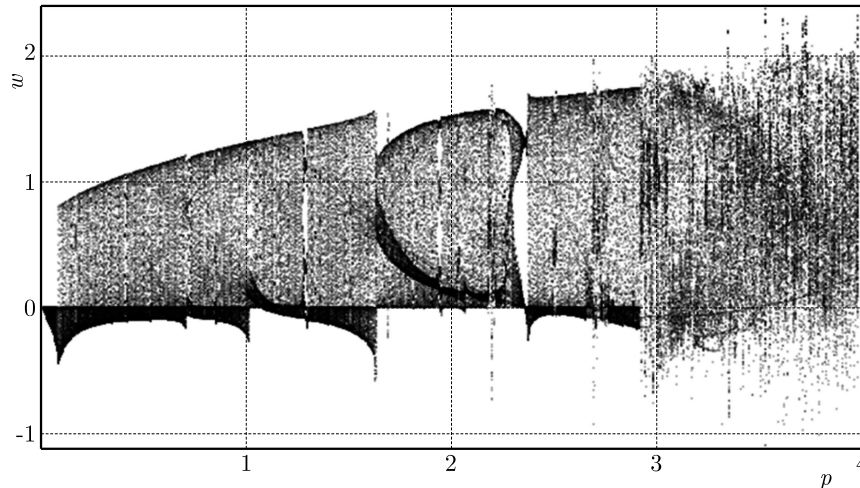


Fig. 7. The bifurcation diagram of the deflection w vs. the load amplitude p

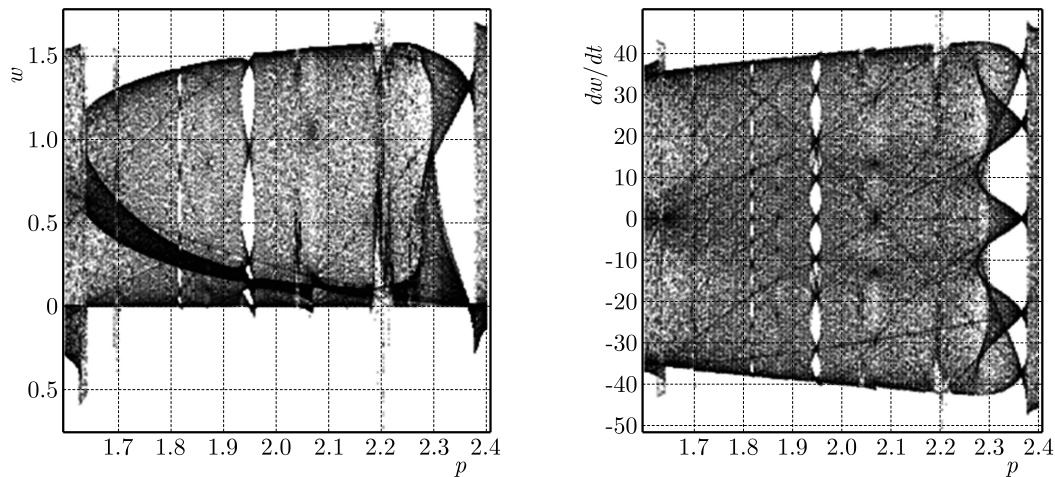


Fig. 8. A blow-up of the bifurcation diagram: the deflection w and the velocity dw/dt vs. the load amplitude p

9. Closing remarks

In this contribution, the tolerance model is shown, which describes geometrically nonlinear vibrations of a periodically inhomogeneous beam. The model is developed by applying the tolerance averaging method directly to the 1D beam theory equations. Hence, the fundamental equations with highly oscillating, periodic, non-continuous functional coefficients are replaced by the equations with constant coefficients. It should be stressed that the aim is to develop a low degree of freedom model that would be able to provide results that are not available for the first order asymptotic models. Some applications of the proposed model including free and forced undamped vibrations are presented. A comparison of linear eigenfrequencies and mode shapes with a finite element model is shown.

The following general remarks can be formulated.

1. It can be observed that the proposed tolerance model makes it possible to investigate the effect of the microstructure size on dynamic problems of periodic beams under consideration, e.g. the “higher order” vibrations related to the beam microstructure.
2. The governing equations of the tolerance model have a physical sense for the unknowns W , U , V^A , $A = 1, \dots, N$, T^K , $K = 1, \dots, M$, being slowly-varying functions.

3. The asymptotic model of periodic beams makes it possible to investigate only lower order (fundamental) vibrations.

The issues anticipated to be addressed in the future work are:

- taking into account the structural and material heterogeneity of the beam and the viscoelastic subsoil,
- more detailed analysis of the solutions to the cell problem,
- detailed analysis of the properties distribution in a periodicity cell,
- analysis of the initial shortening/elongation of the beam axis.

These problems will be investigated in forthcoming papers.

Acknowledgement

The authors are grateful for the support provided by the National Science Centre, Poland (Grant No. 2014/15/B/ST8/03155).

References

1. AWREJCWICZ J., KRYSKO A.V., MROZOWSKI J., SALTYSKOVA O.A., ZHIGALOV M.V., 2011, Analysis of regular and chaotic dynamics of the Euler-Bernoulli beams using finite difference and finite element methods, *Acta Mechanica Sinica*, **27**, 36-43
2. BAKHVALOV N.S., PANASENKO G.P., 1984, *Averaging of Processes in Periodic Media* (in Russian), Nauka, Moskwa
3. BANAKH L., KEMPNER M., 2010, Vibrations of mechanical systems with regular structure, [In:] *Foundations of Engineering Mechanics*, Springer, Berlin
4. BARON E., 2006, On modelling of periodic plates having the inhomogeneity period of an order of the plate thickness, *Journal of Theoretical and Applied Mechanics*, **44**, 3-18
5. BENSOUSSAN A., LIONS J.L., PAPANICOLAOU G., 1978, *Asymptotic Analysis for Periodic Structures*, North-Holland, Amsterdam
6. CHEN T., 2013, Investigations on flexural wave propagation of a periodic beam using multi-reflection method, *Archive of Applied Mechanics*, **83**, 315-329
7. CHEN T., WANG L., 2013, Suppression of bending waves in a periodic beam with Timoshenko beam theory, *Acta Mechanica Solida Sinica*, **26**, 177-188
8. HE W.M., CHEN W.Q., QIAO H., 2013, Frequency estimate and adjustment of composite beams with small periodicity, *Composites: Part B*, **45**, 742-747
9. HRYSIEWICZ Z., KOZIOŁ P., 2013, Wavelet-based solution for vibrations of a beam on a nonlinear viscoelastic foundation due to moving load, *Journal of Theoretical and Applied Mechanics*, **51**, 215-224
10. JĘDRYSIAK J., 1999, Dynamics of thin periodic plates resting on a periodically inhomogeneous Winkler foundation, *Archive of Applied Mechanics*, **69**, 345-356
11. JĘDRYSIAK J., 2013, Modelling of dynamic behaviour of microstructured thin functionally graded plates, *Thin Walled Structures*, **71**, 102-107
12. JĘDRYSIAK J., WOŹNIAK C., 2006, On the propagation of elastic waves in a multiperiodically reinforced medium, *Meccanica*, **41**, 553-569
13. JIKOV V.V., KOZLOV S.M., OLEINIK O.A., 1994, *Homogenization of Differential Operators and Integral Functionals*, Springer Verlag, Berlin-Heidelberg-New York
14. KOLPAKOV A.G., 1991, Calculation of the characteristics of thin elastic rods with a periodic structure, *Journal of Applied Mathematics and Mechanics*, **55**, 358-365
15. KOLPAKOV A.G., 1995, The asymptotic theory of thermoelastic beams, *Journal of Applied Mechanics and Technical Physics*, **36**, 756-763

16. KOLPAKOV A.G., 1998, Application of homogenization method to justification of 1-D model for beam of periodic structure having initial stresses, *International Journal of Solids and Structures*, **35**, 2847-2859
17. KOLPAKOV A.G., 1999, The governing equations of a thin elastic stressed beam with a periodic structure, *Journal of Applied Mathematics and Mechanics*, **63**, 495-504
18. KRYSKO A.V., ZHIGALOV M.V., SALTYKOVA O.A., 2008, Control of complex nonlinear vibrations of sandwich beams, *Russian Aeronautics*, **51**, 238-243
19. LEWIŃSKI T., TELEGA J.J., 2000, *Plates, laminates and shells*, World Scientific Publishing Company, Singapore
20. MAGNUCKI K., JASION P., KRUS M., KULIGOWSKI P., WITTENBECK L., 2013, Strength and buckling of sandwich beams with corrugated core, *Journal of Theoretical and Applied Mechanics*, **51**, 15-24
21. MAZUR-ŚNIADY K., 1993, Macro-dynamics of micro-periodic elastic beams, *Journal of Theoretical and Applied Mechanics*, **31**, 781-793
22. MAZUR-ŚNIADY K., ŚNIADY P., 2001, Dynamic response of a micro-periodic beam under moving load – deterministic and stochastic approach, *Journal of Theoretical and Applied Mechanics*, **39**, 323-338
23. MAZUR-ŚNIADY K., WOŹNIAK C., WIERZBICKI E., 2004, On the modelling of dynamic problems for plates with a periodic structure, *Archive of Applied Mechanics*, **74**, 179-190
24. OLHOFF N., NIU B., CHENG G., 2012, Optimum design of band-gap beam structures, *International Journal of Solids and Structures*, **49**, 3158-3169
25. SANCHEZ-PALENCIA E., 1980, *Non-Homogeneous Media and Vibration Theory*, Lecture Notes in Physics 127, Springer-Verlag, Berlin
26. SEDIGHI H.M., REZA A., ZARE J., 2013, The effect of quintic nonlinearity on the investigation of transversely vibrating buckled Euler-Bernoulli beams, *Journal of Theoretical and Applied Mechanics*, **51**, 959-968
27. SYERKO E., DISKOVSKY A.A., ANDRIANOV I.V., COMAS-CARDONA S., BINETRUY C., 2013, Corrugated beams mechanical behavior modelling by the homogenization method, *International Journal of Solids and Structures*, **50**, 928-936
28. SYLVIA J.E., HULL A.J., 2013, A dynamic model of a reinforced thin plate with ribs of finite width, *International Journal of Acoustics and Vibration*, **18**, 86-90
29. TOMCZYK B., 2007, A non-asymptotic model for the stability analysis of thin bi-periodic cylindrical shells, *Thin Walled Structures*, **45**, 941-944
30. WANG Y.Z., LI F.M., 2014, Nonlinear primary resonance of nano beam with axial initial load by nonlocal continuum theory, *International Journal of Non-Linear Mechanics*, **61**, 74-79
31. WIROWSKI A., 2012, Self-vibration of thin plate with non-linear functionally graded material, *Archives of Mechanics*, **64**, 603-615
32. WOŹNIAK C. ET AL. (EDS.), 2010, *Mathematical Modelling and Analysis in Continuum Mechanics of Microstructured Media*, Silesian University of Technology Press, Gliwice, Poland
33. WOŹNIAK C., MICHALAK B., JĘDRYŃSKI J. (EDS.), 2008, *Thermomechanics of Microheterogeneous Solids and Structures. Tolerance Averaging Approach*, Lodz Technical University Press, Łódź, Poland
34. WOŹNIAK C., WIERZBICKI E., 2000, *Averaging Techniques in Thermomechanics of Composite Solids*, Czestochowa University of Technology Press, Czestochowa, Poland
35. YU D., WENA J., SHEN H., XIAO Y., WEN X., 2012, Propagation of flexural wave in periodic beam on elastic foundations, *Physics Letters A*, **376**, 626-630

IMPLEMENTATION OF THE LQG CONTROLLER FOR A WIND TURBINE TOWER-NACELLE MODEL WITH AN MR TUNED VIBRATION ABSORBER

MACIEJ ROSÓŁ

AGH University of Science and Technology, Department of Automatics and Biomedical Engineering, Cracow, Poland
e-mail: mr@agh.edu.pl

PAWEŁ MARTYNOWICZ

AGH University of Science and Technology, Department of Process Control, Cracow, Poland
e-mail: pmartyn@agh.edu.pl

Vibration of a wind turbine tower is related to fatigue wear, influencing reliability of the whole structure. The current paper deals with the problem of Linear-Quadratic-Gaussian (LQG) tower vibration control using specially designed and built simulation and laboratory tower-nacelle models with a horizontally aligned, magnetorheological (MR) damper based tuned vibration absorber located at the nacelle. Force excitation applied horizontally to the tower itself, or to the nacelle, is considered. The MR damper LQG control algorithm, including the Kalman state observer and LQR (Linear-Quadratic-Regulator) controller is analysed numerically and implemented on the laboratory ground, in comparison with the system with a deactivated absorber. Simulation and experimental results are presented.

Keywords: wind turbine tower vibration, tuned vibration absorber, MR damper, LQG control

1. Introduction

The wind turbines sector is an emerging one nowadays. The wind load (and also sea waves load for offshore structures) that is varying in time as well as rotation of turbine elements are the major contributors to structural vibration of the tower and blades. Cyclic stress the tower is subjected to, may lead to a decrease in reliable operation time due to structure fatigue wear (Enevoldsen and Mork, 1996) or even failure accident. Tower vibration arises due to various excitation sources as variable wind/sea conditions and rotation of turbine elements (Jain, 2011). This vibration is generally lightly damped, especially considering low aeroelastic damping for the first tower lateral mode (Butt and Ishihara, 2012; Hansen *et al.*, 2012; Matachowski and Martynowicz, 2012; Bak *et al.*, 2012). The lateral modes are excited due to the Karman vortices, generator operation, sea waves variable load and rotating machinery unbalance rather than due to direct wind load variation/wind shear/differences in inflow conditions for each of the blades, and the blade passing effect, as for longitudinal modes. In the current research, tower vibration only is being analysed.

The solutions utilised to reduce vibration of wind turbine towers include collective pitch control, generator electromagnetic torque control, and passive/semiactive/active tuned vibration absorbers (TVAs) (Shan and Shan, 2012; Jelavić *et al.*, 2007; Namik and Stol, 2011; Den Hartog, 1985; Oh and Ishihara, 2013; Tsouroukdissian *et al.*, 2011; Rotea *et al.*, 2010). TVAs are widely spread structural vibration reduction solutions for slender structures. In the standard (passive) approach, TVA consists of an additional moving mass, spring and viscous damper whose parameters are tuned to the selected (most often first) mode of the vibration (Den Hartog, 1985; Łatas and Martynowicz, 2012). Passive TVAs work well at the load conditions characterised with a single frequency to which they are tuned, but cannot adapt to a wider excitation

spectrum (Kirkegaard *et al.*, 2002), thus more advanced TVAs are implemented to change/tune TVA operating frequency. Among them, magnetorheological (MR) TVAs are placed (Kirkegaard *et al.*, 2002), as the use of MR damper (instead of viscous damper) guarantees a wide range of the resistance force, fast response times, low sensitivity to temperature changes and fluid contamination, high operational robustness, and minor energy requirements (Kciuk and Martynowicz, 2011; Lord Rheonetic, 2002; Sapiński and Rosól, 2007, 2008; Snamina and Sapiński, 2011; Sapiński and Martynowicz, 2005) as compared to active systems. Simulations and experiments show that the implementation of the MR damper in the TVA system may lead to further vibration reduction in relation to the passive TVA (Martynowicz, 2014b, 2015, 2016; Koo and Ahmadian, 2007).

Within the scope of the current research, there have been specially developed and built tower-nacelle simulation and laboratory models in which all turbine components (nacelle, blades, hub, shaft, generator and possibly gearbox) are represented by nacelle concentrated mass and mass moments of inertia. Regarding variable geometric configuration of the structure resulting from changing rotor angular position, more detailed FEM analysis has been conducted using the full structure model, which demonstrated negligible influence of the rotor angle on tower structural dynamics (Matachowski and Martynowicz, 2012). Both simulation model and laboratory test rig of wind turbine tower-nacelle system give the possibility to model tower vibration under various aerodynamic, hydrodynamic, mechanical unbalance, changeable electromagnetic load, excitation sources (as mentioned before), etc. A horizontal concentrated force generated by the modal shaker may be applied either to the nacelle $P(t)$ or to the tower itself at half of its height $F(t)$. With the use of the MR damper, dedicated control solutions may be realised, in comparison to the system without TVA (i.e. TVA 'locked'). Previous research showed the effectiveness of the ground hook control and its modification, sliding mode control, linear and nonlinear damping, adaptive control and open-loop system with various MR damper constant input current values (Martynowicz, 2014b, 2015, 2016). The Linear-Quadratic-Gaussian (LQG) control approach implementation is analysed within the scope of the current paper. The first bending mode of vibration is analysed here only, as higher modes reduction capabilities with MR TVA located at the nacelle are minor (Martynowicz, 2014b, 2015).

Most of the applications of the LQG controller concern control of civil structures (buildings) excited by severe earth quakes or strong winds. The existing solutions of the LQG semiactive control algorithm use, most frequently, the mathematical model of the analysed mechanical structure (Dyke *et al.*, 1996a,b; Asai *et al.*, 2013; Wang and Dyke, 2013). In opposition to the Linear-Quadratic-Regulator (LQR) algorithm, they do not need measurement of the full-state for all DOFs. The Kalman state observer is responsible for the estimation of unmeasurable state variables, based on the measured positions or accelerations. In many cases, obtaining a sufficiently accurate model is difficult, therefore some authors proposed model-free LQG semiactive control algorithms which do not need an accurate mathematical model (Asai and Spencer Jr., 2014), computing LQG parameters directly from the measurement data (Hjalmarsson *et al.*, 1998; Kawamura, 1998; Favoreel, 1999).

In the present paper, an output feedback strategy based on the measured position at a limited number of structure points is proposed. The LQG controller calculates the desired MR damper force on the basis of the state variables vector restored by the Kalman filter. The LQR problem is solved using a 'black box' input-output linear model identified on the basis of the free vibration response of the tower-nacelle experimental model. Given the measurements of the inputs and outputs of the unknown system, the matrices **A**, **B**, **C** and **D** of the estimate linear system are found. The model order of the 'black box' is selected considering two state variables (position and velocity) for each selected structure point.

The paper is organised as follows. In the next Section, the wind turbine tower-nacelle Comsol/Simulink model with MR TVA is introduced. Then, the laboratory test rig is presented.

LQG controller synthesis including the Kalman filter is further described and followed by Comsol/Simulink simulation and laboratory test rig experimental results. The paper is finished with several conclusions.

2. Wind turbine tower-nacelle model with MR TVA

The beam modelling the tower is arranged vertically. The bottom end of the beam is fixed to the ground via additional foundation frame. A solid body modelling the nacelle is fixed to the upper end of the beam. TVA system incorporating the absorber mass, spring and MR damper is attached to the solid body representing the nacelle, and arranged horizontally. A diagram of the model, including the system of coordinates w - x , is shown in Fig. 1a.

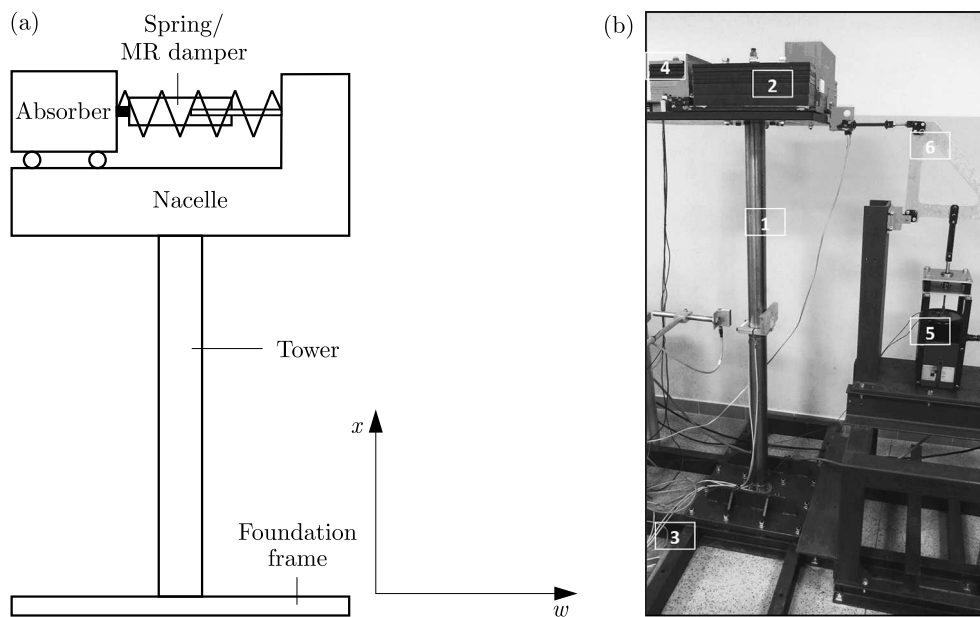


Fig. 1. (a) Diagram of the model, (b) The laboratory test rig

Based on the model assumptions and mathematical calculations results, a Comsol Multiphysics finite element method (FEM) model of the tower-nacelle system was built as a ‘3D Euler Beam’ fixed at the bottom and free at the top, with an additional mass and mass moments of inertia defined at its top. A beam element (of length designated by l) with three nodes has been selected. The two edges are configured by applying material and cross-section parameters of the chosen tower material. The bottom node represents the tower-ground (tower-foundation) restraint, while two other nodes are ‘free’. The node at the tower midpoint (at $x = x_0 = l/2$, see Fig. 1a), where deflection of the 2nd mode is close to maximal, is the ‘load point’, where the horizontal w -axis force F ($F(t)$) may be applied. The node at the top of the tower (at $x = x_1 = l$) corresponds to the nacelle location, thus the mass and mass moments of inertia as well as concentrated load P ($P(t)$) are all assigned here.

The FEM model assumes that angles are small and cross sections are perpendicular to the bending line (Euler-Bernoulli beam model). Also, the Rayleigh model (that is precise within a narrow frequency range only) of the tower material damping is assumed. These assumptions make the developed model to be adequate for small bending angles and within the 1st bending mode frequency neighbourhood only. Also, during the model identification process (subject to separate publication), correction (lowering) of Young’s modulus is necessary as the FEM Euler-Bernoulli beam model is stiffer than the real structure due to neglecting shear deformation and additional restrains input by the finite/limited number of elements.

FEM Comsol Multiphysics model has been exported to MATLAB/Simulink with the ‘General dynamic’ option. During exporting of the ‘Simulink model’, forces F , and P are specified as inputs, while the tower tip (w_{x1}/v_{x1}) and tower midpoint (w_{x0}/v_{x0}) displacements/velocities along the w -axis are defined as output signals. After the exporting, FEM tower-nacelle model is available as a MATLAB structure, and the Comsol Multiphysics model is embedded into Simulink diagram using ‘COMSOL Multiphysics Subsystem’ block. Thus, all 18 FEM model degrees of freedom are a part of the Simulink state vector (COMSOL, 2008).

The MR TVA model is implemented as a standard Simulink diagram. TVA model with the hyperbolic tangent model of RD-1097-1 MR damper (Martynowicz, 2015) including linear bearing guides (see Section 3) friction force, LQG controller block with MR damper optimal (demanded) force output, incorporating the Kalman filter and LQR state feedback loop, linear guides friction force compensation by an MR damper, and MR damper inverse model (to obtain demanded control current) are all embedded in the Simulink diagram. ‘COMSOL Multiphysics Subsystem’ block outputs are fed to the dynamics of MR TVA with mass and stiffness parameters (designated by m and k , respectively) tuned according to Den Hartog (1985). A general structure of the regarded model is shown in Fig. 2. It contains two main blocks: the tower-nacelle system model and the MR TVA model. Its inputs are: F , P , while w_{x0} , v_{x0} , w_{x1} and v_{x1} are the outputs. The forces produced by an MR damper, spring, and bearing guides friction are all added to a force excitation P , (Martynowicz, 2014b, 2015).

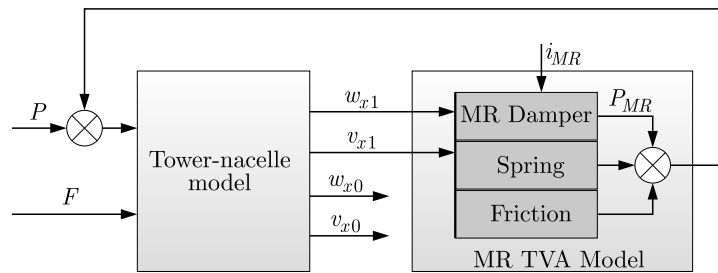


Fig. 2. Structure of the simulation model; F , P – horizontal force applied at the point x_0 and point x_1 , respectively, P_{MR} – MR damper force, i_{MR} – current in the MR damper coil, w_{x0} , v_{x0} – tower midpoint horizontal displacement and velocity, respectively, w_{x1} , v_{x1} – tower tip (nacelle) horizontal displacement and velocity, respectively

3. Laboratory setup

The analysed model has to fulfil various constraints imposed by the laboratory facility and project limitations, among others adequate dimensions, strength and modal masses of the structure, and mass of the absorber corresponding to the commercially available MR damper characteristics, to enable reduction of tower deflection amplitude for the nominal MR damper stroke. It is assumed that at least partial dynamic similarity between the real-world wind turbine (Vensys 82) tower-nacelle system and its scaled model has to be fulfilled, respecting the limited laboratory space and foundation permissible load (Martynowicz, 2014a; Snamina *et al.*, 2014; Martynowicz and Szydło, 2013). Based on all of the assumptions and analyses, a Ti. Gr. 5 alloy rod has been selected to model the wind turbine tower, while Lord’s RD-1097-1 (Lord Rheonetic, 2002) MR damper has been used for TVA, and TMS 2060E lightweight electrodynamic exciter (TMS, 2010) has been selected for excitation purposes. The parameters of TVA have been tuned for the 1st bending mode of vibration (Den Hartog, 1985). After several system reconfigurations, the absorber mass has been selected to be ca. 15% of the modal mass of the 1st bending mode of the tower-nacelle model.

The detailed analysis of a similarity relation between the laboratory model and the full-scale (Vensys 82) structure, including time and length similarity scale factors and determined geometrical and material properties of the model, was presented by Snamina *et al.* (2014). The conducted partial dynamic similarity analysis ensures motion similarity of a selected pair of corresponding points (tower tips).

The laboratory test rig of the wind turbine tower-nacelle with MR TVA system is presented in Fig. 1b. It is build according to the details specified above. It consists of a vertically oriented titanium alloy circular rod 1 (representing wind-turbine tower), and a system of steel plates 2 (representing the nacelle and turbine assemblies) fixed to the top of rod 1, with MR TVA embedded. The rod is rigidly mounted to steel foundation frame 3. MR TVA 4 is an additional mass moving horizontally along linear bearing guides, connected with the assembly representing the nacelle via the spring and RD-1097-1 MR damper in parallel. RD-1097-1 damper, whose force depends on the current fed to its coil, is an actuator of such a vibration reduction system. The MR TVA operates along the same direction as the vibration excitation applied to the system. The force generated by TMS 2060E exciter 5 may be applied either to rod 1 (modelling the tower) midpoint or to the system of steel plates 2 (modelling the nacelle/turbine) with the help of drive train assembly 6 of changeable leverage (enabling changeable force/displacement/velocity ranges). The excitation of the tower resulting from blade rotation, rotating machinery unbalance as well as wind thrust on the rotor may be modelled by a concentrated load P applied to the nacelle/turbine, while the direct (aerodynamic, including blade passing effect, sea waves, ice, etc.) tower loads may be reduced to the resultant concentrated force F applied to the tower itself (e.g. at its midpoint). All the measurements are gathered by PC with MATLAB/Simulink/RT-CON based real-time environment that is also used for the MR damper control and excitation signal generation (Martynowicz, 2015, 2016).

4. LQG Controller synthesis

The LQG (Linear-Quadratic-Gaussian) controllers are built for uncertain linear systems disturbed by additive white Gaussian noises, having incomplete state information (Athans, 1971). The LQG is a combination of the Kalman filter with Linear-Quadratic Regulator (LQR). The separation principle allows each part of the LQG to be designed and tested independently. The LQG controller applies to both linear time-invariant and time-varying systems. It should be noted that the LQG control problem is one of the most fundamental problems of optimal control. Application of a Kalman filter enables to restore unmeasured state variables and then use them in the LQR controller. A typical structure of the LQG regulator is shown in Fig. 3.

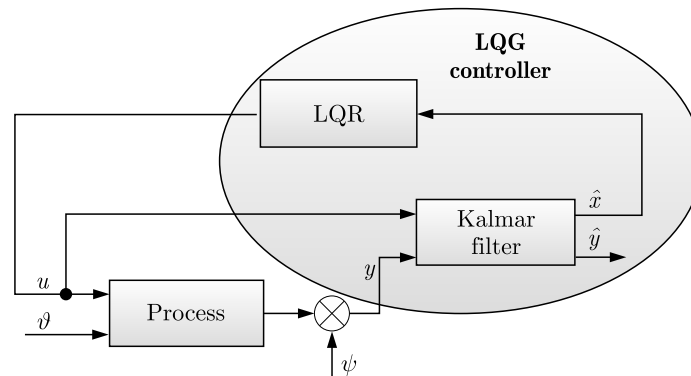


Fig. 3. Structure of a LQG controller; \mathbf{u} – control input of the process, \mathbf{v} – process noise (stochastic), ψ – measurement noise (stochastic), \mathbf{y} – output of the process, $\hat{\mathbf{y}}$ – estimation of the process output, $\hat{\mathbf{x}}$ – estimation of the process state

The present paper concerns a discrete-time LQG control problem. The description of the LQG controller focuses on the following discrete-time linear system of equations, modelling the tower-nacelle with MR TVA system (block ‘Process’ in Fig. 3)

$$\begin{aligned}\mathbf{x}(k+1) &= \mathbf{A}\mathbf{x}(k) + \mathbf{B}\mathbf{u}(k) + \boldsymbol{\vartheta}(k) \\ \mathbf{y}(k) &= \mathbf{C}\mathbf{x}(k) + \mathbf{D}\mathbf{u}(k) + \boldsymbol{\psi}(k)\end{aligned}\quad (4.1)$$

where \mathbf{x} is the state vector, while the process and measurement noises, respectively: $\boldsymbol{\vartheta}(k)$ and $\boldsymbol{\psi}(k)$ are independent, zero mean, white Gaussian random processes, satisfying (\mathbf{Q}_d , \mathbf{R}_d – covariance matrices)

$$E[\boldsymbol{\vartheta}(k)] = E[\boldsymbol{\psi}(k)] = 0 \quad E[\boldsymbol{\vartheta}(k)\boldsymbol{\vartheta}^T(k)] = \mathbf{Q}_d \quad E[\boldsymbol{\psi}(k)\boldsymbol{\psi}^T(k)] = \mathbf{R}_d \quad (4.2)$$

The tower-nacelle model itself (‘Tower-nacelle model’ block in Fig. 2), as presented in Section 2, is linearized with regard to the following four state variables: tower tip (nacelle) horizontal displacement w_{x1} and velocity v_{x1} , and tower midpoint horizontal displacement w_{x0} and velocity v_{x0} . All the other tower-nacelle model state variables produced by the COMSOL Multiphysics FEM model are ignored as not crucial concerning 1st (and even 2nd, regarding future applications) bending mode amplitudes detection and MR TVA control.

The LQG control algorithm can be employed for semi-active control of the tower-nacelle with MR TVA system, assuming P_{MR} force as the control input. Using this algorithm, the optimal control signal P_{MR} , which is the force generated by an MR damper, will be obtained. The MR damper is controlled using a power interface of an analogue type. To induce the MR damper to generate the desired optimal control force, the inverse model of the MR damper is used. This model determines the relationship between the optimal value of the force P_{MR} , actual piston displacement (designated by w_{x12}), actual piston velocity (v_{x12}) and MR damper current, such as: $i_{MR} = f(P_{MR}, w_{x12}, v_{x12})$. However, the displacement signals of the tower-nacelle with MR TVA system are measured only – the velocity signals are not available for the LQR controller and MR damper inverse model. To solve this problem, the velocities are replaced by their estimates produced by the Kalman filter, described in detail in the next Section.

4.1. Kalman filter

The Kalman filter is used to restore unmeasurable variables v_{x1} and v_{x12} , required to implement the LQR controller (and also the MR damper inverse model). This method provides for state (assumed in Section 4.3) of tower-nacelle with MR TVA system estimation, considering the measurement and process noises. It should be noted that in the LQG design, two Kalman filters of the same structure are used separately for v_{x1} and v_{x12} .

Consider the following system

$$\begin{aligned}\mathbf{z}(k+1) &= \mathbf{A}_k\mathbf{z}(k) + \mathbf{B}_k\mathbf{u}(k) + \boldsymbol{\vartheta}(k) \\ \mathbf{y}(k) &= \mathbf{H}_k\mathbf{z}(k) + \boldsymbol{\psi}(k)\end{aligned}\quad (4.3)$$

where: $\mathbf{z} = [w_x, v_x, a_x]^T$ is the state vector that includes displacement w_x (w_{x1} , or w_{x12}), velocity v_x (v_{x1} , or v_{x12}) and acceleration a_x (a_{x1} or a_{x12} , respectively; acceleration is estimated for future applications), while $\boldsymbol{\vartheta}(k)$ and $\boldsymbol{\psi}(k)$ are respectively the process and measurement white noises.

As only w_x displacement is being measured, therefore the following matrices \mathbf{A}_k , \mathbf{B}_k , and \mathbf{H}_k of equations (4.3) are considered (Singhal *et al.*, 2012)

$$\mathbf{A}_k = \begin{bmatrix} 1 & T_0 & T_0^2 \\ 0 & 1 & T_0 \\ 0 & 0 & 1 \end{bmatrix} \quad \mathbf{B}_k = \begin{bmatrix} 0 \\ 0 \\ 0 \end{bmatrix} \quad \mathbf{H}_k = \begin{bmatrix} 1 & 0 & 0 \end{bmatrix}$$

where T_0 is the sampling period of the LQG control algorithm (in the simulations and experiments, $T_0 = 0.001$ s is assumed). For the calculation purposes, the following values of the covariance matrices \mathbf{Q}_k , \mathbf{R}_k are assumed (r is a constant value, Singhal *et al.*, 2012)

$$\mathbf{Q}_k = \begin{bmatrix} T_0^5/20 & T_0^4/8 & T_0^3/6 \\ T_0^4/8 & T_0^3/3 & T_0^2/2 \\ T_0^3/6 & T_0^2/2 & T_0 \end{bmatrix} \quad \mathbf{R}_k = [r]$$

The considered Kalman filter algorithm consists of two basic steps: prediction and correction.

The prediction step:

$$\hat{\mathbf{z}}_k^- = \mathbf{A}_k \hat{\mathbf{z}}_{k-1}^- - \text{predicted value of the state } \mathbf{z},$$

$$\mathbf{P}_k^- = \mathbf{A}_k \mathbf{P}_{k-1}^- \mathbf{A}_k^T + \mathbf{Q}_k - \text{predicted value of the covariance.}$$

The correction step:

$$\mathbf{K}_k = \mathbf{P}_k^- \mathbf{H}_k^T (\mathbf{H}_k \mathbf{P}_k^- \mathbf{H}_k^T + \mathbf{R}_k)^{-1} - \text{gain of the Kalman filter,}$$

$\hat{\mathbf{z}}_k = \hat{\mathbf{z}}_k^- + \mathbf{K}_k [w_x(k) - \mathbf{H}_k \hat{\mathbf{z}}_k^-]$ - optimal, estimated value of the state \mathbf{z} ($w_x(k)$ is the measured displacement value at kT_0 time step),

$$\mathbf{P}_k = (\mathbf{I} - \mathbf{K}_k \mathbf{H}_k) \mathbf{P}_k^- - \text{optimal, estimated value of the covariance (}\mathbf{I}\text{ is the identity matrix).}$$

The above algorithm has been implemented in form of a Simulink diagram. The Kalman filter was tested experimentally on the laboratory test rig. The tower-nacelle with MR TVA system was excited with a chirp-type force of amplitude 130 N applied at the point x_0 ($A(F) = 130$ N). The frequency was changing from 35 Hz to 1 Hz. Figures 4a and 4b present comparison of the displacements and velocities time responses of the tower-nacelle with MR TVA system determined from the experiment and estimated by the Kalman filter. The estimated velocity v_{x1} is compared to the one calculated by the Euler method.

Regarding the displacements, time responses practically coincide (Fig. 4a). Analysis of the velocity signals (Fig. 4b) shows the advantage of the Kalman filter over the simple-differential velocity calculation method.

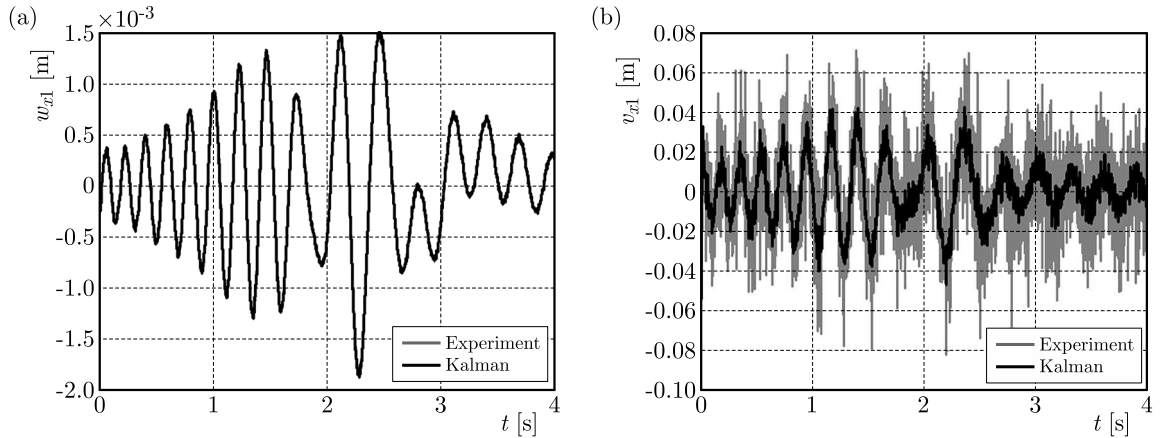


Fig. 4. Comparison of the time responses w_{x1} (a) and v_{x1} (b)

4.2. Linearization of the wind turbine tower-nacelle model

The purpose of the linearization procedure is to obtain a discrete linear model of tower-nacelle system only. The linearization procedure has been carried out using *Ident* tool from MATLAB *Optimization* toolbox. The main parameters for a black-box linear model of the *Ident* tool are set as follows (Ljung, 2015):

- Model structure: general linear state-space model of the 4th order.

- Focus: simulation which approximates dynamics of the model (the transfer function from measured inputs to outputs) with a norm that is given by the input spectrum.
- Estimating method: prediction-error minimization (PEM).

To start the linearization procedure, the reference data are required. These data, describing the relationship between w_{x1} , v_{x1} , w_{x0} , v_{x0} and the MR damper force P_{MR} , may be obtained by performing a simulation test using the nonlinear model of the tower-nacelle system with P_{MR} force as the input. Such a test has been carried out for free vibration of the tower-nacelle model with non-zero initial conditions for the w_{x1} , v_{x1} , w_{x0} and v_{x0} signals, and for the P_{MR} force changing randomly every 0.200 s in the range of ± 10 N. An exemplary P_{MR} pattern used for the linearization procedure is shown in Fig. 5. The continuous system was discretised using a zero-order hold with $T_0 = 0.001$ s.

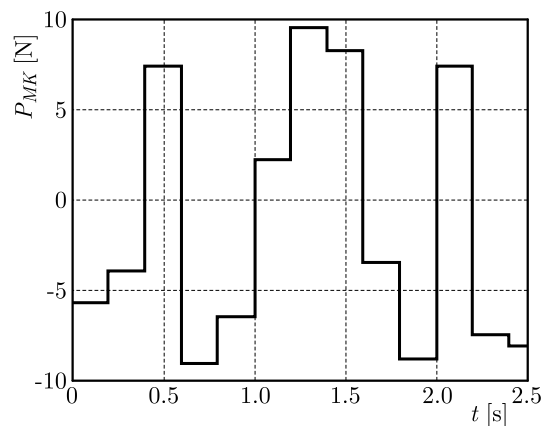


Fig. 5. An exemplary P_{MR} time pattern for the linearization

Figures 6 and 7 show comparison of the reference data (nonlinear model responses, solid lines) and linear model responses of the tower midpoint and tower tip (nacelle) displacements and velocities. The numbers indicating the best fit values are given below each figure (the maximum value is 100). As can be observed, the fit level is high – it exceeds the value of 90 for each state variable. Therefore, it can be concluded that the obtained linear model can be used to implement the LQG regulator.

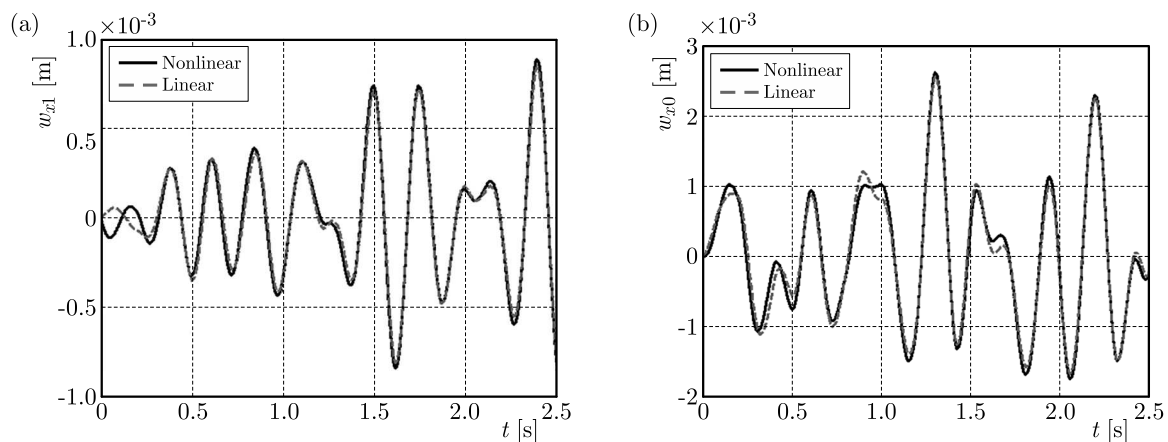


Fig. 6. Comparison of the responses w_{x1} (a) and w_{x0} (b) of nonlinear and linear models; best fits: 94.52 (a) and 95.73 (b)

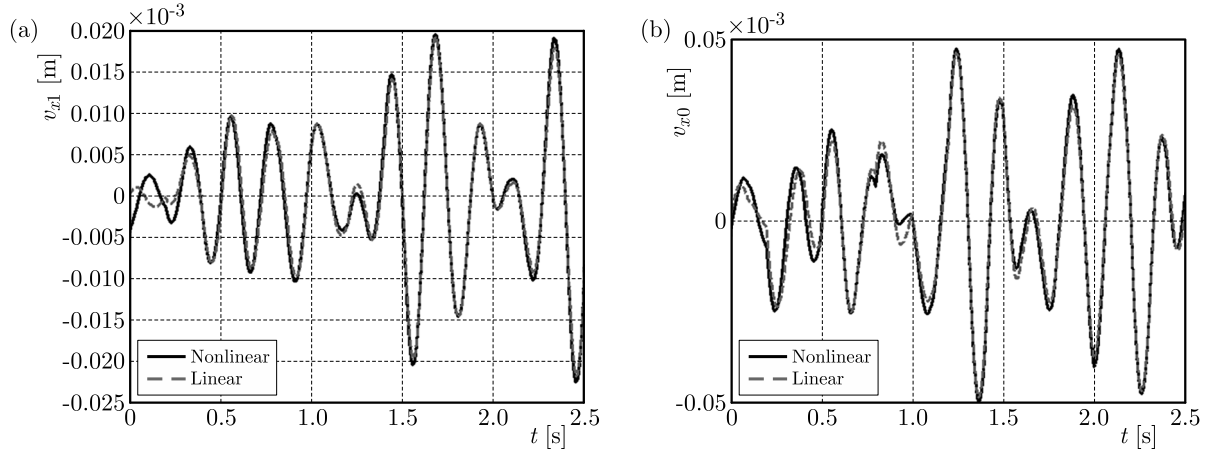


Fig. 7. Comparison of the responses v_{x1} (a) and v_{x0} of nonlinear and linear models; best fits: 94.16 (a) and 94.94 (b)

4.3. DLQR controller

The Discrete Linear-Quadratic Regulator (DLQR) is a state-feedback controller defined for a discrete-time state-space system. DLQR parameters are calculated by solving the optimal problem called the discrete LQR problem. This problem is defined for system dynamics described by a set of linear differential equations and a quadratic cost function.

In this paper, synthesis of a DLQR for a dynamical system described by equations (4.1) is presented. The DLQR optimization problem is solved using *dlqr.m* function (or *dlqry.m*) from MATLAB/Simulink *Optimization* toolbox. The *dlqr.m* function calculates the optimal gain matrix \mathbf{K}_d such that the state-feedback control $\mathbf{u}(k)$ (optimal MR damper force P_{MR})

$$\mathbf{u}(k) = -\mathbf{K}_d \mathbf{x}(k) \quad (4.4)$$

with the assumed state $\mathbf{x}(k) = [w_{x1}(k), v_{x1}(k), w_{x12}(k), v_{x12}(k)]^T$ (w_{x0} and v_{x0} are omitted here being proportional to $w_{x1}(k)$ and $v_{x1}(k)$, respectively, for the 1st bending mode frequency neighbourhood regarded), minimizes the quadratic cost function

$$J = \sum_{k=1}^{\infty} [\mathbf{x}^T(k) \mathbf{Q} \mathbf{x}(k) + \mathbf{u}^T(k) \mathbf{R} \mathbf{u}(k) + 2\mathbf{x}^T(k) \mathbf{N} \mathbf{u}(k)] \quad (4.5)$$

where: $\mathbf{Q} = \mathbf{Q}^T \geq \mathbf{0}$, $\mathbf{R} = \mathbf{R}^T > \mathbf{0}$ and $\mathbf{N} = \mathbf{N}^T \geq \mathbf{0}$.

The DLQR parameters are calculated for the following forms of the matrices \mathbf{Q} and \mathbf{R} , occurring in quality factor

$$\mathbf{Q} = \text{diag}[100, 10, 100, 10] \quad (4.6)$$

with different R values as shown below (denoted by the LQG1), and

$$\mathbf{Q} = \text{diag}[3000, 300, 300, 30] \quad (4.7)$$

with R equal to 0.0005 (denoted by LQG2). The \mathbf{N} matrix is set to zero for both LQG1 and LQG2.

The element values of matrices (4.6) and (4.7) are tuned with emphasis put on the stabilization of the tower-nacelle system position and limited MR damper stroke. Hence, Q_{11} and Q_{33} elements of matrices (4.6), (4.7) are ten times greater than elements Q_{22} and Q_{44} , respectively, while tower-nacelle stabilization purpose dominates over MR damper stroke limitation for LQG2 concept. The maximum control value is limited by the matrix \mathbf{R} .

As the results of calculations, the following values of the DLQR gain \mathbf{K}_d are achieved.

— LQG1 controller

$$\mathbf{K}_d = \begin{cases} \begin{bmatrix} -74.3077 & -11.0044 & -65.6904 & 275.6049 \end{bmatrix} & \text{for } R = 0.0001 \\ \begin{bmatrix} -45.75 & -5.32 & -46.26 & 184.99 \end{bmatrix} & \text{for } R = 0.0002 \\ \begin{bmatrix} -23.7730 & -2.2100 & -28.3578 & 104.9820 \end{bmatrix} & \text{for } R = 0.0005 \end{cases}$$

— LQG2 controller

$$\mathbf{K}_d = \begin{bmatrix} -179.81 & -59.13 & -29.48 & 289.19 \end{bmatrix}$$

In the next step, the DLQR controller and Kalman filter are integrated, forming the LQG controller. The integration stage has been executed according to the scheme shown in Fig. 8 (carets indicate estimates).

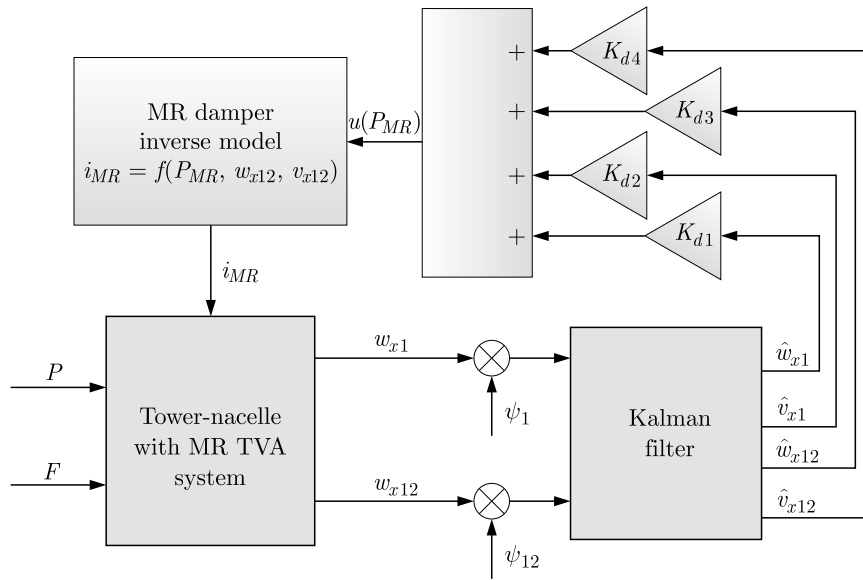


Fig. 8. Structure of the integrated LQG controller

5. Simulation analysis

Within the scope of the simulation analysis, time and frequency characteristics have been obtained. The latter, determined for sine excitation series applied either to the nacelle (excitation force amplitude equal to $A(P) = 61$ N) or to the tower midpoint ($A(F) = 150$ N) are presented below (Figures 9 and 10, see headers). Figures 9a and 10a present output frequency response functions of amplitude $A(w_{x0})$. Figures 9b and 10b show the output frequency response functions of amplitude $A(w_{x1})$. The information present in the legends of all the following figures has the respective meaning: ‘inv’ confirms incorporation of the MR damper inverse model, while ‘Fr’ refers to linear guides friction force (of ca. 1 N) compensation by the MR damper (both of them as described in Section 2).

As can be observed, the $A(w_{x1})$ amplitude output frequency response functions present ca. three times greater values than the respective $A(w_{x0})$ functions. For LQG1 case, an increase in the control weighting value R results in lower feedback gain vector \mathbf{K}_d modulus, and so in less stiffness and less damping present between the protected structure and the absorber. This, in turn, is apparent as higher two maxima amplitudes and lower in-between the two

maxima response. The LQG2 case, characterised with higher weights in Q (especially the weights concerning the tower tip displacement w_{x1} and velocity v_{x1}) and $R = 0.0005$, produces frequency response functions similar to LQG1 controller with the lowest R ($R = 0.0001$).

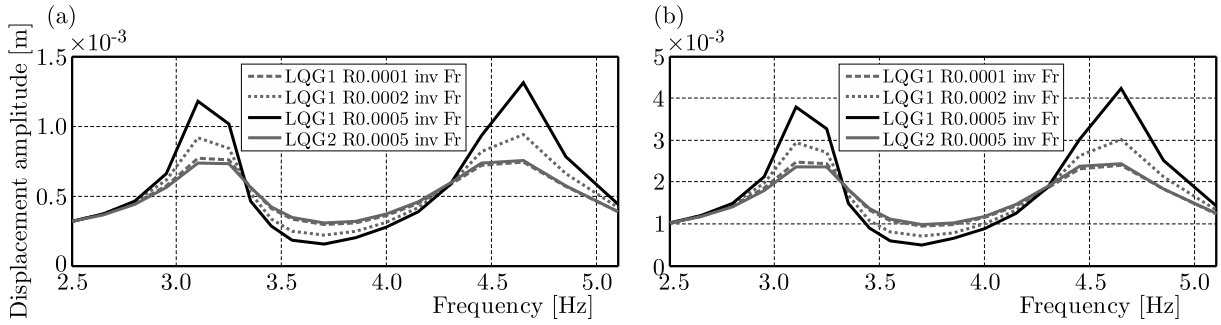


Fig. 9. (a) $A(w_{x0})$ and (b) $A(w_{x1})$ output frequency responses; $A(P) = 61\text{ N}$

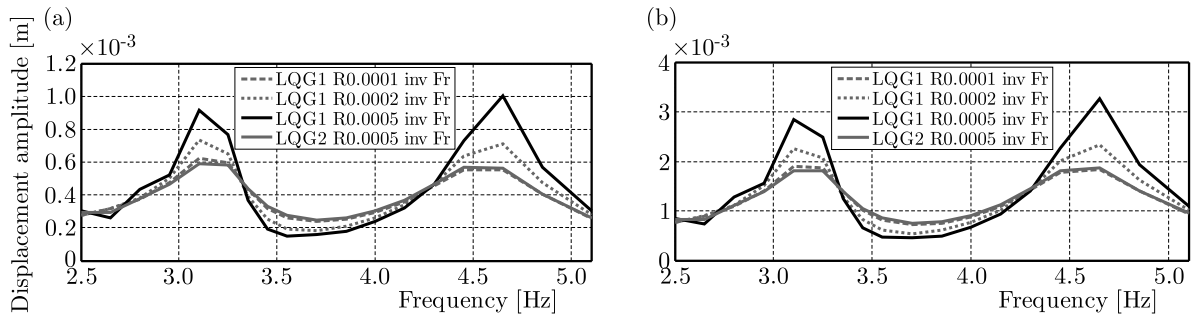


Fig. 10. (a) $A(w_{x0})$ and (b) $A(w_{x1})$ output frequency responses; $A(F) = 150\text{ N}$

6. Experimental analysis

The experimental analysis comprised determination of time and frequency characteristics. The first was a free response test of displacement w_{x1} , obtained for the MR TVA system with selected LQG controllers and the system with MR TVA ‘locked’ (Fig. 11). According to the

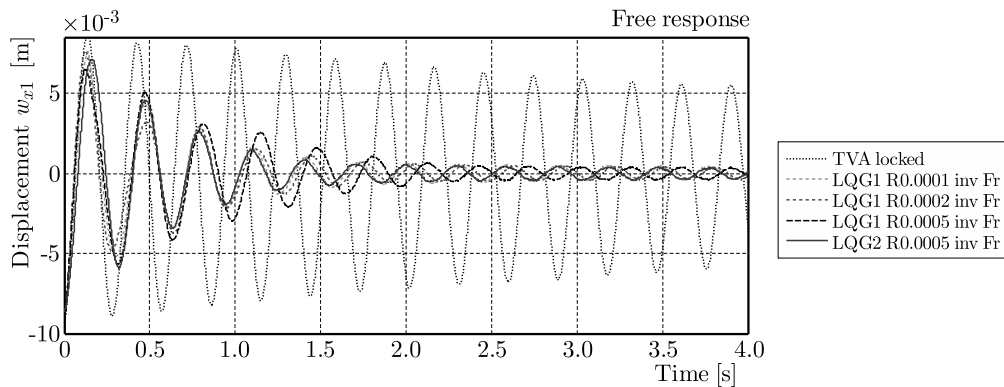


Fig. 11. Time series of displacement w_{x1} – free response of the MR TVA system with LQG controllers and the system with MR TVA ‘locked’

constraints of the laboratory facility, the frequency characteristics (Figs. 12-14) were determined for sine excitation series applied either to the nacelle ($A(P) = 61\text{ N}$; LQG1 system with $R = 0.0001$ and $R = 0.0002$) or to the tower midpoint ($A(F) = 150\text{ N}$; LQG1 and LQG2 systems with $R = 0.0005$). Figures 12a and 13a present the output frequency response functions

of $A(w_{x_0})$ amplitude. Figures 12b and 13b present the output frequency response functions of $A(w_{x_1})$ amplitude. Figure 14 presents output frequency response functions of $A(w_{x_0})$ and $A(w_{x_1})$ amplitudes for the system without TVA (MR TVA ‘locked’).

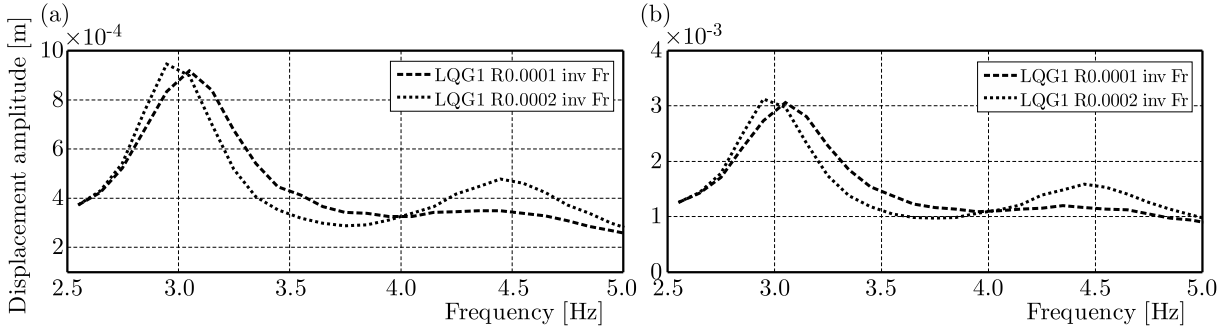


Fig. 12. (a) $A(w_{x_0})$ and (b) $A(w_{x_1})$ output frequency responses; $A(P) = 61$ N

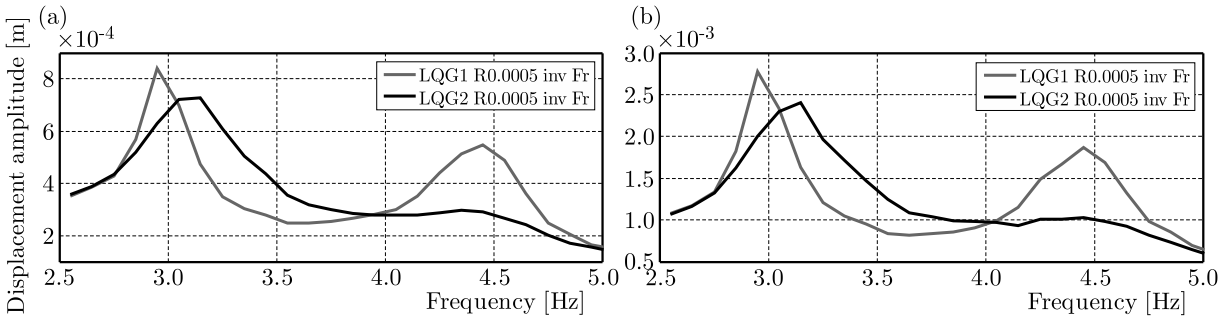


Fig. 13. (a) $A(w_{x_0})$ and (b) $A(w_{x_1})$ output frequency responses; $A(F) = 150$ N

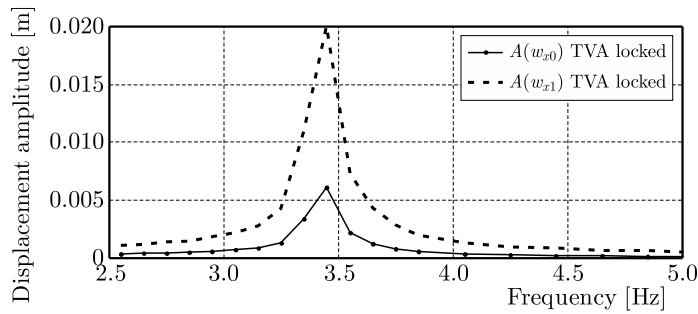


Fig. 14. $A(w_{x_0})$ and $A(w_{x_1})$ output frequency responses; $A(F) = 150$ N

Observing the free response plots, one can conclude that LQG1 algorithm with $R = 0.0001$ and LQG2 algorithm with $R = 0.0005$ provide the best vibration attenuation properties. Regarding the frequency analysis, as for simulations, the $A(w_{x_1})$ amplitude output frequency response functions exhibit ca. three times greater values than the respective $A(w_{x_0})$ functions. LQG1 algorithm with $R = 0.0001$ and $R = 0.0002$ produces comparable results for the excitation series applied to the nacelle, with two maxima apparent for $R = 0.0002$ case. For the excitation applied to the tower midpoint, LQG1 and LQG2 algorithms (both with $R = 0.0005$ weighting value) collation may suggest the latter solution (LQG2) to be preferable, with noticeably lower two maxima amplitudes; however, in-between the two maxima range is better attenuated for LQG1.

7. Conclusion

The obtained results prove the effectiveness of the LQG controller for the considered application. On the basis of the laboratory experiments, almost 10-fold reduction of the displacement w_{x1} amplitude has been observed for the LQG2 system in comparison to the system without MR TVA (TVA ‘locked’) – see Figs. 13b and 14. Implementation of the LQG controller combines the benefits of the LQR state feedback (including system linearization) with noise compensation by the Kalman filter.

Based on the analyses, simulations and laboratory model measurements presented in this paper, and considering force scale factor determination (Snamina and Martynowicz, 2014) in combination with the previous results (Snamina *et al.*, 2014), direct calculation of demanded control signal for a real-world full scale vibration reduction system/MR TVA is possible as well as the calculation of the real-world wind turbine structural deflection and acceleration amplitudes, as for Vensys 82 plant regarded (Martynowicz, 2015).

Acknowledgment

This work has been supported by the Polish National Science Centre (Narodowe Centrum Nauki) under project No. 2286/B/T02/2011/40.

References

1. ASAI T., SPENCER JR. B.F., 2014, Model-free algorithms for seismic response control employing controllable dampers, *Proceedings of the VI World Conference on Structural Control and Monitoring*, Barcelona
2. ASAI T., SPENCER JR. B.F., IEMURA H., CHANG C.-M., 2013, Nature of seismic control force in acceleration feedback, *Structural Control and Health Monitoring*, **20**, 789-803
3. ATHANS M., 1971, The role and use of the stochastic linear-quadratic-Gaussian problem in control system design, *IEEE Transaction on Automatic Control*, **16**, 6, 529-552
4. BAK C., BITSCHKE R., YDE A., KIM T., HANSEN M.H., ZAHLE F., GAUNAA M., BLASQUES J., DOSSING M., WEDEL-HEINEN J.-J., BEHRENS T., 2012, Light rotor: the 10-MW reference wind turbine, *European Wind Energy Association Annual Event*, 16-19.04, Copenhagen, Denmark
5. BUTT U.A., ISHIHARA T., 2012, Seismic load evaluation of wind turbine support structures considering low structural damping and soil structure interaction, *European Wind Energy Association Annual Event*, 16-19.04, Copenhagen, Denmark
6. COMSOL AB, 2008, *COMSOL Multiphysics MATLAB Interface Guide*, COMSOL Version 3.5a, November
7. DEN HARTOG J.P., 1985, *Mechanical Vibrations*, Dover Publications, Mineola, NY
8. DYKE S.J., SPENCER JR. B.F., SAIN M.K., CARLSON J.D., 1996a, A new semi-active control device for seismic response reduction, *Proceedings of the 11th ASCE Engineering Mechanics Specialty Conference*, 886-889
9. DYKE S.J., SPENCER JR. B.F., SAIN M.K., CARLSON J.D., 1996b, Modeling and control of magnetorheological dampers for seismic response reduction, *Smart Materials and Structures*, **5**, 5, 565-575
10. ENEVOLDSEN I., MORK K.J., 1996, Effects of vibration mass damper in a wind turbine tower, *Mechanics of Structures and Machines*, **24**, 2, 155-187
11. FAVOREEL W., DE MOOR B., GEVERS M., VAN OVERSCHEE P., 1999, Closed loop model-free subspace-based LQG-design, *Proceedings of the 7th Mediterranean Conference on Control and Automation (MED99)*, Haifa, Israel, 1926-1939

12. HANSEN M.H., FUGLSANG P., THOMSEN K., KNUDSEN T., 2012, Two methods for estimating aeroelastic damping of operational wind turbine modes from experiments, *European Wind Energy Association Annual Event*, 16-19.04, Copenhagen, Denmark
13. HJALMARSSON H., GEVERS M., GUNNARSSON S., LEQUIN O., 1998, Iterative feedback tuning: theory and applications, *IEEE Control Systems Magazine*, **18**, 26-4.
14. JAIN P., 2011, *Wind Energy Engineering*, McGraw-Hill
15. JELAVIĆ M., PERIĆ N., PETROVIĆ I., 2007, Damping of wind turbine tower oscillations through rotor speed control, *EVER Conference 2007*, March 29-April 1, Monaco
16. KAWAMURA Y., 1998, Direct construction of LQ regulator based on orthogonalization of signals: Dynamical output feedback, *Systems and Control Letters*, **34**, 1-9
17. KCIUK S., MARTYNOWICZ P., 2011, Special application magnetorheological valve numerical and experimental analysis, [In:] *Diffusion and Defect Data – Solid State Data. Pt. B, Solid State Phenomena, Vol. 177: Control Engineering in Materials Processing*, 102-115
18. KIRKEGAARD P.H. ET AL., 2002, Semiactive vibration control of a wind turbine tower using an MR damper, *Structural Dynamics EUROODYN 2001*, H. Grundmann (Edit.), CRC Press
19. KOO J.H., AHMADIAN M., 2007, Qualitative analysis of magneto-rheological tuned vibration absorbers: experimental approach, *Journal of Intelligent Material Systems and Structures*, **18**
20. ŁATAS W., MARTYNOWICZ P., 2012, Modelling of vibration of the tower-nacelle system of a wind power plant with a dynamic damper (in Polish), *Modelowanie Inżynierskie*, **13**, 44, 187-198
21. LJUNG L., 2015, System Identification Toolbox™. User's Guide, MATLAB&Simulink R2015a, The MathWorks Inc., USA
22. Lord Rheonetic, 2002, MR Controllable Friction Damper RD-1097-01 Product Bulletin
23. MARTYNOWICZ P., 2014a, Development of laboratory model of wind turbine's tower-nacelle system with magnetorheological tuned vibration absorber, *Solid State Phenomena*, **208**, 40-51
24. MARTYNOWICZ P., 2014b, Wind turbine's tower-nacelle model with magnetorheological tuned vibration absorber – numerical and experimental analysis, *6WCSCM: Proceedings of the 6th Edition of the World Conference of the International Association for Structural Control and Monitoring (IACSM)*, 15-17.07, Barcelona, Spain
25. MARTYNOWICZ P., 2015, Vibration control of wind turbine tower-nacelle model with magnetorheological tuned vibration absorber, *Journal of Vibration and Control*, doi: 10.1177/1077546315591445
26. MARTYNOWICZ P., 2016, Study of vibration control using laboratory test rig of wind turbine tower-nacelle system with MR damper based tuned vibration absorber, *Bulletin of the Polish Academy of Sciences Technical Sciences*, **64**, 2, 347359
27. MARTYNOWICZ P., SZYDŁO Z., 2013, Wind turbine's tower-nacelle model with magnetorheological tuned vibration absorber: the laboratory test rig, *Proceedings of the 14th International Carpathian Control Conference (ICCC)*, 26-29.05, Rytro, Poland
28. MATACHOWSKI F., MARTYNOWICZ P., 2012, Analysis of dynamics of a wind power plant by making use of Comsol Multiphysics environment (in Polish), *Modelowanie Inżynierskie*, **13**, 44, 209-216
29. NAMIK H., AND STOL K., 2011, Performance analysis of individual blade pitch control of offshore wind turbines on two floating platforms, *Mechatronics*, **21**, 691-703
30. OH S., ISHIHARA T., 2013, A study on structure parameters of an offshore wind turbine by excitation test using active mass damper, *EWEA Offshore*, 19-21.11, Frankfurt
31. ROTEA M.A., LACKNER M.A., SAHEBA R., 2010, Active structural control of offshore wind turbines, *48th AIAA Aerospace Sciences Meeting Including the New Horizons Forum and Aerospace Exposition*, 4-7.01, Orlando, Florida

32. SAPIŃSKI B., MARTYNOWICZ P., 2005, Vibration control in a pitch-plane suspension model with MR shock absorbers, *Journal of Theoretical and Applied Mechanics*, **43**, 3.
33. SAPIŃSKI B., ROSÓŁ M., 2007, MR damper performance for shock isolation, *Journal of Theoretical and Applied Mechanics*, **45**, 1, 133-146
34. SAPIŃSKI B., ROSÓŁ M., 2008, Autonomous control system for a 3 DOF pitch-plane suspension model with MR shock absorbers, *Computers and Structures*, **86**, 3/5, 379-385
35. SHAN W., SHAN M., 2012, Gain scheduling pitch control design for active tower damping and 3p harmonic reduction, *European Wind Energy Association Annual Event*, 16-19.04, Copenhagen, Denmark
36. SINGHAL T., HARIT AKSHAT, VISHWAKARMA D.N., 2012, Kalman filter implementation on an accelerometer sensor data for three state estimation of a dynamic system, *International Journal of Research in Engineering and Technology*, **1**, 6, ISSN 2277-4378
37. SNAMINA J., MARTYNOWICZ P., 2014, Prediction of characteristics of wind turbine's tower-nacelle system from investigation of its scaled model, *6WCSCM: Proceedings of the 6th Edition of the World Conference of the International Association for Structural Control and Monitoring (IACSM)*, 15-17.07, Barcelona, Spain
38. SNAMINA J., MARTYNOWICZ P., ŁATAS W., 2014, Dynamic similarity of wind turbine's Tower-nacelle system and its scaled model, *Solid State Phenomena*, **208**, 29-39
39. SNAMINA J., SAPIŃSKI B., 2011, Energy balance in self-powered MR damper-based vibration reduction system, *Bulletin of the Polish Academy of Sciences Technical Sciences*, **59**, 1, 75-80
40. TMS, 2010, 60 Lbf Modal Shaker, The Modal Shop Inc.
41. TSOUROUKDISSIAN A., CARCANGIU C.E., PINEDA AMO I., MARTIN M., FISCHER T., KUHNLE B., SCHEU M., 2011, Wind turbine tower load reduction using passive and semiactive dampers, *European Wind Energy Association Annual Event*, Brussels
42. WANG Y., DYKE S., 2013, Modal-based LQG for smart base isolation system design in seismic response control, *Structural Control and Health Monitoring*, **20**, 5, 753-768

Manuscript received May 13, 2015; accepted for print January 27, 2016

ON SOME PROBLEMS OF SH WAVE PROPAGATION IN INHOMOGENEOUS ELASTIC BODIES

SEBASTIAN KOWALCZYK, STANISŁAW J. MATYSIAK

*University of Warsaw, Faculty of Geology, Institute of Hydrogeology and Engineering Geology, Warszawa, Poland
e-mail: s.j.matysiak@uw.edu.pl*

DARIUSZ M. PERKOWSKI

Białystok University of Technology, Faculty of Mechanical Engineering, Białystok, Poland

The paper deals with the propagation of shear horizontal (SH) waves in a nonhomogeneous elastic half-space composed of a layer whose shear modulus and mass density have a power dependence on the distance from the lower plane and the periodically stratified half-space. The equation which relates the wave speed to the wave-number and functions of the shear modulus and mass density is derived. The wave velocity is analyzed numerically. Especially, the influence of mechanical properties of the coating layer and the stratified foundation on the wave velocity is presented in the form of figures.

Keywords: displacement, stresses, SH wave, shear modulus, stratified foundation

1. Introduction

The phenomena of wave propagations through the Earth is useful in investigating the internal Earth structure, and it can be helpful in explorations of various materials beneath the Earth's surface. It is well known that the Earth is not perfectly homogeneous and some forms of inhomogeneity exist. Many rocks and soils are stratified and clearly piece-wise homogeneous. Some layers are characterized by mechanical parameters with continuous changing in spatial directions (called as functionally graded materials). The problems of modeling of wave propagations in inhomogeneous elastic bodies play a very important role in applied geophysics civil and mechanical engineering (space structures, fusion reactors). The list of references connected with the problems of wave propagations in inhomogeneous elastic bodies is rather very large (for instance monographs by Birykov *et al.* (1995), Brekhovskikh (1960), Kennet (1983), Nayfeh (1995); papers by Achenbach and Balogun (2010), Alenitsyn (1964), Alshits and Maugin (2005), Cerveny *et al.* (1982), Destrade (2007), Shuvalov *et al.* (2008), Vrettos (1990)). Achenbach and Balogun (2010) dealt with the propagation of anti-plane shear waves in an elastic half-space whose shear modulus and mass density had an arbitrary dependence on the distance from the boundary plane. Alenitsyn (1964) considered the problem of Rayleigh waves in a nonhomogeneous elastic slab. Alshits and Maugin (2005) developed a theory for the elastic wave propagation in an arbitrary layered plane (piece-wise homogeneous or continuously inhomogeneous). The description was based on the transfer matrix approach. The Gaussian beam method of the solution of wave propagation problems in inhomogeneous bodies was applied by Cerveny *et al.* (1982). The seismic Rayleigh waves in an orthotropic elastic half-space with an exponentially graded properties were considered by Destrade (2007). Shuvalov *et al.* (2008) presented some analysis of the problem of shear horizontal waves in transversely inhomogeneous plates. Surface harmonic vibrations of soil deposits with variable shear modulus were analysed by Vrettos (1990).

The problem of SH-wave propagation in anisotropic inhomogeneous layer with directional rigidities and density of mass changing as a power function was investigated by Upadhyay and

Gupta (1972). The authors assumed that the outer layer was fixed to an isotropic homogeneous elastic half-space or to the rigid substrate.

The present paper is concerned with the case of a shear horizontal (SH) wave in an inhomogeneous elastic layer which is assumed to be ideally fixed to a periodically stratified elastic half-space, and the upper boundary plane is free of loadings. The considered layer is characterized by the shear modulus and mass density in the form of power functions of the distance from the lower boundary plane. The substrate is assumed to be composed of periodically repeated two-layered laminae parallel to the boundary plane. Each component of the lamina is a homogeneous and isotropic body. The assumptions connected with the ideal bonding of the components on interfaces lead to a complicated boundary value problem within the framework of the classical theory of elasticity. For this reason, the classic idea is the use of the approximate procedure to replace the heterogeneous medium by an equivalent homogenized model, which gives the average behavior at the macroscopic scale. One of them is the homogenized model with microlocal parameters presented by Matysiak and Woźniak (1987, 1988). This model is derived by using the methods of the nonstandard analysis and taking into account the effects due to the periodic structure of the body. The governing equations of the model are formulated in terms of the unknown macro-displacements and certain extra unknowns being referred to as microlocal parameters. They are described by a relatively simple form of the equations satisfying the conditions of perfect interfacial bonding of constituents. The homogenized model has been successfully applied to a series of problems of the linear elasticity and thermoelasticity (problems of cracks, cavities, inclusions, contact problems, wave propagations), which it was partially resumed in (Matysiak, 1996; Woźniak and Woźniak, 1995). It should be underlined that the homogenization approach has been noticed to produce good physical results, at the same time being rather simple in mathematical aspects (Kulchytsky-Zhyhailo and Kołodziejczyk, 2007; Kulchytsky-Zhyhailo and Matysiak, 2005, 2006; Kulchytsky-Zhyhailo *et al.*, 2006). The wave problems in a periodically layered elastic half-space were investigated by Bielski and Matysiak (1992), Matysiak *et al.* (2009). The same dependence of the shear modulus is taken into account in many papers (see for instance Calladine and Greenwood, 1978; Wang *et al.*, 2003). The same dependence of the shear modulus of the coating layer is considered in the present paper. The distributions of displacements and stresses in an inhomogeneous incompressible elastic half-space caused by line and point loads are considered in (Cerveny *et al.*, 1982). The propagation of surface waves in a linear-elastic, isotropic, compressible half-space with constant mass density and Poisson's ratio and shear modulus varying with depth is considered in (Vrettos, 1990). The useful list of dependence forms for elastic modulus is presented by Wang *et al.* (2003).

2. Formulation and solution of the problem

Consider the problem of shear waves propagation in an elastic nonhomogeneous layer and periodically layered half-space. Let (x_1, x_2, x_3) denote the Cartesian coordinate system such that the layer occupies the region $x_1 \in R$, $0 \leq x_2 \leq H$, $x_3 \in R$, where $H > 0$ is constant thickness of the FGM body, Fig. 1.

Let the upper boundary plane $x_2 = H$ be free of loadings, and the layer is ideally fixed to the periodically two-layered half-space in the plane $x_2 = 0$. Let the stratified half-space be composed of periodically repeated fundamental laminae with thickness δ , which include two homogeneous isotropic sub-layers denoted by 1 and 2 with thicknesses δ_j , $j = 1, 2$, and $\delta = \delta_1 + \delta_2$. Let μ_j , ρ_j , $j = 1, 2$ be the shear modulus and mass densities of the subsequent constituents of the composite half-space. Herein and in the sequel, all quantities (material components, stresses) pertaining to sub-layer 1 and 2 will be labeled by the index j taking values 1 and 2, respectively. The

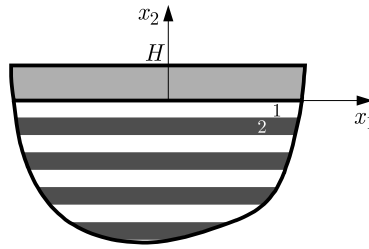


Fig. 1. Scheme of the considered SH problem

considerations are limited to the anti-plane harmonic wave propagation in the $0x_1$ direction. Let $\mathbf{u}(x_1, x_2, t) = (0, 0, u_3(x_1, x_2, t))$ be the displacement vector, where t denotes time. The shear modulus μ and mass density ρ of the upper layer are assumed the same as in (Upadhyay and Gupta, 1972), namely

$$\mu = \mu_0(1 + \alpha x_2)^p \quad \rho = \rho_0(1 + \alpha x_2)^p \tag{2.1}$$

where μ_0, ρ_0, α, p are given constants.

The non-zero stress components σ_{13} and σ_{23} in the coating layer are expressed in the form

$$\begin{aligned} \sigma_{13}(x_1, x_2, t) &= \mu_0(1 + \alpha x_2)^p \frac{\partial u_3(x_1, x_2, t)}{\partial x_1} \\ \sigma_{23}(x_1, x_2, t) &= \mu_0(1 + \alpha x_2)^p \frac{\partial u_3(x_1, x_2, t)}{\partial x_2} \end{aligned} \tag{2.2}$$

The anti-plane wave motion is governed by the following equation

$$\frac{\partial \sigma_{13}}{\partial x_1} + \frac{\partial \sigma_{23}}{\partial x_2} = \rho_0(1 + \alpha x_2)^p \frac{\partial^2 u_3}{\partial t^2} \quad x_1 \in R \quad 0 < x_2 < H \tag{2.3}$$

where the body forces are omitted. From equations (2.2) and (2.3), it follows that

$$\frac{\partial^2 u_3}{\partial x_1^2} + \frac{\alpha p}{1 + \alpha x_2} \frac{\partial u_3}{\partial x_2} + \frac{\partial^2 u_3}{\partial x_2^2} = \frac{\rho_0}{\mu_0} \frac{\partial^2 u_3}{\partial t^2} \quad x_1 \in R \quad 0 < x_2 < H \quad t \in R \tag{2.4}$$

To determine the displacement and stresses in the periodically layered half-space $x_2 < 0$, the homogenized model with microlocal parameters (Bielski and Matysiak, 1992; Kulchytsky-Zhyhailo and Kołodziejczyk, 2007; Kulchytsky-Zhyhailo and Matysiak, 2005, 2006; Kulchytsky-Zhyhailo *et al.*, 2006; Matysiak *et al.*, 2009; Matysiak and Woźniak, 1987, 1988) is applied. Here only a brief outline of the governing equations for the case of anti-plane state of strain will be presented. The homogenized procedure presented by Matysiak and Woźniak (1987, 1988) is based on theorems of the nonstandard analysis and some physical assumptions, which leads, in the case of anti-plane state of strain, to the following approximations

$$\begin{aligned} u_3(x_1, x_2, t) &= w_3(x_1, x_2, t) + h(x_2)q_3(x_1, x_2, t) \approx w_3(x_1, x_2, t) \\ \frac{\partial u_3(x_1, x_2, t)}{\partial x_1} &\approx \frac{\partial w_3(x_1, x_2, t)}{\partial x_1} \quad \frac{\partial u_3(x_1, x_2, t)}{\partial t} \approx \frac{\partial w_3(x_1, x_2, t)}{\partial t} \\ \frac{\partial u_3(x_1, x_2, t)}{\partial x_2} &\approx \frac{\partial w_3(x_1, x_2, t)}{\partial x_2} + h'(x_2)q_3(x_1, x_2, t) \end{aligned} \tag{2.5}$$

where w_3, q_3 are unknowns called macro-displacement and microlocal parameters, respectively. The function h (called the shape function) is given in the form

$$\begin{aligned} h(x_2) &= \begin{cases} x_2 - \frac{1}{2}\delta_1 & \text{for } 0 \leq x_2 \leq \delta_1 \\ -\frac{\eta x_2}{1 - \eta} - \frac{1}{2}\delta_1 + \frac{\delta_1}{1 - \eta} & \text{for } \delta_1 \leq x_2 \leq \delta \end{cases} \\ h(x_2 + \delta) &= h(x_2) \end{aligned} \tag{2.6}$$

and

$$\eta = \frac{\delta_1}{\delta} \quad (2.7)$$

Since $|h(x_2)| < \delta$ for every $x_2 \in R$, then for small δ the terms with h in equations (2.5) are small and are neglected. However, the derivative h' is not small and the terms involving h' cannot be neglected. The form of the shape function h given in (2.6) secures the fulfilment of the conditions of ideal bonding on the composite interfaces. The homogenized model presented by Matysiak and Woźniak (1987, 1988) in the case of anti-plane state of strain leads to the following equations for the unknowns w_3 and q_3

$$\tilde{\mu} \left(\frac{\partial^2 w_3}{\partial x_1^2} + \frac{\partial^2 w_3}{\partial x_2^2} \right) + [\mu] \frac{\partial q_3}{\partial x_2} = \tilde{\rho} \frac{\partial^2 w_3}{\partial t^2} \quad \hat{\mu} q_3 + [\mu] \frac{\partial w_3}{\partial x_2} = 0 \quad (2.8)$$

where

$$\begin{aligned} \tilde{\rho} &= \eta \rho_1 + (1 - \eta) \rho_2 & \tilde{\mu} &= \eta \mu_1 + (1 - \eta) \mu_2 \\ [\mu] &= \eta (\mu_1 - \mu_2) & \hat{\mu} &= \eta \mu_1 + \frac{\eta^2 \mu_2}{1 - \eta} \end{aligned} \quad (2.9)$$

The non-zero stress components $\sigma_{13}^{(j)}$, $\sigma_{23}^{(j)}$, $j = 1, 2$ in the layer of j -th kind are expressed in the form

$$\sigma_{13}^{(j)} = \mu_j \frac{\partial w_3}{\partial x_1} \quad \sigma_{23}^{(j)} = \mu_j \left(\frac{\partial w_3}{\partial x_2} + h'(x_2) q_3 \right) \quad (2.10)$$

Eliminating the microlocal parameter q_3 from (2.8)₁ (2.10) by using (2.8)₂, leads to the equations

$$\tilde{\mu} \frac{\partial^2 w_3}{\partial x_1^2} + C \frac{\partial^2 w_3}{\partial x_2^2} = \tilde{\rho} \frac{\partial^2 w_3}{\partial t^2} \quad (2.11)$$

and

$$\sigma_{13}^{(j)} = \mu_j \frac{\partial w_3}{\partial x_1} \quad \sigma_{23}^{(j)} = C \frac{\partial w_3}{\partial x_2} \quad j = 1, 2 \quad (2.12)$$

where

$$C = \tilde{\mu} - \frac{[\mu]^2}{\hat{\mu}} = \frac{\mu_1 \mu_2}{(1 - \eta) \mu_1 + \eta \mu_2} > 0 \quad (2.13)$$

The following boundary conditions are taken into consideration:

a) on the upper boundary of the FGM layer

$$\sigma_{23}(x_1, H, t) = 0 \quad x_1 \in R \quad t \in R \quad (2.14)$$

b) on the interface $x_2 = 0$ between the FGM layer and the periodically stratified half-space

$$\begin{aligned} u_3(x_1, 0^+, t) &= w_3(x_1, 0^-, t) & \sigma_{23}(x_1, 0^+, t) &= \sigma_{23}^{(1)}(x_1, 0^-, t) \\ x_1 \in R & & t \in R & \end{aligned} \quad (2.15)$$

c) the regularity condition at infinity

$$\lim_{x_2 \rightarrow -\infty} w_3(x_1, x_2, t) = 0 \quad (2.16)$$

Let us consider a SH wave solution of the form

$$u_3(x_1, x_2, t) = U_3(x_2)e^{ik(x_1-ct)} \quad w_3(x_1, x_2, t) = W_3(x_2)e^{ik(x_1-ct)} \quad (2.17)$$

where $i = \sqrt{-1}$, U_3 and W_3 are unknown amplitude of displacement in the outer layer and the periodically layered half-space, respectively, and k and c are the wave number and the phase velocity, respectively. By using equations (2.4) and (2.11) and (2.17), an ordinary differential equation are obtained

$$\frac{d^2U_3(x_2)}{dx_2^2} + \frac{\alpha p}{1 + \alpha x_2} \frac{dU_3(x_2)}{dx_2} + k^2 \left(\frac{c^2}{c_0^2} - 1 \right) U_3(x_2) = 0 \quad 0 < x_2 < H \quad (2.18)$$

and

$$\frac{d^2W_3(x_2)}{dx_2^2} + \frac{k^2}{C} (\tilde{\rho}c^2 - \tilde{\mu}) W_3(x_2) = 0 \quad x_2 < 0 \quad (2.19)$$

where

$$c_0^2 = \frac{\mu_0}{\rho_0} \quad (2.20)$$

The ordinary differential equation of the second order with variable coefficients (2.18) belongs to well-known type (Kamke, 1976, p. 401). Its general solution has the form

$$U_3(x_2) = (1 + \alpha x_2)^{\frac{1-p}{2}} \left[A_1 J_{\frac{|1-p|}{2}} \left(q \left(\frac{1}{\alpha} + x_2 \right) \right) + A_2 Y_{\frac{|1-p|}{2}} \left(q \left(\frac{1}{\alpha} + x_2 \right) \right) \right] \quad 0 < x_2 < H \quad (2.21)$$

where

$$q^2 = k^2 \left(\frac{c^2}{c_0^2} - 1 \right) \quad (2.22)$$

on the assumption that $c > c_0$, and A_1, A_2 are unknown constants, which should be determined from boundary conditions (2.5), and $J_{|1-p|/2}(\cdot), Y_{|1-p|/2}(\cdot)$ are Bessel functions. Equations (2.19) and (2.17) with condition (2.16) lead to the following solution

$$W_3(x_2) = A_3 \exp(\beta x_2) \quad x_2 < 0 \quad \beta^2 = \frac{k^2 \tilde{\mu}}{C} \left(1 - \frac{c^2}{\tilde{c}^2} \right) \quad \tilde{c}^2 = \frac{\tilde{\mu}}{\tilde{\rho}} \quad (2.23)$$

on the assumption that $c < \tilde{c}$ and A_3 is an unknown constant. The constant A_1, A_2, A_3 should be calculated from boundary conditions (2.14) and (2.15).

The further analysis needs to take into consideration two cases: $p \leq 1$ and $p > 1$.

Case 1

Consider that

$$p \leq 1 \quad \text{so} \quad |1 - p| = 1 - p \quad (2.24)$$

To determine the stress component σ_{23} , the following differential relations for the Bessel functions should be applied (Lebediev, 1957)

$$\frac{dz^\nu J_\nu(z)}{dz} = z^\nu J_{\nu-1}(z) \quad \frac{dz^\nu Y_\nu(z)}{dz} = z^\nu Y_{\nu-1}(z) \quad (2.25)$$

Bearing in mind equations (2.2), (2.17), (2.21) and (2.24), it follows that the stress component σ_{23} is expressed in the form

$$\sigma_{23}(x_1, x_2, t) = q\mu_0(1 + \alpha x_2)^{\frac{1+p}{2}} \left[A_1 J_{\frac{-1-p}{2}} \left(q \left(\frac{1}{\alpha} + x_2 \right) \right) + A_2 Y_{\frac{-1-p}{2}} \left(q \left(\frac{1}{\alpha} + x_2 \right) \right) \right] e^{ik(x_1 - ct)} \quad (2.26)$$

where $0 < x_2 < H$.

From boundary condition (2.14) and conditions of continuity (2.15) as well as equations (2.26), (2.17), (2.23), (2.12), (2.21), the following algebraic equations for the unknowns A_1 , A_2 , A_3 are obtained

$$\begin{aligned} A_1 J_{\frac{-1-p}{2}} \left(q \left(\frac{1}{\alpha} + H \right) \right) + A_2 Y_{\frac{-1-p}{2}} \left(q \left(\frac{1}{\alpha} + H \right) \right) &= 0 \\ A_1 J_{\frac{1-p}{2}} \left(\frac{q}{\alpha} \right) + A_2 Y_{\frac{1-p}{2}} \left(\frac{q}{\alpha} \right) &= A_3 \\ \mu_0 q \left[A_1 J_{\frac{-1-p}{2}} \left(\frac{q}{\alpha} \right) + A_2 Y_{\frac{-1-p}{2}} \left(\frac{q}{\alpha} \right) \right] &= C\beta A_3 \end{aligned} \quad (2.27)$$

Eliminating A_3 from the system of equations (2.27), it follows that

$$\begin{aligned} A_1 J_{\frac{-1-p}{2}} \left(q \left(\frac{1}{\alpha} + H \right) \right) + A_2 Y_{\frac{-1-p}{2}} \left(q \left(\frac{1}{\alpha} + H \right) \right) &= 0 \\ A_1 \left[\mu_0 q J_{\frac{-1-p}{2}} \left(\frac{q}{\alpha} \right) - C\beta J_{\frac{1-p}{2}} \left(\frac{q}{\alpha} \right) \right] + A_2 \left[\mu_0 q Y_{\frac{-1-p}{2}} \left(\frac{q}{\alpha} \right) - C\beta Y_{\frac{1-p}{2}} \left(\frac{q}{\alpha} \right) \right] &= 0 \end{aligned} \quad (2.28)$$

The system of algebraic equations (2.28) has a non-zero solution under the following condition

$$\begin{aligned} J_{\frac{-1-p}{2}} \left(q \left(\frac{1}{\alpha} + H \right) \right) \left[\mu_0 q Y_{\frac{-1-p}{2}} \left(\frac{q}{\alpha} \right) - C\beta Y_{\frac{1-p}{2}} \left(\frac{q}{\alpha} \right) \right] \\ - Y_{\frac{-1-p}{2}} \left(q \left(\frac{1}{\alpha} + H \right) \right) \left[\mu_0 q J_{\frac{-1-p}{2}} \left(\frac{q}{\alpha} \right) - C\beta J_{\frac{1-p}{2}} \left(\frac{q}{\alpha} \right) \right] &= 0 \end{aligned} \quad (2.29)$$

Equation (2.29) will be solved numerically.

Case 2

Consider now that

$$p > 1 \quad \text{so} \quad |1 - p| = p - 1 \quad (2.30)$$

To determine the stress component σ_{23} , the following differential relations for the Bessel functions should be applied (Lebediev, 1957)

$$\frac{dz^{-\nu} J_{\nu}(z)}{dz} = -z^{-\nu} J_{\nu+1}(z) \quad \frac{dz^{-\nu} Y_{\nu}(z)}{dz} = -z^{-\nu} Y_{\nu+1}(z) \quad (2.31)$$

Bearing in mind equations (2.2), (2.17), (2.21) and (2.31), it follows that the stress component σ_{23} is expressed in the form

$$\sigma_{23}(x_1, x_2, t) = -q\mu_0(1 + \alpha x_2)^{\frac{1+p}{2}} \left[A_1 J_{\frac{1+p}{2}} \left(q \left(\frac{1}{\alpha} + x_2 \right) \right) + A_2 Y_{\frac{1+p}{2}} \left(q \left(\frac{1}{\alpha} + x_2 \right) \right) \right] e^{ik(x_1 - ct)} \quad (2.32)$$

where $0 < x_2 < H$.

From boundary conditions (2.14) and (2.15) and equations (2.32), (2.17), (2.23), (2.12), (2.21), the following linear algebraic equations for the unknowns A_1, A_2, A_3 are obtained

$$\begin{aligned} A_1 J_{\frac{p+1}{2}} \left(\frac{q}{\alpha} (1 + \alpha H) \right) + A_2 Y_{\frac{p+1}{2}} \left(\frac{q}{\alpha} (1 + \alpha H) \right) &= 0 \\ A_1 J_{\frac{p+1}{2}} \left(\frac{q}{\alpha} \right) + A_2 Y_{\frac{p+1}{2}} \left(\frac{q}{\alpha} \right) &= A_3 \\ -\mu_0 q \left[A_1 J_{\frac{1+p}{2}} \left(\frac{q}{\alpha} \right) + A_2 Y_{\frac{1+p}{2}} \left(\frac{q}{\alpha} \right) \right] &= C\beta A_3 \end{aligned} \tag{2.33}$$

Eliminating A_3 from the system of equations (2.33), it follows that

$$\begin{aligned} A_1 J_{\frac{p+1}{2}} \left(\frac{q}{\alpha} (1 + \alpha H) \right) + A_2 Y_{\frac{p+1}{2}} \left(\frac{q}{\alpha} (1 + \alpha H) \right) &= 0 \\ A_1 \left[\mu_0 q J_{\frac{p+1}{2}} \left(\frac{q}{\alpha} \right) + C\beta J_{\frac{p-1}{2}} \left(\frac{q}{\alpha} \right) \right] + A_2 \left[\mu_0 q Y_{\frac{p+1}{2}} \left(\frac{q}{\alpha} \right) + C\beta Y_{\frac{p-1}{2}} \left(\frac{q}{\alpha} \right) \right] &= 0 \end{aligned} \tag{2.34}$$

The system of algebraic equations (2.34) has non-zero solutions under the following condition

$$\begin{aligned} J_{\frac{p+1}{2}} \left(\frac{q}{\alpha} (1 + \alpha H) \right) \left[\mu_0 q Y_{\frac{p+1}{2}} \left(\frac{q}{\alpha} \right) + C\beta Y_{\frac{p-1}{2}} \left(\frac{q}{\alpha} \right) \right] \\ - Y_{\frac{p+1}{2}} \left(\frac{q}{\alpha} (1 + \alpha H) \right) \left[\mu_0 q J_{\frac{p+1}{2}} \left(\frac{q}{\alpha} \right) + C\beta J_{\frac{p-1}{2}} \left(\frac{q}{\alpha} \right) \right] &= 0 \end{aligned} \tag{2.35}$$

Equation (2.35) will be solved numerically.

3. Numerical results

Equations (2.29) and (2.35) will be solved numerically applying the bisection method. For this aim, the following notations are introduced

$$\psi = \frac{c^2}{c_0^2} \quad \widehat{C} = \frac{C\beta}{\mu_0} \tag{3.1}$$

Case 1

For $p \leq 1$ from (2.28) and (3.1), it follows that

$$\begin{aligned} J_{\frac{-1-p}{2}} \left(\frac{k}{\alpha} \sqrt{\psi - 1} (1 + \alpha H) \right) \left[k \sqrt{\psi - 1} Y_{\frac{-1-p}{2}} \left(\frac{k}{\alpha} \sqrt{\psi - 1} \right) - \widehat{C} Y_{\frac{-1-p}{2}} \left(\frac{k}{\alpha} \sqrt{\psi - 1} \right) \right] \\ - Y_{\frac{-1-p}{2}} \left(\frac{k}{\alpha} \sqrt{\psi - 1} (1 + \alpha H) \right) \left[k \sqrt{\psi - 1} J_{\frac{-1-p}{2}} \left(\frac{k}{\alpha} \sqrt{\psi - 1} \right) - \widehat{C} J_{\frac{-1-p}{2}} \left(\frac{k}{\alpha} \sqrt{\psi - 1} \right) \right] &= 0 \end{aligned} \tag{3.2}$$

Case 2

For $p > 1$ from (3.1) and (2.35), it follows that

$$\begin{aligned} J_{\frac{p+1}{2}} \left(\frac{k}{\alpha} \sqrt{\psi - 1} (1 + \alpha H) \right) \left[k \sqrt{\psi - 1} Y_{\frac{p+1}{2}} \left(\frac{k}{\alpha} \sqrt{\psi - 1} \right) + \widehat{C} Y_{\frac{p+1}{2}} \left(\frac{k}{\alpha} \sqrt{\psi - 1} \right) \right] \\ - Y_{\frac{p+1}{2}} \left(\frac{k}{\alpha} \sqrt{\psi - 1} (1 + \alpha H) \right) \left[k \sqrt{\psi - 1} J_{\frac{p+1}{2}} \left(\frac{k}{\alpha} \sqrt{\psi - 1} \right) + \widehat{C} J_{\frac{p+1}{2}} \left(\frac{k}{\alpha} \sqrt{\psi - 1} \right) \right] &= 0 \end{aligned} \tag{3.3}$$

The obtained numerical results for the dimensionless ratio $\psi = c^2/c_0^2$ are presented in the form of figures. Figure 2a presents the ratio ψ as a function of the parameter p for three cases of $kH = 1, 2, 4$, parameters $\eta = 0.5, \alpha = 0.05$ and ratios $\mu_1/\mu_2 = 4, \mu_1/\mu_0 = 2, \rho_1/\rho_0 = 2$. For $\alpha = 0.05$ and a small values of H being the thickness of the FGM layer it follows from equation

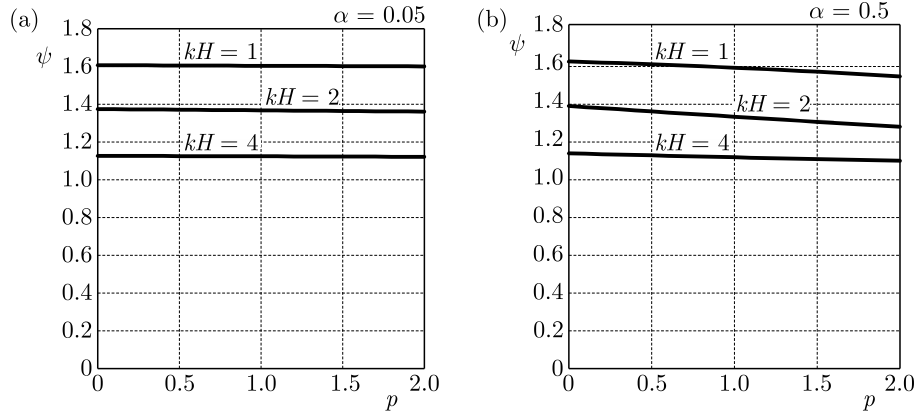


Fig. 2. The distribution of the parameter $\psi = c^2/c_0^2$ as a function of the parameter p for $kH = 1, 2, 4$, $\eta = 0.5$, $\mu_1/\mu_2 = 4$, $\mu_1/\mu_0 = 2$, $\rho_1/\rho_2 = 2$, $\rho_1/\rho_0 = 2$; (a) $\alpha = 0.05$, (b) $\alpha = 0.5$

(2.1) that the coating layer is almost homogeneous for all values of p . For this reason, the values of the ratio ψ are almost constant. A different case is presented in Fig. 2b, where the same values of the parameters as in Fig. 2a are taken into account without the parameter $\alpha = 0.5$. A weak influence of the nonhomogeneity of the coating layer on the wave speed $\psi = c^2/c_0^2$ can be noticed.

Figure 3a presents the distributions of ψ as functions of kH for $\eta = 0.5$, $\mu_1/\mu_0 = 2$, $\rho_1/\rho_0 = 2$, $\alpha = 0.05$, $p = 0.5$ and three cases of values of the ratios: 1 – $\mu_1/\mu_2 = 4$, 2 – $\mu_1/\mu_2 = 6$, 3 – $\mu_1/\mu_2 = 8$. This figure shows that the influence of different features of the sub-layers being components of the considered foundation on the wave speed $\psi = c^2/c_0^2$ is rather small.

The distributions of ψ as a function of the ratio $\mu_1/\mu_2 = \rho_1/\rho_2$ for four cases of values $p = 0, 0.5, 1, 2$ and $\eta = 0.5$, $\mu_1/\mu_0 = 2$, $\rho_1/\rho_0 = 2$, $\alpha = 0.05$, $kH = 1$ are presented in Fig. 3b. The curve numbered by 1 (Fig. 3b) shows the dependence of the ratio ψ for $p = 0$, so it is the homogenous coating layer and the periodically layered foundation. It can be observed that values of ψ decrease together with an increase in the parameter p .

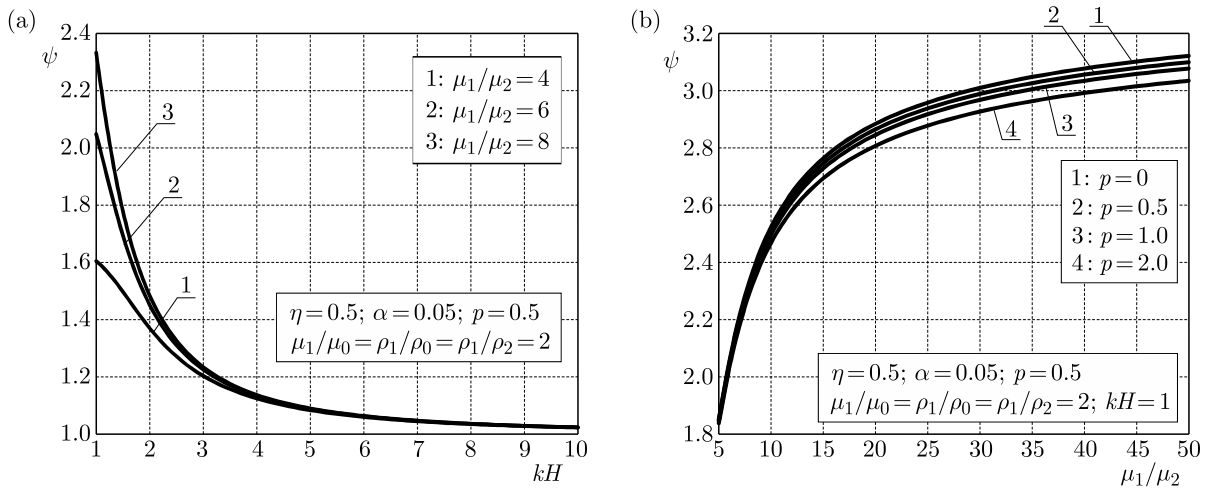


Fig. 3. The distributions of $\psi = c^2/c_0^2$: (a) as a function of kH for 1: $\mu_1/\mu_2 = 4$, 2: $\mu_1/\mu_2 = 6$, 3: $\mu_1/\mu_2 = 8$; (b) as a function of μ_1/μ_2

Figure 4a shows the distributions of the ratio ψ as a function of μ_1/μ_0 for four cases of the ratio $\mu_1/\mu_2 = 4, 6, 8, 10$ and $\eta = 0.5$, $\alpha = 0.05$, $\rho_1/\rho_0 = \rho_1/\rho_2 = 2$, $p = 0.5$, $kH = 1$. The curve numbered by 1 presents the smallest values of ψ for all the considered nonhomogeneities of the periodically layered foundation.

The distributions of the ratio ψ as a function of the parameter η for $\alpha = 0.05$, $\mu_1/\mu_0 = \rho_1/\rho_0 = \rho_1/\rho_2 = 2$, $p = 0.5$, $kH = 1$ and for cases of the ratio $\mu_1/\mu_2 = 4, 6, 8, 10$ are given in Fig. 4b. It can be observed that for $\eta \rightarrow 1$ all curves numbered by 1, 2, 3 and 4 tend to the same point.

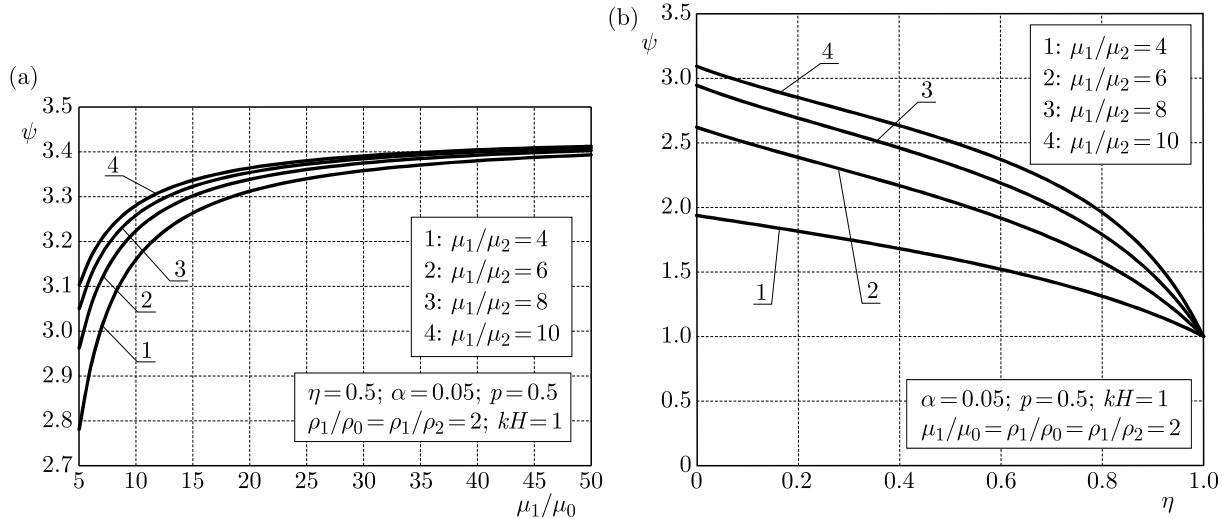


Fig. 4. The distributions of $\psi = c^2/c_0^2$: (a) as a function of μ_1/μ_0 , (b) as a function of η

The limit case $\eta \rightarrow 1$ leads to the homogeneous foundation with the shear modulus $\mu_1 = 2\mu_0$, coated by the FGM layer with the shear modulus and the mass density dependent in the form given by (2.1) with respect to the distance from its lower boundary plane. In the case $\eta \rightarrow 0$, the half-space being the foundation with the shear modulus μ_2 is obtained. The values of μ_2 depend on the taken into account value of the ratio μ_1/μ_2 . From the assumptions in Fig. 4b, it follows that the curves are adequate for the cases: curve 1 for $\mu_0 = 2\mu_2$, curve 2 for $\mu_0 = 3\mu_2$, curve 3 for $\mu_0 = 4\mu_2$ and curve 4 for $\mu_0 = 5\mu_2$, respectively. From Fig. 4b it can be seen that the values of ψ decrease with an increase in the ratio μ_1/μ_2 for fixed values of the parameter η .

4. Final remarks

The problem of SH wave propagation in an elastic nonhomogeneous half-space is considered. The body is assumed to be composed of the FGM layer being a coating and periodically stratified two-layer half-space. The investigations are limited to the anti-plane shear harmonic waves in the nonhomogeneous body on the assumption that the boundary surface is free of loadings. The main aim is to determine the wave speed by using the wave number and the mechanical properties of the components of the half-space. The numerical results present the wave speed in the dimensionless form. The obtained figures show the influence of the nonhomogeneity of the coating layer as well as the nonhomogeneity of the foundation on the wave speed. The assumptions of $p = 0$, $\mu_1 = \mu_2 = \mu_0$, $\rho_1 = \rho_2 = \rho_0$ lead to Love's wave propagation in the homogeneous half-space coated by the homogeneous layer well-known in the literature (see for example Achenbach, 1973; Nowacki, 1970), which is shown in Appendix.

A. Appendix

Taking into account

$$p = 0 \quad \mu_1 = \mu_2 \quad \rho_1 = \rho_2 \tag{A.1}$$

and using equation (2.22), (2.23), (2.9) and (2.13), it follows that

$$C = \mu_1 \quad q = k\sqrt{\frac{c^2}{c_0^2} - 1} \quad \beta = k\sqrt{1 - \frac{c^2}{c_1^2}} \quad c_1^2 = \frac{\mu_1}{\rho_1} \quad c_0 < c < c_1 \quad (\text{A.2})$$

Substituting (A.1) and (A.2) into (2.29) and using following relations (Lebediev, 1957)

$$\begin{aligned} J_{\frac{1}{2}}(z) &= \sqrt{\frac{2}{\pi z}} \sin z & J_{-\frac{1}{2}}(z) &= \sqrt{\frac{2}{\pi z}} \cos z \\ Y_{\frac{1}{2}}(z) &= -J_{-\frac{1}{2}}(z) & Y_{-\frac{1}{2}}(z) &= J_{\frac{1}{2}}(z) \end{aligned} \quad (\text{A.3})$$

we obtain

$$\begin{aligned} \mu_0 q \left[\sin \frac{q}{\alpha} \cos \left(q \left(\frac{1}{\alpha} + H \right) \right) - \cos \frac{q}{\alpha} \sin \left(q \left(\frac{1}{\alpha} + H \right) \right) \right] \\ + \mu_1 \beta \left[\cos \frac{q}{\alpha} \cos \left(q \left(\frac{1}{\alpha} + H \right) \right) + \sin \frac{q}{\alpha} \sin \left(q \left(\frac{1}{\alpha} + H \right) \right) \right] = 0 \end{aligned} \quad (\text{A.4})$$

From equation (A.4), it follows that

$$\mu_1 \beta = \mu_0 q \tan(qH) \quad (\text{A.5})$$

Equation (A.5) agrees with the characteristic equation for the case of Love's wave presented in the monograph by Nowacki (1970) (p. 612, eq. (13)).

References

1. ACHENBACH J.D., 1973, *Wave Propagation in Elastic Solids*, North-Holland Publ. Co., Amsterdam-London
2. ACHENBACH J.D., BALOGUN O., 2010, Anti-plane surface waves on a half-space with depth-dependent properties, *Wave Motion*, **47**, 59-65
3. ALENITSYN A.G., 1964, Rayleigh waves in a nonhomogeneous elastic slab, *Prikladnaya Matematika i Mekhanika*, **28**, 5, 880-888
4. ALSHITS V.I., MAUGIN G.A., 2005, Dynamics of multilayers: elastic waves in an anisotropic graded or stratified plate, *Wave Motion*, **41**, 357-394
5. BIELSKI W.R., MATYSIAK S.J., 1992, Surface waves in a periodic two-layered elastic half-space, *Acta Mechanica*, **91**, 47-55
6. BIRYKOV S.V., GULYAEV YU.V., KRYLOV V.V., PLESKY V.V., 1995, *Surface Acoustic Waves in Inhomogeneous Media*, Springer, Berlin
7. BREKHOVSKIKH L.M., 1960, *Waves in Layered Media*, Academic Press, New York
8. CALLADINE C.R., GREENWOOD J.A., 1978, Line and point loads on a non-homogeneous incompressible elastic half-space, *Quarterly Journal of Mechanics and Applied Mathematics*, **31**, 507-529
9. CERVENY V., POPOV M.M., PSENCIK I., 1982, Computation of wave fields in inhomogeneous media – Gaussian beam approach, *Geophysical Journal of the Royal Astronomical Society*, **70**, 109-128
10. DESTRADE M., 2007, Seismic Rayleigh waves on an exponentially graded, orthotropic elastic half-space, *Proceedings of the Royal Society of London. Series A*, **463**, 495-502
11. KAMKE E., 1976, *Handbook of Ordinary Differential Equations* (in Russian), Science, Moscow

12. KENNETT B.L.N., 1983, *Seismic Wave Propagation in Stratified Media*, Cambridge University Press
13. KULCHYTSKY-ZHYHAILO R., KOŁODZIEJCZYK W., 2007, On axisymmetrical contact problem of pressure of rigid sphere into a periodically two-layered space, *International Journal of Mechanical Science*, **49**, 704-711
14. KULCHYTSKY-ZHYHAILO R., MATYSIAK S.J., 2005, On some heat conduction problem in a periodically two-layered body. Comparative results, *International Communications in Heat and Mass Transfer*, **32**, 332-340
15. KULCHYTSKY-ZHYHAILO R., MATYSIAK S.J., 2006, On distributions in a semi-infinite periodically stratified layer, *Bulletin of the Polish Academy of Science, Technical Sciences*, **54**, 45-49
16. KULCHYTSKY-ZHYHAILO R., MATYSIAK S.J., PERKOWSKI D.M., 2006, On displacements and stresses in a semi-infinite laminated layer. Comparative results, *Meccanica*, **42**, 117-126
17. LEBIEDIEV N.N., 1957, *Special Functions and their Applications* (in Polish), PWN, Warsaw
18. MATYSIAK S.J., 1996, On the microlocal method in modeling of periodically layered composites, *Journal of Theoretical and Applied Mechanics*, **33**, 481-487
19. MATYSIAK S.J., MIESZKOWSKI R., PERKOWSKI D.M., 2009, Surface waves in a periodic half-space with the boundary normal to the layering, *Acta Mechanica*, **207**, 235-243
20. MATYSIAK S.J., WOŹNIAK C., 1987, Micromorphic effects in a modelling of periodic multilayered elastic composites, *International Journal of Engineering Sciences*, **25**, 549-559
21. MATYSIAK S.J., WOŹNIAK C., 1988, On the microlocal modelling of thermoelastic composites, *Journal of Technology Physics*, **29**, 85-97
22. NAYFEH A.H., 1995, *Wave Propagation in Layered Anisotropic Media*, North-Holland, Amsterdam
23. NOWACKI W., 1970, *Theory of Elasticity* (in Polish), PWN, Warsaw
24. SHUVALOV A.L., PONCELET O., KISELEV A.P., 2008, Shear horizontal waves in transversely inhomogeneous plates, *Wave Motion*, **45**, 605-615
25. UPADHYAY S.K., GUPTA O.P., 1972, SH-wave propagation in anisotropic inhomogeneous crustal layer, *Pure and Applied Geophysics*, **95**, 67-73
26. WANG C.D., TZENG C.S., PAN E., LIAO J.J., 2003, Displacements and stresses due to a vertical point load in an inhomogeneous transversally isotropic half-space, *International Journal of Rock Mechanics and Mining Sciences*, **40**, 667-685
27. WOŹNIAK C., WOŹNIAK M., 1995, *Modeling of Composites. Theory and Applications* (in Polish), IFTR Reports, Warsaw
28. RETTOS C., 1990, In-plane vibrations of soil deposits with variable shear modulus. I. Surface wave, *International Journal for Numerical and Analytical Methods in Geomechanics*, **14**, 209-222

MODE OF FAILURE FOR REINFORCED CONCRETE BEAMS WITH GFRP BARS

ABDELMONEM MASMOUDI

*Mechanics, Modelling and Production Laboratory, National School of Engineering of Sfax, University of Sfax, Tunisia
e-mail: abdelmonem.masmoudi@enis.rnu.tn*

MONGI BEN OUEZDOU

*Université de Tunis El Manar, Ecole Nationale d'Ingénieurs de Tunis, LR03ES05 Laboratoire de Génie Civil, Tunis,
Tunisia; e-mail: mongi.benouezdou@enit.rnu.tn*

MOHAMMED HADDAR

Mechanics, Modelling and Production Laboratory, National School of Engineering of Sfax, University of Sfax, Tunisia

Crack propagation in concrete structures is a very complicated process. An experimental method to predict the stress distribution of a cracked GFRP reinforced concrete flexural beam is presented. The beam subjected to four-point bending is internally reinforced with unidirectional GFRP bars. The aim of this investigation is to study the flexural performance of reinforced concrete members strengthened using GFRP bars. For the flexural tests performed on reinforced concrete beams strengthened with GFRP bars, the ultimate load of the beams strengthened with GFRP was reasonably increased. The mode of failure for beams reinforced with GFRP sections is slightly different compared with the traditional beam. The GFRP reinforced concrete beams fail either by concrete crushing at the compression zone or rupture of the GFRP reinforcement.

Keywords: crack propagation, flexural failure, concrete, GFRP bars, stress distribution

1. Introduction

Nowadays, the construction industries around the world face a major problem due to corrosion of steel reinforcement. The cost of maintenance of any deteriorated reinforced concrete structures is very expensive. GFRP composite bars are an excellent alternative to steel bars for reinforcing concrete structures in severe environments.

In the last two decades, a number of studies have been carried out to investigate the flexural response of FRP RC beams (Ritchie, 1991; An *et al.*, 1991; Meier *et al.*, 1993). Therefore, flexural failure is a common phenomenon in the case of concrete members. Plain concrete when subjected to flexural loads fails due to crack propagation. In this work, the effects of several further important parameters on the formation and propagation of cracks in concrete are investigated in order to better understand the decisive phenomena of concrete failure under different loading conditions. When RC beams reach ultimate state with the first two failure modes, the load-carrying capacity of the beams can be easily estimated by applying conventional methods derived using a plane conservation concept.

Experimental studies have been performed to investigate flexural, shear, and failure modes of FRP RC beams (Swamy and Roberts, 1995; Saadatmanesh and Ehsani, 1991; Ritchie *et al.*, 1991; Chajes *et al.*, 1994; Sharif *et al.*, 1994). These studies indicated failure modes that can limit the strengthening effect of FRP retrofitted structures. Recently, four-point bending experiments were performed on FRP strengthened RC beams and compared structural behaviors of beams retrofitted by CFRP (carbon FRP) for flexural strengthening and by GFRP (glass FRP) for shear

strengthening (Kachalakev and McCurry, 2000). The FRP reinforcement technique for bridge and continuous RC beam applications was investigated by Pham and Al-Mahaidi (2004), Ashour (2004). Both studies used CFRP sheets and observed the failure mechanism of the reinforcement beams. The effect of initial load on the structural behavior of FRP RC beams was also studied by Shin and Lee (2003), Wenwei and Guo (2006), who performed experiments on CFRP RC beams under different sustaining loads. The former study showed that the different sustain load levels have influence on the deflection of the beam. The latter study investigated the effect of initial load on the ultimate strength of the CFRP reinforcement RC beams and a theoretical model was proposed that could predict ultimate strength of the beams under sustaining loads. Shear capacity of FRP reinforcement beams was presented (Bencardino *et al.*, 2007; Jayaprakash *et al.*, 2008). The first study tested CFRP reinforcement RC beams cast without shear reinforcements and observed failure modes in shear. It was concluded that the FRP retrofitted RC beams could avoid shear failure if a carefully designed anchorage system was installed in the beams. Another study (Jayaprakash *et al.*, 2008) showed that bi-directionally attached CFRP strips significantly increased the shear capacity of the RC beams. They also investigated the effect of orientation of CFRP strips on ultimate shear capacity as well as crack propagation. The cracking may significantly affect the moment redistribution in continuous members and more accurate assessment of the influence of FRP reinforcement on the behavior of RC elements (Matos *et al.*, 2012).

2. Experimental study

2.1. Materials

For all beams ready mixed concrete was used which had been aged for 28 days. 25 MPa concrete grade was used in the manufacturing of these beams using Ordinary Portland cement and crushed aggregates with maximum size of 12 mm. The initial elasticity modulus E was 34 GPa and the measured tensile strength was 2.1 MPa. The concrete slump was 100 mm. For the internal GFRP reinforcement 4 bars HA12 (diameter of 12 mm) were used. The resistance capacity in shear was provided from 6mm diameter shear reinforcement with 120 mm spacing. Properties of the GFRP and steel bars used in this study and details of beam cross-section are shown in Table 1 (Schock Bauteil GmbH Combar Co., 2006; Aboutaha, 2004). The average ultimate tensile strength was 738 MPa and 400 MPa, respectively for GFRP and steel bars. The modulus of elasticity of the tensile reinforcement bars was 60 GPa and 200 GPa, respectively for GFRP and steel. The beams were casted with concrete with a cover of 20 mm. For the tensile reinforcement, two 12 mm diameter bars were used, and for the construction reinforcement, two 8 mm diameter as the upper reinforcement (Fig. 1).

Table 1. Properties of the GFRP and steel bars used in this study

Type of bar	Glass	Steel
	Nominal diameter 8 and 12 mm	
Tensile modulus of elasticity [GPa]	60 ± 1.9	200 ± 7
Ultimate tensile strength [MPa]	738 ± 22	400 ± 11
Density	2.2	7.85

2.2. Variables of the experiments and beams

In this investigation, four point flexural tests were performed with the experimental variables being shear strengthening or no shear strengthening in the central zone. In our experimental study, we investigated the influence of the internal reinforcement amount in the composite material

Table 2. Composition and characteristics of the concrete

Cement I [kg/m ³]	Water [kg/m ³]	Sand [kg/m ³]	Aggregate (4/12) [kg/m ³]	Aggregate (12/20) [kg/m ³]	Compressive Strength [MPa]	Slump [mm]
350	207	880	300	650	25	100



Fig. 1. GFRP bars reinforcement and the beam cross section

on the RC beam response. Two types of beams are studied, with shear GFRP internal reinforcement in central flexural zone in comparison and with steel internal reinforcement. Three beams were reinforced with GFRP bars (designated BG) and three with steel bars (designated BS). All beams were provided with 6 mm diameter mild stirrup and were designed to fail in flexure. All reinforced concrete beams had span of 1650 mm and rectangular cross section 200 mm × 150 mm. The beam cross section was presented in Fig. 2. All beam tests were carried out using a calibrated 500 kN testing machine with displacement-rate control. The data acquisition system was started a few seconds before load application. The displacement rate of loading was kept constant during the tests (0.005 mm/s). The beam was mounted on cylindrical contacts which were simply supported. Crack width was controlled step by step during loading. The cracks were marked by a color marker directly on each beam.

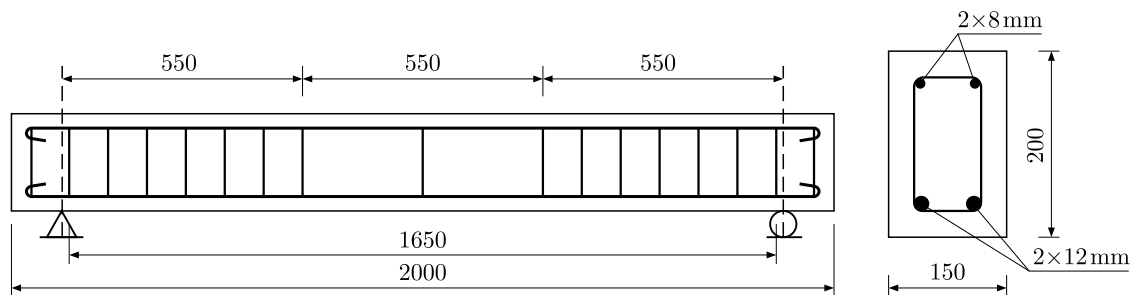


Fig. 2. Beam cross section (all dimensions are in mm)

The objective of this investigation is to study the mechanisms of flexural failure and stress distribution. The mechanical properties enhancement have been evaluated through comparison of the strengthened beams mechanical response with the mechanical response of the control beam with steel internal reinforcement. The beam response has been quantified in terms of stress distribution and deflections at the mid-span. The strain evolution as well as some components of the displacement field has also been monitored.

2.3. Arrangement of strain gauges

Electrical strain deformer was installed on the flexural plate surface. To obtain an accurate deflection reading, four Linear Variable Differential Transducer (LVDT) were also mounted and one at the mid-span and them connected to a data logger. Since the interface meso-crack propagation pattern was known, the monitoring of the local failure behavior could provide information on the crack-initiation point and on the direction of crack propagation. Electrical strain deformation was installed in order to obtain deflection reading by LVDT (Fig. 3). The detectors were installed on the flexural for both steel and GFRP reinforcement and strain versus load plots were considered. The time “zero” was chosen at the beginning of the load history, or at the moment in which the load was applied. Thus, if the local failure is considered as a “moment” in the load history, the sequence of local failures in the monitored spots can reveal the interface crack initiation point and the crack propagation direction. A schematic diagram of testing arrangement is presented in Fig. 3. We used uni-axial strain gages type CEA-06-250-350 with factor gage $2.08 \pm 0.5\%$ and resistance $350.0 \pm 0.5\%$ at 24°C . Figure 4 shows the strain gages fixed to the GFRP bars and attached to the extensometer pont.

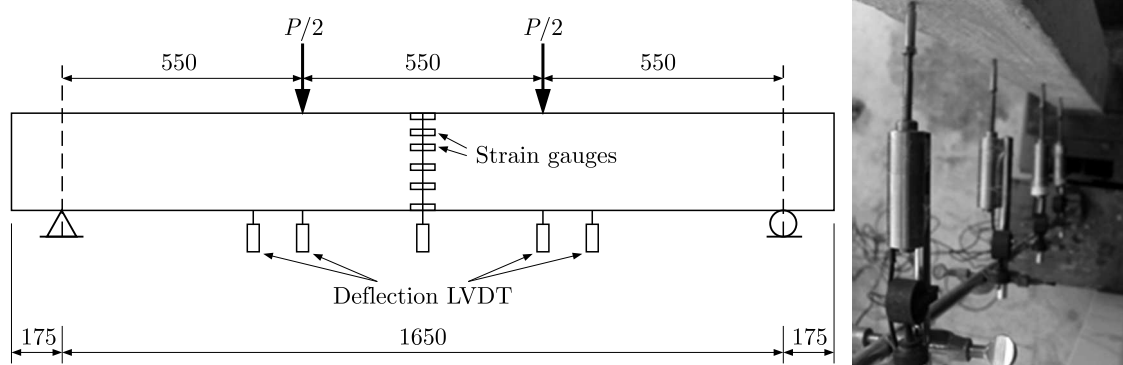


Fig. 3. Schematic diagram of the test set-up

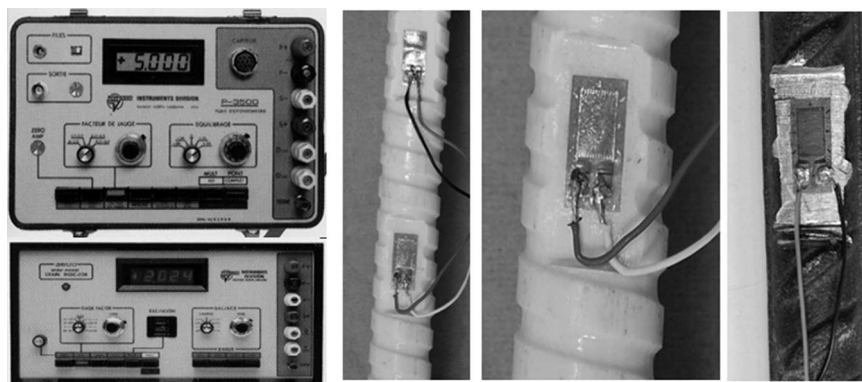


Fig. 4. Gauges for longitudinal deformations

2.4. Longitudinal modulus of elasticity

Uniaxial compression tests on cylindrical samples 16×32 cm were performed to determine the longitudinal modulus of elasticity of concrete used for casting the concrete test beams. The device used showed in Fig. 5 was mounted on a hydraulic press with numerical control. The maximum capacity of this press was 5000 kN with loading speed compression 0.005 mm/s. The longitudinal elastic modulus of the concrete measured on new specimens was identical to

the given average of 34122 MPa. The evolution of the stress in the concrete according to the deformation is shown in Fig. 6.

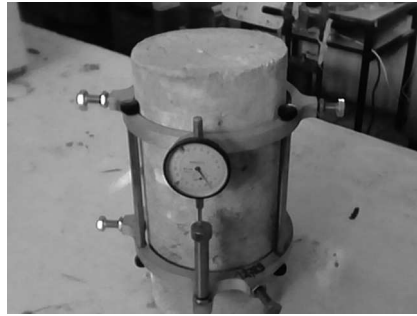


Fig. 5. Test of the longitudinal elasticity modulus

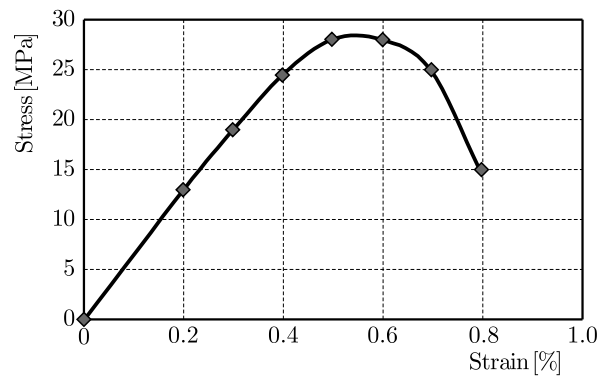


Fig. 6. Evolution of the stress in the concrete vs deformations

3. Analytical study

The term of deformation of the steel in tension ε_{s0} in the case of uncracked section can be expressed by the following expression

$$\varepsilon_{s0} = \frac{Z_0}{Z_1} \left(\varepsilon_{s1} + \frac{N_c}{A_s} \right) \tag{3.1}$$

where Z_0 being the lever arm in the cracked section, Z_1 – lever arm in the uncracked section, N_c – normal tensile stress of concrete.

The deformation of steel in the case of cracked section ε_1 can be found from a conventional calculation by the expression

$$\varepsilon_{s1} = \frac{d - y}{E_c I} M \tag{3.2}$$

where y is the position of the neutral axis in the cracked section, E_c – modulus of elasticity of the concrete, I – inertia of the cracked section.

The conditions of adhesion between reinforcement bars and concrete are modeled involving a scalar variable mechanical damage D (between 0 and 1) given by the following expression

$$\varepsilon_c = \frac{(1 - D)\varepsilon_{s0}}{n} \tag{3.3}$$

where ε_c is the deformation of the concrete area, ε_{s0} – deformation of bar reinforcement in the uncracked section.

From equations (3.1) and (3.3) we can express, in the case of the uncracked concrete section, the normal strains in concrete and in the bars. They are as follows

$$\varepsilon_c = \frac{\varepsilon_{s1}}{\frac{Z_0}{Z_1} \left(\frac{1}{1-D} + \frac{C}{nA_s} \right)} \quad \varepsilon_{s0} = \frac{\varepsilon_{s1}}{\frac{Z_0}{Z_1} \left(1 + \frac{(1-D)C}{nA_s} \right)} \quad (3.4)$$

where C is the contribution of the tensioned concrete surface and n is the equivalence coefficient of concrete steel. We compare the evolution of experimental and theoretical deformations of two reinforcement concrete beams for both BG and BS beams.

4. Presentation and discussion of the test results

4.1. Load-deflection

The load-deflection behavior of all the beams tested is shown in Fig. 7. Initially, all the beams have relatively the same stiffness. However, once the beam cracked, the stiffness of the GFRP reinforced concrete beam decreased at a faster rate compared with the control beam. This resulted in a larger deflection of the GFRP reinforced concrete beam. The recorded deflections near failure for all beams BG, and BS were, 50 mm, and 32 mm, respectively. It can be seen from Fig. 7 that the stiffness of the beams BG was much lower than that of the beam BS. Again, this was due to the lower elastic modulus of the GFRP sections compared with steel reinforcement. At the same load level, the deflection of beams reinforced with GFRP sections was higher by about 2 to 3 times compared with the beam BS. Thus, at the service load, deflection of the beam reinforced with GFRP sections would be higher than in the beam BS and may not satisfy the design criteria. In addition, a larger deflection would also lead to a wider crack width of the beam.

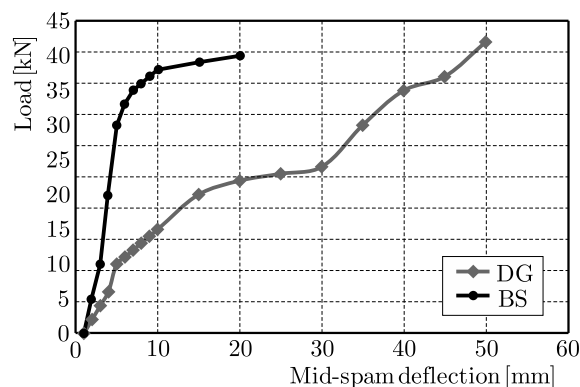


Fig. 7. Load-deflection of all tested beams

4.2. Load-reinforcement strain

The tensile strain of the reinforcements was measured and recorded using electrical strain gauges. The load-reinforcement strain behavior of all the beams tested is shown in Fig. 8. It can be seen that the behavior of the load-reinforcement strain was quite similar to the load-deflection of the beams. An increase in the applied load increased the tensile strain of the reinforcement. From Fig. 8, it can be seen that the bond between concrete and GFRP and steel reinforcements was relatively good. That ensured the transfer of tensile load from concrete to the tensile reinforcements. The experimental results also indicated that the strain of the GFRP reinforcement had linear behavior up to failure. On the other hand, the steel reinforcement

had a yield point before failure. Thus, in the design process, the aspect of ductile behavior of the beam needs to be taken into account based on the type of tensile reinforcement used. The recorded tensile strain near failure for beams BGI and BS were about 15000 and 5000 micro strains, respectively. On the other hand, the steel reinforcement started to yield at about 3200 micro strains. Obviously, the behavior of the steel reinforcement was elastic-plastic while the GFRP section experienced only elastic behavior. These different strain characteristics of the reinforcement have to be considered when the GFRP section is to be used as concrete reinforcement.

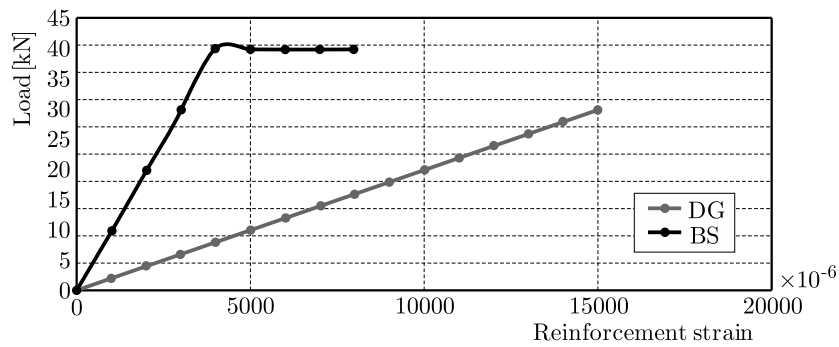


Fig. 8. Load-reinforcement strain of all tested beams

4.3. Failure mode

The recorded experimental results show that all the beams failed in flexure by crushing of concrete at the compression zone. The total number of cracks generated for beams BG and BS were 21 and 6, respectively. Hence, the beam with a lower ultimate load due to a lower elastic modulus experienced a lower number of cracks compared with the beam that had a higher load carrying capacity. In addition, the crack spacing for the beam BS was also larger than beam BG and BS. The measured average crack spacing for beams BG and BS were 40 mm and 130 mm, respectively. It was also observed that the first crack of the GFRP reinforced concrete beams BG was higher by 50% compared with the beam BS. This result was confirmed by Mias *et al.* (2015) who found that the use of GFRP bar reinforcement led to an increase in the average crack spacing and crack width.

The first crack load for GFRP reinforced concrete beams was 5 kN while for the beam BS this value was 10 kN. A schematic diagram of the cracking of all the beams tested in this study is shown in Fig. 9.



Fig. 9. Diagram of the cracking of beams

Crack propagations were observed during the tests. They are illustrated in Fig. 10. In the control specimen, crack initiation occurred at 2.1 kN around the locations where the load was applied. As the applied load increased, cracks propagated from the beam center and loaded points. When the applied load reached 40.2 kN, the reinforcing bar yielded and flexure failure was observed in the specimen. In this load case, the interface crack was initiated at the beam mid-span and propagated towards the support. At the same time, the data collected from the strain deformer placed on the composite material showed that the local failure took place

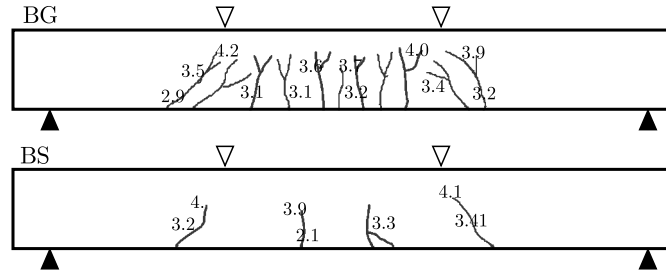


Fig. 10. Level of crack propagation

simultaneously at all monitored regions. Moreover, the simultaneous local failure detected in the composite material coincided with the global failure of the beam and with the “last” local failure on the flexural steel/concrete cover interface. Figures 11 and 12 show that the curve of superior fiber strain ($F\text{-sup}^1$ and $F\text{-sup}^2$) decrease above the load of 25 kN. This means that the concrete was damaged and plasticized. Contrary to the curve of the inferior fiber strain ($F\text{-inf}^1$ and $F\text{-inf}^2$), it was still linear. This result confirms the GFRP linear elastic behavior until rupture. The first cracks appeared in the beam at a load of 25 kN. There were five active cracks with spacing of 62.4 mm in the half span of each beam. Crack widths corresponding to the 45 kN load of the beam were respectively 0.325 mm, 0.315 mm, 0.361, 0.324 and 0.373 mm. We compared the evolution of experimental and theoretical deformations of two reinforcement concrete beams for both types BG and BS. Figures 13 highlights the transfer effort of the reinforcing bar to the concrete in tension. This finding is best seen in the case of the steel beam. An increase in the applied moment generates multiple simultaneous effects. On the one hand, the deterioration of adhesion will continue locally in the portions located between the bending cracks. When degradation is complete, the concrete will not be driven by the reinforcements and mechanically no longer participate. On the other hand, new bending cracks will form in areas closer and closer to the supports. Finally, the area of non-compliance with respect to damage to the adhesive will expand, which means that other sections located between the bending cracks will suffer degradation of adhesion.

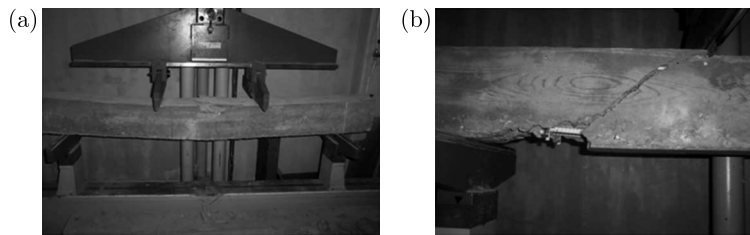


Fig. 11. Beam cracking modes: (a) steel beam, (b) GFRP beam

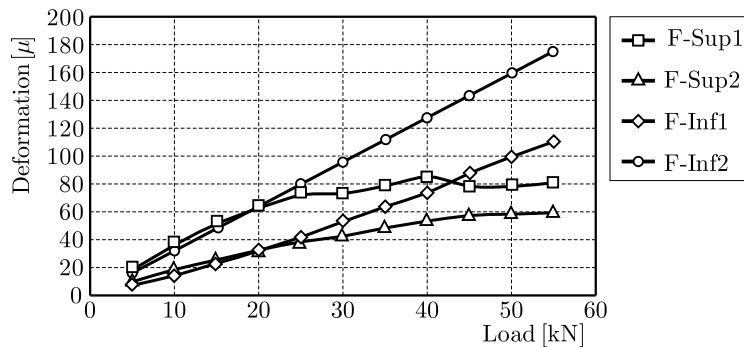


Fig. 12. Strain evolution

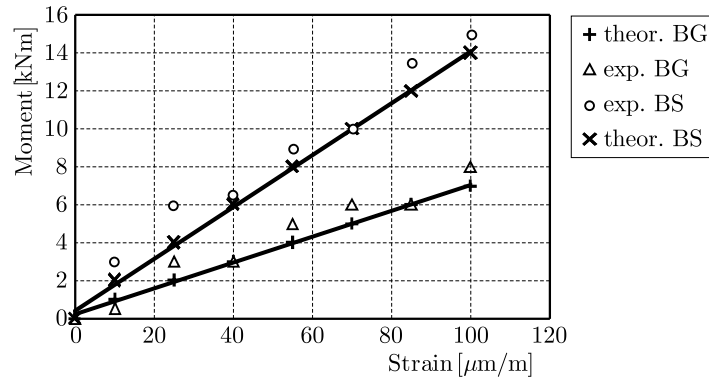


Fig. 13. Evolution of strain in the bar versus moment

The local mechanical behavior has been compared with experimental measurements, the results show good correlations. We can conclude that the local failure mechanism which controls the global failure behavior of the strengthened system takes place in the concrete cover for the beam geometry.

5. Conclusion

In this paper, flexural tests were performed for concrete beams reinforced by GFRP bars. The main conclusions drawn from the study are as follows:

- The concrete beam reinforced with GFRP sections experienced a lower load carrying capacity and stiffness compared with the conventional reinforced concrete beam. This was mainly due to the lower elastic modulus of the GFRP section compared with the steel reinforcement.
- The number of cracks for the beam reinforced with GFRP section was higher than in the conventional beam. In addition, the average crack spacing of the GFRP reinforced concrete beam was also larger compared with the control beam.
- The curve of superior fiber strain ($F\text{-sup}^1$ and $F\text{-sup}^2$) decreased above the load of 25 kN. This means the concrete was damaged and plasticized. Contrary to the curve of the inferior fiber strain ($F\text{-inf}^1$ and $F\text{-inf}^2$) it was still linear. This result confirms the GFRP linear elastic behavior until rupture.
- An increase in the applied moment generates the deterioration of adhesion, and new bending cracks are developed.
- The modes of failure for beams reinforced with GFRP sections were slightly different compared with the control beam. The GFRP reinforced concrete beams fail either by concrete crushing at the compression zone or rupture of the GFRP reinforcement. Failure due to rupture of GFRP reinforcement is not recommended since it may result in catastrophic failure of the structure.

Acknowledgments

The authors would like to thank the manufacturer of the GFRP Combar? (Schöck, Baden-Baden, Germany) for providing GFRP bars and supporting the experimental research. The opinion and analysis presented in this paper are those by the authors.

References

1. ABOUTAHA R., 2004, *Recommended Design for the GFRP Rebar Combar*, Technical Report, Department of Civil and Environmental Engineering, Syracuse University, USA

2. AN W., SAADATMANESH H., EHSANI M.R., 1991, RC beams strengthened with FRP plates. II: Analysis and parametric study, *ASCE Journal of Structural Engineering*, **117**, 11, 3434-3455
3. ASHOUR A.F., EL-REFAIE S.A., GARRITY S.W., 2004, Flexural strengthening of RC continuous beams using CFRP laminates, *Cement and Concrete Composites*, **26**, 765-775
4. BENCARDINO F., SPADEA G., SWAMY R.N., 2007, The problem of shear in RC beams strengthened with CFRP laminates, *Construction and Building Materials*, **21**, 1997-2006
5. CHAJES M.J., THOMSON JR T.A., JANUSZKA T.F., FINCH JR W.W., 1994, Flexural strengthening of concrete beams using externally bonded composite materials, *Construction and Building Materials*, **8**, 3, 191-201
6. Eurocode 2. "Calcul des structures en béton armé, partie 1.1, règles générales et règles pour les bâtiments", AFNOR, 1992
7. JAYAPRAKASH J., SAMAD A.A.A., ABBASOVICH A.A., ALI A.A.A., 2008, Shear capacity of pre-cracked and non-precracked reinforced concrete shear beams with externally bonded bi-directional CFRP strips. *Construction and Building Materials*, **22**, 1148-1165
8. KACHALAKEV D., MCCURRY D.D., 2000, Behavior of full-scale reinforced concrete beams retrofitted for shear and flexural with FRP laminates, *Composites, Part B*, **31**, 445-452
9. MATOS B., CORREIA J.R., CASTRO L.M.S., FRANÇA P., 2012, Structural response of hyperstatic concrete beams reinforced with GFRP bars: effect of increasing concrete confinement, *Composite Structures*, **94**, 1200-1210
10. MEIER U., DEURING M., MEIER M., SCHWEGLER G., 1993, Strengthening of structures with advanced composites, [In:] *Alternative Materials for Reinforcement and Prestressing of Concrete*, J.L. Clarke (Edit.), Blackie Academic and Professional, 153-171
11. MIAS C., TORRES L., GUADAGNINI M., TURON A., 2015, Short and long-term cracking behaviour of GFRP reinforced concrete beams, *Composites, Part B*, **77**, 223-231
12. PHAM H., AL-MAHAIDI R., 2004, Experimental investigation into flexural retrofitting of reinforced concrete bridge beams using FRP composites, *Composite Structures*, **66**, 1/4, 617-625
13. RITCHIE P.A., 1991, External reinforcement of concrete beams using fiber reinforced plastics, *ACI Structural Journal*, **88**, 4, 490-496
14. RITCHIE P.A., THOMAS D.A., LU L.W., CONNELLEY G.M., 1991, External reinforcement of concrete beams using fiber reinforced plastics, *ACI Structural Journal*, **88**, 4, 490-500
15. SAADATMANESH H., EHSANI M.R., 1991, RC beams strengthened with FRP plates. I: Experimental study, *ASCE Journal of Structural Engineering*, **117**, 11, 3417-3433
16. Schock Bauteil GmbH Combar Co., 2006, Design Guideline for Concrete Structures Reinforced with Glass Fiber Reinforced Polymer following the Requirements of DIN 1045-1 and EC2. Design Guide; Issued Germany
17. SHARIF A., AL-SULAIMANI G.J., BASUNBUL I.A., BALUCH M.H., GHALEB B.N., 1994, Strengthening of initially loaded reinforced concrete beams using FRP, *ACI Structural Journal*, **91**, 2, 160-168
18. SHIN Y., LEE C., 2003, Flexural behavior of reinforced concrete beams strengthened with CFRP laminates at different levels of sustaining load, *ACI Structural Journal*, **100**, 2, 231-239
19. SWAMY R.N., ROBERTS H., 1995, Structural behavior of externally bonded steel plated RC beams after long-term exposure, *Structural Engineering*, **73**, 16, 255-261
20. WENWEI W., GUO L., 2006, Experimental study and analysis of RC beams strengthened with CFRP laminates under sustaining load, *International Journal of Solids and Structures*, **43**, 1372-1387

IDENTIFICATION STRATEGY OF ANISOTROPIC BEHAVIOR LAWS: APPLICATION TO THIN SHEETS OF ALUMINIUM A5

AMNA ZNAIDI, OLFA DAGHFAS

National School of Engineers of Tunis, Departement of Mechanical Engineering, Tunis, Tunisie
e-mail: amna.znaidi@laposte.net; daghfasolfa@yahoo.fr

AMEN GAHBICHE

National School of Engineers of Monastir, Mechanical Engineering Laboratory, Monastir, Tunisie
e-mail: amen_gahbiche@yahoo.fr

RACHID NASRI

National School of Engineers of Tunis, Departement of Mechanical Engineering, Tunis, Tunisie
e-mail: rachid.nasri@enit.rnu.tn

Numerical simulation provides a valuable assistance in the controlling of forming processes. The elasto-plastic orthotropic constitutive law is based on the choice of an equivalent stress, a hardening law and a plastic potential. An identification of the model parameters from an experimental database is developed. This database consists in hardening curves and Lankford coefficients of specimens subjected to off-axis tensile tests. The proposed identification strategy is applied to aluminum sheets. The behavior of this material is studied under several solicitations. The anisotropic behavior of the aluminum plate is modeled using the Barlat criterion and the hardening law. The obtained Lankford coefficients are compared to those which are identified by a different strategy.

Keywords: anisotropy, strategy, identification, behavior law, off-axis testing

1. Introduction

Except for certain processes such as molding, a large majority of metal parts is obtained by forming processes during which the material is plastically deformed. They are optimized to reduce the cost, which requires manufacturers to increasingly use numerical simulation and, therefore, need to describe the material behavior.

These simulations are often flawed by a simplified description of the plastic behavior of the material; particularly the anisotropy of rolled sheets (Ghouati and Gelin, 2001; Znaidi, 2004; Haddadi *et al.*, 2006; Kim *et al.*, 2007; Barlat and Lian, 1989). Therefore, it is important to accurately model the plastic behavior of metals in large deformation in order to better predict their behavior of the part during the forming processes (Boubakar and Boisse, 1998; Manget and Perre, 1999; Dogui, 1989).

To describe the plastic behavior of the material, it is necessary to clarify the concept of the load surface related to a plasticity criterion (Barlat and Brem, 1991) that indicates conditions of plastic flow.

The experimental determination of these areas through various mechanical testing and mathematical modeling has been the subject of many inquisitive efforts such as those using the Von Mises criterion because of its implementation in most commercial finite element codes. This criterion is called the energy criterion in which the elastic deformation energy of the material must not exceed a limit value to remain within the elastic range.

In the case of a metal sheet, the material is considered as having orthotropic plasticity where it reserves three preferred directions as it is used in the Hill criterion (Hill, 1948).

Also, to describe the asymmetric behavior in tension and compression such as the anisotropy of a compact hexagonal structure of a metal sheet, Cazacu *et al.* (2008, 2009) proposed a new orthotropic criterion (Barlat and Lian, 1989; Gronostajsk, 2000; Plunkett *et al.*, 2006).

The objective of this work is to provide a model for numerical simulation of forming processes by plastic deformation of thin metal sheets. Hence, the importance of developing a general framework for elasto-plastic orthotropic models (initial orthotropic and isotropic hardening) based on the choice of an equivalent stress and using the Barlat criterion especially for aluminum alloys (Barlat and Brem, 1991), a hardening law and a plastic potential (Znaïdi *et al.*, 2009; Baganna *et al.*, 2010). An identification of the model parameters from an experimental database is developed.

This database consists of many hardening curves from various tests interpreted as homogeneous (Znaïdi, 2004) and their Lankford coefficients (Lankford *et al.*, 1950). Those plates are obtained from a hot-rolling process. We use in our work a method called the Simplex algorithm for computer programming to identify the constitutive parameters of the material behavior. This is an important step. A new identification strategy with its validation will be presented, followed by a comparative study using the Hill criterion.

2. Anisotropic elasto-plastic constitutive laws

The formulation of the anisotropic elasto-plastic behavior in large deformations is well understood now (Znaïdi, 2004; Haddadi *et al.*, 2006; Boubakar and Boisse, 1998; Manget and Perre, 1999): using the formalism of the rotating frame ensures the objectivity of the behavior law regardless of the natural (isotropic, anisotropic) constitutive model functions.

In this work, we focus on the plastic hardening behavior. The materials are considered as incompressible with negligible elastic deformations. The plastic hardening constitutive laws that we have to study fall within the following framework (with the stress tensor)

$$\bar{f}(\bar{\boldsymbol{\sigma}}, \bar{\alpha}) \leq 0 \quad \bar{\alpha} = \mathbf{Q}[\alpha] \quad (2.1)$$

with \mathbf{Q} being the transformation tensor of Lagrange state to Eulerien state. α represents the internal hardening variable

$$\bar{\mathbf{D}} = \lambda \bar{h}(\bar{\boldsymbol{\sigma}}, \bar{\alpha}) \quad \dot{\bar{\alpha}} = \lambda \bar{l}(\bar{\boldsymbol{\sigma}}, \bar{\alpha}) \quad (2.2)$$

with λ as the plastic multiplier that can be determined from the consistency condition $\dot{\bar{f}} = 0$ and $\bar{\mathbf{D}}$ is the plastic deformation rate tensor.

3. Orthotropic plasticity model

Models are formulated for standard generalized materials with isotropic hardening which are described by an internal hardening variable, a law of evolution and an equivalent deformation.

3.1. Internal variable hardening

This work is limited to plastic orthotropic behavior. In fact, the material is initially orthotropic and remains orthotropic. The isotropic hardening is assumed to be captured by a single

scalar internal hardening variable denoted by α . In particular, we will assume that the elastic range evolves homothetically, the yield criterion is then written as follows

$$f(\bar{\boldsymbol{\sigma}}^D, \alpha) = \sigma_c(\bar{\boldsymbol{\sigma}}^D) - \sigma_s(\alpha) \quad (3.1)$$

where $\boldsymbol{\sigma}^D$ is the deviator of the Cauchy stress tensor (incompressible plasticity).

The function $\sigma_c(\bar{\boldsymbol{\sigma}}^D)$ satisfies the following condition

$$\sigma_c(a\bar{\boldsymbol{\sigma}}^D) = a\sigma_c(\bar{\boldsymbol{\sigma}}^D) \quad \text{for all } a > 0 \quad (3.2)$$

This property implies that the normal $\bar{\mathbf{n}}_c = \partial\sigma_c/\partial\bar{\boldsymbol{\sigma}}^D$ is homogeneous of the zero degree with respect to $\bar{\boldsymbol{\sigma}}^D$

$$\begin{aligned} \bar{\mathbf{n}}_c(a\bar{\boldsymbol{\sigma}}^D) &= \bar{\mathbf{n}}_c(\bar{\boldsymbol{\sigma}}^D) \quad \text{for all } a > 0 \\ \bar{\boldsymbol{\sigma}}^D : \bar{\mathbf{n}}_c &= \sigma_c \end{aligned} \quad (3.3)$$

3.2. Evolution law

We assume the existence of a plastic potential $g(\bar{\boldsymbol{\sigma}}^D, \sigma_s(\alpha))$ as follows

$$g(\bar{\boldsymbol{\sigma}}^D, \sigma_s(\alpha)) = \sigma_p(\bar{\boldsymbol{\sigma}}^D) - \sigma_s(\alpha) \quad (3.4)$$

The hardening function $\sigma_s(\alpha)$ plays the role of the thermodynamic function associated with the internal hardening variable α .

The function $\sigma_p(\bar{\boldsymbol{\sigma}}^D)$ is assumed to be orthotropic positively homogeneous in the first degree with respect to $\bar{\boldsymbol{\sigma}}^D$. The evolution law can be written as follows

$$\bar{\mathbf{D}} = \lambda \bar{\mathbf{n}}_p \quad \bar{\mathbf{n}}_p = \frac{\partial\sigma_p}{\partial\bar{\boldsymbol{\sigma}}^D} \quad \dot{\alpha} = -\lambda \frac{\partial g}{\partial\sigma_s} = \lambda \quad (3.5)$$

The hypothesis of associated plasticity implies that the plastic potential g is identically σ_c .

The behavior model will be defined by data from two equivalent stresses, σ_c and σ_p , which are unique and similar. We consider the case of non-associated normality.

3.3. Equivalent deformation

The equivalent deformation is obtained according to one of the following definitions:

— Equivalent deformation under the criterion ε_c

$$\dot{\varepsilon}_c = \frac{1}{\sigma_c}(\bar{\boldsymbol{\sigma}}^D : \bar{\mathbf{D}}) = \frac{1}{\sigma_c}(\boldsymbol{\sigma}^D : \mathbf{D}) = \frac{\lambda\sigma_p}{\sigma_c} \quad (3.6)$$

— Equivalent deformation according to the potential ε_p

$$\dot{\varepsilon}_p = \frac{1}{\sigma_p}(\bar{\boldsymbol{\sigma}}^D : \bar{\mathbf{D}}) = \frac{1}{\sigma_p}(\boldsymbol{\sigma}^D : \mathbf{D}) = \lambda \quad (3.7)$$

4. Orthotropic equivalent stresses

Any orthotropic function $\sigma_c(\bar{\boldsymbol{\sigma}}^D)$ with respect to $\boldsymbol{\sigma}^D$ is written in a general way according to the following invariant:

- isotropy: $\det(\boldsymbol{\sigma}^D)$, $|\boldsymbol{\sigma}^D|$
- transverse isotropy: $\boldsymbol{\sigma}^D : \mathbf{m}_3$, $(\boldsymbol{\sigma}^D)^2 : \mathbf{m}_3$
- orthotropy: $\boldsymbol{\sigma}^D : (\mathbf{m}_1 - \mathbf{m}_2)$, $\sqrt{(\boldsymbol{\sigma}^D)^2 : (\mathbf{m}_1 - \mathbf{m}_2)}$

where $\mathbf{m}_i = \vec{m}_i \otimes \vec{m}_i$ (without summation), \vec{m}_i being the orthonormal orthotropy landmark.

The application of this configuration to the stress deviator gives us

$$\begin{aligned}\bar{x}_1 &= \sqrt{\frac{3}{2}}(\sigma_{11}^D + \sigma_{22}^D) & \bar{x}_2 &= \frac{1}{\sqrt{2}}(\sigma_{11}^D - \sigma_{22}^D) & \bar{x}_3 &= \sqrt{2}\sigma_{12}^D \\ \bar{x}_4 &= \sqrt{2}\sigma_{23}^D & \bar{x}_5 &= \sqrt{2}\sigma_{13}^D\end{aligned}\quad (4.1)$$

Using the special setup of the space deviators, we can write the stress deviator as follows

$$\begin{aligned}|\boldsymbol{\sigma}^D| &= \sqrt{x_1^2 + x_2^2} & \det(\boldsymbol{\sigma}^D) &= \frac{x_1}{\sqrt{6}}\left(x_2^2 - \frac{x_1^2}{3}\right) \\ x_1 &= \sqrt{\frac{3}{2}}(\sigma_1^D + \sigma_2^D) & x_2 &= \frac{1}{\sqrt{2}}(\sigma_1^D - \sigma_2^D)\end{aligned}\quad (4.2)$$

We introduce the angle θ which defines the orientation of $\boldsymbol{\sigma}^D$ in the deviatoric plane

$$x_1 = |\boldsymbol{\sigma}^D| \cos \theta \quad x_2 = |\boldsymbol{\sigma}^D| \sin \theta \quad (4.3)$$

We define the off-axis angle ψ (angle which defines the orientation of the loading directions with respect to the preferred direction of the material) as in the following

$$\bar{x}_1 = x_1 \quad \bar{x}_2 = x_2 \cos 2\psi \quad \bar{x}_3 = x_2 \sin 2\psi \quad (4.4)$$

This allows us to write them in terms of the two angles θ and ψ

$$\bar{x}_1 = |\boldsymbol{\sigma}^D| \cos \theta \quad \bar{x}_2 = |\boldsymbol{\sigma}^D| \sin \theta \cos 2\psi \quad \bar{x}_3 = |\boldsymbol{\sigma}^D| \sin \theta \sin 2\psi \quad (4.5)$$

Using the special setup of the space deviators, the general form of the equivalent orthotropic plane constraint, is thus

$$\sigma_c(\bar{\boldsymbol{\sigma}}^D) = \sigma_c(\bar{x}_1, \bar{x}_2, |\bar{x}_3|) = \frac{|\bar{\boldsymbol{\sigma}}^D|}{f(\theta, 2\psi)} \quad (4.6)$$

Any type of criterion (4.6) can be written in the form

$$f(\theta, 2\psi) = \frac{|\bar{\boldsymbol{\sigma}}^D|}{\sigma_s(\alpha)} \quad (4.7)$$

where θ is the angle that defines the test and ψ the off-axis angle (Baganna *et al.*, 2010; Lankford *et al.*, 1950).

Table 1. Values of θ relative to various tests

Test	Expansions equibiaxes	Simple traction	Large traction	Simple shear
θ	0	$\pi/3$	$\pi/6$	$\pi/2$

5. Identification procedures

5.1. Basic assumption

In this Section, we focus on the phenomenology of plastic behavior; especially modeling plasticity and hardening based on experimental data represented as families of hardening curves, and Lankford coefficient data. In order to simplify our identification process, the following assumptions are adopted:

- Hypothesis 1 – Identification through “small perturbations” process.
- Hypothesis 2 – The tests used are considered as homogeneous tests.
- Hypothesis 3 – We neglect the elastic deformation; the behavior is considered as rigid plastic incompressible.
- Hypothesis 4 – The plasticity surface evolves homothetically (isotropic hardening).
- Hypothesis 5 – All tests are performed in the plane of the sheet resulting in a plane stress condition.

5.2. Limitation of the model

The identified model is defined by:

- An equivalent stress $\sigma_c(\mathbf{A} : \boldsymbol{\sigma}^D)$, σ_c is an isotropic function. It is assumed that the shape is defined by coefficients of the form m_i .

\mathbf{A} – 4th order orthotropic tensor defined by anisotropy coefficients a_i .

- A potential equivalent stress $\sigma_p(\mathbf{A}_p : \boldsymbol{\sigma}^D)$, σ_p is defined by coefficients of the form m'_i and anisotropic coefficients a'_i .
- Hardening curve $\sigma_s(\alpha)$

The tests used for the identification of this model are “radial” and “monotonous” tests

$$\boldsymbol{\sigma} = \sigma \mathbf{a} \quad (5.1)$$

with $\sigma > 0$ and increasing, and \mathbf{a} is constant.

And the deformation tensor is

$$\boldsymbol{\varepsilon} = \varepsilon \mathbf{b} \quad (5.2)$$

Knowing that $\sigma(\varepsilon)$ is determined from experimental tests as $r(\psi)$.

According to the yield criterion (3.1)

$$\sigma_c(\mathbf{q}) - \sigma_s(\alpha) \leq 0 \quad (5.3)$$

where $\mathbf{q} = \mathbf{A}(a_i) : \boldsymbol{\sigma}$, thus $\mathbf{q} = \sigma \mathbf{A}(a_i) : \mathbf{a}$.

So the equivalent stress (positively homogeneous of one degree)

$$\sigma_c(\sigma \mathbf{A} : \mathbf{a}) = \sigma \sigma_c(\mathbf{A} : \mathbf{a}) = \sigma a_e \quad (5.4)$$

The equivalent deformation is determined from the duality relation

$$\dot{\varepsilon}_c = \frac{\sigma \dot{\varepsilon}}{\sigma_c} \quad (5.5)$$

Similar to the equivalent deformation relative to the potential, we write

$$\varepsilon_p = \varepsilon b_e \quad (5.6)$$

When the potential identifies the criterion, we have $b_e = 1/a_e$.

Under these conditions, our hardening curve may be written as in the following

$$\sigma a_e = \sigma_s(\varepsilon b_e) \Rightarrow \sigma = \frac{\sigma_s(\varepsilon b_e)}{a_e} \quad (5.7)$$

First comment

If our hardening curve is shown by an analytical law such as the following law

$$\sigma_s = k(\alpha_0 + \alpha)^n \Rightarrow \sigma = \frac{k(\alpha_0 + \varepsilon b_e)^n}{a_e} = k_{test}(\alpha_{test} + \varepsilon)^n \quad (5.8)$$

$$k_{test} = \frac{k b_e^n}{a_e} \quad \alpha_{test} = \frac{\alpha_0}{b_e}$$

when n is the same for all tests.

A second analytical law

$$\sigma_s = \sigma_0 + k\alpha^n \Rightarrow \sigma = \frac{\sigma_0 + k(\varepsilon b_e)^n}{a_e} \quad (5.9)$$

$$\sigma_s = \sigma_{0test} + k_{test}\varepsilon^n \quad \text{with} \quad \sigma_{0test} = \frac{\sigma_0}{a_e} \quad k_{test} = \frac{k b_e^n}{a_e}$$

In conclusion, we can say that regardless of the analytical law representing the hardening curve and whatever the test, the value of n does not change.

Second comment

We can also begin our identification procedures using the Lankford coefficient as determined from the tensile test by

$$r = \frac{\dot{\varepsilon}_2}{\dot{\varepsilon}_3} = -\frac{1}{1 + \dot{\varepsilon}_1/\dot{\varepsilon}_2} \quad (5.10)$$

We can notice that the Lankford coefficient is independent of ε . This coefficient is equal to one in the case of isotropy, and remains constant in the case of transverse isotropy. However, in the case of orthotropy, it varies depending on the off-axis angle ψ . This coefficient completely characterizes the anisotropy of the sheet when loaded in its plane

$$\dot{\varepsilon} = \lambda \mathbf{n}_p(\sigma \mathbf{a}) \quad a_{T\psi} = \frac{\dot{\varepsilon}_1}{\dot{\varepsilon}_2} = \frac{[n_p(a)]_{11}}{[n_p(a)]_{22}} \quad r(\psi) = -\frac{1}{1 + a_{T\psi}} \quad (5.11)$$

So identifying this coefficient, means determining $a_{T\psi}$ relative to a well chosen model.

6. Results and discussion

This identification strategy requires: (a) an experimental database, (b) criterion for anisotropic plasticity and (c) validation strategy.

In the particular case of aluminum sheets, where anisotropy is present, the identification of this constitutive law requires the identification of:

- The hardening coefficients k and n ,
- The anisotropy coefficients f , g , h , and n notes that a_i has the form factor of m ,
- The Lankford coefficient $r(\psi)$.

The test specimens are cut in different directions relative to the rolling direction of the sheet, according to the geometry defined in Fig. 1.

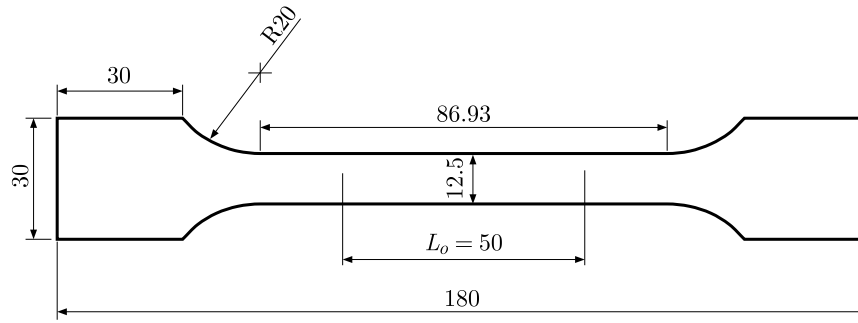


Fig. 1. Test piece in tension. Definition of the systems axis and current dimensions of the active area ($b_0 = 12.5$ mm)

6.1. Identification of k and n

Using the Hollomon law

$$\sigma_s = k\varepsilon^n \quad (6.1)$$

And using the Barlat criterion (Barlat and Brem, 1991)

$$\sigma_c^m = |q_1 - q_2|^m + |q_2 - q_3|^m + |q_1 - q_3|^m \quad (6.2)$$

where q_1 , q_2 and q_3 are the eigenvalues of the tensor \mathbf{q} defined by Eq. (5.3).

Using the plastic Barlat model and respecting the assumptions, the identification of the thin aluminum sheet is equivalent to choosing the coefficients of the model while minimizing the squared difference between the theoretical and experimental results.

In Table 2, we present the values of k and n for different tractions tests.

Table 2. Identification of the constants of the hardening law

ψ	0°	45°	90°
K [daN/mm ²]	15.1117	17.2835	13.8759
n	0.253	0.2316	0.2485

Knowing that the coefficient n is the same for all tests as demonstrated at the beginning of this work. By convention we choose n for traction in the direction $\psi = 0^\circ$ as a reference. For $n = 0.253$, we present different values of k (Table 3).

Table 3. Identification of the constant hardening law for the fixed n

ψ	0°	45°	90°
K [daN/mm ²]	15.1132	18.0828	14.002

In Figs. 2a and 2b, the experimental hardening curves (exp) and the curves identified from the model (ident1) using an average value of n and the curves identified by our model (ident2) are represented. For tensile tests in $\psi = 45^\circ$, the two models (ident1) and (ident2) give a clear fit between the theoretical and experimental results. However, for tests in $\psi = 0^\circ$, identifying these results provides better validation for a good agreement between the experimental and theoretical results for the model (ident2) presented in this work.

6.2. Identification of anisotropic coefficients a_i and shape coefficient m

Our second identification determines the coefficients of anisotropy (f , g , h , n) and the shape coefficient m (Table 4), considering the Barlat criterion (6.2).

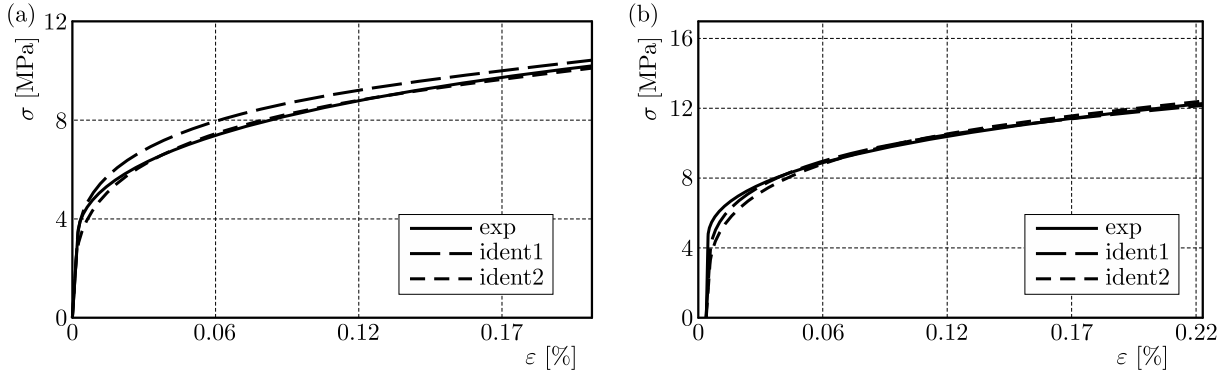


Fig. 2. Identification of the hardening curve: (a) $\psi = 0^\circ$, (b) $\psi = 45^\circ$

Table 4. Identification of anisotropic coefficients and the shape coefficient m

F	g	h	n	m
0.2854	0.2064	0.3335	0.8921	6.9584

6.3. Evolution of the anisotropic and the Lankford coefficient

Using the identified anisotropic coefficients, we represent in Fig. 3a the developments of the Lankford coefficient and the evolution of the anisotropy based on off-axis angles (Fig. 3b).

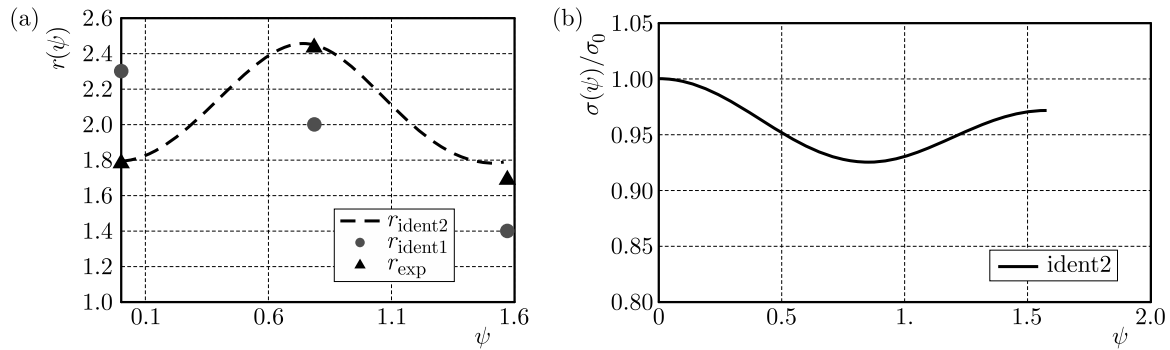


Fig. 3. (a) Evolution of the Lankford coefficient and (b) evolution of the anisotropy based ψ

We find a good agreement between the experimental results and those from the model using the Barlat criterion. We notice an important anisotropy at $\psi = 45^\circ$ (see Fig. 3b). However, the identification using the Hill criterion is not validated by the Lankford coefficient.

6.4. Evolution of the load surface

The model (ident2) allows us to study the load surface on each test. We note that this material is resistant to simple shear much more than to simple traction. In contrast, the plastic flow in wide traction (i.e. the specimen length is comparable to its width) is quickly reached.

7. Validation

We use tensile tests at $\psi = 90^\circ$ in order to validate our model. The results show a good agreement between the theoretical results on the model (using anisotropic coefficients, shape coefficient m) and experimental data (Fig. 5).

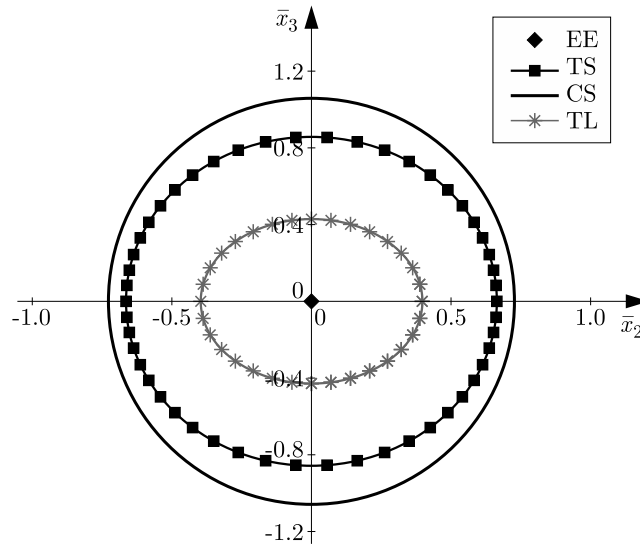


Fig. 4. Evolution of the load surface in the deviatoric plane (\bar{x}_2, \bar{x}_3)

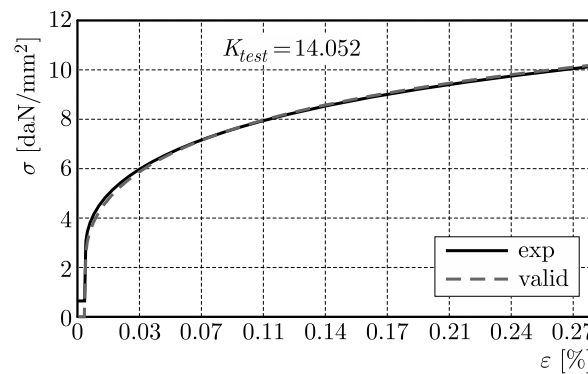


Fig. 5. Validation of the hardening curve at $\psi = 90^\circ$

8. Conclusion

In this work, we show that the identification strategy results can be extracted. This identification has focused both on plastic material parameters of the constitutive law and the Lankford coefficients. Thus, the plastic behavior model: the Hollomon law and the Barlat criterion with 5 parameters are identified.

Validation by comparing the models with the experiment data base has been performed.

The model using the Barlat criterion is in good agreement with the experimental results relating to the Lankford coefficient. It is better than the Hill model.

Following this strategy, we observe very pronounced anisotropy of Aluminum A5 and the load surface for different tests at the end of this identification.

Reference

1. BAGANNA M., ZNAIDI A., KHARROUBI H., NASRI R., 2010, *Identification of Anisotropic Plastic Behavior Laws for Aluminum 2024 after Heat Treatment Materials from Off-Axis Testing*, Toulouse
2. BARLAT F., BREM D.L.J., 1991, A six components yield function for anisotropic materials, *International Journal of Plasticity*, **7**, 693-712

3. BARLAT F., LIAN J., 1989, Plastic behavior and stretchability of sheet metals. Part I: A yield function for orthotropic sheet under plane stress conditions, *International Journal of Plasticity*, **5**, 51-56
4. BOUBAKAR L., BOISSE P., 1998, Anisotropic elastoplastic behavior for numerical analysis of thin shells in great transformations, *Européene Review Mechanics*, **7**, 6
5. CAZACU O., IONESCU I.R., YOON J.W., 2009, Orthotropic strain rate potential for the description of anisotropy in tension and compression of metals, *International Journal of Plasticity*
6. CAZACU O., PLUNKETT B., BARLAT F., 2008, Orthotropic yield criterion description of anisotropy in tension and compression of sheet metals, *International Journal of Plasticity*, **24**, 847-866
7. DOGUI A., 1989, Anisotropic plasticity in large deformation, Doctoral thesis of sciences, University Claude Bernard-Lyon
8. GHOUATI O., GELIN J.C., 2001, A finite element based identification method for complex metallic material behavior, *Computational Materials Science*, 2157-2168
9. GRONOSTAJSK Z., 2000, The constitutive equations for FEM analysis, *Journal of Material Processing Technology*, **106**, 40-44
10. HADDADI H., BOUVIER S., BANU M., MAIER C., TEODOSIU C., 2006, Towards an accurate description of the anisotropic behaviour of sheet metals under large plastic deformations: modelling, numerical analysis and identification, *International Journal of Plasticity*, **22**, 2226-2271
11. HILL R., 1948, A theory of the yielding and plastic flow of anisotropic metals, *Proceedings of Royal Society of London*, **A93**, 281-297
12. KIM D., BARLAT F., BOUVIER S., RABAHALLAH M., BALAN T., CHUNG K., 2007, Non-quadratic anisotropic potential based on linear transformation of plastic strain rate, *International Journal of Plasticity*, **23**, 1380-1399
13. LANKFORD W.I., SNYDER S.C., BAUSHER J.A., 1950, New criteria for predicting the press performance of deep-drawing sheets, *Transactions of American Society for Metals*, **42**, 1196-1232
14. MANGET B., PERRE P., 1999, A large displacement formulation for anisotropic constitutive laws, *European journal of Mecanique*, **18**, 5
15. PLUNKETT B., CAZACU O., BARLAT F., 2006, Orthotropic yield criterion for hexagonal closed packed metals, *International Journal of Plasticity*, **22**, 1171-1194
16. ZNAIDI A., 2004, Plasticity orthotrope in large deformation». PhD thesis at the Faculty of Sciences of Tunis
17. ZNAIDI A., SOULA M., GUELLOUZ S., NASRI R., 2009, *Constitutive Equations Identification Strategies Elastoplastic Anisotropics Heet Material Using Associated and Unassociated Laws of Plasticity*, Marseille

Manuscript received March 5, 2015; accepted for print February 8, 2016

ANALYSIS OF THE STOCHASTIC TECHNICAL STABILITY OF ENGINEERING STRUCTURES ON AN EXAMPLE OF A MOVING CAR

JERZY KISIŁOWSKI

*Kazimierz Pulaski University of Technology and Humanities in Radom, Faculty of Transport and Electrical Engineering,
Radom, Poland; e-mail: jkisolow@kisolowscy.waw.pl*

JAROSŁAW ZALEWSKI

*Warsaw University of Technology, Faculty of Administration and Social Sciences, Warszawa, Poland
e-mail: j.zalewski@ans.pw.edu.pl*

The article presents analysis of the stochastic technical stability of mathematical models (described by the second-order ordinary differential equations) of technical objects, on the example of a moving motor vehicle with the disturbed location of the center of mass, as a result of a non-uniform load. After conducting simulation of motion of a sport vehicle mathematical model, using the MSC Adams/Car software, executing a maneuver of double lane change without completely returning to the original road lane, interpretation of the results in accordance with the given definition has been attempted. Specifically, the aspect of determining the probability of the solution remaining in a certain area of feasible solutions has been highlighted, as well as determination of the magnitude of this probability for stable motion. In addition, attention has been paid to the selection of the upper limit of probability, for which, under certain conditions, stable motion can be determined.

Keywords: stochastic technical stability, mathematical model of motor vehicle, nonlinearity

1. Introduction

Analyses on the safety and dynamics of the means of transport seem an important issue from the scientific research point of view. These studies can be performed on real objects or by using their mathematical models and simulating their motion. One of the problems strictly related to the road traffic safety is the stability of the motor vehicle in different traffic conditions, for example with various vehicle load and road surface conditions. For examination of stability various criteria may be used (Börner and Iserman, 2005; Heinzl *et al.*, 2002; Kaneko *et al.*, 2002; Lenasi *et al.*, 1998; Mokhiamar and Abe, 2002), however not all give clear solutions or allow taking into account random disturbances acting on the examined model.

In the presented analysis, definition of the stochastic technical stability (Bogusz, 1972) is used, because of the possibility to consider random external disturbances acting on the system (derived from an uneven road surface for motor vehicles, see Kisilowski and Zalewski (2008a,b), or from the inequalities of the track for railway vehicles, see Kisilowski *et al.* (1985), Kisilowski and Kardas-Cinal (1993). Furthermore, it is possible to analyse the obtained results on the basis of motion trajectories, which in turn allows making reference to the results or assumptions concerning research on the real motor vehicles.

The aim of this paper is to present examination of the stochastic technical stability on the example of a moving motor vehicle.

2. Description of the considered example

When examining the stochastic technical stability, the following assumptions are made:

- the vehicle body is assumed to be rigid;
- randomly occurring road surface unevenness is described as a stochastic process which is stationary in a broader sense and globally ergodic;
- all coordinate systems are adopted as in Zalewski (2011);
- flexible elements connecting wheel masses to the vehicle body are described by non-linear functions.

Figure 1 shows the physical model of the simulated two-seater sport vehicle in the MSC Adams/Car environment, with degrees of freedom accepted as in Nabagło (2006). This model is assumed to reflect the real vehicle, however no identification concerning this assumption has been performed. The load is represented by two masses corresponding to the driver and the passenger as well as the baggage located in the front of the vehicle (under the bonnet). The location of the center of mass of the vehicle body has been determined in relation to the so-called point “origo” (Fig. 2), which represents the origin of the coordinate system $O_d x_d y_d z_d$ located on the road surface, but moving along with the vehicle.

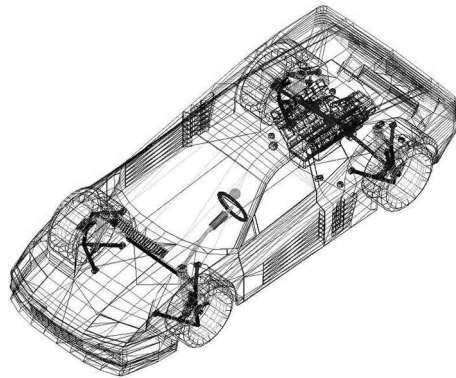


Fig. 1. Full physical model of the examined vehicle. Source: MSC Adams/Car

The suspension in the physical model consists of wishbone arms and McPherson struts. Elastic-damping elements have non-linear characteristics. Power is transferred to the rear wheels, the engine is also mounted at the back of the vehicle. A typical steering system is used.

Assuming that the vehicle body can be represented by a set of cuboids mapping specific parts in a vehicle body, mathematical model of the vehicle is described basing on the works by Gillespie (1992) and Ng (2008), using the equations for translational and rotational motion. It is also supplemented by equations describing both the suspension and the unsprung masses (Nabagło, 2006).

The basic parameters of the sport vehicle model in MSC Adams/Car are:

- mass of the unladen vehicle body $m_{VB} = 995$ kg;
- nominal coordinates of the center of mass of the unladen vehicle body relative to the “origo”: $x_c = 1.5$ m, $y_c = 0$, $z_c = 0.45$ m;
- nominal values of the moments of inertia relative to the axes passing through the “origo” in the unladen vehicle body: $I_{xx} = 401.485$ kg m², $I_{yy} = 2940.237$ kg m², $I_{zz} = 2838,750$ kg m²;
- nominal values of the moments of deviation relative to the axes passing through the “origo” in the unladen vehicle body: $I_{xy} = 0$ kg m², $I_{xz} = 671.625$ kg m², $I_{yz} = 0$ kg m².

For the analysis of motion analysis in extreme conditions, the location of the center of mass in the vehicle body is assumed to have been disturbed resulting from the uneven load. By adding masses of the driver, passenger and baggage, the mass of the entire vehicle is increased, and its distribution in the vehicle changed. The following configuration of disturbances is assumed:

- the vehicle body is loaded with the masses representing the driver $m_d = 74$ kg, passenger $m_p = 105$ kg and the baggage $m_b = 45$ kg. Their distribution in the vehicle body is shown in Figs. 2 and 3.

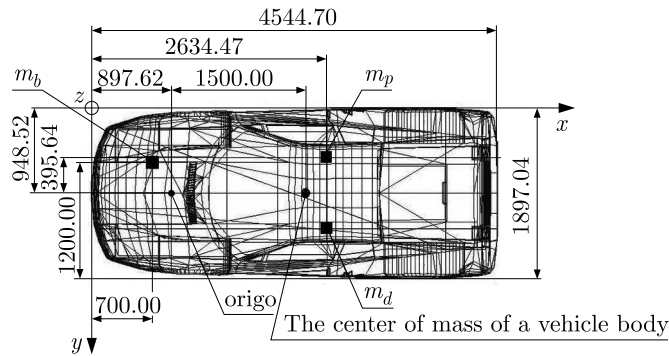


Fig. 2. Distribution of masses loading the vehicle body. Plan view. Source: own research

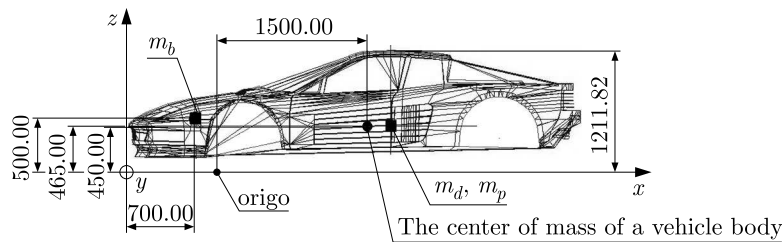


Fig. 3. Distribution of masses loading the vehicle body. Side view. Source: own research

Based on the above assumptions, new coordinates of the center of mass in the laden vehicle body have been determined, which as an effect gave the following results:

- the total mass of the laden vehicle body $m_{VBl} = 1174$ kg;
- coordinates of the center of mass of the laden vehicle body relative to the “origo”: $x_c = 1.562$ m, $y_c = 0.016$ m, $z_c = 0.471$ m;
- moments of inertia of the laden body relative to the axes passing through the “origo”: $I_x = 460$ kg m², $I_y = 3624$ kg m², $I_z = 3464$ kg m²;
- moments of deviation of the laden vehicle body relative to the axes passing through the “origo”: $I_{xy} = 29$ kg m², $I_{xz} = 863$ kg m², $I_{yz} = 8.8$ kg m².

Random disturbances stemming from the road unevenness have been provided using the “2d_stochastic_uneven.rdf” file available in MSC Adams/Car database. The file defines the desired road profile using ARC901 function [16].

Generation of the random disturbances, on the basis of [16], is realised as follows:

- white noise signals are generated based on random variables with almost uniform distribution. Two of these variables are assigned to the road at a distance of every 10 mm;
- the resulting values are integrated over the length of the road argument using the time-discrete filter, in which the independent variable is the road. The effect of this filter is to obtain two approximated realisations of the white noise velocity;

- the obtained signals, having such properties, become road profiles. According to the definition accepted by Múčka (2009), it is assumed that road waviness for the considered example is 2. The research showed that the waviness obtained for the measured road spectral densities ranges between 1.8 and 2.2, see Múčka (2009);
- after that, both the realisations $z_1(s)$, $z_2(s)$ are correlated in order to obtain a profile of the road for the left and right wheels $z_l(s)$, $z_r(s)$ [16]. The correlation coefficient is 0 for the two different road profiles and 1 for the uniform profile. A method of calculating this coefficient is presented the following by formula

$$\begin{aligned} z_l(s) &= z_1(s) + \frac{corr_{rl}}{2}[z_2(s) - z_1(s)] \\ z_r(s) &= z_2(s) + \frac{corr_{rl}}{2}[z_2(s) - z_1(s)] \end{aligned} \quad (2.1)$$

where $corr_{rl}$ is the correlation coefficient between the road profiles for the signal realisations $z_1(s)$, $z_2(s)$.

In the examined vehicle model, the default tire model PAC89 has been removed because it is unable to cooperate with the road profile having random irregularities whose wavelength is smaller than the wheel radius. Instead, the FTIRE model (Flexible Structure Tire odel) has been used, which consists of deformable panels connected by spring elements (Fig. 4).

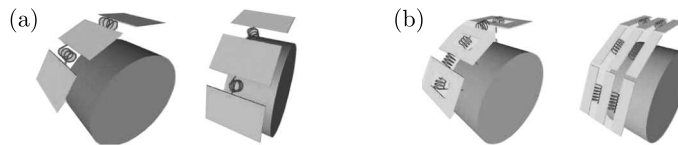


Fig. 4. Schematics of the FTIRE model for (a) radial and (b) circumferential direction.
Source: www.cosin.eu

3. Application of the stochastic technical stability

The definition of the stochastic technical stability is presented, among others, in Bogusz (1972).

Given a system of stochastic equations:

$$\frac{dx}{dt} = f(x, t, \xi(t)) \quad (3.1)$$

where $x = (x_1, \dots, x_n)$ and $f(x, t, y) = (f_1, \dots, f_n)$ and $\xi(t) = (\xi_1, \dots, \xi_n)$ are vectors, whereas $\xi(t)$ for $t \geq 0$ is a stochastic process describing randomly occurring disturbances. For the function $f(x, t, y)$, it is assumed that this function is determined for each $x \in E_n$, $y \in E_n$ and $t \geq 0$. It is also assumed that for the stochastic process $f(0, t, \xi(t))$, there occurs

$$P \left\{ \int_0^T |f(0, t, \xi(t))| dt < \infty \right\} = 1 \quad \text{for each } T > 0 \quad (3.2)$$

Also, the existence of a stochastic process $f(X, t, \xi(t))$ fulfilling the Lipschitz criterion in the interval $[0, T]$ has been assumed, for another process $\eta(t)$ absolutely integrable in the given interval, which can be described as follows

$$|f(x_2, t, \xi(t)) - f(x_1, t, \xi(t))| \leq \eta(t)|x_2 - x_1| \quad (3.3)$$

The result of the above assumptions is the existence of only one solution with the initial conditions $t = t_0$ and $x(t_0) = x_0$, which is an absolutely continuous stochastic process with the probability 1 for $t \geq t_0$.

It has been as well assumed that in the Euclidean space E_n there exist two areas: ω – limited and open as well as Ω – limited and closed, where $\omega \subset \Omega$. The existence of a positive number ε , where $0 < \varepsilon < 1$, and a stochastic process $X(t)$ specified for $t \geq t_0$ has also been assumed.

The initial conditions of each solution are described as $t = t_0$, $x(t_0) = x_0$, and the solution itself as (t, t_0, x_0) .

The definition of stochastic technical stability is: if every solution to equation (3.1), having its initial conditions in ω , belongs to the area Ω with the probability $1 - \varepsilon$, then system (3.1) is stochastically technically stable towards ω and Ω as well as the process $\xi(t)$ with the probability $1 - \varepsilon$ (Fig. 5).

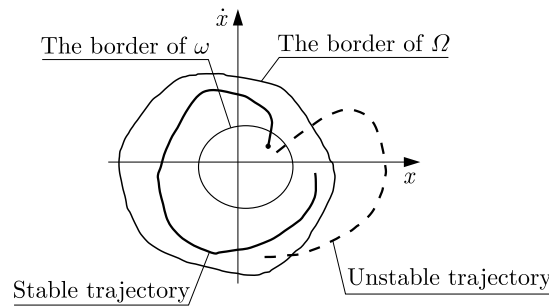


Fig. 5. Graphic interpretation of the stochastic technical stability. Source: Bogusz (1972)

The definition is described by the formula

$$P\{(t, t_0, x_0) \in \Omega\} > 1 - \varepsilon \quad \text{for} \quad \bar{x}_0 \in \omega \tag{3.4}$$

To properly apply the given definition, several additional conditions must be fulfilled. At first, it seems necessary to avoid bifurcation, i.e. a double solution to the nonlinear system taken under consideration. In the theory of nonlinear problems, certain cases can be found where there are two or more solutions of the same system, which gives a misleading picture under certain conditions. In this situation, it is necessary to prove the derivativeness and integrability, especially for functions describing randomly occurring disturbances. The integrability of the stochastic process described by condition (3.2) provides an opportunity to analyse the obtained trajectory of the vehicle in terms of stability studies based on the trajectories, while Lipschitz criterion (3.3) ensures the existence of the derivative of the function describing randomly occurring disturbances, originating from the road in this case.

The Lipschitz criterion may be related to the issues presented by Kuratowski (2012), concerning the existence of derivatives of functions. It is important to determine how the stochastic processes X and η can be related to variables marked for the curve in Fig. 6. Since in Fig. 6 there are variables x and x' that have specific values, so for the processes X and η it can also be assumed that at certain moments they adopt the specific values. Thus, as a result, condition (3.3) provides the relevant slope of the process X realisation with respect to the process η , which is a sort of preservation or warranty of the existence of the derivative in the range between x_1 and x_2 .

In addition, it is important that the stochastic process describing the road surface irregularities is:

- stationary in a broader sense (time invariant), because as it is known the road does not change in time and the irregularities occurring on its surface are located randomly fixed for a specific, also a stationary reference system;

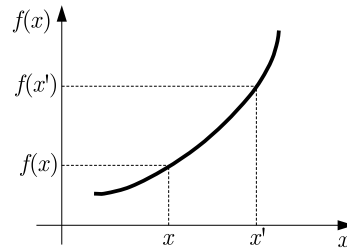


Fig. 6. Graphic interpretation of the Lipschitz criterion for the function $f(x)$. Source: Kuratowski (2012)

- globally ergodic consisting in the fact that the value of the average height of irregularities and their correlation function is equal for various realisations of the process, which provides the ability to conduct analyses based on one realisation. This realisation represents then the whole stochastic process describing road unevenness.

Without the two features mentioned above, it would be impossible to conduct the analysis of the vehicle model motion on the basis of one realisation of the stochastic process describing the randomly occurring road unevenness. It is important from the point of view of disturbances coming from the road. The analysed vehicle model has, as previously mentioned, nonlinear characteristics of its suspension, which still makes it impossible to generalize the obtained results for a set of models with similar features. However, as for the road, providing the above mentioned conditions allows the analysis of various vehicle models on the road with the same characteristics of unevenness.

Another important issue, from the point of view of nonlinear systems analysis, is to determine the initial conditions (the area ω , longitudinal velocity, etc.) as well as a set of feasible solutions (Ω) in which the solution trajectory is considered to be stable.

The last condition is to determine the significance of the number ε , which defines the range of probability at which the solution remains in the feasible area. This number may be a determinant of the stability of the entire system. It is worth noting that, in accordance with the principle of the center of mass in quasi stiff bodies, the motion analysed is that of a representative point (often the center of mass) to which the entire system is referred.

4. Analysis and interpretation of the simulation results

An incomplete double lane change maneuver is analysed, where at the end of the maneuver the vehicle remains roughly in the middle of the width of a single-lane road. The simulation has been carried out for a speed of 120 km/h, reflecting the necessity of an emergency response to the emerging obstacle. The simulation has been carried out in MSC Adams/Car in two configurations:

- vehicle laden with a driver and a passenger having uneven masses, plus a baggage, moving on a flat and dry road surface;
- vehicle laden with a driver and a passenger having uneven masses, plus a baggage, however moving on an icy road surface with randomly occurring irregularities.

During this maneuver, the vehicle covered a distance of approximately 580 m measured in a straight line. The two resulting trajectories for the described case are shown in Fig. 7.

In the presented case, the area ω has been assumed to be a specific width of the road lane, in which the vehicle should remain at the beginning of the maneuver. It is therefore necessary to take into account the overall width of the vehicle applied to the width of the lane. It has been assumed that, in this case, the single lane is about 3 m wide.

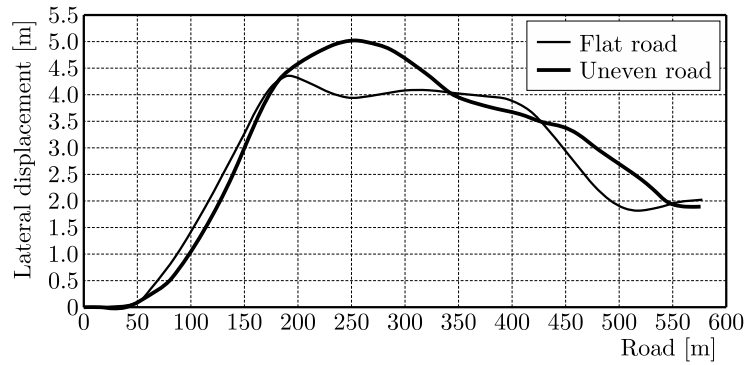


Fig. 7. Lateral motion of the vehicle in relation to the covered distance for the laden vehicle body and both road surface conditions. Source: own research

The area of feasible solutions Ω , containing a part of the trajectory associated with the road length on which the featured maneuver occurs, should be referred to the total width of the road (two lanes). As mentioned previously, the resulting trajectories show the motion of the center of mass of the analysed vehicle. At each point of the trajectories, especially at their most lateral displacements, the entire width of the vehicle should be considered. It has been assumed that the whole width of the road is 6 m, referring to the single-lane, two-way road. The total width of the simulated vehicle model is 1.9 m. As it can be noticed, the trajectory of the vehicle motion on a flat road surface remains in the area of stability. Meanwhile, the trajectory obtained for the more extreme road conditions exits this area.

In Fig. 8, the conditions under which the vehicle remains in a particular lane of the road are schematically illustrated. Let L be the total width, where the vehicle can remain during the maneuver, and L_1 – the width allowable for a representative point (here, the center of mass) of the vehicle.

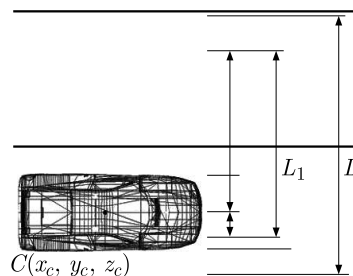


Fig. 8. The conditions of remaining in the specific width of the road, which can be assumed as stable. Source: own research

If the width of the lane is assumed as above, then at a given vehicle width (1.9 m, Fig. 2) the trajectory of the center of mass, as a representative point, may remain in the lane L_1 (about 4 m wide) for stable motion. However, in both cases, the trajectory extends a 4 m width. The conclusion is that the analysed model, for the assumed conditions on a dry and flat road surface, is at the limit of stability and exceeds it for the icy and uneven road surface.

The adoption of the above areas (width of the road) is crucial for the stability examination, namely to find the probability of the solution remaining in a specific area, which is perceived to be stable. It also seems important to define the parameters of the road for which the stability is examined.

In order to examine the stochastic technical stability of the analysed vehicle model during the maneuver, a certain part of the trajectories ranging from 170 to 420 m of the road has been selected, where the hypothetical obstacle avoidance occurs. This selected part is divided into

15 classes $[K_1; K_{15}]$ every 0.1 m (Fig. 9) in terms of lateral displacement. On the axis of the lateral displacement, the classes belonging to the Ω area are marked.

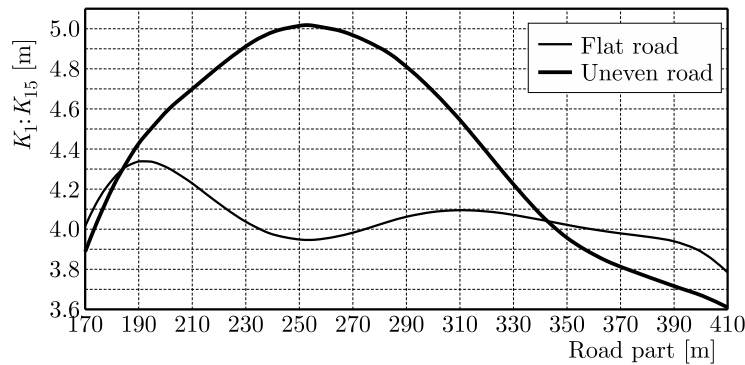


Fig. 9. The selected part of trajectories obtained for the obstacle avoidance with the division of Ω into disjoint classes $[K_1; K_{15}]$. Source: own research

The frequencies of events for the obstacle avoidance [170 m; 410 m] have been calculated for every 20 m step of the road, which gave 12 subintervals.

Implementation of the disturbances took place in the domains of the road, height of road irregularities and their wavelengths. After transformation by velocity, the time, amplitude and frequency domains have been obtained. The frequencies of events have been calculated, where the solution remains in a certain class of Ω (acceptable width of the lane). Equation (4.1) has been used, however with replacing the time with the road length as the area of specificity of the considered system

$$W(K_j) = \frac{T_{K_j}}{T} = \frac{T_{K_j}V}{TV} = \frac{S_{K_j}}{S} = \frac{N_{K_j}\Delta s}{N\Delta s} = \frac{N_{K_j}}{N} \quad (4.1)$$

where: T_{K_j} is the time when the model remains in the given class; T – total time necessary to complete the considered part of the road; S_{K_j} – road length in the given intervals for which the model remains in the given class; S – total distance of the discussed part of the road; N_{K_j} – number of sub-intervals for which the solution remains in the given class; N – number of all sub-intervals.

Research on the stochastic technical stability of a motor vehicle model has been made by comparing the trajectories of motion and the frequencies of the solution remaining in every class of the area Ω . Attention has been paid to deviation of the trajectory from the nominal position. The nominal position has been assumed for the trajectory of the vehicle moving on a flat and dry road surface (curve indicated by a thin line).

For the area of feasible solutions, two lanes of 6 m wide road have been assumed. The minimum width of the lane in accordance with the regulation of the Minister of Transport and Maritime Economy from 2 March 1999 is 2.5 m. Therefore, in accordance with Fig. 9, it has been assumed that the stable motion occurs when the center of mass of the vehicle model of a certain width does not exceed a predetermined distance from the middle line dividing the road into two lanes (half width of L_1).

It has also been assumed that the car avoiding the obstacle at a speed of 100 km/h should fit in the width of about 4 m of the 6 m wide road. It results from the study of the vehicle center of mass trajectory, so the width of the vehicle should be taken into account. When the motion is disturbed, i.e. when the center of mass of the car model exceeds the accepted range of a 4 m wide road part (icy surface), the outer wheels are dangerously close to the edge of the road or may remain in contact with the shoulder.

The maximum amplitude values of the trajectory of the vehicle with the disturbed center of mass, for a dry road surface, are near the border of stability. For the icy road, the trajectory trespasses the accepted area of stability.

In Tables 1 and 2, the frequencies of events are presented on both the flat and dry as well as uneven and icy road surfaces. Significant differences are found in classes 3, 4, 5 and 14.

Table 1. Frequencies of events for the solution remaining in the given class of the area Ω . Analysis for the flat road surface. Source: own research

Class	1	2	3	4	5	6	7	8	9	10	11	12	13	14	15
N_{K_j}	0	1	0	4	6	0	1	1	0	0	0	0	0	0	0
$W(K_j)$	0	0.077	0	0.308	0.462	0	0.077	0.077	0	0	0	0	0	0	0

Table 2. Frequencies of events for the solution remaining in the given class of the area Ω . Analysis for the uneven road surface. Source: own research

Class	1	2	3	4	5	6	7	8	9	10	11	12	13	14	15
N_{K_j}	1	1	2	1	0	0	1	0	1	1	0	1	1	2	1
$W(K_j)$	0.077	0.077	0.154	0.077	0	0	0.077	0	0.077	0.077	0	0.077	0.077	0.154	0.077

In order to relate the results to the definition of stochastic technical stability, the probability of a solution remaining in a certain class of the feasible solutions area Ω should be determined first, and then the parameter ε defined by formula (3.4) related to it.

It has been assumed that the probability of the solution remaining in the certain class is closely related to the frequencies determined in Tables 1 and 2. In both tables, the total frequency of event rate is equal to 1, thus using the formula

$$W(K_j) = \frac{N_{K_j}}{\sum N_{K_j}} \tag{4.2}$$

where: $W(K_j)$ is the frequency of the solution remaining in the j -th class; N_{K_j} – number of events in the j -th class; $\sum N_{K_j}$ – total number of events in all classes, it can be concluded that the frequency can be used to determine the probability.

Then, if the width of Ω is divided, e.g., into 15 classes and treated as an area in which the trajectory as a whole remains with the probability equal to 1, then using to the parameter ε the width of feasible solutions can be narrowed to such, that only the trajectory of the stable vehicle motion should fit without changing the area Ω but only adjusting the stable area for specific requirements. The parameter ε should be adopted by subtracting as many classes from the width of the road (Ω) as under the above accepted principles correspond to the stable area.

For the presented case, the parameter ε should adopt a value corresponding to the eight lower classes $[K_1; K_8]$ occupied by the trajectory of motion obtained for the dry and flat road surface, i.e. $\varepsilon = 8/15 = 0.53$, and the probability according to formula (3.4) $P = 1 - \varepsilon = (15 - 8)/15 = 0.47$, respectively.

As a consequence of the presented considerations, the probability of the whole trajectory remaining in the stable area should, in the presented case, be greater than or equal to 0.47, which, for the trajectory of the vehicle on a dry and flat road, is fulfilled. For a trajectory that would run closer to the axis of the road, this probability would likely be significantly greater than 0.47. For the trajectory of the vehicle on an uneven and icy road, the probability of remaining in the stable area (subtracting 14 classes) is close to zero.

5. Conclusions

Based on the simulation of the vehicle motion in Adams/Car, trajectories have been obtained in two different road conditions. They show that a seemingly slight disturbance of the center of mass in the vehicle can have a greater impact on the stochastic technical stability of the vehicle motion, the greater the bad traffic conditions are.

In addition, for vehicles after an accident repair, it seems that on the basis of stability examination it would be possible to apply such a vehicle for admission to further exploitation.

Also, it has been shown how to use the definition of stochastic technical stability of mathematical models in examination of the technical objects in different conditions. The versatility of this method can provide testing in different environments (not just in the case of road vehicles). The greatest advantage of the presented method is the possibility of making an analysis based on the obtained trajectory and a comparison with the stability of real objects (example for motor vehicles presented in Zalewski (2011)).

The scope of further research can cover the stochastic technical stability analysis for different mathematical models in different road conditions and for different maneuvers.

References

1. BOGUSZ W., 1972, *Technical Stability* (in Polish), Warszawa 1972, PWN
2. BÖRNER M., ISERMANN R., 2005, The characteristic velocity stability indicator for passenger cars, *Vehicle System Dynamics*, **43**, 8
3. GILLESPIE T.D., 1992, Fundamentals of vehicle dynamics, *SAE International*
4. HEINZL P., LUGNER P., PLÖCHL M., 2002, Stability control of a passenger car by combined additional steering and unilateral braking, *Supplement to Vehicle System Dynamics*, **37**
5. KANEKO T., KAGEYAMA I., TSUNASHIMA H., 2002, Braking stability of articulated vehicles on highway, *Supplement to Vehicle System Dynamics*, **37**
6. KISIŁOWSKI J., CHOROMAŃSKI W., ŁOPATA H., 1985, Investigation of technical stochastic stability of lateral vibrations of mathematical model of rail vehicle, *Engineering Transactions*, **33**
7. KISIŁOWSKI J., KARDAS-CINAL E., 1993, On a certain method of examining stability of mathematical models of railway vehicles with disturbances occurring in teal objects, *VSD Supplement to vol. 23, Proceedings of 13th IAVSD Symposium Held in Chendu, Sichuan, P.R. China, August 23-27*
8. KISIŁOWSKI J., ZALEWSKI J., 2008a, Chosen problems of examination of car stability, *Archives of Transport Systems Telematics*, **1**, 1
9. KISIŁOWSKI J., ZALEWSKI J., 2008b, On a certain possibility of practical application of stochastic technical stability, *Maintenance and Reliability*, **37**, 1
10. KURATOWSKI K., 2012, *Differential and Integral Calculus: Functions of One Variable* (in Polish), PWN, Warsaw
11. LENASI J., DANON G., ŽEŽELIJ S., 1998, Lateral stability of a braking vehicle on the friction limit, *Supplement to Vehicle System Dynamics*, **29**
12. MOKHIAMAR O., ABE M., 2002, Combined lateral force and yaw moment control to maximize stability as well as vehicle responsiveness during evasive manouvering for active handling safety, *Supplement to Vehicle System Dynamics*, **37**
13. MÚČKA P., 2009, Sensitivity of road unevenness indicators to road waviness, *Journal of Testing and Evaluation (JTE)*, February

14. NABAGŁO T., 2006, Synthesis of semi-active suspension control system with magneto-rheological elements (in Polish), Doctoral Thesis, Cracow University of Technology, Kraków, Poland
15. NG L., 2008, Reinforcement learning of dynamic collaborative driving, Doctoral thesis, Waterloo, Ontario, Canada
16. Using Adams, MSC Software Corporation
17. ZALEWSKI J., 2011, Modelling of the influence of car body disturbances on the stability of motion of road vehicle (in Polish), Doctoral Thesis, Warsaw University of Technology, Warszawa, Poland

Manuscript received March 16, 2015; accepted for print February 10, 2016

LOAD DISTRIBUTION IN THE WORM MESHING

HENRYK G. SABINIĄK

Technical University of Lodz, Łódź, Poland
e-mail: henryk.sabiniak@p.lodz.pl

The paper presents a theoretical analysis of deflections of circular and rectangular cantilever plates of an elastically built-in edge. The problem has been solved using the finite difference method. A method of determination of load distribution between two plates being in contact along an arbitrary line has been presented. Different shapes of these plates constitute models of mating of cylindrical and globoidal worm meshings. To verify the presented theory of searching for load distributions along the contact lines in these meshings, experimental investigations with the freezing of stresses in the cylindrical worm meshing have been carried out. Directions of investigations that would specify further theoretical considerations over load distribution in globoidal gear meshings have been indicated.

Keywords: finite differences, circular plate, cantilever plates, worm teeth, load distribution

Notations

A – distance of axes, auxiliary constant
 D – binding rigidity of plate
 E, ν – Young's modulus and Poisson's ratio
 F, F_i – force and force acting at point i of contact line, respectively
 $F_i^1(r_i, \varphi_i), F_i^2(r_i, \varphi_i)$ – force acting at point i of contact line of plate 1 and 2, respectively
 F_w – inter tooth force
 $K_{r,\varphi}^{r_i,\varphi_i}$ – dimensionless parameter of deflection of plate
 R, R_n – minimum and maximum radius of the plate, respectively
 R_z – radius of tooth tips of worm wheel
 h – plate thickness
 m – module
 p – screw parameter
 q – linear load
 r – average radius of circular cantilever plates
 r_g – radius of globoid of worm wheel
 r_n – radius of cylinder pitch of worm
 z_1 – number of teeth of worm
 $(r, \varphi), (r_i, \theta, z), (x, y, z)$ – polar, cylindrical and rectangular coordinates, respectively
 α_n – pressure angle
 β – angle between contact line and rubbing speed vector
 φ_1 – angle of rotation of worm
 ω – deflection

$\omega_0(r, \varphi), \omega_0^1(r, \varphi), \omega_0^2(r, \varphi)$ – deflection at point of coordinates (r, φ) corresponding to total load acting on plate, plate 1 and plate 2, respectively

$\omega_i(r, \varphi)$ – deflection at point of coordinates (r, φ) caused by concentrated force $F_i(r_i, \varphi_i)$ acting on plate

Indices: I, II, III – numbers of the contact lines.

1. Introduction

The compactness of construction, silent running and the possibility of obtaining a large transmission ratio on one stage, cause the worm gears to be one of the most popular types of toothed gears.

At the stage of designing cylindrical and globoidal worm gears, there are actually two problems to be dealt with: rubbing speed and load distribution in the meshing.

Great rubbing speeds in the meshing are characteristic for worm gears. This is their negative feature, since they are the source of power losses which, in turn, change into heat during the operation of the gear. This problem is well-known to the constructors of worm gears who can lessen this negative effect while designing by a proper selection of tooth profile geometry, a shift in the profile and the selection of material (Buckingham, 1960; Niemann and Winter, 1983; Crosher, 2002; Dudás, 2005).

On the other hand, load distribution in the worm gear meshing can be considered unknown or hardly known. The knowledge of distribution of load along the contact lines of the mating teeth and the related distribution of stresses in the tooth foot, as well as of the laws governing the above will enable one – through constructional procedures at the design stage – to obtain such a distribution of load that will allow increasing the durability of the meshing or its load-carrying capacity.

The widespread use of rectangular and circular cantilever plates in machines and structures as their real elements, or as physical-mathematical models of real systems, makes it necessary for the designer to become better-acquainted with the deformability of cantilever plates replacing real fragments of machine parts. The present work aims at solving a number of problems concerning the cantilever plate theory, with the special question being their adaptation to globoidal and cylindrical worm meshings.

2. The basics of the worm meshing theory

The external surface (tip diameter) of the worm and the surface of the globoid and the external (maximum) diameter of the worm wheel interpenetrate and define the area in which the mating of the worm teeth and the worm wheel takes place. The determination of the area of mating and the contact line will be presented basing on the simplest example from the point of view of meshing geometry, namely for the gear with a worm of the profile of Archimedes teeth. Archimedes worms are characterized by a rectilinear profile in the axial section, while the front section of these worms is in the shape of the Archimedes spiral.

The geometry of such a worm meshing can be described by the formulae (Litwin, 1959)

$$\begin{aligned} [p(\Theta - \varphi_1) - r_i \tan \alpha_n] \left(\cos \Theta \tan \alpha_n + \frac{p \sin \Theta}{r_i} \right) - r_i \cos \Theta = r_n \\ x = r_i \sin \Theta \quad y = r_i \cos \Theta \quad z = p(\Theta - \varphi_1) - r_i \tan \alpha_n \quad p = \frac{mz_1}{2} \end{aligned} \quad (2.1)$$

If $\varphi_1 = \text{const}$, then equations (2.1) define instantaneous contact lines for a given angle of rotation of the worm. The contact between the worm teeth and the worm wheel for a given gear

takes place only in the area common for both these elements. This area is referred to as a tooth contact area (mashing area). In other words, the tooth contact area (Fig. 1) is a working part of the meshing area limited by the above-mentioned areas of the worm pair (Fig. 1) (Sabiniak, 1996); namely:

- the apex diameter of the worm d_z (curve a),
- the globoidal area of the worm wheel with the radius r_g corresponding to it (curve b),
- the maximum diameter of the worm wheel R_z (curve c).

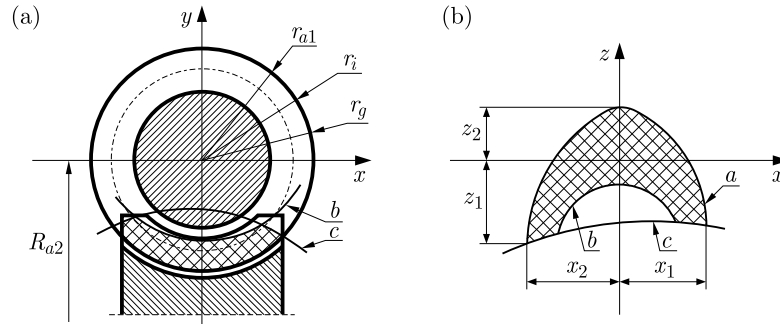


Fig. 1. The area of meshing of the worm pair: (a) in the front section, (b) in the horizontal projection

To define the tooth contact area, one must determine:

- curve a (Fig. 1), assuming $r_i = r_g$ in equations (2.1), i.e. replace an arbitrary radius of the cylinder with the external radius of the worm,
- curve b ; then in equations (2.1) one must substitute $r_i = r_g$, and add the globoid equation

$$(x + A)^2 - \left(A - \sqrt{r_g^2 - y^2} \right)^2 + z^2 = 0 \quad (2.2)$$

- curve c , by considering simultaneously equations (2.1) and the equation of the external cylinder of the worm wheel

$$z^2 + (A + r_i \cos \Theta)^2 = R_z^2 \quad (2.3)$$

The tooth contact area and the course of the contact lines for the established value of the angle φ_1 is shown, by way of example, in Fig. 1 (Sabiniak, 1996).

3. The characteristics of the contact lines in the worm meshing

The course of the contact lines in the tooth contact area has a significant effect on the operating parameters of the gear.

Modern tendencies in the construction of worm gears aim at finding such a position for the contact lines as to let angle β , which they form with the vector of the rubbing speed (Fig. 2), approach 90° . Favorable conditions are then created for the formation of an oil film, and the amount of heat in the mashing is simultaneously reduced. In addition, the shape of the contact lines has a decisive effect on the load distribution (which will be presented further). In turn, the course of the contact line largely depends on the profile of the mating surfaces of the teeth and the worm wheel addendum modification coefficient. In principle, there are two groups of profiles:

- rectilinear profiles,
- curvilinear profiles.

The first group comprises all worms made using a rotational tool of a rectilinear profile or those that have a straight line in any section. The following profiles can be distinguished here:

- Archimedes profiles,
- rectilinear in the section perpendicular to the helix on the tooth reference cylinder,
- evolvent,
- conoidal.

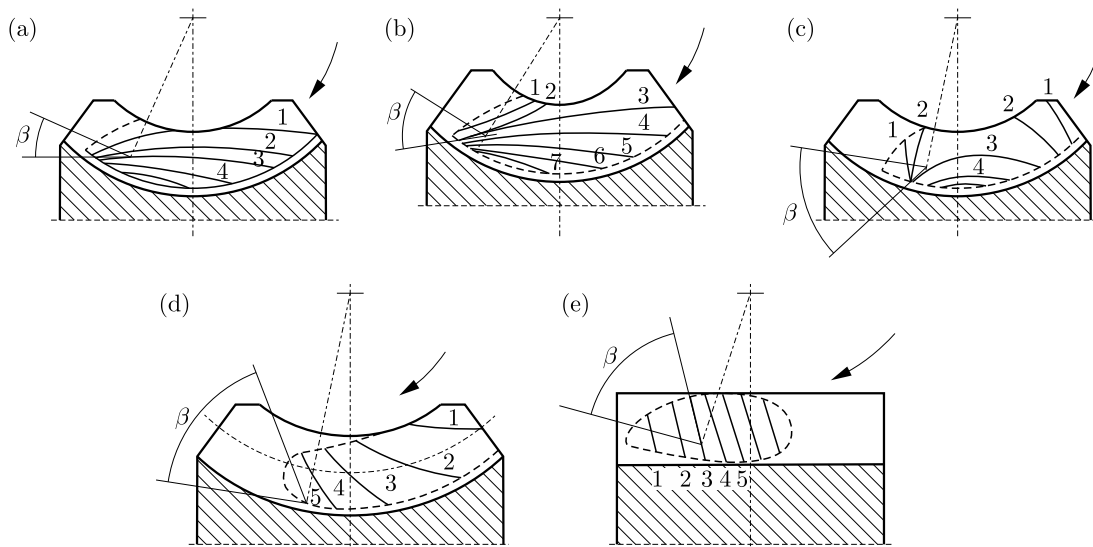


Fig. 2. The course of the contact lines and values of the angle in gears with the following worms:
 (a) cylindrical of the profile of Archimedes teeth, (b) cylindrical of the evolvent teeth profile,
 (c) cylindrical of the circular-concave teeth profile, (d) cylindrical of the circular-convex teeth profile,
 (e) globoidal

The contact of the teeth of the worm and the worm wheel in the gears with a rectilinear worm is a contact of two convex surfaces, which results in the formation of great inter tooth pressures. Then, small equivalent radii of the curvatures of the profiles along the contact line occur.

In the group of curvilinear profiles, the following worms can be distinguished:

- of a circular-concave profile in the axial section, Cavex,
- of a circular-convex profile in the axial section.

Of the profiles discussed so far, worm gears with a globoidal worm (Fig. 2e) have the best conditions for the formation of an oil film. Moreover, at least one more pair of teeth mates in the case of cylindrical worm gears. The technology of making globoidal worms requires making use of special machines. They are also troublesome to check. However, their operating properties are superior to all the ones discussed hitherto.

4. Load distribution along the contact line in the worm meshing

While solving the problem of load distribution along the contact lines in the worm meshing, it has been assumed that the tooth of the worm or the worm wheel is a cantilever plate having one edge built-in elastically (Sabiniak, 1992). The bar between the plates illustrates the contact line and ensures the transfer of load from one plate – a tooth – to another along the contact line required (Figs. 3a and 3b).

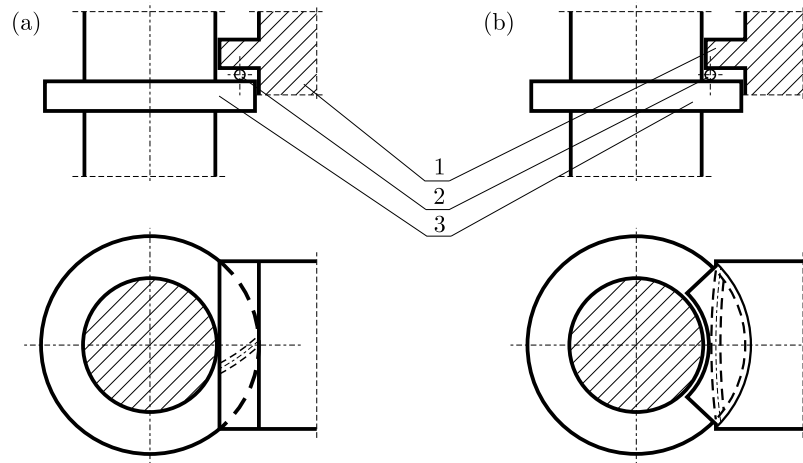


Fig. 3. (a) The model of meshing of the globoidal worm gear: 1 – tooth of the cylindrical wheel, 2 – bar illustrating the contact line, 3 – worm tooth; (b) the model of meshing of the cylindrical worm gear: 1 – worm wheel tooth, 2 – bar illustrating the contact line, 3 – worm tooth

Prior to the determination of load distribution, the question of deformability of the plate, depending on its geometric parameters and material constants, has been solved by forming matrices of rigidity of the plates (Sabiniak, 1982, 1992). Calculations of the strains (or more precisely, of the dimensionless parameters of deflection of the plate $K_{r,\varphi}^{r_i,\varphi_i}$) have been made for each type of the plate (circular cantilever plate and a circular plate in the shape of a circular sector) by applying the concentrated force to appropriately selected places. These appropriately selected places are nodes of the net superimposed on the plates, through which contact lines pass.

Basing on these results, one could start searching for load distribution along the contact line (Fig 3 and 4), assuming at the same time that:

- the continuous load will be replaced with a number of concentrated forces (Sabiniak, 1992; Umezawa *et al.*, 1969; Jaramillo, 1950)

$$F_i = \int_{l_{i-1}}^{l_i} q dl \quad (4.1)$$

- the total strain of the plate is a superposition of the previously obtained deflections from particular, independently acting concentrated forces (Sabiniak, 2012; Sabiniak and Woźniak, 1988)

$$\omega_0(r, \varphi) = \sum_{i=1}^{i=n} \omega(r_i, \varphi_i) \quad (4.2)$$

- the algebraic sum of deflections of both plates along the contact line is a constant value

$$\omega_0^1(r, \varphi) + \omega_0^2(r, \varphi) = \omega = \text{const} \quad (4.3)$$

- the forces of reciprocal interaction in the corresponding points along the contact line of both plates are equal to each other

$$F_i^1(r_i, \varphi_i) = F_i^2(r_i, \varphi_i) \quad (4.4)$$

- the sum of forces acting in particular nodes of the contact line must be equal to the inter tooth force

$$F_w = \sum_{i=1}^{i=n} F_i(r_i, \varphi_i) \quad (4.5)$$

5. The mating of circular cantilever plates and those in the shape of the circular sector

The deflection of the plate at the point of coordinates (r, φ) , caused by the action of the concentrated force applied at the point of coordinates (r, φ) , has the form

$$\omega_i(r, \varphi) = \frac{h^2}{\pi D} K_{r, \varphi}^{r_i, \varphi_i} F_i(r_i, \varphi_i) \quad (5.1)$$

where $K_{r, \varphi}^{r_i, \varphi_i} = f(R, R_1, R_n, E, F, F_i, F_w, h, r_i, v, \varphi, \varphi_i)$ have been taken from work (Sabiniak, 1992; Umezawa *et al.*, 1969; Jaramillo, 1950).

The total deflection of the plate at the point of coordinates (r, φ) will be the sum of deflections from particular forces acting on the plate

$$\omega_0(r, \varphi) = \frac{h^2}{\pi D} \sum_{i=1}^{i=n} K_{r, \varphi}^{r_i, \varphi_i} F_i(r_i, \varphi_i) \quad (5.2)$$

When the contact lines do not pass exactly through the nodes of the net, interpolation is performed. If the point of the contact line, e.g. K (Fig. 4) is on the line of the net between two nodes, then the dimensionless parameter of deflection of the plate K_K for such a point is determined from the dependence $K_K = a_2 K_A + a_1 K_B$, where $a_1 + a_2 = 1$. If the point of the contact line L is not on any line of the net (Fig. 4), then the dimensionless parameter of deflection of the plate of such a point is determined from the dependence $K_L = c_2(b_2 K_E + b_1 K_D) + c_1(b_2 K_B + b_1 K_C)$, assuming that $b_1 + b_2 = c_1 + c_2 = 1$.

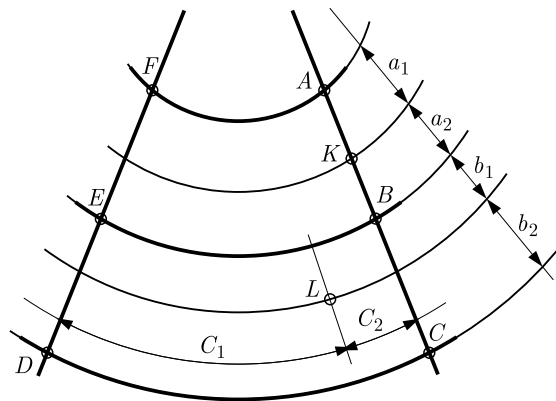


Fig. 4. The interpolation of the deflections of the plate points that do not coincide with the nodes

For the dimensionless parameters of deflections of the plate in particular points of the line of contact (5.2) thus calculated, condition (4.3) can be employed. If the number of the concentrated forces replacing the constant load, equal to the nodes lying on the contact line is i , then – following the application of condition (4,3) – a system of i linear equations containing $i + 1$ unknowns (particular forces in the nodes and the total deflection) will be obtained in each node. The missing equation is obtained by equating the sum of force acting in particular nodes of the contact line to the resultant force acting on the plate (4.5).

In the toothed gears it results from the action of the inter tooth force (Sabiniak, 1982, 1992; Umezawa, 1974). The course of calculation procedure will be shown using an example.

6. A numerical example

Find the distribution of the inter tooth force between two cantilever plates:

- the circular (of steel) with material constants $E_1 = 2.06 \cdot 10^{11} \text{ N/m}^2$ and $\nu_1 = 0.3$ and dimensions $R_{n1} = 60 \text{ mm}$ – the external radius of the circular plate – of the worm convolution apexes, $R_1 = 38 \text{ mm}$ – the internal radius of the circular plate – of the bases of the worm convolution and $h_1 = 7.5 \text{ mm}$ – the thickness of the circular plate equal to the average thickness of the worm teeth;
- in the shape of the circular sector (of bronze) with material constants $E_2 = 10^{11} \text{ N/m}^2$ and $\nu_2 = 0.35$ and the dimensions $R_2 = 62 \text{ mm}$ – the external radius of the plate in the shape of the circular sector – the radius of the bases of the worm wheel teeth, $R_2 = 40 \text{ mm}$ – the internal radius of the plate in the shape of the circular sector – the radius of apexes of the teeth of the worm wheel and $h_2 = 12 \text{ mm}$ – the thickness of the plate in the shape of the circular sector equal to the average thickness of the worm wheel tooth contacting each other along the line shown in Fig. 5 and designated as number I. The deflections of the circular cantilever plate made of steel (the worm) in particular points of the contact line amount to

$$\begin{aligned}
 \omega_{50,-45}^1 &= \frac{h_1^2}{\pi D_1} (K_{50,-45}^{50,-45} F_{50,-45} + K_{50,-45}^{50,-40} F_{50,-40} + \dots + K_{50,-45}^{50,40} F_{50,40} + K_{50,-45}^{50,45} F_{50,45}) \\
 \omega_{50,-40}^1 &= \frac{h_1^2}{\pi D_1} (K_{50,-40}^{50,-45} F_{50,-45} + K_{50,-40}^{50,-40} F_{50,-40} + \dots + K_{50,-40}^{50,40} F_{50,40} + K_{50,-40}^{50,45} F_{50,45}) \\
 &\vdots \\
 \omega_{50,40}^1 &= \frac{h_1^2}{\pi D_1} (K_{50,40}^{50,-45} F_{50,-45} + K_{50,40}^{50,-40} F_{50,-40} + \dots + K_{50,40}^{50,40} F_{50,40} + K_{50,40}^{50,45} F_{50,45}) \\
 \omega_{50,45}^1 &= \frac{h_1^2}{\pi D_1} (K_{50,45}^{50,-45} F_{50,-45} + K_{50,45}^{50,-40} F_{50,-40} + \dots + K_{50,45}^{50,40} F_{50,40} + K_{50,45}^{50,45} F_{50,45})
 \end{aligned} \tag{6.1}$$

Identical dependences must, of course, be written for the cantilever plate in the shape of the circular sector made of bronze (the worm wheel). From the symmetry of the system occurring for this case, it can be clearly seen that

$$\begin{aligned}
 F_{50,-45} &= F_{50,45} \\
 F_{50,-40} &= F_{50,40} \\
 &\vdots \\
 F_{50,-5} &= F_{50,5} \\
 F_{50,0} &= F_{50,0}
 \end{aligned} \tag{6.2}$$

Expression (6.1) and the one obtained in the similar manner for the plate made of bronze, must be substituted into condition (4.3), taking at the same time dependences (4.4) and (6.2) into account. Then, while replacing the continuous load along the contact line with the concentrated forces, 19 in number, and making transformations, a system of 10 linear homogeneous equations will be obtained

$r = 50 \text{ mm}$
 $E_1 = 2.06 \cdot 10^{11} \text{ N/m}^2$
 $\nu_1 = 0.3$
 $E_2 = 10^{11} \text{ N/m}^2$
 $\nu_2 = 0.35$
 $h_1 = 7.5 \text{ mm}$
 $h_2 = 12 \text{ mm}$

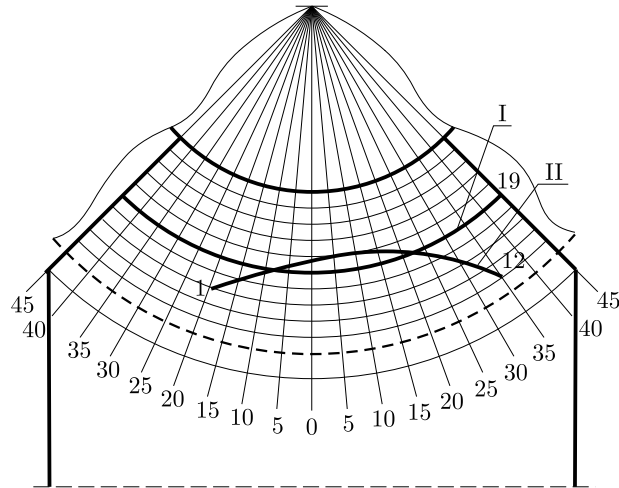


Fig. 5. The net of division and the contact lines in the cylindrical worm meshing

$$\begin{aligned}
 \omega_{50,-45}^1 + \omega_{50,-45}^2 - \omega &= 0 \\
 \omega_{50,-40}^1 + \omega_{50,-40}^2 - \omega &= 0 \\
 \vdots & \\
 \omega_{50,-5}^1 + \omega_{50,-5}^2 - \omega &= 0 \\
 \omega_{50,0}^1 + \omega_{50,0}^2 - \omega &= 0
 \end{aligned} \tag{6.3}$$

Substituting the values of $K_{r,\varphi}^{r_i,\varphi_i}$ calculated in works (Sabiniak, 1982, 1986, 1992) and adding condition (4.5), the following system of equations is obtained, allowing one to determine forces in particular nodes of the net.

The calculation results are graphically presented in Fig. 6.

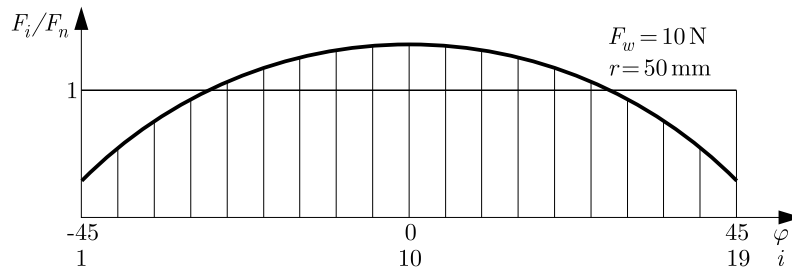


Fig. 6. The load distribution for contact line I according to Fig. 5

7. The mating of circular and rectangular cantilever plates

While searching for load distribution along the contact line in the globoidal meshing, the same formulae (4.1)-(5.2) are applied.

Additional calculations are required only in the case of making linear equations for contact line I (Fig. 7). Contact line I does not pass precisely through the net nodes. In this case, interpolation is also used for finding the coefficients $K_{r,\varphi}^{r_i,\varphi_i}$, (Fig. 4). The procedure described refers to the calculations carried out for both the polar and rectangular coordinates.

It has been decided that – for the rectangular plate – the nodes would occur where contact line I would cross horizontal lines of the net. Following such an assumption, with the interpolation

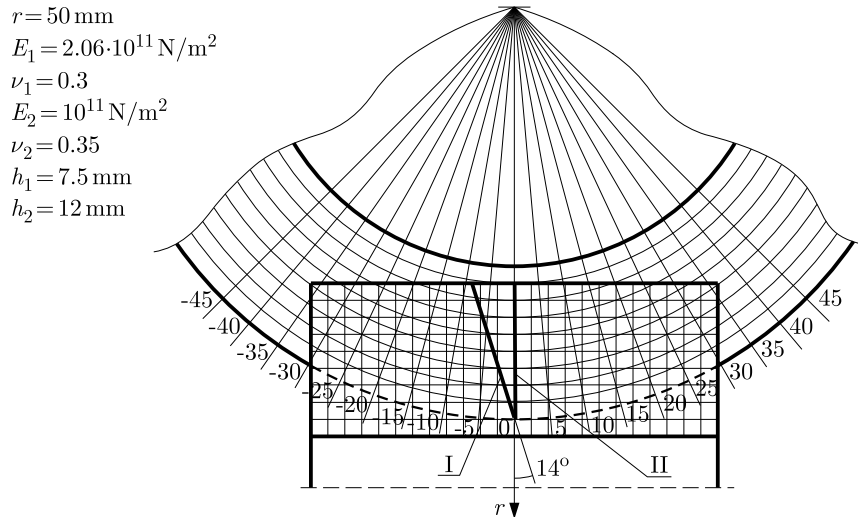


Fig. 7. The net of division and the contact lines in the globoidal worm meshing

of the coefficient $K_{r,\varphi}^{r_i,\varphi_i}$ for a plate in the shape of the circular sector, four adjacent points for the net of polar coordinates are taken into consideration, as described in Section 4, and only two adjacent points for the net of rectangular coordinates.

The shape and designations of the contact lines are shown in Fig. 7, while the load distributions corresponding to particular contact lines in Figs. 8. The distributions of load obtained for these lines do not differ radically, which results from a slight difference in the course of these lines.

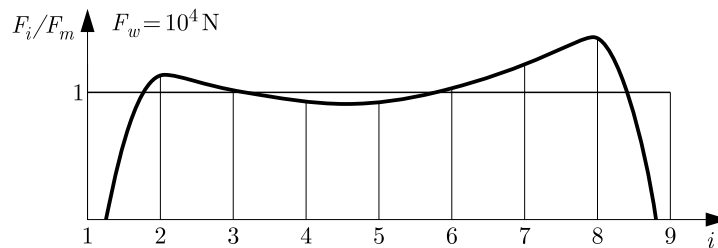


Fig. 8. The load distribution for contact line I according to Fig. 9

8. The results of theoretical and experimental investigations

Figure 9 presents the course of the contact lines on particular teeth of the worm wheel in the worm gear studied, obtained during experimental investigations.

Figure 10 presents the stresses that occurred in the cylindrical worm meshing. The concentration of stresses in particular points of contact for particular teeth is characteristic here.

Figure 11 is a diagram of changes in contact stresses along the contact line.

The contact line for tooth 6 (Fig. 9) can be equated to contact line I in Fig. 5. Here is a slight divergence between the course of the contact line in the tooth contact area. Thus, the stresses of Fig. 11 can be compared with the load distribution in Fig. 6. As there are principally different quantities “stress” and “force” in these figures, there is no justification for comparing them with respect to absolute values. However, as has been mentioned at the beginning of the paper, experimental investigations aimed at the qualitative verification of the theory of load distribution along the contact line (are not?) discussed in the present work.

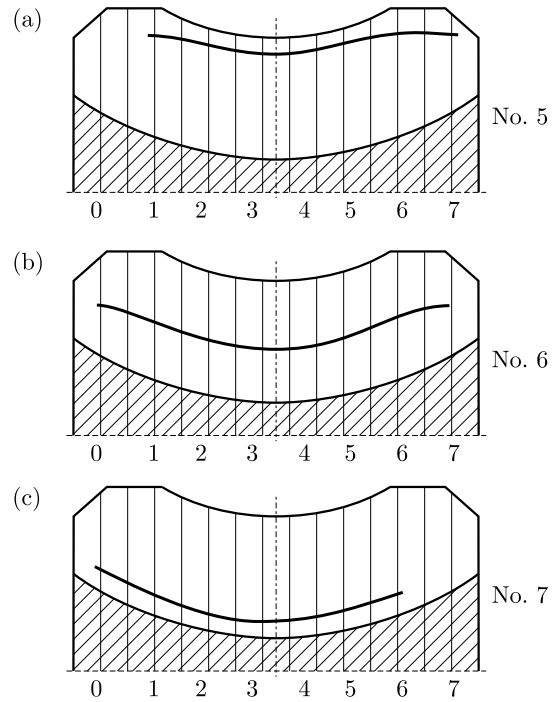


Fig. 9. The real contact lines in the worm gear under investigation: (a) for the worm wheel tooth entering the meshing, designated by number 5, (b) for the central worm wheel tooth being in the meshing, designated by number 6, (c) for the worm wheel tooth leaving the meshing, designated by number 7

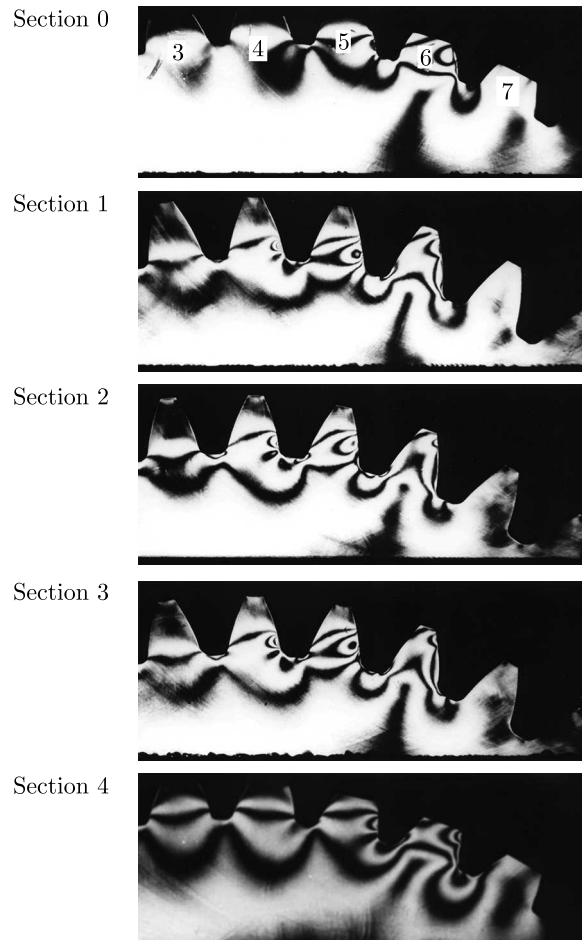


Fig. 10. The state of stresses in the cylindrical worm meshing in particular sections of the worm wheel according to Fig. 9

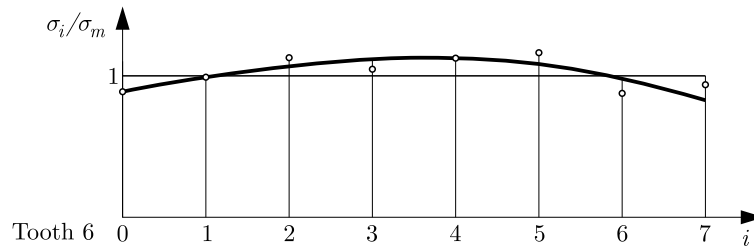


Fig. 11. The changes in the contact stresses along the contact line in the cylindrical worm meshing

In other words: if the load changes, its character along the contact line decreases, increases, rapidly concentrates, fades, etc. The change in contact stresses should be of the same character in the same places. The stresses in the tooth foot should assume a similar, although slightly milder, character. When comparing Figs. 11 and 6 with this respect, a similarity of the course of load distribution and contact stresses along the contact lines discussed can be easily observed.

9. Directions of further investigations

The present work constitutes solely one of the problems which, as will be presented below, has not been fully dealt with. It is one in the whole range of problems related to globoidal meshings.

As has been mentioned in the works (Sabiniak, 1982, 1986, 1992; Hayman and Sabiniak, 1986; Predki, 1991), owing to its specificity, globoidal meshings possess a serious difficulty in scientific studies, both theoretical and experimental. The skill of finding load distribution along any contact line is a fundamental problem, the knowledge of which allows passing on to further investigations in this field. The use of the knowledge and the load distribution along the contact line is connected to finding an answer to the question: how will the mating surfaces of the teeth be deformed under such a load? The problem of hertzian pressures along with the Bielajew problem (Niemann and Winter, 1983) is currently relatively well-known and there seems to be no difficulty in the adaptation of this knowledge to globoidal meshings.

The next step, which appears the obvious thing to do, is the introduction of an elastothermohydrodynamic oil film between the mating teeth. Such attempts are already in progress.

If the oil film is to be considered, then the next step is the introduction of temperature into the meshing and finding its distributions, both in the oil film and in particular mating teeth. It is clear that a great amount of heat is released during the operation of worm gears. Thus, the question arises what portion of the energy is changed into heat, and how it is dissipated. There are works concerning basic studies on plates where the thermal problem has been solved. However, temperature has been treated as a boundary condition there (Jaramillo, 1950; Timoshenko and Woinovsky-Krieger, 1959; Umezawa *et al.*, 1969; Kączkowski, 1980). The solutions in thermal investigations of plates thus presented are difficult to interpret physically and cannot be practically applied in the problem discussed. The attempts at tackling the heat problem of worm gears aim rather at operational uses than at elucidating the phenomena occurring in the worm meshing.

The development of numerical methods in mathematics, particularly of the finite element and finite difference methods (Sabiniak, 2012), allows finding load distributions in worm meshings when the thickness of the tooth, as a plate, changes arbitrarily, which will probably be the next stage in further research.

However, the problem of distribution of the load into particular pairs of mating teeth has yet not been solved (Litwin, 1959; Niemann and Winter, 1983; Crosher, 2002; Dudás, 2005).

Either the problem of strain of the worm as a shaft has not been solved.

The deflections occurring in bearings and strains of the body should not be either forgotten (Sabiniak and Woźniak, 1988).

All the above questions, as well as problems waiting to be solved, are static problems. One can only realize the difficulties of the subject presented if motion is introduced.

10. Summary

Basing on the presented theoretical considerations and experimental investigations, as well as on the results obtained, the following conclusions emerge:

1. The finite difference method used with regard to the search for deflections of cantilever plates under arbitrary normal load offers in the solutions of these plates a very good accuracy (Figs. 4-11). In particular, if boundary conditions are carefully selected, then the divergence between the theoretical and experimental results are not greater than 14%.
2. The theoretical and experimental results obtained are in good agreement both for cylindrical and globoidal worm gears, which confirms the rightness of the presented theory of searching for load distributions in the worm meshing (Sabiniak, 2007).
3. The experimental method selected for the verification of the theory presented here should be considered fully justified, although it has already been used for seeking the state of stresses in the meshing. Its application for the presentation of the state of stresses in the worm meshing only confirms the versatility of this method.
4. The results obtained indicate that the existing method of finding the radial course of the contact lines in the tooth contact area (Niemann and Winter, 1983; Litwin, 1959; Crosher, 2002; Dudás, 2005) must be verified. It seems that the method of obtaining the radial course of the contact lines in the tooth contact area by using a great addendum modification in the profile and circular profile of the meshing, at the cost of decreasing the tooth contact area, and first of all, the length of the contact lines occurring simultaneously in the tooth contact area, seems unjustified. A greater length of the contact line significantly reduces the local stress of the materials and generally of the mating teeth thereby improving the load-carrying capacity of the gear and its resistance to wear. Hence, the durability and efficiency of the meshing will increase with length of the contact line in the tooth contact area. It should be remembered, however, that the “straightening” of the contact lines in the tooth contact area impairs, in turn, conditions for the formation of an oil film.
5. The above conclusions show that globoidal worm gears are superior to cylindrical worm gears both with respect to their load-carrying capacity and life, which is nothing new. The above results have again confirmed this truth. The problem that remains is the cost of such a worm in relation to e.g. 1 KW of the power transmitted. This is not so obvious.
6. A change in the character of the course of the contact line in the tooth contact area also changes radically the character of the load distribution.
7. The results obtained are to be used for the modification of the profile of the teeth in order to “equalize” the existing load distribution along the contact line.

References

1. BUCKINGHAM E., 1960, *Design and Manufacture of All Resection Worm and Spiral Gear Drives*, The Industrial Press, New York
2. CROSHER W.P., 2002, *Design and Application of the Worm Gear*, ASME, USA
3. DUDÁS I., 2005, *The Theory and Practice of Worm Gear Drives*, Elsevier

4. HAYMANN J., SABINIĄK H.G., 1993, Bestimmung der Spannungen in der Schneckengetriebeverzahnung mit Hilfe des Spannungsoptischen Erstarrungsverfahrens, *Zeszyty Naukowe Politechniki Łódzkiej, Mechanika*, **83**, 103-122
5. JARAMILLO T.J., 1950, Deflections and moments due to a concentrated load on a cantilever plate of infinite length, *Journal of Applied Mechanics*, March, 67-72
6. KĄCZKOWSKI Z., 1980, *Plates – Static Calculations* (in Polish), Arkady, Warszawa
7. LITWIN B.L., 1959, *Teoria zubczatych zaceplenii* (in Russian), Izd. Nauka, Moskwa
8. NIEMANN G., WINTER H., 1983, *Maschinenelemente*, Band III, Springer-Verlag, Berlin, Heidelberg, New York, Tokio
9. PREDKI W., 1991, Stand der Schneckengetriebeentwicklung, *Konstruktion*, **43**, 233-238
10. SABINIĄK H.G., 1982, Load distribution along the line of contact of two cantilever plates as models of the tooth of a toothed gear (in Polish), *Zeszyty Naukowe Politechniki Łódzkiej, Mechanika*, **64**, 71-82
11. SABINIĄK H.G., 1986, Load distribution between two cantilever plates contacting each other along a straight line (in Polish), *Zeszyty Naukowe Politechniki Łódzkiej, Mechanika*, **70**, 31-40
12. SABINIĄK H.G., 1992, *Lastverteilung längs der Berührungslinie zweier Kragplatten, betrachtet als Modell für die Zähne eines Zylinder- und Globoidschneckengetriebes*, Technische Universität, Chemnitz, Dissertation B
13. SABINIĄK H.G., 1996, Real meshing zone in worm gear (in Polish), *Przegląd Mechaniczny*, **20**, 10-12, 18-20
14. SABINIĄK H.G., 2007, *Load Capacity and Durability of Worm Gears* (in Polish), Monografie Politechniki Łódzkiej
15. SABINIĄK H.G., 2012, The method of finite differences in solutions concerning circular plate, *Key Engineering Materials.*, **490**, 305-311
16. SABINIĄK H.G., WOŹNIAK K., 1988, Operating properties of the worm gear with a convex worm and of circular-convex profil, *Conference of Gearing*, Zhengzhou, China
17. TIMOSHENKO S., WOINOWSKY-KRIEGER S., 1959, *Theory of Plates and Shells*, Mc Graw Hill Book Company Inc., New York, Toronto, London
18. UMEZAWA K., 1974, The meshing test on helical gears under load transmission, *Bulletin of the Japan Society of Mechanical Engineers*, **17**, 112
19. UMEZAWA K., ISHIKAWA J., HAYASHI K., 1969, Deflections due to a concentrated load on a cantilever thick plate of finite length gears, *Bulletin of the Japan Society of Mechanical Engineers*, **12**, 53

Manuscript received May 14, 2015; accepted for print February 12, 2016

COMPARISON OF EXPLICIT AND IMPLICIT FORMS OF THE MODIFIED POINT MASS TRAJECTORY MODEL

LESZEK BARANOWSKI

Military University of Technology, Faculty of Mechatronics and Aerospace, Warszawa, Poland
e-mail: leszek.baranowski@wat.edu.pl

BŁAŻEJ GADOMSKI, JACEK SZYMONIK

PIT-RADWAR S.A., Warszawa, Poland
e-mail: blazej.gadomski@pitradwar.com; jacek.szymonik@pitradwar.com

PRZEMYSŁAW MAJEWSKI

PIT-RADWAR S.A., Warszawa, Poland and
University of Warsaw, Chair of Mathematical Methods in Physics, Warsaw, Poland
e-mail: przemek.majewski@gmail.com

The article compares the results of trajectory computation for a 35 mm projectile using two forms (explicit and implicit) of the modified point-mass trajectory model. All necessary ammunition parameters (aerodynamic coefficients, dimensions, mass etc.) and initial conditions for differential equations are provided. The results of numerical integration (using non-stiff fourth-order Runge-Kutta solver) are presented in form of projectile trajectories projections onto vertical and horizontal planes. Data tables comparing both models in terms of projectile position and velocity in chosen time steps are also attached.

Keywords: exterior ballistics, projectile motion, MPMTM, equations of motion, projectile trajectory

1. Introduction

One of the requirements for algorithms implemented in Fire Control Systems (e.g. probability calculation via initial condition error propagation, finding fire-control solution) is limited runtime. Some of FCS algorithms require the use of a certain model of the projectile trajectory. The basic approach to projectile trajectory calculations is to use a Modified Point-Mass Trajectory Model (MPMTM), also known as the four degree-of-freedom model or the Lieske model (after an American R. Lieske, who initiated its widespread usage), whose foundations were introduced by Lieske and Reiter (1966). One of the MPMTM implementations is presented in (STANAG 4355, 2009) and exemplary calculations based on it were published by Baranowski (2013), McCoy (1999), Coleman *et al.* (2003).

A significant weakness of this MPMTM representation is the iterative method for determining the yaw of repose, which makes this approach time consuming. In order to overcome this limitation, a new explicit form of the MPMTM was proposed by Baranowski *et al.* (2016).

The aim of this paper is to compare both implicit and explicit forms of MPMTM. The two model variations are analyzed in terms of the obtained results and runtime. Firstly, we characterize the differential equations describing motion of the projectile for both forms. We also provide initial conditions for the equations of motion as well as other necessary parameters of the mathematical model such as:

- physical parameters of the chosen 35 mm ammunition;

- values of aerodynamic coefficients of the projectile;
- atmospheric conditions used in simulation tests.

Calculations of 35 mm projectile trajectories are conducted for standard atmospheric conditions (STANAG 4119, 2007) considering three different scenarios, i.e.:

- no wind present along the projectile trajectory;
- homogeneous cross wind introduced along the projectile trajectory;
- homogeneous tail wind introduced along the projectile trajectory.

The runtimes of integration of the projectile path for different elevation angles for both the explicit and implicit forms have been measured and later compared. In order to enhance model analysis, we have used MATLAB scripts and built-in functions.

2. Projectile motion models

2.1. Modified point-mass trajectory model (MPMTM) – implicit form

The basic MPMTM is a conventional point-mass model but, in addition, the instantaneous equilibrium yaw is calculated at each time step along the trajectory. It provides estimates of yaw and drag, lift, and Magnus force effects resulting from the yaw of repose. The assumptions made at the stage of model derivation require that the projectile is dynamically stable, only the most essential forces and moments are taken into account, transition processes in projectile oscillatory motion around its center of mass are ignored due to replacement of the total angle of attack α_t with the yaw of repose α_e .

The mathematical model of artillery projectile 3D motion, according to the implicit form of the MPMTM, contains the following equations (Baranowski, 2013; Coleman *et al.*, 2003):

- dynamic differential equation of motion of the projectile center of mass

$$m\dot{\mathbf{u}} = \mathbf{DF} + \mathbf{LF} + \mathbf{MF} + m\mathbf{g} \quad (2.1)$$

- dynamic equation for rotation around the projectile axis of symmetry

$$\frac{d\mathbf{p}}{dt} = \frac{\pi\rho d^4 v C_{spin}}{8I_x} \mathbf{p} \quad (2.2)$$

- equation of the yaw of repose vector

$$\boldsymbol{\alpha}_e = -\frac{8I_x p(\mathbf{v} \times \dot{\mathbf{u}})}{\pi\rho d^3 (C_{M_\alpha} + C_{M_{\alpha^3}} \alpha_e^2) v^4} \quad (2.3)$$

where \mathbf{DF} , \mathbf{LF} , \mathbf{MF} , \mathbf{g} are the drag, lift, Magnus and gravity force vector, respectively

$$\begin{aligned} \mathbf{DF} &= -\frac{\pi\rho d^2}{8} [C_{D_0} + C_{D_{\alpha^2}} (Q_D \alpha_e)^2] v \mathbf{v} & \mathbf{LF} &= \frac{\pi\rho d^2 f_L}{8} (C_{L_\alpha} + C_{L_{\alpha^3}} \alpha_e^2) v^2 \boldsymbol{\alpha}_e \\ \mathbf{MF} &= -\frac{\pi\rho d^3 Q_{MP} C_{mag-f}}{8} (\boldsymbol{\alpha}_e \times \mathbf{v}) & m\mathbf{g} &= -mg \begin{bmatrix} 0 \\ 1 \\ 0 \end{bmatrix} \end{aligned} \quad (2.4)$$

The meaning of letter symbols used in equations (2.1)-(2.4) is as follows: ρ – density of air, d – caliber of the projectile, m – mass of the projectile, v – velocity of the projectile with respect to the air: $v = u - w$, u – velocity of the projectile with respect to a ground – fixed reference system,

w – velocity of the wind, p – angular velocity of the spinning motion, I_x – moment of inertia along the axis of the projectile, C_{spin} – spin damping coefficient, $C_{M\alpha}$ – overturning moment coefficient, $C_{M\alpha^3}$ – cubic overturning moment coefficient, C_{D0} – drag force coefficient, $C_{D\alpha^2}$ – yaw drag coefficient, $C_{L\alpha}$ – lift force coefficient, $C_{L\alpha^3}$ – cubic lift force coefficient, C_{mag-f} – Magnus force coefficient, i, f_L, Q_M, Q_D – fitting factors for the drag, lift, Magnus force and yaw drag, respectively, g – gravitational acceleration.

In the above equations of motion of the projectile, the Coriolis force is neglected. In our calculations we assumed (unlike in the model described in STANAG 4355) constant gravity force along the projectile trajectory as we considered only ground firing trajectories. It is worth mentioning that we also assumed $C_{M\alpha^3} = C_{L\alpha^3} = 0$ during the simulations (as a result of linear dependency of C_L and C_M on α).

2.2. Modified point-mass trajectory model – explicit form

In the form presented in the previous Section, the vector α_e depends on $\dot{\mathbf{u}}$, which results in a differential equation being defined by an implicit function. The derivation of the explicit MPMTM was introduced by Baranowski *et al.* (2016). In the equations of motion of the projectile, the Coriolis force is neglected and the gravitational force is constant. The differential equations for the final form of the explicit model are as follows:

$$\dot{\mathbf{x}} = \mathbf{v} + \mathbf{w} \tag{2.5}$$

where \mathbf{x} is the three-dimensional position vector

$$\begin{aligned} \dot{p} &= \frac{\rho v^2}{2I_x} S d C_{spin} \hat{p} & S &= \frac{\pi d^2}{4} \\ \dot{v} &= -\frac{\rho v^2}{2m} S \left[C_{D0} + \hat{C}_{D\alpha^2} \left(\frac{2mg}{\rho v^2 S} \right)^2 \frac{\hat{I}_x^2 \hat{p}^2 \cos^2 \gamma_a}{(1 - \hat{I}_x \hat{p}^2 \hat{C}_{mag-f})^2 + (\hat{I}_x \hat{p} \hat{C}_{L\alpha})^2} \right] - g \sin \gamma_a \end{aligned} \tag{2.6}$$

and¹

$$\begin{bmatrix} \dot{\gamma}_a \\ \dot{\chi}_a \cos \gamma_a \end{bmatrix} = -\frac{g}{v} \frac{\cos \gamma_a}{(1 - \hat{I}_x \hat{p}^2 \hat{C}_{mag-f})^2 + (\hat{I}_x \hat{p} \hat{C}_{L\alpha})^2} \begin{bmatrix} 1 - \hat{I}_x \hat{p}^2 \hat{C}_{mag-f} \\ \hat{I}_x \hat{p} \hat{C}_{L\alpha} \end{bmatrix} \tag{2.7}$$

Dimensionless coefficients used in equations are

$$\hat{I}_x = \frac{I_x}{m d^2} \quad \hat{p} = \frac{p d}{v} \tag{2.8}$$

The above equations describe the case in which the wind is homogeneous within the interval of integration, i.e. $\dot{\mathbf{w}} = 0$. Please note, that rigorously it is not equivalent to a constant wind, merely that the wind is constant along the flight path. Nevertheless, in practice, such phenomena are almost impossible to occur in ballistics. The dimensionless coefficients are given as

$$\hat{C}_{D\alpha^2} = \frac{C_{D\alpha^2}}{(C_{M\alpha})^2} \quad \hat{C}_{L\alpha} = \frac{C_{L\alpha}}{C_{M\alpha}} \quad \hat{C}_{mag-f} = \frac{C_{mag-f}}{C_{M\alpha}} \tag{2.9}$$

Let us recall that from (Baranowski *et al.*, 2016) it follows that the explicit and implicit forms of the MPMTM are equivalent.

¹ γ_a is the elevation angle of \mathbf{v} measured from the horizontal direction, i.e. the air-path inclination angle and χ_a is the azimuth angle of \mathbf{v} , i.e. the air-path azimuth angle.

3. Physical model

The flight simulation computer program of artillery projectiles requires determination of the so-called physical model (Koruba *et al.*, 2010; Kowaleczko and Żyłuk, 2009; Ładyżyńska-Kozdraś, 2012) which includes the following characteristics:

- geometries, mass and inertial, aerodynamic characteristics of the projectile,
- surrounding environment (density, viscosity, temperature, pressure, velocity and wind direction depending on weather, flight altitude, etc.).

35 mm TP-T ammunition parameters used in the simulation tests are as follows:

- projectile mass $m = 0.55$ kg,
- projectile muzzle velocity $v = 1180$ m/s,
- projectile calibre $d = 0.035$ m,
- projectile axial moment of inertia $I_x = 0.97 \cdot 10^{-4}$ kg m².

In the process of trajectory generation, we have used aerodynamic coefficients obtained for 35 mm TP-T ammunition from PRODAS software (Baranowski and Furmanek, 2013). The coefficients of aerodynamic drag, lift force and spin dumping moment have been interpolated using polynomials in the following form (Pope, 1978; Shanks and Walton, 1957)

$$C(\text{Ma}) = (1 + s)A(r) + (1 - s)B(r) \quad (3.1)$$

where

$$\begin{aligned} A(r) &= a_0 + a_1r + a_2r^2 & B(r) &= b_0 + b_1r + b_2r^2 \\ s &= \frac{r}{\sqrt{(1 - L^2)r^2 + L^2}} & r &= \frac{\text{Ma}^2 - K^2}{\text{Ma}^2 + K^2} \end{aligned} \quad (3.2)$$

where $C(\text{Ma})$ is an aerodynamic coefficient dependent on the Mach number and $a_0, a_1, a_2, b_0, b_1, b_2, K, L$ are parameters to be identified. Figures 1a and 1b present aerodynamic drag and lift force coefficients in nodes and the result of polynomial interpolation with the use of polynomial (3.1). Gridded data piecewise cubic Hermite interpolation (MATLAB griddedInterpolant class) has been used to represent the induced drag and Magnus force coefficients.

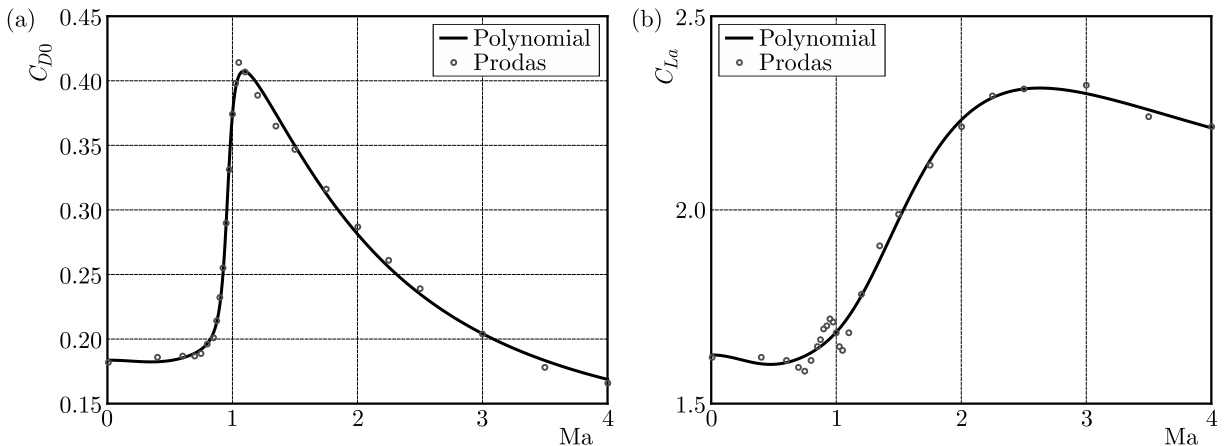


Fig. 1. Drag (a) and lift (b) force coefficient as a function of the Mach number

In order to compare explicit and implicit forms of the MPMTM, the projectile is “shot” from the origin at $[0, 0, 0]$ along the x axis with the quadrant elevation QE equal to 710 mils – the

angle of the maximum range for chosen 35 mm ammunition. The initial angular velocity of the spinning motion is calculated using

$$p = \frac{2\pi v}{27.57d} \quad (3.3)$$

where the number 27.57 reflects the length of the revolution of the rifling in caliber units. The initial time instance is obviously gauged to zero. As it was mentioned before, the gravitational force is constant along the projectile trajectory with the gravitational acceleration $g = 9.80665 \text{ m/s}^2$. The flight of projectile is simulated in standard atmospheric conditions (ISO 2533, 1975) both without and with homogeneous non-zero wind.

4. Simulation tests results

In this Section we present and compare the results of flight simulation tests of the 35 mm TP-T projectile using both the implicit and the explicit form of the MPMTM. The parameters of the model and initial conditions for the differential equations of motion used are presented in Section 3. We also compare the time needed by both models to generate trajectories for different elevation angles.

4.1. Results for standard atmospheric conditions

Figures 2a and 2b present trajectory projections on the vertical and horizontal plane, respectively. An assumption has been made that there is no wind within the integration interval. Based on the plotted trajectories one cannot unambiguously decide whether there are any differences between two models. In order to analyze the results in a more detailed way, differential equations of motion were integrated using a non-stiff fourth-order Runge-Kutta solver.

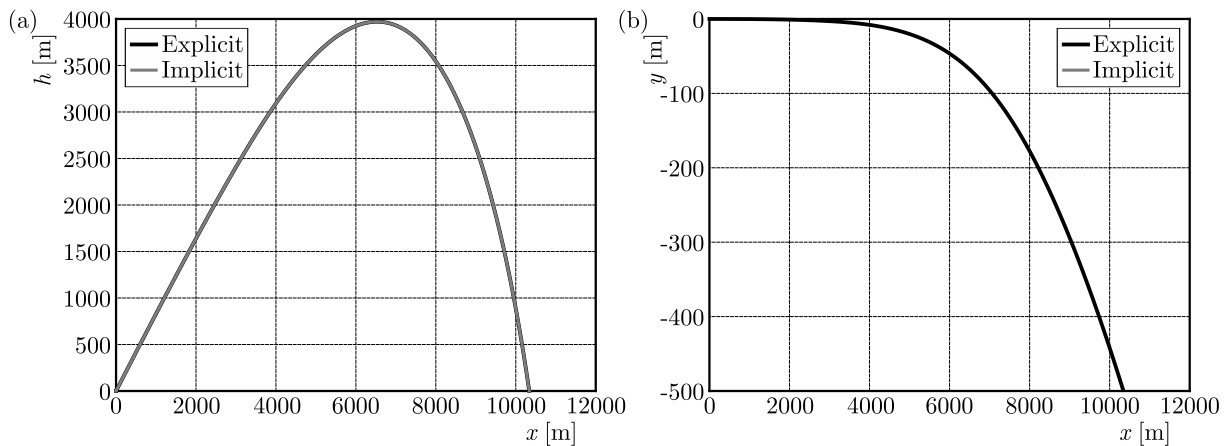


Fig. 2. Projection of the trajectory of 35 mm TP-T projectile on the vertical plane (a) and horizontal plane (b); standard atmosphere without wind

Tables 1-4 contain information on projectile position and velocity in several chosen moments of time calculated for the implicit and explicit form of the MPMTM. The differences observed in these tables are the result of the precision² used during simulations (1e-12).

²Tolerance set for the integration method is a measure of the error relative to the size of each solution component. Roughly, it controls the number of correct digits in all solution components *MATLAB 2014b Documentation*

While comparing the models presented in Section 2, it is important to remember (when the wind velocity is non-zero) that they return projectile velocities in different reference frames:

- explicit model returns velocity in the air-flow³ reference system,
- implicit model returns velocity in the the anti-aircraft gun reference system.

Figure 3 visualizes absolute errors of the projectile position and velocity for two forms of the MPMTM.

Table 1. Comparison of the projectile horizontal position (x -coordinate) in chosen moments of time; standard atmosphere without wind

Time of flight [s]	x -explicit [m]	x -implicit [m]	Δx [m]
5	2.879740543380384e+03	2.879740543380467e+03	-8.276401786133647e-11
10	4.283281165179276e+03	4.283281165179690e+03	-4.138200893066824e-10
15	5.352708930364734e+03	5.352708930365055e+03	-3.210516297258437e-10
20	6.274635184339581e+03	6.274635184339474e+03	1.073203748092055e-10
30	7.827993890946567e+03	7.827993890945661e+03	9.067662176676095e-10
40	9.071956738403202e+03	9.071956738401780e+03	1.422449713572860e-09
50	1.001379407012815e+04	1.001379407012648e+04	1.669832272455096e-09

Table 2. Comparison of the projectile horizontal position (y -coordinate) in chosen moments of time; standard atmosphere without wind

Time of flight [s]	y -explicit [m]	y -implicit [m]	Δy [m]
5	-2.615179706617644	-2.615179706628132	1.048805486902893e-11
10	-10.437812368269643	-10.437812368304497	3.485389754587231e-11
15	-27.482113983932305	-27.482113983970038	3.773337198254012e-11
20	-57.329128551977114	-57.329128551940180	-3.693401140481001e-11
30	-1.609880120207460e+02	-1.609880120205749e+02	-1.710418473521713e-10
40	-3.035886033713625e+02	-3.035886033711299e+02	-2.325464265595656e-10
50	-4.443484747573776e+02	-4.443484747571376e+02	-2.399360710114706e-10

Table 3. Comparison of the projectile vertical h -coordinate in chosen moments of time; standard atmosphere without wind

Time of flight [s]	h -explicit [m]	h -implicit [m]	Δh [m]
5	2.318321798332399e+03	2.318321798332298e+03	1.009539118967950e-10
10	3.260802764803827e+03	3.260802764803513e+03	3.137756721116602e-10
15	3.756859479068482e+03	3.756859479067962e+03	5.197762220632285e-10
20	3.959477637219192e+03	3.959477637218932e+03	2.596607373561710e-10
30	3.644341649231496e+03	3.644341649231876e+03	-3.801687853410840e-10
40	2.533030738575992e+03	2.533030738576817e+03	-8.244569471571594e-10
50	8.539543121131945e+02	8.539543121141693e+02	-9.747509466251358e-10

³Air-frame reference system has been chosen as the most convenient for calculations

Table 4. Comparison of the projectile velocity in chosen moments of time; standard atmosphere without wind

Time of flight [s]	v -explicit [m/s]	v -implicit [m/s]	Δv [m/s]
5	4.582123481454996e+02	4.582123481455023e+02	-2.671640686457977e-12
10	2.694330549712324e+02	2.694330549712641e+02	-3.177547114319168e-11
15	2.084609346355481e+02	2.084609346355003e+02	4.780531526193954e-11
20	1.738563395829701e+02	1.738563395828820e+02	8.813572094368283e-11
30	1.584999648980999e+02	1.584999648980213e+02	7.861444828449748e-11
40	1.814453824749712e+02	1.814453824749252e+02	4.595790414896328e-11
50	2.034057467881448e+02	2.034057467881248e+02	1.995204002014361e-11

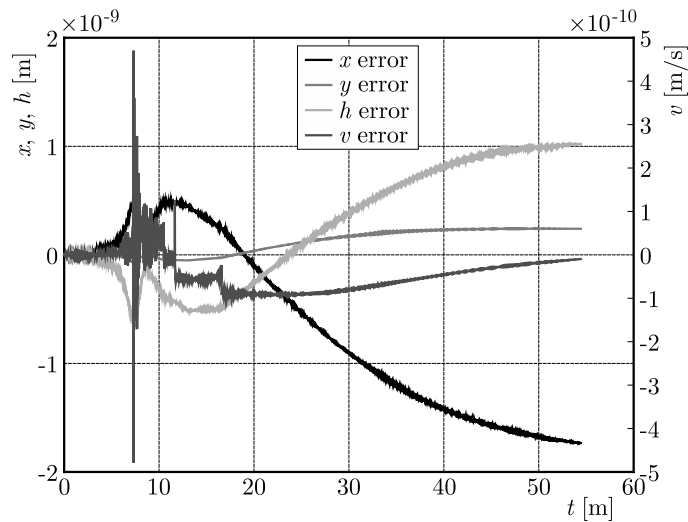


Fig. 3. Absolute differences of projectile position and velocity as a function of time for the explicit and implicit form of the MPMTM; standard atmosphere, no wind

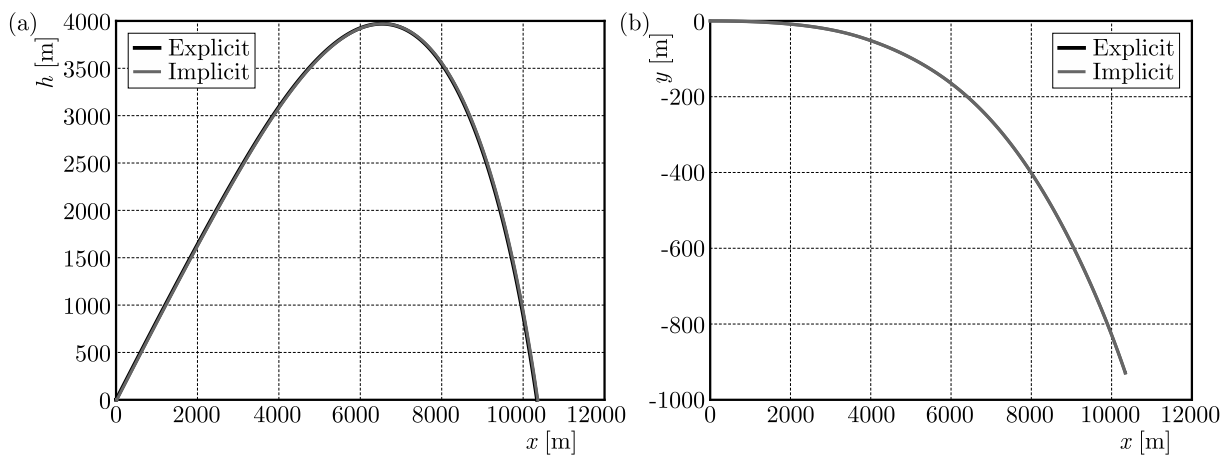


Fig. 4. Projection of the trajectory of 35 mm TP-T projectile on the vertical plane (a) and horizontal plane (b); standard atmosphere, cross wind -10 m/s

4.2. Results for standard atmospheric conditions with cross wind

Figures 4a and 4b present trajectory projections in the case of the presence of homogeneous cross wind blowing with the velocity -10 m/s (other conditions remain the same as in the previous case). Aside from figures, we also publish tables with the results of integration of the differential equations for both forms of the MPMTM (Tables 5 to 8). Absolute differences between respective values are shown in the tables as well as in Fig. 5.

Table 5. Comparison of the projectile horizontal position (x -coordinate) in chosen moments of time; standard atmosphere, homogeneous cross wind (-10 m/s)

Time of flight [s]	x -explicit [m]	x -implicit [m]	Δx [m]
5	2.879759177098334e+03	2.879759177098053e+03	$-2.810338628478348e-10$
10	4.283361832919431e+03	4.283361832918131e+03	$-1.300577423535287e-09$
15	5.352944802665610e+03	5.352944802661354e+03	$-4.256435204297304e-09$
20	6.275169112336884e+03	6.275169112329893e+03	$-6.990376277826726e-09$
30	7.829612391519409e+03	7.829612391508746e+03	$-1.066291588358581e-08$
40	9.075093437693744e+03	9.075093437681275e+03	$-1.246917236130685e-08$
50	1.001843598545247e+04	1.001843598543946e+04	$-1.301486918237060e-08$

Table 6. Comparison of the projectile horizontal position (y -coordinate) in chosen moments of time; standard atmosphere, homogeneous cross wind (-10 m/s)

Time of flight [s]	y -explicit [m]	y -implicit [m]	Δy [m]
5	-20.786332880295095	-20.786332880260023	$3.507238943711855e-11$
10	-63.095834383862190	-63.095834383657966	$2.042241931121680e-10$
15	$-1.183192056414523e+02$	$-1.183192056408177e+02$	$6.345430847431999e-10$
20	$-1.879744883329794e+02$	$-1.879744883319200e+02$	$1.059447640727740e-09$
30	$-3.744560742377584e+02$	$-3.744560742362193e+02$	$1.539149252494099e-09$
40	$-6.032941561003266e+02$	$-6.032941560987131e+02$	$1.613557287782896e-09$
50	$-8.336302688008207e+02$	$-8.336302687993701e+02$	$1.450530362490099e-09$

Table 7. Comparison of the projectile vertical h -coordinate in chosen moments of time; standard atmosphere, homogeneous cross wind (-10 m/s)

Time of flight [s]	h -explicit [m]	h -implicit [m]	Δh [m]
5	2.318313372013739e+03	2.318313372014125e+03	$3.865352482534945e-10$
10	3.260776306927196e+03	3.260776306929160e+03	$1.963144313776866e-09$
15	3.756809955845482e+03	3.756809955850505e+03	$5.022684490540996e-09$
20	3.959406864678785e+03	3.959406864686925e+03	$8.139977580867708e-09$
30	3.644234110531493e+03	3.644234110544769e+03	$1.327543941442855e-08$
40	2.532897496773589e+03	2.532897496790511e+03	$1.692160367383622e-08$
50	8.538100257788867e+02	8.538100257975424e+02	$1.865566900960403e-08$

Table 8. Comparison of the projectile velocity in chosen moments of time; standard atmosphere, homogeneous cross wind (-10 m/s)

Time of flight [s]	v -explicit [m/s]	v -implicit [m/s]	Δv [m/s]
5	4.582266925378976e+02	4.582266925378934e+02	$-4.206412995699793e-12$
10	2.694372225018485e+02	2.694372225017880e+02	$-6.048139766789973e-11$
15	2.084647377666492e+02	2.084647377662564e+02	$-3.927880243281834e-10$
20	1.738602908045667e+02	1.738602908041290e+02	$-4.376374818093609e-10$
30	1.585036690668833e+02	1.585036690664340e+02	$-4.492619609663962e-10$
40	1.814475179841104e+02	1.814475179838305e+02	$-2.798401510517579e-10$
50	2.034062035223828e+02	2.034062035223219e+02	$-6.087930159992538e-11$

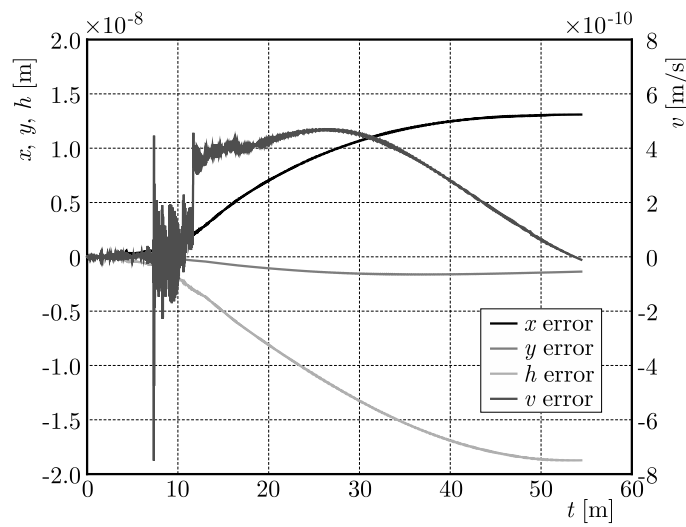


Fig. 5. Absolute differences of projectile position and velocity as a function of time for the explicit and implicit form of the MPMTM; standard atmosphere, homogeneous crosswind (-10 m/s)

4.3. Results for standard atmospheric conditions with tail wind

Figures 6a and 6b present trajectories projections in the case of the presence of homogeneous tail wind blowing with the velocity 10 m/s (other conditions remain the same as described in 4.1).

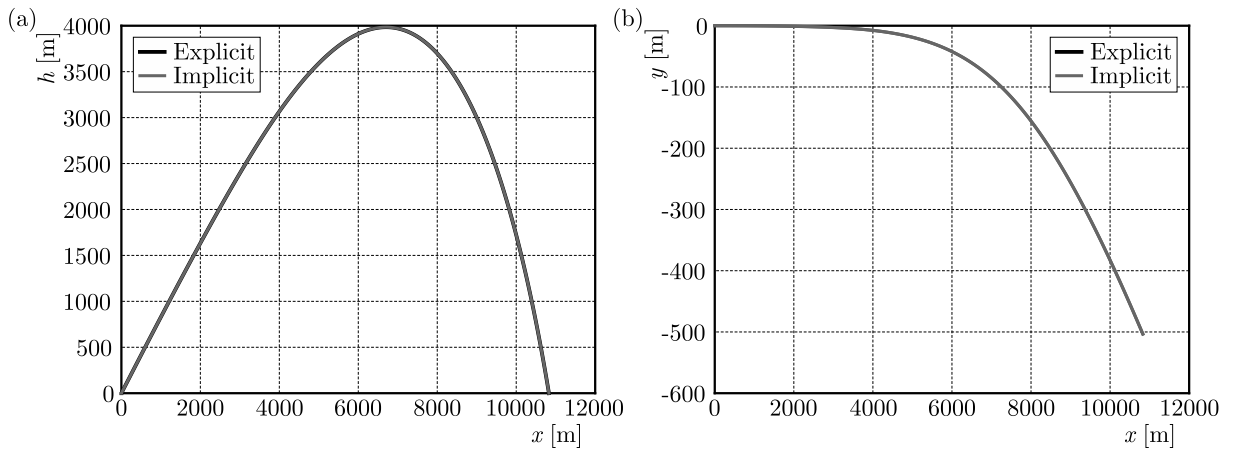


Fig. 6. Projection of the trajectory on the vertical plane (a) and horizontal plane (b); standard atmosphere, tail wind 10 m/s

Table 9. Comparison of the projectile horizontal position (x -coordinate) in chosen moments of time; standard atmosphere, homogeneous tail wind (10 m/s)

Time of flight [s]	x -explicit [m]	x -implicit [m]	Δx [m]
5	2.899745751481406e+03	2.899745751481390e+03	1.637090463191271e-11
10	4.342170882757351e+03	4.342170882757300e+03	5.093170329928398e-11
15	5.455738001516948e+03	5.455738001517138e+03	-1.891748979687691e-10
20	6.423191936662845e+03	6.423191936663049e+03	-2.037268131971359e-10
30	8.070359880147351e+03	8.070359880147523e+03	-1.718944986350834e-10
40	9.410976469705320e+03	9.410976469705542e+03	-2.219167072325945e-10
50	1.045149163528715e+04	1.045149163528757e+04	-4.165485734120011e-10

Table 10. Comparison of the projectile horizontal position (y -coordinate) in chosen moments of time; standard atmosphere, homogeneous tail wind (10 m/s)

Time of flight [s]	y -explicit [m]	y -implicit [m]	Δy [m]
5	-2.614508424916781	-2.614508424914710	-2.071232074740692e-12
10	-10.447910913790327	-10.447910913786751	-3.575806317712704e-12
15	-27.533351120232908	-27.533351120240553	7.645439836778678e-12
20	-57.473911630279034	-57.473911630223405	-5.562839078265824e-11
30	-1.616578103374976e+02	-1.616578103373247e+02	-1.728892584651476e-10
40	-3.052317376261908e+02	-3.052317376259557e+02	-2.351043804083020e-10
50	-4.470705154062585e+02	-4.470705154060170e+02	-2.415276867395733e-10

Table 11. Comparison of the projectile vertical h -coordinate in chosen moments of time; standard atmosphere, homogeneous tail wind (10 m/s)

Time of flight [s]	h -explicit [m]	h -implicit [m]	Δh [m]
5	2.319843392772728e+03	2.319843392772747e+03	-1.955413608811796e-11
10	3.265607481624752e+03	3.265607481624821e+03	-6.821210263296962e-11
15	3.765857597754436e+03	3.765857597754508e+03	-7.230482879094780e-11
20	3.972340990237719e+03	3.972340990238237e+03	-5.184119800105691e-10
30	3.663900131717957e+03	3.663900131719271e+03	-1.313765096710995e-09
40	2.557278531390514e+03	2.557278531392392e+03	-1.878106559161097e-09
50	8.802228281796221e+02	8.802228281817677e+02	-2.145611688320059e-09

Table 12. Comparison of the projectile velocity in chosen moments of time; standard atmosphere, homogeneous tail wind (10 m/s)

Time of flight [s]	v -explicit [m/s]	v -implicit [m/s]	Δv [m/s]
5	4.556196037618452e+02	4.556196037618386e+02	6.593836587853730e-12
10	2.686771069413229e+02	2.686771069413665e+02	-4.354205884737894e-11
15	2.077692047266052e+02	2.077692047266444e+02	-3.922195901395753e-11
20	1.731362186963469e+02	1.731362186963497e+02	-2.728484105318785e-12
30	1.578228372701631e+02	1.578228372701328e+02	3.029754225281067e-11
40	1.810541039539512e+02	1.810541039539235e+02	2.768274498521350e-11
50	2.033211141640507e+02	2.033211141640362e+02	1.458033693779726e-11

Tables 9-12 present exemplary results of the projectile trajectory calculations using both forms of the MPMTM. Absolute differences between the respective values are shown in the tables as well as in Fig. 7.

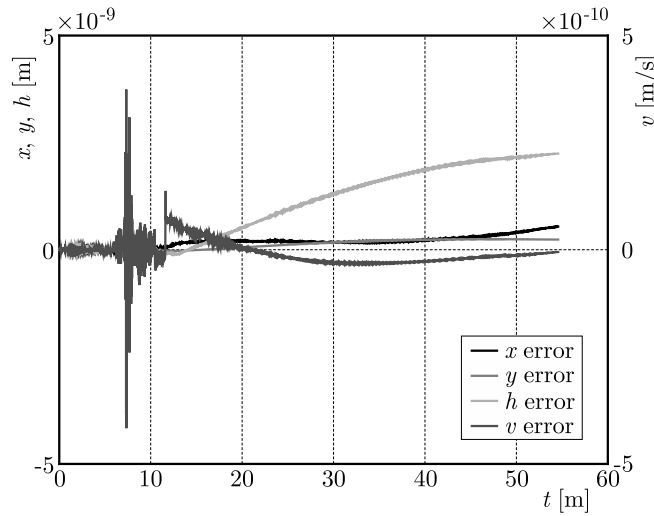


Fig. 7. Absolute differences of projectile position and velocity as a function of time for the explicit and implicit form of the MPM model; standard atmosphere, homogeneous tail wind (10 m/s)

4.4. Calculation time

Another aspect that we have taken under consideration is the runtime needed for the necessary computations. Figure 8b shows the time needed for trajectory generation for different elevation angles: 10 to 710 mil with the interval of 20 mils. As mentioned before, the differential equations have been integrated using the non-stiff fourth-order Runge-Kutta solver ode45. The stopping condition for numerical integration was the moment when the projectile reached the point of fall⁴.

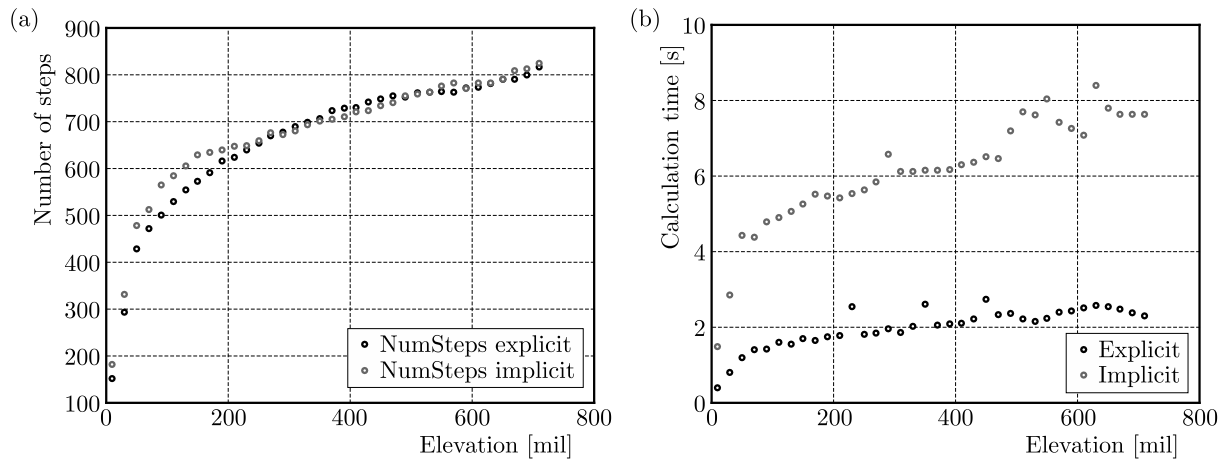


Fig. 8. (a) Number of steps for the implicit and explicit forms of the MPMTM using the ode45 solver; (b) comparison of the trajectory calculation time for both forms of the MPMTM

As it can be seen, the explicit model needs much less time (up to 4 times less) to calculate the trajectory. Figure 8a shows statistics drawn from the ode45 solver – the aggregate number of steps (both successful and failed). One can easily notice that the solver needs much less time

⁴The point of intersection between the trajectory and the weapon level surface *STANAG 4119*, 2007

for the explicit form of MPMTM despite a similar number of steps and function evaluations (Fig. 8a).

5. Conclusions

The aim of this paper is to compare an implicit form of the MPMTM with the explicit one, which was derived by Baranowski *et al.* (2016). As it is shown in Section 4, simulations of the 35 mm TP-T projectile trajectory gives the same results for both model forms in the following cases:

- standard atmosphere without the presence of wind within the whole integration interval;
- standard atmosphere with homogeneous side wind within the whole integration interval;
- standard atmosphere with homogeneous tail wind within the whole integration interval.

Furthermore, it is shown that the explicit MPMTM can integrate differential equations of motion up to 4 times faster than the implicit form, which is solely attributed to the fact that the explicit analytic formula for the yaw of repose has been derived. This freed us from the cost of unnecessary FLOPS needed to approximate α_e . The great reduction of runtime in the explicit model is of great importance and can significantly enhance the process of aerodynamic coefficients identification. This process, based on ammo data and firing tables (ground and anti-aircraft), needs time consuming calculations, i.e. finding local minima of complicated functions (given by ODEs) in multi-dimensional parameter spaces, with the impossible aim of finding the global minimum – the ideal fit. Moreover, an explicit formula does not have convergence issues which might appear in the implicit method. It seems justified to apply the explicit form of the MPMTM to the identification process of aerodynamic coefficients on which we will focus in our future work.

Acknowledgement

This paper was created as a part of the development project No. O ROB 0046 03 001 financed by Polish National Centre for Research and Development in the period between 2012 and 2015.

References

1. BARANOWSKI L., 2013, Feasibility analysis of the modified point mass trajectory model for the need of ground artillery fire control systems, *Journal of Theoretical and Applied Mechanics*, **51**, 3, 511-522
2. BARANOWSKI L., FURMANEK W., 2013, The problem of validation of the trajectory model of 35 mm calibre projectile TP-T in the normal conditions (in Polish), *Problemy Techniki Uzbrojenia*, **125**, 35-44
3. BARANOWSKI L., GADOMSKI B., MAJEWSKI P., SZYMONIK J., 2016, Explicit “ballistic M-model”: a refinement of the implicit “modified point mass trajectory model”, *Bulletin of the Polish Academy of Sciences – Technical Sciences*, **64**, 1, 81-89
4. COLEMAN N., MAY R., NEELAKANDAN M., PAPANAGOPOULOS G., UDOMKESMALEE S., LIN C.F., POLITOPOULOS A., 2003, Fire control solution using robust MET data extraction and impact point prediction, *4th International Conference on Control and Automation ICCA '03*, Montreal, 770-774
5. ISO 2533, 1975, *The ISO Standard Atmosphere*, U.S. Government Printing Office, Washington, D.C.
6. KORUBA Z., DZIOPA Z., KRZYSZTOFIK I., 2010, Dynamics and control of a gyroscope-stabilized platform in a self-propelled anti-aircraft system, *Journal of Theoretical and Applied Mechanics*, **48**, 1, 5-26

7. KOWALECZKO G., ŻYLUK A., 2009, Influence of atmospheric turbulence on bomb release, *Journal of Theoretical and Applied Mechanics*, **47**, 1, 69-90
8. ŁADYŻYŃSKA-KOZDRAŚ E., 2012, Modeling and numerical simulation of unmanned aircraft vehicle restricted by non-holonomic constraints, *Journal of Theoretical and Applied Mechanics*, **50**, 1, 251-268
9. LIESKE R.F., REITER M.L., 1966, *Equations of Motion for a Modified point Mass Trajectory*, U.S. Army Ballistic Research Laboratory, Report No. 1314
10. MATLAB 2014b Documentation
11. MCCOY R.L., 1999, *Modern Exterior Ballistics. The Launch and Flight Dynamics of Symmetric Projectiles*, Schiffer Publishing
12. POPE R.L., 1978, *The Analysis of Trajectory and Solar Aspect Angle Records of Shell Flights. Theory and Computer Programs*, Department of Defence, Defence Science and Technology Organisation, Weapons Systems Research Laboratory
13. SHANKS D., WALTON T.S., 1957, *A New General Formula for Representing the Drag on a Missile Over the Entire Range of Mach Number*, NAVORD Report 3634, May
14. STANAG 4119, 2007, *Adoption of a Standard Cannon Artillery Firing Table Format*, Ed. 2
15. STANAG 4355, 2009, *The Modified Point Mass and Five Degrees of Freedom Trajectory Models*, Ed. 3

Manuscript received July 22, 2015; accepted for print February 18, 2016

METAMORPHOSES OF RESONANCE CURVES IN SYSTEMS OF COUPLED OSCILLATORS

JAN KYZIOŁ, ANDRZEJ OKNIŃSKI

Kielce University of Technology, Kielce, Poland

e-mail: kyziol@tu.kielce.pl; fizao@tu.kielce.pl

We study dynamics of two coupled periodically driven oscillators in a general case and compare it with two simplified models. Periodic steady-state solutions to these system equations are determined within the Krylov-Bogoliubov-Mitropolsky approach. Amplitude profiles are computed. These two equations, each describing a surface, define a 3D curve – intersection of these surfaces. In the present paper, we analyse metamorphoses of amplitude profiles induced by changes of control parameters in three dynamical systems studied. It is shown that changes of the dynamics occur in the vicinity of singular points of these 3D curves.

Keywords: coupled oscillators, amplitude profiles, singular points

1. Introduction

We study dynamics of two coupled nonlinear oscillators, one of which being driven by an external periodic force. Equations of motion are

$$\begin{aligned} m\ddot{x} - V(\dot{x}) - R(x) + V_e(\dot{y}) + R_e(y) &= F(t) \\ m_e(\ddot{x} + \ddot{y}) - V_e(\dot{y}) - R_e(y) &= 0 \end{aligned} \tag{1.1}$$

where x is the position of primary mass m , y is the relative position of another mass m_e attached to m and R , V and R_e , V_e are nonlinear elastic restoring and nonlinear forces of internal friction for masses m , m_e , respectively (we use convention $\dot{x} \equiv dx/dt$, etc.). A dynamic vibration absorber is a typical mechanical model described by (1.1) (in this case m is usually much larger than m_e) (Den Hartog, 1985; Oueini *et al.*, 1999).

Dynamics of coupled, externally and/or parametrically driven oscillators, is very complex. Indeed, there are many interesting nonlinear phenomena present in this class of dynamical systems. There exists a large body of analytical and numerical studies documenting multistability, symmetry breaking, attractors merging, synchronisation, existence of exotic attractors and various transitions to chaos (Bi, 2004; Brezetskyi *et al.*, 2015; Chen and Xu, 2010; Danzl and Moehlis, 2010; Dudkowski *et al.*, 2014; Kuznetsov *et al.*, 2009; Laxalde *et al.*, 2006; McFarland *et al.*, 2005; Pikovsky *et al.*, 2003; Sabarathinam *et al.*, 2013; Warmiński, 2010).

In our earlier papers, we have designed a method based on the theory of singular points of 2D curves, permitting computation of parameter values at which qualitative changes (metamorphoses) of 2D amplitude curves occur, see Kyzioł and Okniński (2013) and references therein. We have also shown that metamorphoses of amplitude profiles are visible in bifurcation diagrams as qualitative changes of dynamics (bifurcations). Recently, our approach has been generalized to the case of 3D resonance curves and applied to compute bifurcations in dynamical system (1.1) with small nonlinearities in the main mass frame (Kyzioł, 2015). It is thus possible to treat system (1.1) as a small perturbation of model with linear functions $R(x)$, $V(\dot{x})$ analyzed in Kyzioł and Okniński (2013) (let us recall that in this case internal motion can be separated

off, leading to a simpler equation for the corresponding amplitude profile) and use the results obtained by Kyzioł and Okniński (2013). We show that the method is a powerful tool to predict bifurcations of nonlinear resonances present in such dynamical systems.

In the paper by Awrejcewicz (1995), the author outlined a programme, based on the Implicit Function Theorem, to “define and find different branches intersecting at singular points” of amplitude equations. In the present paper, we are working in a more general context of theory of singular points of algebraic curves (Wall, 2004; Hartmann, 2003).

We investigate the following hierarchy of dynamical systems of form (1.1): we consider functions R, V, R_e, V_e for which (a) system of equations can be reduced to one second-order effective equation of relative motion, (b) fourth-order equation for variable y can be separated off, (c) it is impossible to separate variables. We analyse approximate analytic solutions (amplitude profiles) obtained within the Krylov-Bogoliubov-Mitropolsky (KBM) method (Nayfeh, 1981; Awrejcewicz and Krysko, 2006), using theory of algebraic curves. More exactly, singular points of amplitude profiles are computed. We demonstrate that qualitative changes of dynamics, referred to as metamorphoses, induced by changes of control parameters, occur in neighbourhoods of singular points of amplitude profiles, see also Kyzioł and Okniński (2011, 2013) and references therein.

The paper is organized as follows. In the next Section, equations (1.1), (2.1) are transformed into non-dimensional form. In Section 4, implicit equations for resonance surfaces $A(\omega), B(\omega)$ are derived within the Krylov-Bogoliubov-Mitropolsky approach, where the amplitudes A, B correspond to small and large masses, respectively. The problem is more difficult than before because these two equations are coupled. In Section 5, we review necessary facts from theory of algebraic curves which are used to compute singular points on three-dimensional resonance curve (intersection of resonance surfaces $A(\omega), B(\omega)$). In Section 6, computational results are presented. Our results are summarized in the last Section.

2. Equations of motion

In what follows the function $F(t)$ is assumed in form $F(t) = f \cos(\omega t)$. When all the functions R, V, R_e, V_e are nonlinear, namely

$$\begin{aligned} R(x) &= -\alpha x - \gamma x^3 & R_e(y) &= -\alpha_e y - \gamma_e y^3 \\ V(\dot{x}) &= -\nu \dot{x} - \beta \dot{x}^3 & V_e(\dot{y}) &= -\nu_e \dot{y} - \beta_e \dot{y}^3 \end{aligned} \quad (2.1)$$

then we deal with the general case of Eq. (1.1). For linear functions R, V

$$\begin{aligned} R(x) &= -\alpha x & R_e(y) &= -\alpha_e y - \gamma_e y^3 \\ V(\dot{x}) &= -\nu \dot{x} & V_e(\dot{y}) &= -\nu_e \dot{y} + \beta_e \dot{y}^3 \end{aligned} \quad (2.2)$$

it is possible to separate off the variable y to obtain the following equation for relative motion (Kyzioł and Okniński, 2013)

$$\widehat{L}(\mu \ddot{y} - V_e(\dot{y}) - R_e(y)) + \epsilon m_e \widehat{K} y = F \cos(\omega t) \quad (2.3)$$

where

$$\begin{aligned} \widehat{L} &= M \frac{d^2}{dt^2} + \nu \frac{d}{dt} + \alpha & \widehat{K} &= \left(\nu \frac{d}{dt} + \alpha \right) \frac{d^2}{dt^2} & F &= m_e \omega^2 f \\ \epsilon &= \frac{m_e}{M} & \mu &= \frac{m m_e}{M} & M &= m + m_e \end{aligned}$$

Finally, assuming $m_e \ll m$, i.e. $\epsilon \ll 1$, we can reject the term proportional to ϵ to obtain an approximate equation which can be integrated partly to yield the effective equation (Kyzioł and Okniński, 2011)

$$\begin{aligned} \mu\ddot{y} + \nu_e\dot{y} - \beta_e\dot{y}^3 + \alpha_e y + \gamma_e y^3 &= F(t) \\ F(t) &= \frac{-m_e\omega^2 f}{\sqrt{M^2\left(\omega^2 - \frac{\alpha}{M}\right)^2 + \nu^2\omega^2}} \cos(\omega t + \delta) \end{aligned} \quad (2.4)$$

where transient states are neglected.

3. Equations in non-dimensional form

Equations (1.1), (2.1) are transformed into non-dimensional form (Kyzioł, 2015). We introduce non-dimensional time τ and frequency Ω and rescale variables x, y

$$t = \sqrt{\frac{\mu}{\alpha_e}}\tau \quad \omega = \sqrt{\frac{\alpha_e}{\mu}}\Omega \quad x = \sqrt{\frac{\alpha_e}{\gamma_e}}u \quad y = \sqrt{\frac{\alpha_e}{\gamma_e}}z \quad (3.1)$$

to get

$$\begin{aligned} \ddot{u} + \widehat{H}\dot{u} + c\dot{u}^3 + \widehat{a}u + du^3 - \widehat{\kappa}(h\dot{z} + b\dot{z}^3 + z + z^3) &= \lambda \cos(\Omega\tau) \\ \ddot{z} + h\dot{z} + b\dot{z}^3 + z + z^3 - \widehat{H}\dot{u} - c\dot{u}^3 - \widehat{a}u - du^3 &= -\lambda \cos(\Omega\tau) \end{aligned} \quad (3.2)$$

and new parameters read

$$\begin{aligned} a &= \frac{\mu\alpha}{M\alpha_e} & b &= \frac{\beta_e}{\gamma_e}\left(\frac{\alpha_e}{\mu}\right)^{\frac{3}{2}} & c &= \frac{\beta(\alpha_e)^{\frac{3}{2}}}{\sqrt{\mu}m\gamma_e} & d &= \frac{\mu\gamma}{m\gamma_e} \\ h &= \frac{\nu_e}{\sqrt{\mu\alpha_e}} & H &= \frac{\nu}{M}\sqrt{\frac{\mu}{\alpha_e}} & G &= \frac{1}{\alpha_e}\sqrt{\frac{\gamma_e}{\alpha_e}}f & \kappa &= \frac{m_e}{m} \\ \lambda &= \frac{\kappa}{\kappa+1}G & \widehat{H} &= H(1+\kappa) & \widehat{a} &= a(1+\kappa) & \widehat{\kappa} &= \frac{\kappa}{\kappa+1} \end{aligned} \quad (3.3)$$

where

$$M = m + m_e \quad \mu = \frac{mm_e}{M} \quad \dot{u} \equiv \frac{du}{d\tau} \quad \dot{z} \equiv \frac{dz}{d\tau}$$

Note that \ddot{u} is eliminated from the second of Eqs. (1.1).

4. Nonlinear resonances

System of equations (3.2) is written in form

$$\begin{aligned} \frac{d^2u}{d\tau^2} + \Omega^2u + \varepsilon(\sigma u + g(\dot{u}, u, \dot{z}, z, \tau)) &= 0 \\ \frac{d^2z}{d\tau^2} + \Omega^2z + \varepsilon(\sigma z + k(\dot{u}, u, \dot{z}, z, \tau)) &= 0 \end{aligned} \quad (4.1)$$

where

$$\begin{aligned} \varepsilon\sigma &= \Theta^2 - \Omega^2 & \widehat{H} &= \varepsilon\widehat{H}_0 & \widehat{a} &= \varepsilon\widehat{a}_0 & b &= \varepsilon b_0 & c &= \varepsilon c_0 \\ \Theta^2 &= \varepsilon\Theta_0^2 & d &= \varepsilon d_0 & h &= \varepsilon h_0 & \varepsilon\delta_0 &= 1 & \lambda &= \varepsilon\lambda_0 \end{aligned} \quad (4.2)$$

and functions $g(\dot{u}, u, \dot{z}, z, \tau)$, $k(\dot{u}, u, \dot{z}, z, \tau)$ are defined in (Kyzioł, 2015). Equations (4.1) have been prepared in such a way that for $\varepsilon = 0$ the solutions are $u(\tau) = B \cos(\Omega\tau + \psi)$, $z(\tau) = A \cos(\Omega\tau + \varphi)$.

We shall now look for 1 : 1 resonance using the Krylov-Bogoliubov-Mitropolsky (KBM) perturbation approach (Nayfeh, 1981; Awrejcewicz and Krysko, 2006). For a small nonzero ε , the solutions to Eqs. (4.1) are assumed in form

$$\begin{aligned} u(\tau) &= B \cos(\Omega\tau + \psi) + \varepsilon u_1(B, \psi, \tau) + \dots \\ z(\tau) &= A \cos(\Omega\tau + \varphi) + \varepsilon z_1(A, \varphi, \tau) + \dots \end{aligned} \quad (4.3)$$

with slowly varying amplitudes and phases

$$\begin{aligned} \frac{dA}{d\tau} &= \varepsilon M_1(A, \varphi) + \dots & \frac{dB}{d\tau} &= \varepsilon P_1(B, \psi) + \dots \\ \frac{d\varphi}{d\tau} &= \varepsilon N_1(A, \varphi) + \dots & \frac{d\psi}{d\tau} &= \varepsilon Q_1(B, \psi) + \dots \end{aligned} \quad (4.4)$$

Proceeding as described in (Kyzioł, 2015), we obtain finally equations for the amplitudes A, B

$$L_1(A, B, \Omega; \Lambda) = 0 \quad L_2(A, B, \Omega; \Lambda) = 0 \quad (4.5)$$

where Λ denotes parameters and

$$\begin{aligned} L_1 &= Z((\eta_4^2 + u_2^2)(u_1^2 + \eta_2^2) + \hat{\kappa}X^2u_3) - (\hat{\kappa} - 1)^2(u_1^2 + \eta_2^2)\lambda^2 \\ u_1 &= \hat{\kappa}X + \eta_1 \quad u_2 = \hat{\kappa}X + \eta_3 \quad u_3 = \hat{\kappa}X^2 + 2\eta_2\eta_4 - 2u_1u_2 \end{aligned} \quad (4.6)$$

$$L_2 = \frac{Y}{(\hat{\kappa} - 1)^2} [u_4^2 + (\hat{\kappa}Xu_5 + \eta_1\eta_3 - \eta_2\eta_4)^2] - \lambda^2X^2 \quad (4.7)$$

$$u_4 = \hat{\kappa}X(\eta_2 + \eta_4) + \eta_1\eta_4 + \eta_2\eta_3 \quad u_5 = (\hat{\kappa} - 1)X + \eta_1 + \eta_3$$

$$\eta_1 = \left(\frac{3}{4}Y + 1 - X\right)(\hat{\kappa} - 1) \quad \eta_2 = \Omega\left(\frac{3}{4}bXY + h\right)(\hat{\kappa} - 1) \quad (4.8)$$

$$\eta_3 = \left(\hat{a} + \frac{3}{4}dZ - X\right)(\hat{\kappa} - 1) \quad \eta_4 = \Omega\left(\frac{3}{4}cXZ + \hat{H}\right)(\hat{\kappa} - 1)$$

$$X = \Omega^2 \quad Y = A^2 \quad Z = B^2 \quad (4.9)$$

If we put $c = d = 0$ in Eqs.(4.6), (4.7) and (4.8) (or $\beta = \gamma = 0$ in Eqs. (2.1)) then the function L_2 becomes independent on B . In this case, it is possible to separate variables in Eqs. (1.1), (2.2) obtaining the fourth-order effective equation for the small mass (Kyzioł and Okniński, 2013). The function L_2 , defined above, for $c = d = 0$ is equal to the function $L(X, Y)$ defined in Eq. (4.1) in (Kyzioł and Okniński, 2013).

5. Metamorphoses of the amplitude profiles

In the preceding Section, we have obtained two implicit equations (4.5) for amplitude profiles. Each of these equations describes a surface in a three dimensional space (A, B, Ω) . Intersection of the surfaces $L_1 = 0, L_2 = 0$ is a 3D curve, and in singular points of this curve all three minors of the rectangular matrix

$$\mathbf{M} = \begin{bmatrix} L'_{1,A} & L'_{1,B} & L'_{1,\Omega} \\ L'_{2,A} & L'_{2,B} & L'_{2,\Omega} \end{bmatrix} \quad (5.1)$$

are zero (Hartmann, 2003), where $L'_{1,A} = \partial L_1 / \partial A$, etc. Equations (4.5) and these conditions are used to compute singular points. We have shown in our previous papers that qualitative changes of dynamics, induced by changes of control parameters, occur in neighbourhoods of singular points of amplitude profiles (Kyzioł and Okniński, 2011, 2013; Kyzioł, 2015).

6. Amplitude profiles and bifurcation diagrams

Applying the KBM method to effective equation (2.4) we obtain approximate formula $y(t) = A \cos(\omega t + \varphi)$ where dependence of A on ω is given by an implicit equation $F_1(A, \omega; \Lambda) = 0$. The form of the function F_1 can be found in Kyzioł and Okniński (2011). In Fig. 1a, this implicit function is shown just after an isolated point $(A, \omega) = (1.124, 1.784)$ has been born.

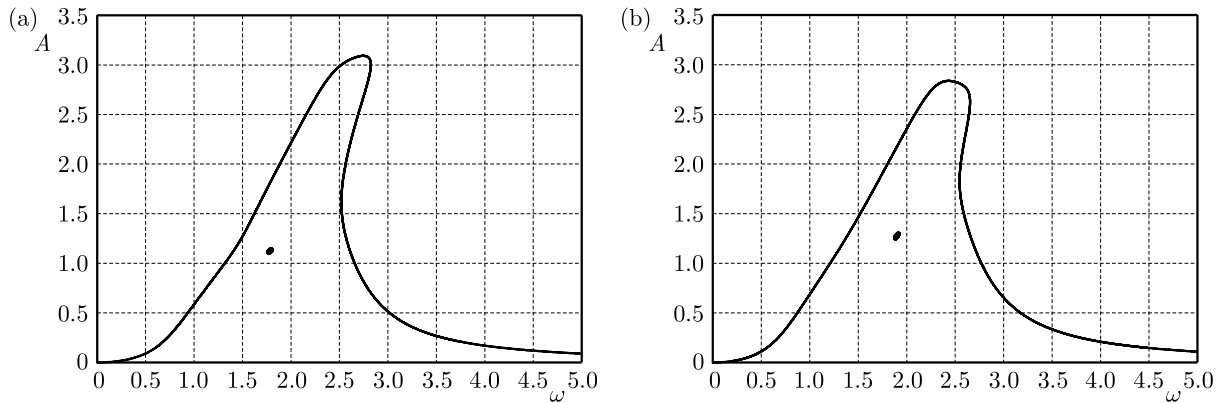


Fig. 1. Amplitude profile $F_1(A, \omega; \Lambda) = 0$ (a) and $F_2(A, \omega; \Lambda) = 0$ (b) with an isolated point

Then, applying the KBM method to fourth-order equation (2.3) we obtain the corresponding implicit amplitude equation $F_2(A, \omega; \Lambda) = 0$. The form of F_2 has been described in Kyzioł and Okniński (2013). In Fig. 1b, we see that an isolated point $(A, \omega) = (1.274, 1.899)$ has been just born. Similarity of the amplitude profiles shows that effective equation (2.4) is a good approximation to fourth-order equation (2.3). Bifurcation diagrams show indeed the birth of new branches of solutions in both models (Kyzioł and Okniński, 2011, 2013).

Now we consider the general case with small nonlinearities in the main mass frame, $c = 0.001$, $d = 0.02$, so that the system of equations (1.1), (2.1) is a small perturbation of model (1.1), (2.2), with other parameters being equal $a = 6$, $b = 0.001$, $h = 0.5$, $H = 0.7$, $\kappa = 0.05$, $\gamma = 2.011615 \stackrel{df}{=} \gamma_{cr}$.

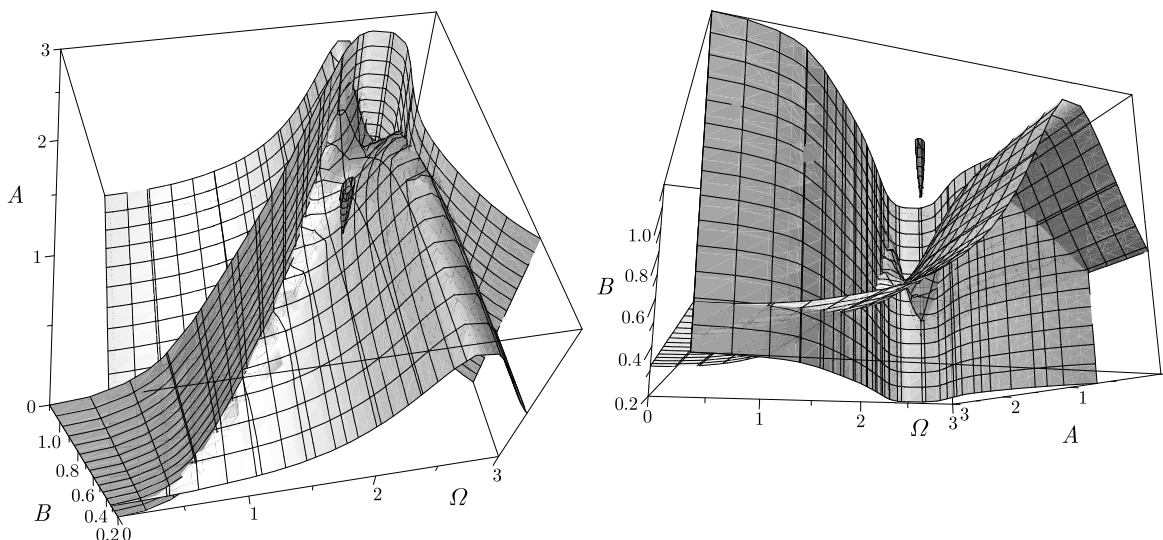


Fig. 2. Resonance surfaces before the singular point is formed, left figure. The conical structure does not intersect the lower surface, right figure

Resonance surfaces (4.5) are shown in Figs. 2 before the singular point is formed, the singular point being $(A, B, \Omega) = (1.276, 0.620, 1.902)$ and $\gamma = 2.015 > \gamma_{cr}$, where the surfaces in the right

figure have been rotated to show that the additional conical surface does not pierce the other surface yet, and, after formation of the singular point, $\gamma = 1.995 < \gamma_{cr}$, in Fig. 3.

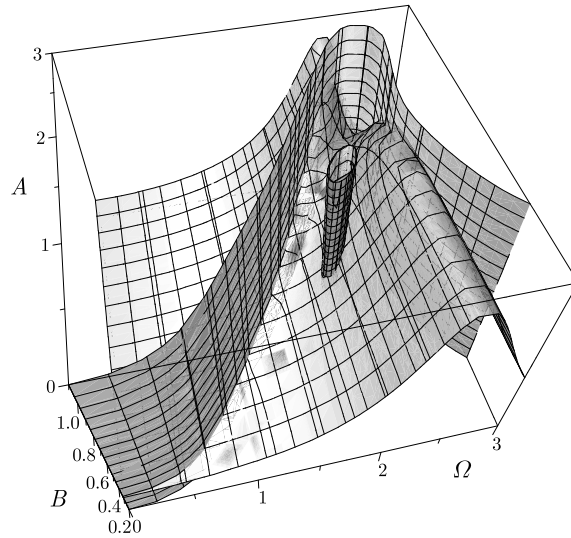


Fig. 3. Resonance surfaces $L_1(A, B, \Omega; A) = 0$ and $L_2(A, B, \Omega; A) = 0$ with an additional tubular structure intersecting the lower surface

The corresponding bifurcation diagrams, one with a new branch near $\Omega = 1.9$, are shown in Figs. 4.

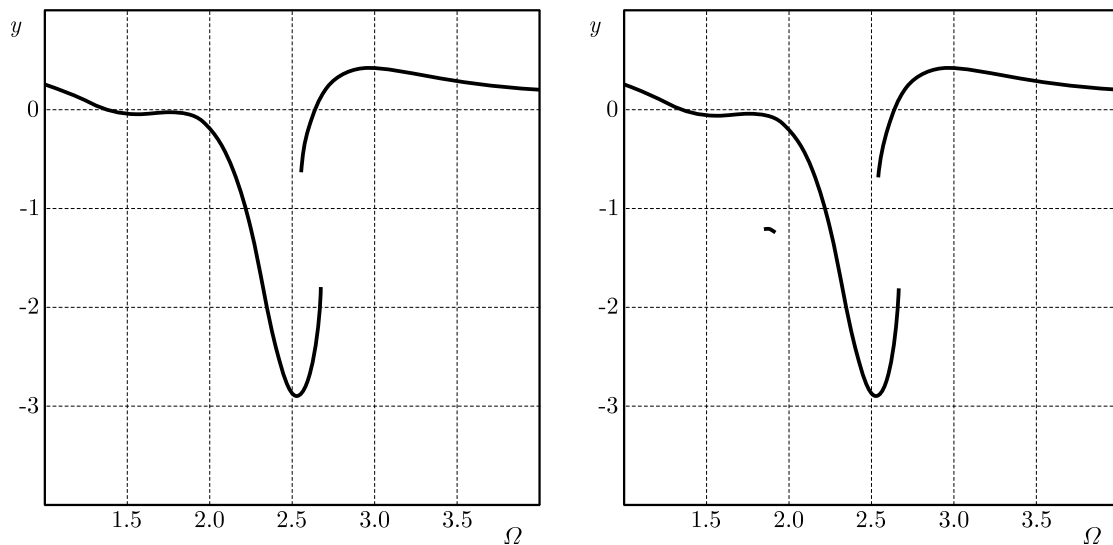


Fig. 4. Bifurcation diagram before formation of the singular point (left figure) and after (right figure)

7. Discussion

In the present work, we continue study of the general case of dynamics of two coupled periodically driven oscillators, cf. Eq. (1.1), initiated in Kyzioł (2015). More exactly, we have investigated: (a) model (1.1), (2.1) with small parameters α , γ ; (b) model (1.1), (2.2) with $\alpha = 0$, $\gamma = 0$ (in this case, dynamics of small mass can be separated off, see Eq. (2.3)); (c) and approximate effective equation (2.4).

We have studied the amplitude (resonance) equations for steady states, obtained via the KBM approach, within the theory of singular points of 2D and 3D algebraic curves (Wall, 2004; Hartmann, 2003). Analysis of the resonance curves in cases (b), (c) has been relatively simple since we have been dealing with one implicit equation of form $F(A, \Omega; \Lambda) = 0$, describing a 2D curve only (Kyzioł and Okniński, 2011, 2013). The general case is more difficult since there are two amplitude equations, $L_1(A, B, \Omega; \Lambda) = 0$, $L_2(A, B, \Omega; \Lambda) = 0$, which describe two surfaces. Conditions for singular points of the 3D curve – intersection of these surfaces – are also more complex: they are given by two equations (4.5) and three equations $\det(\mathbf{M}) = 0$ with matrix \mathbf{M} given by (5.1).

Bifurcations diagrams shown in Figs. 4 confirm that a qualitative change of dynamics – birth of a new branch of a nonlinear resonance – occurs in the neighbourhood of the singular point of the 3D curve defined by amplitude equations (4.5).

Acknowledgement

The present paper is an extended version of the article published in the Proceedings of the conference: PCM-CMM-2015 – 3rd Polish Congress of Mechanics and 21st Computer Methods in Mechanics, September 8th-11th 2015, Gdańsk, Poland.

References

1. AWREJCEWICZ J., 1995, Modified Poincaré method and implicit function theory, [In:] *Nonlinear Dynamics: New Theoretical and Applied Results*, Awrejcewicz J. (Edit.), Akademie Verlag, Berlin, 215-229
2. AWREJCEWICZ J., KRYSKO V.A., 2006, *Introduction to Asymptotic Methods*, Chapman and Hall (CRC Press), New York
3. BI Q., 2004, Dynamical analysis of two coupled parametrically excited van der Pol oscillators, *International Journal of Non-Linear Mechanics*, **39**, 33-54
4. BREZETSKYI S., DUDKOWSKI D., KAPITANIAK T., 2015, Rare and hidden attractors in Van der Pol-Duffing oscillators, *European Physical Journal Special Topics*, **224**, 1459-1467
5. CHEN H., XU Q., 2010, Global bifurcations in externally excited autoparametric systems, *International Journal of Non-Linear Mechanics*, **45**, 766-792
6. DANZL P., MOEHLIS J., 2010, Weakly coupled parametrically forced oscillator networks: existence, stability, and symmetry of solutions, *Nonlinear Dynamics*, **59**, 661-680
7. DEN HARTOG J.P., 1985, *Mechanical Vibrations*, 4th ed., Dover Publications, New York
8. DUDKOWSKI D., MAISTRENKO Y., KAPITANIAK T., 2014, Different types of chimera states: An interplay between spatial and dynamical chaos, *Physical Review E*, **90**, 032920
9. HARTMANN E., 2003, *Geometry and Algorithms for Computer Aided Design*, Darmstadt University of Technology, Darmstadt
10. KUZNETSOV A.P., STANKEVICH N.V., TURUKINA L.V., 2009, Coupled van der Pol-Duffing oscillators: phase dynamics and structure of synchronization tongues, *Physica D*, **238**, 1203-1215
11. KYZIOŁ J., 2015, Metamorphoses of resonance curves for two coupled oscillators: The case of small non-linearities in the main mass frame, *International Journal of Non-Linear Mechanics*, **76**, 164-168
12. KYZIOŁ J., OKNIŃSKI A., 2011, Coupled nonlinear oscillators: metamorphoses of resonance curves. The case of the approximate effective equation, *Acta Physica Polonica B*, **42**, 2063-2076
13. KYZIOŁ J., OKNIŃSKI A., 2013, Exact nonlinear fourth-order equation for two coupled oscillators: metamorphoses of resonance curves, *Acta Physica Polonica B*, **44**, 35-47

14. LAXALDE D., THOUVEREZ F., SINOUE J.-J., 2006, Dynamics of a linear oscillator connected to a small strongly non-linear hysteretic absorber, *International Journal of Non-Linear Mechanics*, **41**, 969-978
15. MCFARLAND D.M., BERGMAN L.A., VAKAKIS A.F., 2005, Experimental study of non-linear energy pumping occurring at a single fast frequency, *International Journal of Non-Linear Mechanics*, **40**, 891-899
16. NAYFEH A.H., 1981, *Introduction to Perturbation Techniques*, John Wiley & Sons, New York
17. OUEINI S.S., NAYFEH A.H., PRATT J.R., 1999, A review of development and implementation of an active nonlinear vibration absorber, *Archive of Applied Mechanics*, **69**, 585-620
18. PIKOVSKY A., ROSENBLUM M., KURTHS J., 2003, *Synchronization: A Universal Concept in Non-linear Sciences*, Cambridge University Press, Cambridge
19. SABARATHINAM S., THAMILMARAN K., BORKOWSKI L., PERLIKOWSKI P., BRZESKI P., STEFANSKI A., KAPITANIAK T., 2013, Transient chaos in two coupled, dissipatively perturbed Hamiltonian Duffing oscillators, *Communications in Nonlinear Science and Numerical Simulation*, **18**, 3098-3107
20. WALL C.T.C., 2004, *Singular Points of Plane Curves*, Cambridge University Press, New York
21. WARMIŃSKI J., 2010, Nonlinear normal modes of a self-excited system driven by parametric and external excitations, *Nonlinear Dynamics*, **61**, 677-689

Manuscript received October 1, 2015; accepted for print February 18, 2016

APPLICATION OF THE DIFFERENTIAL TRANSFORM METHOD TO THE FREE VIBRATION ANALYSIS OF FUNCTIONALLY GRADED TIMOSHENKO BEAMS

ÖZGE ÖZDEMİR

Istanbul Technical University, Faculty of Aeronautics and Astronautics, Maslak, Istanbul, Turkey
e-mail: ozdemirozg@itu.edu.tr

In this study, free vibration characteristics of a functionally graded Timoshenko beam that undergoes flapwise bending vibration is analysed. The energy expressions are derived by introducing several explanatory figures and tables. Applying Hamilton's principle to the energy expressions, governing differential equations of motion and boundary conditions are obtained. In the solution part, the equations of motion, including the parameters for rotary inertia, shear deformation, power law index parameter and slenderness ratio are solved using an efficient mathematical technique, called the differential transform method (DTM). Natural frequencies are calculated and effects of several parameters are investigated.

Keywords: differential transform method, functionally graded beam, Timoshenko beam

1. Introduction

The concept of Functionally Graded Materials (FGMs) was originated from a group of material scientists in Japan as means of preparing thermal barrier materials (Loy *et al.*, 1999). FGMs are special composites that have continuous variation of material properties in one or more directions to provide designers with the ability to distribute strength and stiffness in a desired manner to get suitable structures for specific purposes in engineering and scientific fields such as design of aircraft and space vehicle structures, electronic and biomedical installations, automobile sector, defence industries, nuclear reactors, electronics, transportation sector, etc. As a consequence, it is important to understand static and dynamic behavior of FGMs, so it has been an area of intense research in the recent years. Especially, functionally graded beam (FGB) structures have become a fertile area of research since beam structures have been widely used in aeronautical, astronautical, civil, mechanical and other kinds of installations. Several research papers provide a good introduction and further references on the subject (Alshorbagy *et al.*, 2011; Chakraborty *et al.*, 2003; Giunta *et al.*, 2011; Huang and Li, 2010; Kapuria *et al.*, 2008; Lai *et al.*, 2012; Li, 2008; Loja *et al.*, 2012; Lu and Chen, 2005; Thai and Vo, 2012; Wattanasakulpong *et al.*, 2012; Zhong and Yu, 2007).

Due to the increasing application trend of FGMs, several beam theories have been developed to examine the response of FGBs. The Classical Beam Theory (CBT), i.e. Euler Bernoulli Beam Theory, is the simplest theory that can be applied to slender FGBs. The first order shear deformation theory (FSDT), i.e. Timoshenko Beam Theory, is used for the case of either short beams or high frequency applications to overcome the limitations of the CBT by accounting for the transverse shear deformation effect. Bhimaraddi and Chandrashekhara (1991) derived laminated composite beam equations of motion using the first-order shear deformation plate theory (FSDPT). Dadfarnia (1997) developed a new beam theory for laminated composite beams using the assumption that the lateral stresses and all derivatives with respect to the lateral coordinate in the plate equations of motion are ignored.

In this study, which is an extension of the author's previous works (Kaya and Ozdemir Ozgumus, 2007; Kaya and Ozdemir Ozgumus, 2010; Ozdemir Ozgumus and Kaya, 2013), free vibration analysis of a functionally graded Timoshenko beam that undergoes flapwise bending vibrations is performed. At the beginning of the study, expressions for both kinetic and potential energies are derived in a detailed way by using explanatory tables and figures. In the next step, governing differential equations of motion are obtained applying Hamilton's principle. In the solution part, the equations of motion, including the parameters for rotary inertia, shear deformation, power law index parameter and slenderness ratio are solved using an efficient mathematical technique, called the differential transform method (DTM). Natural frequencies are calculated and effects of the parameters, mentioned above, are investigated. The calculated results are compared with the ones in open literature. Consequently, it is observed that there is a good agreement between the results which proves the correctness and accuracy of the DTM.

2. Beam model

The governing differential equations of motion are derived for the free vibration analysis of a functionally graded Timoshenko beam model with a right-handed Cartesian coordinate system which is represented by Fig. 1.

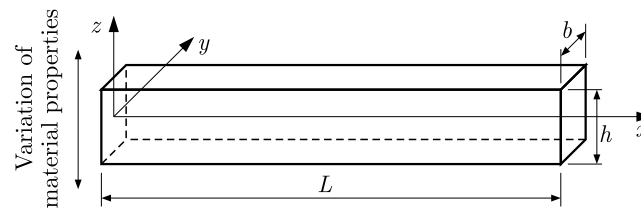


Fig. 1. Functionally graded beam model and the coordinate system

Here a uniform, functionally graded Timoshenko beam of length L , height h and width b which has the cantilever boundary condition at point O is shown. The xyz -axes constitute a global orthogonal coordinate system with the origin at the root of the beam. The x -axis coincides with the neutral axis of the beam in the undeflected position, the y -axis lies in the width direction and the z -axis lies in the depth direction.

3. Formulation

3.1. Functionally graded beam formulation

Material properties of the beam, i.e. modulus of elasticity E , shear modulus G , Poisson's ratio ν and material density ρ are assumed to vary continuously in the thickness direction z as a function of the volume fraction, and the properties of the constituent materials according to a simple power law.

According to the rule of mixture, the effective material property $P(z)$ can be expressed as follows

$$P(z) = P_t V_t + P_b V_b \quad (3.1)$$

where P_t and P_b are the material properties at the top and bottom surfaces of the beam while V_t and V_b are the corresponding volume fractions. The relation between the volume fractions is given by

$$V_t + V_b = 1 \quad (3.2)$$

The volume fraction of the top constituent of the beam V_t is assumed to be given by

$$V_t = \left(\frac{z}{h} + \frac{1}{2}\right)^k \quad k \geq 0 \tag{3.3}$$

where k is a non-negative power law index parameter that dictates the material variation profile through the beam thickness.

Considering Eqs. (3.1)-(3.3), the effective material property can be rewritten as follows

$$P(z) = (P_t - P_b)\left(\frac{z}{h} + \frac{1}{2}\right)^k + P_b \tag{3.4}$$

It is evident from Eq.(4) that when $z = h/2$, $E = E_t$, $\nu = \nu_t$, $G = G_t$, $\rho = \rho_t$ and when $z = -h/2$, $E = E_b$, $\nu = \nu_b$, $G = G_b$ and $\rho = \rho_b$.

3.2. Displacement field and strain field

The cross-sectional and the longitudinal views of a Timoshenko beam that undergoes extension and flapwise bending deflections are given in Figs. 2a and 2b, respectively. Here, the reference point is chosen, and is represented by P_0 before deformation and by P after deformation.

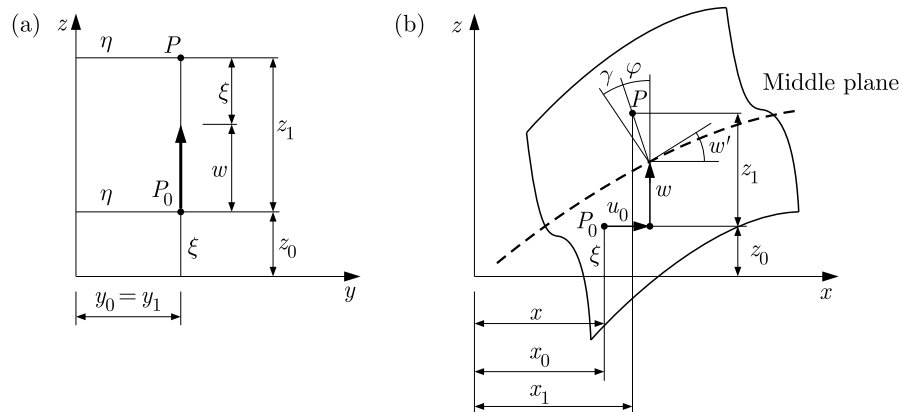


Fig. 2. (a) Cross-sectional view, (b) longitudinal view of the Timoshenko beam

Here, η is the offset of the reference point from the z -axis, ξ is the offset of the reference point from the middle plane, x is the offset of the reference point from the z -axis, u_0 is the elongation, w is the flapwise bending displacement, φ is the rotation due to bending and γ is the shear angle.

Considering Figs. 2a and 2b, the coordinates of the reference point are obtained as follows:
 — before deflection (coordinates of P_0)

$$x_0 = x \quad y_0 = \eta \quad z_0 = \xi \tag{3.5}$$

— after deflection (coordinates of P)

$$x_1 = x + u_0 + \xi\varphi \quad y_1 = \eta \quad z_1 = w + \xi \tag{3.6}$$

The position vectors of the reference point are represented by \mathbf{r}_0 and \mathbf{r}_1 before and after deflection, respectively. Therefore, $d\mathbf{r}_0$ and $d\mathbf{r}_1$ can be written as follows

$$\begin{aligned} d\mathbf{r}_0 &= dx\mathbf{i} + d\eta\mathbf{j} + d\xi\mathbf{k} \\ d\mathbf{r}_1 &= [(1 + u'_0 + \xi\varphi')]dx\mathbf{i} + d\eta\mathbf{j} + (w'dx + d\xi)\mathbf{k} \end{aligned} \tag{3.7}$$

where $(\cdot)'$ denotes differentiation with respect to the spanwise coordinate x .

The classical strain tensor ε_{ij} may be obtained by using the following equilibrium equation given by Eringen (1980)

$$d\mathbf{r}_1 \cdot d\mathbf{r}_1 - d\mathbf{r}_0 \cdot d\mathbf{r}_0 = 2[d\mathbf{x} \ d\eta \ d\xi][\varepsilon_{ij}] \begin{bmatrix} dx \\ d\eta \\ d\xi \end{bmatrix} \tag{3.8}$$

where

$$[\varepsilon_{ij}] = \begin{bmatrix} \varepsilon_{xx} & \varepsilon_{x\eta} & \varepsilon_{x\xi} \\ \varepsilon_{\eta x} & \varepsilon_{\eta\eta} & \varepsilon_{\eta\xi} \\ \varepsilon_{\xi x} & \varepsilon_{\xi\eta} & \varepsilon_{\xi\xi} \end{bmatrix} \tag{3.9}$$

Substituting Eqs. (3.7) into Eq. (3.8), the components of the strain tensor ε_{ij} are obtained as follows

$$\begin{aligned} \varepsilon_{xx} &= u'_0 + \frac{(u'_0)^2}{2} + \frac{(w')^2}{2} + u'_0\varphi'\xi + \varphi'\xi + \frac{(\varphi')^2}{2}\xi^2 \\ \gamma_{x\eta} &= 0 \qquad \gamma_{x\xi} = (w' + \varphi) + \varphi\varphi'\xi - u'_0\varphi \end{aligned} \tag{3.10}$$

where ε_{xx} , $\gamma_{x\eta}$ and $\gamma_{x\xi}$ are the axial strain and the shear strains, respectively.

In this work, only ε_{xx} , $\gamma_{x\eta}$ and $\gamma_{x\xi}$ are used in the calculations because, as noted by Hodges and Dowell (1974) for long slender beams, the axial strain ε_{xx} is dominant over the transverse normal strains $\varepsilon_{\eta\eta}$ and $\varepsilon_{\xi\xi}$. Moreover, the shear strain $\gamma_{\eta\xi}$ is by two orders smaller than the other shear strains $\gamma_{x\xi}$ and $\gamma_{x\eta}$. Therefore, $\varepsilon_{\eta\eta}$, $\varepsilon_{\xi\xi}$ and $\gamma_{\eta\xi}$ are neglected.

In order to obtain simpler expressions for the strain components given by Eqs. (3.10), higher order terms can be neglected, so an order of magnitude analysis is performed by using the ordering scheme taken from Hodges and Dowell (1974) and introduced in Table 1.

Table 1. Ordering scheme for the Timoshenko beam model

Term	Order
w'	$O(\varepsilon)$
φ	$O(\varepsilon)$
$w' + \varphi$	$O(\varepsilon^2)$
u'_0	$O(\varepsilon^2)$
φ'	(ε^2)

Hodges and Dowell (1974) used the formulation for an Euler-Bernoulli beam, so in this study their formulation is modified for the Timoshenko beam, and a new expression $w' + \varphi = O(\varepsilon^2)$ is added to their ordering scheme as a contribution to literature.

Considering Table 1, Eqs. (3.10) are simplified as follows

$$\varepsilon_{xx} = u'_0 + \frac{(u'_0)^2}{2} + \frac{(w')^2}{2} + \varphi'\xi \qquad \gamma_{x\eta} = 0 \qquad \gamma_{x\xi} = w' + \varphi \tag{3.11}$$

3.3. Potential energy

The expression for potential energy is given by

$$U = \frac{1}{2} \int_0^l \int_A (\sigma_{xx}\varepsilon_{xx} + \tau_{x\xi}\gamma_{x\xi}) dA dx = \frac{b}{2} \int_0^l \int_{-h/2}^{h/2} (\sigma_{xx}\varepsilon_{xx} + \tau_{x\xi}\gamma_{x\xi}) d\xi dx \tag{3.12}$$

The axial force N , the bending moment M and the shear force Q that act on a laminate at the midplane are expressed as follows (Kollar and Springer, 2003)

$$N = b \int_{-h/2}^{h/2} \sigma dz \quad M = b \int_{-h/2}^{h/2} z\sigma dz \quad Q = b \int_{-h/2}^{h/2} \tau dz \quad (3.13)$$

Substituting Eqs. (3.11) into Eq. (3.12) and considering Eqs. (3.13), the following expression is obtained

$$U = \frac{1}{2} \int_0^l \left\{ N_x \left[u_0' + \frac{(w')^2}{2} \right] + M_x \varphi' + Qz(w' + \varphi) \right\} dx \quad (3.14)$$

where

$$N_x = \bar{A}_{11}u_0' + \bar{B}_{11}\varphi' \quad M_x = \bar{B}_{11}u_0' + \bar{D}_{11}\varphi' \quad Q = \bar{A}_{55}\gamma_{x\xi} \quad (3.15)$$

Here, the stiffness coefficients are obtained as follows

$$[\bar{A}_{11} \quad \bar{B}_{11} \quad \bar{D}_{11}] = \int_A E(z)[1 \quad z \quad z^2] dA \quad \bar{A}_{55} = K \int_A G(z) dA \quad (3.16)$$

where K is defined as the shear correction factor that takes the value of $K = 5/6$ for rectangular cross sections.

Substituting Eqs. (3.15) into Eq. (3.14) gives

$$U = \frac{1}{2} \int_0^l [\bar{A}_{11}(u_0')^2 + 2\bar{B}_{11}u_0'\varphi' + \bar{D}_{11}(\varphi')^2 + \bar{A}_{55}(w' + \varphi)] dx \quad (3.17)$$

Referring Eq. (3.17), variation of the potential energy is obtained as follows

$$\delta U = \int_0^l [(\bar{A}_{11}u_0' + \bar{B}_{11}\varphi')\delta u_0' + (\bar{B}_{11}u_0' + \bar{D}_{11}\varphi')\delta\varphi' + \bar{A}_{55}(w' + \varphi)(\delta w' + \delta\varphi)] dx \quad (3.18)$$

3.4. Kinetic energy

The position vector of the point P shown in Fig. 2 is given by

$$\mathbf{r} = (x + u_0 + \xi\varphi)\mathbf{i} + w\mathbf{k} \quad (3.19)$$

Considering Eq. (3.19), the velocity vector of this point is obtained as follows

$$\mathbf{V} = \frac{\partial \mathbf{r}}{\partial t} = (\dot{u}_0 + \xi\dot{\varphi})\mathbf{i} + \dot{w}\mathbf{k} \quad (3.20)$$

Hence, the velocity components are

$$V_x = \dot{u}_0 + \xi\dot{\varphi} \quad V_y = 0 \quad V_z = \dot{w} \quad (3.21)$$

The kinetic energy expression is given by

$$T = \frac{1}{2} \int_0^l \int_A \rho(z)(V_x^2 + V_y^2 + V_z^2) dA dx = \frac{b}{2} \int_0^l \int_{-h/2}^{h/2} \rho(z)(V_x^2 + V_y^2 + V_z^2) d\xi dx \quad (3.22)$$

where $\rho(z)$ is the effective material density.

Substituting the velocity components into Eq. (3.22) and taking the variation of kinetic energy gives

$$\delta T = \int_0^l [I_1(\dot{u}_0 \delta \dot{u}_0 + \dot{w} \delta \dot{w}) + I_2(\dot{u}_0 \delta \dot{\varphi} + \dot{\varphi} \delta \dot{u}_0) + I_3 \dot{\varphi} \delta \dot{\varphi}] dx \quad (3.23)$$

where I_1 , I_2 and I_3 are the inertial characteristics of the beam given by

$$[I_1 \ I_2 \ I_3] = \int_A \rho(z) [1 \ z \ z^2] dA \quad (3.24)$$

3.5. Equations of motion and the boundary conditions

Hamilton's principle is expressed as follows

$$\int_{t_1}^{t_2} \delta(U - T) dt = 0 \quad (3.25)$$

Substituting Eqs. (3.18)–(3.23) into Eq. (3.25) gives the equations of motion and the boundary conditions as follows:

— equations of motion

$$\begin{aligned} \overline{A}_{11} u_0'' + \overline{B}_{11} \varphi'' &= I_1 \ddot{u}_0 + I_2 \ddot{\varphi} & \overline{A}_{55} (w'' + \varphi') &= I_1 \ddot{w} \\ \overline{D}_{11} \varphi'' + \overline{B}_{11} u_0'' - \overline{A}_{55} (w' + \varphi) &= I_2 \ddot{u}_0 + I_3 \ddot{\varphi} \end{aligned} \quad (3.26)$$

— boundary conditions

$$\begin{aligned} x = 0 & \quad u_0(0, t) = w(0, t) = \varphi(0, t) = 0 \\ x = L & \quad \overline{A}_{11} u_0'(L, t) + \overline{B}_{11} \varphi'(L, t) = 0 & \overline{A}_{55} [w'(L, t) + \varphi(L, t)] = 0 \\ & \quad \overline{D}_{11} \varphi(L, t) + \overline{B}_{11} u_0'(L, t) - \overline{A}_{55} (w' + \varphi) = 0 \end{aligned} \quad (3.27)$$

In order to investigate free vibration of the beam model considered in this study, a sinusoidal variation of u_0 , w and φ with a circular natural frequency ω is assumed, and the functions are approximated as

$$u_0(x, t) = \overline{u}(x) e^{i\omega t} \quad w(x, t) = \overline{w}(x) e^{i\omega t} \quad \varphi(x, t) = \overline{\varphi}(x) e^{i\omega t} \quad (3.28)$$

Substituting Eqs. (3.28) into the equations of motion, i.e. Eqs. (3.26), and into the boundary conditions, i.e. Eqs. (3.27), the following dimensionless equations are obtained as follows:

— equations of motion

$$\begin{aligned} \gamma^2 \tilde{u}^{**} + \alpha^2 \tilde{\varphi}^{**} + \lambda^2 (\tilde{u} + \mu^2 \tilde{\varphi}) &= 0 & \frac{\tilde{w}^{**} + \tilde{\varphi}}{\tau^2} + \lambda^2 \tilde{w} &= 0 \\ \tau^2 (\alpha^2 \tilde{u}^{**} + \tilde{\varphi}^{**} + \mu^2 \lambda^2 \tilde{u}) + (r^2 \tau^2 \lambda^2 - 1) \tilde{\varphi} - \tilde{w}^* &= 0 \end{aligned} \quad (3.29)$$

— boundary conditions

$$\begin{aligned} x = 0 & \quad \tilde{u}(0, t) = \tilde{w}(0, t) = \tilde{\varphi}(0, t) = 0 \\ x = L & \quad \gamma^2 \tilde{u}^* + \alpha^2 \tilde{\varphi}^*(L, t) = 0 & \frac{1}{\tau^2} [\tilde{w}^*(L, t) + \tilde{\varphi}(L, t)] = 0 \\ & \quad \alpha^2 \tilde{u}^*(L, t) + \tilde{\varphi}^*(L, t) = 0 \end{aligned} \quad (3.30)$$

Here, the dimensionless parameters are defined as

$$\begin{aligned} \tilde{w} &= \frac{\bar{w}}{L} & \tilde{u} &= \frac{\bar{u}}{L} & \tilde{\varphi} &= \varphi & \gamma^2 &= \frac{\bar{A}_{11}L^2}{\bar{D}_{11}} & \tau^2 &= \frac{\bar{D}_{11}}{\bar{A}_{55}L^2} \\ \lambda^2 &= \frac{I_1L^4\omega^2}{\bar{D}_{11}} & \mu^2 &= \frac{I_2}{I_1L} & r^2 &= \frac{I_3}{I_1L^2} & \alpha^2 &= \frac{\bar{B}_{11}L}{\bar{D}_{11}} \end{aligned} \quad (3.31)$$

4. Differential Transform Method

The Differential Transform Method (DTM) is a transformation technique based on the Taylor series expansion and is a useful tool to obtain analytical solutions of differential equations. In this method, certain transformation rules are applied, and the governing differential equations and the boundary conditions of the system are transformed into a set of algebraic equations in terms of the differential transforms of the original functions, and the solution of these algebraic equations gives the desired solution of the problem.

Consider a function $f(x)$ which is analytical in a domain \mathcal{D} and let $x = x_0$ represent any point in \mathcal{D} . The function $f(x)$ is then represented by a power series whose center is located at x_0 . The differential transform of the function $f(x)$ is given by

$$F[k] = \frac{1}{k!} \left(\frac{d^k f(x)}{dx^k} \right)_{x=x_0} \quad (4.1)$$

where $f(x)$ is the original function and $F[k]$ is the transformed function. The inverse transformation is defined as

$$f(x) = \sum_{k=0}^{\infty} (x - x_0)^k F[k] \quad (4.2)$$

Combining Eq. (4.1) and Eq. (4.2), we get

$$f(x) = \sum_{k=0}^{\infty} \frac{(x - x_0)^k}{k!} \left(\frac{d^k f(x)}{dx^k} \right)_{x=x_0} \quad (4.3)$$

Considering Eq. (4.3), it is noticed that the concept of differential transform is derived from the Taylor series expansion. However, the method does not evaluate the derivatives symbolically.

In actual applications, the function $f(x)$ is expressed by a finite series and Eq. (4.3) can be written as follows

$$f(x) = \sum_{k=0}^m \frac{(x - x_0)^k}{k!} \left(\frac{d^k f(x)}{dx^k} \right)_{x=x_0} \quad (4.4)$$

which means that the rest of the series

$$f(x) = \sum_{k=m+1}^{\infty} \frac{(x - x_0)^k}{k!} \left(\frac{d^k f(x)}{dx^k} \right)_{x=x_0} \quad (4.5)$$

is negligibly small. Here, the value of m depends on the convergence of natural frequencies.

Theorems that are frequently used in the transformation procedure are introduced in Table 2, and theorems that are used for boundary conditions are introduced in Table 3.

After applying DTM to Eqs. (3.29) and (3.30), the transformed equations of motion and boundary conditions are obtained as follows:

Table 2. DTM theorems used for equations of motion

Original function	Transformed function
$f(x) = g(x) \pm h(x)$	$F[k] = G[k] \pm H[k]$
$f(x) = \lambda g(x)$	$F[k] = \lambda G[k]$
$f(x) = g(x)h(x)$	$F[k] = \sum_{l=0}^k G[k-l]H[l]$
$f(x) = \frac{d^n g(x)}{dx^n}$	$F[k] = \frac{(k+n)!}{k!} G[k+n]$
$f(x) = x^n$	$F[k] = \delta(k-n) = \begin{cases} 0 & \text{if } k \neq n \\ 1 & \text{if } k = n \end{cases}$

Table 3. DTM theorems used for boundary conditions

$x = 0$		$x = 1$	
Original B.C.	Transformed B.C.	Original B.C.	Transformed B.C.
$\frac{df(0)}{dx} = 0$	$F(0) = 0$	$f(1) = 0$	$\sum_{k=0}^{\infty} F(k) = 0$
$\frac{df}{dx}(0) = 0$	$F(1) = 0$	$\frac{df}{dx}(1) = 0$	$\sum_{k=0}^{\infty} kF(k) = 0$
$\frac{d^2 f}{dx^2}(0) = 0$	$F(2) = 0$	$\frac{d^2 f}{dx^2}(1) = 0$	$\sum_{k=0}^{\infty} k(k-1)F(k) = 0$
$\frac{d^3 f}{dx^3}(0) = 0$	$F(3) = 0$	$\frac{d^3 f}{dx^3}(1) = 0$	$\sum_{k=0}^{\infty} (k-1)(k-2)kF(k) = 0$

— equations of motion

$$\begin{aligned}
 & \gamma^2(k+1)(k+2)U[k+2] + \alpha^2(k+1)(k+2)\varphi[k+2] + \lambda^2(U[k] + \mu^2\varphi[k]) = 0 \\
 & \frac{1}{\tau^2}(k+1)(k+2)W[k+2] + \lambda^2W[k] + \frac{1}{\tau^2}(k+1)\varphi[k+1] = 0 \\
 & \alpha^2(k+1)(k+2)U[k+2] + (k+1)(k+2)\varphi[k+2] + \lambda^2\mu^2U[k] + \left(r^2\lambda^2 - \frac{1}{\tau^2}\right)\varphi[k] \\
 & \quad - \frac{1}{\tau^2}(k+1)W[k+1] = 0
 \end{aligned} \tag{4.6}$$

— boundary conditions

$$\begin{aligned}
 x = 0 \quad & U[k] = W[k] = \varphi[k] = 0 \\
 x = L \quad & \gamma^2 \sum_{k=0}^{\infty} kU[k] + \alpha^2 \sum_{k=0}^{\infty} k\varphi[k] = 0 \quad \frac{1}{\tau^2} \left(\sum_{k=0}^{\infty} (kW[k] + \varphi[k]) \right) = 0 \\
 & \alpha^2 \sum_{k=0}^{\infty} kU[k] + \sum_{k=0}^{\infty} k\varphi[k] = 0
 \end{aligned} \tag{4.7}$$

5. Results and discussions

In the numerical analysis, two cases are studied. In the first case, natural frequencies of a pure aluminum Timoshenko beam with simply-simply supported (SS) end conditions and, in the second case, a functionally graded Timoshenko beam with clamped free (CF) boundary conditions are calculated. Effects of the slenderness ratio L/h and the power law index parameter k on the

natural frequencies are investigated. The results are presented in related tables. In order to validate the calculated results, comparisons with the studies in open literature are made and a very good agreement between the results is observed, which proves the correctness and accuracy of the Differential Transform Method. It is believed that the tabulated results can be used as references by other researchers to validate their results.

Case 1. Pure aluminum simply supported beam

Table 4. Material properties of the aluminum Timoshenko beam

Property	Aluminum (Al)
Elasticity modulus E	70 GPa
Material density ρ	2700 kg/m ³
Poisson's ratio ν	0.23

Variation of the first five natural frequencies of the S-S pure aluminum Timoshenko beam with respect to the slenderness ratio L/h is given in Table 5. When the calculated results are compared with the ones given by Sina *et al.* (2009), a very good agreement between the results is observed.

Table 5. Dimensionless natural frequencies of the pure aluminum Timoshenko beam

Frequency $\lambda = \frac{\omega L^2}{h} \sqrt{\frac{\rho_m}{E_m}}$	Slenderness ratio L/h					
	10	20	30	40	50	100
Fundamental	2.87896	2.91515	2.92204	2.92447	2.92559	2.92709
Sina <i>et al.</i> (2009)	2.879	–	2.922	–	–	2.927
2nd NF	10.9963	11.5159	11.6224	11.6606	11.6784	11.7024
3rd NF	23.1528	25.3995	25.9107	26.0988	26.1876	26.3078
4th NF	32.2814	43.9854	45.4901	46.0634	46.3380	46.7137
5th NF	38.0919	64.5627	69.9845	71.3222	71.9741	72.8788

Case 2. FG Timoshenko beam

The FG beam is made of aluminum (Al) at the top and alumina (Al_2O_3) at the bottom. The effective beam properties change through the beam thickness according to the power law. The material properties of the FG beam are displayed in Table 6.

Table 6. Material properties of the FG beam

Property	Aluminum (Al)	Alumina (Al_2O_3)
Elasticity modulus E	70 GPa	380 GPa
Material density ρ	2702 kg/m ³	3960 kg/m ³
Poisson's ratio ν	0.3	0.3

Variation of the fundamental natural frequency of the C-F functionally graded Timoshenko beam according to the power law exponent for $L/h = 20$ is given in Table 7. When the calculated results are compared with the ones given by Şimşek (2010), a very good agreement between the results is observed.

Table 7. Dimensionless fundamental frequencies of the C-F FG Timoshenko beam

Frequency	Power law exponent k							
$\lambda = \frac{\omega L^2}{h} \sqrt{\frac{\rho_m}{E_m}}$	0	0.2	0.5	1	2	5	10	Full metal
Fundamental	1.94955	1.81407	1.66026	1.50103	1.36966	1.30373	1.26493	1.01297
Şimsek (2010)	1.94957	1.81456	1.66044	1.50104	1.36968	1.30375	1.26495	1.01297

In Table 8, variation of the dimensionless natural frequencies of the C-F functionally graded Timoshenko beam with respect to the power law exponent k and the slenderness ratio L/h is presented.

Table 8. Variation of the dimensionless natural frequencies of the C-F functionally graded Timoshenko beam with respect to the power law exponent k and the slenderness ratio L/h

		k						
L/h	0	0.2	0.5	1	2	5	10	Full metal
3	1.80329	1.6829	1.54468	1.39885	1.27348	1.19956	1.15684	0.936972
	8.21514	7.72196	7.12189	6.44425	5.77913	5.22620	4.96530	4.26852
	9.06941	8.675	8.23136	7.7081	7.05971	6.19459	5.64279	4.71239
	17.9802	16.9703	15.7499	14.3438	12.9094	11.6647	11.0314	9.34237
	26.4033	25.1248	23.5417	21.6204	19.4397	17.1022	15.8590	–
4	1.86385	1.73735	1.59278	1.44141	1.31344	1.24242	1.20111	0.96844
	9.42868	8.8443	8.15412	7.39468	6.68493	6.15895	5.8858	4.89906
	12.0925	11.5548	10.931	10.1889	9.27327	8.07187	7.35535	6.28319
	21.5877	20.3297	18.8307	17.1413	15.4804	14.1093	13.3796	11.2168
	34.5928	32.7263	30.451	27.8043	25.0665	22.6209	21.4285	18.0754
5	1.89441	1.76476	1.61692	1.46276	1.33353	1.26419	1.2237	0.98432
	10.2025	9.55154	8.79239	7.97167	7.23018	6.72424	6.44766	5.30114
	15.1157	14.4404	13.6505	12.7061	11.5406	10.0258	9.14605	7.85398
	24.2839	22.8225	21.0981	19.1875	17.3683	15.9509	15.1753	12.6177
	40.3144	38.0031	35.2454	32.1226	29.0171	26.3775	24.9471	20.9484
10	1.93806	1.80382	1.65126	1.49308	1.36215	1.29547	1.25629	1.007
	11.6155	10.8294	9.92996	8.98688	8.18692	7.73783	7.4778	6.03531
	30.2314	28.5306	26.2115	23.7423	21.5708	19.8231	18.204	15.708
	30.5505	28.8901	27.3023	25.3998	23.0609	20.4233	19.5414	15.8738
	55.4176	51.8978	47.8058	43.39	39.4041	36.6649	35.1095	28.7945
15	1.94655	1.81139	1.65791	1.49895	1.3677	1.30157	1.26267	1.01141
	11.9506	11.1299	10.1949	9.22147	8.40836	7.97825	7.72685	6.20943
	32.4399	30.247	27.7372	25.1042	22.8681	21.6068	20.8769	16.8555
	45.347	43.3142	40.921	38.0455	34.4964	29.9319	27.3397	23.5619
	60.9894	56.9502	52.3063	47.394	43.1404	40.553	39.057	31.6896
20	1.94955	1.81407	1.66026	1.50103	1.36966	1.30373	1.26493	1.01297
	12.0753	11.2415	10.293	9.30821	8.49032	8.06791	7.8202	6.27423
	33.2016	30.9307	28.3406	25.6387	23.3723	22.1529	21.4418	17.2513
	60.4627	57.7447	54.1446	49.0496	44.62	39.8473	36.4316	31.4159
	63.4443	59.1681	54.6767	50.7988	46.1299	42.3338	40.8514	32.9651

In Fig. 3, convergence of the first five natural frequencies with respect to the number of terms N used in DTM application is shown, where $L/h = 5$ and $k = 0.5$. To evaluate up to the fifth natural frequency to five-digit precision, it has been necessary to take 45 terms.

Additionally, it is seen that higher modes appear when more terms are taken into account in DTM application. Thus, depending on the order of the required modes, one must try a few values for the term number at the beginning of the calculations in order to find the adequate number of terms. For instance, only $N = 50$ is enough for the results given in Tables 5, 7 and 8.

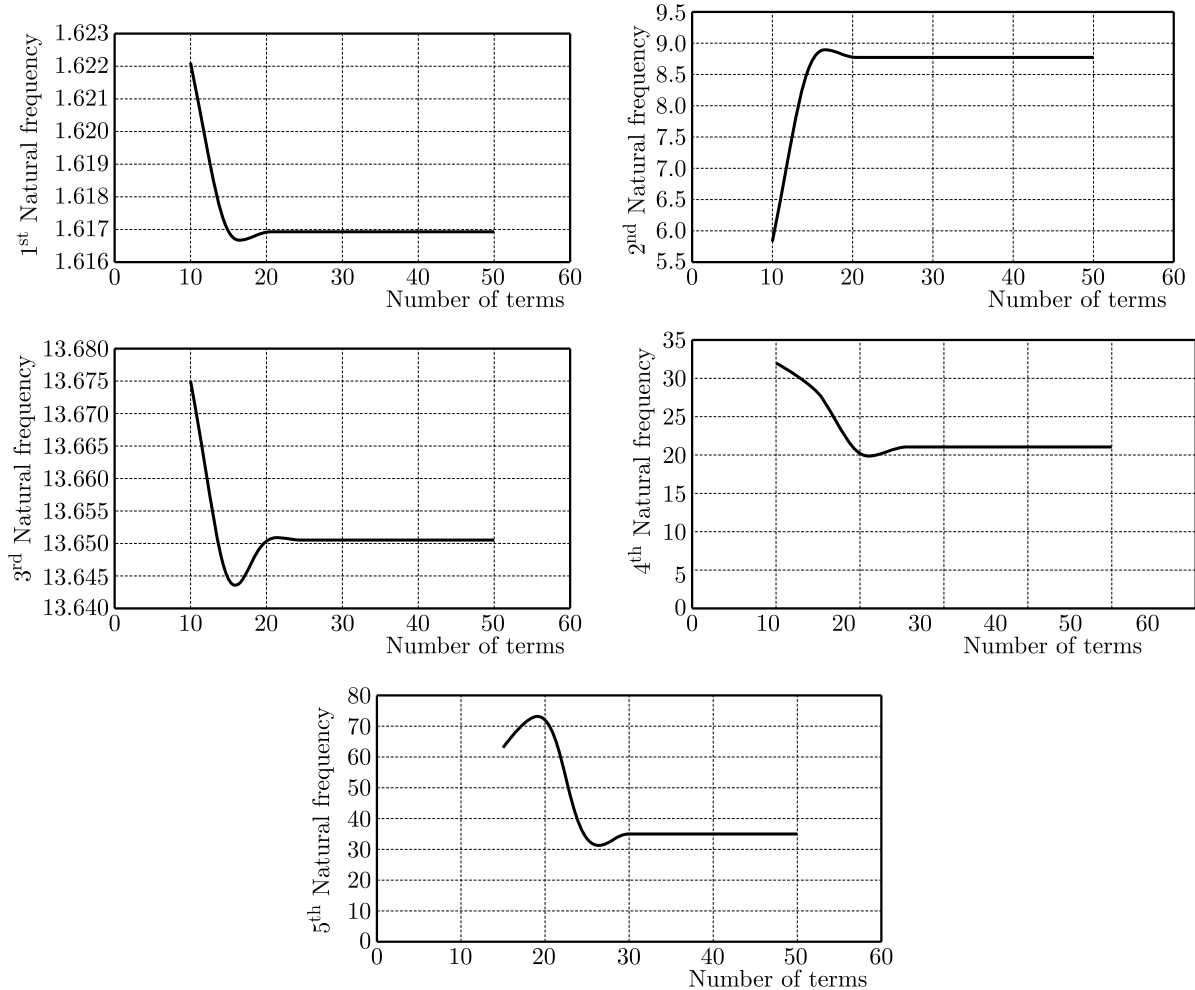


Fig. 3. Convergence of the first five natural frequencies with respect to the number of terms N

6. Conclusion

In this study, formulation of a functionally graded Timoshenko beam that undergoes flapwise bending vibration is derived by introducing several explanatory figures and tables. Applying Hamilton's principle to the obtained energy expressions, governing differential equations of motion and the boundary conditions are derived. In the solution part, the equations of motion, including the parameters for rotary inertia, shear deformation, power law index parameter and slenderness ratio are solved using an efficient mathematical technique, called the differential transform method (DTM). Natural frequencies are calculated and effects of the above mentioned parameters are investigated.

Considering the calculated results, the following conclusions are reached:

- As the slenderness ratio L/h increases, the natural frequencies increase;
- The effect of the slenderness ratio on the frequencies is negligible for long FG beams (i.e., $L/h \geq 20$);
- The natural frequencies decrease as the value of the power-law exponent k increases.

7. Future work

According to the author's knowledge, the Differential Transform Method has not been applied to functionally graded Timoshenko beams in literature before. Therefore, this gap is aimed to be fulfilled in this paper. However, in this study, a functionally graded Timoshenko beam with a power-law gradient is considered and the efficiency of DTM has not been examined for other gradients such as exponent gradient (Tang *et al.*, 2014; Hao and Wei, 2016; Li *et al.*, 2013; Wang *et al.*, 2016). The examination of the DTM efficiency for other gradient types can be considered as a challenging future work.

References

1. ALSHORBAGY A.E., ELTAHER M.A., MAHMOUD F.F., 2011, Free vibration characteristics of a functionally graded beam by finite element method, *Applied Mathematical Modelling*, **35**, 412-425
2. BHIMARADDI A., CHANDRASHEKHARA K., 1991, Some observation on the modeling of laminated composite beams with general lay-ups, *Composite Structures*, **19**, 371-380
3. CHAKRABORTY A., GOPALAKRISHNAN S., REDDY J.N., 2003, A new beam finite element for the analysis of functionally graded materials, *International Journal of Mechanical Sciences*, **45**, 519-539
4. DADFARNIA M., 1997, Nonlinear forced vibration of laminated beam with arbitrary lamination, M.Sc. Thesis, Sharif University of Technology
5. DENG H.D., WEI C., 2016, Dynamic characteristics analysis of bi-directional functionally graded Timoshenko beams, *Composite Structures*, in press
6. ERINGEN A.C., 1980, *Mechanics of Continua*, Robert E. Krieger Publishing Company, Huntington, New York
7. GIUNTA G., CRISAFULLI D., BELOUETTAR S., CARRERA E., 2011, Hierarchical theories for the free vibration analysis of functionally graded beams, *Composite Structures*, **94**, 68-74
8. HODGES D.H., DOWELL E.H., 1974, Nonlinear equations of motion for the elastic bending and torsion of twisted nonuniform rotor blades, *NASA Technical Report*, NASA TN D-7818
9. HUANG Y., LI X.F., 2010, A new approach for free vibration of axially functionally graded beams with non-uniform cross-section, *Journal of Sound and Vibration*, **329**, 2291-2303
10. KAPURIA S., BHATTACHARYYA M., KUMAR A.N., 2008, Bending and free vibration response of layered functionally graded beams: a theoretical model and its experimental validation, *Composite Structures*, **82**, 390-402
11. KAYA M.O., OZDEMIR OZGUMUS O., 2007, Flexural-torsional-coupled vibration analysis of axially loaded closed-section composite Timoshenko beam by using DTM, *Journal of Sound and Vibration*, **306**, 495-506
12. KAYA M.O., OZDEMIR OZGUMUS O., 2010, Energy expressions and free vibration analysis of a rotating uniform timoshenko beam featuring bending-torsion coupling, *Journal of Vibration and Control*, **16**, 6, 915-934
13. KOLLAR L.R., SPRINGER G.S., 2003, *Mechanics of Composite Structures*, Cambridge University Press, United Kingdom
14. LAI S.K., HARRINGTON J., XIANG Y., CHOW K.W., 2012, Accurate analytical perturbation approach for large amplitude vibration of functionally graded beams, *International Journal of Non-Linear Mechanics*, **47**, 473-480
15. LI X.F., 2008, A unified approach for analyzing static and dynamic behaviors of functionally graded Timoshenko and Euler-Bernoulli beams, *Journal of Sound and Vibration*, **318**, 1210-1229

16. LI X.F., KANG Y.A., WU J.X., 2013, Exact frequency equation of free vibration of exponentially functionally graded beams, *Applied Acoustics*, **74**, 3, 413-420
17. LOJA M.A.R., BARBOSA J.I., MOTA SOARES C.M., 2012, A study on the modelling of sandwich functionally graded particulate composite, *Composite Structures*, **94**, 2209-2217
18. LOY C.T., LAM K.Y., REDDY J.N., 1999, Vibration of functionally graded cylindrical shells, *International Journal of Mechanical Science*, **41**, 309-324
19. LU C.F., CHEN W.Q., 2005, Free vibration of orthotropic functionally graded beams with various end conditions, *Structural Engineering and Mechanics*, **20**, 465-476
20. OZDEMIR OZGUMUS O., KAYA M.O., 2013, Energy expressions and free vibration analysis of a rotating Timoshenko beam featuring bending-bending-torsion coupling, *Archive of Applied Mechanics*, **83**, 97-108
21. SINA S.A., NAVAZI H.M., HADDADPOUR H., 2009, An analytical method for free vibration analysis of functionally graded beams, *Materials and Design*, **30**, 741-747
22. ŞİMSEK M., 2010, Fundamental frequency analysis of functionally graded beams by using different higher-order beam theories, *Nuclear Engineering and Design*, **240**, 697-705
23. TANG A.Y., WU J.X., LI X.F., LEE K.Y., 2014, Exact frequency equations of free vibration of exponentially non-uniform functionally graded Timoshenko beams, *International Journal of Mechanical Sciences*, **89**, 1-11
24. THAI H.T., VO T.P., 2012, Bending and free vibration of functionally graded beams using various higher-order shear deformation beam theories, *International Journal of Mechanical Sciences*, **62**, 57-66
25. WANG Z., WANG X., XU G., CHENG S., ZENG T., 2016, Free vibration of two directional functionally graded beams, *Composite Structures*, **135**, 191-198
26. WATTANASAKULPONG N., PRUSTY B.G., KELLY D.W., HOFFMAN M., 2012, Free vibration analysis of layered functionally graded beams with experimental validation, *Materials and Design*, **36**, 182-190
27. ZHONG Z., YU T., 2007, Analytical solution of a cantilever functionally graded beam, *Composites Science and Technology*, **67**, 481-488

Manuscript received November 29, 2015; accepted for print February 18, 2016

HOMOTOPY ANALYSIS OF A FORCED NONLINEAR BEAM MODEL WITH QUADRATIC AND CUBIC NONLINEARITIES

SHAHRAM SHAHLAEI-FAR, AIRTON NABARRETE, JOSÉ MANOEL BALTHAZAR

Aeronautics Institute of Technology, ITA, São José dos Campos, Brazil

e-mail: shazzz_85@yahoo.de

This study investigates forced nonlinear vibrations of a simply supported Euler-Bernoulli beam on a nonlinear elastic foundation with quadratic and cubic nonlinearities. Applying the homotopy analysis method (HAM) to the spatially discretized governing equation, we derive novel analytical solutions and discuss their convergence to present nonlinear frequency responses with varying contributions of the nonlinearity coefficients. A comparison with numerical solutions is conducted and nonlinear time responses and phase planes are compared to the results from linear beam theory. The study demonstrates that apart from nonlinear problems of free vibrations, HAM is equally capable of solving strongly nonlinear problems of forced vibrations.

Keywords: forced nonlinear vibration, HAM, quadratic and cubic nonlinearities, Galerkin method

1. Introduction

Nonlinear vibrations of a simply supported Euler-Bernoulli beam on a nonlinear elastic foundation with distributed quadratic and cubic nonlinearities subject to harmonic excitation are, in nondimensional form, governed by (Abe, 2006)

$$\frac{\partial^2 w}{\partial t^2} + \frac{\partial^4 w}{\partial x^4} + 2\mu \frac{\partial w}{\partial t} + \alpha_2 w^2 + \alpha_3 w^3 = F(x) \cos(\Omega t) \quad (1.1)$$

subject to the boundary conditions

$$w = \frac{\partial^2 w}{\partial x^2} = 0 \quad \text{at} \quad x = 0, 1 \quad (1.2)$$

where w is the displacement of the beam, μ is the viscous damping coefficient, α_2 and α_3 are the quadratic and cubic nonlinearity coefficients, respectively, and $F(x)$ and Ω are the distribution and frequency of the harmonic load, respectively.

Abe (2006) provided numerical solutions for the cases of primary resonance and subharmonic resonance of the order one-half by means of the finite difference and shooting method, the first applied directly to Eqs. (1.1) and (1.2) and the latter to their spatially discretized form using the Galerkin method. He concluded that the Galerkin discretization yields more accurate results than the direct approach. Considering only small amplitude vibrations, he also obtained perturbative approximate solutions using the method of multiple scales (MMS) (Nayfeh and Mook, 1979) applied directly to Eq. (1.1) modeled as a weakly nonlinear system involving small perturbation parameters. However, Abe *et al.* (1998,a,b,c, 2000) showed that for the direct approach it is unlikely to obtain highly accurate solutions as it is not possible to define a detuning parameter in the quadratic form between the natural and the excitation frequency.

The present work provides accurate analytical solutions to Eqs. (1.1) and (1.2) using the homotopy analysis method (HAM) introduced by Liao (Liao, 1992, 1995, 2003, 2004, 2009,

2012; Liao and Cheung, 1998; Liao and Tan, 2007) to investigate the case when the excitation frequency is close to the natural frequency of the fundamental mode. Making no use of small or large parameters, this method allows us to consider the general nonlinear distributed-parameter system for small as well as large amplitude vibrations. Thus it overcomes the requirement for the MMS to model the problem as a weakly nonlinear system involving only small finite amplitudes. To ensure accurate results, we reduce the governing equation to an ordinary nonlinear differential equation with the Galerkin method before applying HAM. For the convergence analysis of the obtained analytical solutions, we plot the so-called h -curves for higher-order approximations and achieve the optimal value of h by minimizing the square residual of the governing equation for a chosen order of the approximation. We verify our higher-order solutions by comparison with numerical solutions given by the fourth-order Runge-Kutta method. Demonstrating how powerful a first-order approximation of HAM already is, we derive explicit closed-form solutions of the mean of motion, amplitude and phase of the generalized coordinate to present frequency response curves for various values of the quadratic and cubic nonlinearity coefficients addressing the cases of softening- and hardening-type behavior. Moreover, we compare the nonlinear time responses and their respective phase planes for different values of the quadratic nonlinearities to the results from linear beam theory.

HAM has seen extensive successful applications to highly nonlinear problems in science and engineering (Wen and Cao, 2007; Hoseini *et al.*, 2008; Pirbodaghi *et al.*, 2009; Abbasbandy and Shivanian, 2011; Mastroberardino, 2011; Mehrizi *et al.*, 2012; Mohammadpour *et al.*, 2012; Mustafa *et al.*, 2012; Sedighi *et al.*, 2012; Ray and Sahoo, 2015). Previous applications of HAM have been mainly devoted to nonlinear differential equations of free vibratory continuous systems. As seen in Eq. (1.1), the important case of forced nonlinear vibrations of a damped system involving cubic and quadratic nonlinearities, where the mean of motion cannot be disregarded, poses a greater challenge with respect to finding analytical solutions and understanding nonlinear behavior. Our results provide an example, applicable to other beam models and boundary conditions, of a forced nonlinear vibratory system in which HAM yields accurate convergent solutions for all values of the relevant parameters.

2. Governing differential equation

The model is discretized by the Galerkin method with $w(x, t) = W(t)\phi(x)$, where $\phi(x) = \sqrt{2}\sin(\pi x)$ is the normalized eigenfunction of the fundamental mode and $W(t)$, the corresponding time-dependent amplitude, is the generalized coordinate. Thus, governing equation (1.1) is reduced to the nonlinear ordinary differential equation

$$\ddot{W} + 2\mu\dot{W} + \omega^2 W + \frac{8\sqrt{2}}{3\pi}\alpha_2 W^2 + \frac{3}{2}\alpha_3 W^3 = f \cos(\Omega t - \varphi) \quad (2.1)$$

and without loss of generality subject to the initial conditions

$$W(0) = \delta + A \quad \dot{W}(0) = 0 \quad (2.2)$$

where $\omega = \pi^2$ is the normalized natural frequency of the fundamental mode, $f = \int_0^1 F(x)\phi(x) dx$ is the first modal force, A is an unknown amplitude and $\delta = (1/T)\int_0^T W(t) dt$ is the mean of motion being generally nonzero for oscillations with the quadratic nonlinearity. The dot represents differentiation with respect to time t . Note that, for convenience and without loss of generality, we introduce the phase angle φ in the expression of the harmonic load as a quantity to be determined.

Defining the variables

$$\tau = \Omega t \quad W(t) = \delta + AV(\tau) \quad (2.3)$$

and inserting them into Eqs. (2.1) and (2.2), we obtain

$$\begin{aligned} \Omega^2 A \frac{\partial^2 V(\tau)}{\partial \tau^2} + \Omega 2\mu A \frac{\partial V(\tau)}{\partial \tau} + \omega^2(\delta + AV(\tau)) + \frac{8\sqrt{2}}{3\pi} \alpha_2(\delta + AV(\tau))^2 \\ + \frac{3}{2} \alpha_3(\delta + AV(\tau))^3 = f_1 \cos \tau + f_2 \sin \tau \end{aligned} \quad (2.4)$$

subject to the initial conditions

$$V(0) = 1 \quad \frac{\partial V(0)}{\partial \tau} = 0 \quad (2.5)$$

with the constants f_1 and f_2 satisfying

$$f_1^2 + f_2^2 = f^2 \quad \varphi = \arctan \frac{f_2}{f_1} \quad (2.6)$$

3. Homotopy analysis method

The homotopy analysis method is a nonperturbative analytical technique for solving nonlinear differential equations. By means of an embedding parameter ranging from zero to one, it transforms a nonlinear differential equation into an infinite number of linear differential equations and derives a family of solution series.

The periodic solution to Eq. (2.4) can be expressed by a set of base functions

$$\{\sin(m\tau), \cos(m\tau) \mid m = 1, 2, 3, \dots\} \quad (3.1)$$

such that

$$V(\tau) = \sum_{k=1}^{infy} (\alpha_k \sin(k\tau) + \beta_k \cos(k\tau)) \quad (3.2)$$

where α_k and β_k are coefficients to be determined. We choose the initial guess as

$$V_0 = \cos \tau \quad (3.3)$$

which satisfies the initial conditions of Eq. (2.5). To ensure the rule of solution expression given by Eq. (3.2), we choose the linear operator to be

$$\mathcal{L}[\phi(\tau, q)] = \Omega^2 \left(\frac{\partial^2 \phi(\tau, q)}{\partial \tau^2} + \phi(\tau, q) \right) \quad (3.4)$$

with the property

$$\mathcal{L}[C_1 \sin \tau + C_2 \cos \tau] = 0 \quad (3.5)$$

where C_1 and C_2 are constants of integration. According to Eq. (2.4), we define the nonlinear operator

$$\begin{aligned} \mathcal{N}[\phi(\tau, q), \Lambda(q), \Delta(q)] = \Omega^2 \Lambda(q) \frac{\partial^2 \phi(\tau, q)}{\partial \tau^2} + 2\mu \Omega \Lambda(q) \frac{\partial \phi(\tau, q)}{\partial \tau} \\ + \omega^2(\Delta(q) + \Lambda(q)\phi(\tau, q)) + \frac{8\sqrt{2}}{3\pi} \alpha_2(\Delta(q) + \Lambda(q)\phi(\tau, q))^2 \\ + \frac{3}{2} \alpha_3(\Delta(q) + \Lambda(q)\phi(\tau, q))^3 - f_1 \cos \tau - f_2 \sin \tau \end{aligned} \quad (3.6)$$

where $q \in [0, 1]$ is the embedding parameter, $\phi(\tau, q)$ is a function of τ and q , $\Lambda(q)$ and $\Delta(q)$ are functions of q . The zeroth-order deformation equation is given by

$$(1 - q)\mathcal{L}[\phi(\tau, q) - V_0(\tau)] = qhH(\tau)\mathcal{N}[\phi(\tau, q), \Lambda(q), \Delta(q)] \quad (3.7)$$

where $h \neq 0$ is the convergence-control parameter and $H(\tau)$ a nonzero auxiliary function. For $q = 0$ and $q = 1$ we have

$$\begin{aligned} \phi(\tau, 0) &= V_0(\tau) & \phi(\tau, 1) &= V(\tau) & \Lambda(0) &= A_0 \\ \Lambda(1) &= A & \Delta(0) &= \delta_0 & \Delta(1) &= \delta \end{aligned} \quad (3.8)$$

Thus, the function $\phi(\tau, q)$ varies from the initial guess $V_0(\tau)$ to the desired solution as q varies from 0 to 1. The Taylor expansions of $\phi(\tau, q)$, $\Lambda(q)$ and $\Delta(q)$ with respect to q are

$$\begin{aligned} \phi(\tau, q) &= V_0(\tau) + \sum_{m=1}^{infy} V_m(\tau)q^m & \Lambda(q) &= A_0 + \sum_{m=1}^{infy} A_m q^m \\ \Delta(q) &= \delta_0 + \sum_{m=1}^{infy} \delta_m q^m \end{aligned} \quad (3.9)$$

where

$$V_m(\tau) = \frac{1}{m!} \frac{\partial^m \phi(\tau, q)}{\partial q^m} \Big|_{q=0} \quad A_m = \frac{1}{m!} \frac{\partial^m \Lambda(q)}{\partial q^m} \Big|_{q=0} \quad \delta_m = \frac{1}{m!} \frac{\partial^m \Delta(q)}{\partial q^m} \Big|_{q=0} \quad (3.10)$$

Choosing properly the auxiliary function $H(\tau)$ and the convergence-control parameter h , the series in Eqs. (3.9) converge when $q = 1$, such that

$$V(\tau) = V_0(\tau) + \sum_{m=1}^{infy} V_m(\tau) \quad A = A_0 + \sum_{m=1}^{infy} A_m \quad \delta = \delta_0 + \sum_{m=1}^{\infty} \delta_m \quad (3.11)$$

Differentiating zeroth-order equation (3.7) m times with respect to q , dividing it by $m!$ and setting $q = 0$, the m -th order deformation equation is obtained as

$$\mathcal{L}[V_m(\tau) - \chi_m V_{m-1}(\tau)] = hH(\tau)R_m(\mathbf{V}_{m-1}, \mathbf{A}_{m-1}, \boldsymbol{\delta}_{m-1}) \quad (3.12)$$

subject to the initial conditions

$$V_m(0) = \frac{\partial V_m(0)}{\partial \tau} = 0 \quad (3.13)$$

where

$$\begin{aligned} \chi_m &= \begin{cases} 0 & m \leq 1 \\ 1 & m > 1 \end{cases} & \mathbf{V}_{m-1} &= [V_0(\tau), V_1(\tau), \dots, V_{m-1}(\tau)] \\ \mathbf{A}_{m-1} &= [A_0, A_1, \dots, A_{m-1}] & \boldsymbol{\delta}_{m-1} &= [\delta_0, \delta_1, \dots, \delta_{m-1}] \end{aligned} \quad (3.14)$$

and

$$\begin{aligned}
R_m(\mathbf{V}_{m-1}, \mathbf{A}_{m-1}, \boldsymbol{\delta}_{m-1}) &= \frac{1}{(m-1)!} \frac{d^{m-1} \mathcal{N}[\phi(\tau, q), \Lambda(q), \Delta(q)]}{dq^{m-1}} \Big|_{q=0} \\
&= \Omega^2 A_{m-1} \frac{\partial^2 V_{m-1}}{\partial \tau^2} + 2\mu\Omega A_{m-1} \frac{\partial V_{m-1}}{\partial \tau} + \omega^2 (\delta_{m-1} + A_{m-1} V_{m-1}) \\
&\quad + \frac{8\sqrt{2}}{3\pi} \alpha_2 \sum_{n=0}^{m-1} (\delta_n + A_n V_n) (\delta_{m-1-n} + A_{m-1-n} V_{m-1-n}) \\
&\quad + \frac{3}{2} \alpha_3 \sum_{n=0}^{m-1} \left(\sum_{j=0}^n (\delta_j + A_j V_j) (\delta_{n-j} + A_{n-j} V_{n-j}) \right) \\
&\quad \cdot (\delta_{m-1-n} + A_{m-1-n} V_{m-1-n}) - (1 - \chi_m) (f_1 \cos \tau + f_2 \sin \tau) \\
&= C_{m,0} + \sum_{k=1}^{l(m)} \left(c_{m,k}(\mathbf{V}_{m-1}, \mathbf{A}_{m-1}, \boldsymbol{\delta}_{m-1}) \cos(k\tau) + d_{m,k}(\mathbf{V}_{m-1}, \mathbf{A}_{m-1}, \boldsymbol{\delta}_{m-1}) \sin(k\tau) \right)
\end{aligned} \tag{3.15}$$

For the nonzero auxiliary function to obey the rule of solution expression and the rule of coefficient ergodicity, we choose it to be

$$H(\tau) = \cos(2\tau) \tag{3.16}$$

where κ is an integer. It can be determined uniquely as $H(\tau) = 1$.

According to the property of the linear operator, if the terms $\sin \tau$ and $\cos \tau$ exist in R_m , the secular terms $\tau \cos \tau$ and $\tau \sin \tau$ will appear in the final solution, therefore $c_{m,1}$ and $d_{m,1}$ have to be equal to zero. Moreover, if $C_{m,0} \neq 0$, a constant term will appear in the final solution violating the rule of solution expression, thus it must be set to zero.

The general solution to Eq. (3.12) for $m \geq 1$ is derived to be

$$V_m(\tau) = \chi_m V_{m-1}(\tau) + \frac{h}{\Omega^2} \sum_{k=2}^{l(m)} \frac{c_{m,k} \cos(k\tau) + d_{m,k} \sin(k\tau)}{1 - k^2} + C_1 \sin \tau + C_2 \cos \tau \tag{3.17}$$

where C_1 and C_2 need to be determined by the initial conditions in Eq. (3.13).

For the first-order approximation ($m=1$) we obtain from Eq. (3.15)

$$\begin{aligned}
R_1(\mathbf{V}_0, \mathbf{A}_0, \boldsymbol{\delta}_0) &= -\Omega^2 A_0 \cos \tau - 2\mu\Omega A_0 \sin \tau + \omega^2 (\delta_0 + A_0 \cos \tau) \\
&\quad + \frac{8\sqrt{2}}{3\pi} \alpha_2 (\delta_0 + A_0 \cos \tau)^2 + \frac{3}{2} \alpha_3 (\delta_0 + A_0 \cos \tau)^3 - f_1 \cos \tau \\
&\quad - f_2 \sin \tau = \frac{8\sqrt{2}}{6\pi} \alpha_2 A_0^2 + \left(\omega^2 + \frac{9}{4} \alpha_3 \right) \delta_0 + \frac{8\sqrt{2}}{3\pi} \alpha_2 \delta_0^2 + \frac{3}{2} \alpha_3 \delta_0^3 \\
&\quad + \left(-\Omega^2 A_0 + \omega^2 A_0 + \frac{16\sqrt{2}}{3\pi} \alpha_2 \delta_0 A_0 + \frac{9}{2} \alpha_3 \delta_0^2 A_0 + \frac{9}{8} \alpha_3 A_0^3 - f_1 \right) \cos \tau \\
&\quad + (-2\mu\Omega A_0 - f_2) \sin \tau + \left(\frac{8\sqrt{2}}{6\pi} \alpha_2 A_0^2 + \frac{9}{8} \alpha_3 \delta_0 A_0^2 \right) \cos(2\tau) + \frac{3}{8} \alpha_3 A_0^3 \cos(3\tau) \\
&= C_{1,0} + \sum_{k=1}^{l(1)=3} \left(c_{1,k}(\mathbf{V}_0, \mathbf{A}_0, \boldsymbol{\delta}_0) \cos(k\tau) + d_{1,k}(\mathbf{V}_0, \mathbf{A}_0, \boldsymbol{\delta}_0) \sin(k\tau) \right)
\end{aligned} \tag{3.18}$$

with $d_{1,2} = d_{1,3} = 0$. Enforcing the constant term and the coefficients of $\sin \tau$ and $\cos \tau$ to be equal to zero, and using the conditions in Eq. (2.6), we obtain steady state solutions of the mean of motion δ_0 , the amplitude A_0 and the phase φ , respectively, as

$$\delta_0 = -\frac{16\sqrt{2}\alpha_2}{27\alpha_3\pi} - \frac{K_1}{27\alpha_3\sqrt[3]{2\pi}\sqrt[3]{K_2 + \sqrt{K_2^2 + 4K_1^3}}} + \frac{1}{54\alpha_3\sqrt[3]{2\pi}} \sqrt[3]{K_2 + \sqrt{K_2^2 + 4K_1^3}} \tag{3.19}$$

with

$$K_1 = -2048\alpha_2^2 + 162\alpha_3\pi(9A_0^2\alpha_3\pi + 4\pi^5) \quad K_2 = -131072\sqrt{2}\alpha_2^3 + 62208\sqrt{2}\alpha_2\alpha_3\pi^6$$

and

$$\begin{aligned} & \left((\omega^2 - \Omega^2)A_0 + \frac{16\sqrt{2}}{3\pi}\alpha_2\delta_0A_0 + \frac{9}{2}\alpha_3\delta_0^2A_0 + \frac{9}{8}\alpha_3A_0^3 \right)^2 + (-2\mu\Omega A_0)^2 = f^2 \\ \varphi &= \arctan \frac{2\mu\Omega}{\Omega^2 - \omega^2 - \frac{16\sqrt{2}}{3\pi}\alpha_2\delta_0 - \frac{9}{2}\alpha_3\delta_0^2 - \frac{9}{8}\alpha_3B} \\ B &= \frac{\omega^2\delta_0 + \frac{8\sqrt{2}}{3\pi}\alpha_2\delta_0^2 + \frac{3}{2}\alpha_3\delta_0^3}{\frac{9}{4}\alpha_3\delta_0 + \frac{8\sqrt{2}}{6\pi}\alpha_2} \end{aligned} \quad (3.20)$$

Finally, solving the first-order deformation equation of Eq. (3.12), the general solution is

$$\begin{aligned} V_1(\tau) &= \frac{h}{\Omega^2} \sum_{k=2}^{l(1)=3} \frac{c_{1,k}}{1-k^2} \cos(k\tau) + C_1 \sin \tau + C_2 \cos \tau \\ &= \frac{h}{\Omega^2} \left(\left(\frac{4\sqrt{2}}{9\pi}\alpha_2 + \frac{3}{4}\alpha_3\delta_0 \right) A_0^2 (\cos \tau - \cos(2\tau)) + \frac{3}{64}\alpha_3 A_0^3 (\cos \tau - \cos(3\tau)) \right) \end{aligned} \quad (3.21)$$

where the constants C_1 and C_2 are obtained from the initial conditions in Eq. (3.13).

Thus, with Eqs. (3.11), the first-order approximation of $W(t)$ becomes

$$\begin{aligned} W(t) &= \delta + AV(\tau) \approx \delta_0 + A_0(V_0(\tau) + V_1(\tau)) \\ &= \delta_0 + \frac{h}{\Omega^2} \left(\left(\frac{\Omega^2}{h} A_0 + \frac{4\sqrt{2}}{9\pi}\alpha_2 A_0^3 + \frac{3}{4}\alpha_3\delta_0 A_0^3 + \frac{3}{64}\alpha_3 A_0^4 \right) \cos(\Omega t) \right. \\ &\quad \left. + \left(\frac{4\sqrt{2}}{9\pi}\alpha_2 A_0^3 + \frac{3}{4}\alpha_3\delta_0 A_0^3 \right) \cos(2\Omega t) + \frac{3}{64}\alpha_3 A_0^4 \cos(3\Omega t) \right) \end{aligned} \quad (3.22)$$

4. Convergence of HAM solution

Applying HAM to a nonlinear problem results in a family of solution series which depend on the convergence-control parameter h . In order to ensure the convergence and rate of the approximation for the HAM solution, valid convergence regions for the auxiliary parameter h need to be obtained. By means of plotting h -curves this can be achieved and thus a convergent solution series is guaranteed. Since a valid region comprises a range of possible values of h , the optimal choice is obtained by minimizing the square residual of the governing equation for a given order of the approximation. For this, we consider the N th-order approximations of Eqs. (3.11) given by

$$V_N(\tau) = V_0(\tau) + \sum_{m=1}^N V_m(\tau) \quad A = A_0 + \sum_{m=1}^N A_m \quad \delta = \delta_0 + \sum_{m=1}^N \delta_m \quad (4.1)$$

Inserting Eqs. (4.1)-(4.3) into Eq. (3.6) with $q = 1$, we can define the square residual error for the N -th order approximation as

$$e_N(h) = \int_0^1 (\mathcal{N}[V_N(\tau), A_N, \delta_N])^2 d\tau \quad (4.2)$$

The solution series is convergent when $e_N(h) \rightarrow 0$ as $N \rightarrow \infty$. The optimal value of h for a given order N of the approximation is obtained by the solution of the algebraic equation

$$\frac{de_N}{dh} = 0 \quad (4.3)$$

It is to be noted that the calculation for each order is done separately and not iteratively.

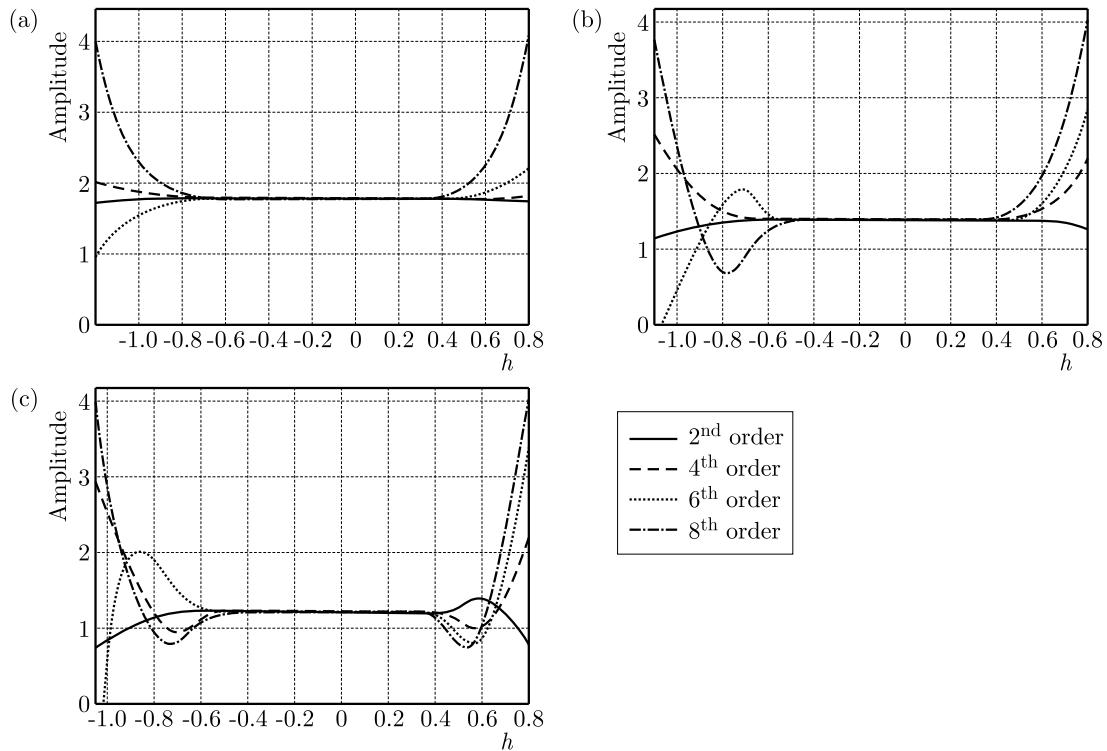


Fig. 1. h -curves of the amplitude A for $\alpha_2 = 5$: (a) $\alpha_3 = 0.5$, (b) $\alpha_3 = 1$, (c) $\alpha_3 = 1.5$

Figure 1 shows the effect of the auxiliary parameter on the solution convergence for higher-order approximations. The valid region is characterized by the flat portion which is common to all h -curves displayed. The corresponding optimal values of h for varying values of the cubic nonlinearity coefficient α_3 are presented in Table 1 using the software Mathematica.

5. Discussion of results

A simply supported Euler-Bernoulli beam resting on a nonlinear elastic foundation with quadratic and cubic nonlinearities is considered. First, higher-order approximations from the general solution in Eq. (3.17), obtained with the software Mathematica, are compared to numerical results. Secondly, considering the first-order approximation of HAM, the frequency response curves of the amplitude obtained in Eq. (3.20)₁ are presented for different values of the quadratic and cubic nonlinearity coefficients. Moreover, the nonlinear time response curves and phase planes are compared to the results from linear beam theory showing the effect of these nonlinearities upon the distributed-parameter system.

In Fig. 2, the accuracy of nonlinear time responses obtained by a sixth-order HAM approximation for $\alpha_2 = 5$ is validated by comparison with the numerical results achieved by the fourth-order Runge-Kutta method for varying values of α_3 and the corresponding optimal values of the auxiliary parameter h . There is accurate agreement between the analytical and numerical results.

Table 1. Optimal values of h and minimum values of e_N for $\mu = 0.05$, $F(x) = \sqrt{2}\sin(\pi x)$, $\alpha_2 = 5$

α_3	N	Optimal value of h	Minimum value of e_N
0.5	2	-0.3567	$8.374 \cdot 10^{-4}$
	4	-0.3324	$1.705 \cdot 10^{-7}$
	6	-0.3286	$4.119 \cdot 10^{-9}$
	8	-0.3045	$7.805 \cdot 10^{-11}$
1	2	-0.2943	$5.096 \cdot 10^{-2}$
	4	-0.2755	$1.643 \cdot 10^{-5}$
	6	-0.2619	$4.295 \cdot 10^{-6}$
	8	-0.2578	$9.349 \cdot 10^{-8}$
1.5	2	-0.2581	$6.912 \cdot 10^{-1}$
	4	-0.2319	$3.782 \cdot 10^{-2}$
	6	-0.2247	$2.186 \cdot 10^{-4}$
	8	-0.2169	$6.237 \cdot 10^{-6}$

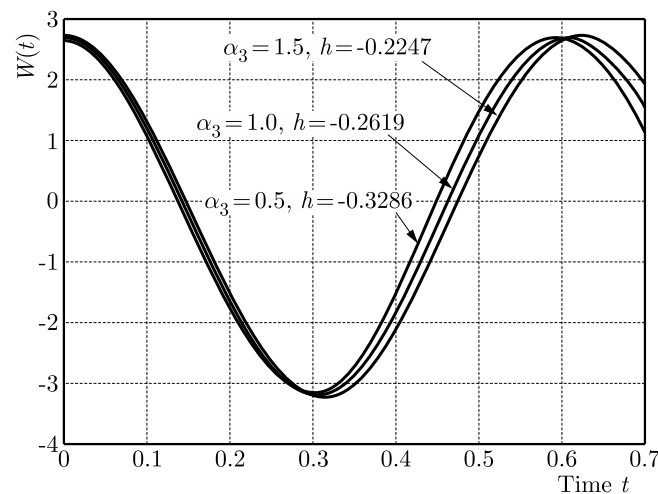


Fig. 2. Comparison of sixth-order HAM solutions (solid line) with numerical results by the fourth-order Runge-Kutta method (symbols)

Fixing $\alpha_2 = 5$ and $\alpha_3 = 0.5$ and using the optimal values of h from Table 1, approximations of order 2, 4, 6 and 8 are compared to numerical results (fourth-order Runge-Kutta) in Table 2. The results show that low-order approximations by HAM agree well with numerical solutions, although by increasing the order of HAM iterations, the accuracy increases.

For the rest of this Section, we consider the first-order approximation by HAM. In Fig. 3, we investigate the influence of the nonlinearity coefficients on the frequency response curves, that is, we show the variation of the response curves with α_2 for different values of α_3 . In Fig. 3a, as the excitation frequency Ω nears the fundamental frequency ω , the response of the system exhibits hardening-spring nonlinear characteristics due to the cubic nonlinearity. Increasing the value of α_3 , this hardening-type behavior is further increased. In the presence of both α_2 and α_3 , in Fig. 3b, the response is almost linear (for $\alpha_3 = 0.5$) suggesting that the magnitude of the nonlinearities cancel each other out. Further increase of α_3 results, as in the previous case, in hardening-type behavior. Figure 3c predicts softening- as well as hardening-type responses for increasing values of α_3 demonstrating the softening effect of the quadratic nonlinearity. This transition is also evident in Fig. 3d, whereby the softening-spring effect is more pronounced. For higher values of the quadratic nonlinearity, the softening effect on the system becomes more distinctive.

Table 2. Comparison of higher-order HAM solutions with numerical results for $\mu = 0.05$, $F(x) = \sqrt{2}\sin(\pi x)$, $\alpha_2 = 5$, $\alpha_3 = 0.5$

Time t	HAM solution				Numerical results
	2-nd order	4-th order	6-th order	8-th order	
0	2.70874	2.71538	2.71796	2.71923	2.71925
0.1	1.34795	1.35269	1.35344	1.35416	1.35418
0.2	-1.50326	-1.51083	-1.51278	-1.51490	-1.51492
0.3	-3.21418	-3.21964	-3.22461	-3.22791	-3.22793
0.4	-2.15817	-2.16227	-2.16435	-2.16520	-2.16521
0.5	0.65104	0.66129	0.66483	0.66659	0.66662
0.6	2.61598	2.62004	2.62135	2.62337	2.62339
0.7	1.92956	1.93118	1.93207	1.93479	1.93480

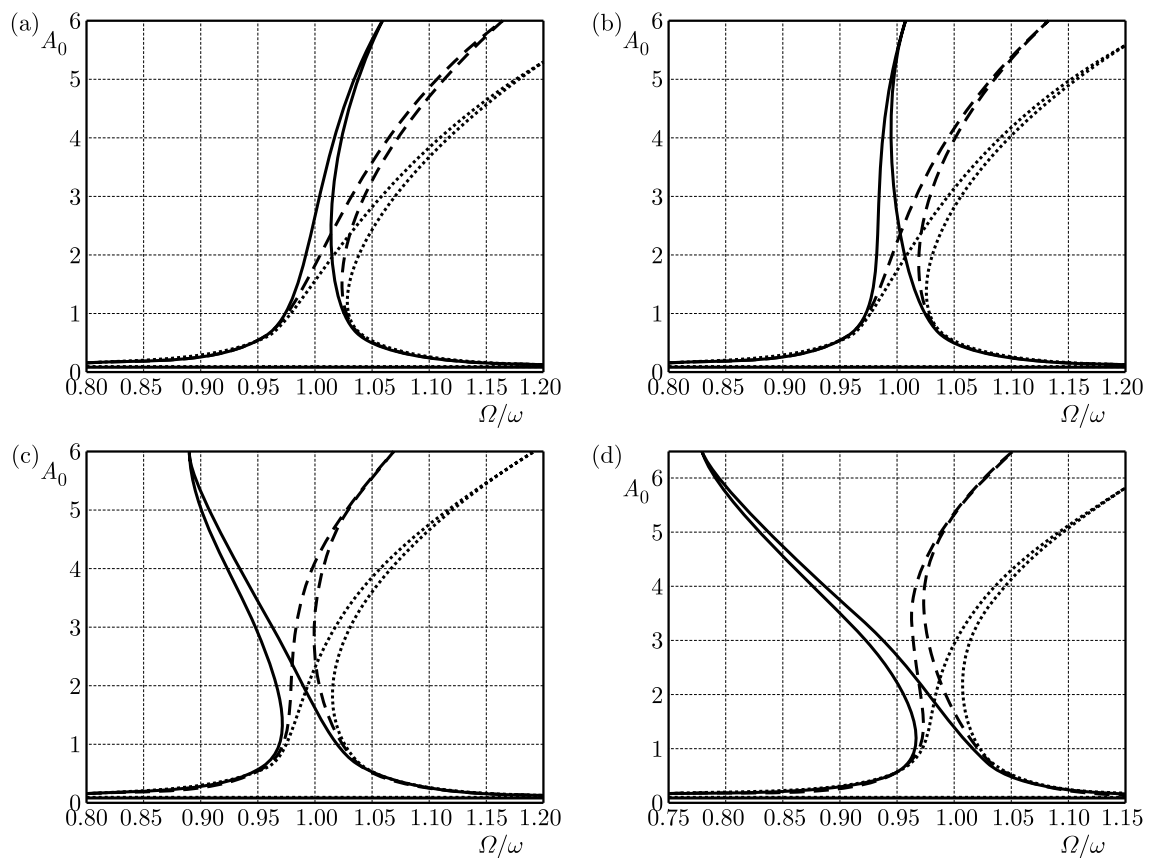


Fig. 3. Amplitude-frequency curves for $\mu = 0.05$, $F(x) = \sqrt{2}\sin(\pi x)$, $\alpha_3 = 0.5$ (solid line), $\alpha_3 = 1$ (dashed line), $\alpha_3 = 1.5$ (dotted line): (a) $\alpha_2 = 5$, (b) $\alpha_2 = 7.4$, (c) $\alpha_2 = 10.5$, (d) $\alpha_2 = 12$

Investigating the impact of the quadratic nonlinearity on the distributed-parameter system we compare, in Fig. 4, the nonlinear time responses obtained by HAM with those from linear beam theory maintaining a fixed value for α_3 and varying values of the quadratic nonlinearity coefficient α_2 . The optimal value of h is obtained by solving Eq. (4.5) for $N = 1$. It is evident that for lower values of α_2 there is more agreement between the linear and nonlinear time response, whereas by increasing the value of α_2 , the difference becomes considerable.

In Fig. 5, the phase planes for both nonlinear and linear responses are presented for different values of α_2 while fixing $\alpha_3 = 0.5$. With an increase in α_2 , the phase planes significantly diverge from their linear counterparts emphasizing the effect of the quadratic nonlinearity term on

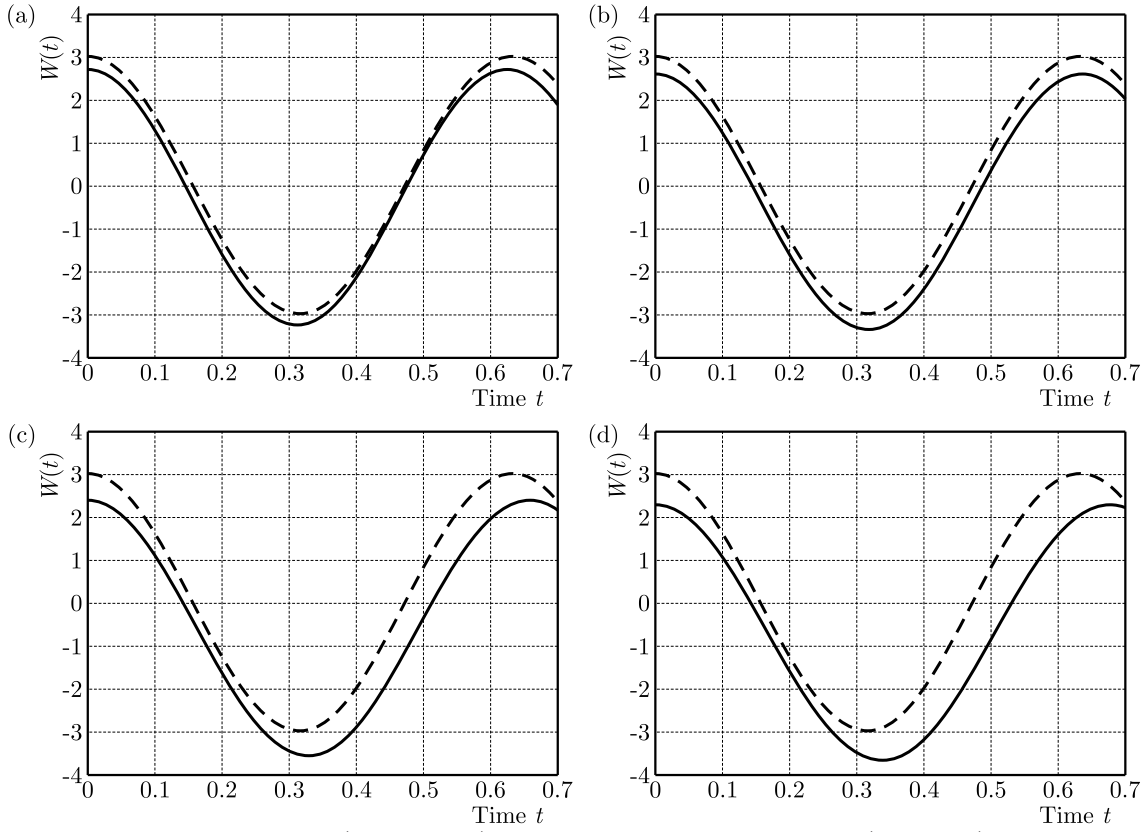


Fig. 4. Linear time response (dashed line) versus nonlinear time response (solid line) for $\mu = 0.05$, $F(x) = \sqrt{2} \sin(\pi x)$, $\alpha_3 = 0.5$, $h = -0.3719$: (a) $\alpha_2 = 5$ ($\Omega/\omega = 0.9806$), (b) $\alpha_2 = 7.4$ ($\Omega/\omega = 0.9910$), (c) $\alpha_2 = 10.5$ ($\Omega/\omega = 1.0075$), (d) $\alpha_2 = 12$ ($\Omega/\omega = 1.0160$)

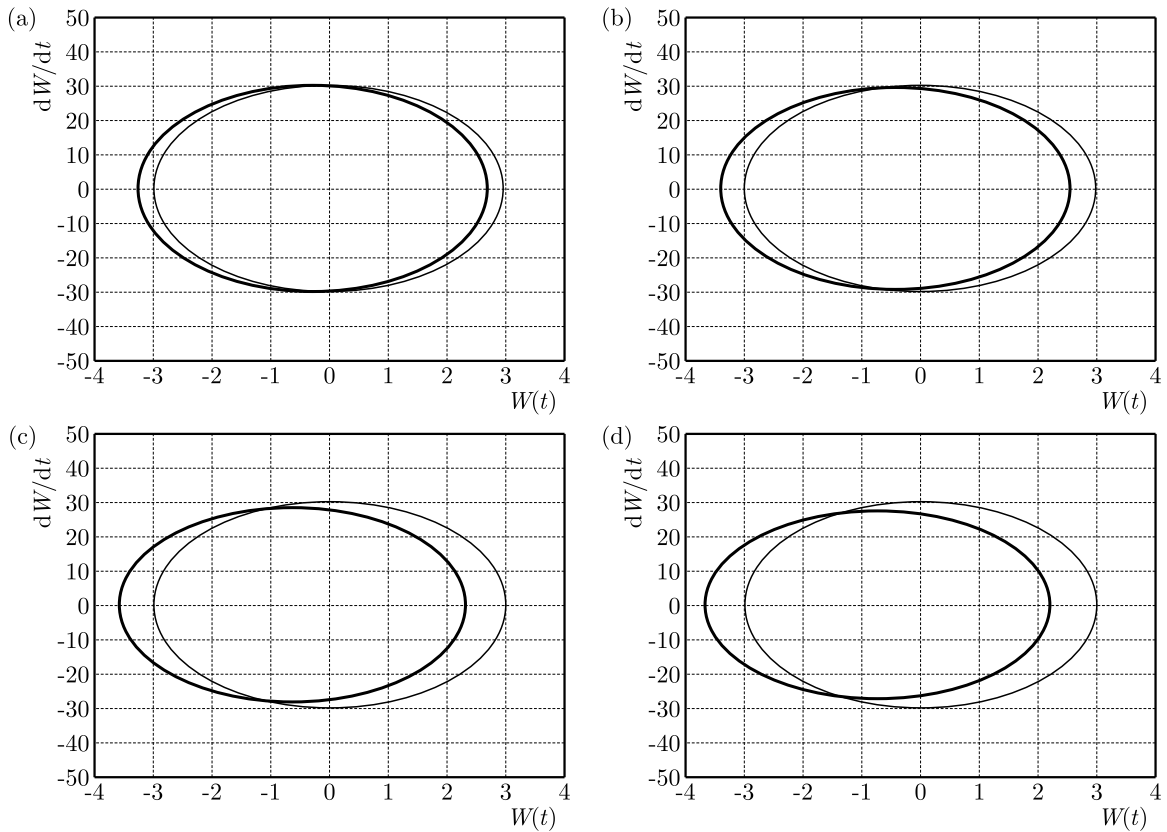


Fig. 5. Phase plane of linear response (thin line) versus nonlinear response (thick line) for $\mu = 0.05$, $F(x) = \sqrt{2} \sin(\pi x)$, $\alpha_3 = 0.5$, $h = -0.3719$: (a) $\alpha_2 = 5$ ($\Omega/\omega = 0.9806$), (b) $\alpha_2 = 7.4$ ($\Omega/\omega = 0.9910$), (c) $\alpha_2 = 10.5$ ($\Omega/\omega = 1.0075$), (d) $\alpha_2 = 12$ ($\Omega/\omega = 1.0160$)

the system when the excitation frequency is close to the natural frequency of the fundamental mode.

It should be noted that the analysis presented in this study can be expanded to predict beam responses for different boundary conditions. To this end, the mode shape $\phi(x)$ satisfying the boundary conditions at both ends should be inserted into $w(x, t) = W(t)\phi(x)$ for the spatial discretization by the Galerkin method. The solutions can then be derived analogously with the methodology described in Section 3.

6. Conclusion

The present study provides analytical solutions to forced nonlinear vibrations of a simply supported Euler-Bernoulli beam resting on a nonlinear elastic foundation with quadratic and cubic nonlinearities using the homotopy analysis method. The convergence of the solution has been investigated by optimizing the value of the auxiliary convergence-control parameter h . Using the optimal values of h , higher-order solutions by HAM have been compared to numerical results demonstrating the effectiveness of the method for low-order approximations and varying values of the cubic nonlinearity. The derived closed-form solution of the amplitude yields frequency response curves for various values of the quadratic and cubic nonlinearity coefficients presenting their softening-/hardening-type effect on the distributed-parameter system. Phase planes and nonlinear time response curves illustrate the considerable difference with respect to the results from linear beam theory for various values of the quadratic nonlinearity coefficient. The findings reveal that HAM is a general solution method that can successfully address highly nonlinear problems of forced vibrations.

Acknowledgement

The authors acknowledge the financial support received during this work from CAPES and the MCT/CNPq/FAPEMIG-National Institute of Science and Technology on Smart Structures in Engineering, grant number 574001/2008-5.

References

1. ABBASBANDY S., SHIVANIAN E., 2011, Predictor homotopy analysis method and its application to some nonlinear problems, *Communications in Nonlinear Science and Numerical Simulation*, **16**, 2456-2468
2. ABE A., 2006, On non-linear vibration analyses of continuous systems with quadratic and cubic non-linearities, *International Journal of Non-Linear Mechanics*, **41**, 873-879
3. ABE A., KOBAYASHI Y., YAMADA G., 1998a, Analysis of subharmonic resonance of moderately thick antisymmetric angle-ply laminated plates by using method of multiple scales, *Journal of Sound and Vibration*, **217**, 467-484
4. ABE A., KOBAYASHI Y., YAMADA G., 1998b, Internal resonance of rectangular laminated plates with degenerate modes, *JSME International Journal, Series C*, **41**, 718-726
5. ABE A., KOBAYASHI Y., YAMADA G., 1998c, Two-mode response of simply supported, rectangular laminated plates, *International Journal of Non-Linear Mechanics*, **33**, 675-690
6. ABE A., KOBAYASHI Y., YAMADA G., 2000, Non-linear vibration characteristics of clamped laminated shallow shells, *Journal of Sound and Vibration*, **234**, 405-426
7. HOSEINI S.H., PIRPODAGHI T., ASGHARI M., FARRAHI G.H., AHMADIAN M.T., 2008, Nonlinear free vibration of conservative oscillators with inertia and static type cubic nonlinearities using homotopy analysis method, *Journal of Sound and Vibration*, **316**, 263-273

8. LIAO S.J., 1992, Proposed homotopy analysis techniques for the solution of nonlinear problems, Ph.D. Dissertation, Shanghai Jiao Tong University, Shanghai
9. LIAO S.J., 1995, An approximate solution technique which does not depend upon small parameters: a special example, *International Journal of Non-Linear Mechanics*, **30**, 371-380
10. LIAO S.J., 2003, *Beyond Perturbation: Introduction to Homotopy Analysis Method*, Chapman & Hall/CRC Press, Boca Raton
11. LIAO S.J., 2004, On the homotopy analysis method for nonlinear problems, *Applied Mathematics and Computation*, **147**, 499-513
12. LIAO S.J., 2009, Notes on the homotopy analysis method: some definitions and theorems, *Communications in Nonlinear Science and Simulation*, **14**, 983-997
13. LIAO S.J., 2012, *Homotopy Analysis Method in Nonlinear Differential Equations*, Springer Education Press, Heidelberg
14. LIAO S.J., CHEUNG A.T., 1998, Application of homotopy analysis method in nonlinear oscillations, *Journal of Applied Mechanics*, **65**, 914-922
15. LIAO S.J., TAN Y., 2007, A general approach to obtain series solutions of nonlinear differential equations, *Studies in Applied Mathematics*, **119**, 297-355
16. MASTROBERARDINO A., 2011, Homotopy analysis method applied to electrohydrodynamic flow, *Communications in Nonlinear Science and Numerical Simulation*, **16**, 2730-2736
17. MEHRIZI A.A., VAZIFESHENAS Y., DOMAIRRY G., 2012, New analysis of natural convection boundary layer flow on a horizontal plate with variable wall temperature, *Journal of Theoretical and Applied Mechanics*, **50**, 4, 1001-1010
18. MOHAMMADPOUR A., ROKNI E., FOOLADI M., KIMIAEIFAR A., 2012, Bernoulli-Euler beams under different boundary conditions with non-linear Winkler type foundation, *Journal of Theoretical and Applied Mechanics*, **50**, 2, 339-355
19. MUSTAFA M., HAYAT T., HENDI A.A., 2012, Influence of melting heat transfer in the stagnation-point flow of a Jeffrey fluid in the presence of viscous dissipation, *Journal of Applied Mechanics*, **79**, 2, 4501-4505
20. NAYFEH A.H., MOOK D.T., 1979, *Nonlinear Oscillations*, Wiley, New York
21. PIRBODAGHI T., AHMADIAN M.T., FESANGHARY M., 2009, On the homotopy analysis method for non-linear vibration of beams, *Mechanics Research Communications*, **36**, 143-148
22. RAY S.S., SAHOO S., 2015, Traveling wave solutions to Riesz time-fractional Camassa-Holm equation in modeling for shallow-water waves, *Journal of Computational and Nonlinear Dynamics*, **10**, 6, 1026-1030
23. SEDIGHI H.M., SHIRAZI K.H., ZARE J., 2012, An analytic solution of transversal oscillation of quintic non-linear beam with homotopy analysis method, *International Journal of Non-Linear Mechanics*, **47**, 777-784
24. WEN J., CAO Z., 2007, Sub-harmonic resonances of nonlinear oscillations with parametric excitation by means of the homotopy analysis method, *Physics Letters A*, **371**, 427-431

NUMERICAL ANALYSIS OF THE INFLUENCE OF LATERAL SUSPENSION PARAMETERS ON THE RIDE QUALITY OF RAILWAY VEHICLES

MĂDĂLINA DUMITRIU

*Politehnica University of Bucharest, Department of Railway Vehicles, Romania
e-mail: madalinadumitriu@yahoo.com*

This paper deals with the influence of parameters of the lateral suspension on the ride quality of railway vehicles during running on a track with lateral deviations, compared to the designing geometry. The ride quality is evaluated at speed 200 km/h, based on lateral accelerations in three reference points of the vehicle carbody. The values corresponding to these accelerations are derived from numerical simulations on a non-linear model of the vehicle with 21 degrees of freedom. The results thus obtained validate a series of features in vibrational behaviour of the railway vehicle and the possibility to improve the ride quality by the best possible selection of the suspension parameters.

Keywords: railway vehicle, ride quality, lateral suspension, vibration behaviour, R.M.S. acceleration

1. Introduction

During running, a railway vehicle is subjected to permanent vibrations that can be limited by the suspension to a level that would not affect the dynamic performance of the vehicle. The ability of the vehicle to comply with the transport requirements in terms of the level of vibrations to which they can be subjected, and are dependent on the vehicle type, passengers, goods or the locomotive staff, is assigned a high value by the ride quality (Garg and Dukkipati, 1984). This criterion is considered when evaluating the dynamic behaviour of the railway vehicle for the homologation and its admission into international traffic, besides safety and track fatigue (UIC 518 Leaflet, 2009).

From the perspective of ride quality, the evaluation of dynamic behaviour of railway vehicles mainly involves finding solutions to certain issues of vibrations, which can be dealt with experimentally and theoretically. As a matter of fact, it is about the determination of the acceleration value at the vehicle carbody level, during either line testing (Dumitriu, 2014) or in a virtual environment, based on a numerical model of the vehicle (Sharma, 2011). Numerical simulations are useful tools to estimate the dynamic behaviour of the railway vehicle and to optimize its dynamic performance even at the designing stage, followed by the investigation of the issues emerging during exploitation. In comparison with the line testing that is costly and requires considerable investment of time and effort and may be affected by out-of-control series of variables, numerical simulations have a certain advantage as they allow the examination of the dynamic behaviour of the vehicle even in the vicinity of extreme circumstances that cannot be marked out during real testing conditions (Evans and Berg, 2009; Schupp, 2003).

The numerical evaluation of ride quality is possible via software applications developed on the basis of certain vehicle/track system models. During the modelling stage, which needs to be considered, the railway vehicle represents a complex oscillating system that vibrates both in the vertical and lateral directions. Nevertheless, due to the fact that the vehicle construction generally complies with the rules of geometrical symmetry, both inertial and elastic, vertical motions can be regarded as uncoupled from the lateral ones, hence separately studied.

As for the lateral vibrations, they are a consequence of the fact that rolling surfaces of the wheels, rigidly fixed on the wheelset, have inversed concavities and are maintained by track lateral irregularities (Iwnicki, 2006). The lateral vibrations are of particular importance, both for vehicle stability and for ensuring ride quality and comfort of passengers. Indeed, the essential features of such vibrations is the tendency to become unstable when the velocity goes beyond a certain value – the critical speed, and unstable running of the vehicle can lead to extreme situations – vehicle derailment and track damage. This is the reason why most studies have been focused on the issue of vehicle stability dealt with from different perspectives – methods of stability evaluation (Polach and Kaiser, 2012; Polach, 2006), stability optimization (Mazzola *et al.*, 2010; He and McPhee, 2002), influence of suspension parameters and wheel/rail contact conditions upon the critical speed (Dabin *et al.*, 2012; Huang *et al.*, 2013; Lee and Cheng, 2005; Serajian, 2013; Park *et al.*, 2011), analysis of the stability in curving (Cheng *et al.*, 2009; Zboinski and Dusza, 2010, 2011).

The paper talks about the issue of ride quality in comparison with lateral vibrations of the vehicle, in terms of analysis of the influence of the primary and secondary suspension (stiffness and lateral damping) upon lateral acceleration at the level of the vehicle carbody. This analysis aims to bring a quality identification of the solutions by which the carbody lateral acceleration can be minimised, thus giving the vehicle the best dynamic performance in terms of ride quality. It is about a problem that, to the best knowledge of the author, has not been yet approached from this viewpoint. A literature survey only mentions sensitivity analysis that evaluates the effect of elastic properties in the suspension of the railway vehicles upon the dynamic behaviour of the vehicle regarding safety, track fatigue, ride quality (Suarez *et al.*, 2013). On the whole, eight different elastic and damping properties were considered, excluding lateral damping of the primary suspension.

To reach the goal of this paper, a non-linear complex model with 21 degrees of freedom of the vehicle/track system is recommended. It allows examination of vehicle vibrations during circulation on a track with lateral irregularities. The non-linear nature of the model comes from wheel/rail creep forces, lateral reaction of the rail acting on the wheelset when its clearance on the track is consumed and the load is transferred between the wheels of each wheelset.

To calculate the wheel/rail creep forces, the non-linear Polach model is applied (Polach, 1999) that is herein extended by introducing the influence of the load transfer between the wheels of the same wheelset upon creep coefficients. The results derived from numerical simulations validate the possibility to improve ride quality by a good selection of lateral suspension parameters – lateral damping of the secondary suspension or lateral stiffness of the primary suspension.

2. The model of the vehicle/track system

Figures 1 and 2 feature the mechanical model of the vehicle/track system herein used for numerical evaluation of ride quality of a railway vehicle during running at velocity V on a track with lateral irregularities. The vehicle is represented with a non-linear mechanical model of 21-degrees of freedom, comprising of 7 rigid bodies representing the carbody, suspended masses of the bogies (the bogies' chassis) as well as four wheelsets connected via Kelvin-Voigt type elements by which the elastic and damping elements of the two suspension levels are modelled.

The vehicle carbody is described by a rigid body with three degrees of freedom and the following motions: lateral y_c , roll φ_c and yaw α_c . The bogie chassis is also modelled as a three-degrees of freedom rigid body, namely lateral y_{bi} , roll φ_{bi} and yaw α_{bi} , with $i = 1$ or 2 . It should be noted that $2a_c$ means the vehicle wheelbase and $2a_b$ – the bogie wheelbase.

As for the wheelsets, they are considered to be able to perform the following independent motions: lateral translation $y_{wj,(j+1)}$ and rotation around the vertical wheelset – yaw $\alpha_{wj,j+1}$,

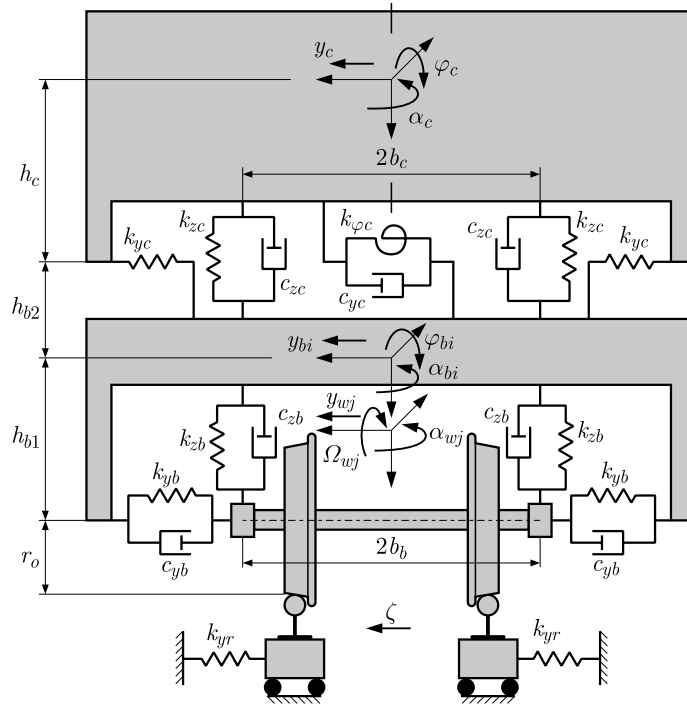


Fig. 1. The mechanical model of the vehicle/track system – front view

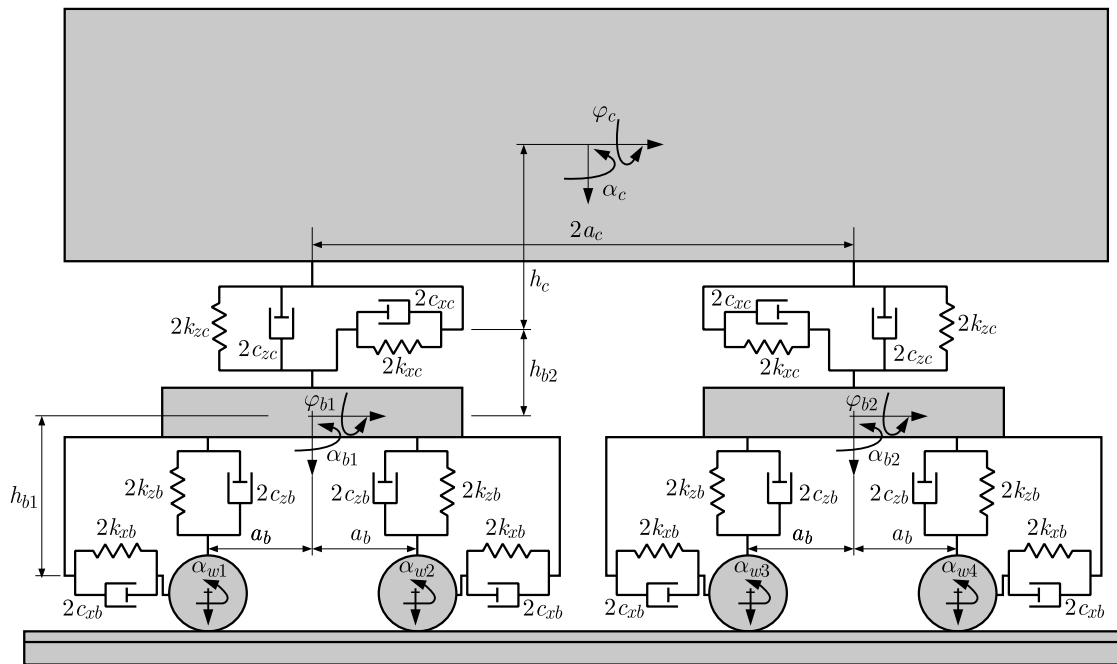


Fig. 2. The mechanical model of the vehicle/track system – side view

where $j = 2i - 1$, with $i = 1$ or 2 , having in mind that the bogie i has the wheelsets j and $j + 1$. Similarly, the wheelset rotates around its own axis at the angular speed $\Omega_{wj,(j+1)} = V/r_o + \omega_{wj,j+1}$, where $\omega_{wj,j+1}$ is angular sliding speed of the wheelset compared to V/r_o , and r_o is radius of the rolling circle when the wheelset occupies the median position on the track. Likewise, due to shape of the rolling profiles, the wheelset performs two more motions, namely rolling and bouncing, which are not independent, but affect the wheelset lateral motion on the track.

The elastic elements of the secondary suspension can be deformed after vertical, lateral and longitudinal directions and they have the rigidities of k_{zc} , k_{yc} and k_{xc} . In order to restrict the roll, each bogie has an anti-roll torsion bar system whose stiffness is $k_{\varphi c}$. In the vertical direction, the secondary suspension of the bogie has two dampers with the damping constant c_{zc} , while in the horizontal direction there is only one damper with the constant c_{yc} . The anti-hunting dampers that are mounted on the lateral sides of the bogies have the damping constant c_{xc} . It is mentioned that the plane of the secondary suspension is at height h_c referred to the carbody mass centre and at height h_{b2} referred to the bogie mass centre, while the lateral base of the secondary suspension is $2b_c$. The elements of the primary suspension whose lateral base is $2b_c$ also operate in the three directions and have rigidities k_{xb} , k_{yb} , k_{zb} and damping constants c_{xb} , c_{yb} and c_{zb} . The Kelvin-Voigt systems located in the axles plane at height h_{b1} referred to the bogie mass centre are modelling their elastic driving.

As for the track lateral irregularities, they are described by a pseudo-stochastic function $\zeta(x)$, written as

$$\zeta(x) = \sum_{k=0}^N Z_k \cos(\Omega_k + \varphi_k) \quad (2.1)$$

where Z_k is the amplitude of the spectral component corresponding to the wave number Ω_k , and φ_k is the lag of the spectral component k' for which a uniform random distribution is selected. The amplitude of each spectral component is established on the basis of the power spectral density of the track irregularities described in accordance with ORE B176 and specifications included in the UIC 518 Leaflet regarding the track geometrical quality.

Against each wheelset, the track lateral irregularities are described by the function $\zeta_{j,(j+1)}(x_{j,(j+1)})$ dependent on the distance along the track, such as

$$\zeta_{j,j+1}(x_{j,j+1}) = \begin{cases} 0 & \text{for } x_{j,j+1} \leq 0 \\ \zeta(x_{j,j+1}) & \text{for } x_{j,j+1} > 0 \end{cases} \quad (2.2)$$

where, depending on the wheelset position in the vehicle unit, $x_{j,j+1}$ is as below:

— for $i = 1$

$$x_1 = x \quad x_2 = x - a_b \quad (2.3)$$

— for $i = 2$

$$x_3 = x - 2a_c \quad x_4 = x - 2a_b - 2a_c \quad (2.4)$$

where the abscissa x is calculated as a function of the time moment t , $x = Vt$.

During circulation on a tangent track, the wheelsets usually follow the trajectory given by the track alignment without consuming the clearance on the track. This occurs when the vehicle exhibits stable behaviour. Under such circumstances, the wheel/rail contact takes place on the rolling surface of the profiles and the contact geometry can be described by linear relations, as for the S78 wheel profile (used in C.F.R. – the Romanian Railway Tracks) and for the UIC 60 rail profile (Dumitriu, 2013). However, there are exceptional situations, such as the loss of stability or the existence of an isolated defect of great amplitude, when it is possible to consume the wheelset clearance on the track and shocks between the wheel flange and the inside rail flank. The modelling of these latter situations is possible by the introduction of a lateral reaction with a non-linear characteristic, which operates upon the outer wheel where the wheelset has consumed the clearance on the track σ (Lee and Cheng, 2005). The equation for such a force is

$$Y_{\sigma j,j+1} = H\left(|y_{wj,j+1} - \zeta_{j,j+1}| - \frac{\sigma}{2}\right) \operatorname{sgn}(y_{wj,j+1} - \zeta_{j,j+1}) k_{yr} \left(|y_{wj,j+1} - \zeta_{j,j+1}| - \frac{\sigma}{2}\right) \quad (2.5)$$

where k_{yr} is the rail lateral stiffness and $H(\cdot)$ is Heaviside's unit step function.

3. The equations of motion of the vehicle

The equations of lateral, roll and yaw motions of the vehicle carbody are written as below

$$\begin{aligned}
 & m_c \ddot{y}_c + c_{yc} [2(\dot{y}_c + h_c \dot{\varphi}_c) - (\dot{y}_{b1} + \dot{y}_{b2}) + h_{b2}(\dot{\varphi}_{b1} + \dot{\varphi}_{b2})] \\
 & \quad + 2k_{yc} [2(y_c + h_c \varphi_c) - (y_{b1} + y_{b2}) + h_{b2}(\varphi_{b1} + \varphi_{b2})] = 0 \\
 & J_{xc} \ddot{\varphi}_c + 2c_{zc} b_c^2 [2\dot{\varphi}_c - (\dot{\varphi}_{b1} + \dot{\varphi}_{b2})] + c_{yc} h_c [2(\dot{y}_c + h_c \dot{\varphi}_c) - (\dot{y}_{b1} + \dot{y}_{b2}) + h_{b2}(\dot{\varphi}_{b1} + \dot{\varphi}_{b2})] \\
 & \quad + (k_{\varphi c} + 2k_{zc} b_c^2) [2\varphi_c - (\varphi_{b1} + \varphi_{b2})] \\
 & \quad + 2k_{yc} h_c [2(y_c + h_c \varphi_c) - (y_{b1} + y_{b2}) + h_{b2}(\varphi_{b1} + \varphi_{b2})] - m_c g h_c \varphi_c = 0 \\
 & J_{zc} \ddot{\alpha}_c + 2c_{xc} b_c^2 [2\dot{\alpha}_c - (\dot{\alpha}_{b1} + \dot{\alpha}_{b2})] + c_{yc} a_c [2a_c \dot{\alpha}_c - (\dot{y}_{b1} - \dot{y}_{b2}) + h_{b2}(\dot{\varphi}_{b1} - \dot{\varphi}_{b2})] \\
 & \quad + 2k_{xc} b_c^2 [2\alpha_c - (\alpha_{b1} + \alpha_{b2})] + 2k_{yc} a_c [2a_c \alpha_c - (y_{b1} - y_{b2}) + h_{b2}(\varphi_{b1} - \varphi_{b2})] = 0
 \end{aligned} \tag{3.1}$$

where m_c represents mass of the carbody, J_{xc} is the inertia moment of the carbody around the longitudinal axis, and J_{zc} – the inertia moment of the carbody around the vertical axis.

For $i = 1, 2$ and $j = 2i - 1$, the equations of motion for the lateral displacement, roll and yaw of the bogies are as follows

$$\begin{aligned}
 & m_b \ddot{y}_{bi} + c_{yc} (\dot{y}_{bi} - h_{b2} \dot{\varphi}_{bi} - \dot{y}_c - h_c \dot{\varphi}_c \mp a_c \dot{\alpha}_c) + 2c_{yb} [2(\dot{y}_{bi} + h_{b1} \dot{\varphi}_{bi}) - (\dot{y}_{wj} + \dot{y}_{w(j+1)})] \\
 & \quad + 2k_{yc} (y_{bi} - h_{b2} \varphi_{bi} - y_c - h_c \varphi_c \mp a_c \alpha_c) + 2k_{yb} [2(y_{bi} + h_{b1} \varphi_{bi}) - (y_{wj} + y_{w(j+1)})] = 0 \\
 & J_{xb} \ddot{\varphi}_{bi} + 2c_{zc} b_b^2 (\dot{\varphi}_{bi} - \dot{\varphi}_c) + c_{yc} h_{b2} (h_{b2} \dot{\varphi}_{bi} - \dot{y}_{bi} + \dot{y}_c + h_c \dot{\varphi}_c \pm a_c \dot{\alpha}_c) \\
 & \quad + 2c_{yb} h_{b1} [2(h_{b1} \dot{\varphi}_{bi} + \dot{y}_{bi}) - (\dot{y}_{wj} + \dot{y}_{w(j+1)})] + 4c_{zb} b_b^2 \dot{\varphi}_{bi} + (k_{\varphi c} + 2k_{zc} b_c^2) (\varphi_{bi} - \varphi_c) \\
 & \quad + 2k_{yc} h_{b2} (h_{b2} \varphi_{bi} - y_{bi} + y_c + h_c \varphi_c \pm a_c \alpha_c) \\
 & \quad + 2k_{yb} h_{b1} [2(h_{b1} \varphi_{bi} + y_{bi}) - (y_{wj} + y_{w(j+1)})] \\
 & \quad + \left[4k_{zb} b_b^2 - g \left(h_{12} \frac{m_c}{2} + h_{b1} m_b \right) \right] \varphi_{bi} = 0 \quad \text{with} \quad h_{12} = h_{b1} + h_{b2} \\
 & J_{zb} \ddot{\alpha}_{bi} + 2c_{xc} b_b^2 (\dot{\alpha}_{bi} - \dot{\alpha}_c) + 2c_{xb} b_b^2 [2\dot{\alpha}_{bi} - (\dot{\alpha}_{wj} + \dot{\alpha}_{w(j+1)})] \\
 & \quad + 2c_{yb} a_b [2a_b \dot{\alpha}_{bi} - (\dot{y}_{wj} - \dot{y}_{w(j+1)})] + 2k_{xc} b_b^2 (\alpha_{bi} - \alpha_c) \\
 & \quad + 2k_{xb} b_b^2 [2\alpha_{bi} - (\alpha_{wj} + \alpha_{w(j+1)})] + 2k_{yb} a_b [2a_b \alpha_{bi} - (y_{wj} - y_{w(j+1)})] = 0
 \end{aligned} \tag{3.2}$$

where m_b represents suspended mass of the bogie, J_{xb} is the inertia moment of the bogie chassis around the longitudinal axis and J_{zb} – inertia moment of the bogie chassis around the vertical axis.

For the wheelsets j and $j + 1$, the equations of lateral displacement and yaw motions and the equation for rotary motion around the wheelset axis with $i = 1, 2$ and $j = 2i - 1$, are

$$\begin{aligned}
 & m_w \ddot{y}_{wj,j+1} + 2c_{yb} (\dot{y}_{wj,j+1} - \dot{y}_{bi} - h_{b1} \dot{\varphi}_{bi} \mp a_b \dot{\alpha}_{bi}) + 2k_{yb} (y_{wj,j+1} - y_{bi} - h_{b1} \varphi_{bi} \mp a_b \alpha_{bi}) \\
 & \quad = Y_{j,(j+1)1} + Y_{j,(j+1)2} - Y_{\sigma j,j+1} \\
 & J_{zw} \ddot{\alpha}_{wj,j+1} + 2c_{xb} b_b^2 (\dot{\alpha}_{wj,j+1} - \dot{\alpha}_{bi}) + 2k_{xb} b_b^2 (\alpha_{wj,j+1} - \alpha_{bi}) \\
 & \quad + J_{yw} \frac{V}{r_o} \dot{\varphi}_{wj,j+1} = -e_o (X_{j,(j+1)1} - X_{j,(j+1)2}) \\
 & J_{yw} \dot{\omega}_{wj,j+1} = -r_o (X_{j,(j+1)1} + X_{j,(j+1)2})
 \end{aligned} \tag{3.3}$$

where m_w is mass of the wheelset; e_o , r_o – coordinates of the wheel-rail contact points when the wheelset is in the median position on the track; J_{xw} , J_{yw} and J_{zw} – wheelset inertia moments. The term $J_{yw} (V/r_o) \dot{\varphi}_{wj,j+1}$ corresponds to the gyroscopic moment due to the combined effect of wheelset rotary motion around its own axis with roll motion. $X_{j,(j+1)1,2}$ are longitudinal forces

and $Y_{j,(j+1)1,2}$ represent guidance forces acting upon the wheelsets j and $j + 1$, respectively, in the wheel/rail contact points 1 or 2.

The above equations are added to the equations for bouncing and roll of the wheelsets, the motions that are dependent on the lateral displacement of the wheelset on the track. These equations are used to calculate the normal contact wheel/rail forces. When considering that the bounce coming from the lateral displacement of the wheelset on the track is very low (Wickens, 2005), the inertia effect of the wheelset mass in the vertical direction can be thus neglected. Hence, the balance equation for the vertical forces can be written as

$$Q_{j,(j+1)1} + Q_{j,(j+1)2} = 2Q_o \tag{3.4}$$

where $Q_{j,(j+1)1,2}$ are vertical loads in the wheel/rail contact points and Q_o is the static load acting on the wheel.

The equation for the wheelset roll motion is

$$\begin{aligned} J_{xw}\ddot{\varphi}_{wj,j+1} - J_{yw}\frac{V}{r_o}\dot{\alpha}_{wj,j+1} - 2b_b^2c_{zb}\dot{\varphi}_{bi} - 2b_b^2k_{zb}\varphi_{bi} \\ = r_o(Y_{j,(j+1)1} + Y_{j,(j+1)2}) + e_o(Q_{j,(j+1)1} - Q_{j,(j+1)2}) + r_oY_{\sigma j,j+1} \end{aligned} \tag{3.5}$$

where the term $J_{yw}(V/r_o)\dot{\alpha}_{wj,j+1}$ corresponds to the gyroscopic moment due to the combined effect of rotary motion of the wheelset around its own axis with the yaw motion.

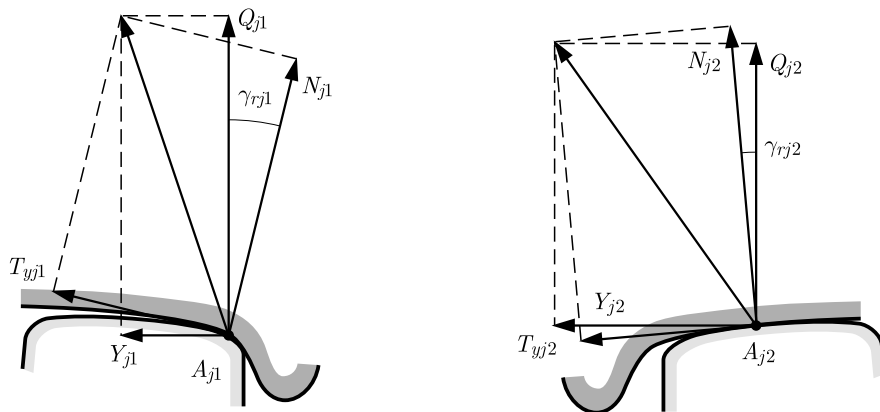


Fig. 3. he wheel/rail contact forces acting in the cross wheel-rail section

The wheel/rail contact forces, namely the longitudinal forces, guidance forces and the vertical loads are expressed as a function of the longitudinal components $T_{xj,(j+1)1,2}$ and lateral $T_{yj,(j+1)1,2}$ of the creep forces and the normal reactions $N_{j,(j+1)1,2}$ in the wheel/rail contact points. As an example, the equations for the wheelsets j (see Fig. 3) can be therefore written

$$\begin{aligned} X_{j1,2} &= T_{xj1,2} \\ Y_{j1,2} &= T_{yj1,2} \cos \gamma_{rj1,2} \mp N_{j1,2} \sin \gamma_{rj1,2} \\ Q_{j1,2} &= \pm T_{yj1,2} \sin \gamma_{rj1,2} + N_{j1,2} \cos \gamma_{rj1,2} \end{aligned} \tag{3.6}$$

where $\gamma_{rj1,2}$ stand for the wheel/rail contact angles against the track reference system. Since the contact angles are small on the rolling surface areas, the equation below can be used

$$\gamma_{rj1,2} = \gamma_o \pm (y_{wj1,2} - \zeta_j) \frac{1}{\rho_w - \rho_r} \frac{e_o + \rho_w \gamma_o}{e_o - r_o \gamma_o} \tag{3.7}$$

where γ_o is the wheel/rail contact angle for the median position of the wheelset on the track and ρ_w and ρ_r represent the curvature radii of the wheel-rail rolling profiles, respectively.

According to Polach's friction nonlinear model (Polach, 1999), the components of creep forces have the following forms

$$\begin{aligned}
 T_{xj1,2} &= -\frac{2\mu N_{j1,2}}{\pi} \left(\frac{\kappa_{j1,2}}{1 + \kappa_{j1,2}^2} + \arctan \kappa_{j1,2} \right) \frac{\nu_{xj1,2}}{\nu_{cj1,2}} \\
 T_{yj1,2} &= -\mu N_{j1,2} \left\{ \frac{2}{\pi} \left(\frac{\kappa_{j1,2}}{1 + \kappa_{j1,2}^2} + \arctan \kappa_{j1,2} \right) \frac{\nu_{yj1,2}}{\nu_{cj1,2}} \right. \\
 &\quad \left. + \frac{9}{16} a_{j1,2} K_{Mj1,2} \left[1 + 6.3 \left(1 - e^{(-a/b)_{j1,2}} \right) \right] \frac{\nu_{sj1,2}}{\nu_{cj1,2}} \right\}
 \end{aligned} \tag{3.8}$$

where μ is the friction coefficient, $\nu_{xj1,2}$ and $\nu_{yj1,2}$ represent the longitudinal and the lateral components of the creepage in the wheel/rail contact points, $\nu_{cj1,2}$ – creepage corrected by the spin, and $a_{j1,2}$ and $b_{j1,2}$ stand for the semiaxes of the contact ellipse.

To calculate the creepage in the wheel/rail contact points, the following equations are used

$$\begin{aligned}
 \nu_{xj1,2} &= \mp \frac{y_{wj} - \zeta_j}{r_o} \gamma_e - \frac{\omega_{wj} r_o}{V} \mp \frac{e_o \dot{\alpha}_{wj}}{V} \\
 \nu_{yj1,2} &= \frac{1}{V} (\phi \dot{y}_{wj} - \lambda \dot{\zeta}_j) - \alpha_{wj} \quad \lambda = \frac{r_o \gamma_o}{e_o - r_o \gamma_o} \quad \phi = 1 + \lambda \\
 \nu_{cj1,2} &= \sqrt{\nu_{xj1,2}^2 + \nu_{ycj1,2}^2}
 \end{aligned} \tag{3.9}$$

where

$$\gamma_e = \frac{\rho_r \gamma_o}{\rho_w - \rho_r} \frac{e_o + \rho_r \gamma_o}{e_o - r_o \gamma_o} \tag{3.10}$$

is the equivalent conicity and $\nu_{ycj1,2}$ represents the lateral component of the creepage corrected by the spin.

In order to calculate $\nu_{ycj1,2}$, the relations below are applied

$$\nu_{ycj1,2} = \begin{cases} \nu_{yj1,2} + a_{j1,2} \nu_{sj1,2} & \text{for } |\nu_{yj1,2} + a_{j1,2} \nu_{sj1,2}| > |\nu_{yj1,2}| \\ \nu_{yj1,2} & \text{for } |\nu_{yj1,2} + a_{j1,2} \nu_{sj1,2}| \leq |\nu_{yj1,2}| \end{cases} \tag{3.11}$$

where $\nu_{sj1,2}$ is the spin defined as below

$$\nu_{sj1,2} = \frac{\dot{\alpha}_{wj}}{V} \mp \left(\frac{1}{r_o} + \frac{\omega_{wj}}{V} \right) \gamma_{wj1,2} \tag{3.12}$$

where $\gamma_{wj1,2}$ represent the wheel/rail contact angles compared to the wheelset reference system

$$\gamma_{wj1,2} = \gamma_o \pm (y_{wj1,2} - \zeta_j) \frac{1}{\rho_w - \rho_r} \frac{e_o + \rho_r \gamma_o}{e_o - r_o \gamma_o} \tag{3.13}$$

To determine the semiaxes of the wheel/rail contact ellipse, the Hertz equations will be used as a function of the normal force and the curves of the rolling profiles.

As for the coefficient $\kappa_{j1,2}$ in equations (3.8), it can be calculated from

$$\kappa_{j1,2} = \frac{1}{4} \frac{G \pi a_{j1,2} b_{j1,2} C_{ii}}{\mu N_{j1,2}} \nu_{cj1,2} \tag{3.14}$$

where G is the transverse elasticity modulus and C_{ii} is a constant defined by Polach depending on the Kalker coefficients C_{11} and C_{22} (Kalker, 1967)

$$C_{ii} = \sqrt{\left(C_{11} \frac{\nu_{xj1,2}}{\nu_{j1,2}} \right)^2 + \left(C_{22} \frac{\nu_{yj1,2}}{\nu_{j1,2}} \right)^2} \quad \nu_{j1,2} = \sqrt{\nu_{xj1,2}^2 + \nu_{yj1,2}^2} \tag{3.15}$$

The coefficient $K_{Mj1,2}$ in relation (3.8)₂ is

$$K_{Mj1,2} = |\kappa_{sj1,2}| \left(\frac{\delta_{j1,2}^3}{3} - \frac{\delta_{j1,2}^2}{2} + \frac{1}{6} \right) - \frac{1}{3} \sqrt{(1 - \delta_{j1,2}^2)^3} \quad (3.16)$$

where

$$\delta_{j1,2} = \frac{\kappa_{sj1,2}^2 - 1}{\kappa_{sj1,2}^2 + 1} \quad \kappa_{sj1,2} = \frac{8Gb_{j1,2}\sqrt{a_{j1,2}b_{j1,2}}}{3\mu N_{j1,2}} \frac{C_{23}\nu_{ycj1,2}}{1 + 2\pi[1 - e^{-(a/b)_{j1,2}}]} \quad (3.17)$$

while mentioning that C_{23} is the coefficient calculated by Kalker (1967) for the spin.

The next step is calculation of the normal reactions $N_{j,1,2}$ in the wheel/rail contact points of the wheelsets j . After some calculations, equations (3.4) and (3.5) become

$$\begin{aligned} q_{j1}N_{j1} + q_{j2}N_{j2} &= 2Q_o \\ (r_o p_{j1} - e_o q_{j1})N_{j1} + (r_o p_{j2} + e_o q_{j2})N_{j2} &= -c_j \end{aligned} \quad (3.18)$$

in which

$$\begin{aligned} c_j &= J_{xo}\ddot{\varphi}_{oj} - J_{yo}\frac{V}{r_o}\dot{\alpha}_{oj} - 2b_b^2c_{zb}\dot{\varphi}_{bi} - 2b_b^2k_{zb}\varphi_{bi} - r_oY_{\sigma j} \\ q_{j1,2} &= 1 \mp \left(K_{j1,2}\frac{\nu_{yj1,2}}{\nu_{cj1,2}} + K_{sj1,2}\frac{\nu_{sj1,2}}{\nu_{cj1,2}} \right) \gamma_{rj1,2} \\ p_{j1,2} &= K_{j1,2}\frac{\nu_{yj1,2}}{\nu_{cj1,2}} + K_{sj1,2}\frac{\nu_{sj1,2}}{\nu_{cj1,2}} \pm \gamma_{rj1,2} \end{aligned} \quad (3.19)$$

where

$$\begin{aligned} K_{j1,2} &= \frac{2\mu}{\pi} \left(\frac{\kappa_{j1,2}}{1 + \kappa_{j1,2}^2} + \arctan \kappa_{j1,2} \right) \\ K_{sj1,2} &= \frac{9\mu}{16} a_{j1,2} K_{Mj1,2} \left[1 + 6.3 \left(1 - e^{-(a/b)_{j1,2}} \right) \right] \end{aligned} \quad (3.20)$$

It is worth mentioning that the set of equations (3.18) is non-linear because the coefficients $q_{j1,2}$ and $p_{j1,2}$ depend on the normal forces $N_{j1,2}$. The solution to the set can be derived by simple iterations via the equations

$$N_{j1} = \frac{2(r_o p_{j2} + e_o q_{j2})Q_o + q_{j2}c_j}{r_o(q_{j1}p_{j2} - q_{j2}p_{j1}) + 2e_o q_{j1}q_{j2}} \quad N_{j2} = \frac{-q_{j1}c_j - 2(r_o p_{j1} - e_o q_{j1})Q_o}{r_o(q_{j1}p_{j2} - q_{j2}p_{j1}) + 2e_o q_{j1}q_{j2}} \quad (3.21)$$

Equations of motion (3.1)-(3.3) can be solved by the Runge-Kutta method and relations (3.21) are used iteratively for each integration step in the calculation of the wheel/rail contact normal forces.

4. Numerical analysis

This Section features the results of numerical simulations regarding the influence of parameters of the lateral suspension on ride quality in the railway vehicle at velocity of 200 km/h on a track with lateral irregularities. The evaluation of ride quality is based on the lateral R.M.S. acceleration, calculated in three reference points on the carbody longitudinal axis and at the floor level – at the carbody centre and above the two bogies.

The parameters of the vehicle numerical model are shown in Table 1. To calculate geometrical parameters of the wheel/rail contact, the S78 profile wheel and the UIC 60 rail with the standard

Table 1. Parameters of the numerical model

$m_c = 34000$ kg	$2c_{xc} = 50$ kNs/m
$m_b = 3200$ kg	$c_{yc} = 15.205$ kNs/m
$m_w = 1650$ kg	$2c_{zc} = 34.44$ kNs/m
$J_{xc} = 57460$ kgm ²	$2k_{xc} = 340$ kN/m
$J_{zc} = 2456500$ kgm ²	$2k_{yc} = 340$ kN/m
$J_{xb} = 3200$ kgm ²	$2k_{zc} = 1.2$ MN/m
$J_{zb} = 5000$ kgm ²	$k_{\varphi c} = 10$ kNm
$J_{xw} = J_{zw} = 928.125$ kgm ²	$4c_{xb} = 100$ kNs/m
$J_{yw} = 349.14$ kgm ²	$4c_{yb} = 35.77$ kNs/m
$2a_c = 19$ m	$4c_{zb} = 52.21$ kNs/m
$2a_b = 2.56$ m	$4k_{xb} = 140$ MN/m
$h_c = 1.3$ m	$4k_{yb} = 10$ MN/m
$h_{b1} = 0.25$ m; $h_{b2} = 0.2$ m	$4k_{zb} = 4.4$ MN/m
$2b_b = 2b_c = 2$ m	$k_{yr} = 100$ MN/m
$\sigma = 12$ mm	$\mu = 0.36$

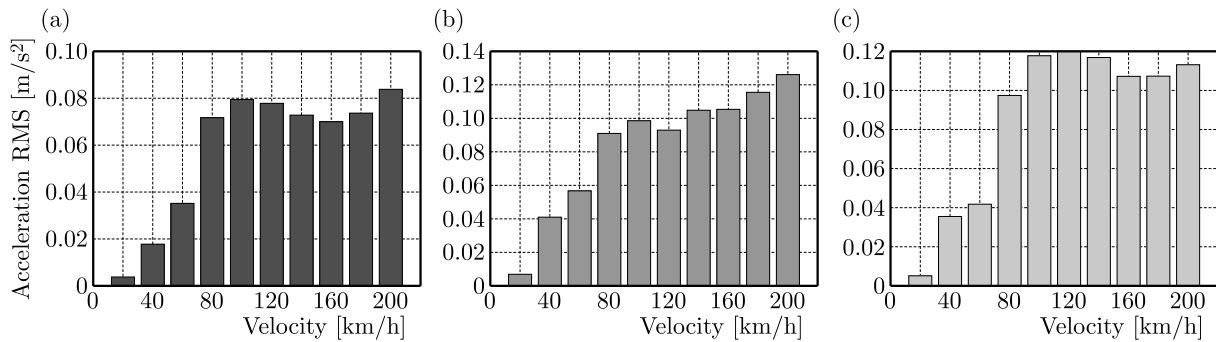


Fig. 4. The lateral R.M.S. acceleration of the carbody: (a) at the carbody centre, (b) above the front bogie, (c) above the rear bogie

C.F.R. of 1/20 are considered. When the wheelset occupies the median position on the track with the normal gauge, the coordinates of the wheel/rail contact points are $r_o = 0.4598$ m, $e_o = 0.754$ m and $\gamma_o = 0.0495$, and the profiles radii are: $\rho_w = 500$ mm and $\rho_r = 300$ mm (Dumitriu, 2013). The equivalent conicity is $\gamma_e = 0.1237$.

For the reference parameters of the numerical model presented in Table 1, Fig. 4 shows the lateral R.M.S. acceleration calculated in the three reference points of the carbody, ranging from 20 to 200 km/h. The velocity increases along with the lateral acceleration, which is not uniform due to the geometrical filtering effect coming from the vehicle wheelbases. Further on, it should be noted that, irrespective of the velocity, the acceleration is lower at the carbody centre and rises against the bogies. Also, it exhibits different behaviour of the vehicle in the reference points located above the two bogies. Should the carbody critical point in terms of vibrations is that reference point, where the acceleration is higher, this point can be identified against either the front bogie or the rear bogie, depending on the velocity. Thus, the carbody critical point is found above the front bogie up to velocity of 60 km/h. When the speed increases, the critical point migrates over the rear bogie – in this reference point, the carbody acceleration has the maximum value for velocities going from 80 to 160 km/h. When the vehicle travels at a speed of 180 or 200 km/h, the reference point above the front bogie is the carbody critical point.

Figure 5 shows the carbody lateral R.M.S. acceleration of the vehicle at the velocity of 200 km/h for values of the secondary suspension lateral stiffness ranging from 10^4 N/m to $5 \cdot 10^5$ N/m. The higher k_{yc} , the worse ride quality is, a fact also visible in the continuous increase of the acceleration. For instance, for the reference value of the lateral stiffness, the R.M.S. acceleration is 0.084 m/s^2 – at the carbody centre; 0.126 m/s^2 – above the front bogie; 0.113 m/s^2 – above the rear bogie. If k_{yc} goes up to $5 \cdot 10^5$ N/m, the following values of acceleration will be obtained: 0.237 m/s^2 – at the carbody centre; 0.329 m/s^2 – above the front bogie; 0.363 m/s^2 – above the rear bogie. It is an increase of about circa three times of the lateral acceleration at the vehicle carbody level.

The diagrams in Fig. 5 also reveal an interesting fact, namely that for a rise in the lateral stiffness of the secondary suspension, the carbody critical point migrates from one reference point to another. Thus, for k_{yc} ranging from 10^4 N/m to $1.7 \cdot 10^5$ N/m, the critical point is located above the front bogie, while for k_{yc} as $5 \cdot 10^5$ N/m, this point is the carbody reference point against the rear bogie.

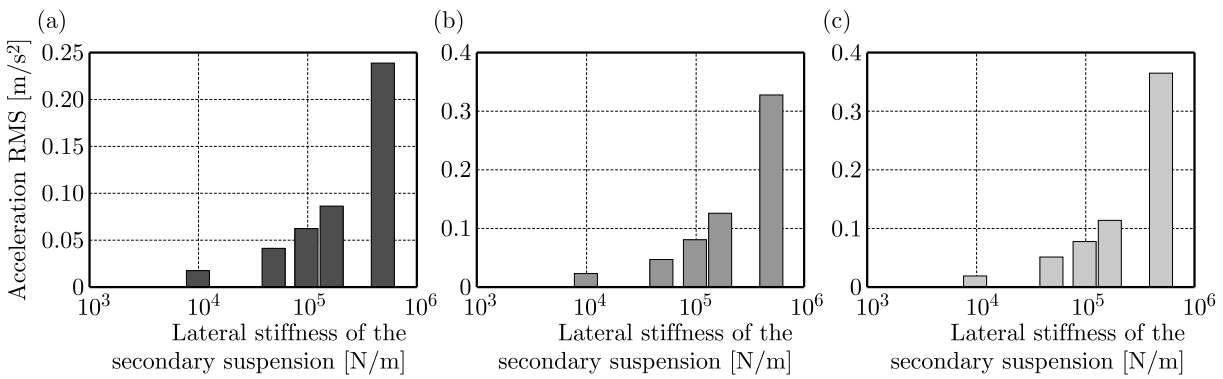


Fig. 5. The influence of the lateral stiffness of the secondary suspension upon ride quality: (a) at the carbody centre, (b) above the front bogie, (c) above the rear bogie

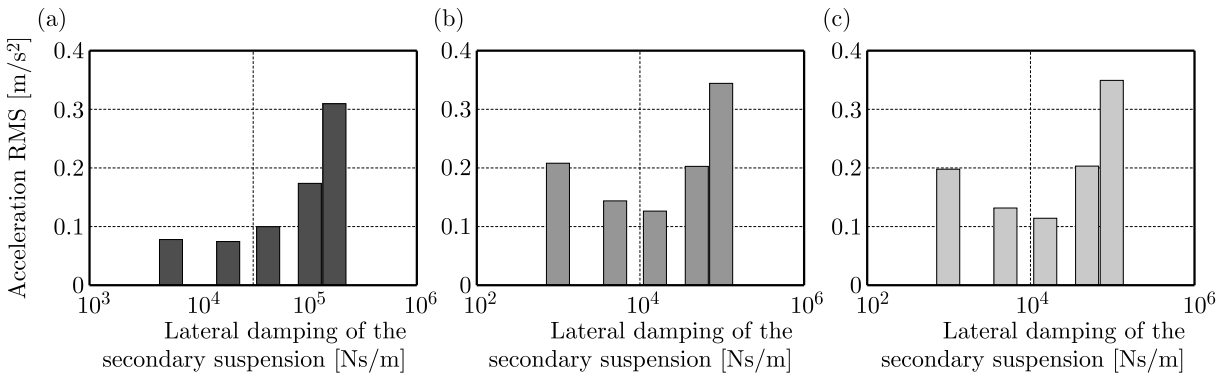


Fig. 6. The influence of the lateral damping of the secondary suspension upon ride quality: (a) at the carbody centre, (b) above the front bogie, (c) above the rear bogie

Upon examining the diagrams in Fig. 6, the observation is that there is a value of the lateral damping of the secondary suspension for which the lateral acceleration in any of the carbody reference points has the minimum value. At the carbody centre, where the level of vibrations is lower, the minimum acceleration is calculated for $c_{yc} = 5 \cdot 10^3$ Ns/m. On the other hand, the same thing happens above the bogies for higher values of the lateral damping, which is here the reference value itself ($c_{yc} = 1.52 \cdot 10^4$ Ns/m). The conclusion is that an increase in the lateral damping of the secondary suspension up to a certain value generally improves ride quality. Over this limit, the damping has a contrary effect, evident in a significant rise of the

R.M.S. acceleration. For instance, this acceleration is 0.074 m/s^2 for $c_{yc} = 5 \cdot 10^3 \text{ Ns/m}$ at the carbody centre. When raising the lateral damping up to 10^5 Ns/m , the acceleration becomes 0.31 m/s^2 . The same thing occurs in the reference points above the bogies. Thus, above the front bogie, the R.M.S. acceleration is 0.126 m/s^2 for $c_{yc} = 1.52 \cdot 10^4 \text{ Ns/m}$; when c_{yc} reaches 10^5 Ns/m , the acceleration goes up to 0.345 m/s^2 . Another observation is related to the fact that the lateral damping of the secondary suspension influences the position of the critical point of the carbody. In this case, it is about its migration from the front bogie to the rear bogie, when c_{yc} is 10^5 Ns/m .

The diagrams in Fig. 7 help with further examination of the influence of the lateral stiffness of the primary suspension upon ride quality, thus considering values of k_{yb} between 10^6 N/m and $5 \cdot 10^7 \text{ N/m}$. For $k_{yb} = 5 \cdot 10^6 \text{ N/m}$, the lateral R.M.S. acceleration calculated in the carbody reference points has the minimum value: 0.080 m/s^2 – at the carbody centre; 0.121 m/s^2 – against the front bogie; 0.106 m/s^2 – against the rear bogie. On the other hand, for the above cases, a change in the lateral stiffness of the primary suspension does not lead to the movement of the carbody critical point, which remains above the front bogie.

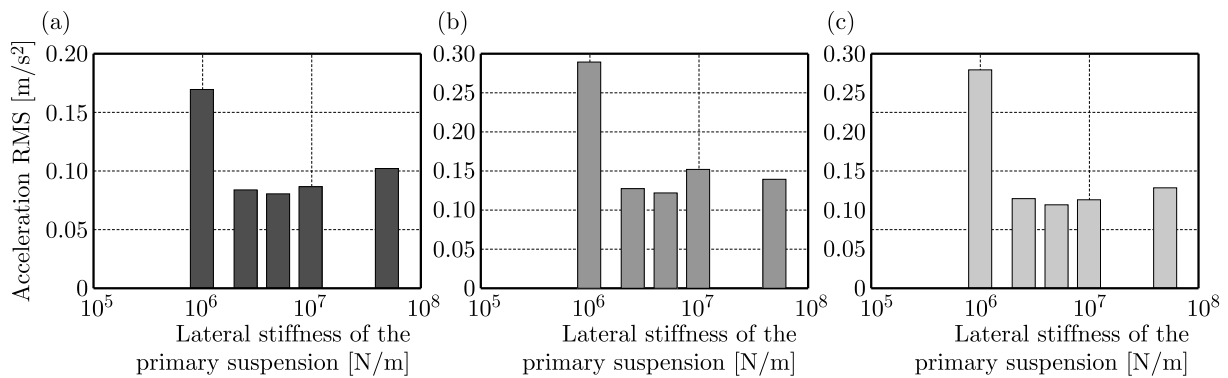


Fig. 7. The influence of the lateral stiffness of the primary suspension upon ride quality: (a) at the carbody centre, (b) above the front bogie, (c) above the rear bogie

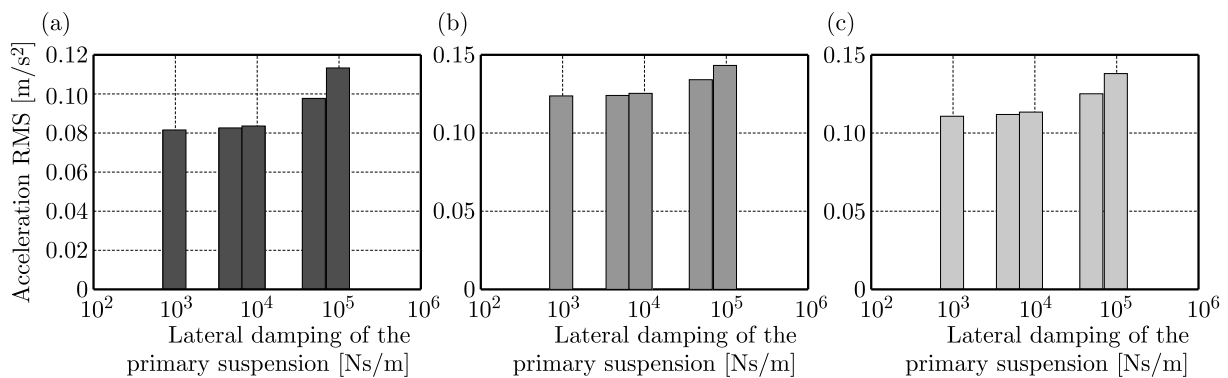


Fig. 8. The influence of the lateral damping of the primary suspension upon ride quality: (a) at the carbody centre, (b) above the front bogie, (c) above the rear bogie

The influence of lateral damping of the primary suspension upon ride quality is evident in the diagrams in Fig. 8. They include the results regarding the lateral R.M.S. acceleration for values of c_{yb} within the interval of $10^3, 10^4, 10^5 \text{ Ns/m}$. It can be observed that lateral damping of the primary suspension does not have a significant influence upon the R.M.S. acceleration. However, for better ride quality, it is desirable to have the lowest possible lateral damping of the primary suspension. To validate this hypothesis, let us look at the results corresponding to the limit values of the interval defined for c_{yb} . Thus, for $c_{yb} = 10^3 \text{ Ns/m}$, the R.M.S. acceleration in the

carbody reference points is 0.081 m/s^2 – at the carbody centre; 0.124 m/s^2 – above the front bogie; 0.111 m/s^2 – above the rear bogie. For $c_{yb} = 10^5 \text{ Ns/m}$, the results are as such: 0.113 m/s^2 – at the carbody centre; 0.144 m/s^2 – above the front bogie; 0.138 m/s^2 – above the rear bogie. As for the position of the carbody critical point, it can be proven that this corresponds to the reference point above the first bogie, irrespective of the value of c_{yb} being considered.

5. Conclusions

The paper hereby examines the influence of suspension parameters upon ride quality compared to lateral vibrations of a railway vehicle during running on a track with lateral irregularities. The ride quality is evaluated by numerical simulations, based on the lateral accelerations in three reference points of the carbody – at its centre and above the bogies.

The results thus obtained validate, on one hand, some features of lateral vibrations of the railway vehicle and, on the other hand, the possibility to improve ride quality by the best possible selection of the lateral suspension parameters.

It has been shown that, irrespective of the velocity, the lateral acceleration is lower at the carbody centre and higher above the bogies. Similarly, the asymmetry of the carbody vibrations has been noticed in the reference points against the two bogies. The concept of the carbody critical point in terms of the vibration level has been introduced as being that reference point where the acceleration has the highest value. Its position depends on velocity and parameters of the secondary suspension.

The analysis of the influence of the suspension parameters on the carbody lateral acceleration has confirmed that the most appropriate values of the lateral damping in the secondary suspension or of the lateral stiffness in the primary suspension can be identified. For these values, the carbody acceleration can be lowered to minimum, hence enabling the vehicle to have the best dynamic performance in terms of ride quality. Likewise, the lateral stiffness of the secondary suspension can significantly affect ride quality under certain conditions.

References

1. CHENG Y.C., LEEB, S.Y., CHEN, H.H., 2009, Modeling and nonlinear hunting stability analysis of high-speed railway vehicle moving on curved track, *Journal Sound and Vibration*, **324**, 139-160
2. DABIN C., LI L., JIN X., XIAO X., DING J., 2012, Influence of vehicle parameters on critical hunting speed based on Ruzicka model, *Chinese Journal of Mechanical Engineering*, **25**, 1, 536-542
3. DUMITRIU M., 2013, Modelling the geometric contact between wheels and the rails of a track with horizontal irregularity, *Mechanical Journal Fiability and Durability*, **1**, 116-122
4. DUMITRIU M., 2014, On-line running tests for validating the numerical simulations of the vertical dynamic behavior in railway vehicles, *Applied Mechanics and Materials*, **657**, 609-613
5. EVANS J., BERG M., 2009, Challenges in simulation of rail vehicle dynamics, *Vehicle System Dynamics*, **47**, 1023-1048
6. GARG V.K., DUKKIPATI R.V., 1984, *Dynamics of Railway Vehicle Systems*, Academic Press, New York
7. HE Y., MCPHEE J., 2002, Optimization of the lateral stability of rail vehicles, *Vehicle System Dynamics*, **38**, 5, 361-390
8. HUANG C., ZENG J., LIANG S., 2013, Carbody hunting investigation of a high speed passenger car, *Journal of Mechanical Science and Technology*, **27**, 8, 2283-2292
9. IWNICKI S., 2006, *Handbook of Railway Vehicle Dynamics*, CRC Press Taylor & Francis Group

10. KALKER J.J., 1967, On the rolling contact of two elastic bodies in the presence of dry friction, Ph.D. Thesis, Delft
11. LEE S.Y., CHENG Y.C., 2005, Hunting stability analysis of high-speed railway vehicle trucks on tangent tracks, *Journal of Sound and Vibration*, **282**, 881-898
12. MAZZOLA L., ALFI S., BRUNI S., 2010, A method to optimize stability and wheel wear in railway bogies, *International Journal of Railway*, **3**, 3, 95-105
13. ORE B 176, 1989, Bogies with steered or steering wheelsets, Report No.1: Specifications and preliminary studies, Vol. 2, Specification for a bogie with improved curving characteristics
14. PARK J.P., KOH H.I., KIM N.P., 2011, Parametric study of lateral stability for a railway vehicle, *Journal of Mechanical Science and Technology*, **25**, 7, 1657-1666
15. POLACH O., 1999, A fast wheel-rail forces calculation computer code, *Vehicle System Dynamics*, **33**, 728-739
16. POLACH O., 2006, On non-linear methods of bogie stability assessment using computer simulations, *Proceedings of the Institution of Mechanical Engineers, Part F: Journal of Rail and Rapid Transit*, **220**, 13-27
17. POLACH O., KAISER I., 2012, Comparison of methods analyzing bifurcation and hunting of complex rail vehicle models, *Journal of Computational and Nonlinear Dynamics*, **7**, 041005-1 - 041005-8
18. SCHUPP G., 2003, Simulation of railway vehicles: Necessities and applications, *Mechanics Based Design of Structures and Machines*, **31**, 3, 297-314
19. SERAJIAN R., 2013, Parameters' changing influence with different lateral stiffness on nonlinear analysis of hunting behavior of a bogie, *Vibroengineering. Journal of Measurements in Engineering*, **1**, 4, 195-206
20. SHARMA R.C., 2011, Parametric analysis of rail vehicle parameters influencing ride behavior, *International Journal of Engineering, Science and Technology*, **3**, 8, 54-65
21. SUAREZ B., MERA J.M. , MARTINEZ M.L. JOSE, CHOVER J.A., 2013, Assessment of the influence of the elastic properties of rail vehicle suspensions on safety, ride quality and track fatigue, *Vehicle System Dynamics*, **51**, 2, 280-300
22. UIC 518 Leaflet, 2009, Testing and approval of railway vehicles from the point of view of their dynamic behaviour – Safety – Track Fatigue – Ride Quality
23. WICKENS A.H., 2005, *Fundamentals of rail vehicles dynamics: guidance and stability*, Taylor & Francis e-Library
24. ZBOINSKI K., DUSZA M., 2010, Self-exciting vibrations and Hopf's bifurcation in non-linear stability analysis of rail vehicles in a curved track, *European Journal of Mechanics – A/Solids*, **29**, 190-203
25. ZBOINSKI K., DUSZA M., 2011, Extended study of railway vehicle lateral stability in a curved track, *Vehicle System Dynamics*, **49**, 789-810

ON THE TURBULENT BOUNDARY LAYER OF A DRY GRANULAR AVALANCHE DOWN AN INCLINE. II – CLOSURE MODEL AND NUMERICAL SIMULATIONS

CHUNG FANG

National Cheng Kung University, Department of Civil Engineering, Tainan City, Taiwan
e-mail: cfang@mail.ncku.edu.tw

Dynamic responses of the closure relations, specific turbulent Helmholtz free energy and turbulent viscosity are postulated followed by experimental calibrations. The established closure model is applied to analyses of a gravity-driven stationary avalanche with incompressible grains down an incline. While the mean velocity and volume fraction increase from their minimum values on the plane toward maximum values on the free surface exponentially, two-fold turbulent kinetic energies and dissipations evolve in a reverse manner. Most two-fold turbulent kinetic energies and dissipations are confined within the thin turbulent boundary layer immediately above the plane, with *nearly vanishing* two-fold turbulent kinetic energies and *finite* two-fold turbulent dissipations in the passive layer. The two layers are similar to those of Newtonian fluids in turbulent boundary layer flows, and are preferable recognized by the distributions of turbulent kinetic energies and dissipations.

Keywords: closure model, gravity-driven flow, passive layer, turbulent boundary layer

1. Introduction

This paper continues Fang (2016b), hereafter referred to as Part I. The balance equations of the mean fields for *isothermal flows with incompressible grains* are summarized in the following

$$\begin{aligned}
 0 &= \dot{\nu} + \bar{\nu} \nabla \cdot \bar{\mathbf{v}} & \mathbf{0} &= \bar{\gamma} \bar{\nu} \dot{\bar{\mathbf{v}}} - \text{div}(\bar{\mathbf{t}} + \mathbf{R}) - \bar{\gamma} \bar{\nu} \bar{\mathbf{b}} \\
 0 &= \bar{\gamma} \bar{\nu} \ell \ddot{\bar{\nu}} - \nabla \cdot (\bar{\mathbf{h}} + \mathbf{H}) - \bar{\gamma} \bar{\nu} \bar{f} & \mathbf{0} &= \dot{\bar{\mathbf{Z}}} - \bar{\Phi} \quad (\dot{\bar{\mathbf{Z}}} \equiv \dot{\bar{\mathbf{Z}}} - [\bar{\Omega}, \bar{\mathbf{Z}}]) \\
 0 &= \bar{\gamma} \bar{\nu} \dot{k} - \mathbf{R} \cdot \bar{\mathbf{D}} - \nabla \cdot \mathbf{K} + \bar{\gamma} \bar{\nu} \varepsilon & 0 &= \bar{\gamma} \bar{\nu} \dot{s} - \ell \mathbf{H} \cdot \nabla \dot{\bar{\nu}} - \nabla \cdot \mathbf{L} + \bar{\gamma} \bar{\nu} H
 \end{aligned} \tag{1.1}$$

for which

$$\mathcal{P} = \{\bar{p}, \bar{\nu}, \bar{\mathbf{v}}, \bar{\mathbf{Z}}, \vartheta^M, \vartheta^T, \vartheta^G\} \quad \mathcal{C} = \{\bar{\mathbf{t}}, \mathbf{R}, \bar{\mathbf{h}}, \mathbf{H}, \bar{f}, \bar{\Phi}, k, s, \mathbf{K}, \mathbf{L}, \varepsilon, H\} \tag{1.2}$$

are introduced respectively as the primitive mean fields and closure relations based on the turbulent state space given by

$$\mathcal{Q} = \{\nu_0, \bar{\nu}, \dot{\bar{\nu}}, \mathbf{g}_1, \bar{\gamma} = c_1, \mathbf{g}_2, \vartheta^M = c_2, \mathbf{g}_3, \vartheta^T, \mathbf{g}_4, \vartheta^G, \mathbf{g}_5, \bar{\mathbf{D}}, \bar{\mathbf{Z}}\} \quad \mathcal{C} = \hat{\mathcal{C}}(\mathcal{Q}) \tag{1.3}$$

with c_1 and c_2 are constants, and $\mathbf{g}_2 = \mathbf{g}_3 = \mathbf{0}$. Quantities in (1.1)-(1.3) have been defined in Part I. Müller-Liu entropy principle has been investigated to derive the equilibrium closure relations, with the results summarized in Table 1, in which the subscript E denotes that the indexed quantity is evaluated at an equilibrium state, defined viz.,

$$\mathcal{Q}|_E \equiv (\nu_0, \bar{\nu}, 0, \mathbf{g}_1, c_1, \mathbf{0}, c_2, \mathbf{0}, \vartheta^T, \mathbf{0}, \vartheta^G, \mathbf{0}, \mathbf{0}, \bar{\mathbf{Z}}) \quad \mathcal{Q}^D \equiv (\dot{\bar{\nu}}, \mathbf{g}_3, \mathbf{g}_4, \mathbf{g}_5, \bar{\mathbf{D}}) \tag{1.4}$$

with \mathcal{Q}^D the dynamic sub-state space, upon which the dynamic closure relations should depend.

Table 1. Thermodynamically consistent equilibrium closure relations (Fang, 2016b)

$\psi^T = \hat{\psi}^T(\nu_0, \bar{\nu}, \nabla \bar{\nu}, \bar{\gamma} = c_1, \vartheta^M = c_2, \vartheta^T, \vartheta^G, \bar{\mathbf{Z}})$	$\bar{\beta} = \bar{\gamma} \bar{\nu} \psi_{\bar{\nu}}^T$	
$\bar{\gamma} \bar{\nu} k = \bar{\gamma} \bar{\nu} \vartheta^M \psi_{,\vartheta^T}^T$	$\bar{\gamma} \bar{\nu} s = \bar{\gamma} \bar{\nu} \vartheta^M \psi_{,\vartheta^G}^T$	
$\bar{\gamma} \bar{\nu} \varepsilon _E = 0$	$\bar{\gamma} \bar{\nu} H _E = 0$	$\bar{\Phi} _E = \mathbf{0}$
$\mathbf{K} _E = (\vartheta^M - \vartheta^T) \bar{\gamma} \bar{\nu} \varepsilon_{,\mathbf{g}_4} _E + (\vartheta^M - \vartheta^G) \bar{\gamma} \bar{\nu} H_{,\mathbf{g}_4} _E - \bar{\gamma} \bar{\nu} \vartheta^M \psi_{,\bar{\mathbf{Z}}}^T \cdot \bar{\Phi}_{,\mathbf{g}_4} _E$		
$\mathbf{L} _E = (\vartheta^M - \vartheta^T) \bar{\gamma} \bar{\nu} \varepsilon_{,\mathbf{g}_5} _E + (\vartheta^M - \vartheta^G) \bar{\gamma} \bar{\nu} H_{,\mathbf{g}_5} _E - \bar{\gamma} \bar{\nu} \vartheta^M \psi_{,\bar{\mathbf{Z}}}^T \cdot \bar{\Phi}_{,\mathbf{g}_5} _E$		
$\ell(\vartheta^M \bar{\mathbf{h}} + \vartheta^G \mathbf{H}) = \bar{\gamma} \bar{\nu} \vartheta^M \psi_{,\mathbf{g}_1}^T$	$\mathbf{H} = \ell \mathbf{R} \mathbf{g}_1$	
$\bar{f} _E = (\ell)^{-1} \left\{ (\bar{p} - \bar{\beta}) / (\bar{\gamma} \bar{\nu}) + (1 - \vartheta^T / \vartheta^M) \varepsilon_{,\dot{\nu}} _E + (1 - \vartheta^G / \vartheta^M) H_{,\dot{\nu}} _E - \psi_{,\bar{\mathbf{Z}}}^T \cdot \bar{\Phi}_{,\dot{\nu}} _E \right\}$		
$\bar{\mathbf{t}} _E = -\bar{\nu} \bar{p} \mathbf{I} - \bar{\gamma} \bar{\nu} \psi_{,\mathbf{g}_1}^T \otimes \mathbf{g}_1 + \bar{\gamma} \bar{\nu} \psi_{,\bar{\mathbf{Z}}}^T \cdot \bar{\Phi}_{,\bar{\mathbf{D}}} _E$		
$\mathbf{R} _E = -(\vartheta^M / \vartheta^T - 1) \bar{\gamma} \bar{\nu} \varepsilon_{,\mathbf{D}} _E - (\vartheta^M / \vartheta^T - \vartheta^G / \vartheta^T) \bar{\gamma} \bar{\nu} H_{,\mathbf{D}} _E$		

In Section 2, the dynamic responses of the closure relations are postulated by a quasi-static theory, followed by the specific postulates of the turbulent Helmholtz free energy, viscosities and the hypoplastic model for rate-independent characteristics. The established closure model is applied to analyses of a gravity-driven stationary avalanche down an incline in Section 3. Numerical simulations are compared with laminar flow solutions. The study is concluded in Section 4.

2. Zero-order closure model

2.1. Dynamic response

It is assumed that the closure relations consist of the equilibrium and dynamic parts viz.

$$\mathcal{C} = \mathcal{C}|_E + \mathcal{C}^D \quad \mathcal{C} \in \{\bar{\mathbf{t}}, \mathbf{R}, \bar{\Phi}, \mathbf{K}, \mathbf{L}, \bar{f}, \bar{\gamma} \bar{\nu} \varepsilon, \bar{\gamma} \bar{\nu} H\} \quad (2.1)$$

Specifically, $\bar{\mathbf{t}}^D$, \mathbf{R}^D , \bar{f}^D , $\bar{\gamma} \bar{\nu} \varepsilon^D$, $\bar{\gamma} \bar{\nu} H^D$, \mathbf{K}^D and \mathbf{L}^D are assumed to be the quasi-static expressions of \mathcal{Q}^D given by

$$\begin{aligned} \mathbf{0} &= \bar{\mathbf{t}}^D - \epsilon^M \dot{\nu} \mathbf{I} - \lambda^M (\text{tr } \bar{\mathbf{D}}) \mathbf{I} - 2\mu^M \bar{\mathbf{D}} & \mathbf{0} &= \mathbf{R}^D - \epsilon^T \dot{\nu} \mathbf{I} - \lambda^T (\text{tr } \bar{\mathbf{D}}) \mathbf{I} - 2\mu^T \bar{\mathbf{D}} \\ 0 &= \bar{f}^D + \zeta \dot{\nu} + \delta (\text{tr } \bar{\mathbf{D}}) & 0 &= \bar{\gamma} \bar{\nu} \varepsilon^D - f_1 \dot{\nu} - f_2 (\text{tr } \bar{\mathbf{D}}) - f_3 (\mathbf{g}_4 \cdot \mathbf{g}_4) \\ 0 &= \bar{\gamma} \bar{\nu} H^D - f_4 \dot{\nu} - f_5 (\text{tr } \bar{\mathbf{D}}) - f_6 (\mathbf{g}_5 \cdot \mathbf{g}_5) & \mathbf{0} &= \mathbf{K}^D + f_7 \mathbf{g}_4 \quad \mathbf{0} = \mathbf{L}^D + f_8 \mathbf{g}_5 \end{aligned} \quad (2.2)$$

with ϵ^M , ϵ^T , ζ , f_1 , f_3 , f_4 , f_{6-8} being scalar functions of $(\nu_0, \bar{\nu}, \bar{\gamma}, \vartheta^M, \vartheta^T, \vartheta^G)$; and λ^M , λ^T , δ , μ^M , μ^T , f_2 , f_5 scalar functions depending additionally on the three invariants ($I_{\bar{\mathbf{D}}}^1, I_{\bar{\mathbf{D}}}^2, I_{\bar{\mathbf{D}}}^3$) of $\bar{\mathbf{D}}$ given by $I_{\bar{\mathbf{D}}}^1 \equiv \text{tr } \bar{\mathbf{D}}$, $I_{\bar{\mathbf{D}}}^2 \equiv 0.5(\text{tr}^2 \bar{\mathbf{D}} - \text{tr } \bar{\mathbf{D}}^2)$ and $I_{\bar{\mathbf{D}}}^3 \equiv \det \bar{\mathbf{D}}$.

In equation (2.2), Truesdell's equi-presence principle is used, by which $(\vartheta^M \bar{\mathbf{t}}^D + \vartheta^T \mathbf{R}^D)$ and \bar{f}^D depend explicitly and linearly on $\dot{\nu}$ and $\bar{\mathbf{D}}$; $\bar{\gamma} \bar{\nu} \varepsilon^D$ and $\bar{\gamma} \bar{\nu} H^D$ depend explicitly and linearly on $\dot{\nu}$, $\bar{\mathbf{D}}$, \mathbf{g}_4 and \mathbf{g}_5 ; \mathbf{K}^D and \mathbf{L}^D depend explicitly and linearly on \mathbf{g}_4 and \mathbf{g}_5 , respectively, motivated by the Fourier law. Thus, a dry granular avalanche is considered a Stokes or Reiner-Rivlin fluid. Scalar functions μ^M and μ^T are respectively the *material viscosity* and *phenomenological (turbulent) viscosity* induced by turbulent fluctuation. Equation (2.2) has been applied for creeping, dense and rapid laminar flows, and for weak turbulent dense flows as the first approximation (Fang, 2008, 2009, 2016a; Fang and Wu, 2014; Kirchner and Teufel, 2002; Wang and Hutter, 1999).

2.2. Turbulent Helmholtz free energy, material and turbulent viscosities

It is assumed that ψ^T consists of an elastic part, ψ_e^T , and a rate-independent part, ψ_f^T , viz.

$$\psi^T = \psi_e^T(\nu_0, \bar{\nu}, \mathbf{g}_1, \bar{\gamma}, \vartheta^M, \vartheta^T, \vartheta^G) + \psi_f^T(I_{\bar{\mathbf{Z}}}^1, I_{\bar{\mathbf{Z}}}^2, I_{\bar{\mathbf{Z}}}^3) \quad (2.3)$$

with the irreversible effect confined within ψ_f^T (Fang, 2009; Kirchner and Teufel, 2002; Wang and Hutter, 1999). Following the previous works, ψ_e^T is assumed to be expanded in a Taylor series about $\bar{\nu} = \bar{\nu}_m$ and $|\mathbf{g}_1| = 0$, with $\bar{\nu}_m$ the critical mean volume fraction at which shearing is decoupled from dilatation, see Fang (2009), Savage (1993), Wang and Hutter (2001)

$$\begin{aligned} \psi_e^T &= \left\{ \alpha_0 (\bar{\nu} - \bar{\nu}_m)^2 + \beta_0 \left(\frac{\bar{\nu}_m}{\bar{\nu}_\infty - \bar{\nu}} \right)^2 \mathbf{g}_1 \cdot \mathbf{g}_1 \right\} \mathcal{F}_c \\ \mathcal{F}_c &= \sum_{n=0}^{n=2} \frac{1}{n!} \left\{ \left(\frac{\vartheta^T}{\vartheta^M} \right)^n + \left(\frac{\vartheta^G}{\vartheta^M} \right)^n \right\} - 1 \end{aligned} \quad (2.4)$$

with $\bar{\nu}_\infty$ the value of $\bar{\nu}$ corresponding to the densest possible packing of the grains, and $\{\alpha_0, \beta_0\}$ depending on $\{\bar{\nu}_m, \bar{\gamma}, \vartheta^M\}$. Equation (2.4) is an extension of its laminar flow counterpart with \mathcal{F}_c accounting for the influence of turbulent fluctuation, motivated by the nonlinear characteristics of rapid flows (Pudasaini and Hutter, 2007; Rao and Nott, 2008; Wang and Hutter, 2001). It asserts that smaller two-fold granular coldnesses result in smaller free energy.

The specific forms of the material viscosity μ^M and turbulent viscosity μ^T are given by

$$\mu^M = \mu_0 \bar{\gamma}^2 \left(\frac{\bar{\nu}_m}{\bar{\nu}_\infty - \bar{\nu}} \right)^8 \Xi \quad \mu^T = \mu_0 \bar{\gamma}^2 (\mathcal{F}_c - 1) \left(\frac{\bar{\nu}_m}{\bar{\nu}_\infty - \bar{\nu}} \right)^8 \Xi \quad (2.5)$$

with $\Xi = \hat{\Xi}(I_{\bar{\mathbf{D}}}^1, I_{\bar{\mathbf{D}}}^2, I_{\bar{\mathbf{D}}}^3)$, and $\mu_0 = \hat{\mu}_0(\nu_0, \vartheta^M)$, a positive constant. They are postulated followed by the previous works (Fang, 2009; Kirchner and Teufel, 2002), with the power 8 a curve-fitting (Savage, 1993), and the dependency of μ^T on ϑ^T and ϑ^G motivated by Newtonian fluids in turbulent flow. Both μ^M and μ^T assert that total stress is larger in turbulent flows than in laminar flows. For laminar flows, both ϑ^T and ϑ^G vanish, yielding the vanishing μ^T .

2.3. Hypoplasticity

A hypoplastic model of $\bar{\Phi}$ is given by (Fellin, 2013; Fuentes *et al.*, 2012; Niemunis *et al.*, 2009)

$$\bar{\Phi} = \hat{\Phi}(\bar{\nu}, \bar{\mathbf{D}}, \bar{\mathbf{Z}}) = f_s(\bar{\nu}, I_{\bar{\mathbf{Z}}}^1) \left\{ a^2 \bar{\mathbf{D}} + \check{\mathbf{Z}} \operatorname{tr}(\check{\mathbf{Z}} \bar{\mathbf{D}}) + f_d(\bar{\nu}) a (\check{\mathbf{Z}} + \check{\mathbf{Z}}^*) \|\bar{\mathbf{D}}\| \right\} \quad (2.6)$$

for rate-independent characteristics, with $\check{\mathbf{Z}} = \bar{\mathbf{Z}} / \operatorname{tr}(\bar{\mathbf{Z}})$, the versor of $\bar{\mathbf{Z}}$; $\check{\mathbf{Z}}^* = \check{\mathbf{Z}} - \mathbf{I}/3$, the deviator of $\check{\mathbf{Z}}$; $\|\bar{\mathbf{D}}\| = \sqrt{\operatorname{tr} \bar{\mathbf{D}}^2}$; and a a positive constant. The scalar functions f_s and f_d are respectively the stiffness and density factors. The constant a is related to the stress state $\bar{\mathbf{Z}}_c$ and frictional angle φ_c in the critical state, and can be determined empirically (Bauer and Herle, 2000; Buscamera, 2014; Marcher *et al.*, 2000). Equation (2.6) is used to account for the rate-independent features of dry granular systems, with the benefits that (1) distinction between loading and unloading is automatically accomplished, and (2) elastic/inelastic deformations need not *a priori* be distinguished; information about yield surface and plastic potential is no longer necessary.

2.4. Closure relations

With these, the closure relations of an isochoric flow are given by

$$\begin{aligned}
0 &= \bar{\gamma}\bar{\nu}k - \bar{\gamma}\bar{\nu}\left[\alpha_0(\bar{\nu} - \bar{\nu}_m)^2 + \beta_0\left(\frac{\bar{\nu}_m}{\bar{\nu}_\infty - \bar{\nu}}\right)^2(\mathbf{g}_1 \cdot \mathbf{g}_1)\right]\left(1 + \frac{\vartheta^T}{\vartheta^M}\right) \\
0 &= \bar{\gamma}\bar{\nu}\varepsilon - f_1\dot{\bar{\nu}} - f_2(\text{tr } \bar{\mathbf{D}}) - f_3(\mathbf{g}_4 \cdot \mathbf{g}_4) \\
0 &= \bar{\gamma}\bar{\nu}H - f_4\dot{\bar{\nu}} - f_5(\text{tr } \bar{\mathbf{D}}) - f_6(\mathbf{g}_5 \cdot \mathbf{g}_5) \\
0 &= \bar{\gamma}\bar{\nu}s - \bar{\gamma}\bar{\nu}\left[\alpha_0(\bar{\nu} - \bar{\nu}_m)^2 + \beta_0\left(\frac{\bar{\nu}_m}{\bar{\nu}_\infty - \bar{\nu}}\right)^2(\mathbf{g}_1 \cdot \mathbf{g}_1)\right]\left(1 + \frac{\vartheta^G}{\vartheta^M}\right) \\
\mathbf{0} &= \ell(\vartheta^M \bar{\mathbf{h}} + \vartheta^G \mathbf{H}) - 2\beta_0 \bar{\gamma}\bar{\nu}\vartheta^M \mathcal{F}_c \left(\frac{\bar{\nu}_m}{\bar{\nu}_\infty - \bar{\nu}}\right)^2 \mathbf{g}_1 \\
\mathbf{0} &= \mathbf{K} + f_7 \mathbf{g}_4 \quad \mathbf{0} = \mathbf{L} + f_8 \mathbf{g}_5 \\
0 &= \bar{f} - \frac{\bar{p}}{\bar{\gamma}\bar{\nu}\ell} + \frac{2}{\ell}\left[\alpha_0(\bar{\nu} - \bar{\nu}_m) + \frac{\beta_0 \bar{\nu}_m^2}{(\bar{\nu}_\infty - \bar{\nu})^3}(\mathbf{g}_1 \cdot \mathbf{g}_1)\right]\mathcal{F}_c - \left(1 - \frac{\vartheta^T}{\vartheta^M}\right)\frac{f_1}{\bar{\gamma}\bar{\nu}\ell} \\
&\quad - \left(1 - \frac{\vartheta^G}{\vartheta^M}\right)\frac{f_4}{\bar{\gamma}\bar{\nu}\ell} + \zeta\dot{\bar{\nu}} + \delta(\text{tr } \bar{\mathbf{D}}) \\
\mathbf{0} &= \bar{\mathbf{t}} - (-\bar{\nu}p + \epsilon^M \dot{\bar{\nu}} + \lambda^M \text{tr } \bar{\mathbf{D}})\mathbf{I} - f_s(\zeta_1 \mathbf{I} + \zeta_2 \bar{\mathbf{Z}} + \zeta_3 \bar{\mathbf{Z}}^2) \\
&\quad + 2\beta_0 \bar{\gamma}\bar{\nu}\mathcal{F}_c \left(\frac{\bar{\nu}_m}{\bar{\nu}_\infty - \bar{\nu}}\right)^2 \mathbf{g}_1 \otimes \mathbf{g}_1 - 2\mu_0 \bar{\gamma}^2 \left(\frac{\bar{\nu}_m}{\bar{\nu}_\infty - \bar{\nu}}\right)^8 \sqrt{|I_{\bar{\mathbf{D}}}^2|} \bar{\mathbf{D}} \\
\mathbf{0} &= \mathbf{R} - \left[-\left(\frac{\vartheta^M}{\vartheta^T} - 1\right)f_2 - \left(\frac{\vartheta^M}{\vartheta^T} - \frac{\vartheta^G}{\vartheta^T}\right)f_5 + \epsilon^T \dot{\bar{\nu}} + \lambda^T \text{tr } \bar{\mathbf{D}}\right]\mathbf{I} \\
&\quad - 2\mu_0 \bar{\gamma}^2 (\mathcal{F}_c - 1) \left(\frac{\bar{\nu}_m}{\bar{\nu}_\infty - \bar{\nu}}\right)^8 \sqrt{|I_{\bar{\mathbf{D}}}^2|} \bar{\mathbf{D}}
\end{aligned} \tag{2.7}$$

where the Cayley-Hamilton theorem and the notations

$$\begin{aligned}
c_1 &= \psi_{f, I_{\bar{\mathbf{Z}}}^1}^T & c_2 &= \psi_{f, I_{\bar{\mathbf{Z}}}^2}^T & c_3 &= \psi_{f, I_{\bar{\mathbf{Z}}}^3}^T \\
(I_{\bar{\mathbf{Z}}}^1)_{, \bar{\mathbf{Z}}} &= \mathbf{I} & (I_{\bar{\mathbf{Z}}}^2)_{, \bar{\mathbf{Z}}} &= I_{\bar{\mathbf{Z}}}^1 \mathbf{I} - \bar{\mathbf{Z}} & (I_{\bar{\mathbf{Z}}}^3)_{, \bar{\mathbf{Z}}} &= I_{\bar{\mathbf{Z}}}^2 \bar{\mathbf{Z}}^{-1} \\
\zeta_1 &= a^2(c_1 + c_2 I_{\bar{\mathbf{Z}}}^1) - c_3 a^2 I_{\bar{\mathbf{Z}}}^2 I_{\bar{\mathbf{Z}}}^3 & \zeta_3 &= c_3 a^2 (I_{\bar{\mathbf{Z}}}^3)^2 \\
\zeta_2 &= (c_1 + c_2 I_{\bar{\mathbf{Z}}}^1)(I_{\bar{\mathbf{Z}}}^1)^{-1} - c_2(a^2 + (I_{\bar{\mathbf{Z}}}^1)^{-2} \text{tr } \bar{\mathbf{Z}}^2) + c_3 I_{\bar{\mathbf{Z}}}^3 (3(I_{\bar{\mathbf{Z}}}^1)^{-2} + a^2 I_{\bar{\mathbf{Z}}}^1)
\end{aligned} \tag{2.8}$$

have been used. For laminar flows, (2.7) reduce to those in previous work (Fang, 2009). Two-fold turbulent kinetic energies in (2.7)₁ and (2.7)₄ are determined once $\bar{\nu}$ is known.

The field equations of $\{\bar{p}, \bar{\mathbf{v}}, \bar{\nu}, \vartheta^T, \vartheta^G, \bar{\mathbf{Z}}\}$ are obtained by substituting (2.7) into (1.1). Since the system is mathematically likely well-posed, one has the chance to obtain the primitive mean fields. In applying (2.7), the phenomenological parameters $\alpha_0, \beta_0, f_{1-8}, f_s, f_d, a, \epsilon^M, \lambda^M, \epsilon^T, \lambda^T, \mu_0, \zeta_{1-3}, \bar{\nu}_m$ and $\bar{\nu}_\infty$ need be prescribed. Since detailed information of them is insufficient, numerical simulation is restricted to a parametric study.

3. Gravity-driven flow

3.1. Field equations and boundary conditions

Consider a fully-developed, isochoric, two-dimensional *stationary avalanche* down an incline, as shown in Fig. 1. It is assumed that

$$\begin{aligned}
\bar{\mathbf{v}} &= [\bar{u}(y), \bar{v}(y), 0] & \bar{\nu} &= \bar{\nu}(y) & \bar{p} &= \bar{p}(y) \\
\vartheta^T &= \vartheta^T(y) & \vartheta^G &= \vartheta^G(y) & \bar{Z}_{ij} &= \bar{Z}_{ij}(y)
\end{aligned} \tag{3.1}$$

with $\bar{v}/\bar{u} \sim 0$; $u' \neq 0$, $v' \neq 0$; $\{i, j\} = (x, y)$, motivated by the assumptions that $\alpha_{,x} \ll \alpha_{,y}$ for any quantity α in simple turbulent shear flows of Newtonian fluids (Batchelor, 1993). The flow corresponds to the *critical state* defined as the state in which $\dot{\bar{\rho}} = 0$ and $\dot{\bar{\mathbf{Z}}} = \mathbf{0}$ (Ai *et al.*, 2014; Kirchner and Teufel, 2002). Since in the critical state f_d is set to be unity, equations (1.1)₄ and (2.6) reduce to

$$\mathbf{0} = f_s \left\{ a_c^2 \bar{\mathbf{D}} + \check{\bar{\mathbf{Z}}} \operatorname{tr}(\check{\bar{\mathbf{Z}}}\bar{\mathbf{D}}) + a_c(\check{\bar{\mathbf{Z}}} + \check{\bar{\mathbf{Z}}}^*) \|\bar{\mathbf{D}}\| \right\} \quad (3.2)$$

with $a_c = \sqrt{8/27} \sin \varphi_c$, and φ_c the critical friction angle (Kirchner and Teufel, 2002). Since f_s does not vanish generally, substituting (3.1) into (3.2) yields

$$\begin{aligned} 0 &= \check{\bar{Z}}_{xx} \check{\bar{Z}}_{xy} m + a_c \left(2\check{\bar{Z}}_{xx} - \frac{1}{3} \right) & 0 &= \check{\bar{Z}}_{yy} \check{\bar{Z}}_{xy} m + a_c \left(2\check{\bar{Z}}_{yy} - \frac{1}{3} \right) \\ 0 &= a_c^2 m + \check{\bar{Z}}_{xy}^2 m + 2a_c \check{\bar{Z}}_{xy} \end{aligned} \quad (3.3)$$

with $m \equiv \bar{D}_{xy}/\|\bar{\mathbf{D}}\| = \bar{D}_{xy}/|\bar{D}_{xy}|$. A non-trivial solution to (3.3) is only that $\bar{Z}_{xx} = \bar{Z}_{yy}$ and $\bar{Z}_{xy} = -m\sqrt{8/3} \sin \varphi_c \bar{Z}_{yy}$. Thus, equation (1.1)₄ is decoupled from other mean balance equations. For further identification, a specific form of f_s is given by (Bauer and Herle, 2000)

$$f_s = \left(\frac{1 - \bar{v}_s}{1 - \bar{v}} \right)^m \quad m = 1 \quad (3.4)$$

with \bar{v}_s the minimum mean volume fraction; and unity power justified for most cases (Herle and Gudehus, 2000; Marcher *et al.*, 2000; Niemunis *et al.*, 2009).

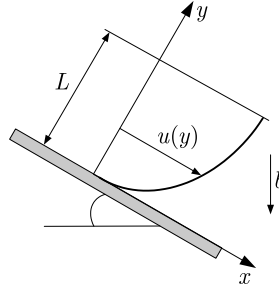


Fig. 1. Gravity-driven stationary avalanche down an incline and the coordinate

With these, the field equations are obtained

$$\begin{aligned} 0 &= \frac{d}{dy} \left\{ \frac{1 - \bar{v}_s}{1 - \bar{v}} (\zeta_2 \bar{Z}_{xy} + \zeta_3 \bar{Z}_{xy}^2) + \mu_0 \bar{\gamma}^2 \mathcal{F}_c \left(\frac{\bar{v}_m}{\bar{v}_\infty - \bar{v}} \right)^8 \left(\frac{d\bar{u}}{dy} \right)^2 \right\} + \bar{\gamma} \bar{v} b \sin \theta \\ 0 &= \frac{d\bar{t}_{yy}}{dy} - \bar{\gamma} \bar{v} \cos \theta \\ 0 &= \frac{d}{dy} \left\{ \frac{2\beta_0 \bar{\gamma} \bar{v} \mathcal{F}_c}{\ell} \left(\frac{\bar{v}_m}{\bar{v}_\infty - \bar{v}} \right)^2 \frac{d\bar{v}}{dy} \right\} + \frac{1}{\bar{v} \ell} \left\{ -\bar{t}_{yy} + \frac{1 - \bar{v}_s}{1 - \bar{v}} l (\zeta_1 + \zeta_2 \bar{Z}_{yy} + \zeta_3 \bar{Z}_{yy}^2) \right. \\ &\quad \left. - 2\alpha_0 \bar{\gamma} \bar{v}^2 (\bar{v} - \bar{v}_m) \mathcal{F}_c - 2\beta_0 \bar{\gamma} \bar{v} \left(\frac{\bar{v}_m}{\bar{v}_\infty - \bar{v}} \right)^2 \left(\frac{d\bar{v}}{dy} \right)^2 \frac{\bar{v}_\infty \mathcal{F}_c}{\bar{v}_\infty - \bar{v}} \right\} \\ 0 &= \mu_0 \bar{\gamma}^2 (\mathcal{F}_c - 1) \left(\frac{\bar{v}_m}{\bar{v}_\infty - \bar{v}} \right)^8 \left(\frac{d\bar{u}}{dy} \right)^3 - f_7 \frac{d^2 \vartheta^T}{dy^2} - f_3 \left(\frac{d\vartheta^T}{dy} \right)^2 \\ 0 &= -f_8 \frac{d^2 \vartheta^G}{dy^2} - f_6 \left(\frac{d\vartheta^G}{dy} \right)^2 \end{aligned} \quad (3.5)$$

for $\bar{u}(y)$, $\bar{v}(y)$, $\bar{t}_{yy}(y)$, $\vartheta^T(y)$ and $\vartheta^G(y)$, in which $\bar{p}(y)$ is replaced by $\bar{t}_{yy}(y)$ for simplicity.

Although solid boundaries have been demonstrated to act as energy sources and sinks of the turbulent kinetic energy of the grains (e.g. Pudasaini and Hutter, 2007; Richman and Marciniec, 1990), and the conventional no-slip condition for \bar{u} does not hold (Savage, 1993). The field observations suggest that the no-slip condition can still be used as the first approximation (Pudasaini and Hutter, 2007; Rao and Nott, 2008), with which a fixed value of \bar{v} is assumed. As motivated by the finite turbulent kinetic energies and dissipations on solid boundaries of Newtonian fluids in turbulent boundary layer flows (Batchelor, 1993; Tsinober, 2009), finite two-fold turbulent kinetic energies and dissipations on the plane are assumed through the prescriptions of ϑ^T and ϑ^G , respectively. On the other hand, field observations suggest that the grains on the free surface interlock with one another to form a kind of inelastic network. Due to a significant density difference between the grains and the air, the shear stress is negligible, yielding vanishing normal gradients of \bar{u} and \bar{v} . However, the air entrainment on the free surface provides a finite normal stress, giving a rise to nonvanishing \bar{t}_{yy} and normal gradients of ϑ^T and ϑ^G (Pudasaini and Hutter, 2007; Rao and Nott, 2008; Wang and Hutter, 2001). Thus, BCs for (3.5) are postulated by:

— for $y = 0$

$$\bar{u} = 0 \quad \bar{v} = \bar{v}_b \quad \vartheta^T = \vartheta_b^T \quad \vartheta^G = \vartheta_b^G \tag{3.6}$$

— for $y = L$

$$\frac{d\bar{u}}{dy} = 0 \quad \frac{d\bar{v}}{dy} = 0 \quad \frac{d\vartheta^T}{dy} = a_T \quad \frac{d\vartheta^G}{dy} = a_G \quad \bar{t}_{yy} = \bar{t}_b \tag{3.7}$$

with the superscript b denoting the boundary values.

3.2. Nondimensionalisation

With the dimensionless parameters defined in Table 2, in which V_0 is the characteristic velocity of the flow, equations (3.5) are recast in dimensionless forms

$$\begin{aligned} 0 &= \frac{d}{d\tilde{y}} \left\{ \frac{1 - \bar{v}_m \tilde{v}_s}{1 - \bar{v}_m \tilde{v}} \Xi_1 + \frac{\tilde{\mathcal{F}}_c}{(\tilde{v}_\infty - \tilde{v})^8} \left(\frac{d\tilde{u}}{d\tilde{y}} \right)^2 \right\} + S_1 \tilde{v} \sin \theta \\ 0 &= \frac{d\tilde{\pi}}{d\tilde{y}} + S_2 \tilde{v} \cos \theta \\ 0 &= \frac{d}{d\tilde{y}} \left\{ \frac{2\tilde{v} \tilde{\mathcal{F}}_c}{(\tilde{v}_\infty - \tilde{v})^2} \frac{d\tilde{v}}{d\tilde{y}} \right\} + \frac{1}{\tilde{v}} \left\{ \tilde{\pi} + \frac{1 - \bar{v}_m \tilde{v}_s}{1 - \bar{v}_m \tilde{v}} \Xi_2 - 2\tilde{v}^2 (\tilde{v} - 1) - \frac{2\tilde{v} \tilde{v}_\infty \tilde{\mathcal{F}}_c}{(\tilde{v}_\infty - \tilde{v})^3} \left(\frac{d\tilde{v}}{d\tilde{y}} \right)^2 \right\} \\ 0 &= \frac{\chi_1 (\tilde{\mathcal{F}}_c - 1)}{(\tilde{v}_\infty - \tilde{v})^8} \left(\frac{d\tilde{u}}{d\tilde{y}} \right)^3 - \frac{d^2 \tilde{\vartheta}^T}{d\tilde{y}^2} - \chi_2 \left(\frac{d\tilde{\vartheta}^T}{d\tilde{y}} \right)^2 \\ 0 &= -\frac{d^2 \tilde{\vartheta}^G}{d\tilde{y}^2} - \chi_3 \left(\frac{d\tilde{\vartheta}^G}{d\tilde{y}} \right)^2 \end{aligned} \tag{3.8}$$

for $\tilde{u}(\tilde{y})$, $\tilde{v}(\tilde{y})$, $\tilde{\pi}(\tilde{y})$, $\tilde{\vartheta}^T(\tilde{y})$ and $\tilde{\vartheta}^G(\tilde{y})$, with $\tilde{\mathcal{F}}_c = 1 + \tilde{\vartheta}^T + \tilde{\vartheta}^G + (\tilde{\vartheta}^T)^2 + (\tilde{\vartheta}^G)^2$, and the dimensionless BCs:

— for $\tilde{y} = 0$

$$\tilde{u} = 0 \quad \tilde{v} = \tilde{v}_b \quad \tilde{\vartheta}^T = \tilde{\vartheta}_b^T \quad \tilde{\vartheta}^G = \tilde{\vartheta}_b^G \tag{3.9}$$

— for $\tilde{y} = \tilde{L}$

$$\frac{d\tilde{u}}{d\tilde{y}} = 0 \quad \frac{d\tilde{v}}{d\tilde{y}} = 0 \quad \frac{d\tilde{\vartheta}^T}{d\tilde{y}} = \tilde{a}_T \quad \frac{d\tilde{\vartheta}^G}{d\tilde{y}} = \tilde{a}_G \quad \tilde{\pi} = \tilde{\pi}_b \tag{3.10}$$

Table 2. Dimensionless parameters

$\xi^2 = \frac{\alpha_0}{\beta_0} = \frac{1}{\ell^2}$	$\tilde{y} = \xi y$	$\tilde{L} = \xi L$	$\tilde{\nu} = \frac{\bar{\nu}}{\bar{\nu}_m}$	$\tilde{u} = \frac{\bar{u}}{V_0}$
$\tilde{\nu}_\infty = \frac{\bar{\nu}_\infty}{\bar{\nu}_m}$	$\tilde{n}u_b = \frac{\bar{\nu}_b}{\bar{\nu}_m}$	$\tilde{\vartheta}^T = \frac{\vartheta^T}{\vartheta^M}$	$\tilde{\vartheta}^G = \frac{\vartheta^G}{\vartheta^M}$	
$\Xi_1 = \frac{\zeta_2 \bar{Z}_{xy} + \zeta_3 \bar{Z}_{xy}^2}{\mu_0 \bar{\gamma}^2 V_0^2 \xi^2}$	$\Xi_2 = \frac{\zeta_1 + \zeta_2 \bar{Z}_{yy} + \zeta_3 \bar{Z}_{yy}^2}{\alpha_0 \bar{\gamma} \bar{\nu}_m^3}$	$S_1 = \frac{\bar{\nu}_m b}{\mu_0 \bar{\gamma} V_0^2 \xi^3}$		
$S_2 = \frac{b}{\alpha_0 \bar{\nu}_m^2 \xi}$	$\chi_1 = \frac{\mu_0 \bar{\gamma} V_0^3 \xi}{f_7 \vartheta^M}$	$\chi_2 = \frac{f_3 \vartheta^M}{f_7}$	$\chi_3 = \frac{f_6 \vartheta^M}{f_8}$	
$\tilde{\pi} = \frac{-\bar{t}_{yy}}{\alpha_0 \bar{\gamma} \bar{\nu}_m^3}$	$\tilde{\nu}_s = \frac{\bar{\nu}_s}{\bar{\nu}_m}$	$\tilde{\pi}_b = \frac{-\bar{t}_b}{\alpha_0 \bar{\gamma} \bar{\nu}_m^3}$	$\tilde{\vartheta}_b^T = \frac{\vartheta_b^T}{\vartheta^M}$	
$\tilde{\vartheta}_b^G = \frac{\vartheta_b^G}{\vartheta^M}$	$\tilde{a}_T = \frac{a_T}{\vartheta^M \xi}$	$\tilde{a}_G = \frac{a_G}{\vartheta^M \xi}$		

Equations (3.8)-(3.10) define a nonlinear BVP, with \tilde{L} being the effect of flow thickness; S_2 the effect of gravity; S_1 the influence of viscosity for fixed S_2 ; Ξ_1 and Ξ_2 the hypoplastic effect; χ_1 the relative contribution between viscosity and turbulent kinetic energy flux; χ_2 and χ_3 the relative significances between two-fold turbulent kinetic energy fluxes and dissipations. For implementation of numerical simulation, the values of $\bar{\nu}_m$, $\bar{\nu}_b$, $\bar{\nu}_\infty$ and $\bar{\nu}_s$ are given by $\bar{\nu}_b = 0.51$, $\bar{\nu}_m = 0.555$, $\bar{\nu}_\infty = 0.644$, $\bar{\nu}_s = 0.25$ (thus, $\tilde{\nu}_b = 0.919$, $\tilde{\nu}_\infty = 1.16$, $\tilde{\nu}_s = 0.451$), with fixed values of ϑ_b^T , ϑ_b^G and \bar{t}_b assumed as a first approximation (Bauer and Herle, 2000; Fang and Wu, 2014; Savage, 1993; Wang and Hutter, 1999).

Two-point nonlinear BVP (3.8)-(3.10) is solved numerically by using the iterative methods with a successive under-relaxation scheme (Fang and Wu, 2014; Wang and Hutter, 1999; Wendt, 2009). So, sequences of the primitive mean fields are calculated at each iteration step, which are incorporated into the next step, until demanded convergence is reached. Moreover, integrating last Eq. (3.8) yields an analytical solution of $\tilde{\vartheta}^G(\tilde{y})$ under a fixed value of χ_3 , viz., $\tilde{\vartheta}^G = \tilde{\vartheta}_b^G + \chi_3^{-1} \ln((1 - \tilde{a}_G \chi_3 (\tilde{L} - \tilde{y})) / (1 - \tilde{a}_G \chi_3 \tilde{L}))$, indicating that $\tilde{\vartheta}^G$ increases logarithmically from the plane toward the free surface, and corresponding to the previous works (Fang, 2009, 2016b; Fang and Wu, 2014).

3.3. Numerical results

Numerical tests show that only the relative magnitudes of the $\tilde{\nu}$ -, \tilde{u} -, $\tilde{\vartheta}^T$ - and ϑ^G -profiles are influenced by the variations in S_1 and χ_{1-3} , but the tendencies remain unchanged. Thus, $S_1 = 0.02$ and $\chi_1 = \chi_2 = \chi_3 = 0.01$ are used, with $\tilde{\vartheta}_b^T = \tilde{\vartheta}_b^G = 0.1$ for finite turbulent kinetic energies and dissipations on the boundary (Pudasaini and Hutter, 2007; Rao and Nott, 2008). Since Ξ_1 and Ξ_2 are of equal importance (Fang, 2009; Kirchner and Teufel, 2002), they are set equal. In all figures, the normalized calculated values are displayed for comparison.

Figure 2 illustrates the profiles of $\tilde{\nu}$, \tilde{u} , $\tilde{\gamma} \tilde{\nu}_s$, $\tilde{\gamma} \tilde{\nu} k$, $\tilde{\gamma} \tilde{\nu} H$ and $\tilde{\gamma} \tilde{\nu} \varepsilon$ for variations in $\tilde{L} = [10, 15, 20]$ indicated by the arrows, with $\tilde{a}_T = \tilde{a}_G = 0.1$, $\Xi_1 = \Xi_2 = 0.01$, $\tilde{\pi}_b = 0.01$ and $S_2 = 0.02$. The solid lines are the simulated results; the dashed lines are the laminar flow solutions from Fang (2009); the dotted line are Newtonian fluid characteristics in a laminar flow. Increasing \tilde{L} tends to enlarge the difference in $\tilde{\nu}$ between the free surface and plane, as shown in Fig. 2a. This results from the weight of the granular body: when the flow is thicker, larger compressive stress applies on the grains in the thin layer immediately above the plane (the *turbulent boundary layer*, *TBL*), with maximum shearing there, causing the grains to collide intensively with one another and resulting in smaller values of $\tilde{\nu}$. Above this thin layer, there exists a relatively thick layer (the *passive layer*, *PL*), in which the grains form a kind of inelastic network and behave as a lump

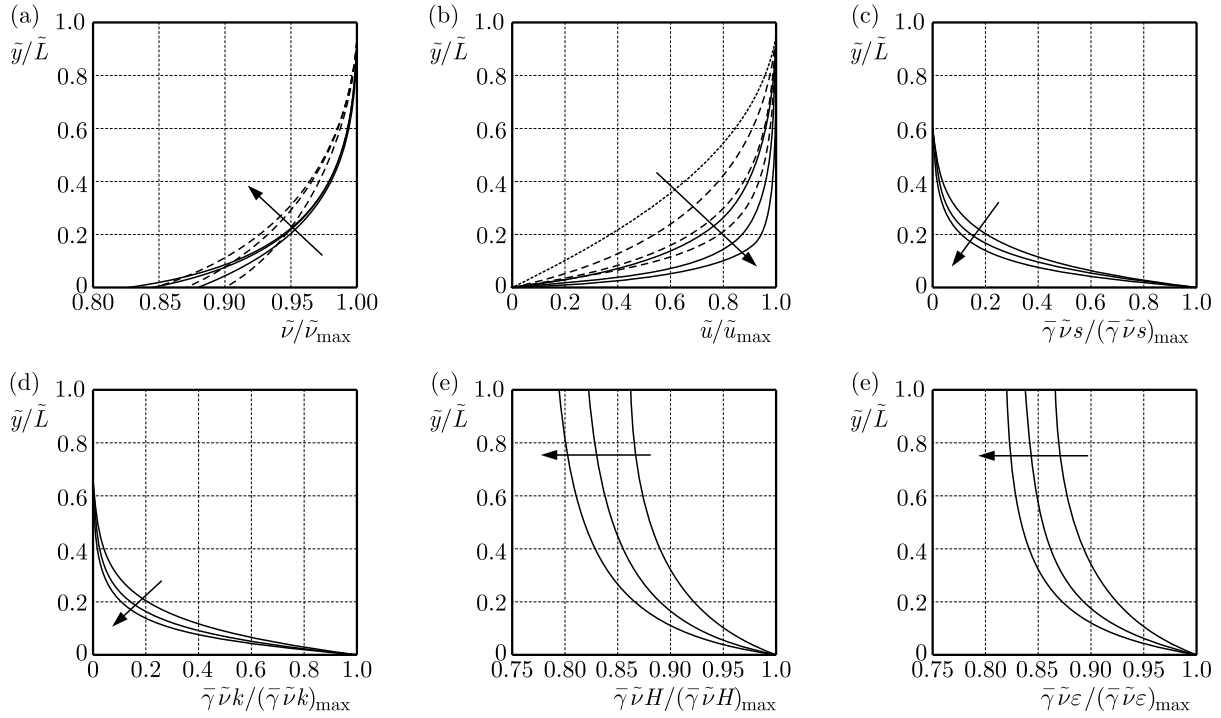


Fig. 2. Normalized profiles of \tilde{v} , \tilde{u} , $\bar{\gamma}\tilde{\nu}s$, $\bar{\gamma}\tilde{\nu}k$, $\bar{\gamma}\tilde{\nu}H$, $\bar{\gamma}\tilde{\nu}\varepsilon$, with $\tilde{L} = [10, 15, 20]$ indicated by the arrows. Dashed lines: laminar flow solutions; dotted line: laminar Newtonian flow

solid with nearly uniform \tilde{v} and \tilde{u} , as displayed in Figs. 2a and 2b. As \tilde{L} increases, the TBL becomes thinner with larger \tilde{u} -gradients at the interface between two layers. When compared with laminar flow solutions, the \tilde{v} - and \tilde{u} -profiles are more convex, with larger amplitudes in the PL. These are due to the influence of turbulent kinetic energy and dissipation, to be discussed later.

Two-fold turbulent kinetic energies in Figs. 2c and 2d decrease from their maximum values in the plane toward *nearly vanishing values* on the free surface exponentially. Similar tendencies appear for the profiles of $\bar{\gamma}\tilde{\nu}H$ and $\bar{\gamma}\tilde{\nu}\varepsilon$ in Figs. 2e and 2f, except for *finite* values on the free surface. As \tilde{L} increases, $\bar{\gamma}\tilde{\nu}s$, $\bar{\gamma}\tilde{\nu}k$, $\bar{\gamma}\tilde{\nu}H$ and $\bar{\gamma}\tilde{\nu}\varepsilon$ decrease more obviously. These correspond not only to those of Newtonian fluids in turbulent boundary layer flows, but also are justified, for turbulent kinetic energy and dissipation should assume maximum values in the regions where shearing is maximum, and a larger turbulent kinetic energy induces larger turbulent dissipation (Batchelor, 1993; Tsinober, 2009). Although in Newtonian fluids and dry granular avalanches the turbulent kinetic energies and dissipations evolve in a similar manner, their vanishing values on the free surface are identified for Newtonian fluids, while it is not so for dry granular avalanches. These reflect the discrete nature of dry granular systems.

Although the TBL and PL can be identified by the profiles of ν and u in laminar formulations (e.g. Fang, 2009; Wang and Hutter, 1999), they are preferably recognized by the distributions of $\bar{\gamma}\tilde{\nu}s$, $\bar{\gamma}\tilde{\nu}k$, $\bar{\gamma}\tilde{\nu}H$ and $\bar{\gamma}\tilde{\nu}\varepsilon$. In the PL, the dominant grain-grain interaction is the long-term one, causing the grains to form a kind of inelastic network to yield nearly vanishing $\bar{\gamma}\tilde{\nu}s$ and $\bar{\gamma}\tilde{\nu}k$, and finite $\bar{\gamma}\tilde{\nu}H$ and $\bar{\gamma}\tilde{\nu}\varepsilon$. On the other hand, the grains in the TBL are dominated by the short-term interaction, giving a rise to intensive turbulent fluctuation with significant $\bar{\gamma}\tilde{\nu}s$, $\bar{\gamma}\tilde{\nu}k$, $\bar{\gamma}\tilde{\nu}H$ and $\bar{\gamma}\tilde{\nu}\varepsilon$, resulting in larger \tilde{v} and \tilde{u} in the PL, when compared with laminar flow solutions.

Figure 3 illustrates the profiles of \tilde{v} , \tilde{u} , $\bar{\gamma}\tilde{\nu}s$, $\bar{\gamma}\tilde{\nu}k$, $\bar{\gamma}\tilde{\nu}H$ and $\bar{\gamma}\tilde{\nu}\varepsilon$ for variations in $S_2 = [0.01, 0.035, 0.07]$ indicated by the arrows, with $\tilde{a}_T = \tilde{a}_G = 0.1$, $\tilde{L} = 15$, $\Xi_1 = \Xi_2 = 0.01$ and $\tilde{\pi}_b = 0.01$. Increasing S_2 tends to enhance the gravitational effect, resulting in more convex \tilde{v} - and \tilde{u} -profiles in Figs. 3a and 3b. This goes back to the influence of a larger grain weight. As

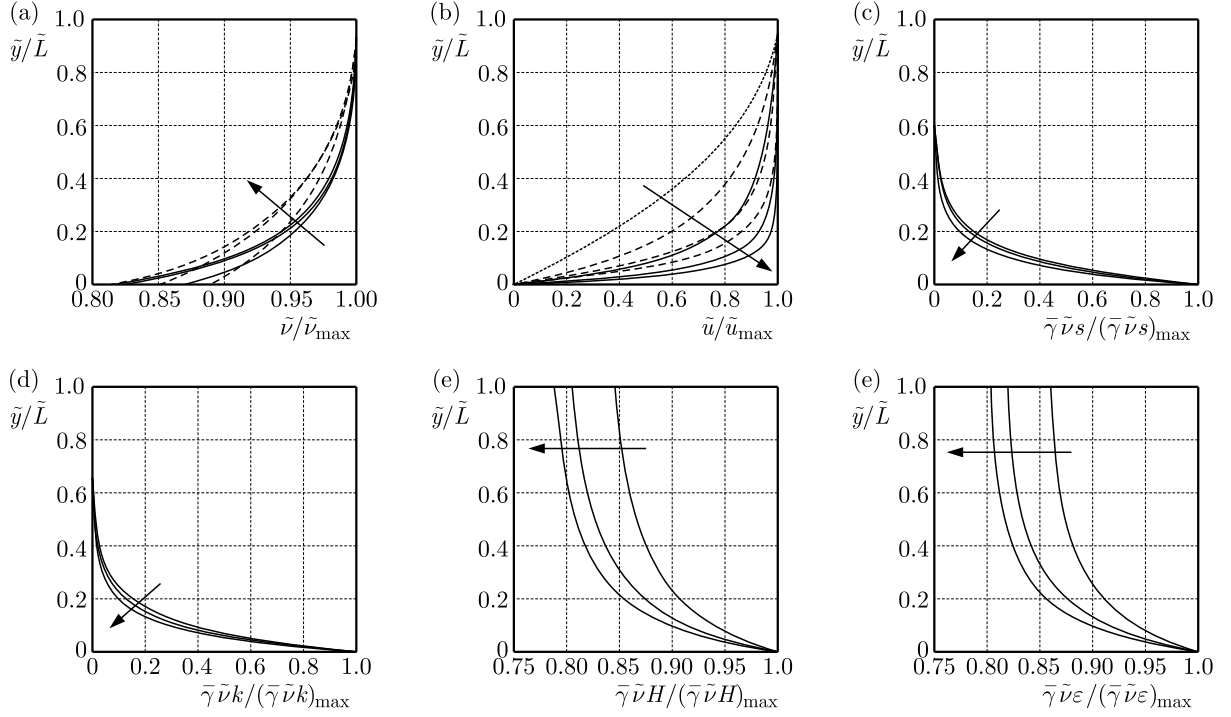


Fig. 3. Normalized profiles of $\tilde{\nu}$, \tilde{u} , $\tilde{\gamma}\tilde{\nu}s$, $\tilde{\gamma}\tilde{\nu}k$, $\tilde{\gamma}\tilde{\nu}H$, $\tilde{\gamma}\tilde{\nu}\epsilon$, with $S_2 = [0.01, 0.035, 0.07]$ indicated by the arrows. Dashed lines: laminar flow solutions; dotted line: laminar Newtonian flow

S_2 increases, most $\tilde{\gamma}\tilde{\nu}s$, $\tilde{\gamma}\tilde{\nu}k$, $\tilde{\gamma}\tilde{\nu}H$ and $\tilde{\gamma}\tilde{\nu}\epsilon$ are confined within even thinner TBLs, resulting in more energetic grain collisions there, as shown in Figs. 3c-3f. In addition, $\tilde{\gamma}\tilde{\nu}s$, $\tilde{\gamma}\tilde{\nu}k$, $\tilde{\gamma}\tilde{\nu}H$ and $\tilde{\gamma}\tilde{\nu}\epsilon$ evolve with similar tendencies described in Fig. 2. Due to the distributions of two-fold turbulent kinetic energies, the $\tilde{\nu}$ - and \tilde{u} -profiles are more convex than their laminar-flow counterparts.

The influence of $\tilde{\pi}_b$ is summarized in Fig. 4, with $\tilde{a}_T = \tilde{a}_G = 0.1$, $\Xi_1 = \Xi_2 = 0.01$, $\tilde{L} = 15$, $S_2 = 0.02$ and $\tilde{\pi}_b = [0.01, 0.1, 0.25]$ indicated by the arrows. Increasing $\tilde{\pi}_b$ is to apply larger normal traction on the free surface, exciting the grains in the TBL to collide with one another more vigorously. This reduces base friction, resulting in more convex $\tilde{\nu}$ - and \tilde{u} -profiles in Figs. 4a and 4b, and thicker PLs. Figures 4c-4f show that as $\tilde{\pi}_b$ increases, $\tilde{\gamma}\tilde{\nu}s$, $\tilde{\gamma}\tilde{\nu}k$, $\tilde{\gamma}\tilde{\nu}H$ and $\tilde{\gamma}\tilde{\nu}\epsilon$ are confined mostly in the TBL and decrease exponentially from the plane toward the free surface. The profiles of $\tilde{\nu}$ and \tilde{u} are more convex than their laminar flow counterparts due to the influences of $\tilde{\gamma}\tilde{\nu}s$, $\tilde{\gamma}\tilde{\nu}k$, $\tilde{\gamma}\tilde{\nu}H$ and $\tilde{\gamma}\tilde{\nu}\epsilon$.

Simulations for variations in Ξ_1 and Ξ_2 are summarized in Fig. 5, with $\Xi_1 = \Xi_2 = [0.01, 0.05, 0.1]$ indicated by the arrows; $\tilde{a}_T = \tilde{a}_G = 0.1$, $\tilde{\pi}_b = 0.01$, $\tilde{L} = 15$ and $S_2 = 0.02$. When Ξ_1 and Ξ_2 increase, the hypoplastic effect inside a granular RVE is enhanced, which weakens the frictional contact between the grains in the TBL, giving a rise to reduced $\tilde{\gamma}\tilde{\nu}s$, $\tilde{\gamma}\tilde{\nu}k$, $\tilde{\gamma}\tilde{\nu}H$ and $\tilde{\gamma}\tilde{\nu}\epsilon$ with thinner TBLs. With an enhanced hypoplastic effect, most $\tilde{\gamma}\tilde{\nu}s$, $\tilde{\gamma}\tilde{\nu}k$, $\tilde{\gamma}\tilde{\nu}H$ and $\tilde{\gamma}\tilde{\nu}\epsilon$ are confined within even thinner TBLs, which are equally recognized in the $\tilde{\nu}$ - and \tilde{u} -profiles.

Calculations for variations in \tilde{a}_T and \tilde{a}_G are given in Fig. 6, with $\tilde{a}_T = \tilde{a}_G = [0.01, 0.025, 0.05]$ indicated by the arrows; $\Xi_1 = \Xi_2 = 0.01$, $\tilde{\pi}_b = 0.01$, $S_2 = 0.02$ and $\tilde{L} = 15$. Equal values of \tilde{a}_T and \tilde{a}_G are used for simplicity. Increasing \tilde{a}_T and \tilde{a}_G allows more fluxes of $\tilde{\gamma}\tilde{\nu}s$ and $\tilde{\gamma}\tilde{\nu}k$ enter into the granular body from the free surface, inducing more $\tilde{\gamma}\tilde{\nu}H$ and $\tilde{\gamma}\tilde{\nu}\epsilon$ for counter-balance. This yields more thicker PLs, illustrated by more convex profiles of $\tilde{\nu}$, \tilde{u} , $\tilde{\gamma}\tilde{\nu}s$, $\tilde{\gamma}\tilde{\nu}k$, $\tilde{\gamma}\tilde{\nu}H$ and $\tilde{\gamma}\tilde{\nu}\epsilon$. These correspond to field observations, for in the PL, the grains are interlocked and behave as a lump solid, causing $\tilde{\gamma}\tilde{\nu}H$ and $\tilde{\gamma}\tilde{\nu}\epsilon$ to overcome $\tilde{\gamma}\tilde{\nu}s$ and $\tilde{\gamma}\tilde{\nu}k$.

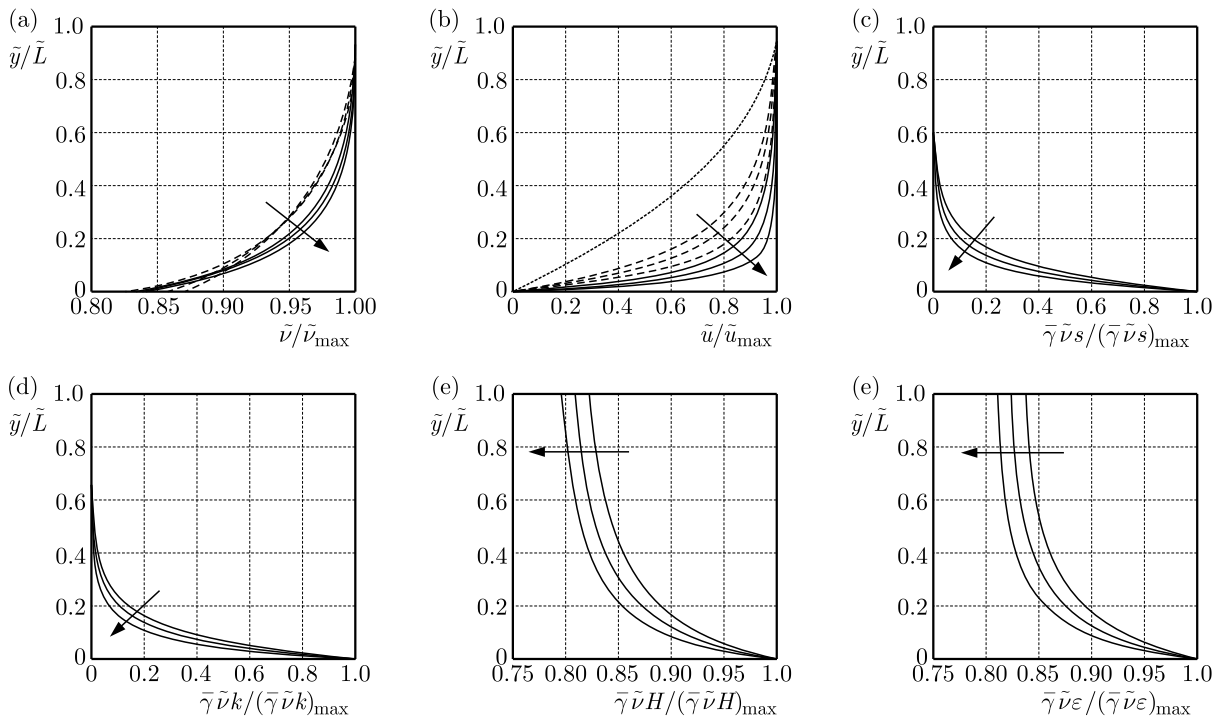


Fig. 4. Normalized profiles of \tilde{v} , \tilde{u} , $\tilde{\gamma}\tilde{\nu}s$, $\tilde{\gamma}\tilde{\nu}k$, $\tilde{\gamma}\tilde{\nu}H$, $\tilde{\gamma}\tilde{\nu}\epsilon$, with $\tilde{\pi}_b = [0.01, 0.1, 0.25]$ indicated by the arrows. Dashed lines: laminar flow solutions; dotted line: laminar Newtonian flow

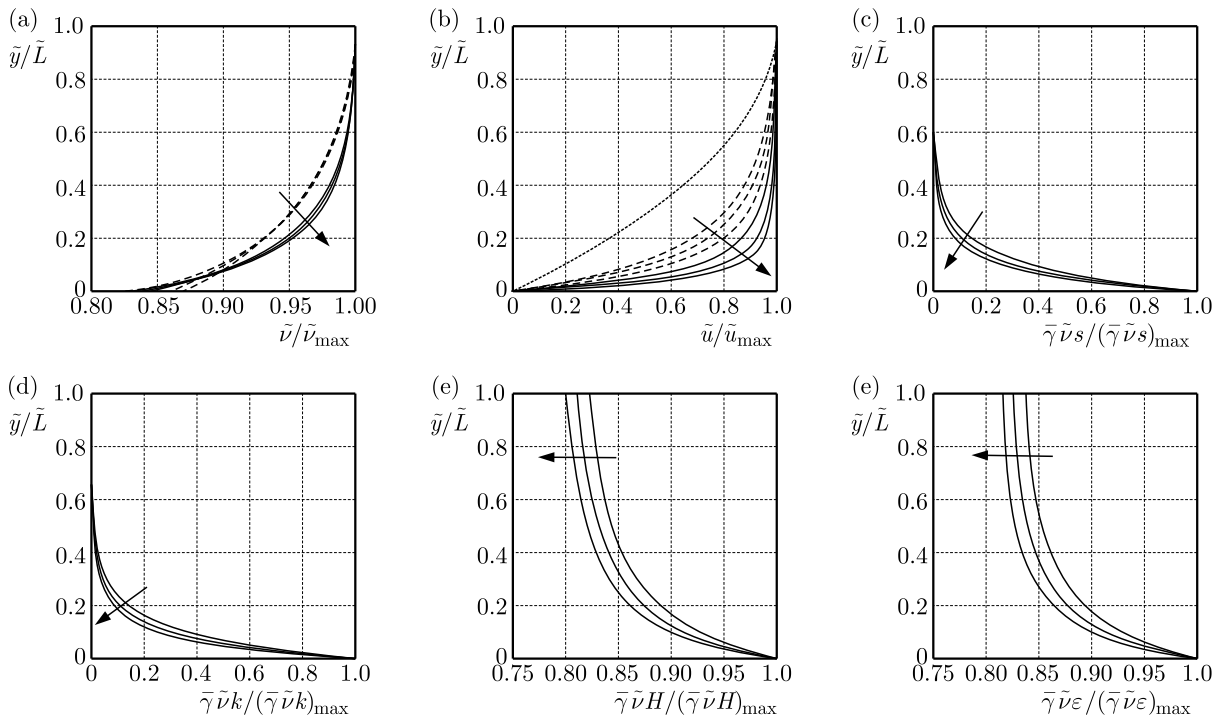


Fig. 5. Normalized profiles of \tilde{v} , \tilde{u} , $\tilde{\gamma}\tilde{\nu}s$, $\tilde{\gamma}\tilde{\nu}k$, $\tilde{\gamma}\tilde{\nu}H$, $\tilde{\gamma}\tilde{\nu}\epsilon$, with $\Xi_1 = \Xi_2 = [0.01, 0.5, 0.1]$ indicated by the arrows. Dashed lines: laminar flow solutions; dotted line: laminar Newtonian flow

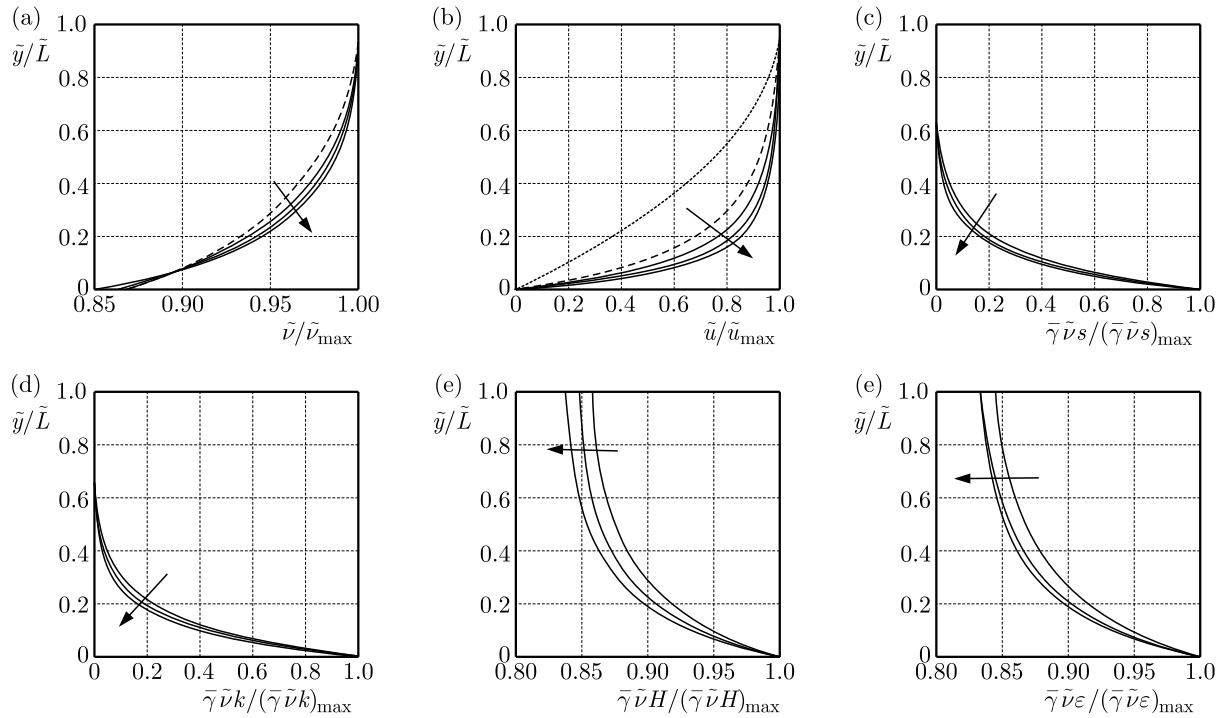


Fig. 6. Normalized profiles of \tilde{v} , \tilde{u} , $\tilde{\gamma v}_s$, $\tilde{\gamma v}_k$, $\tilde{\gamma v}_H$, $\tilde{\gamma v}_\varepsilon$, with $\tilde{a}_T = \tilde{a}_G = [0.01, 0.025, 0.05]$ indicated by the arrows. Dashed lines: laminar flow solutions; dotted line: laminar Newtonian flow

4. Conclusions and discussions

The derived equilibrium closure relations in Part I (Fang, 2016b) have been implemented to obtain a zero-order closure model, which has been applied to analyses of a stationary avalanche down an incline; numerical simulations have been compared with laminar flow solutions.

While \tilde{v} and \tilde{u} evolve from their minimum values on the plane toward maximum values on the free surface, $\tilde{\gamma v}_s$, $\tilde{\gamma v}_k$, $\tilde{\gamma v}_H$ and $\tilde{\gamma v}_\varepsilon$ distribute in a reverse manner, with most of them confined within the TBL immediately above the plane. Above this, there exists a PL in which the grains behave as a lump solid with nearly uniform \tilde{v} and \tilde{u} . In the TBL, the grains are dominated by the short-term interaction, giving a rise to intensive turbulent fluctuation with significant turbulent kinetic energy and dissipation, while those in the PL are dominated by the long-term interaction to form a kind of inelastic network. Two layers are preferable recognized from the turbulent kinetic energy and dissipation profiles.

The TBL and PL of a dry granular avalanche are similar to those of Newtonian fluids in turbulent boundary layer flows. Although the turbulent kinetic energies and dissipations evolve in a similar manner, their vanishing values on the free surface are found for Newtonian fluids, while nearly vanishing turbulent kinetic energies and finite turbulent dissipations are obtained for granular avalanches, resulted from their discrete nature and different dominant grain-grain interactions in the TBL and PL. Discrepancies in the estimated \tilde{v} - and \tilde{u} -profiles from the laminar flow solutions suggest that the energy cascade induced by turbulent fluctuation needs to be considered for better estimations on the characteristics of dry granular avalanches.

Acknowledgements

The author is indebted to the Ministry of Science and Technology, Taiwan, for the financial support through the project MOST 103-2221-E-006-116-. The author also thanks the editor and Professor Janusz Badur for the detailed comments and suggestions which led to improvements.

References

1. AI J., LANGSTON P.A., YU H.-S., 2014, Discrete element modeling of material non-coaxiality in simple shear flows, *International Journal for Numerical and Analytical Methods in Geomechanics*, **38**, 6, 615-635
2. BATCHELOR G.K., 1993, *The Theory of Homogeneous Turbulence*, Cambridge University Press, Cambridge New York
3. BAUER E., HERLE I., 2000, Stationary states in hypoplasticity, [In:] *Constitutive Modeling of Granular Materials*, Kolymbas D. (ed.), Springer Verlag, Berlin, 167-192
4. BUSCAMERA G., 2014, Uniqueness and existence in plastic models for unsaturated soils, *Acta Geotechnica*, **9**, 313-327
5. FANG C., 2008, Modeling dry granular mass flows as elasto-visco-hypoplastic continua with microstructural effects. II. Numerical simulations of benchmark flow problems, *Acta Mechanica*, **197**, 191-209
6. FANG C., 2009, Gravity-driven dry granular slow flows down an inclined moving plane: a comparative study between two concepts of the evolution of porosity, *Rheologica Acta*, **48**, 971-992
7. FANG C., 2016a, A k - ε turbulent closure model of an isothermal dry granular dense matter, *Continuum Mechanics and Thermodynamics*, **28**, 4, 1048-1069
8. FANG C., 2016b, On the turbulent boundary layer of a dry granular avalanche down an incline. I. Thermodynamic analysis, *Journal of Theoretical and Applied Mechanics*, **54**, 3, 1051-1062
9. FANG C., WU W., 2014, On the weak turbulent motions of an isothermal dry granular dense flow with incompressible grains. Part II. Complete closure models and numerical simulations, *Acta Geotechnica*, **9**, 739-752
10. FELLIN W., 2013, Extension to barodesy to model void ratio and stress dependency of the K_0 value, *Acta Geotechnica*, **8**, 561-565
11. FUENTES W., TRIANTAFTLLIDIS T., LIZCANO A., 2012, Hypoplastic model for sands with loading surface, *Acta Geotechnica*, **7**, 177-192
12. HERLE I., GUDEHUS G., 1999, Determination of parameters of a hypoplastic constitutive model from properties of grain assemblies, *Mechanics of Cohesive and Frictional Materials*, **4**, 461-485
13. KIRCHNER N., TEUFEL A., 2002, Thermodynamically consistent modeling of abrasive granular materials. II: Thermodynamic equilibrium and applications to steady shear flows, *Proceeding of Royal Society London A*, **458**, 3053-3077
14. MARCHER TH., VERMEER P.A., WOLFFERSDORF P.-A., 2000, Hypoplastic and elastoplastic modeling – a comparison with test data, [In:] *Constitutive Modeling of Granular Materials*, Kolymbas D. (ed.), Springer Verlag, Berlin, 353-371
15. NIEMUNIS A., GRANDAS-TAVERA C.E., PRADA-SARMIENTO L.F., 2009, Anisotropic visco-hypoplasticity, *Acta Geotechnica*, **4**, 293-314
16. PUDASAINI S., HUTTER K., 2007, *Avalanche Dynamics*, Springer Verlag, Berlin Heidelberg
17. RAO K.K., NOTT P.R., 2008, *Introduction to Granular Flows*, Cambridge University Press, London New York
18. RICHMAN M.W., MARCINIEC R.P., 1990, Gravity-driven granular flows of smooth, inelastic spheres down bumpy inclines, *Journal of Applied Mechanics*, **57**, 1036-1043
19. SAVAGE S.B., 1993, Mechanics of granular flows, [In:] *Continuum Mechanics in Environmental Sciences and Geophysics*, Hutter K. (ed.), Heidelberg, Springer, 467-522
20. TSINOBER A., 2009, *An Informal Conceptual Introduction to Turbulence*, Springer, Heidelberg
21. WANG Y., HUTTER K., 1999, A constitutive theory of fluid-saturated granular materials and its application in gravitational flows, *Rheologica Acta*, **38**, 214-223
22. WANG Y., HUTTER K., 2001, Granular material theories revisited, [In:] *Geomorphological Fluid Mechanics*, Balmforth N.J., Provenzale A. (eds.), Heidelberg, Springer, 79-107
23. WENDT J.F., 2009, *Computational Fluid Dynamics: An Introduction*, Springer, Berlin Heidelberg

ANALYSIS OF A CROSS-CHANNEL MICROMIXER THROUGH THE DYNAMICS OF TRACER GRADIENT

MICHEL GONZALEZ

CNRS, UMR 6614/CORIA, Site Universitaire du Madrillet, Saint-Etienne du Rowray, France

e-mail: michel.gonzalez@coria.fr

The study aims at showing how the dynamics of tracer gradient accounts for the stirring mechanism produced by a periodically forced flow relevant to practical mixing operation. The numerical simulation uses the equations for the orientation and norm of the tracer gradient and an analytic model for velocity. To a large extent, the micromixer properties over different ranges of the Strouhal number are explained through the response of the tracer gradient orientation to the tilting of strain principal axes resulting from flow forcing. The analysis also reveals a rich picture of stirring as the Strouhal number is varied.

Keywords: Low-Reynolds number flows, mixing enhancement, micromixers

1. Introduction

In fluid flows used for mixing, stretching caused by stirring raises the contact areas and draws fluid portions to be mixed together, which hastens the molecular diffusion flux. Low-Reynolds number flows, by contrast to turbulent flows, do not start the stretching-driven cascade bringing about the shrinking of scales down to the diffusive lengthscale. Mixing of a weakly diffusive material, then, may need significant time – or distance – to be achieved. Efficient mixing has thus to be controlled, which needs precise knowledge of the stirring properties of the flow. This question is crucial in microfluidics. Chemical, biological and medical applications, in particular, have given rise to significant investigation in this field both on the practical and academic levels (Nguyen and Wu, 2005; Capretto *et al.*, 2011; Lee *et al.*, 2011).

The gradient of a scalar – heat, contaminant... – is the finest level at which the problem of mixing can be tackled, for it gives a direct insight into the stirring mechanisms. This approach is also plainly suited to the physics of mixing. As the gradient direction and magnitude respectively correspond to the striation orientation and thickness – fine structures meaning large gradients, the tracer gradient features are indeed closely connected to the structure of mixing patterns. The growth rate of the tracer gradient shows the conditions in which stirring may enhance the diffusion fluxes and is thus a key quantity. Although strain intensity matters, the alignment of the tracer gradient within the strain eigenframe may be the determining factor. The role of alignment may be especially critical in non-stationary regimes in which the dynamics of the tracer gradient – through its response to unsteady mechanical action – drives the growth rate. Previous studies addressed the dynamics of the scalar gradient orientation (Lapeyre *et al.*, 2001; Garcia *et al.*, 2005) and its role in the mechanism of the gradient growth was pointed out (Garcia *et al.*, 2008; Gonzalez and Paranthoën, 2010).

The present study is focused on the kinematics of a tracer gradient in a periodically forced cross-channel micromixer. The purpose is twofold: i) addressing the role of the tracer gradient dynamics in stirring produced by a practical mixing device; ii) assessing the relevance of the tracer gradient approach to the analysis of stirring in this kind of device. It seems that the operation of such a micromixer has not been studied through the response of a vector field yet.

The device is an active mixer in which the material flowing in the main channel is stirred by forcing a pulsating flow in the side channels, a standard geometry in microfluidics. Previous works (Niu and Lee, 2003; Tabeling *et al.*, 2004; Lee *et al.*, 2007) addressed the conditions in which chaotic advection is triggered and enhances mixing in this system. In this basic geometry, stirring properties are ruled by two parameters, namely the Strouhal number St , and the velocity ratio α – the ratio of maximum pulsating velocity to the maximum velocity in the main channel. Okkels and Tabeling (2004) and Lee *et al.* (2007) analysed the folding rate of interface segments and the mean finite-time Lyapunov exponent, respectively, by spanning both St and α .

In this work, St is varied for two values of α . The flowfield is simulated by the kinematic model of Niu and Lee (2003) and the Lagrangian, diffusionless equation for the tracer gradient is solved in terms of orientation and norm. The stirring properties of the flow are scrutinised through the mean growth rate of the tracer gradient norm for small to large Strouhal numbers.

2. Cross-channel micromixer model

A detailed description of a practical, periodically forced cross-channel micromixer was given by Lee *et al.* (2007). A simple sketch of the device is shown in Fig. 1.

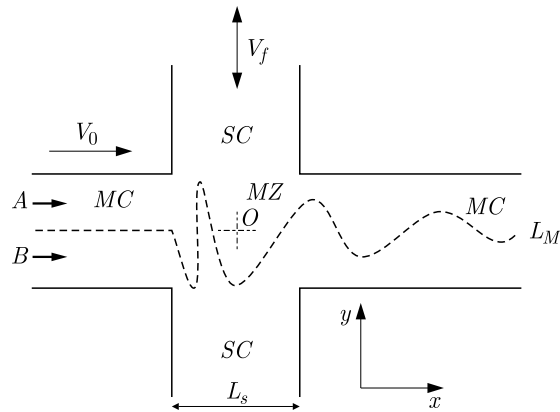


Fig. 1. Sketch of the cross-channel micromixer; MC – main channel, SC – side channel, MZ – mixing zone

The velocity field is simulated by the kinematic two-dimensional model proposed by Niu and Lee (2003). The flowfield is splitted over different parts of the micromixer and, assuming very low Reynolds number, the velocity field in the mixing zone is approximated as the linear combination of the velocity fields in the main and side channels. The latter are assumed to be parabolic, the velocity is steady in the main channel and periodic in the side channel. The flowfield model is expressed as follows:

— main channel

$$u = V_0 \left[1 - \left(\frac{2y}{L_M} \right)^2 \right] \quad v = 0 \quad (2.1)$$

— side channel

$$u = 0 \quad v = V_f \left[1 - \left(\frac{2x}{L_S} \right)^2 \right] \cos \omega_f t \quad (2.2)$$

— mixing zone

$$u = V_0 \left[1 - \left(\frac{2y}{L_M} \right)^2 \right] \quad v = V_f \left[1 - \left(\frac{2x}{L_S} \right)^2 \right] \cos \omega_f t \quad (2.3)$$

This model was shown to be consistent with experimental data – including the chaotic regime – (Lee *et al.*, 2007).

It is straightforward to derive the strain rate, $\sigma = \sqrt{\sigma_n^2 + \sigma_s^2}$ – with $\sigma_n = \partial u/\partial x - \partial v/\partial y$ and $\sigma_s = \partial u/\partial y + \partial v/\partial x$ being the normal and shear strain components – and the vorticity, $\omega = \partial v/\partial x - \partial u/\partial y$ from Eqs. (2.1)-(2.3). The orientation of the strain principal axes in the fixed frame of reference (x, y) is defined by the angle Φ through $\tan(2\Phi) = \sigma_n/\sigma_s$. As $\sigma_n = 0$ in the whole flowfield, the strain rate reduces to $\sigma = |\sigma_s|$. The orientation of strain principal axes is a simple piecewise function defined as

$$\Phi = \begin{cases} 0 & \text{for } \sigma_s > 0 \\ \pi/2 & \text{for } \sigma_s < 0 \end{cases} \quad (2.4)$$

The local structure of the flow is defined by $Q = \sigma^2 - \omega^2$ ($Q > 0$ in hyperbolic regions and $Q < 0$ in elliptic regions; Okubo, 1970; Weiss, 1991). The flow structure in the side channel is a pure shear and $Q = 0$ in this part of the micromixer. In the mixing zone, where $Q \sim xy \cos \omega_f t$, the Eulerian local structure is periodic in time as already mentioned by Lee *et al.* (2007). However, the evolution of Q along Lagrangian trajectories is of course more complex.

3. Tracer gradient equations

The general equation for the gradient \mathbf{G} of a diffusionless scalar – or tracer – is

$$\frac{D\mathbf{G}}{Dt} = -\mathbf{A}^T \mathbf{G} \quad (3.1)$$

where $\mathbf{A} = \nabla \mathbf{u}$ is the velocity gradient tensor. With $\mathbf{G} = |\mathbf{G}|(\cos \theta, \sin \theta)$, Eq. (3.1) gives the Lagrangian equations for the orientation and norm of \mathbf{G} (Lapeyre *et al.*, 1999)

$$\frac{D\theta}{Dt} = \frac{1}{2} \{ \omega - \sigma \cos[2(\theta + \Phi)] \} \quad \frac{2}{|\mathbf{G}|} \frac{D|\mathbf{G}|}{Dt} = -\sigma \sin[2(\theta + \Phi)] \quad (3.2)$$

The growth rate, $\eta = (1/|\mathbf{G}|)(D|\mathbf{G}|/Dt)$, takes the minimum value $-\sigma/2$ for \mathbf{G} aligning with the extensional strain direction defined by $\theta_e = -\Phi + \pi/4$ and reaches the maximum value $\sigma/2$, when \mathbf{G} aligns with the compressive strain direction given by $\theta_c = -\Phi - \pi/4$.

As a result of the alternating behaviour of Φ , Eq. (2.4), the tracer gradient experiences unsteady forcing through its orientation with respect to the strain principal axes. As is shown in this study, the variations of Φ are actually essential to explain the mean growth rate of the tracer gradient in function of the flow properties.

The Lagrangian dynamics of the tracer gradient orientation is derived by solving Eq. (3.2)₁ together with the tracking of particles given by $D\mathbf{x}/Dt = \mathbf{u}$ with \mathbf{x} being the position vector and \mathbf{u} the modelled velocity field in the mixer. The growth rate of the tracer gradient is then directly given by Eq. (3.2)₂ without solving for the gradient norm. High growth rate indicates good stirring properties through fast enhancement of local gradients.

The numerical method is a fourth-order Runge-Kutta scheme. Initially, 1000 particles are located on a line at $y = 0$ from $x = -L_S/2$ to $x = L_S/2$. As we are strictly interested in the properties of a single mixing cavity – and not a series of elemental micromixers, each particle leaving the computational domain at $x = L_S/2$ is reinjected at $(x, y) = (-L_S/2, 0)$ with the initial condition $\theta = \pi/2$ for the orientation of the tracer gradient, which mimics the tracking of an interface between two different scalar quantities – say, A and B as shown in Fig. 1. The numerical timestep is $\Delta t = T_f/3200$ with $T_f = 2\pi/\omega_f$ being the time period of the flow forcing. Statistics are derived by averaging over all the instantaneous values computed along the

Lagrangian paths during a time interval $T = 200T_f$. As T amounts to several mean residence time – 50 at least – this is enough to account for the differences in residence time over the particle ensemble. Averaging over the values recorded on Lagrangian trajectories is denoted by brackets. Those averaged quantities duly include Lagrangian information on the evolution of the tracer gradient. Integrating along trajectories – for the strain and growth rates, for instance – strictly shows the same behaviour.

4. General features of the kinematics of tracer gradient

The stirring properties of the cross-channel device are described by the amplitude parameter, $\alpha = V_f/V_0$ and the Strouhal number $St = L_S/V_0T_f$ (Okkels and Tabeling, 2004; Lee *et al.*, 2007). In this study, the influence of the Strouhal number is analysed for $\alpha = 1$ and $\alpha = 3$ with $L_M = L_S = 1$.

The Lagrangian evolution of the tracer gradient tightly depends on the residence time inside the micromixer cavity. The mean residence time T_r of a particle injected at $(-L_S/2, 0)$ and leaving the mixing zone at section $x = L_S/2$ is shown in Fig. 2. For a given value of the Strouhal number, the residence time in the side channels – and thus T_r – obviously grows with α . At large Strouhal numbers, the time spent in the side channels tends to zero and T_r approaches the convection timescale $T_c = L_S/V_0$ as expected. The ratio of the residence time to the time period of the flow forcing $T_r/T_f = StT_r/T_c$, thus varies as St at large St values, as shown by the plot of T_r/T_f .

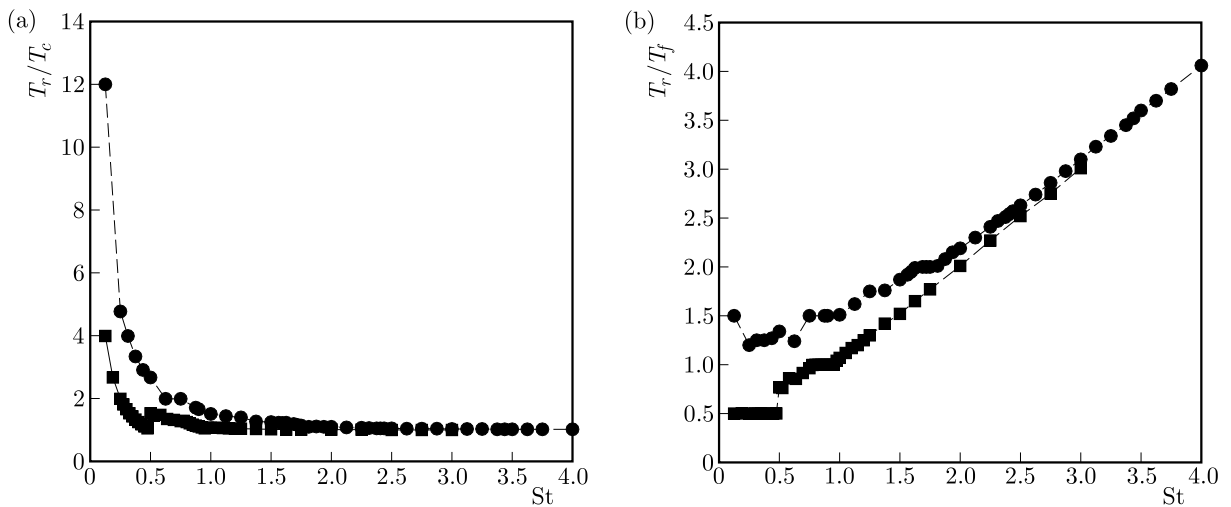


Fig. 2. Mean residence time in the micromixer cavity; (a) T_r/T_c , with $T_c = L_S/V_0$ being the convection timescale, (b) T_r/T_f , with T_f being the time period of the flow forcing; squares: $\alpha = 1$, circles: $\alpha = 3$

Overall, the evolution of the tracer gradient derived from the tracking of particles injected at $(-L_S/2, 0)$ is dominated by rotation. At small Strouhal numbers, however, they are more likely to experience a pure shear regime as a result of significant time spent in the side channels. This behaviour is shown by the plots of the respective strain ($Q > 0$), rotation ($Q < 0$) and shear ($Q = 0$) events ratios along the Lagrangian paths (Fig. 3).

The dependence of the tracer gradient dynamics upon the Strouhal number in terms of the orientation and norm growth rate reveals a rich phenomenology. From the plot of $\langle \eta \rangle / \langle \sigma \rangle$ – which gives a measure of the efficiency of the micromixer (Fig. 4), Strouhal number ranges promoting good stirring are found together with narrow ranges where stirring is certainly quite poor. While

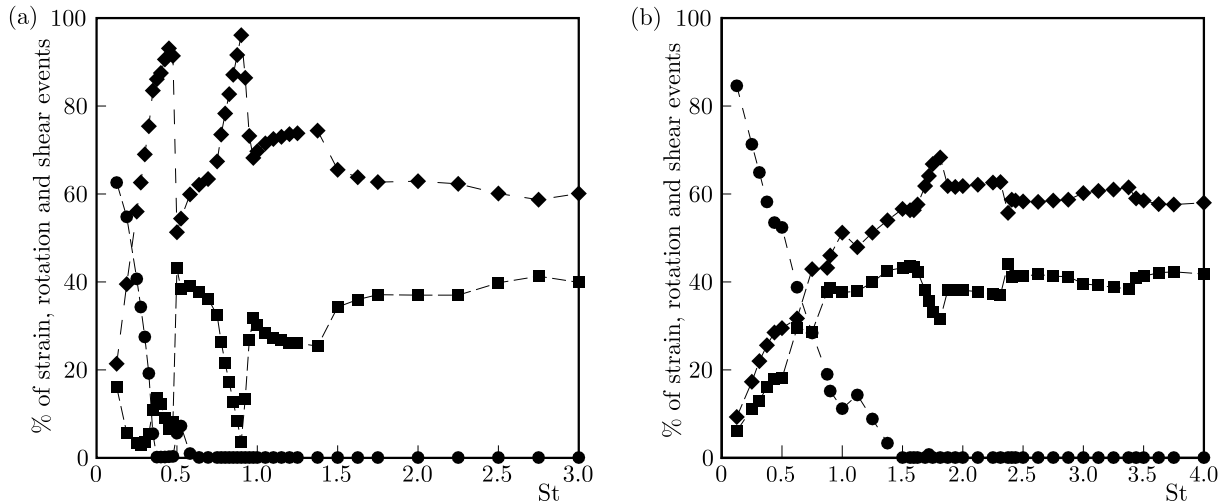


Fig. 3. Ratios of strain-, rotation- and shear-dominated events along the Lagrangian paths vs. Strouhal number; (a) $\alpha = 1$, (b) $\alpha = 3$; squares: strain, diamonds: rotation, circles: shear

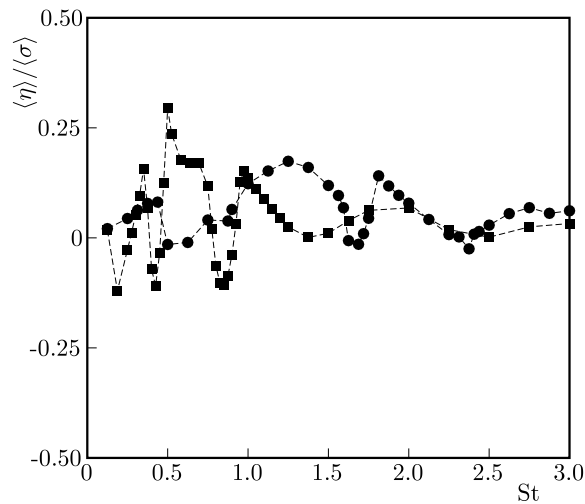


Fig. 4. Ratio of the mean growth rate to the mean rate of strain, $\langle \eta \rangle / \langle \sigma \rangle$, vs. Strouhal number; squares: $\alpha = 1$, circles: $\alpha = 3$

its theoretical maximum value is 0.5, $\langle \eta \rangle / \langle \sigma \rangle$ reaches 0.29 for $\alpha = 1$ and 0.17, at best, for $\alpha = 3$. This is due to a moderate statistical alignment of the tracer gradient with the compressional strain which most likely results from overall prevailing rotation.

The rather weak alignment of \mathbf{G} with compressional strain is confirmed by Fig. 5 displaying $\langle \sigma \rangle$, $\langle -\sin \zeta \rangle$ – with $\zeta = 2(\theta + \Phi)$ – and $\langle \eta \rangle$ in function of the Strouhal number. Far from unity – the value reached when \mathbf{G} is parallel to compression, the maximum for $\langle -\sin \zeta \rangle$ is 0.31 for $\alpha = 1$ and 0.16 for $\alpha = 3$. The mean growth rate depends on the strain level, but the dependence on the tracer gradient orientation through $\sin \zeta$ is stronger. This is clear beyond $St \simeq 0.7$ for $\alpha = 1$ and $St \simeq 1$ for $\alpha = 3$. These results thus suggest that the stirring properties of the flow can be mainly explained in terms of the dynamics of tracer gradient orientation. As the tracer gradient is locally normal to the interface separating the material to be mixed, this view agrees with analyses based on the deformation of interface segments (Okkels and Tabeling, 2004; Tabeling *et al.*, 2004).

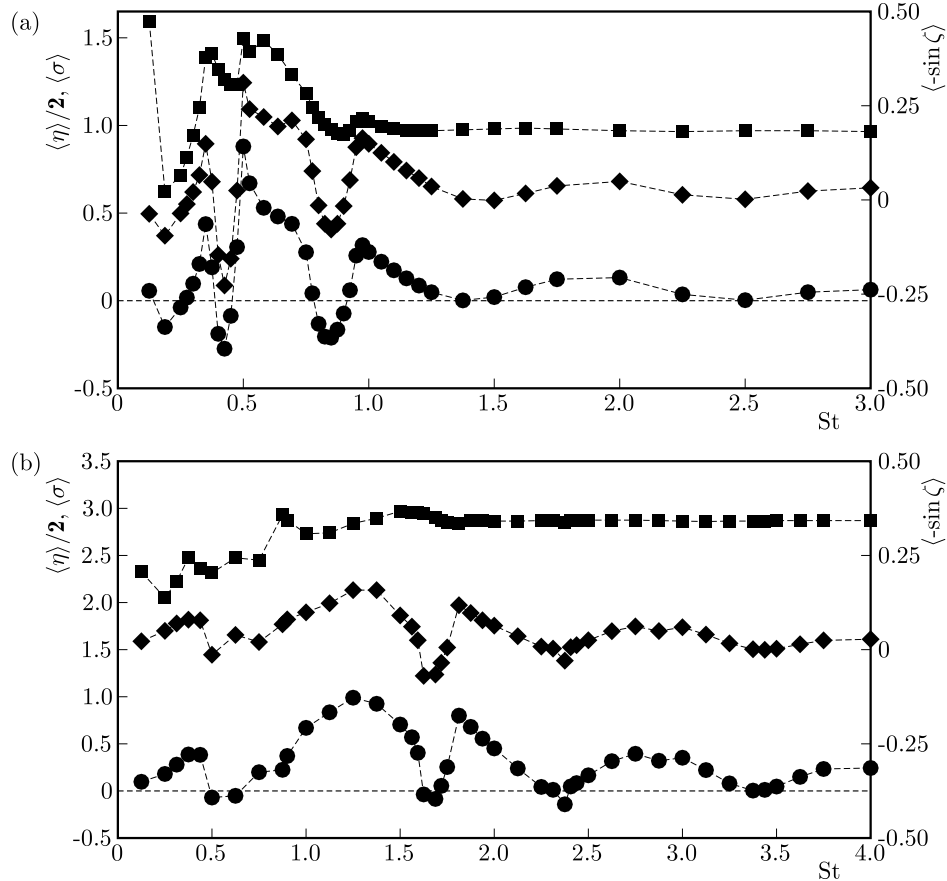


Fig. 5. Mean rate of strain $\langle\sigma\rangle$ statistical alignment given by $\langle-\sin\zeta\rangle$ and mean growth rate $\langle\eta\rangle$ vs. Strouhal number; (a) $\alpha = 1$, (b) $\alpha = 3$; squares: $\langle\sigma\rangle/2$, diamonds: $\langle-\sin\zeta\rangle$, circles: $\langle\eta\rangle$

5. Dependence of stirring properties on the Strouhal number

5.1. Small Strouhal number

Figure 6 confirms that the mean residence time inside the side channels is significant at small Strouhal numbers. As a result, the statistics of tracer gradient orientation in this range of the Strouhal number is governed by pure shear ($Q = 0$).

From Eq. (2.2), the transversal velocity v and the shear component of strain σ_s are in phase in the side channels, where Lagrangian particles move with $x = \text{const}$. Each turning back of a Lagrangian particle in the side channel thus coincides with a $\pi/2$ -tilting of the strain principal axes, Eq. (2.4), that makes $\sin\zeta$ – and hence η – change sign; the way back is always covered with the sign reversed for the growth rate which, on average, is therefore close to zero in the side channels. Figure 7 shows the trajectories as well as the Lagrangian histories of σ , $\sin\zeta$ and η for $\alpha = 1$ and $St = 0.125$.

The mean values conditioned on pure shear $\langle-\sin\zeta|Q = 0\rangle$ and $\langle\eta|Q = 0\rangle$, are close to zero up to $St \simeq 0.35$ (Fig. 8a). The same behaviour for $\alpha = 3$ is displayed in Fig. 8b.

5.2. Large Strouhal number

The behaviour of the tracer gradient at large Strouhal numbers is governed by the tilting of strain principal axes in the mixing zone. The tilting of strain principal axes occurs in the elliptic regions; it is easy to show, from the expressions for σ_s and Q , that σ_s changes sign – which also amounts to $\sigma = 0$ – only if $Q < 0$. As St is increased, the mean tilting frequency f_Φ

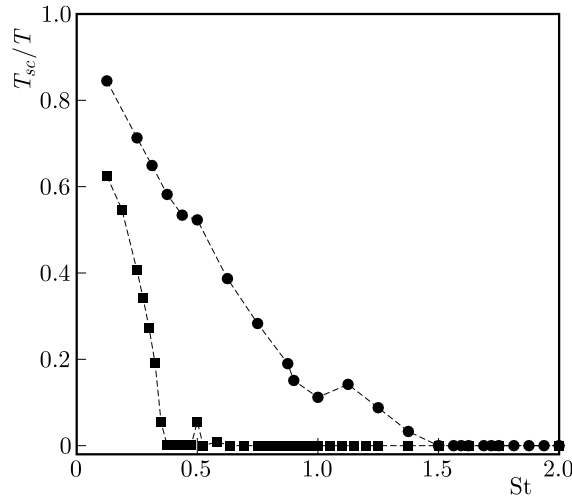


Fig. 6. Mean ratio T_{SC}/T of time spent in the side channels during simulation; squares: $\alpha = 1$; circles: $\alpha = 3$

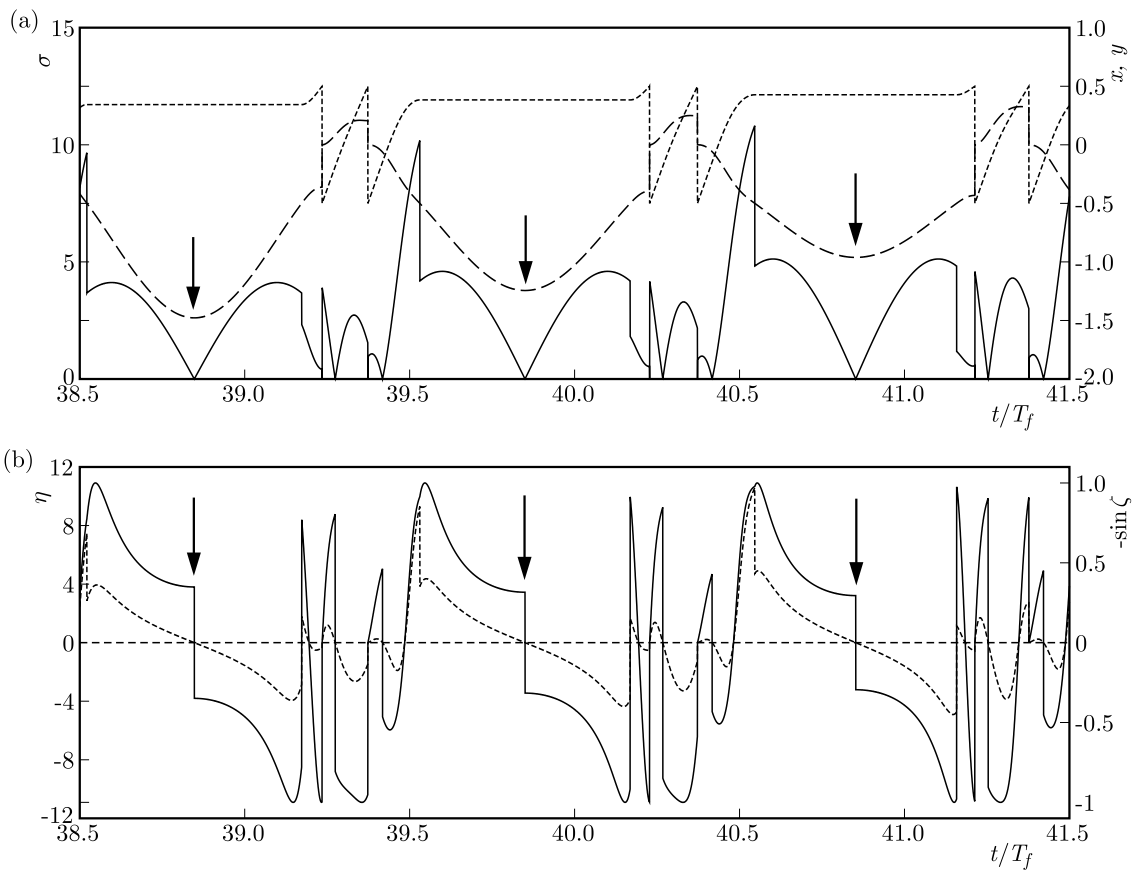


Fig. 7. Lagrangian signals for $\alpha = 1$ and $St = 0.125$; (a) solid line: σ , short dash: x , long dash: y ; (b) solid line: $-\sin \zeta$, dashed line: η ; each arrow shows a turning back in a side channel

grows linearly as shown in Fig. 9 ($T_r \simeq T_c$ at large Strouhal numbers, Fig. 2). At large Strouhal numbers, the tracer gradient thus experiences faster and faster changes in the strain direction. The latter become too fast for the tracer gradient to respond and its orientation gets closer and closer to the direction of a bisector of strain principal axes for which $\sin \zeta = 0$ – and $\eta = 0$. As a result, the mean growth rate decays at large Strouhal numbers.

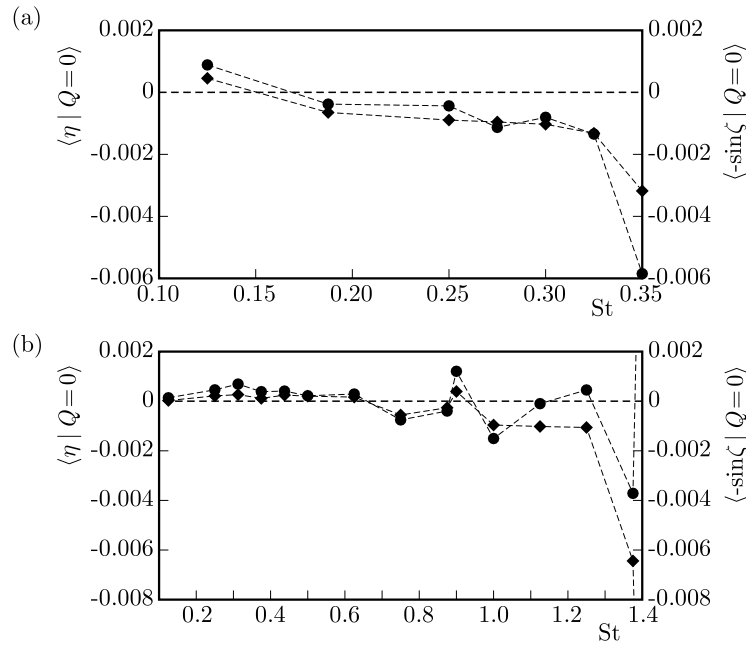


Fig. 8. Mean values of $-\sin \zeta$ and η conditioned on pure shear vs. Strouhal number; (a) $\alpha = 1$, (b) $\alpha = 3$; diamonds: $\langle -\sin \zeta | Q = 0 \rangle$, circles: $\langle \eta | Q = 0 \rangle$

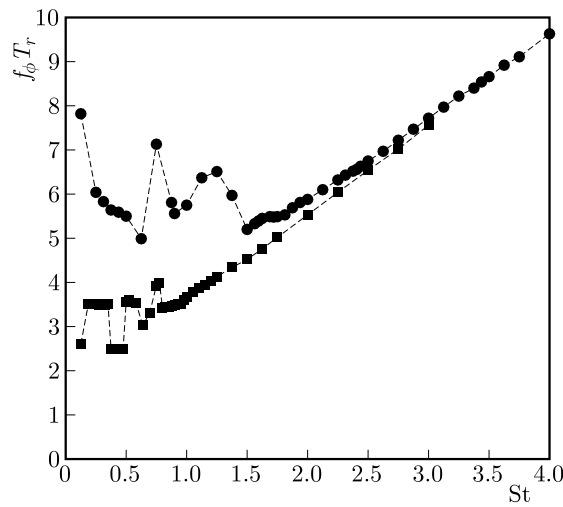


Fig. 9. Mean tilting frequency of strain principal axes normalised by the mean residence time in the mixing cavity vs. Strouhal number; squares: $\alpha = 1$; circles: $\alpha = 3$

On a more general level, this mechanism is clearly reminiscent of the nonadiabatic regime of the scalar gradient response to unsteady forcing in which the scalar gradient does not keep up with fast changes in strain persistence – or in strain principal axes direction (Garcia *et al.*, 2008; Gonzalez and Paranthoën, 2010). The probability density function (p.d.f) of the tracer gradient orientation (Fig. 10) shows the gradual preferential alignment with a bisector of strain principal axes at large Strouhal numbers.

For $\alpha = 1$, the variance of $\sin \zeta$ is 0.243, 0.102 and 0.0707 at $St = 2, 3$ and 4 , respectively; for $\alpha = 3$ these values are 0.687, 0.548 and 0.396. The tendency is less marked when $\alpha = 3$ for which higher strain and vorticity levels result in a better response of the tracer gradient to the mechanical action of the velocity gradient.

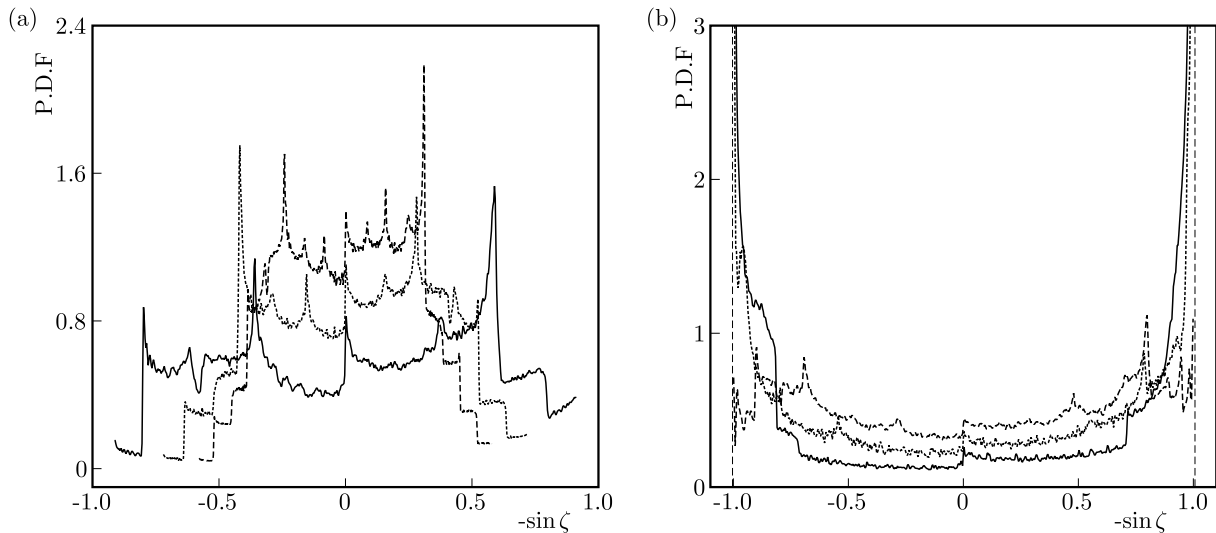


Fig. 10. P.d.f.'s of tracer gradient orientation; (a) $\alpha = 1$, (b) $\alpha = 3$; solid line: $St = 2$, short dash: $St = 3$, long dash: $St = 4$

5.3. Middle-range Strouhal number

5.3.1. Vanishing mean growth rate and resonance phenomenon

Poor stirring properties are also found for Strouhal number ranges in which the mean residence time takes special values. For $\alpha = 1$, the mean growth rate is virtually zero – 0.021 and 0.0030, while the maximum value is 0.88 – at $St = 1.5$ and $St = 2.5$ (Fig. 5) where $T_r/T_f = 1.52$ and 2.52, respectively (Fig. 2). For $\alpha = 3$ $\langle \eta \rangle = 0.012$ – maximum value: 0.99 – at $St = 3.4375$ for which $T_r/T_f = 3.52$. These results are reminiscent of the resonance phenomenon found by Okkels and Tabeling (2004) in which the folding rate of an interface segment falls to zero when $T_r/T_f = (n + 1/2)$ – with $n \in \mathbb{N}$. The authors show that a resonance occurs when the perturbation of a point on the interface developing within the first half of the mixing region is reversed and strictly offset in the second part – incidentally, this needs $n \geq 1$. The analysis in terms of the tracer gradient orientation agrees with this mechanism. Figure 11, plotted for $\alpha = 1$ and $St = 1.5$, shows that the interplay between the periodic flow forcing and the position on a trajectory brings about a symmetric Lagrangian signal of strain over the residence time inside the mixing cavity.

Especially, the strain tilting events felt by the tracer gradient along a Lagrangian path are symmetric. They occur for $\sigma = 0$, namely whenever $y + \alpha x \cos \omega_f t = 0$, which is true near the center of the cavity – where $x = y = 0$, but also at any position provided that x , y and t fulfill the latter condition – as shown in Fig. 11. The special behaviour of strain results in a symmetric signal for $\sin \zeta$ and thus for η which, on average, cancels out over the mean residence time. This analysis is confirmed by the Lagrangian plots for $\alpha = 1$ and $St = 2.5$ as well as for $\alpha = 3$ and $St = 3.4375$ (not shown). Figure 11 also displays the Lagrangian evolution of Q .

5.3.2. Negative mean growth rate

Negative values of the mean growth rate are found over narrow ranges of the Strouhal number and especially for $\alpha = 1$ (Fig. 5). They obviously result from a statistical alignment of the tracer gradient closer to the extensive than to the compressive strain direction. In these special conditions, the flowfield opposes stirring which may prevent mixing. While $\langle \eta \rangle / \langle \sigma \rangle = -0.025$, at best, for $\alpha = 3$, the most significant negative values of $\langle \eta \rangle$ for $\alpha = 1$ are found at $St = 0.1875$, 0.425 and 0.85 where $\langle \eta \rangle / \langle \sigma \rangle = -0.12$, -0.11 and -0.11 , respectively. In this ranges of the

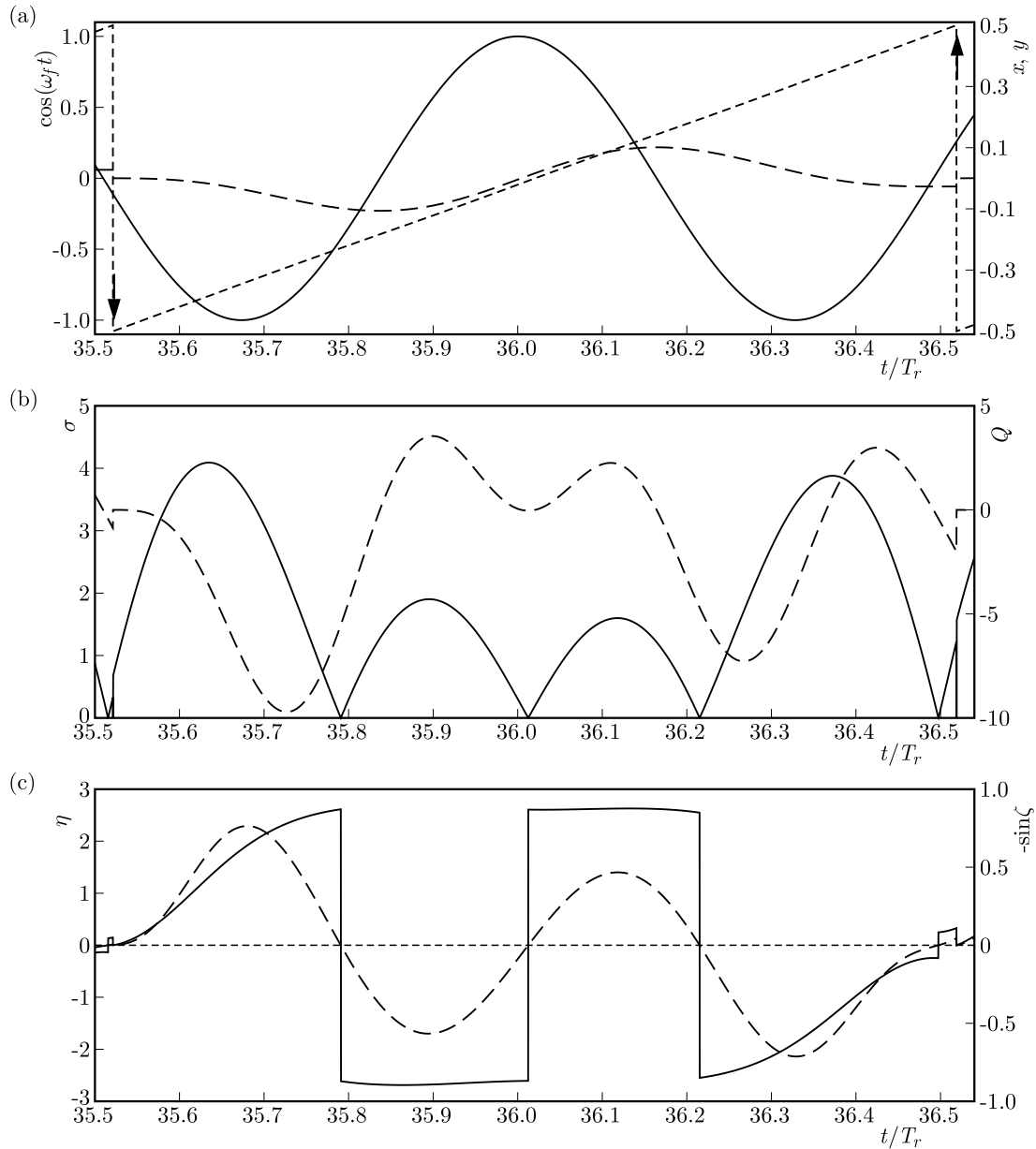


Fig. 11. Lagrangian signals for $\alpha = 1$ and $St = 1.5$; (a) solid line: $\cos \omega_f t$, short dash: x , long dash: y ; the arrows show the injection and exit of the Lagrangian particle; (b) solid line: σ , dashed line: Q ; (c) solid line: $-\sin \zeta$, dashed line: η

Strouhal number, T_r/T_f takes special values ~ 0.5 for $St = 0.1875$ and 0.425 , ~ 1 for $St = 0.85$ (Fig. 2). At $St = 0.1875$, the tracer gradient evolution is mainly governed by shear (Section 5.1). At $St = 0.425$ and 0.85 , both the flow structure and orientation dynamics explain the negative values of the mean growth rate. As shown in Fig. 3, the ratio of rotation events sharply peaks near these St values and the tracer gradient essentially experiences an elliptic regime. And the sharp drops of $-\sin \zeta$ at $St = 0.425$ and 0.85 (Fig. 12), showing statistical alignment near the extensive strain direction, deepen negative $\langle \eta \rangle$.

At those Strouhal numbers, this statistical alignment with extensive strain in hyperbolic regions is explained by unsteadiness. In fact, the time spent in the hyperbolic regime is much too short for strain to bring back the tracer gradient from the extensive to the compressive direction after tiltings occurring in the elliptic regions.

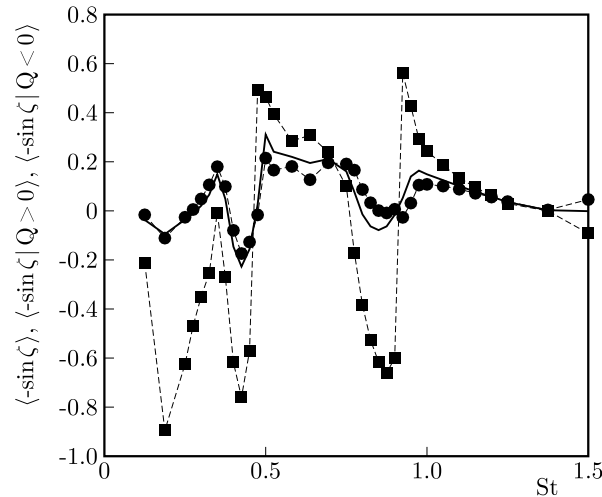


Fig. 12. Statistical orientation of the tracer gradient; $\alpha = 1$; solid line: $\langle -\sin \zeta \rangle$, squares: conditioning on hyperbolic events, $\langle -\sin \zeta | Q > 0 \rangle$, circles: conditioning on elliptic events, $\langle -\sin \zeta | Q < 0 \rangle$

5.3.3. Maximum mean growth rate

Finally, good stirring must be restricted to moderate Strouhal numbers away from the small and large Strouhal number ranges where the tilting of strain principal axes make the mean growth rate collapse (Sections 5.1 and 5.2). In addition, T_r/T_f must not take special values resulting in limiting mechanisms such as resonances. Then, good stirring conditions are found, roughly, from $St = 0.48$ to 0.75 for $\alpha = 1$ and $St = 0.95$ to 1.6 for $\alpha = 3$ (Figs. 4 and 5) with peak values at $St = 0.5$ and 1.25 , respectively. In a pure kinematic view, these findings are consistent. The ratio of strain-dominated events as well as the mean strain rate indeed reach maximum values over those Strouhal number ranges (Figs. 3 and 5). And the maximum of $\langle -\sin \zeta \rangle$ agrees with the peak values of $\langle \eta \rangle$. As already mentioned by Lee *et al.* (2007), optimal stirring is thus ensured by the values of the control parameters, St and α , defining the best conditions for particles to reach a hyperbolic region and spend enough time therein. Figure 13 shows the Lagrangian signals for $\alpha = 1$ and $St = 0.5$.

By $x = cte$ -segments, the trajectories inside the cavity reveal the inroads into the side channels. As a possible result of the chaotic behaviour, they do not display any clear periodic features. Instead, it appears that a particle may either cross the mixing zone straight or spend a variable time inside the side channel. The sample signals also confirm the significant ratio of strain-dominated events as well as the relative large time spent by the tracer gradient near the compressive direction of strain.

6. Conclusion

This study confirms that despite the significant role of the strain level, the response of the tracer gradient orientation to unsteady strain is a key mechanism to explain the stirring properties of a periodically forced, cross-channel micromixer.

This approach also gives a detailed insight into the micromixer properties. At small Strouhal numbers, the mean growth rate of the tracer gradient shrinks, thus showing poor stirring; the major part of the mean residence time is spent in the side channels where the periodic, symmetric reversing of the orientation of the tracer gradient with respect to the strain principal axes cancels its growth rate. At large Strouhal numbers, the tracer gradient does not respond to the fast

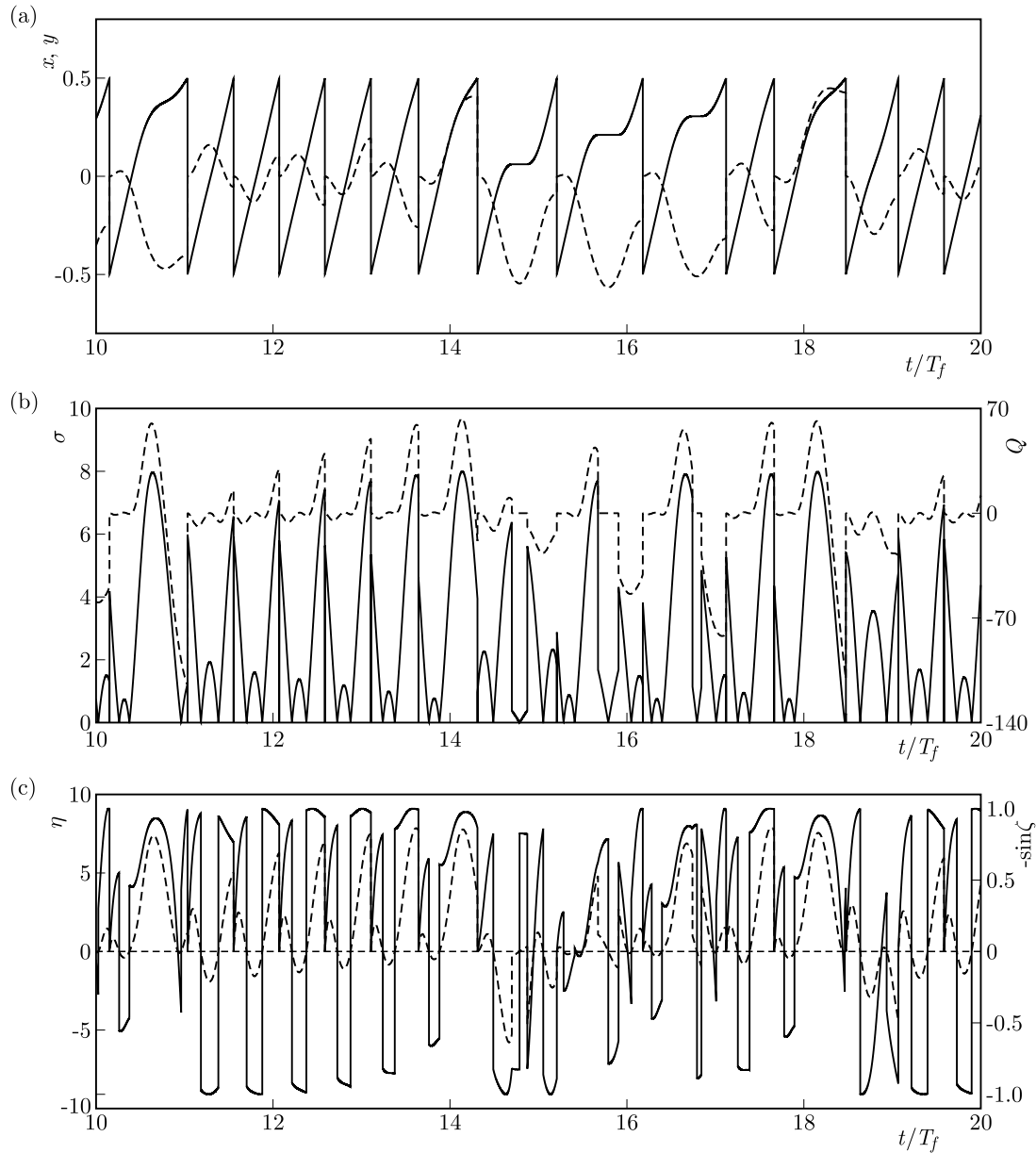


Fig. 13. Lagrangian signals for $\alpha = 1$ and $St = 0.5$; (a) solid line: x , dashed line: y , (b) solid line: σ , dashed line: Q ; (c) solid line: $-\sin \zeta$, dashed line: η

changes in the strain direction caused by flow forcing and aligns closer and closer to a bisector of strain principal axes where the growth rate vanishes.

Good stirring conditions are found in the middle range of the Strouhal number. They are fulfilled at Strouhal numbers for which the hyperbolic regime prevails and the mean strain rate reaches its maximum values on Lagrangian trajectories, namely within $St = 0.48$ to 0.75 for $\alpha = 1$ and $St = 0.95$ to 1.6 for $\alpha = 3$ with peak values at $St = 0.5$ and 1.25 , respectively. Poor stirring, however, may occur in narrow windows of the Strouhal number where the mean growth rate either vanishes – which precisely corresponds to the resonance phenomenon pointed out by Okkels and Tabeling (2004) – or takes negative values as a result of both the flow structure and dynamics of tracer gradient orientation when the elliptic regime prevails along the Lagrangian trajectories.

References

1. CAPRETTO L., CHENG W., HILL M., ZHANG X., 2011, Micromixing within microfluidic devices, *Topics in Current Chemistry*, **304**, 27-68
2. GARCIA A., GONZALEZ M., PARANTHOËN P., 2005, On the alignment dynamics of a passive scalar gradient in a two-dimensional flow, *Physics of Fluids*, **17**, 117102
3. GARCIA A., GONZALEZ M., PARANTHOËN P., 2008, Nonstationary aspects of passive scalar gradient behaviour, *European Journal of Mechanics B/Fluids*, **27**, 433-443
4. GONZALEZ M., PARANTHOËN P., 2010, On the role of unsteady forcing of tracer gradient in local stirring, *European Journal of Mechanics B/Fluids*, **29**, 143-152
5. LAPEYRE G., HUA B.L., KLEIN P., 2001, Dynamics of the orientation of active and passive scalars in two-dimensional turbulence, *Physics of Fluids*, **13**, 251-264
6. LAPEYRE G., KLEIN P., HUA B.L., 1999, Does the tracer gradient vector align with the strain eigenvectors in 2D turbulence?, *Physics of Fluids*, **11**, 3729-3737
7. LEE C.-Y., CHANG C.-L., WANG Y.-N., FU L.-M., 2011, Microfluidic mixing: a review, *International Journal of Molecular Sciences*, **12**, 3263-3287
8. LEE Y.-K., SHIH C., TABELING P., HO C.-M., 2007, Experimental study and nonlinear dynamic analysis of time-periodic micro chaotic mixers, *Journal of Fluid Mechanics*, **575**, 425-448
9. NGUYEN N.-T., WU Z., 2005, Micromixers – a review, *Journal of Micromechanics and Microengineering*, **15**, R1-R16
10. NIU X., LEE Y.-K., 2003, Efficient spatial-temporal chaotic mixing in microchannels, *Journal of Micromechanics and Microengineering*, **13**, 454-462
11. OKKELS F., TABELING P., 2004, Spatiotemporal resonances in mixing of open viscous fluids, *Physical Review Letters*, **92**, 038301
12. OKUBO A., 1970, Horizontal dispersion of floatable particles in the vicinity of velocity singularities such as convergences, *Deep-Sea Research*, **17**, 445-454
13. TABELING P., CHABERT M., DODGE A., JULLIEN C., OKKELS F., 2004, Chaotic mixing in cross-channel micromixers, *Philosophical Transactions of the Royal Society of London A*, **362**, 987-1000
14. WEISS J., 1991, The dynamics of enstrophy transfer in two-dimensional hydrodynamics, *Physica D*, **48**, 273-294

THE GENERAL FORM OF THE ELASTIC STRESS AND DISPLACEMENT FIELDS OF THE FINITE CRACKED PLATE

ALI EHSAN SEIF, MOHAMMAD ZAMAN KABIR

Department of Civil Engineering, Amirkabir University of Technology (Tehran Polytechnic), Tehran, Iran
e-mail: seyf@aut.ac.ir; mzkabir@aut.ac.ir (corresponding author)

In this paper, the general forms of in-plane fields of a finite cracked plate have been achieved in the elastic range by expanding the potential functions of the infinite cracked plate about the crack tip. Subsequently, the stress intensity at the crack tip has been obtained. In addition, the numerical models have been provided by the finite element method. The effect of finite sizes on the stress and displacement fields has been detected and to validate the obtained analytical relations, the least-squares curve fitting has been used. Moreover, the calculated stress intensity correction factors have been compared with the existing results in the literature.

Keywords: finite cracked plate, least-squares curve fitting, general series form

1. Introduction

As Sadd (2005) explains, the stress singularity and displacement discontinuity are two characteristics of crack problems which lead to some complexity in solving these types of problems in the theory of elasticity. Solving many of crack problems will be done only by assuming the infinity of boundaries. Using this assumption, boundary conditions can be applied and the problem may be solvable. In the real problems with limited boundaries, usually, the results of infinite problems are used by applying a correction factor related to the finite size of the problem. The well known case is the use of geometry correction factor for the stress intensity at the crack tip in a finite cracked plate.

A wide range of studies using analytical and numerical methods are taken to determine the stress intensity correction factor or other stress and displacement fields at the crack tip. Isida (1971) estimated the value of the stress intensity at the crack tip by considering a special power series form for the stresses of finite cracked plates. Wu *et al.* used the weight function method to calculate the stress intensity under different loading conditions (Wu and Carlsson, 1983; Wu, 1984; Wu and Chen, 1989). Rice (1972), Ng and Lau (1999), Kiciak *et al.* (2003) and Jones *et al.* (2004) are further studies for the use of the weight function method in the crack problems. Many studies like Meng *et al.* (1998), Rangelova *et al.* (2003), Sahli *et al.* (2007) and Chen and Wang (2008) used numerical methods such as finite element and boundary element methods to observe the stress intensity or other fields at the crack-tip under different loading conditions.

Most of these studies examined only the near crack tip fields, especially the stress intensity factor and do not study the changes of stress and displacements at a distance far from the crack. Although there is no close form solution for the finite cracked plate, this study intends to extend the basic relations of infinite cracked plates and obtain the general power series form for the elastic stress and displacement fields of the finite crack plate so that it can be used for both near and far from the crack tip. To confirm the capability of the obtained analytical functions, some square plates with various crack lengths are modeled and analyzed with the finite element method. Then, the least-squares curve fitting is used to fit the analytical series functions to the numerically obtained stress and displacement profiles.

2. Analytical approach

2.1. Infinite cracked plate

Figure 1 shows the central crack with length $2a$ in an infinite plate which is under a uniform tension σ_o perpendicular to the crack direction.

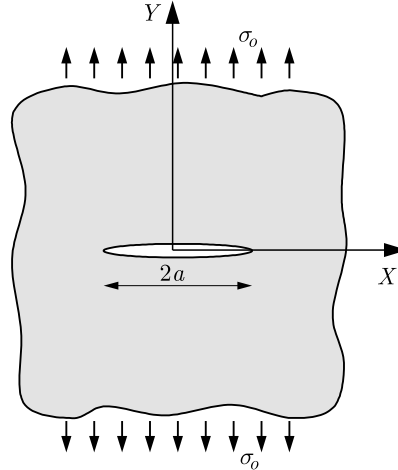


Fig. 1. Central cracked plate under tension

The classic solution of the infinite cracked plate using the complex variable method is available in many references such as Sadd (2005). Considering the complex coordinate $Z = X + iY$ and $i = \sqrt{-1}$, two complex potential functions γ and ψ are used with the following relations for the elastic problem shown in Fig. 1

$$\gamma(Z) = \frac{\sigma_o}{4} \left(2\sqrt{Z^2 - a^2} - Z \right) \quad \psi(Z) = \frac{\sigma_o}{4} \left(Z - \frac{a}{\sqrt{Z^2 - a^2}} \right) \quad (2.1)$$

Based on the potential functions, the stress combinations become

$$\sigma_y + \sigma_x = 2(\gamma' + \bar{\gamma}') \quad \sigma_y - \sigma_x + 2i\tau_{xy} = 2(\bar{Z}\gamma'' + \psi') \quad (2.2)$$

where the prime and the over-bar signs denote derivative with respect to Z and the complex conjugate, respectively, which results

$$\sigma_y + \sigma_x = \sigma_o \operatorname{Re} \left(\frac{2Z}{\sqrt{Z^2 - a^2}} - 1 \right) \quad \sigma_y - \sigma_x + 2i\tau_{xy} = \sigma_o \left[\frac{a^2(Z - \bar{Z})}{\sqrt{(Z^2 - a^2)^3}} + 1 \right] \quad (2.3)$$

in which Re is the real part. The corresponding displacements U and V respectively along X and Y can also be expressed by

$$2\mu(U + iV) = k\gamma - Z\bar{\gamma}' - \bar{\psi} \quad (2.4)$$

or

$$2\mu(U + iV) = \frac{\sigma_o}{4} \left[\frac{2(a^2 - Z\bar{Z})}{\sqrt{(\bar{Z}^2 - a^2)^3}} + k(\sqrt{Z^2 - a^2} - Z) + 1 - 2\bar{Z} \right] \quad (2.5)$$

Since E and ν are the modulus of elasticity and Poisson's ratio, $\mu = E/2(1 + \nu)$ and $k = (3 - \nu)/(1 + \nu)$ for plane stress problems. By setting X and Y in relations (2.3) and (2.5), simpler forms of the stress and displacement can be obtained for specific cases. For example, for $Y = 0$ and consequently $Z = \bar{Z} = X$, the value of the shear stress τ_{xy} is zero and the profiles of the normal stresses and displacements in the X direction are expressed as follows:

— for $X \leq a$

$$\begin{aligned} \sigma_y &= 0 & \sigma_x &= -\sigma_o \\ V &= \frac{2\sigma_o}{E} \sqrt{a^2 - X^2} & U &= -\frac{\sigma_o X}{E} \end{aligned} \tag{2.6}$$

— for $X > a$

$$\begin{aligned} \sigma_y &= \frac{\sigma_o X}{\sqrt{X^2 - a^2}} & \sigma_x &= \sigma_y - \sigma_o \\ V &= 0 & U &= \frac{\sigma_o}{E} [(1 - \nu)\sqrt{X^2 - a^2} - X] \end{aligned} \tag{2.7}$$

Likewise, in the case $X = 0$ we have $Z = -\bar{Z} = iY$, and hence

$$\begin{aligned} \sigma_y &= \frac{\sigma_o Y^3}{\sqrt{(Y^2 + a^2)^3}} & \sigma_x &= \sigma_o \left[\frac{Y(Y^2 + 2a^2)}{\sqrt{(Y^2 + a^2)^3}} - 1 \right] \\ V &= \frac{\sigma_o}{E} \left[\frac{2a^2 + (1 - \nu)Y^2}{\sqrt{a^2 + Y^2}} + \nu Y \right] & U &= 0 \end{aligned} \tag{2.8}$$

Equations (2.6) to (2.8), which are obtained on the assumption of infinite dimensions, can be used for both near crack-tip and areas away from that. But in the real problems with finite sizes, the boundary conditions affect the stress and displacement fields. These effects become more, away from the crack tip and near the boundaries and they rule out the use of infinite plate relations for the finite one. In Fig. 2, the distribution of stresses σ_{xx} and σ_{yy} on the axes X and Y of a finite cracked plate are schematically compared with the infinite ones under the same tension stress σ_o .

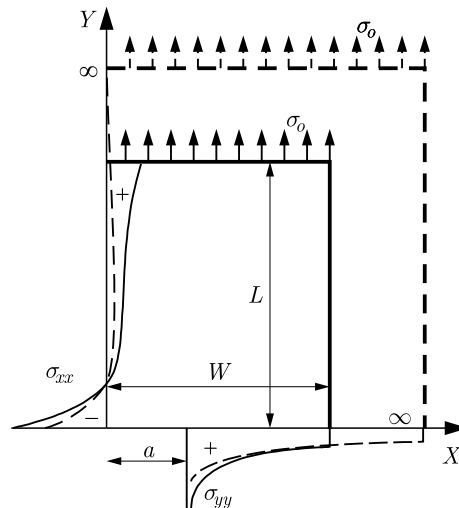


Fig. 2. Comparison of the stress distribution in one quarter of a finite cracked plate (solid line) and the infinite one (dash line) under the same tension; (+) for tensile and (-) for compressive stresses

2.2. Finite cracked plate

Ng and Lau (1999) used a method based on the expansion of field functions around the crack tip to get the general form of the stress intensity at the crack tip. In that method, using a variable transformation, the crack opening function V from (2.6)₃ is expanded around the crack tip and consequently, the general form of the stress intensity is obtained as the infinite series.

Present study uses the same method to obtain the general forms of all stresses and displacements around the crack tip and away from that. For this purpose, the variable transformation based on the parameters defined in Fig. 1 is

$$t = Z^2 - a^2 \quad (2.9)$$

so that at the crack tip we have $t = 0$. Using (2.1) and the new variable t , let the general form of the potentials be taken as follows

$$\gamma = \frac{\sigma_o}{4}[\omega(t) - B_0Z] \quad \psi = \frac{\sigma_o}{2}[B_0Z - \varphi(t)] \quad (2.10)$$

where $\omega(t)$ and $\varphi(t)$ are two basic functions of t and B_0 is an unknown coefficient. Comparing equations (2.1) with (2.10), it can be concluded that for the infinite cracked plate we have $B_0 = 1$, $\omega(t) = 2\sqrt{t}$ and $\varphi(t) = a^2/\sqrt{t}$. As Ng and Lau (1999) mentioned, according to the theory of linear elastic fracture mechanics, all the stresses and displacements in the vicinity of the crack tip are similar for any two cracks under arbitrary boundary conditions; thus the general form of the basic functions ω and φ near the crack tip will be

$$\omega_{NT} = 2A_o\sqrt{t} \quad \varphi_{NT} = \frac{A_o a^2}{\sqrt{t}} \quad (2.11)$$

where subscript NT denotes near tip. Subsequently, the normalized form of the basic functions with respect to the near tip can be defined as follows

$$G(t) = \frac{\omega(t)}{\omega_{NT}} \quad F(t) = \frac{\varphi(t)}{\varphi_{NT}} \quad (2.12)$$

Now, to reach the series form for basic functions, normalized forms (2.12) can be expanded in Taylor series about the crack tip ($t = 0$)

$$\begin{aligned} G(t) &= G(0) + \frac{G^{(1)}(0)}{1!}t + \frac{G^{(2)}(0)}{2!}t^2 + \dots + \frac{G^{(n)}(0)}{n!}t^n + \dots \\ F(t) &= F(0) + \frac{F^{(1)}(0)}{1!}t + \frac{F^{(2)}(0)}{2!}t^2 + \dots + \frac{F^{(n)}(0)}{n!}t^n + \dots \end{aligned} \quad (2.13)$$

where $F(n)$ and $G(n)$ denote the n -th derivatives of F and G with respect to t which are subject to the boundary conditions and the loading and, generally, can be used as the unknown coefficients in the series. It should be noted that approaching the crack tip, G and F are close to 1 so that at the crack tip ($t = 0$) we have $G(0) = F(0) = 1$. Hence after simplifying (2.13) and using (2.11) and (2.12), the general form of the basic functions would be

$$\begin{aligned} \omega(t) &= 2\sqrt{t}(A_0 + A_1t + A_2t^2 + \dots + A_nt^n + \dots) = \sum_{n=0}^{\infty} 2A_nt^{n+1/2} \\ \varphi(t) &= \frac{a^2}{\sqrt{t}}(A_0 + A_1t + A_2t^2 + \dots + A_nt^n + \dots) = \sum_{n=0}^{\infty} a^2 A_nt^{n-1/2} \end{aligned} \quad (2.14)$$

Finally, using (2.9) and substituting (2.14) respectively into (2.10), the general forms of the potentials would be expressed as follows

$$\gamma = \frac{\sigma_o}{4} \left[\sum_{n=0}^{\infty} 2A_n(Z^2 - a^2)^{n+1/2} - B_0Z \right] \quad \psi = \frac{\sigma_o}{2} \left[B_0Z - \sum_{n=0}^{\infty} a^2 A_n(Z^2 - a^2)^{n-1/2} \right] \quad (2.15)$$

Using above equations, the general forms of the stress and displacement fields can be achieved for the whole finite cracked plate with arbitrary boundary conditions. Substituting equations (2.15) into (2.2) and doing some mathematical works, each component of the stress can be expressed separately

$$\begin{aligned} \sigma_x &= \frac{\sigma_o}{2} \operatorname{Re} \left\{ \sum_{n=0}^{\infty} A_n H_n \left[2Z^2(Z - n\bar{Z}) - a^2 \left(\frac{2n+3}{2n+1} Z - \bar{Z} \right) \right] \right\} - B_0 \sigma_o \\ \sigma_y &= \frac{\sigma_o}{2} \operatorname{Re} \left\{ \sum_{n=0}^{\infty} A_n H_n \left[2Z^2(Z + n\bar{Z}) - a^2 \left(\frac{6n+1}{2n+1} Z + \bar{Z} \right) \right] \right\} \\ \tau_{xy} &= \frac{\sigma_o}{2} \operatorname{Im} \left\{ \sum_{n=0}^{\infty} A_n H_n \left[2Z^2(n\bar{Z}) - a^2 \left(\frac{2n-1}{2n+1} Z + \bar{Z} \right) \right] \right\} \end{aligned} \tag{2.16}$$

where Re and Im are the real and imaginary parts, respectively, and

$$H_n = (2n + 1)(Z^2 - a^2)^{n-3/2} \tag{2.17}$$

In the same way, the displacements are obtained in the series forms by using (2.15) and (2.4)

$$\begin{aligned} U &= \frac{\sigma_o}{4\mu} \operatorname{Re} \left[\sum_{n=0}^{\infty} A_n J_n - B_0 \left(\frac{k-1}{2} Z + \bar{Z} \right) \right] \\ V &= \frac{\sigma_o}{4\mu} \operatorname{Im} \left[\sum_{n=0}^{\infty} A_n J_n - B_0 \left(\frac{k-1}{2} Z + \bar{Z} \right) \right] \end{aligned} \tag{2.18}$$

in which

$$J_n = k(Z^2 - a^2)^{n+1/2} - [(2n + 1)Z\bar{Z} - a^2](\bar{Z}^2 - a^2)^{n-1/2} \tag{2.19}$$

As it will be shown, equations (2.16) to (2.19) as general forms of the stresses and displacements can be used for finite cracked plates. It is necessary to note that the obtained equations are not limited to fields near the crack tip and can get stresses and displacements away from that and close to the boundaries. Although forms (2.16) to (2.19) are so complex, simplified equations can be obtained for special cases. For example, for $Y = 0$, the profiles of non-zero stresses and displacements are expressed as follows:

— for $X \leq a$

$$\begin{aligned} \sigma_x &= -B_0 \sigma_o & U &= -\frac{\sigma_o}{E} B_0 X \\ V &= \frac{2\sigma_o}{E} \sum_{n=0}^{\infty} A_n (-1)^n (a^2 - X^2)^{n-1/2} \left(a^2 - X^2 - \frac{1+\nu}{2} n X^2 \right) \end{aligned} \tag{2.20}$$

— for $X > a$

$$\begin{aligned} \sigma_x &= \sigma_o \sum_{n=0}^{\infty} A_n X (X^2 - a^2)^{n-3/2} [X^2 - a^2 - (2n - 1)n X^2] - B_0 \sigma_o \\ \sigma_y &= \sigma_o \sum_{n=0}^{\infty} A_n X (X^2 - a^2)^{n-3/2} [(4n + 1)(X^2 - a^2) + (2n - 1)n X^2] \\ U &= \frac{\sigma_o}{E} \sum_{n=0}^{\infty} A_n (X^2 - a^2)^{n-1/2} [(1 - \nu)(X^2 - a^2) - (1 + \nu)n X^2] - \frac{\sigma_o}{E} B_0 X \end{aligned} \tag{2.21}$$

Likewise, in the case $X = 0$

$$\begin{aligned}\sigma_x &= \sigma_o \sum_{n=0}^{\infty} A_n(n+1)(-1)^n Y(Y^2 + a^2)^{n-3/2} [2a^2 + (2n+1)Y^2] - B_0\sigma_o \\ \sigma_y &= \sigma_o \sum_{n=0}^{\infty} A_n(-1)^n Y(Y^2 + a^2)^{n-3/2} [2na^2 - (2n+1)(n-1)Y^2] \\ V &= \frac{\sigma_o}{E} \sum_{n=0}^{\infty} A_n(-1)^n (Y^2 + a^2)^{n-1/2} [2a^2 + Y^2(1-\nu - n(1+\nu))] + \frac{\sigma_o}{E} B_0\nu Y\end{aligned}\quad (2.22)$$

2.3. Calculation of the stress intensity

As mentioned, based on the principles of linear elastic fracture mechanics theory, the stress and displacement fields near the crack tip have the same general forms for different boundary conditions; but their value is a function of the stress intensity at the crack tip. In other words, the stress intensity at the crack tip can be calculated from the fields of stress and displacements near the crack tip. With regard to the first mode of fracture, the stress intensity K_I can be obtained from the stress field at $Y = 0$ and $X \geq a$ as follows

$$K_I = \lim_{r \rightarrow 0} \sigma_y \sqrt{2\pi r} \quad r = X - a \quad (2.23)$$

Now, using the dimensionless variable $x = X/a$, if (2.21)₂ is used with the above equation, it will be

$$K_I = \lim_{x \rightarrow 1} \sigma_o \sqrt{\pi a} \sum_{n=0}^{\infty} \frac{A_n x}{\sqrt{x+1}} [(4n+1)(x^2-1)^n + (2n-1)nx^2(x^2-1)^{n-1}] \quad (2.24)$$

or

$$K_I = \sigma_o \sqrt{\pi a} [A_0(1) + A_1(3) + A_2(0) + \dots + A_n(0) + \dots] \quad (2.25)$$

As can be seen, despite numerous terms in series (2.21)₂, the stress intensity at the crack tip is related to the first two terms of the series. In the field of linear fracture mechanics, for cracked problems with finite sizes, the so-called correction factor β is defined as the dimensionless ratio of $K_I/\sigma_o\sqrt{\pi a}$ that includes the effect of boundary conditions and finite sizes. Hence, (2.25) can be rewritten as follows

$$\beta = \frac{K_I}{\sigma_o \sqrt{\pi a}} = A_0 + 3A_1 \quad (2.26)$$

Likewise, the stress intensity factor can be obtained based on the displacement field at $Y = 0$ and $X \leq a$

$$K_I = \lim_{r \rightarrow 0} \frac{EV}{4} \sqrt{\frac{2\pi}{r}} \quad r = a - X \quad (2.27)$$

in which E is Young's modulus, and substituting (2.20)₃ into (2.27) we have

$$\frac{K_I}{\sigma_o \sqrt{\pi a}} = \lim_{x \rightarrow 1} \sum_{n=0}^{\infty} \frac{A_n x}{\sqrt{x+1}} [(4n+1)(x^2-1)^n + (2n-1)nx^2(x^2-1)^{n-1}] \quad (2.28)$$

and thus

$$K_I = \sigma_o \sqrt{\pi a} \left[A_0(1) + A_1 \left(\frac{1+\nu}{2} \right) + A_2(0) + \dots + A_n(0) + \dots \right] \quad (2.29)$$

It should be noted that coefficients A_n in (2.25) and (2.29) are not necessarily identical, and each will be obtained independently by fitting the curves of stress and displacements. But the remarkable thing is that, as a result obtained by the stress field, this time also the stress intensity is related to the first two terms of the displacement field series. In other words, the first two terms in series (2.20)₃ to (2.22)₃ or generally (2.16) to (2.18) are related to the fields near crack tip, and the other terms describe the effects of boundary conditions on the fields away from the crack tip. However, using (2.29), the correction factor will be obtained based on the displacement field as follows

$$\beta = \frac{K_I}{\sigma_o \sqrt{\pi a}} = A_0 + \frac{1 + \nu}{2} A_1 \quad (2.30)$$

3. Numerical modeling and verifications

In order to assess the applicability of the analytical series for the finite cracked plate, the numerical models are provided in ABAQUS environment. In this context, the stress and displacement profiles have been extracted from the results of the prepared numerical models for specific cases discussed in Section 2 and using the technique of least-square curve fitting have been compared with the analytical results. Finally, the results of this comparison are presented in tables and charts. Figure 3 shows the geometric parameters of the finite cracked plate under uniaxial tensile load. Next, the description of the numerical models has been offered.

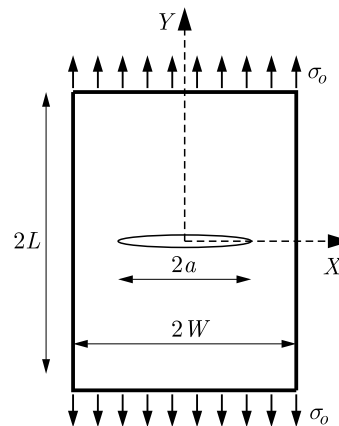


Fig. 3. The finite plate with a central cracked under tension

3.1. Numerical modeling specifications

The numerical models have been made in ABAQUS environment using 4-node doubly curved general-purpose shell elements S4R. After some mesh size sensitivity analysis, the proper finite element mesh with 3600 elements and an adequate refinement near the crack tips is illustrated in Fig. 4.

As can be seen from equations (2.23) to (2.30), the stress intensity is independent of the material properties (E and ν) and the plate thickness t . The correction factor β is also only related to the geometry of the plate. Therefore, several models of the square cracked plate ($L = W$) have been developed with different aspect ratios $a/W = 0.2 \sim 0.5$. It should be noted that in these models, the constant parameters are $E = 200$ GPa, $\nu = 0.3$, $t = 1$ mm, $W = 200$ mm and all exterior edges are free to move in the plane.

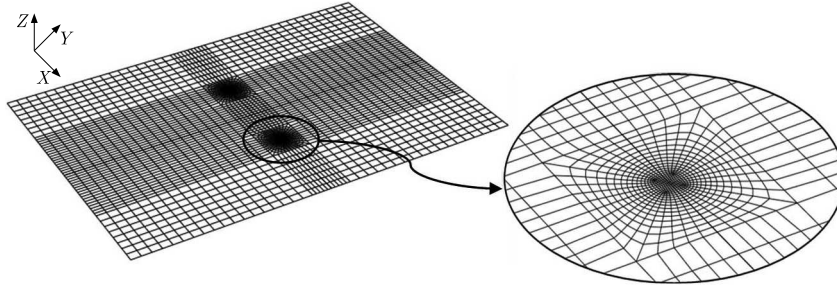


Fig. 4. Typical finite element mesh and crack tip detail

3.2. Stress and displacement fields of the finite and infinite cracked plates

Comparison of the normal stresses in the finite and infinite cracked plate is shown schematically in Fig. 2. In this Section, more complete and accurate comparison is made using the results of the finite element models. For this purpose, normalized curves of the stress and displacement profiles from the numerical models of the finite cracked plates are plotted against the existing theory relations of the infinite cracked plates in Figs. 5 to 8.

Figure 5 is related to the stresses σ_x and σ_y at $Y = 0$ and $X \leq a$. As can be seen, the general form of the stress σ_x for the finite cracked plates is similar to that of the infinite cracked plate that have been adapted to the conditions of zero stress at the free edges of the plate. But in the case of the stress σ_y , the limited size of the plate effectively changes the form of the curves. As expected, this effect is greater for plates with a larger relative crack length a/W . Moreover, with increasing crack length, the stress σ_y is increased in areas near the crack tip which, based on the principles of fracture mechanics, it is affected by increasing the stress intensity. But away from the crack tip, that trend will be changed under the influence of boundary conditions so that the tensile stresses at the free edges of the plate are unexpectedly increased with the increasing relative crack length.

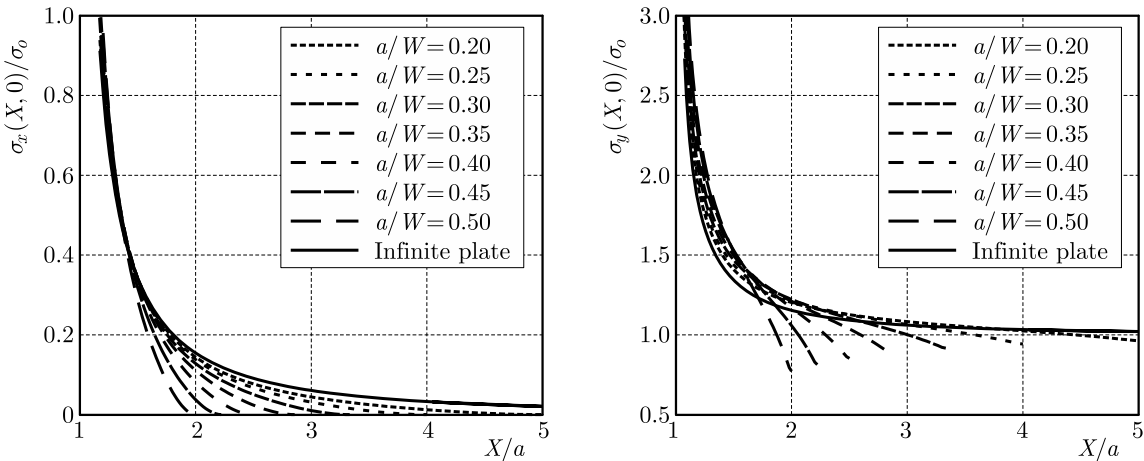


Fig. 5. Stress profiles at $Y = 0$ and $X \geq a$ from numerical results of finite cracked plates (dash lines) in comparison with theoretical profiles of the infinite cracked plate (solid lines)

According to Fig. 6, the general form of the curves for the displacement U in the finite cracked plates is similar to that of the infinite cracked plate in both linear and nonlinear parts. Likewise, in the case of crack opening displacement V , due to the remoteness of the free edges of the plates, the boundary conditions have the least impact on the general form of the curves. In terms of quantity, with the increasing relative crack length, the values of both displacements U and V are expectedly increased so that even in the normalized curves (with respect to the crack length), larger crack curves are above the smaller ones.

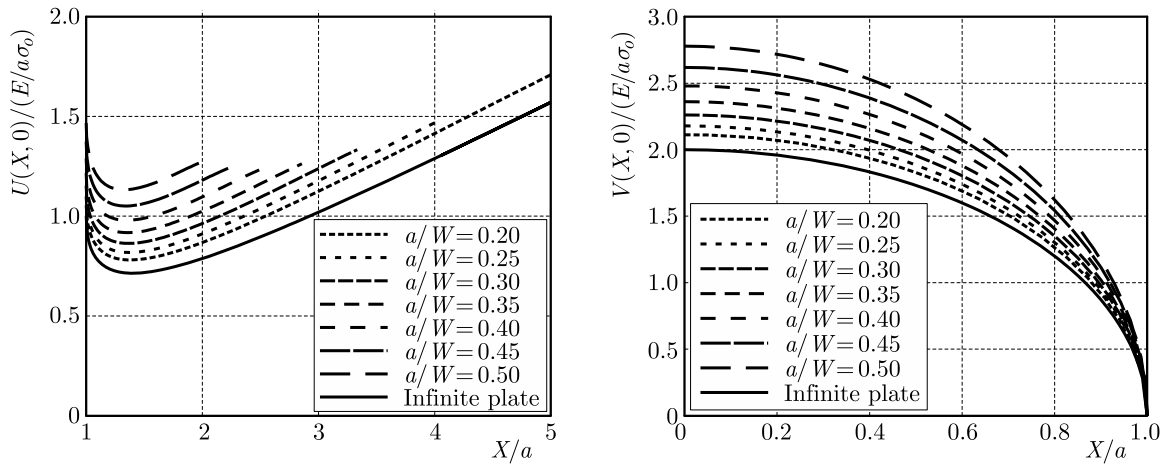


Fig. 6. Displacement profiles at $Y = 0$ and $X \geq a$ from numerical results of finite cracked plates (dash lines) in comparison with theoretical profiles of the infinite cracked plate (solid lines)

Figure 7 shows the stresses σ_x and σ_y at $X = 0$. In the case of stress σ_x , all curves show that the maximum compressive stress appears at the crack edge and decreases getting away from that. Subsequently, the compressive stress reaches zero at a distance of about $Y = 0.8a$ and then with a change of sign, it goes into the tensile phase. As can be seen, the maximum difference between the curves appears in the tensile phase so that for the infinite cracked plate, the curve is directed toward the edges and finally approaches zero; but the curves related to the finite cracked plates are upward near the edges and in most cases, the maximum tensile stress occurs at the edge. In the case of stress σ_y , a significant difference between the overall trend of the curves related to the finite and infinite cracked plate cannot be viewed. The same result can be seen for the displacement V at $X = 0$ in Fig. 8. Comparison of all stress and displacement curves indicates that the finite sizes of the plate affect the general form of the stresses more than the displacements. This effect is more for the plates with a larger relative crack length and the maximum difference between the finite and infinite cracked plates occurs away from the crack tip and near the outer boundaries.

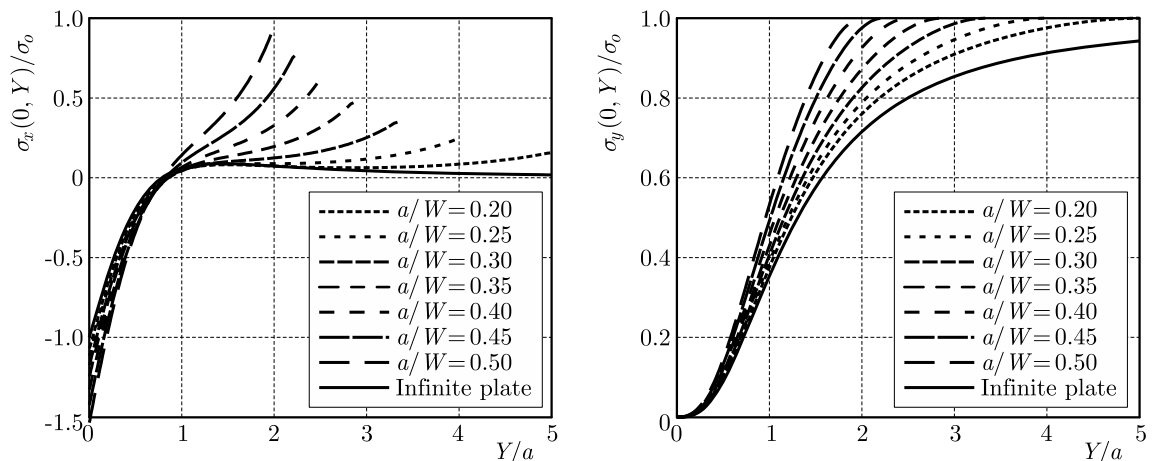


Fig. 7. Stress profiles at $X = 0$ from numerical results of finite cracked plates (dash lines) in comparison with theoretical profiles of the infinite cracked plate (solid lines)

On the whole, it can be said that the theory relations of the infinite cracked plate cannot satisfy the boundary conditions of finite cracked plates. Also in terms of overall form of some in-plane fields, those relations have considerable differences with the results of the finite cracked

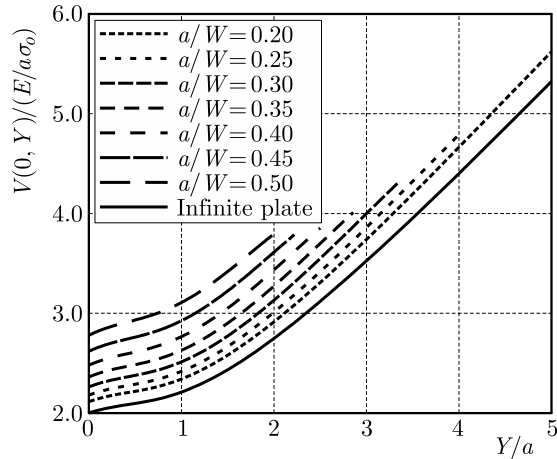


Fig. 8. Displacement profiles at $X = 0$ from numerical results of finite cracked plates (dash lines) in comparison with theoretical profiles of the infinite cracked plate (solid lines)

plates. In this regard, the general forms of stresses and displacements fields are presented in Section 2.2 and their application for the finite cracked plates will be examined in the following Section.

3.3. Validation of the analytical approach

In order to validate the presented analytical approach, using the least-squares technique, the curves of the series obtained in Section 2.2 are fitted to the stress and displacement profiles derived from the numerical models for the finite plates. In the curve fitting, three relative crack lengths of $a/W = 0.2, 0.35, 0.5$ are selected as small, medium and large cracks, and the minimum terms of the series are chosen so that so-called coefficient of determination R^2 with the precision of three decimal places is equal to 1. The results are presented in Figs. 9 to 12 and the curve fit parameters have been inserted into every curve, where R^2 is the coefficient of determination and N is the number of series terms used in the curve fitting. It should be noted that during the curve fitting, the stress singularity at the tip of the crack can cause errors and reduce the accuracy of the results. Therefore, as shown in Fig. 9, the normalized stress fields σ_x and σ_y at $Y = 0$ and $X \geq a$ are multiplied by the dimensionless term of $\sqrt{(X/a)^2 - 1}$ to avoid the errors and then the curve fitting has been done.

As can be seen, in all cases, the desired accuracy has been achieved only using a limited number of the series terms. The same results of displacement fields for this zone are shown in Fig. 10. By comparing Figs. 9 and 10, it can be seen that with the same accuracy in curve fitting, the number of required terms for displacement fields are always less than the number of terms needed for stress fields.

Figure 11 shows the curve fitting results of σ_x and σ_y at $X = 0$. As noted in Section 3.2, in the tensile phase of stress σ_x , the overall trend of the curves related to the finite cracked plates are different from the theory relations of the infinite cracked plate; but as can be seen in Fig. 11, the obtained analytical series with only 3 terms are accountable for such a dissimilar trend and with a high accuracy fit on the numerical results achieved for the finite cracked plates. In total, for both stresses σ_x and σ_y , using 3 terms of the series gives the desired accuracy. Figure 12 also represents the same results for the displacement fields at $X = 0$.

3.4. The stress intensity and correction factor

In Section 2.3, the stress intensity and, consequently, correction factor are obtained based on the first two terms of the series related to the stress σ_y and displacement V at $Y = 0$. In this Section, using the results of curve fitting, the correction factor has been attained from (2.26)

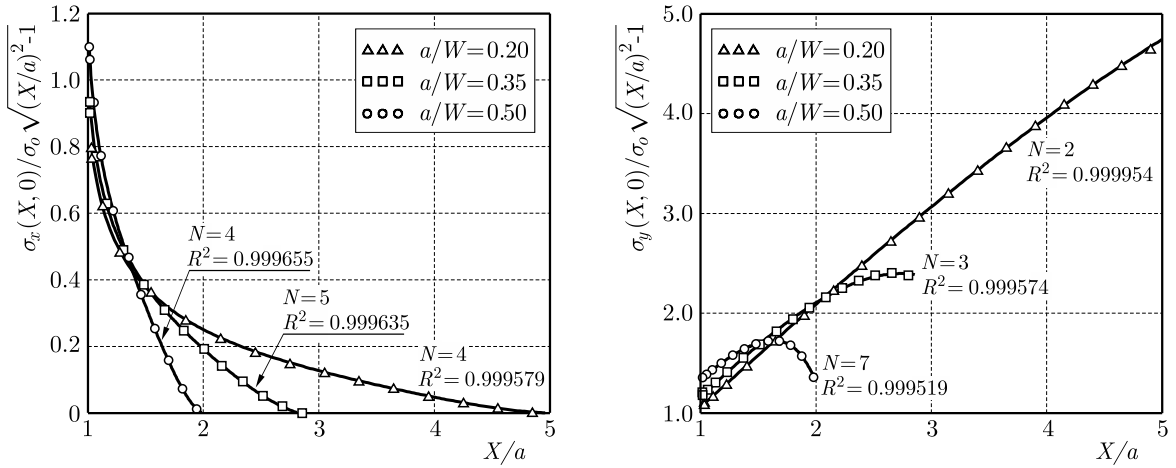


Fig. 9. Theoretical series curves (solid lines) related to stress fields at $Y = 0$ and $X \geq a$ fitted to numerical results (symbols)

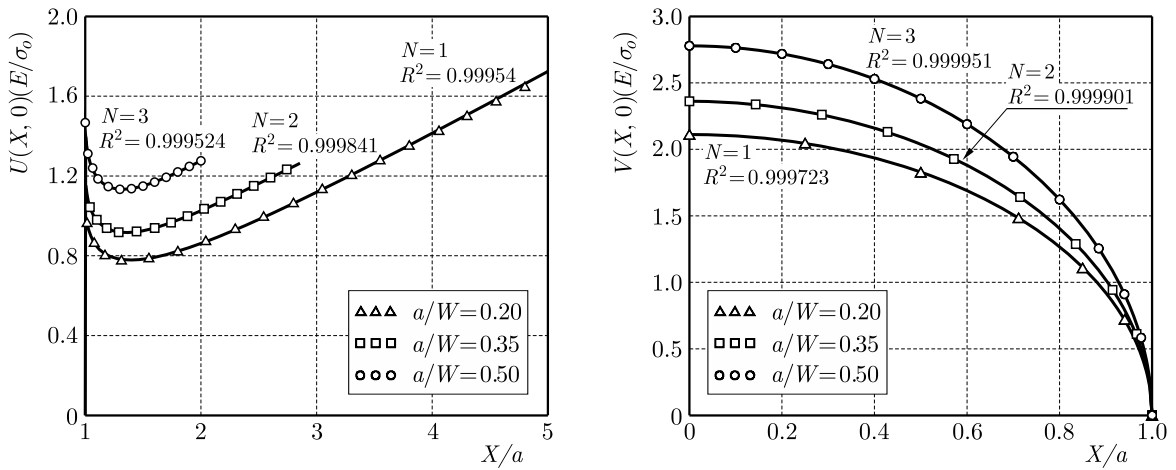


Fig. 10. Theoretical series curves (solid lines) related to displacement fields at $Y = 0$ fitted to numerical results (symbols)

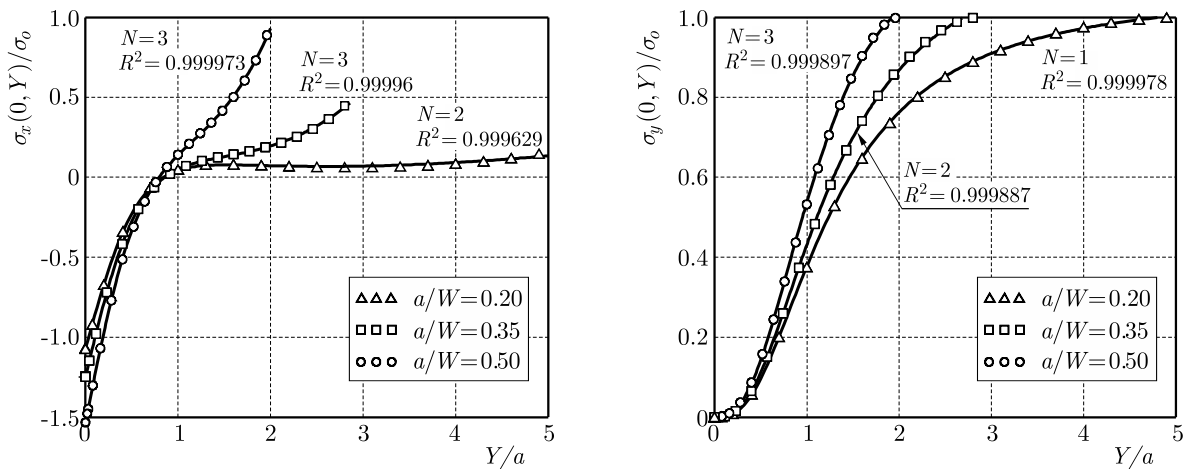


Fig. 11. Theoretical series curves (solid lines) related to stress fields at $X = 0$ fitted to numerical results (symbols)

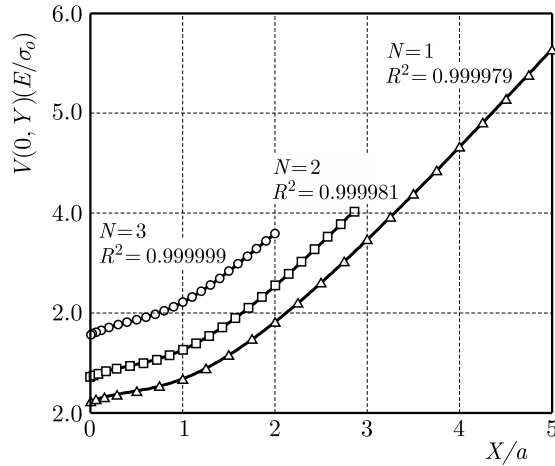


Fig. 12. Theoretical series curves (solid lines) related to displacement fields at $X = 0$ fitted to numerical results (symbols)

and (2.30) and is presented in Table 1 for three relative crack lengths of $a/W = 0.2, 0.35, 0.5$ in which the columns A_0 and A_1 contain the resulting coefficients of the curve fitting and the column β represents the evaluated correction factors from (2.26) and (2.30). Moreover, in order to validate the results, the related correction factors from Isida (1971) are presented in the column β_{REF} , and in the last column, the percentage difference between the results is provided.

Table 1. Correction factor from curve fitting process and the reference by Isida (1971)

a/W	Field	A_0	A_1	β	β_{REF}	Error [%]
0.20	$S_y(X, 0)$	1.05860	-0.00076	1.05633	1.055	0.13
	$V(X, 0)$	1.05496	-0.00153	1.05397	1.055	0.10
0.35	$S_y(X, 0)$	1.18793	-0.00762	1.16507	1.170	0.38
	$V(X, 0)$	1.17125	-0.00944	1.16511	1.170	0.38
0.50	$S_y(X, 0)$	1.41167	-0.03556	1.30498	1.334	2.18
	$V(X, 0)$	1.35431	-0.03491	1.33162	1.334	0.18

As can be seen, the analytical results of the present paper agree well with the results of Isida (1971). The maximum difference is 2.18%. It is also observed that for different crack lengths, the calculated correction factors based on the displacement filed are always more accurate than the stress filed because firstly, the displacement at the crack tip is not singular as the stress field and secondly, in the finite element method, the obtained displacement fields are continuous at the boundaries of elements while there is no such continuity for the stress fields.

4. Conclusion

Since there is no closed form solution for finite cracked plates, in this paper, the general forms of stress and displacement fields of the finite cracked plate are achieved by expanding potential functions of an infinite cracked plate about the crack tip. In addition to analytical relations, numerical models of the finite cracked plate with different crack lengths have been provided in ABAQUS environment. Based on the numerical results, the stress and displacement profiles are plotted against the existing theory relations of infinite cracked plates. The plotted curves show that finite sizes of the plate affect the general form of stresses more than displacements, and the maximum difference between the finite and infinite cracked plates occurs away from the crack tip and near the outer boundaries. The observed difference indicates that the theory relations of

the infinite cracked plate cannot satisfy the boundary conditions of the finite cracked plates and also in terms of overall form of some in-plane fields, those relations have considerable differences with the results of the finite cracked plates.

Accordingly, using the least-squares curve fitting, the obtained theoretical series for stresses and displacements of the finite cracked plates have been compared with the finite element results. The presented results indicate that the obtained analytical series with a limited number of terms are accountable for such a dissimilar trend and with a high accuracy fit to the numerical results achieved for the finite cracked plates. For example, the coefficient of determination R^2 with precision of three decimal places is equal to 1 by choosing only 7 terms of the series for singular stresses and 3 terms for other stress and displacement fields.

Moreover, by calculating the stress intensity on the basis of stress and displacement series, it has been shown that the stress intensity and the related correction factor β are related to the first two terms of the series. Using the analytical relations with the results of curve fitting, the correction factors have been attained for some relative crack lengths and compared with the results of Isida (1971). The comparison shows that the analytical results of the present paper agree well with the results of Isida (1971), and the maximum difference is 2.18%.

References

1. CHEN C.H., WANG C.L., 2008, Stress intensity factors and T-stresses for offset double edge-cracked plates under mixed-mode loadings, *International Journal of Fracture*, **152**, 149-162
2. ISIDA M., 1971, Effect of width and length on stress intensity factors of internally cracked plates under various boundary conditions, *International Journal of Fracture Mechanics*, **7**, 301-316
3. JONES R., PENG D., PITT S., WALLBRINK C., 2004, Weight functions, CTOD, and related solutions for cracks at notches, *Engineering Failure Analysis*, **11**, 79-114
4. KICIAK A., GLINKA G., BURNS D.J., 2003, Calculation of stress intensity factors and crack opening displacements for cracks subjected to complex stress fields, *Journal of Pressure Vessel Technology*, **125**, 260-266
5. MENG G., CHEN S., LIU H., WANG Z., 1998, The influence of plate size with double cracks on stress intensity factor, *Communications in Numerical Methods In Engineering*, **14**, 429-436
6. NG S.W., LAU K.J., 1999, A new weight function expression for through cracks, *Engineering Fracture Mechanics*, **64**, 515-537
7. RANGELOVA T., DINEVAB P., GROSS D., 2003, A hyper-singular traction boundary integral equation method for stress intensity factor computation in a finite cracked body, *Engineering Analysis with Boundary Elements*, **27**, 9-21
8. RICE J.R., 1972, Some remarks on elastic crack-tip stress fields, *International Journal of Solids and Structures*, **8**, 751-758
9. SADD M.H., 2005, *Elasticity: Theory, Applications and Numerics*, Elsevier Inc., Oxford
10. SAHLI A., BOUTCHICHA D., BELARBI A., RAHMANI O., 2007, Stress intensity solutions for cracked plates by the dual boundary method, *Strength of Materials*, **39**, 5, 513-522
11. WU X.R., CARLSSON J., 1983, The generalised weight function method for crack problems with mixed boundary conditions, *Journal of The Mechanics and Physics of Solids*, **31**, 6, 485-497
12. WU X.R., 1984, Approximate weight functions for center and edge cracks in finite bodies, *Engineering Fracture Mechanics*, **20**, 1, 35-49
13. WU X.R., CHEN X.G., 1989, Wide-range weight function for center cracks, *Engineering Fracture Mechanics*, **33**, 6, 877-886

A PCM-WATER HEAT EXCHANGER WITH POLYMERIC HOLLOW FIBRES FOR LATENT HEAT THERMAL ENERGY STORAGE: A PARAMETRIC STUDY OF DISCHARGING STAGE

JIŘÍ HEJČÍK, PAVEL CHARVÁT, LUBOMÍR KLIMEŠ

*Brno University of Technology, Department of Thermodynamics and Environmental Engineering, Brno, Czech Republic
e-mail: hejcik@fme.vutbr.cz; charvat@fme.vutbr.cz; klimes@fme.vutbr.cz*

ILYA ASTROUSKI

*Brno University of Technology, Heat Transfer and Fluid Flow Laboratory, Brno, Czech Republic
e-mail: astrouski@fme.vutbr.cz*

The paper presents a theoretical parametric study into latent heat thermal energy storage (LHTES) employing polymeric hollow fibres embedded in a phase change material (PCM). The polymeric hollow fibres of five inner diameters between 0.5 mm and 1.5 mm are considered in the study. The effectiveness-NTU method is employed to calculate the thermal performance of a theoretical LHTES unit of the shell-and-tube design. The results indicate that the hollow fibres embedded in a PCM can mitigate the drawback of low thermal conductivity of phase change materials. For the same packing fraction, the total heat transfer rates between the heat transfer fluid and the PCM increase with the decreasing diameter of the hollow fibres. This increase in the heat transfer rate and thus the efficiency of the heat exchange to some extent compensate for the energy consumption of the pump that also increases with the decreasing fibre diameter.

Keywords: polymeric hollow fibre, heat exchanger, latent heat thermal energy storage, phase change materials

1. Introduction

The polymeric hollow fibre heat exchanger (PHFHE) is a relatively novel type of heat exchanger that employs thin-wall polymeric fibres for separation of heat transfer fluids. The hollow fibres can be produced by the extrusion process from a variety of polymers such as polypropylene (PP), polyethylene (PE), polyether ether ketone (PEEK) as well as from certain polymers with increased conductivity. The PHFHEs are an alternative to conventional metal heat exchangers for low temperature applications (Zarkadas and Sirkar, 2004).

A number of heat transfer devices was constructed and tested for both liquid and gaseous heat transfer fluids. One of the most common designs of a PHFHE is the one similar to the shell-and-tube heat exchanger. The PHFHEs have rather high ratios between the heat transfer area and the volume (around $1400 \text{ m}^2/\text{m}^3$). Zarkadas and Sirkar (2004) reported the overall heat transfer coefficients of these devices between $647 \text{ W}/\text{m}^2\text{K}$ and $1314 \text{ W}/\text{m}^2\text{K}$ for water-to-water heat transfer application. It was shown that the overall conductance per unit of volume of the PHFHE (around $1.2 \cdot 10^6 \text{ W}/\text{m}^3\text{K}$) is larger than in the case of conventional metallic shell-and-tube exchangers and slightly less than in the case of the plate heat exchangers. Song *et al.* (2010) presented a lab study aimed at the use PHFHEs in the thermal desalination process. The metallic heat exchangers suffer from corrosive behaviour of salt water while the plastics withstand salt water quite well. The two experimental lab-scale PHFHEs were of the shell-and-tube design and contained solid polypropylene hollow fibres (950 and 2750, respectively) with

the outer diameter of 0.58 mm and the wall thickness of 0.075 mm. The experimental PHFHEs had large values of packing fraction (0.59 and 0.63, respectively) and the surface area/volume ratios of $3061 \text{ m}^2/\text{m}^3$ and $3290 \text{ m}^2/\text{m}^3$, respectively. The heat transfer performance of the PHFHEs was studied for a hot brine (80°C to 98°C) – cold water (8°C to 25°C) system as well as for a steam (101°C to 113°C) – cold water (8°C to 25°C) system as these systems are typically encountered in thermal desalination plants. The overall heat transfer coefficient as high as $2000 \text{ W}/\text{m}^2\text{K}$ was achieved, which was close to the limiting value imposed by the PP wall thickness ($2660 \text{ W}/\text{m}^2\text{K}$). The overall conductance per unit of volume was around $6.1 \cdot 10^5$ - $3.5 \cdot 10^6 \text{ W}/\text{m}^3\text{K}$, which is higher than that of metallic shell-and-tube heat exchangers and comparable with the best plate heat exchangers.

The present paper deals with a theoretical study aimed at application of PHFHEs in the latent heat thermal energy storage. The polymeric hollow fibres embedded in a phase change material (PCM) represent a way to increase the heat transfer rates between the heat transfer fluid (HTF) and the PCM. The analysis has been performed for a PCM-water latent heat thermal energy storage (LHTES) unit of the shell-and-tube design where the tubes are polymeric hollow fibres and the shell is filled with a PCM.

2. Fluid flow and heat transfer in polymeric hollow fibres

The polymeric hollow fibres have the inner diameter of around 10^{-3} m . Therefore, the fluid flow and heat transfer in hollow fibres is essentially the fluid flow and heat transfer in minichannels as classified by Kandlikar and Grande (2003) where the minichannels were channels with diameter between $200 \mu\text{m}$ and 3 mm . The fluid flow in minichannels is characterized by low Reynolds numbers. A number of correlations for minichannels and microchannels can be found in Tullius *et al.* (2012). It has been shown that the fluid flow and heat transfer in minichannels is in a good agreement with the criteria established for channels of much larger diameters (Herwig and Hausner, 2003; Celata *et al.*, 2006; Dutkowski, 2008). A significant deviation could occur in microchannels of very small diameters – only a few micrometers. Such channel diameters are close to the free mean path of the molecules where the assumption of continuum in the case of fluid flow no longer applies. However, the polymeric hollow fibres used in the PHFHEs do not have the inner diameter of less than 0.1 mm ($100 \mu\text{m}$) and the assumption of the continuum for heat and mass transfer is valid. Also, the decreasing diameter of a channel translates into increasing pressure drop. Since the pressure drop significantly influences operating costs of heat exchangers, the fluid velocities in the polymeric hollow fibres need to be rather small to achieve reasonable pressure drops. Figure 1 shows the pressure drop of 1 meter length of the hollow fibres

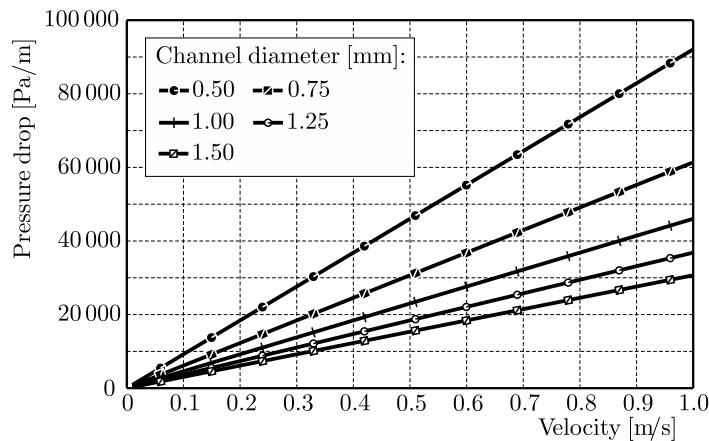


Fig. 1. Pressure drop as a function of the channel diameter and water velocity

of five inner diameters between 0.5 mm and 1.5 mm. The Reynolds number for all the cases was $Re \leq 2000$, which means laminar flow. The Nusselt number in the case of the laminar flow only depends on the boundary condition; a constant heat flux or a constant wall temperature. The Nusselt number is defined as $Nu = hd/k$ where h is the heat transfer coefficient, d is the inner diameter and k is the thermal conductivity of the fluid. The Nusselt number for laminar flow in a circular channel is $Nu = 4.36$ for the constant heat flux through the wall of the channel and $Nu = 3.66$ for constant wall temperature (Incropera *et al.*, 2006). It can be concluded from the definition of the Nusselt number that the heat transfer coefficient increases rapidly for channel diameters below 1 mm (microchannels). However, it is important to not overestimate the influence of heat transfer coefficient on the overall heat transfer rates.

3. Hollow fibres embedded in phase change materials

The phase change materials (PCMs) as the media for LHTES have received a lot of attention in the last two decades (Oró *et al.*, 2012; Sharma *et al.*, 2009; Zalba *et al.*, 2003). In contrast to sensible heat storage, the phase change of a material offers a relatively high thermal storage capacity and energy storage density in a narrow temperature interval around the temperature of the phase change. Nonetheless, the practical application of the PCMs in LHTES is still relatively limited. One of the reasons is rather low thermal conductivity of most PCMs (Jegadheeswaran and Pohekar, 2009). Many possibilities to increase the heat transfer rates between the heat transfer fluid (HTF) and the PCM have been proposed; from extended heat transfer surfaces (Al-Abidi *et al.*, 2014; Kozak *et al.*, 2014) to metal foams (Zhao *et al.*, 2010) and to nanoparticles (Raam Dheep and Sreekumar, 2014). This paper discusses the potential use of polymeric hollow fibres embedded in a PCM as a way to increase the heat transfer rates between the PCM and the heat transfer fluid. Five inner diameters of hollow fibres are considered: 0.5 mm, 0.75 mm, 1 mm, 1.25 mm and 1.5 mm. The wall thickness of the fibres is proposed in a way to achieve the same hoop stress in the wall of the fibre for the same HTF pressure. This assumption leads to a constant ratio between the outer and the inner diameter of the fibre and consequently to the same value of the thermal resistance of heat conduction through the fibre wall (per unit of length).

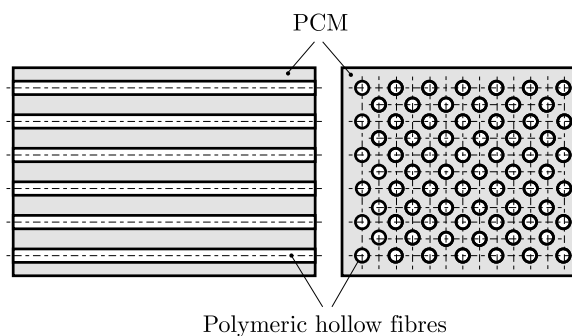


Fig. 2. Polymeric hollow fibres embedded in the PCM

Figure 2 shows a schematic view of polymeric hollow fibres embedded in a phase change material. The theoretical analysis presented in this paper focuses on the thermal performance of such an arrangement in thermal energy storage. The hexagonal pattern of the hollow fibres was considered as shown in Fig. 3. In this pattern, the distance between any two adjacent hollow fibres is the same since the distances of the fibres are the sides of equilateral triangles. The distance of the fibres, called the pitch and marked P_T in Fig. 3, is usually expressed in relation to the diameter of the tube (polymeric hollow fibre in this case). The ratio between the pitch P_T

and the outer fibre diameter D in the design of the conventional fluid-to-fluid shell-and-tube heat exchangers is between 1.25 and 1.5. This is equivalent to the packing fraction (the ratio of the tube bundle cross section area to the shell cross section area) between 0.58 (for $P_T/D = 1.25$) and 0.4 (for $P_T/D = 1.5$).

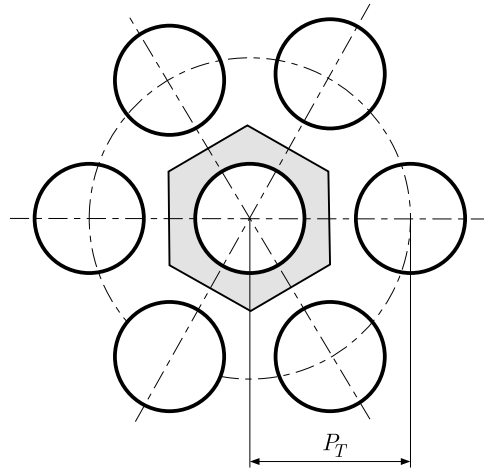


Fig. 3. Hexagonal arrangement of the fibres

Various combinations of the fibre inner diameter d and the fibre pitch P_T produce values of the heat exchanger area density between $548 \text{ m}^2/\text{m}^3$ and $2369 \text{ m}^2/\text{m}^3$, see Fig. 4. The situation in Fig. 4 applies to fluid-to-fluid heat exchangers. It shows that it is possible to reach high thermal performance with a small volume of the heat exchanger with the use of hollow fibres, because a decrease in the fibre diameter leads to a simultaneous increase in the heat transfer coefficient and the area density. However, the largest value of area density is reached for the combination of the minimal fibre diameter and the smallest fibre pitch. Hence, a very small volume of the phase change material remains around the fibres. This significantly reduces the overall thermal storage capacity of LHTES units with this design. Therefore, the packing fraction of the shell-and-tube LHTES units with PCMs needs to be much smaller than in the case of the shell-and-tube heat exchangers for fluid-to-fluid heat transfer. In the present study, the ratio $P_T/D = 10$ that provides much larger volume and thus overall thermal capacity of the PCM is used. In general, the smaller the P_T/D ratio the higher overall heat transfer rates between the PCM and the heat transfer fluid can be achieved. An optimal P_T/D ratio would depend on the purpose and operating conditions of the LHTES unit.

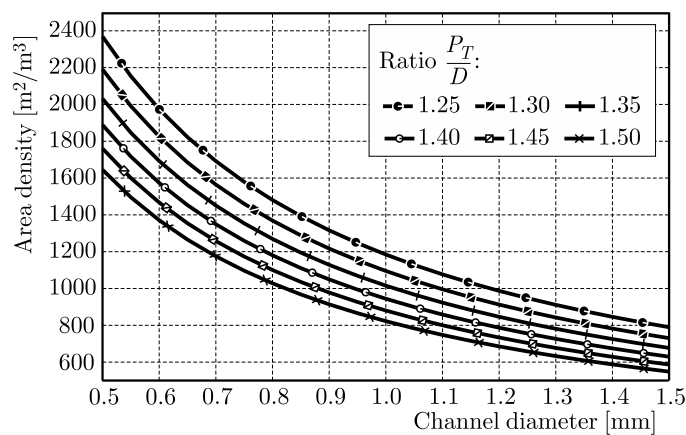


Fig. 4. Area density for different fibre diameters and P_T/D ratios

The presented parametric study takes into account both the heat transfer in the hollow fibres and the amount of stored energy. Several assumptions and simplifications have been adopted in the study. The phase change of the PCM is considered isothermal (taking place at constant temperature). This assumption has frequently been adopted by other authors, e.g. Aadmi *et al.* (2015), Hu and Patniak (2014), Zivkovic and Fuji (2001). The amount of the heat storage material belonging to one hollow fibre has been calculated from the hexagonal section (grey area in Fig. 3) and the length of the fibre. The thickness of the melted/solidified layer of the PCM along the length of the fibre is considered to be constant. The analysis of the thermal behaviour of hollow fibres in the LHTES unit has been based on the ε -NTU methodology (Tay *et al.*, 2012) where the thermal performance characteristics of a heat exchanger are described by the equations

$$\varepsilon = 1 - e^{-NTU} \quad NTU = \ln\left(\frac{1}{1 - \varepsilon}\right) \quad (3.1)$$

where ε is the heat exchanger effectiveness and NTU is the Number of Transfer Units. Since the phase change occurs at a constant temperature T_{melt} , the medium with minimal heat capacity rate C_{min} is the heat transfer fluid. The heat exchanger effectiveness thus represents the efficiency of charging (or discharging) of heat by means of the HTF, and it can be expressed by the following equation

$$\varepsilon = \frac{T_{in} - T_{out}}{T_{in} - T_{melt}} \quad (3.2)$$

where T_{in} is the HTF inlet temperature, T_{out} is the HTF outlet temperature and T_{melt} is PCM melting temperature. The heat transfer rate used for charging/discharging is calculated from the parameter NTU, which is defined as

$$NTU = \frac{UA}{C_{min}} \quad (3.3)$$

where U is the overall heat transfer coefficient, A is the heat transfer area and C_{min} is the minimal heat capacity rate, which is the product of mass flow rate \dot{m}_{HTF} and the specific heat c_{HTF} of the HTF, $C_{min} = \dot{m}_{HTF}c_{HTF}$.

The UA parameter is derived from the thermal storage geometry and the physical properties of the HTF and it is equal to the inverted value of the overall thermal resistance. Three thermal resistances are taken into account in the parametric study. The first one is the convective thermal resistance inside the hollow fibre, based on the heat transfer coefficient for the fully developed laminar flow with the constant wall temperature ($Nu = 3.66$). The second thermal resistance is the conductive resistance of the fibre wall. Finally, the third resistance is the heat transfer resistance through the solid PCM material which built up around the fibre surface during the discharge of heat from thermal energy storage. The resistance of the melted PCM around the fibre surface would be used in the case of charging of the thermal storage. The thermal resistance of the melting/solidification front is neglected and the UA value has been calculated using following equation

$$\frac{1}{UA} = \sum_i R_i = \frac{1}{h_{in}\pi dL} + \frac{\ln \frac{D}{d}}{2\pi k_w L} + \frac{\ln \frac{D_{PCM}}{D}}{2\pi k_{PCM} L} \quad (3.4)$$

where h_{in} is the heat transfer coefficient inside the fibre, d is the inner diameter of the hollow fibre, L is the fibre length, D is the fibre outer diameter, k_w is the thermal conductivity of the fibre wall, D_{PCM} is the diameter on which the melting/solidification front is located and k_{PCM} is the thermal conductivity of the solid PCM surrounding the fibre.

4. Results and discussion

Quasi-steady-state thermal calculations have been carried out for comparison of several hollow fibre diameters in the LHTES unit. The heat loss to the ambient environment is neglected as is a common assumption in theoretical studies (Belusko *et al.*, 2012; Pinnau and Breitkopf, 2015; Daugenet-Frick *et al.*, 2015). The study focuses on heat transfer between the HTF and the PCM and not on the overall thermal performance of an actual LHTES unit, so it has been justifiable to assume an adiabatic shell of the unit. Nevertheless, it needs to be emphasized that the heat loss to the ambient environment can significantly influence the real-life operation of LHTES units. The internal volume of the LHTES unit is considered 1 m^3 and the PHFHE consisted of 1 m long fibres that are assembled in the hexagonal pattern (Fig. 3) with the pitch $P_T/D = 10$. Therefore, the packing fraction is the same for all fibre diameters and the LHTES unit contains the same weight of PCM in all studied cases. The calculations start with the LHTES unit containing the liquid PCM at the melting temperature. The heat stored in the unit is discharged by water flowing through the hollow fibres (the water flow rate was 60 l/min). The initial condition is $D_{\text{PCM}} = D$ at the time $t = 0$, which means the PCM thermal resistance is equal to zero. The calculations have been performed with the time step $\Delta t = 30 \text{ s}$. The input data for calculations and the considered parameters of the LHTES unit are presented in Tables 1 and 2.

Table 1. LHTES unit parameters

Parameter	Simulation				
	1	2	3	4	5
d	0.5 mm	0.75 mm	1 mm	1.25 mm	1.5 mm
D	0.7 mm	1.05 mm	1.4 mm	1.75 mm	2.1 mm
P_T	7 mm	10.5 mm	14 mm	17.5 mm	21 mm
Number of fibres	23 565	10 473	5 891	3 770	2 618

Table 2. Calculation inputs and parameters

PCM properties	
Melting temperature T_{melt}	30°C
Latent heat	200 kJ/kg
Density	760 kg/m^3
Thermal conductivity (solid) k_{PCM}	0.2 W/mK
HTF – water	
Inlet temperature T_{in}	25°C
Flow rate \dot{m}_{HTF}	60 l/min
Fibre material	
Thermal conductivity	0.18 W/mK
Volume	1 m^3
Amount of PCM	753 kg
Latent heat capacity	1.5 GJ
Packing fraction	0.009

Figure 5 shows the time needed to discharge heat from the LHTES unit in the case of five hollow fibre diameters. It is evident that the LHTES unit with the small diameter fibres is more efficient as it takes less time to solidify all the PCM. This corresponds with the results presented in Fig. 6 that shows the heat exchanger efficiency as a function of the solid fraction. The heat transfer efficiency of the small diameter fibres remains high during the entire heat

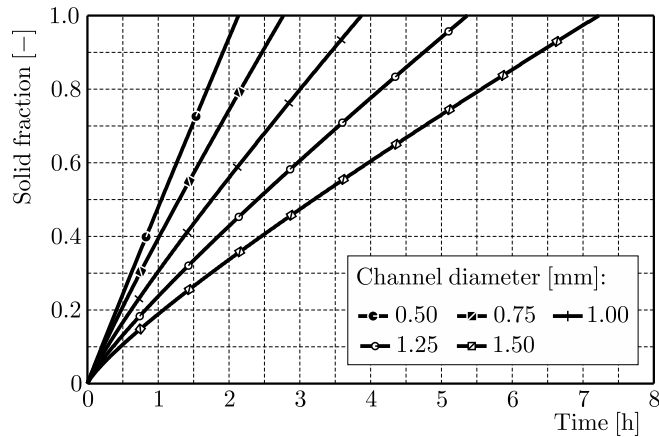


Fig. 5. Time vs. solid fraction for different fibre diameters

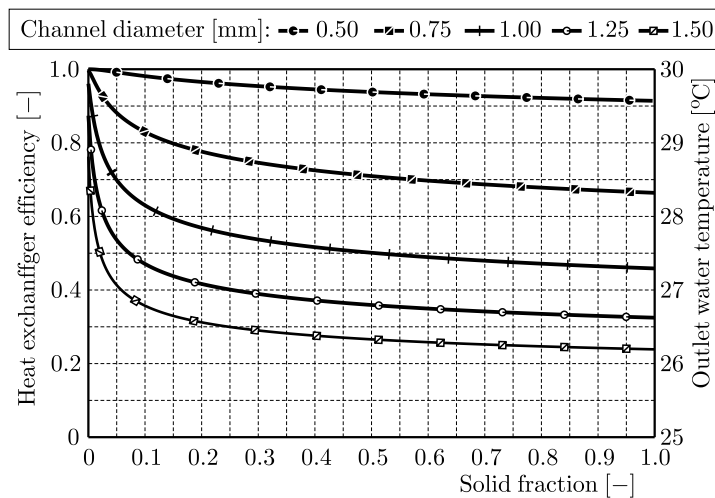


Fig. 6. Heat exchanger efficiency and outlet water temperature as functions of the solid fraction

discharge process. It is the result of very high heat transfer area of the hollow fibres with the small diameter which are surrounded by quite a thin layer of the PCM.

The efficiency of the heat exchanger influences the outlet temperature of the water as can be seen in Eq. (3.2). Even when the solidification of the PCM takes place at a constant temperature, as assumed in this study, the outlet water temperature changes during the heat discharge process, see Fig. 6. This fact can have significant consequences for real-life operation of LHTES. One of the advantages of LHTES is that heat is stored and released in a narrow temperature interval around the melting point of the heat storage medium (PCM). If there is a certain requirement on the minimum outlet temperature of the HTF, the total thermal storage capacity of a LHTES unit may not be utilized as the HTF outlet temperature drops below the required value during discharge of heat.

A high efficiency of the heat exchanger with small diameter fibres is countered by a higher pressure drop. The pressure drop in the case of 0.5 mm hollow fibres is almost 9 times higher than that in the case of 1.5 mm fibres. This translates into an increase in the pump power for the same water flow rates and the same packing fraction. Figure 7 shows the pump power as a function of the flow rate for the considered LHTES unit. The pump power has been obtained as

$$P_p = \frac{\dot{V} \Delta p}{\eta} \tag{4.1}$$

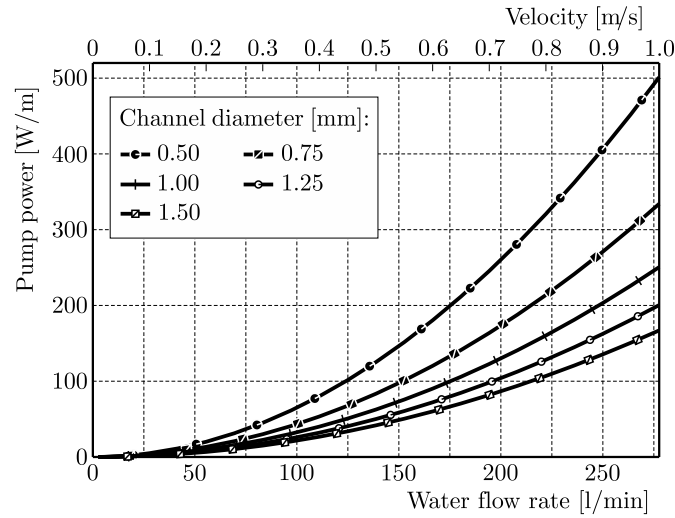


Fig. 7. Pump power as a function of the water flow rate

where \dot{V} is the volumetric flow rate, Δp is the pressure drop and η is the efficiency of the pump. For the sake of comparison, a constant efficiency of the pump $\eta = 0.85$ is considered in all cases. Though the required pump power increases with the decreasing inner diameter of the fibre. A better efficiency of the heat exchangers with small diameters of the fibres reduces the overall energy consumed by the pump during a heat storage cycle. As can be seen in Fig. 5, the time needed to discharge the heat from the heat storage unit is much shorter in the case of 0.5 mm fibres than in the case of 1.5 mm fibres.

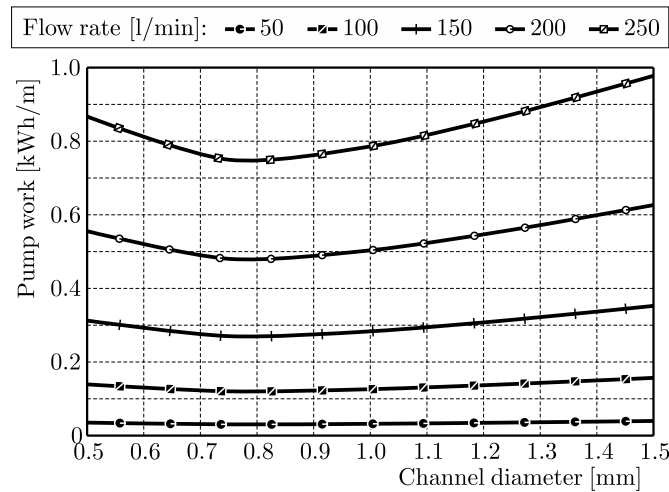


Fig. 8. Pump power as a function of the channel diameter

Figure 8 shows the energy consumed by a pump during the heat discharge period. The energy is obtained as

$$E = \int_0^t P_p dt \quad (4.2)$$

where t is the time needed for the discharge of the heat from the LHTES unit and P_p is the pump power given by Eq. (4.1). As can be seen in Fig. 8, the curves of energy consumption have a minimum for certain diameters of the hollow fibres. A parameter similar to COP can be defined as a ratio between the amount of heat charged into and/or discharged from the LHTES unit

and the energy consumed by the pump. Such a parameter can then be used in multi-criterion optimization of the design of the LHTES units with polymeric hollow fibres.

The presented parametric study is relatively simple but it shows the potential of the polymeric hollow fibre heat exchangers in the latent heat thermal energy storage. There are many obstacles to overcome in design and manufacturing of such units, e.g. LHTES units containing tens of thousands of hollow fibres would be both difficult and costly to produce. For these reasons, the small units for short-term thermal energy storage with high heat storage and heat release rates seem to be a more promising area of application of PHFHE than the large-scale thermal energy storage. One area of application could be automotive industry where various ways of LHTES have been studied in the last several years (Kim *et al.*, 2010; Javani *et al.*, 2014; Kauranen *et al.*, 2010).

5. Conclusions

The polymeric hollow fibre heat exchangers (PHFHEs) provide a large surface area density that can compensate for the small thermal conductivity of phase change materials (PCMs) in the latent heat thermal energy storage (LHTES). Moreover, PHFHEs are resistant to corrosive behaviour of some PCMs and heat transfer fluids. The results of the conducted parametric study are in line with the expectations and they indicate strengths and weaknesses of the PHFHE in LHTES in terms of heat transfer between the heat transfer fluid and the PCM. The efficiency of the PHFHE in LHTES decreases with the increasing solid fraction of a PCM. For the constant mass of a PCM, constant length of the hollow fibres and constant packing fraction, the heat transfer rates and the efficiency increase with the decreasing diameter of the hollow fibres. An increase in the packing fraction leads to an increase in the heat transfer rates but at the expense of decreasing energy storage density. For a constant packing fraction, the diameter of the hollow fibre can be found that provides the maximum ratio between the stored heat and the pump energy.

Acknowledgement

The research leading to the presented results was supported by the Czech Science Foundation under contract number P101/11/P538 and GA15-19162S.

References

1. AADMI M., KARKRI M., EL HAMMOUTI M., 2015, Heat transfer characteristics of thermal energy storage for PCM (phase change material) melting in horizontal tube: Numerical and experimental investigations, *Energy*, **85**, 339-352, DOI: 10.1016/j.energy.2015.03.085
2. AL-ABIDI A.A., MAT S., SOPIAN K., SULAIMAN M.Y., MOHAMMAD A.T., 2014, Experimental study of melting and solidification of PCM in a triplex tube heat exchanger with fins, *Energy and Buildings*, **68**, 33-41, DOI: 10.1016/j.enbuild.2013.09.007
3. BELUSKO M., HALAWA E., BRUNO F., 2012, Characterising PCM thermal storage systems using the effectiveness-NTU approach, *International Journal of Heat and Mass Transfer*, **55**, 13/14, 3359-3365, DOI: 10.1016/j.ijheatmasstransfer.2012.03.018
4. CELATA G.P., CUMO M., MARCONI V., MCPHAIL S.J., ZUMMO G., 2006, Microtube liquid single-phase heat transfer in laminar flow, *International Journal of Heat and Mass Transfer*, **49**, 19/20, 3538-3546, DOI: 10.1016/j.ijheatmasstransfer.2006.03.004
5. DAGUENET-FRICK X., GANTENBEIN P., FRANK E., FUMEY B., WEBER R., 2015, Development of a numerical model for the reaction zone design of an aqueous sodium hydroxide seasonal thermal energy storage, *Solar Energy*, **121**, 17-30, DOI: 10.1016/j.solener.2015.06.009.

6. DUTKOWSKI K., 2008, Experimental investigations of Poiseuille number laminar flow of water and air in minichannels, *International Journal of Heat and Mass Transfer*, **51**, 25/26, 5983-5990, DOI: 10.1016/j.ijheatmasstransfer.2008.04.070
7. HERWIG H., HAUSNER O., 2003, Critical view on new results in micro-fluid mechanics: an example, *International Journal of Heat and Mass Transfer*, **46**, 5, 935-937, DOI: 10.1016/S0017-9310(02)00306-X
8. HU X., PATNAIK S.S., 2014, Modeling phase change material in micro-foam under constant temperature condition, *International Journal of Heat and Mass Transfer*, **68**, 677-682, DOI: 10.1016/j.ijheatmasstransfer.2013.09.054
9. INCROPERA F.P., DEWITT D.P., BERGMAN T.L., LAVINE A.S., 2006, *Fundamentals of Heat and Mass Transfer*, Wiley, New York
10. JAVANI N., DINCER I., NATERER G.F., 2014, New latent heat storage system with nanoparticles for thermal management of electric vehicles, *Journal of Power Sources*, **268**, 718-727, DOI: 10.1016/j.jpowsour.2014.06.107
11. JEGADHEESWARAN S., POHEKAR S.D., 2009, Performance enhancement in latent heat thermal storage system: A review, *Renewable and Sustainable Energy Reviews*, **13**, 9, 2225-2244, DOI: 10.1016/j.rser.2009.06.024
12. KANDLIKAR S.G., GRANDE W.J., 2003, Evolution of microchannel flow passages: thermohydraulic performance and fabrication technology, *Heat Transfer Engineering*, **24**, 1, 3-17, DOI: 10.1080/01457630304040
13. KAURANEN P., ELONEN T., WIKSTRÖM L., HEIKKINEN J., LAURIKKO J., 2010, Temperature optimisation of a diesel engine using exhaust gas heat recovery and thermal energy storage (diesel engine with thermal energy storage), *Applied Thermal Engineering*, **30**, 6/7, 631-638, DOI: 10.1016/j.applthermaleng.2009.11.008
14. KIM K., CHOI K., KIM Y., LEE K., LEE K., 2010, Feasibility study on a novel cooling technique using a phase change material in an automotive engine, *Energy*, **35**, 1, 478-484, DOI: 10.1016/j.energy.2009.10.015
15. KOZAK Y., ROZENFELD T., ZISKIND G., 2014, Close-contact melting in vertical annular enclosures with a non-isothermal base: Theoretical modeling and application to thermal storage, *International Journal of Heat and Mass Transfer*, **72**, 114-127, DOI: 10.1016/j.ijheatmasstransfer.2013.12.058
16. ORÓ E., DE GRACIA A., CASTELL A., FARID M.M., CABEZA L.F., 2012, Review on phase change materials (PCMs) for cold thermal energy storage applications, *Applied Energy*, **99**, 513-533, DOI: 10.1016/j.apenergy.2012.03.058
17. PINNAU S., BREITKOPF C., 2015, Determination of thermal energy storage (TES) characteristics by Fourier analysis of heat load profiles, *Energy Conversion and Management*, **101**, 343-351, DOI: 10.1016/j.enconman.2015.05.055
18. RAAM DHEEP G., SREEKUMAR A., 2014, Influence of nanomaterials on properties of latent heat solar thermal energy storage materials – A review, *Energy Conversion and Management*, **83**, 133-148, DOI: 10.1016/j.enconman.2014.03.058
19. SHARMA A., TYAGI V.V., CHEN C.R., BUDDHI D., 2009, Review on thermal energy storage with phase change materials and applications, *Renewable and Sustainable Energy Reviews*, **13**, 2, 318-345, DOI: 10.1016/j.rser.2007.10.005
20. SONG L., LI B., ZARKADAS D., CHRISTIAN S., SIRKAR K., 2010, Polymeric hollow-fiber heat exchangers for thermal desalination processes, *Industrial and Engineering Chemistry Research*, **49**, 23, 11961-11977, DOI: 10.1021/ie100375b
21. TAY N.H.S., BELUSKO M., BRUNO F., 2012, An effectiveness-NTU technique for characterising tube-in-tank phase change thermal energy storage systems, *Applied Energy*, **91**, 1, 309-319, DOI: 10.1016/j.apenergy.2011.09.039

22. TULLIUS J.F., TULLIUS T.K., BAYAZITOGU Y., 2012, Optimization of short micro pin fins in minichannels, *International Journal of Heat and Mass Transfer*, **55**, 15/16, 3921-3932, DOI: 10.1016/j.ijheatmasstransfer.2012.03.022
23. ZALBA B., MARIN J.M., CABEZA L.F., MEHLING H., 2003, Review on thermal energy storage with phase change: materials, heat transfer analysis and applications, *Applied Thermal Engineering*, **23**, 3, 251-283, DOI: 10.1016/S1359-4311(02)00192-8
24. ZARKADAS D.M., SIRKAR K.K., 2004, Polymeric hollow fiber heat exchangers: An alternative for lower temperature applications, *Industrial and Engineering Chemistry Research*, **43**, 25, 8093-8106, DOI: 10.1021/ie040143k
25. ZHAO C.Y., LU W., TIAN Y., 2010, Heat transfer enhancement for thermal energy storage using metal foams embedded within phase change materials (PCMs), *Solar Energy*, **84**, 8, 1402-1412, DOI: 10.1016/j.solener.2010.04.022
26. ZIVKOVIC B., FUJII I., 2001, An analysis of isothermal phase change of phase change material within rectangular and cylindrical containers, *Solar Energy*, **70**, 1, 51-61, DOI: 10.1016/S0038-092X(00)00112-2

Manuscript received January 14, 2016; accepted for print March 3, 2016

BAND GAP PROPERTIES OF PERIODIC TAPERED BEAM STRUCTURE USING TRAVELING WAVE METHOD

TUANJIE LI

School of Electromechanical Engineering, Xidian University, Xi'an, China
e-mail: tjlh888@126.com

XIAOFEI MA

Xi'an Institute of Space Radio Technology, Xi'an, China

QIAN ZHANG, ZUOWEI WANG

School of Electromechanical Engineering, Xidian University, Xi'an, China

The wave motion equations of a tapered beam with respect to axial, torsional and flexural deformations are deduced including the transmission and waveguide equations. Combining the force equilibrium and displacement coordination conditions at the junction, we obtain the relation between the wavenumber and frequency, and the band gap properties of periodic tapered beam structures by the Bloch theorem. The modeling accuracy and efficiency of the traveling wave method are verified by the finite element method. The band gap properties of periodic tapered and uniform beam structures are analyzed and compared for the same materials and lengths as well as the same volumes.

Keywords: band gap, periodic structure, traveling wave method, Bloch theorem, tapered beam

1. Introduction

In the field of space technology, the majority of structures are complex structures, such as truss structures, frame structures and honeycomb sandwich plate structures. The basic elements of these structures are rods, beams, and plates, etc. For the convenience of manufacturing, most structures are usually built by these basic elements into periodic structures. The wave-bearing properties of periodic structures are governed by their geometries. Wave motion in periodic structures exhibits characteristic frequency intervals called pass and stop bands over which wave motion can or can not occur, respectively. There may be an opportunity to tailor materials to achieve desired band gap characteristics, such that wave propagation is prevented in specified frequency ranges. Therefore, the research on the band gap properties of periodic structures is of significance for vibration isolation design and control of the actual structures in practical engineering.

The analysis of band gap properties of periodic structures dates back to the investigations by Brillouin (1953). He deduced the relation between frequency and wavenumber to describe band gap properties of periodic structures: electric filters and crystal lattices. While since 1960s, the periodic structures consisting of beam-type elements have been attracting great attention in the mechanics and engineering technologies. Many different methods were applied to study the elastic wave propagation in beam-type periodic structures, including lump mass method in Wang *et al.* (2005), transfer matrix method in Li and Wang (2005) and Yu *et al.* (2012), plane wave expansion method in Wang *et al.* (2007), finite element method in Denys (2009) and Liu and Gao *et al.* (2007), boundary element method in Li *et al.* (2013), spectral element method in Wen *et al.* (2014) and Wu *et al.* (2015) and reverberation-ray matrix method in Guo and Fang (2013).

Based on the Euler-Bernoulli theorem, Wen *et al.* (2005) calculated the band gap properties of flexural waves of periodic binary straight beam structures by the plane wave expansion method and the vibration attenuation spectra of a finite sample by the finite element method. A novel vibration isolation structure is designed by using band gap properties of flexural waves. Doyle (1989) proposed an analytical spectral element method to obtain accurate wave solutions in the frequency domain based on the vibration equations.

The existing researches on band gap properties of beam-type periodic structures mainly have two aspects of shortcomings. One shortcoming is that the methods lack enough accuracy or versatility. The spectral element method does not have exact wave solutions for all complex structures. Therefore, it is generally used to address band gap properties of one-dimensional periodic structures. The finite element method discretizes a continuous structure into a structure with limited degrees of freedom, which results in a discrete error. The displacement of each member is described by the specified interpolation function. This simplification causes the interpolation error. Due to these errors, the finite element method has large errors for in dynamical analysis of the structures. The other shortcoming is that all mentioned references are based on uniform beams, rarely based on tapered beams. A tapered beam has changeable stiffness along the axial direction due to variable sectional area. They can improve strength and reduce weight for space applications. In addition, they have changeable flexural wavenumber varying with the sectional area. This paper combines the exact traveling wave method with the Bloch theorem to investigate the band gap properties of tapered periodic structures.

The layout of the paper is as follows. First, the traveling wave model of a tapered beam is established. Then, based on the model and Bloch theorem, the relation between wavenumber and frequency is deduced. Finally, simulations to verify the traveling wave model and analysis of the band gap properties of periodic tapered and uniform beam structures are presented.

2. Traveling wave model of the tapered beam

The vibration of structures can be considered as superposition of different frequencies and modes of elastic waves. The Fourier transform of each mode of elastic waves is called a wave mode. The different wave modes are related to different frequencies and coupled by both the transmission relation of a member and the scattering relation of a junction. The dynamical characteristics of the overall structures can be described by assembling all wave modes of members.

2.1. Traveling wave model of a member

We define the coordinate systems for a member as shown in Fig. 1. $x'y'z'$ is the global coordinate system, and xyz is the local coordinate system.

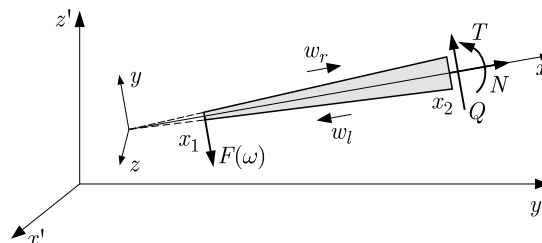


Fig. 1. Coordinate systems of a member

In Fig. 1, w_l and w_r are the left and right traveling wave modes of the member, respectively. In the local coordinate system, the right traveling waves propagate along the x -axis in the positive direction. x_1 and x_2 are position coordinates of the endpoints of the tapered beam and

the subscripts 1 and 2 indicate the number of endpoints of the junction. N is the axial force, T is the torsion with respect to x -axis, and Q is the transverse force, $F(\omega)$ is the external stimulation.

The displacement and force of the member in the global coordinate system are expressed by

$$\mathbf{P} = \begin{Bmatrix} \mathbf{U} \\ \mathbf{F} \end{Bmatrix} = \mathbf{M}_t \begin{Bmatrix} \mathbf{u} \\ \mathbf{f} \end{Bmatrix} = \mathbf{M}_t \mathbf{Y}(x, \omega) \begin{Bmatrix} w_l \\ w_r \end{Bmatrix} \tag{2.1}$$

where \mathbf{U} and \mathbf{F} are the displacement and force vectors in the global coordinate system, and \mathbf{u} and \mathbf{f} are the displacement and force vectors in the local coordinate system, respectively. \mathbf{M}_t is the coordinate transformation matrix between the global and local coordinate systems, $\mathbf{Y}(x, \omega)$ is the state transfer matrix and ω is the frequency of the external stimulation.

The wave modes of the endpoints of the tapered beam are related by a transmission matrix

$$\begin{Bmatrix} w_l \\ w_r \end{Bmatrix} \Big|_{x_2} = \tau(x_2, x_1, \omega) \begin{Bmatrix} w_l \\ w_r \end{Bmatrix} \Big|_{x_1} \tag{2.2}$$

where $\tau(x_2, x_1, \omega)$ is the transmission matrix characterizing the variations of the amplitudes and phases of each traveling wave. The waveguide and transmission equations (Eqs. (2.1) and (2.2)) are together called the traveling wave model of the member.

Based on the Euler-Bernoulli beam theory in Riedel and Kang (2006), the specific forms of above equations of the tapered beam are derived in the following.

2.2. Waveguide equations of the tapered beam

Generally, the beam structure contains three types of wave modes: axial wave mode, torsional wave mode and flexural wave mode. The thin and straight tapered beam shown in Fig. 1 is assumed to be the ideal elastomer. Then, the length of the beam is $l = x_2 - x_1$, and the sectional area of a tapered beam $A(x)$ is a function of x . This function is assumed to be $A(x) = A_0 x^2/a^2$, where a is the variation factor of the sectional area, A_0 is the standard sectional area of the referenced uniform beam in Riedel and Kang (2006).

2.2.1. Axial waveguide equation

The force analysis of the tapered beam with respect to stretching and compression deformations is shown in Fig. 2. The force equilibrium equation of an infinitesimal unit is

$$\rho \frac{1}{2} [A(x + dx) + A(x)] dx \frac{\partial^2 u}{\partial t^2} = \left(N + \frac{\partial N}{\partial x} dx \right) - N = E \frac{\partial A(x) u}{\partial x} dx \tag{2.3}$$

where ρ is density, and $u(x, t)$ is the axial displacement.

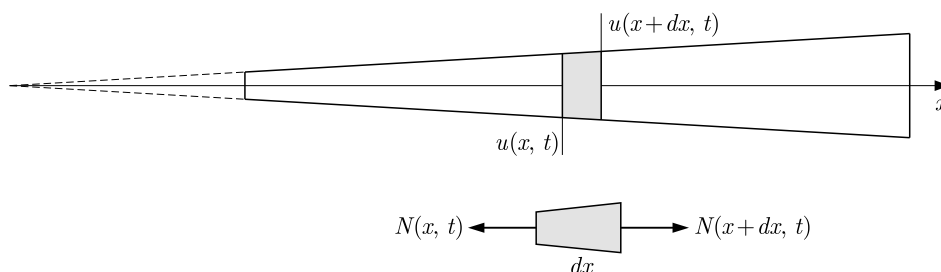


Fig. 2. Axial deformation of the tapered beam

The coefficient of the quadratic differential term of u in Eq. (2.3) must be simplified to obtain analytical wave solutions. We adopt Taylor series expansion of $A(x + dx)$ to obtain the approximation relation

$$[A(x + dx) + A(x)]dx \approx 2A(x)dx + \frac{\partial A(x)}{\partial A(x)}d^2x \tag{2.4}$$

By omitting the second-order terms of dx in Eq. (2.4), we can further simplify Eq. (2.3) as

$$\rho A(x)dx \frac{\partial^2 u(x, t)}{\partial t^2} = EA(x) \frac{\partial^2 u(x, t)}{\partial x^2} dx + E \frac{\partial u(x, t)}{\partial x} \frac{dA(x)}{dx} dx \tag{2.5}$$

where E is the elasticity modulus. With separation of variables $u(x, t) = \hat{u}(x, \omega)e^{j\omega t}$, the equation of motion of the axial wave is given by

$$\frac{\partial^2 \hat{u}}{\partial x^2} + \frac{2}{x} \frac{\partial \hat{u}}{\partial x} + \frac{\rho\omega^2}{E} \hat{u} = 0 \tag{2.6}$$

The general solution to Eq. (2.6) is

$$\hat{u}(x, \omega) = u_l + u_r = \frac{c_{ul}}{k_\alpha x} \exp\left[j\left(k_\alpha x - \frac{\pi}{2}\right)\right] + \frac{c_{ur}}{k_\alpha x} \exp\left[-j\left(k_\alpha x - \frac{\pi}{2}\right)\right] \tag{2.7}$$

where u_l and u_r are the undetermined left and right axial traveling wave modes, respectively. The axial wavenumber $k_\alpha = \sqrt{\rho\omega^2/E}$ depends on the density, elasticity modulus and frequency except the sectional area.

Based on Eq. (2.7), the waveguide equation is expressed by

$$\begin{Bmatrix} \hat{u} \\ N \end{Bmatrix} = \begin{bmatrix} 1 & 1 \\ -\frac{EA}{x} + jk_\alpha EA & -\frac{EA}{x} - jk_\alpha EA \end{bmatrix} \begin{Bmatrix} u_l \\ u_r \end{Bmatrix} \tag{2.8}$$

The corresponding transmission equation of wave modes is

$$\begin{Bmatrix} u_l \\ u_r \end{Bmatrix}_{|x=x_2} = \text{diag}\left(\frac{x_1}{x_2} e^{jk_\alpha l}, \frac{x_1}{x_2} e^{-jk_\alpha l}\right) \begin{Bmatrix} u_l \\ u_r \end{Bmatrix}_{|x=x_1} \tag{2.9}$$

2.2.2. Torsional waveguide equation

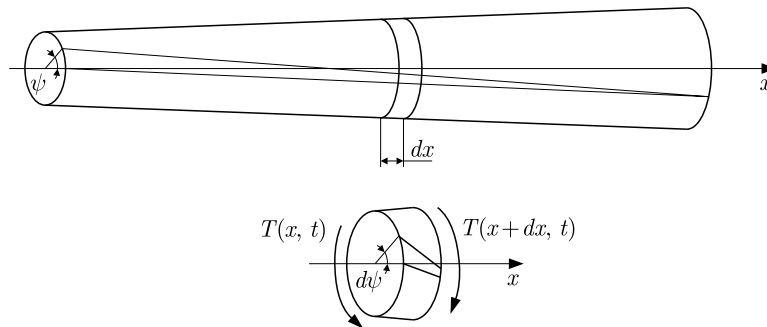


Fig. 3. Torsional deformation of the tapered beam

The torsional motion of the tapered beam is shown in Fig. 3, where $\psi(x, t)$ indicates the angle with respect to the x -axis. The moment equilibrium equation of the infinitesimal unit is given as

$$\rho I_p(x)dx \frac{\partial^2 \psi(x, t)}{\partial t^2} = T(x + dx) - T(x) = \frac{\partial T(x, t)}{\partial x} dx \tag{2.10}$$

$$T = GI_p \frac{\partial \psi}{\partial x}$$

where I_P is the polar moment of inertia of the section and G is the shear modulus.

Setting $\psi(x, t) = \overline{\phi(x, \omega)}e^{j\omega t}$, we can obtain the torsional motion equations as follows

$$\frac{\partial^2 \phi}{\partial x^2} + \frac{4}{x} \frac{\partial \phi}{\partial x} + \frac{\rho\omega^2}{G} \phi = 0 \tag{2.11}$$

In a similar way, the waveguide equation of the torsional wave is

$$\begin{Bmatrix} \phi \\ T \end{Bmatrix} = \begin{bmatrix} 1 + \frac{j}{k_t x} & 1 - \frac{j}{k_t x} \\ \left(-\frac{3}{x} - \frac{3j}{k_t x^2} + jk_t\right)GI_P & \left(-\frac{3}{x} + \frac{3j}{k_t x^2} - jk_t\right)GI_P \end{bmatrix} \begin{Bmatrix} \phi_l \\ \phi_r \end{Bmatrix} \tag{2.12}$$

where ϕ_l and ϕ_r are the undetermined left and right torsional traveling wave modes, respectively. The torsional wavenumber $k_t = \sqrt{\rho\omega^2/G}$ is related to the density, shear modulus and frequency, and is independent of the sectional area.

The transmission equation of the torsional wave is described as

$$\begin{Bmatrix} \phi_l \\ \phi_r \end{Bmatrix} \Big|_{x=x_2} = \text{diag} \left(\frac{x_1^2}{x_2^2} e^{jk_t l}, \frac{x_1^2}{x_2^2} e^{-jk_t l} \right) \begin{Bmatrix} \phi_l \\ \phi_r \end{Bmatrix} \Big|_{x=x_1} \tag{2.13}$$

2.2.3. Flexural waveguide equation

The flexural stress analysis of the tapered beam is shown in Fig. 4, where $w_y(x, t)$ is the y -axis deflection of the beam, $I_z = \int_A y^2 dA$ indicates the moment of inertia of the section with respect to the z -axis. M_z is the bending moment with respect to the z -axis and the distribution force is $q = \partial^2 M_z / \partial x^2$. The force equilibrium equation of the flexural motion of the infinitesimal element in the plane xy is

$$\frac{\partial^2}{\partial x^2} \left(EI_z \frac{\partial^2 w_y(x, t)}{\partial x^2} \right) = \rho A \frac{\partial^2 w_y(x, t)}{\partial t^2} \tag{2.14}$$

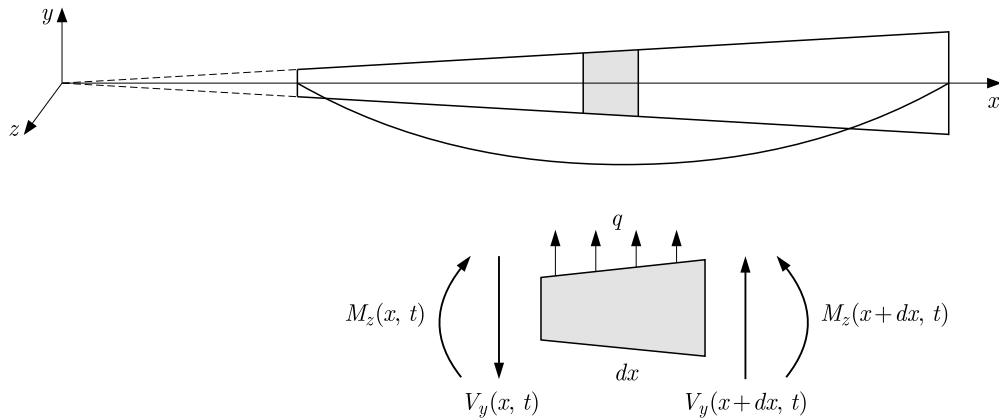


Fig. 4. Flexural deformation of the tapered beam

With the expression of $w_y(x, t) = \hat{w}_y(x, \omega)e^{j\omega t}$, Eq. (2.14) yields the wave equation of motion

$$x^2 \frac{\partial^4 \hat{w}_y}{\partial x^4} + 8x \frac{\partial^3 \hat{w}_y}{\partial x^3} + 12x^2 \frac{\partial^2 \hat{w}_y}{\partial x^2} - \frac{4\pi a^2 \rho\omega^2}{EA_0} \hat{w}_y = 0 \tag{2.15}$$

The general solution to Eq. (2.15) is

$$\hat{w}_y = w_{y1} + w_{y2} + w_{y3} + w_{y4} \tag{2.16}$$

where

$$\begin{aligned} w_{y1} &= \frac{c_{y1}}{\sqrt[5]{x^4}} \exp\left[j\left(2k_z x - \frac{\pi}{4}\right)\right] & w_{y2} &= \frac{c_{y2}}{\sqrt[5]{x^4}} \exp\left(2k_z x - \frac{j\pi}{4}\right) \\ w_{y3} &= \frac{c_{y3}}{\sqrt[5]{x^4}} \exp\left[-j\left(2k_z x - \frac{\pi}{4}\right)\right] & w_{y4} &= \frac{c_{y4}}{\sqrt[5]{x^4}} \exp\left(-2k_z x - \frac{j\pi}{4}\right) \end{aligned}$$

Differently from the wavenumber of axial and torsional wave modes, the wavenumber of the flexural wave mode $k_z = \sqrt[4]{\rho A \omega^2 / (EI_z)}$ not only depends on the density, frequency, elasticity modulus and moment of inertia of area, but also on the sectional area. Therefore, the wavenumber of flexural wave mode of the tapered beam varies with the sectional area. For convenient calculation, the position variable of the section x is separated from k_z , i.e. $k_z = k'_z / \sqrt{x}$, where $k'_z = \sqrt[4]{4\pi a^2 \rho \omega^2 / (EA_0)}$ is a constant.

Then, the waveguide equation of the flexural wave mode is

$$\begin{Bmatrix} \widehat{w}_y \\ \varphi_z \\ V_y \\ M_z \end{Bmatrix} = \begin{bmatrix} 1 & 1 & 1 & 1 \\ a_{y1} + ja_{y2} & a_{y1} + a_{y2} & a_{y1} - ja_{y2} & a_{y1} - a_{y2} \\ m_{31} & m_{32} & m_{33} & m_{34} \\ m_{41} & m_{42} & m_{43} & m_{44} \end{bmatrix} \begin{Bmatrix} w_{y1} \\ w_{y2} \\ w_{y3} \\ w_{y4} \end{Bmatrix} \quad (2.17)$$

where $m_{31} = EI_z(a_{y3} - ja_{y4} - a_{y5} + ja_{y2}^3)$, $m_{32} = EI_z(a_{y3} - a_{y4} + a_{y5} - a_{y2}^3)$, $m_{33} = EI_z(a_{y3} + ja_{y4} - a_{y5} - ja_{y2}^3)$, $m_{34} = EI_z(a_{y3} + a_{y4} + a_{y5} + a_{y2}^3)$, $m_{41} = EI_z[-(9a_{y1}/(4x)) - (3ja_{y2}/x) - a_{y2}^2]$, $m_{42} = EI_z[-(9a_{y1}/(4x)) - (3a_{y2}/x) + a_{y2}^2]$, $m_{43} = EI_z[-(9a_{y1}/(4x)) + (3ja_{y2}/x) - a_{y2}^2]$, $m_{44} = EI_z[-(9a_{y1}/(4x)) + (3a_{y2}/x) + a_{y2}^2]$, and $\varphi_z = \partial \widehat{w}_y / \partial x$ is the bending angle with respect to the z -axis and $V_y = EI_z \partial^3 \widehat{w}_y / \partial x^3$ is the shear force with respect to the y -axis. Some coefficients in Eq. (2.17) are $a_{y1} = -5/(4x)$, $a_{y2} = k'_z / \sqrt{x}$, $a_{y3} = 585/(64x^3)$, $a_{y4} = 177k'_z / (16\sqrt{x^5})$, $a_{y5} = 21k'_z{}^2 / (4x^2)$. The transmission equation of the flexural wave modes is

$$\begin{Bmatrix} w_l \\ w_r \end{Bmatrix}_{|x=x_2} = \text{diag}\left(a_{y6} e^{2jk'_z a_{y7}}, a_{y6} e^{2k'_z a_{y7}}, a_{y6} e^{-2jk'_z a_{y7}}, a_{y6} e^{-2k'_z a_{y7}}\right) \begin{Bmatrix} w_l \\ w_r \end{Bmatrix}_{|x=x_1} \quad (2.18)$$

where $w_l = \{w_{y1}, w_{y2}\}^T$, $w_r = \{w_{y3}, w_{y4}\}^T$, $a_{y6} = \sqrt[4]{x_1^5/x_2^5}$, $a_{y7} = \sqrt{x_2} - \sqrt{x_1}$.

Due to flexural deformation of the beam with the circular cross-section, in the plane xy and xz there is rotational symmetry with respect to x -axis. Similarly, $k_y = k'_y / \sqrt{x}$, where $k'_y = \sqrt[4]{4\pi a^2 \rho \omega^2 / (EA_0)}$ is a constant. The waveguide equation and the transmission equation of wave modes in the plane xz are obtained just replacing I_z and k_z by I_y and k_y .

2.2.4. Spatial beam element

As the wave motion couples the axial, torsional and flexural wave modes, the corresponding \mathbf{u} , \mathbf{f} , \mathbf{w}_l and \mathbf{w}_r in Eq. (2.1) can be defined by

$$\begin{aligned} \mathbf{u} &= \left\{ \widehat{u} \quad \widehat{w}_y \quad \widehat{w}_z \quad \phi \quad \varphi_y \quad \varphi_z \right\}^T & \mathbf{f} &= \left\{ N \quad V_y \quad V_z \quad T \quad M_y \quad M_z \right\}^T \\ \mathbf{w}_l &= \left\{ w_l \quad w_{y1} \quad w_{z1} \quad \phi_l \quad w_{y2} \quad w_{z2} \right\}^T & \mathbf{w}_r &= \left\{ w_r \quad w_{y3} \quad w_{z3} \quad \phi_r \quad w_{y4} \quad w_{z4} \right\}^T \end{aligned} \quad (2.19)$$

For the sake of simplicity, the state transfer matrix of tapered beam is described as

$$Y = \begin{bmatrix} Y_{ul} & Y_{ur} \\ Y_{fl} & Y_{fr} \end{bmatrix} \quad (2.20)$$

where Y_{ul} , Y_{ur} , Y_{fl} and Y_{fr} can be obtained by Eqs. (2.8), (2.12) and (2.17).

The transmission matrix of the spatial tapered beam is obtained as

$$t(x_2, x_1, \omega) = \begin{bmatrix} t'(x_2 - x_1) & 0 \\ 0 & t'(x_1 - x_2) \end{bmatrix} \quad (2.21)$$

where $t'(x_2 - x_1)$ and $t'(x_1 - x_2)$ can be found from Eqs. (2.9), (2.13) and (2.18).

3. Band gap properties of periodic tapered beam structure

The periodic beam structure shown in Fig. 5 is rigidly composed of tapered beam units. Each periodic unit has two tapered beams with different materials rigidly connected together at the junction \mathbf{H} . \mathbf{U}_{nB}^R and \mathbf{F}_{nB}^R indicate the output displacement and force of the n -th periodic unit. The superscript R and L denote the right and left endpoints of the tapered beam, respectively. According to the force equilibrium and displacement coordination at the junction, we obtain the following relation of state vectors:

— beam A and beam B

$$\mathbf{F}_{nA}^R + \mathbf{F}_{nB}^L = \mathbf{0} \quad \mathbf{U}_{nA}^R = \mathbf{U}_{nB}^L \quad (3.1)$$

— periodic units n and $n - 1$

$$\mathbf{F}_{(n-1)B}^R + \mathbf{F}_{nA}^L = \mathbf{0} \quad \mathbf{U}_{(n-1)B}^R = \mathbf{U}_{nA}^L \quad (3.2)$$

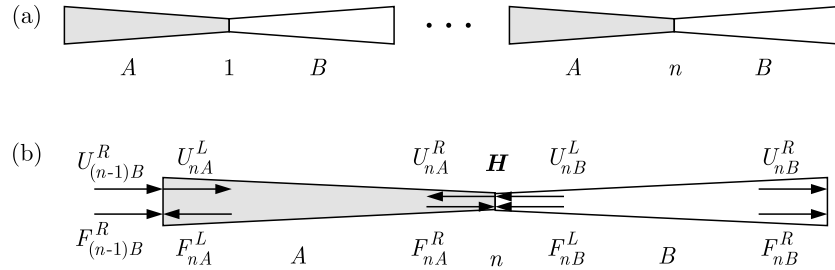


Fig. 5. Periodic tapered beam structure; (a) periodic tapered beam structure, (b) periodic unit

According to the connection relationship of periodic units in Fig. 5, $\mathbf{P}_{(n-1)B}^R = \{\mathbf{U}_{(n-1)B}^R, \mathbf{F}_{(n-1)B}^R\}^T$ is the input state vector of the n -th unit, $\mathbf{P}_{nB}^R = \{\mathbf{U}_{nB}^R, \mathbf{F}_{nB}^R\}^T$ is the output state vector of the n -th periodic unit. With Eqs. (3.1) and (3.2), the relationship of state vectors between two tapered beams of the periodic unit and between two periodic units are given by

$$\mathbf{P}_{nA}^R = \text{diag}(\mathbf{I}, -\mathbf{I})\mathbf{P}_{nB}^L \quad \mathbf{P}_{(n-1)B}^R = \text{diag}(\mathbf{I}, -\mathbf{I})\mathbf{P}_{nA}^L \quad (3.3)$$

The state vectors $\mathbf{P}_{ni_2}^{i_1} = \{\mathbf{U}_{ni_2}^{i_1}, \mathbf{F}_{ni_2}^{i_1}\}^T$ and the wave modes vector $\mathbf{W}_{nA}^{i_1} = \{w_{nl}, w_{nr}\}^T$ are defined, where the superscript i_1 indicates R or L and the subscript i_2 indicates A or B . According to waveguide equation Eq. (2.1) and transmission equation Eq. (2.2), we get

$$\mathbf{P}_{ni_2}^{i_1} = \text{diag}(\mathbf{I}, -\mathbf{I})\mathbf{V}_{ni_2}\mathbf{Y}_{ni_2}^{i_1}\mathbf{W}_{ni_2}^{i_1} \quad \mathbf{W}_{ni_2}^R = T_{ni_2}\mathbf{W}_{ni_2}^L \quad (3.4)$$

where \mathbf{I} is a 3×3 identity matrix and \mathbf{V}_n is the coordinate transformation of the tapered beam i_2 of the n -th periodic unit.

If m is the number of periods, the relation of the input and output state vectors of the $(n+m)$ -th periodic unit can be obtained based on Eqs. (3.1)-(3.4)

$$\begin{aligned} \mathbf{P}_{(n+m)B}^R &= \mathbf{A}_{(n+m-1)B}\mathbf{B}_{(n+m-1)A}\mathbf{P}_{(n+m-1)B}^R \\ \mathbf{A}_{(n+m-1)B} &= \mathbf{V}_{(n+m-1)B}\mathbf{Y}_{(n+m-1)B}^R\mathbf{T}_{(n+m-1)B}^{L \rightarrow R}(\mathbf{Y}_{(n+m-1)B}^L)^{-1}(\mathbf{V}_{(n+m-1)B})^{-1} \\ \mathbf{B}_{(n+m-1)A} &= \mathbf{V}_{(n+m-1)A}\mathbf{Y}_{(n+m-1)A}^R\mathbf{T}_{(n+m-1)A}^{R \rightarrow L}(\mathbf{Y}_{(n+m-1)A}^L)^{-1}(\mathbf{V}_{(n+m-1)A})^{-1} \end{aligned} \quad (3.5)$$

where the subscript $L \rightarrow R$ indicates the coordinate transformation matrix from the left endpoint to the right endpoint, similarly $R \rightarrow L$.

The relation between the input state vector of the n -th and the output state vector of $(n+m)$ -th periodic unit is

$$\mathbf{P}_{(n+m)B}^R = \mathbf{A}_{(n+m-1)B} \mathbf{B}_{(n+m-1)A} \mathbf{P}_{(n+m-1)B}^R = \prod_{j=n+m}^{n+1} \mathbf{A}_{(j-1)B} \mathbf{B}_{(j-1)A} \mathbf{P}_{nB}^R = \mathbf{C} \mathbf{P}_{nB}^R \quad (3.6)$$

where

$$\mathbf{C} = \prod_{j=n+m}^{n+1} \mathbf{A}_{(j-1)B} \mathbf{B}_{(j-1)A}$$

The undetermined state vectors of Eq. (3.6) are much larger than the number of equations. Therefore, Eq. (3.6) is a multiple solutions problem. More equations are needed to obtain the analytical solutions. The state vectors of different periodic units are related by the Bloch theorem. The relation describing the input and output state vectors between the n -th and $(n+m)$ -th periodic unit by the Bloch theorem is given as

$$\mathbf{P}_{(n+m)B}^R = \text{diag}(e^{jkmb} \mathbf{I}, -e^{jkmb} \mathbf{I}) = \mathbf{D} \mathbf{P}_{nB}^R \quad (3.7)$$

where k is the wavenumber of the periodic unit, b is the length of the periodic unit.

Combining Eq. (3.6) with Eq. (3.7), the following expression is obtained

$$(\mathbf{C} - \mathbf{D}) \mathbf{P}_{nB}^R = \mathbf{0} \quad (3.8)$$

If the matrix determinant $\det(\mathbf{C} - \mathbf{D}) = 0$, we can get the relation between the wavenumber and frequency, and the band gap properties.

4. Numerical simulations

Two numerical examples are applied to illustrate the proposed method of the tapered beam. The first one is to analyze the vibration response of the tapered cantilever beam with flexural deformations. The veracity and superiority of the proposed method are revealed by comparing with the results of the finite element method. The second one is to compare the differences between the band gap properties of the periodic tapered and uniform beam structure.

4.1. Dynamic response analysis

A transverse stimulation applied to the endpoint 1 of the cantilever tapered beam shown in Fig. 1 is $F(\omega) = e^{j\omega t}$ and the other endpoint 2 is fixed. The material and geometrical parameters are listed in Table 1.

Table 1. Material and geometrical parameters of the tapered beam

Elasticity modulus E [Pa]	Density ρ [kg/m ³]	Poisson's ratio μ	Length L [m]	Variation factor a	Standard area A_0 [m ²]
$2.0 \cdot 10^9$	7800	0.3	1	2	$5.0 \cdot 10^{-4}$

The frequency response of the transverse displacement of the free end is shown in Fig. 6. The results of the traveling wave model are compared with those of the finite element method. In Fig. 6, the results of the traveling wave method are displayed by the black solid line, and the finite element results obtained by 20 elements and 5 elements per member are shown by the grey dash dot line and black dash line, respectively.

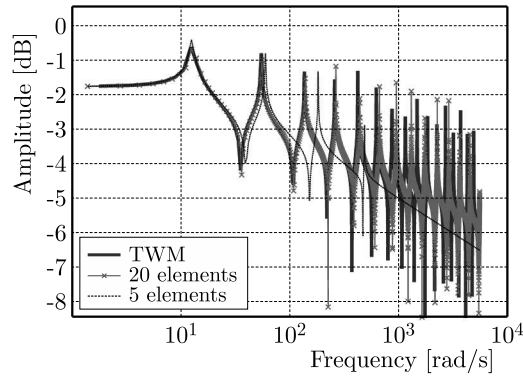


Fig. 6. Frequency response of transverse displacement of the free end

As shown in Fig. 6, the results of the traveling wave model well coincide with the finite element results obtained by 20 elements per member in the low frequency range, which verifies the veracity of the proposed traveling wave method. In the frequency range of 0-1100 rad/s, just 3 resonance peaks are found for finite element results obtained by 5 elements per member. As the number of disperse elements increases, more resonance peaks appear, and the finite element results are converge to the results of the traveling wave method.

4.2. Band gap analysis

A periodic unit of the periodic tapered beam structure is shown in Fig. 5. The corresponding material and geometrical parameters are listed in Table 2.

Table 2. Material and geometrical parameters of periodic unit

Items	Tapered beam		Uniform beam	
	<i>A</i>	<i>B</i>	<i>A</i>	<i>B</i>
Elastic modulus <i>E</i> [Pa]	$8.43 \cdot 10^9$	$1.10 \cdot 10^{11}$	$8.43 \cdot 10^9$	$1.10 \cdot 10^{11}$
Density ρ [kg/m ³]	1210	2730	1210	2730
Poisson's ratio μ [-]	0.3	0.3	0.3	0.3
Length <i>L</i> [m]	0.5	0.5	0.5	0.5
Variation factor <i>a</i>	2	2	–	–
Standard area <i>A</i> ₀ [m ²]	$1.59 \cdot 10^{-2}$	$1.59 \cdot 10^{-2}$	–	–
Sectional area <i>A</i> [m ²]	–	–	$6.28 \cdot 10^{-3}$	$6.28 \cdot 10^{-3}$

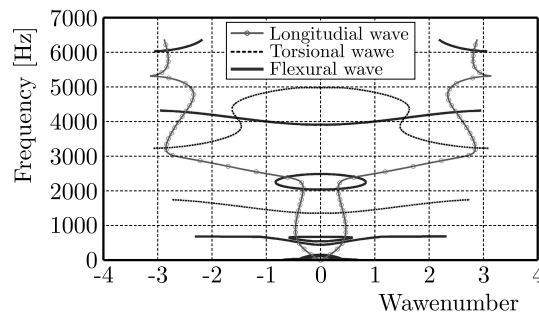


Fig. 7. Band gap properties in three kinds of waves

The band gap properties of the periodic tapered beam structure are shown in Fig. 7. It can be noted that no stop band is found for the axial wave and two stop bands are found for the torsional wave: 0 Hz-1353 Hz and 1758 Hz-3229 Hz. The flexural wave has four stop

bands: 152.9 Hz-445.9 Hz, 684.7 Hz-2038 Hz, 2484 Hz-3908 Hz and 4318 Hz-6025 Hz. The frequency range 0 Hz-152.9 Hz is the pass band for the axial wave and the flexural wave, but the stop band for the torsional wave, which is called the partial stop band. Other partial stop bands are 152.9 Hz-445.9 Hz, 684.7 Hz-1758 Hz, 1758 Hz-2038 Hz, 2484 Hz-3229 Hz, 3229 Hz-3908 Hz and 4318 Hz-6025 Hz. In the frequency range 152.9 Hz-445.9 Hz, only the axial wave contributes to the wavenumber. Therefore, the material or structural parameters of the axial wave can be changed to make it a stop band to prevent wave propagation.

The group velocity of waves is defined as $v = d\omega/dk$. The value of the group velocity represents the speeds of the wave energy transmission. The group velocity curve of the torsional wave is shown in Fig. 8. The group velocity is non-zero in the pass bands 1353 Hz-1758 Hz and 3229 Hz-5003 Hz. The group velocity equals to zero in the stop bands 0 Hz-1353 Hz and 1758 Hz-3229 Hz, which indicates no energy propagation in the stop bands. It can be observed from Fig. 8 that the group velocity changes with the frequency in the pass band, and the fastest velocity of the energy propagation is at the frequency 3904 Hz. The velocities of the energy transmission in high frequencies are much faster than that in low frequencies.

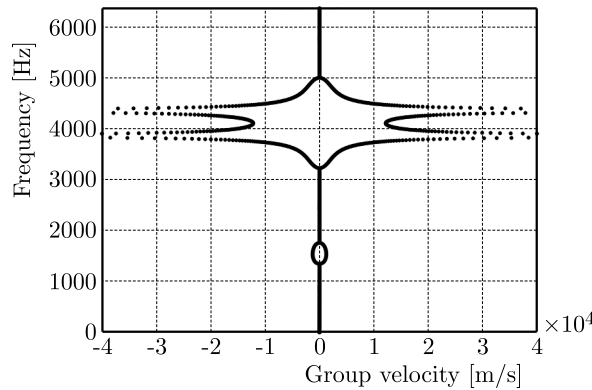


Fig. 8. Group velocity curve of the torsional wave

The material and geometrical parameters of the periodic uniform beam structure are listed in Table 2. The comparisons of band gap properties between the periodic tapered and uniform beam structures with respect to axial, torsional and flexural waves are respectively shown in Fig. 9. The axial wave has three stop bands and the torsional wave has five stop bands. Similarly, the flexural wave has six stop bands. Among these stop bands, no waves can propagate through structure in the frequency ranges 414 Hz-675.2 Hz, 1143 Hz-1341 Hz and 3322 Hz-3723 Hz, which are called the complete stop bands. The other stop bands are the partial stop bands.

As shown in Fig. 9a, the axial wave of the periodic tapered beam structure has no stop bands while that of the periodic uniform beam structure has three stop bands: 1032 Hz-2430 Hz, 2975 Hz-4634 Hz and 5357 Hz-6010 Hz. It can be inferred that the filter in certain frequency ranges that are complete pass bands for the axial wave and complete stop bands for torsional and flexural waves can be achieved by the periodic tapered beam structure with variational sectional area. Furthermore, the curve slope of the periodic tapered beam structure representing the velocity of energy propagation is bigger than that of the periodic uniform beam structure at the frequency range 0 Hz-2000 Hz.

Referring to Fig. 9b, the torsional wave of the periodic tapered beam structure has two stop bands and five stop bands are for the torsional waves of the periodic uniform beam structure: 640.1 Hz-1506 Hz, 1844 Hz-2873 Hz, 3322 Hz-3726 Hz, 4264 Hz-4841 Hz and 5236 Hz-6293 Hz. But the stop bands of the periodic tapered beam structure covering a large frequency range are relatively wider than those of the periodic uniform beam structure. It means that the bearing capacity of the torsional force of the periodic tapered beam structure is much better than that

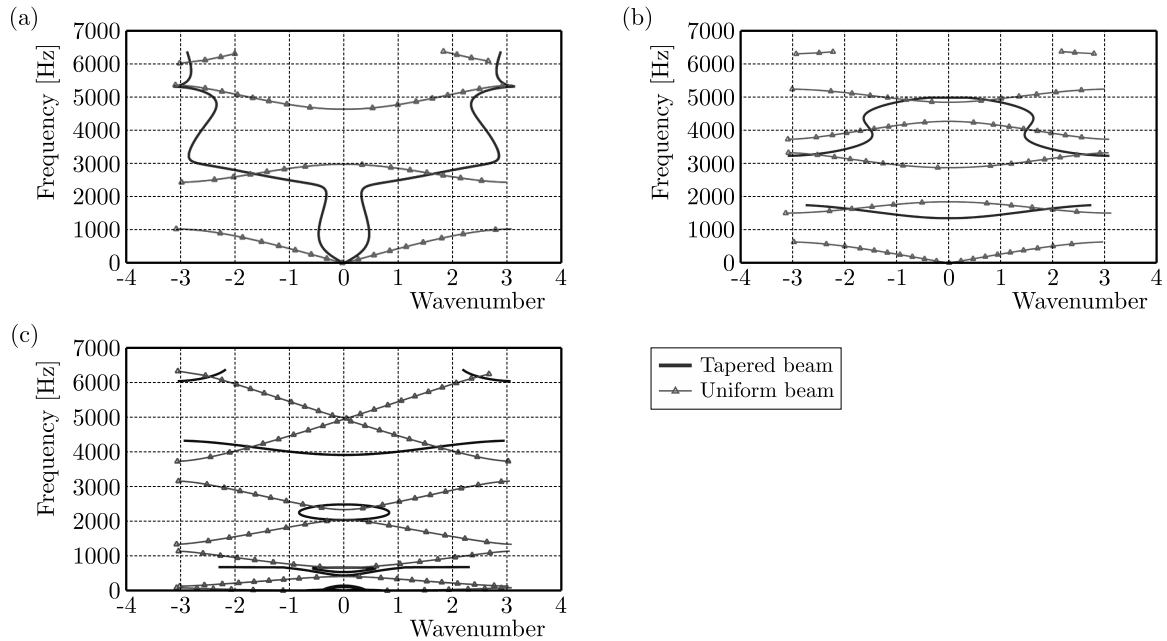


Fig. 9. Comparison of band gap properties of the: (a) axial wave, (b) torsional wave, (c) flexural wave

of the periodic uniform beam structure. Furthermore, the first stop band of the periodic tapered beam structure covers the whole low frequencies 0 Hz-1353 Hz. Therefore, the periodic tapered beam structure is very suitable for vibration isolation of torsional motion.

Referring to Fig. 9c, the frequency range of stop bands of the flexural wave of the periodic uniform beam structure is small. The widest frequency range is just 567 Hz, which is much smaller than that of the periodic tapered beam, 1707 Hz. It means that the bearing capacity of the flexural force of the periodic tapered beam structure is much better than that of the periodic uniform beam structure. The high frequency ranges of stop bands of the periodic tapered beam structure are as approximately the same as those in low frequencies due to the wavenumber changing with the sectional area.

5. Conclusions

In this paper, the traveling wave model of the tapered beam is established including the transmission and waveguide equations with respect to the axial, torsional and flexural deformations. Combining these equations with the Bloch theorem, band gap properties of the periodic tapered beam and the periodic uniform beam are analyzed and compared. Some conclusions are summarized as follows.

- Compared with the conventional finite element method, the traveling wave method has higher precision in mid and high frequencies as well as shorter calculation time and less memory occupation. This is because the traveling wave method uses the continuous model to exactly describe the transmission relationship of the member as well as the force equilibrium and displacement coordination conditions of the junction.
- Compared with the uniform beam, the wavenumbers of axial and torsional waves of the tapered beam cannot change with variable sectional area, while the wavenumbers of the flexural wave decrease with an increase in the sectional area.
- The stop bands of the periodic tapered beam structure are wider than those of the periodic uniform beam structure. The periodic tapered beam structure has more advantages over

the periodic uniform beam structure to achieve vibration isolation and filtering in some frequency ranges.

Acknowledgment

This project is supported by National Natural Science Foundation of China (Grant No. 51375360, U1537213).

References

1. BRILLOUIN L., 1953, *Wave Propagation in Periodic Structures: Electric Filters and Crystal Lattices*, McGraw-Hill Book Company Inc., New York
2. DENYS J.M., 2009, The forced vibration of one-dimensional multi-coupled periodic structures: An application to finite element analysis, *Journal of Sound and Vibration*, **319**, 282-304
3. DOYLE J.F., 1989, *Wave Propagation in Structures: an FFT-Based Spectral Analysis Methodology*, Springer-Verlag, New York
4. GUO Y.Q., FANG D.N., 2013, Analysis and interpretation of longitudinal waves in periodic multi-phase rods using the method of reverberation-ray matrix combined with the floquet-bloch theorem, *Journal of Vibration and Acoustics*, **136**, 122-136
5. LI F.L., WANG Y.S., ZHANG C.Z., YU G.L., 2013, Boundary element method for band gap calculations of two-dimensional solid phononic crystals, *Engineering Analysis with Boundary Elements*, **37**, 225-235
6. LI F.M., WANG Y.S., 2005, Study on wave localization in disordered periodic layered piezoelectric composite structures, *International Journal of Solids and Structures*, **42**, 6457-6474
7. LIU Y., GAO L.T., 2007, Explicit dynamic finite element method for band-structure calculations of 2D phononic crystals, *Solid State Communications*, **144**, 89-93
8. RIEDEL C.H., KANG B., 2006, Free vibration of elastically coupled dual-span curved beams, *Journal of Sound and Vibration*, **290**, 820-838
9. WANG G., WEN J.H., WEN X.S., 2005, Quasi-one-dimensional phononic crystals studied using the improved lumped-mass method: application to locally resonant beams with flexural wave band gap, *Physical Review B*, **71**, 104302
10. WANG Y.Z., LI F.M., HUANG W.H., WANG Y.S., 2007, Effects of inclusion shapes on the band gaps in two-dimensional piezoelectric phononic crystals, *Journal of Physics: Condensed Matter*, **19**, 496204
11. WEN J., WANG G., YU D.L., ZHAO H.G., LIU Y.Z., 2005, Theoretical and experimental investigation of flexural wave propagation in straight beams with periodic structures: Application to a vibration isolation structure, *Journal of Applied Physics*, **97**, 114907-114910
12. WEN S.R., LU N.L., WU Z.J., 2014, Dynamic property analysis of the space-frame structure using the spectral element method, *Waves Random Complex Medium*, **24**, 404-420
13. WU Z.J., LI F.M., ZHANG C., 2015, Vibration band-gap properties of three-dimensional Kagome lattices using the spectral element method, *Journal of Sound and Vibration*, **341**, 162-173
14. YU D.L., WEN J.H., SHEN H.J., XIAO Y., WEN X.S., 2012, Propagation of flexural wave in periodic beam on elastic foundations, *Physical Letter A*, **376**, 626-630

STUDY OF A MEMS HYBRID THERMO-PZT MICRO ACTUATOR

HASAN POURROSTAMI, NAVID SEYED KAZEM VILIANI

Department of Mechanical Engineering, Islamic Azad University, Abhar Branch, I.R. Iran
e-mail: a.pourrostami@gmail.com

The current study presents an analytical model for a MEMS cantilever based hybrid thermo-piezoelectric micro actuator. The micro actuator structure consists of a unimorph type bending piezoelectric beam and a passive layer which uses the thermal bimorph principle. Primarily, under electrical and thermal loadings, the governing equations of motion are derived. After verification of the results, the deflection analysis of the micro actuator is performed. Moreover, the equivalent force at the actuator tip is obtained. To provide efficient optimization, the effects of the micro actuator geometrical and materials properties on the actuator tip deflection and force are investigated.

Keywords: hybrid micro actuator, thermo-piezoelectric, deflection, force analysis

1. Introduction

Micro actuators are broadly used in miniaturized systems or devices such as micro-valves and micro-switches. These actuators are designed differently from classical actuators and are mainly employed to produce mechanical motion in these devices. In order to fulfill the required performances, micro actuators need to be designed with high resolution, good accuracy, quick response time and high range of positioning capability.

Among different types of actuation mechanisms which can be classified into thermal, electrostatic, magnetic, piezoelectric and other categories, thermal and piezoelectric ones are the most prized due to their remarkable characteristics and high compatibility with MEMS devices. Some of these noticeable features in piezoelectric actuators are high positioning accuracy, rapid response time, more mechanical power. While the distinguishable feature of electrothermal actuators is a large output force with reasonable displacement.

Both piezoelectric and electrothermal micro actuators are used in the variety of applications which include micro gripper (Nguyen and Ho, 2004; Capparelli *et al.*, 2002), scanning probe arrays (Zheng and Lu, 2004), micro positioning applications (De Cicco and Morten, 2009; Jain *et al.*, 2005) and control valves (Roberts and Li, 2003). It should be noted that the use of electrothermal micro actuators are more common. This is due to the fact that they can be easily fabricated and operated at small drive voltages. This group of actuators is ideally suited for applications that demand relatively high-output forces. However, they consume much power and show slow response time (Alwan and Aluru, 2009). On the other hand, piezoelectric actuators have the advantage of high positioning accuracy, more sensitivity and rapid response, but when compared to electrothermal micro actuators, they suffer from the limited range of deformation (Ha and Kim, 2002).

Combination of these two classes of micro actuators as a hybrid micro actuator removes their limitations and leads to modified characteristics such as low power consumption, better response time and more deflection. Rakotondrabe and Ivan (2010) attempted to integrate electrothermal and piezoelectric actuation mechanisms. They employed the thermal bimorph principle and a piezocantilever micro actuator which was made up of a piezoelectric and a passive layer. A Peltier

module (as an external source of heat generation) was used to provide temperature variation. They used the thermal network approach to model the micro actuator. The main difference between the current research and the Rakotondrabe research is the problem-solution approach. They used the thermal network approach to model the micro actuator. In this research, the elasticity approach is used to model the micro actuator. In the elasticity approach, there is better control on designing parameters such as geometrical and material properties of the micro actuator.

Although physical modeling and temperature characterization of multi/bi layered piezoelectric cantilevers have also been studied by some researchers (Tadmor and Kósa, 2003; Ballas, 2007; Rakotondrabe *et al.*, 2008), there is still a gap in knowledge for optimized selection of the micro actuator material and geometry based on the design requirements.

Recently, the deflection analysis of a U shape hybrid thermo-piezoelectric micro actuator, in which the piezoelectric actuation mechanism was based on d_{33} strain coefficient, has been performed (Pourrostami *et al.*, 2012). In the research, the piezoelectric material properties were varied by temperature and the effects of piezoelectric material properties on the deflection of micro actuator were studied which provided efficient optimization for selecting the piezoelectric material.

The main objective of this research is the study of the effects of geometrical and material properties of the micro actuator to provide efficient optimization on its performance.

In this paper, a MEMS hybrid cantilevered thermo-piezoelectric micro actuator with d_{31} actuation mechanism is developed. The micro actuator geometry is based on the presented model by Rakotondrabe and Ivan (2010). In the current study based on strength of the material, the actuator tip deflection and force are studied. Furthermore, to provide efficient optimization, the effects of the micro actuator geometrical and materials properties are investigated.

2. Actuator modeling

The configuration of the MEMS hybrid cantilevered thermo-piezoelectric micro actuator is illustrated in Fig. 1. This micro actuator is made of a Lead-Zirconate-Titanate Piezoceramic (PZT) cantilever beam and a passive elastic layer (Rakotondrabe and Ivan, 2010). By applying an electrical field, the piezoelectric layer expands (or contracts) and consequently the cantilever beam bends over. Moreover, due to the existence of a difference between thermal expansions of different layers when the micro actuator is subjected to a temperature variation, the secondary bending will be induced.

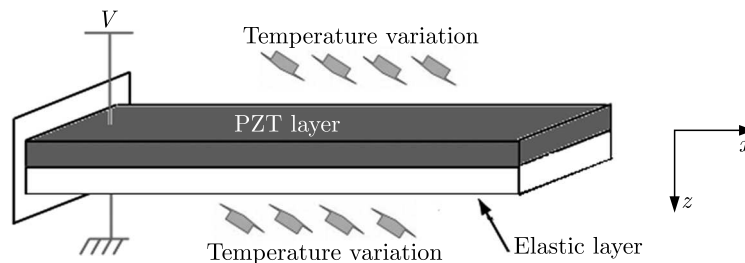


Fig. 1. The structure of the hybrid thermo-piezoelectric micro actuator (Rakotondrabe and Ivan, 2010)

Piezoelectric ceramics have very high electrical resistivity (more than $10^9 \Omega\text{m}$) which prevents them from any heat generation by passing electric current through the material. Therefore, in order to have thermal actuation in piezoelectric beams, an additional external heat source is needed. Based on the small size of the micro actuator, usually a uniform temperature variation on the surfaces of micro beams is considered (Rakotondrabe and Ivan, 2010). In this model,

the classical Euler-Bernoulli beam theory (EBT) is considered, and it is assumed that the shear and electrostriction effects are negligible. Also x - z plane stress and x - y plane strain are enforced (Devoe and Pisano, 1997).

2.1. Constitutive relations

For the piezoelectric materials, the general constitutive relations are (Kargarnovin *et al.*, 2007)

$$\boldsymbol{\varepsilon} = \mathbf{S}^E \boldsymbol{\sigma} - \mathbf{d}^T \mathbf{E} \quad \mathbf{F} = \mathbf{d} \boldsymbol{\sigma} - \boldsymbol{\epsilon}^T \mathbf{E} \quad (2.1)$$

In which $\boldsymbol{\sigma}$, $\boldsymbol{\varepsilon}$, \mathbf{E} and \mathbf{D} represents the columns of stress components, strain components, electrical field components and electric displacement components, respectively. Also \mathbf{S}^E , \mathbf{d} and $\boldsymbol{\epsilon}$ are the compliance matrix at the constant electric field, the piezoelectric strain constant matrix and the dielectric permittivity matrix.

On the assumption of the x - z plane strain which is reasonable for a wide flat micro beam, the strain component in the y -direction is zero. Setting $\varepsilon_y = 0$ in equation (2.1)₁, σ_y yields to

$$\sigma_y = -\frac{1}{s_{22}}(s_{12}\sigma_x + s_{23}\sigma_z + d_{31}E_z) \quad (2.2)$$

When the temperature is applied, by substituting equation (2.2) into equations (2.1), the constitutive equation reduces to

$$\begin{aligned} \varepsilon_x &= \bar{s}_{11}\sigma_x + \bar{s}_{13}\sigma_z + \bar{d}_{31}E_z + \alpha\Delta T & \varepsilon_x &= \bar{s}_{13}\sigma_x + \bar{s}_{33}\sigma_z + \bar{d}_{33}E_z \\ D_z &= \bar{d}_{31}\sigma_x + \bar{d}_{33}\sigma_z + \bar{\epsilon}_{33}E_z \end{aligned} \quad (2.3)$$

It should be noticed that because of small height and width of the micro actuator in comparison with its length, the thermal expansions in the y and z directions are neglected. Also the reference temperature is room temperature. \bar{s}_{11} , \bar{s}_{13} , \bar{s}_{33} , \bar{d}_{31} , \bar{d}_{33} and $\bar{\epsilon}_{33}$ are reduced material constants of the piezoelectric for the plain stress assumed

$$\begin{aligned} \bar{s}_{11} &= s_{11} - \frac{s_{12}^2}{s_{22}} & \bar{s}_{13} &= s_{13} - \frac{s_{12}s_{23}}{s_{22}} & \bar{s}_{33} &= s_{33} - \frac{s_{23}^2}{s_{22}} \\ \bar{d}_{31} &= d_{31} - \frac{s_{12}}{s_{22}}d_{31} & \bar{d}_{33} &= d_{33} - \frac{s_{23}}{s_{22}}d_{31} & \bar{\epsilon}_{33} &= \epsilon_{33} - \frac{d_{31}^2}{s_{22}} \end{aligned} \quad (2.4)$$

Rewriting the constitutive relations in terms of stress-strain components, we get

$$\begin{bmatrix} \sigma_x \\ \sigma_z \end{bmatrix} = \begin{bmatrix} \bar{c}_{11} & \bar{c}_{13} \\ \bar{c}_{13} & \bar{c}_{33} \end{bmatrix} \left(\begin{bmatrix} \varepsilon_x \\ \varepsilon_z \end{bmatrix} - \begin{bmatrix} \bar{d}_{31}E_z \\ \bar{d}_{33}E_z \end{bmatrix} \right) \quad (2.5)$$

where \bar{c}_{11} , \bar{c}_{13} and \bar{c}_{33} are reduced stiffness components of the piezoelectric beam. They are expressed by

$$\bar{c}_{11} = \frac{\bar{s}_{33}}{\bar{s}_{11}\bar{s}_{33} - \bar{s}_{13}^2} \quad \bar{c}_{13} = -\frac{\bar{s}_{13}}{\bar{s}_{11}\bar{s}_{33} - \bar{s}_{13}^2} \quad \bar{c}_{33} = \frac{\bar{s}_{11}}{\bar{s}_{11}\bar{s}_{33} - \bar{s}_{13}^2} \quad (2.6)$$

For a transversely isotropic piezoelectric beam with a small aspect ratio, the thickness in the z -direction is stress free. Therefore, it is plausible to set $\sigma_z = 0$. By setting $\sigma_z = 0$ in equation (2.5), ε_z yields

$$\varepsilon_z = -\frac{1}{\bar{c}_{33}}[\bar{c}_{13}(\varepsilon_x - \bar{d}_{31}E_z) - \bar{c}_{33}\bar{d}_{33}E_z] \quad (2.7)$$

By substituting equation (2.7) into equations (2.3)₃ and (2.5), when the uniform temperature variation is applied, the constitutive equation reduces to

$$\sigma_x^p = E_p(\varepsilon_x - \bar{d}_{31}E_z\alpha_p\Delta T) \quad D_z = \bar{d}_{31}E_p\varepsilon_x + (\bar{\varepsilon}_{33} - \bar{d}_{31}^2E_p)E_z \quad (2.8)$$

where α_p and E_p are the thermal expansion coefficient and the effective elasticity modulus of the PZT layer. For the one dimensional piezoelectric beam under considered assumptions, the effective elasticity modulus is

$$E_p = \bar{\varepsilon}_{11} - \frac{\bar{c}_{13}^2}{\bar{\varepsilon}_{33}} \quad (2.9)$$

For the elastic beam under plane strain and stress assumptions by applying temperature, the constitutive relation in terms of stress-strain components is

$$\sigma_x^e = E_e(\varepsilon_x - \alpha_e\Delta T) \quad (2.10)$$

where α_e is the thermal expansion coefficient of the elastic beam and E_e is the effective elasticity modulus of the elastic beam for the plane strain. It can be obtained from

$$E_e = \frac{E}{1 - \nu^2} \quad (2.11)$$

3. Deflection analysis

The deflection of the HTP micro actuator can be derived by applying static equilibrium and strain compatibility between the layers (Devoe and Pisano 1997). Figure 2 shows a cross section of the micro actuator.

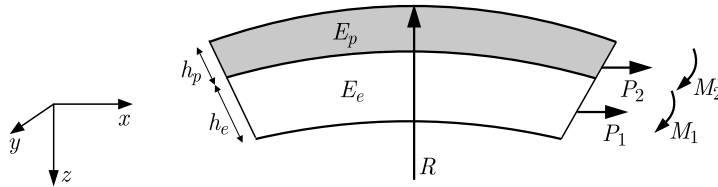


Fig. 2. The cross section of the hybrid thermo-piezoelectric micro actuator (Devoe and Pisano 1997)

In Fig. 2, R represents radius of the curvature, h_e and h_p are heights of the elastic and piezoelectric beams. P_1 , P_2 , M_1 and M_2 are axial forces and moments at the cross-section of two layers. Furthermore, E_e and E_p are the effective elasticity modulus of the elastic and piezoelectric micro beams, respectively.

The curvature $1/R$ of the curve $y(x)$ is expressed as follows

$$\frac{1}{R} = \frac{d^2y}{dx^2} \quad (3.1)$$

Then

$$y = \frac{x^2}{2R} \quad (3.2)$$

The maximum deflection is found at the tip of the micro actuator ($x = L$). Using the following equations, the requirements for force and moment equilibrium are satisfied (Devoe and Pisano 1997)

$$P_1 + P_2 = 0 \quad \frac{h_e}{2}P_1 + \left(h_e + \frac{h_p}{2}\right)P_2 + \frac{E_e h_e^3 + E_p h_p^3}{12R} = 0 \quad (3.3)$$

The total strain in the elastic layer is due to axial force, bending moment and thermal effect, while the piezoelectric effect causes an additional strain component in the PZT beam. To satisfy the strain compatibility between two layers, we can write

$$\varepsilon_{axial} + \varepsilon_{bending} + \varepsilon_{thermal} = \varepsilon_{axial} + \varepsilon_{bending} + \varepsilon_{thermal} + \varepsilon_{piezo}$$

$$\frac{P_1}{E_e h_e} + \frac{h_e}{2R} + \alpha_e \Delta T = \frac{P_2}{E_p h_p} - \frac{h_p}{2R} + \alpha_p \Delta T + \frac{d_{31}}{h_p} V \quad (3.4)$$

where V , ΔT and d_{31} are the applied voltage, temperature variation and piezoelectric transverse strain constant, respectively.

To determine the actuator curvature, the system of equations in a matrix form is rewritten

$$\begin{bmatrix} 1 & 1 & 0 \\ \frac{h_e}{2} & h_e + \frac{h_p}{2} & \frac{E_e h_e^3 + E_p h_p^3}{12} \\ \frac{1}{E_e h_e} & -\frac{1}{E_p h_p} & \frac{h_e + h_p}{2} \end{bmatrix} \begin{bmatrix} P_1 \\ P_2 \\ \frac{1}{R} \end{bmatrix} = \begin{bmatrix} 0 \\ 0 \\ (\alpha_p - \alpha_e) \Delta T + \frac{d_{31}}{h_p} V \end{bmatrix} \quad (3.5)$$

By solving equation (3.5) for the curvature $1/R$, the actuator tip deflection using equation (3.2) is

$$\delta = \frac{3L^2(h_e + h_p)E_e E_p h_e h_p}{E_p^2 h_p^4 + E_e h_e E_p h_p (4h_p^2 + 6h_e h_p + 4h_e^2) + E_e^2 h_e^4} \left(-\frac{\bar{d}_{31}}{h_p} V + (\alpha_p - \alpha_e) \Delta T \right) \quad (3.6)$$

where L is the total length of the actuator.

4. Deflection analysis

The equivalent generated force of the micro actuator can be obtained by the using actuator tip deflection and stiffness

$$F = K\delta = \frac{3E_{eq}I_{eq}}{L^3}\delta \quad (4.1)$$

where K is the stiffness, E_{eq} and I_{eq} are the equivalent elasticity modulus and moment of inertia of the two layers, respectively.

The method used to calculate the equivalent beam is based on the construction of an equivalent homogeneous section that is mechanically equivalent to the initial, heterogeneous, section (see Fig. 3). To keep flexural rigidity in the equivalent homogeneous section, the method of normalization of widths by the elasticity modulus is used. In this method, the ratio of the elastic beam width b_e to the piezoelectric beam width b_p should be equal to the ratio of their elasticity moduli

$$\frac{b_e}{b_p} = \frac{E_e}{E_p} \quad (4.2)$$

To calculate the equivalent moment of inertia, it is essential to find the location of the neutral axis of the equivalent homogeneous section h_{eq}

$$h_{eq} = \frac{\sum A_i h_i}{\sum A_i} = \frac{h_p E_p \left(h_e + \frac{h_p}{2} \right) + \frac{1}{2} h_e^2 E_e}{h_p E_p + h_e E_e} \quad (4.3)$$

The equivalent moment of inertia is then expressed as follows:

$$I_{eq} = \frac{b_p}{12} \frac{E_p^2 h_p^4 + 4h_p h_e \left(h_p^2 + \frac{3}{2} h_p h_e + h_e^2 \right) E_p E_e + E_e^2 h_e^4}{(E_e h_e + E_p h_p) E_p} \quad (4.4)$$

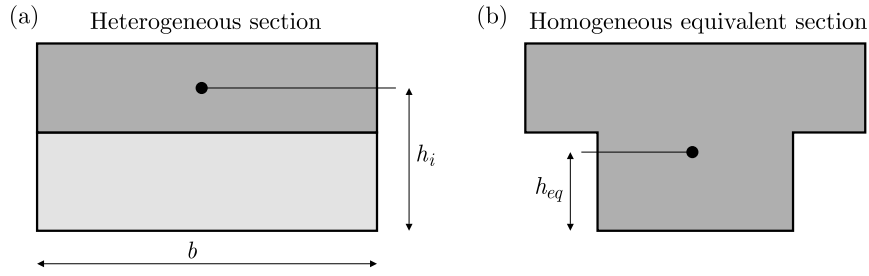


Fig. 3. (a) The cross section of the actuator with piezoelectric and elastic layers, (b) the equivalent homogenous beam section

The equivalent generated force of the micro actuator can be obtained using equations (3.6), (4.1) and (4.4)

$$F = \frac{3 E_p E_e h_e h_p (h_e + h_p) b}{4 L (E_e h_e + E_p h_p)} \left(-\frac{\bar{d}_{31}}{h_p} V + (\alpha_p - \alpha_e) \Delta T \right) \quad (4.5)$$

5. Results and discussion

Based on the developed relations, the governing derived equations for the deflection and force of the actuator are solved numerically using the data listed in Tables 1 and 2 for geometrical and material properties, respectively. In the current study, PZT-5H and copper are used as active piezoelectric and passive elastic layers whose geometry and materials are exactly the same as the one which was presented in the experimental model by Rakotondrabe and Ivan (2010). In the first step, the validity of the obtained results is verified by comparing with the reported and experimental results (Devoe and Pisano 1997; Rakotondrabe and Ivan, 2010). Then, in order to have an optimized design, the effects of geometrical and material properties on the actuator performance are studied.

Several researches have been done on the temperature dependence of the PZT material properties which show that for PZT-5H: i) piezoelectric strain constants d_{31} and d_{33} increase with temperature while d_{15} remains almost constant, ii) piezoelectric dielectric constants ϵ_{11} and ϵ_{33} increase with temperature, iii) for the mentioned temperature range, the elastic constants do not remarkably change with temperature (Hooker, 1998). In the current study, for verification of the results (based on the experimental results by Rakotondrabe and Ivan (2010)) the working temperature of the PZT-5H is considered 50°C. The PZT-5H material properties at room and working temperature are listed in Table 2. Also it is assumed that the variation of material properties of the copper layer with temperature are negligible (Rakotondrabe and Ivan, 2010).

Table 1. Geometrical data for the actuator (Rakotondrabe and Ivan, 2010)

Length of the actuator, L [mm]	15
Width of the actuator, b [mm]	2

5.1. Verifications

From Eq. (3.6), it is clear that the actuator tip deflection is a linear function of the applied voltage and temperature. Substituting $\Delta T = 0$ in Eq. (3.6), the hybrid micro actuator converts to the unimorph piezoelectric micro actuator (Devoe and Pisano 1997). Furthermore, based on the experimental results, two linear models have been proposed for variation of deflection versus

Table 2. Material properties (Rakotondrabe and Ivan, 2010; Hooker, 1998)

Title	Symbol	Value
PZT-5H		
Compliance matrix component [m^2/N]	s_{11}	$16.5 \cdot 10^{-12}$
Compliance matrix component [m^2/N]	s_{33}	$20.7 \cdot 10^{-12}$
Compliance matrix component [m^2/N]	s_{12}	$-4.78 \cdot 10^{-12}$
Compliance matrix component [m^2/N]	s_{13}	$-8.45 \cdot 10^{-12}$
Piezoelectric transverse strain constant [V/m]	d_{31}	$-100 \cdot 10^{-12}$
Expansion coefficient [$1/^\circ\text{C}$]	α_p	$3.6 \cdot 10^{-6}$
Elastic layer (copper)		
Axial elastic constant [Pa]	E	$125 \cdot 10^9$
Poisson's ratio [-]	ν	0.35
Expansion coefficient [$1/^\circ\text{C}$]	α_e	$1.7 \cdot 10^{-6}$

voltage and temperature (Rakotondrabe and Ivan, 2010). In this Section, the analytical results are compared with those from the proposed linear models.

Figure 4 shows the variation of the actuator tip deflection versus the applied voltage when $\Delta T = 0^\circ\text{C}$, $h_p = 0.2 \text{ mm}$ and $h_e = 0.1 \text{ mm}$. The results follow a linear trend and the analytical result is in a good agreement with the experimental result.

In the next step, the actuator tip deflection as a function of the applied temperature is plotted (see Fig. 4b) at $V = 0$ when $h_p = 0.2 \text{ mm}$ and $h_e = 0.1 \text{ mm}$, respectively. As it is seen in Fig. 4b, when a uniform temperature distribution is applied, the deflection variation is changed linearly.

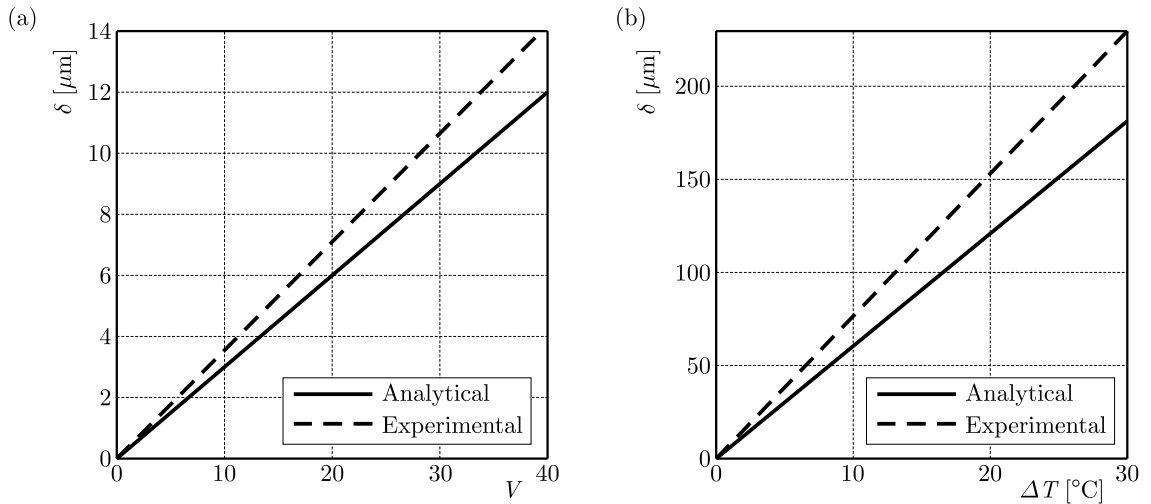


Fig. 4. The actuator tip deflection versus applied voltage (a) and uniform temperature variation (b)

The present difference between the two obtained results is due to the pyroelectric effect. The pyroelectricity is generation of an electric charge on a crystal by a change in temperature. The change in temperature slightly modifies positions of atoms within the crystal structure such that the polarization of the material changes. This polarization change gives a rise to the voltage across the crystal. As a result, the generated voltage causes greater deflection.

5.2. Geometry effects

In this Section, the variations of heights of the piezoelectric and elastic layers on the actuator deflection and force are studied. Figure 5a illustrates the variation of the actuator tip deflection versus height of the elastic layer for two different heights of the PZT layer when $\Delta T = 25^\circ\text{C}$, $V = 40\text{ V}$. Referred to this figure, smaller heights of PZT and elastic layers enable the actuator to deflect more efficiently.

Figure 5b shows the variation of the actuator force versus height of the elastic layer for two different heights of the PZT layer when $\Delta T = 25^\circ\text{C}$, $V = 40\text{ V}$. Contrarily, greater heights of the PZT and elastic layers generate large forces in the actuator. Therefore, optimization of heights of the PZT and elastic layers can lead to the maximum efficiency of the micro actuator.

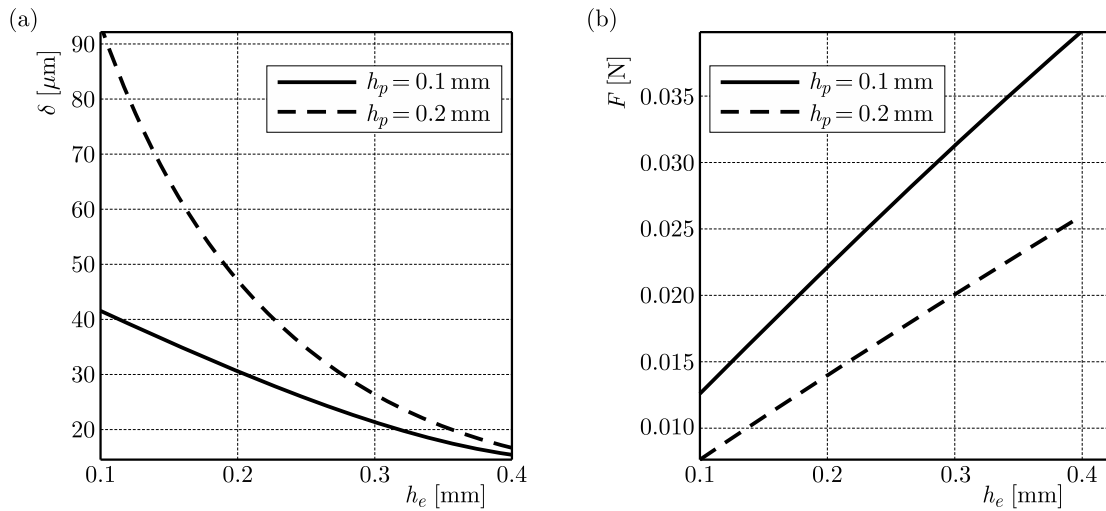


Fig. 5. (a) The actuator tip deflection versus height of the elastic layer for different heights of the PZT layer; (b) the actuator force versus height of the elastic layer for two different heights of the PZT layer

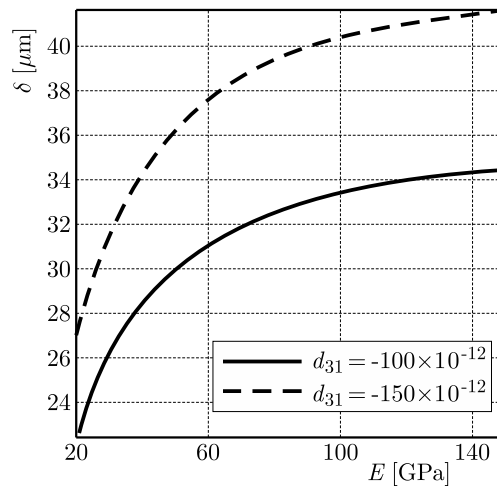


Fig. 6. The actuator tip deflection versus elasticity modulus of the elastic layer

5.3. Material property effects

In the present Section, the effects of the piezoelectric strain constant d_{31} and the elasticity modulus of the elastic layer E on the actuator deflection are investigated. The variation of actuator deflection versus elasticity modulus of the elastic layer are plotted in Fig. 6 for

$\Delta T = 25^\circ\text{C}$, $V = 40\text{ V}$, $h_p = 0.2\text{ mm}$ and $h_e = 0.1\text{ mm}$, respectively. There is a nonlinear variation trend when the elasticity modulus of the elastic layer increases. It means that a stiffer elastic layer leads to a greater deflection and force in the actuator. Furthermore, when the piezoelectric strain constant d_{31} increases indirectly with the temperature, the actuator deflection and force rise.

6. Conclusion

In the present study, static analysis is performed for the proposed MEMS hybrid micro actuator which applies both the piezoelectric and thermal actuation. To sum up, the most important conclusions arising from this study are as follows:

- By increasing the applied voltage and temperature gradient, the actuator force and tip deflection linearly increase.
- The actuator tip deflection is decreased upon an increase in the heights of PZT and elastic layers.
- An indirect increase in the piezoelectric transverse strain constant d_{31} by growth of the temperature give a rise to the actuator force and tip deflection.
- Making use of a stiffer elastic layer rises the nonlinear increasing trend of the actuator force and tip deflection.
- Increasing the temperature not only increases thermal expansions of the layers and, as a result, increases deflection, but also affects the piezoelectric strain constant, which enlarges deflection as well.

References

1. ALWAN A., ALURU N., 2009, Analysis of hybrid electrothermomechanical microactuators with integrated electrothermal and electrostatic actuation, *Journal of Microelectromechanical Systems*, **18**, 1126-1136
2. BALLAS R., 2007, Piezoelectric Multilayer Beam Bending Actuators, Static and Dynamic Behavior and Aspects of Sensor Integration, Springer, 1st Edit., ISBN: 978-3-540-32641-0
3. CAPPARELLI D.J., FRECKER M.I., SIMPSON T.W., SNYDER A., 2002, Design of a PZT bimorph actuator using a metamodel-based approach, *ASME Journal of Mechanical Design*, **124**, 354-357
4. DE CICCIO G., MORTEN B., 2009, Thick-film piezoelectric actuators for micro positioning, *Journal of Intelligent Material Systems and Structures*, **20**, 1689-1697
5. DEVOE D., PISANO P., 1997, Modeling and optimal design of piezoelectric cantilever microactuator, *Journal of Microelectromechanical Systems*, **6**, 3, 266-270
6. HA S., KIM Y., 2002, Analysis of a piezoelectric multi-morph in extensional and flexural motions, *Journal of Sound and Vibration*, **253**, 5, 1001-1014
7. HOOKER M.W., 1998, *Properties of PZT-Based Piezoelectric Ceramics Between -150 and 250°C* , Lockheed Martin Engineering & Science Co., Hampton, Virginia
8. JAIN A., QU H., TODD S., XIE H., 2005, A thermal bimorph micromirror with large bi-directional and vertical actuation, *Sensors and Actuators A: Physical*, **122**, 9-15
9. KARGARNOVIN M.H., NAJAFIZADEH M.M., VILIANI N.S., 2007, Vibration control of a functionally graded material plate patched with piezoelectric actuators and sensors under a constant electric charge, *Smart Materials and Structures*, **16**, 1252-1259
10. NGUYEN N.T., HO S., 2004, A polymeric microgripper with integrated thermal actuators, *Journal of Micromechanics and Microengineering*, **14**, 969-974

11. POURROSTAMI H., KARGARNOVIN M.H., ZOHOOR H., 2012, Modeling and analytical solution of hybrid thermopiezoelectric micro actuator and performance study under changing of different parameters, *Mechanics of Advanced Material and Structure*, **22**, 10, 785-793
12. RAKOTONDRABE M., DIOUF M., LUTZ P., 2008, Robust feed forward-feedback control of a hysteretic piezocantilever under thermal disturbance, *IFAC World Congress*, Seoul Corea, July 2008, 13725-13730
13. RAKOTONDRABE M., IVAN I., 2010, Development and dynamic modeling of a new hybrid thermo-piezoelectric microactuator, *IEEE Transactions on Robotics*, **26**, 1077-1085
14. ROBERTS D.C., LI H., 2003, A piezoelectric microvalve for compact high frequency high-differential pressure hydraulic micropumping systems, *Journal of Microelectromechanical Systems*, **12**, 81-92
15. TADMOR E., KÓSA G., 2003, Electromechanical coupling correction for piezoelectric layered beams, *Journal of Microelectromechanical Systems*, **12**, 899-906
16. ZHENG L., LU M., 2004, A large-displacement CMOS micromachined thermal actuator with comb electrodes for capacitive sensing, *Sensors and Actuators A: Physical*, **136**, 2, 697-703

Manuscript received August 17, 2015; accepted for print March 7, 2016

A MODE-III CRACK WITH VARIABLE SURFACE EFFECTS

XU WANG

School of Mechanical and Power Engineering, East China University of Science and Technology, Shanghai, China
e-mail: xuwang@ecust.edu.cn

PETER SCHIAVONE

University of Alberta, Department of Mechanical Engineering, Edmonton, Canada
e-mail: p.schiavone@ualberta.ca

We study the contribution of variable surface effects to the antiplane deformation of a linearly elastic material with a mode-III crack. The surface elasticity is incorporated using a modified version of the continuum based surface/interface model of Gurtin and Murdoch. In our discussion, the surface moduli are not constant but vary along the crack surfaces. Using Green's function method, the problem is reduced to a single first-order Cauchy singular integro-differential equation, which is solved numerically using Chebyshev polynomials and a collocation method. Our results indicate that the gradient of the surface shear modulus exerts a significant influence on the crack opening displacement and on the singular stress field at the crack tips.

Keywords: surface elasticity, variable surface moduli, mode-III crack, Cauchy singular integro-differential equation

1. Introduction

The analysis of deformation of an elastic solid incorporating a crack is critical for the understanding of failure modes and in the general stress analysis of engineering materials. Traditional modeling via the use of linear elastic fracture mechanics (LEFM) ignores the contributions of surface energies, surface tension and surface stresses. The high surface area to volume ratio present at the nanoscale dictates that any continuum-based model of deformation should incorporate the separate contribution of surface mechanics (Sharma and Ganti, 2004). Recently, the continuum-based surface/interface model proposed by Gurtin, Murdoch and co-workers (Gurtin and Murdoch, 1975; Gurtin *et al.*, 1998) has been incorporated in the analysis of several typical crack problems (see for example, Kim *et al.*, 2010, 2011a,b; Antipov and Schiavone, 2011; Wang, 2015; Wang and Schiavone, 2015, 2016). It was first proved by Walton (2012) and later corroborated by Kim *et al.* (2013) that the contribution of surface elasticity (based on the Gurtin-Murdoch model) to LEFM would, at best, reduce the classical strong square root singularity to a weaker logarithmic singularity.

The Gurtin-Murdoch surface elasticity model essentially models a material surface as a thin elastic membrane (of separate elasticity) perfectly bonded to the surrounding bulk material (see, for example, Steigmann and Ogden, 1997; Chen *et al.*, 2007; Antipov and Schiavone, 2011; Markenscoff and Dundurs, 2014). In recent studies, the incorporation of surface elasticity into LEFM models has been confined to the simple case in which the surface moduli are constant along the crack surfaces (Kim *et al.*, 2010, 2011a,b; Antipov and Schiavone, 2011; Wang, 2015; Wang and Schiavone, 2015, 2016).

This work aims to study, for the first time, the effects of variable surface moduli in a classical mode-III crack problem arising in the antiplane shear deformation of a linearly isotropic elastic

solid. Specifically, the corresponding surface shear modulus is varied linearly along the upper and lower crack surfaces. By considering a distribution of screw dislocations on the crack, the problem is reduced to a single first-order Cauchy singular integro-differential equation for the unknown dislocation density which is solved numerically using Chebyshev polynomials and the collocation method. Numerical results are presented to demonstrate how the variable surface shear modulus influences the dislocation density, crack opening displacement and the singular stress field near the crack tips.

2. Bulk and surface elasticity

2.1. The bulk elasticity

In a fixed rectangular coordinate system x_i ($i = 1, 2, 3$), the equilibrium and stress-strain relations for an isotropic elastic bulk solid are well-known to be

$$\sigma_{ij,j} = 0 \quad \sigma_{ij} = 2\mu\varepsilon_{ij} + \lambda\varepsilon_{kk}\delta_{ij} \quad \varepsilon_{ij} = \frac{1}{2}(u_{i,j} + u_{j,i}) \quad (2.1)$$

Here, $i, j, k = 1, 2, 3$ and we sum over repeated indices; λ and μ are the Lamé constants of the bulk material; σ_{ij} and ε_{ij} are respectively the components of the stress and strain tensors in the bulk; u_i is the i -th component of the displacement vector \mathbf{u} and δ_{ij} is the Kronecker delta.

For the antiplane shear deformation of an isotropic elastic material, the two shear stress components σ_{31} and σ_{32} and the out-of-plane displacement $w = u_3(x_1, x_2)$ can be expressed in terms of a single analytic function $f(z)$ of the complex variable $z = x_1 + ix_2$ as

$$\sigma_{32} + i\sigma_{31} = \mu f'(z) \quad w = \text{Im}\{f(z)\} \quad (2.2)$$

2.2. The surface elasticity

The equilibrium conditions on the surface incorporating interface/surface elasticity can be expressed as (Gurtin and Murdoch, 1975; Gurtin *et al.*, 1998; Ru, 2010)

$$\begin{aligned} \sigma_{\alpha j} n_j \underline{e}_\alpha + \sigma_{\alpha\beta, \beta}^s \underline{e}_\alpha &= 0 && \text{tangential direction} \\ [\sigma_{ij} n_i n_j] &= \sigma_{\alpha\beta}^s \kappa_{\alpha\beta} && \text{normal direction} \end{aligned} \quad (2.3)$$

where $\alpha, \beta = 1, 3$; \underline{e}_α are the bases for the surface; n_i are the components of the unit normal vector to the surface; $[\cdot]$ denotes the jump of the corresponding quantities across the surface; $\sigma_{\alpha\beta}^s$ are the components of the surface stress tensor and $\kappa_{\alpha\beta}$ are those of the curvature tensor of the surface. In addition, the constitutive equations on the isotropic surface are given by

$$\sigma_{\alpha\beta}^s = \sigma_0 \delta_{\alpha\beta} + 2(\mu^s - \sigma_0) \varepsilon_{\alpha\beta}^s + (\lambda^s + \sigma_0) \varepsilon_{\gamma\gamma}^s \delta_{\alpha\beta} + \sigma_0 \nabla_s \mathbf{u} \quad (2.4)$$

where $\varepsilon_{\alpha\beta}^s$ is the surface strain tensor, σ_0 is the surface tension, λ^s and μ^s are the two surface Lamé parameters, ∇_s is the surface gradient and $\gamma = 1, 3$. In contrast to previous studies in this area, here it is assumed that λ^s and μ^s can vary along the surface.

3. A mode-III crack with variable surface effects

Consider the antiplane shear deformation of a linearly elastic and homogeneous isotropic solid weakened by a finite crack $\{-a \leq x_1 \leq a, x_2 = 0\}$. The crack surfaces are traction-free and the solid is subjected to a uniform remote shear stress σ_{32}^∞ . Let the upper and lower half-planes be designated the “+” and “-” sides of the crack, respectively.

From Eq. (2.3), the boundary conditions on the crack surfaces can be written as

$$\begin{aligned} \sigma_{13,1}^s + (\sigma_{23})^+ - (\sigma_{23})^- &= 0 && \text{on the upper crack face} \\ \sigma_{13,1}^s + (\sigma_{23})^+ - (\sigma_{23})^- &= 0 && \text{on the lower crack face} \end{aligned} \tag{3.1}$$

where $(\sigma_{23})^-$ in Eq. (3.1)₁ and $(\sigma_{23})^+$ in Eq. (3.1)₂ are zero.

In the current setting, we have from the surface constitutive equations in Eq. (2.4) that

$$\sigma_{13}^s = 2[\mu^s(x_1) - \sigma_0]\varepsilon_{13}^s \tag{3.2}$$

which indicates that the surface shear modulus is not constant but indeed variable along the upper and lower crack surfaces.

By making use of Eq. (3.2) and assuming a coherent interface ($\varepsilon_{\alpha\beta}^s = \varepsilon_{\alpha\beta}$), Eqs. (3.1) are written as

$$\begin{aligned} (\sigma_{23})^+ &= -[\mu^s(x_1) - \sigma_0]u_{3,11}^+ - \frac{d[\mu^s(x_1) - \sigma_0]}{dx_1}u_{3,1}^+ && \text{on the upper crack face} \\ (\sigma_{23})^- &= +[\mu^s(x_1) - \sigma_0]u_{3,11}^- + \frac{d[\mu^s(x_1) - \sigma_0]}{dx_1}u_{3,1}^- && \text{on the lower crack face} \end{aligned} \tag{3.3}$$

or equivalently

$$\begin{aligned} (\sigma_{23})^+ + (\sigma_{23})^- &= -[\mu^s(x_1) - \sigma_0](u_{3,11}^+ - u_{3,11}^-) - \frac{d[\mu^s(x_1) - \sigma_0]}{dx_1}(u_{3,1}^+ - u_{3,1}^-) \\ (\sigma_{23})^+ - (\sigma_{23})^- &= -[\mu^s(x_1) - \sigma_0](u_{3,11}^+ + u_{3,11}^-) - \frac{d[\mu^s(x_1) - \sigma_0]}{dx_1}(u_{3,1}^+ + u_{3,1}^-) \end{aligned} \tag{3.4}$$

The problem can be formulated by considering a distribution of line dislocations with density $b(x_1)$ on the crack. Consequently, the analytic function $f(z)$ can be written in the following form

$$f(z) = \frac{1}{2\pi} \int_{-a}^a b(\xi) \ln(z - \xi) d\xi + \frac{\sigma_{32}^\infty}{\mu} z \tag{3.5}$$

From the above expression, it follows that

$$\begin{aligned} f'_+(x_1) &= -\frac{ib(x_1)}{2} + \frac{1}{2\pi} \int_{-a}^a \frac{b(\xi)}{x_1 - \xi} d\xi + \frac{\sigma_{32}^\infty}{\mu} \\ f'_-(x_1) &= \frac{ib(x_1)}{2} + \frac{1}{2\pi} \int_{-a}^a \frac{b(\xi)}{x_1 - \xi} d\xi + \frac{\sigma_{32}^\infty}{\mu} \end{aligned} \tag{3.6}$$

where $-a < x_1 < a$, The subscripts “+” and “-” here indicate limiting values as we approach the crack from the upper and lower half-planes, respectively.

It is not difficult to verify that the boundary condition in Eq. (3.4)₂ is automatically satisfied with $f(z)$ given by Eq. (3.5). On the other hand, the boundary condition in Eq. (3.4)₁ leads to the following first-order Cauchy singular integro-differential equation for the unknown density function $b(x_1)$

$$-\frac{\mu}{\pi} \int_{-a}^a \frac{b(\xi)}{\xi - x_1} d\xi + 2\sigma_{32}^\infty = [\mu^s(x_1) - \sigma_0]b'(x_1) + \frac{d[\mu^s(x_1) - \sigma_0]}{dx_1}b(x_1) \quad -a < x_1 < a \tag{3.7}$$

From Eqs. (3.6), we deduce that

$$\Delta w = w^+ - w^- = - \int_{-a}^{x_1} b(\xi) \, d\xi \quad -a < x_1 < a \quad (3.8)$$

Consequently, for a single-valued displacement in the case of a contour surrounding the crack surface we require that

$$\int_{-a}^a b(\xi) \, d\xi = 0 \quad (3.9)$$

In what follows, we assume that $\mu^s(x_1) - \sigma_0$ is a linear function of the coordinate x_1 and is given by

$$\mu^s(x_1) - \sigma_0 = \mu_0 \left(1 + \frac{k}{a} x_1 \right) \quad -a < x_1 < a \quad (3.10)$$

where $\mu_0 (> 0)$ and $k (-1 < k < 1)$ are two constants. The constant k can be considered as a parameter characterizing the gradient of the surface shear modulus $\mu^s(x_1)$ along the surfaces.

Using Eq. (3.10), Eq. (3.7) simplifies to

$$-\frac{\mu}{\pi} \int_{-a}^a \frac{b(\xi)}{\xi - x_1} \, d\xi + 2\sigma_{32}^\infty = \mu_0 \left(1 + \frac{k}{a} x_1 \right) b'(x_1) + \frac{\mu_0 k}{a} b(x_1) \quad -a < x_1 < a \quad (3.11)$$

Comparing Eq. (3.11) with Eq. (23) in Kim *et al.* (2010) reveals that a nonzero gradient parameter k will result in an additional term $b(x_1)$ on the right-hand side of the equation. In the next Section, we present an approach based on Chebyshev polynomials and an adapted collocation method to solve Eq. (3.11) numerically together with the auxiliary condition in Eq. (3.9).

4. Solution to the singular integro-differential equation

We begin by setting $x = x_1/a$ in Eq. (3.11). For convenience, we write $b(x) = b(ax) = b(x_1)$. As a result, Eqs. (3.9) and (3.11) can be written in the following normalized form

$$\int_{-1}^1 \frac{\hat{b}(t)}{t-x} \, dt = -\pi S_e (1+kx) \hat{b}'(x) - \pi S_e k \hat{b}(x) + 2\pi \quad -1 < x < 1 \quad (4.1)$$

$$\int_{-1}^1 \hat{b}(t) \, dt = 0$$

where

$$\hat{b}(x) = \frac{\mu b(x)}{\sigma_{32}^\infty} \quad S_e = \frac{\mu_0}{a\mu} \quad (4.2)$$

Define the inverse operator T^{-1} by

$$T^{-1}\psi(x) = \frac{1}{\pi\sqrt{1-x^2}} \int_{-1}^1 \psi(t) \, dt - \frac{1}{\pi^2\sqrt{1-x^2}} \int_{-1}^1 \frac{\sqrt{1-t^2}\psi(t)}{t-x} \, dt \quad -1 < x < 1 \quad (4.3)$$

and apply to Eq. (4.1)₁ to obtain

$$\hat{b}(x) = \frac{1}{\pi\sqrt{1-x^2}} \int_{-1}^1 \hat{b}(t) dt - \frac{1}{\pi\sqrt{1-x^2}} \int_{-1}^1 \frac{\sqrt{1-t^2}[-S_e(1+kt)\hat{b}'(t) - S_ek\hat{b}(t) + 2]}{t-x} dt \quad (4.4)$$

Multiply both sides of Eq. (4.4) by $\sqrt{1-x^2}$ and using the condition in Eq. (4.1)₂, we obtain

$$\hat{b}(x)\sqrt{1-x^2} = -\frac{1}{\pi} \int_{-1}^1 \frac{\sqrt{1-t^2}[-S_e(1+kt)\hat{b}'(t) - S_ek\hat{b}(t) + 2]}{t-x} dt \quad (4.5)$$

We assume that the unknown function $\hat{b}(x)$ can be approximated by the following expansion

$$\hat{b}(x) = \sum_{m=0}^N c_m T_m(x) \quad (4.6)$$

where $T_m(x)$ represents the m th Chebyshev polynomial of the first kind.

By inserting Eq. (4.6) into Eq. (4.5), and making use of the following identities

$$\begin{aligned} \frac{dT_m(x)}{dx} &= mU_{m-1}(x) & 2xU_m(x) &= U_{m+1}(x) + U_{m-1}(x) \\ \int_{-1}^1 T_m(t) dt &= \begin{cases} \frac{1+(-1)^m}{1-m^2} & m \neq 1 \\ 0 & m = 1 \end{cases} \\ \int_{-1}^1 \frac{U_m(t)\sqrt{1-t^2}}{t-x} dt &= -\pi T_{m+1}(x) \\ \int_{-1}^1 \frac{T_m(t)\sqrt{1-t^2}}{t-x} dt &= \int_{-1}^1 \frac{[U_m(t) - tU_{m-1}(t)]\sqrt{1-t^2}}{t-x} dt \\ &= \int_{-1}^1 \frac{U_m(t)\sqrt{1-t^2}}{t-x} dt - x \int_{-1}^1 \frac{U_{m-1}(t)\sqrt{1-t^2}}{t-x} dt - \int_{-1}^1 U_{m-1}(t)\sqrt{1-t^2} dt \\ &= -\pi T_{m+1}(x) + \pi x T_m(x) - \frac{\pi}{2}\delta_{m1} - \pi x \delta_{m0} \end{aligned} \quad (4.7)$$

with $U_m(x)$ being the m -th Chebyshev polynomial of the second kind, we finally arrive at

$$\begin{aligned} c_0(\sqrt{1-x^2} + S_ekx) + \sum_{m=1}^N c_m \left[S_ek \left(1 + \frac{m}{2} \right) T_{m+1}(x) \right. \\ \left. + (\sqrt{1-x^2} + S_em - S_ekx) T_m(x) + \frac{S_ekm}{2} T_{m-1}(x) \right] = 2x \end{aligned} \quad (4.8)$$

If we select the collocation points given by $x = -\cos(i\pi/N)$ for $i = 1, 2, \dots, N$, Eqs. (4.8) and (4.1)₂ further reduce to the following algebraic equations

$$\begin{aligned}
 &c_0 \left(\sqrt{1 - \left(\cos \frac{i\pi}{N} \right)^2} - S_e k \cos \frac{i\pi}{N} \right) + \sum_{m=1}^N c_m \left[(-1)^{m+1} S_e k \left(1 + \frac{m}{2} \right) \cos \frac{(m+1)i\pi}{N} \right. \\
 &\quad \left. + (-1)^m \left(\sqrt{1 - \left(\cos \frac{i\pi}{N} \right)^2} + S_e m + S_e k \cos \frac{i\pi}{N} \right) \cos \frac{mi\pi}{N} \right. \\
 &\quad \left. + (-1)^{m-1} \frac{S_e k m}{2} \cos \frac{(m-1)i\pi}{N} \right] = -2 \cos \frac{i\pi}{N} \quad i = 1, 2, \dots, N \tag{4.9} \\
 &\sum_{m=0, m \neq 1}^N \frac{1 + (-1)^m}{1 - m^2} c_m = 0
 \end{aligned}$$

The $(N + 1)$ unknowns c_m , $m = 0, 1, 2, \dots, N$ can be uniquely determined by solving the $(N + 1)$ independent equations in Eqs. (4.9).

5. Numerical results and discussion

In Figs. 1a and 1b, we illustrate the distributions of the dislocation density $b(x)$ and the crack opening displacement Δw for four values of the gradient parameter k with $S_e = 1$. It is observed from the two figures that: (i) $b(x)$ is no longer an odd function of x and Δw is no longer an even function of x for $k \neq 0$; (ii) as k increases from zero, the magnitude of $b(-1) < 0$ increases considerably whereas that of $b(1) > 0$ decreases only marginally; (iii) as k increases from zero, Δw increases significantly for the majority of the left portion of the crack and shrinks only marginally for a small part of the right portion of the crack. It is observed from Eq. (3.10) that the surface shear modulus for $x < 0$ always decreases and that for $x > 0$ always increases as k increases from zero. This means that the left section of the crack becomes softer as opposed to the right portion which becomes stiffer as k increases from zero. For example, when $k = 0.99$, $\mu^s(-1) - \sigma_0 = 0.01\mu_0$ and $\mu^s(+1) - \sigma_0 = 1.99\mu_0$. In this case, the crack surface in the immediate neighbourhood of the left crack tip exhibits a minimal surface effect. Thus $-\hat{b}(-1)$ should be considerably large since it becomes infinite in the absence of any surface effect. In fact, the numerical result shows that $\hat{b}(-1) \approx -30$.

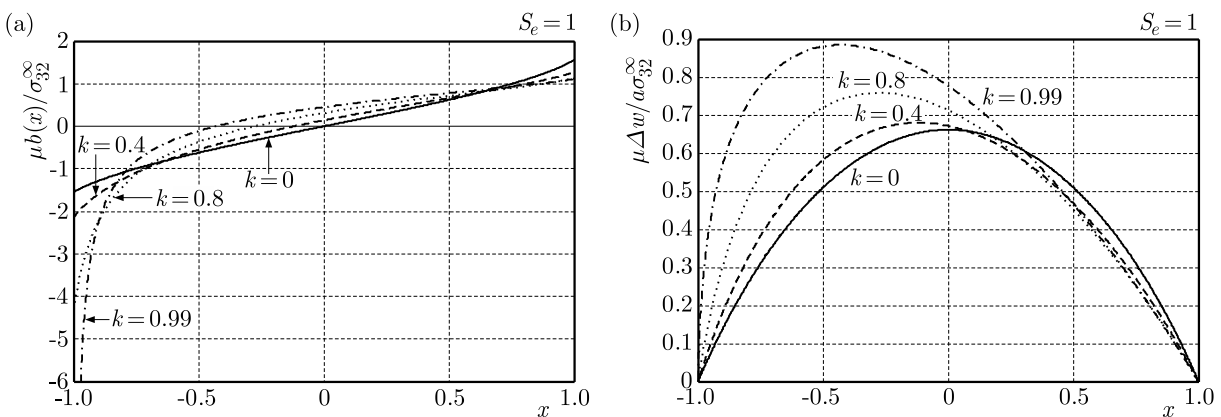


Fig. 1. The distribution of $b(x)$ (a) and Δw (b) for four values of the gradient parameter $k = 0, 0.4, 0.8, 0.99$ with $S_e = 1$

In Figs. 2a and 2b, we illustrate the variations of $b(x)$ and Δw for three sets of surface parameters: $S_e = 1, k = 0.8$; $S_e = 1.8, k = 0$; $S_e = 0.2, k = 0$. The surface shear modulus at the left crack tip for $S_e = 1, k = 0.8$ is simply equal to the constant surface shear modulus in the case $S_e = 0.2, k = 0$; the surface shear modulus at the right crack tip when $S_e = 1, k = 0.8$ is

just the constant surface shear modulus for the case $S_e = 1.8, k = 0$. It is observed from Fig. 2a that $\hat{b}(-1) = -4.4524$ for $S_e = 1, k = 0.8$ and $\hat{b}(-1) = -4.8444$ for $S_e = 0.2, k = 0$. These two values of \hat{b} are clearly close to each other. In addition, $\hat{b}(1) = 1.1282$ for $S_e = 1, k = 0.8$ and $\hat{b}(1) = 0.9538$ for $S_e = 1.8, k = 0$. Again, these two values of \hat{b} are close. From Fig. 2b we see that Δw for $S_e = 1, k = 0.8$ is greater than that for $S_e = 1.8, k = 0$ and is smaller than that for $S_e = 0.2, k = 0$. This observation is in agreement with the conclusion reached in Antipov and Schiavone (2011) that surface effects decrease the crack opening displacement. Intuitively, our observations are consistent with the physics of the problem.

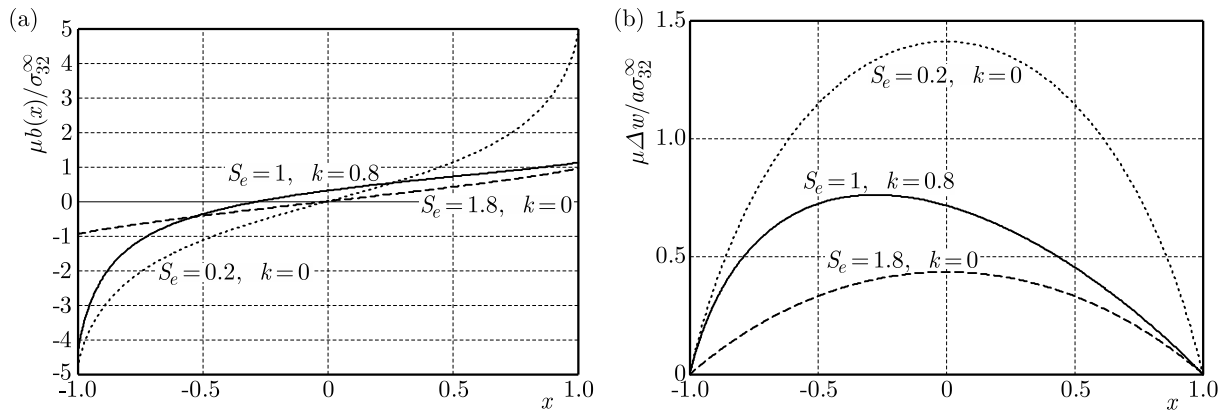


Fig. 2. The distribution of $b(x)$ (a) and Δw (b) for three sets of the surface parameters: $S_e = 1, k = 0.8$; $S_e = 1.8, k = 0$; $S_e = 0.2, k = 0$

Once $\hat{b}(x)$ is known, the stress field can be obtained from

$$\frac{\sigma_{32}}{\sigma_{32}^\infty} + i\frac{\sigma_{31}}{\sigma_{32}^\infty} = \frac{1}{2\pi} \int_{-1}^1 \frac{\hat{b}(t)}{\hat{z} - t} dt + 1 \tag{5.1}$$

where $\hat{z} = z/a$. Since $\hat{b}(x)$ is finite at $x = \pm 1$, the stresses exhibit a logarithmic singularity at the crack tips as follows

$$\begin{aligned} \frac{\sigma_{32}}{\sigma_{32}^\infty} + i\frac{\sigma_{31}}{\sigma_{32}^\infty} &= -\frac{\hat{b}(1)}{2\pi} \ln(z - a) + O(1) & \text{as } z \rightarrow a \\ \frac{\sigma_{32}}{\sigma_{32}^\infty} + i\frac{\sigma_{31}}{\sigma_{32}^\infty} &= \frac{\hat{b}(-1)}{2\pi} \ln(z + a) + O(1) & \text{as } z \rightarrow -a \end{aligned} \tag{5.2}$$

We illustrate in Fig. 3 the stress component σ_{32} along the negative real axis for four values of the gradient parameter k with $S_e = 1$. As k increases from zero, the material in the proximity of the left crack tip becomes softer. Consequently, as illustrated in Fig. 3, the stress increases. For any value of k , the stress is consistently lower than that found from the corresponding classical solution $\sigma_{32}/\sigma_{32}^\infty = |x|/\sqrt{x^2 - 1}$ in the absence of surface effects. In order to verify the logarithmic singularity at the crack tips, the near tip distribution of σ_{32} along the negative real axis outside the crack is shown in Fig. 4. Seemingly, σ_{32} is a linear function of $\ln(-x - 1)$ for a fixed value of k . Thus the logarithmic singularity at the crack tip is verified numerically. From Fig. 4 we can also calculate the pre-factors of the logarithmic term as: -0.2738 for $k = 0$; -0.3798 for $k = 0.4$; -0.7758 for $k = 0.8$; -4.8376 for $k = 0.99$. The theoretical values from Eq. (5.2)₂ give: -0.2481 for $k = 0$; -0.3448 for $k = 0.4$; -0.7086 for $k = 0.8$; -4.7396 for $k = 0.99$. Clearly, the calculated pre-factors well approximate the theoretical values.

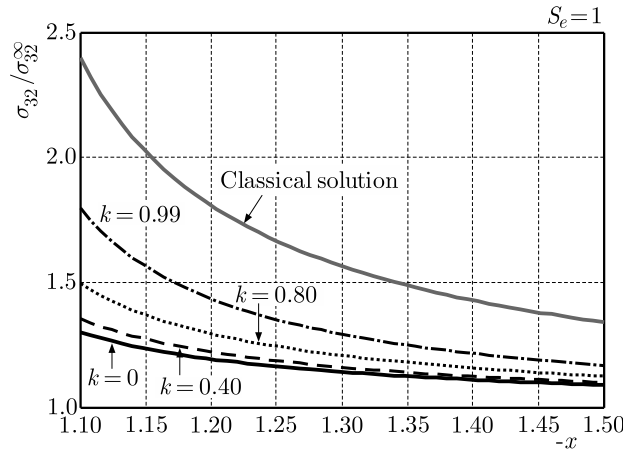


Fig. 3. σ_{32} along the negative real axis for four values of the gradient parameter $k = 0, 0.4, 0.8, 0.99$ with $S_e = 1$

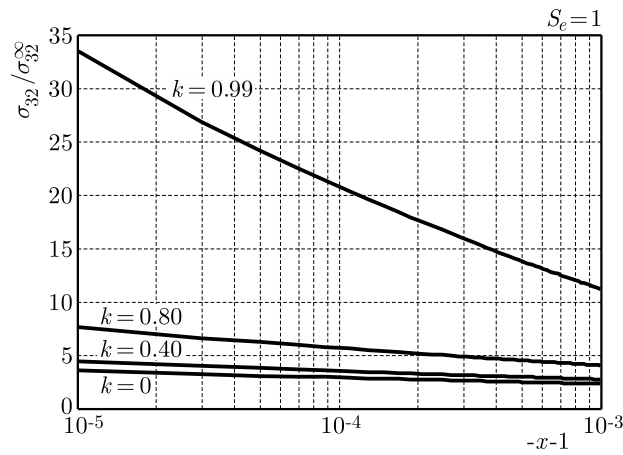


Fig. 4. The near tip distribution of σ_{32} along the negative real axis outside the crack

6. Conclusions

In this paper, we utilize a modified version of the Gurtin-Murdoch model to examine the effects of variable surface shear modulus in a mode-III fracture problem arising in the antiplane shear deformation of a linearly elastic solid. The method of Green’s functions is used to obtain an exact complete solution valid throughout the entire domain of interest (including at the crack tips) by reducing the problem to a Cauchy singular integro-differential equation of the first-order which is solved numerically using an adapted collocation method. Numerical results demonstrate clearly that the gradient of the surface shear modulus exerts a significant influence on the distributions of dislocation density on the crack, crack opening displacement and stress distribution near the crack tips. The numerical results also verify that the resulting analysis is correct and that the proposed collocation method is an effective tool in the analysis of crack problems in the presence of variable surface effects.

Acknowledgements

This work is supported by the National Natural Science Foundation of China (Grant No.: 11272121) and through a Discovery Grant from the Natural Sciences and Engineering Research Council of Canada (Grant # RGPIN 155112).

References

1. ANTIPOV Y.A., SCHIAVONE P., 2011, Integro-differential equation for a finite crack in a strip with surface effects, *Quarterly Journal of Mechanics and Applied Mathematics*, **64**, 87-106
2. CHEN T., DVORAK G.J., YU C.C., 2007, Size-dependent elastic properties of unidirectional nano-composites with interface stresses, *Acta Mechanica*, **188**, 39-54
3. GURTIN M.E., MURDOCH A., 1975, A continuum theory of elastic material surfaces, *Archive for Rational Mechanics and Analysis*, **57**, 291-323
4. GURTIN M.E., WEISSMULLER J., LARCHE F., 1998, A general theory of curved deformable interface in solids at equilibrium, *Philosophical Magazine*, **A78**, 1093-1109
5. KIM C.I., RU C.Q., SCHIAVONE P., 2013, A clarification of the role of crack-tip conditions in linear elasticity with surface effects, *Mathematics and Mechanics of Solids*, **18**, 59-66
6. KIM C.I., SCHIAVONE P., RU C.Q., 2010, The effects of surface elasticity on an elastic solid with mode-III crack: complete solution, *ASME Journal of Applied Mechanics*, **77**, 021011-1–021011-7
7. KIM C.I., SCHIAVONE P., RU C.Q., 2011a, Analysis of plane-strain crack problems (mode I and mode II) in the presence of surface elasticity, *Journal of Elasticity*, **104**, 397-420
8. KIM C.I., SCHIAVONE P., RU C.Q., 2011b, Effect of surface elasticity on an interface crack in plane deformations, *Proceedings of the Royal Society of London. Series A*, **467**, 3530-3549
9. MARKENSCOFF X., DUNDURS J., 2014, Annular inhomogeneities with eigenstrain and interphase modeling, *Journal of the Mechanics and Physics of Solids*, **64**, 468-482
10. RU C.Q., 2010, Simple geometrical explanation of Gurtin-Murdoch model of surface elasticity with clarification of its related versions, *Science China*, **53**, 536-544
11. SHARMA P., GANTI S., 2004, Size-dependent Eshelby's tensor for embedded nano-inclusions incorporating surface/interface energies, *ASME Journal of Applied Mechanics*, **71**, 663-671
12. STEIGMANN D.J., OGDEN R.W., 1997, Plane deformations of elastic solids with intrinsic boundary elasticity, *Proceedings of the Royal Society of London. Series A*, **453**, 853-877
13. WALTON J.R., 2012, A note on fracture models incorporating surface elasticity, *Journal of Elasticity*, **109**, 95-102
14. WANG X., 2015, A mode III arc shaped crack with surface elasticity, *Zeitschrift für Angewandte Mathematik und Physik*, **66**, 1987-2000
15. WANG X., SCHIAVONE P., 2015, A mode III interface crack with surface strain gradient elasticity, *Journal of Integral Equations and Applications*, **28**, 123-148
16. WANG X., SCHIAVONE P., 2016, Bridged cracks of mode III with surface elasticity, *Mechanics of Materials*, **95**, 125-135

METHOD FOR SHIP'S ROLLING PERIOD PREDICTION WITH REGARD TO NON-LINEARITY OF GZ CURVE

WOJCIECH WAWRZYŃSKI, PRZEMYSŁAW KRATA

Gdynia Maritime University, Faculty of Navigation, Department of Ship Operation, Gdynia, Poland

e-mail: w.wawrzynski@wn.am.gdynia.pl; p.krata@wn.am.gdynia.pl

The paper deals with the problem of prediction of the rolling period. A special emphasis is put on the practical application of the new method for rolling period prediction with regard to non-linearity of the GZ curve. The one degree-of-freedom rolling equation is applied with using the non-linear stiffness moment and linear damping moment formulas. A number of ships are considered to research the discrepancies between the pending GM-based IMO-recommended method and the results of conducted numerical simulations performed for a wide range of operational loading conditions. Since the research shows some drawbacks of the IMO formula for the ship rolling period, a new formula is worked out and proposed instead.

Keywords: ship natural roll period, GZ approximation, rolling prediction, safety against capsizing

1. Introduction

A ship performing in rough sea conditions experiences complex motions which are the outcome of the combination of linear displacements and rotations considering each axis of the reference system. With regard to a ship safety, the greatest concern is related to its rolling oscillations. The main parameters of the rolling equation are: inertia, damping, stiffness and excitation. Each of them reveals a significant nonlinearity and its proper application has an impact on the obtained results.

Generally, potentially dangerous situations that may cause capsizing of a ship that remains intact, can be divided into resonant and non-resonant ones (Błocki, 2000). The non-resonant situations are mainly the outcome of two possible scenarios. First of all, they are caused by a combination of the ship rolling motion and a dynamic gust of wind. The scenario is well described by weather criteria of stability in accordance with the IMO IS-Code (IMO, 2009). Secondly, they are caused by the loss of stability on following or quartering seas when the wave crest is amidships. Furthermore, broaching and surfriding may be classified as non-resonant phenomena which may lead to capsizing (IMO, 2007).

The resonant situations may be divided into parametric resonance and synchronous rolling. The first one occurs mainly on following and quartering seas and is caused by inducing instability and an increase in the rolling amplitude due to the periodic variation of ships stability characteristics, not as a result of direct roll excitation. The synchronous rolling takes place usually at beam seas when the encounter period is close to the natural period of ship roll or half of this period (IMO, 2007).

The above-mentioned adverse phenomena represent a real threat to the ship safety. Also they are very complex and have significantly nonlinear characteristics. As a result, there is a great amount of research that has been undertaken worldwide for many years. The literature review shows a list of works taking into consideration various aspects of ships rolling motion. Some of the older works on the topic of damping of rolling are worth mentioning, see Cardo *et al.*

(1994), Haddara and Bennett (1989), Himeno (1981). Among newer papers, there is a significant number of worthwhile works devoted to the synchronous rolling and parametric rolling in the context of development of the second generation of intact stability criteria (Belenky *et al.*, 2011; Holden *et al.*, 2007; Neves and Rodriguez, 2006, 2009; Shin *et al.*, 2004; Umeda, 2013). Also, there is a noteworthy quantity of works dedicated to various mathematical models of rolling, mainly with regard to nonlinearities existing in particular components of the roll equation or a system of motion equations in the case of the coupling analysis (Bulian, 2005; Contento *et al.*, 1996; Francescutto and Contento, 1999; Taylan, 2000). The importance of the influence of the mathematical model used was presented by Spanos and Papanikolaou (2009) who presents a comparison of results of calculations of rolling on waves using 14 different, recognized simulations programs. The consistency of some results left much to be desired giving the room for further researches in this field.

There is a group of works where one of the goals was to describe relatively simple analytical formulas enabling one to calculate singular rolling characteristics, for example the maximum rolling amplitude that a ship may reach in parametric rolling conditions (Shin *et al.*, 2004).

In many of the above-mentioned papers the natural roll frequency, which strongly determines the resonance mode of motion, is used as one of the rolling equation parameters. Unfortunately, this frequency is calculated on the basis of the initial metacentric height of a ship, most often with the use of a simple formula recommended in the IMO IS Code. However, this metacentric height is valid for small angles of heel, normally up to about 7 degrees, which do not pose a threat to the ship stability. The rolling frequency varies for greater amplitudes. The influence of the rolling amplitude on its frequency and, consequently, on the rolling period was investigated by Contento *et al.* (1996). In the paper by Kruger and Kluwe (2008), the authors directly suggest that variations of the rolling period should be taken into account and the energy balance method is proposed for the equivalent metacentric height calculation. This current paper is a continuation of the former work regarding the period prediction of ships natural rolling.

2. Applied model of rolling

The most commonly used model of rolling, which neglects any couplings from motions taking place in other than rolling degrees of freedom may be given by the following formula

$$(I_x + A_{44})\ddot{\phi} + B_e\dot{\phi} + K(\phi) = M_w \cos(\omega_e t) \quad (2.1)$$

where I_x denotes the transverse moment of ship inertia; A_{44} is the moment of added mass due to water dragging by the rolling hull; B_e is the equivalent linear roll damping coefficient, $K(\phi)$ describes the righting moment, e.g. stiffness of the ship, M_w is the external heeling moment exciting rolling and ω_e is the encounter frequency of waves. Although, the roll damping is significantly nonlinear and the equivalent linear roll damping coefficient B_e depends on the amplitude, the frequency and the ship speed (Himeno, 1981; Uzunoglu and Guedes Soares, 2015), for the sake of simplicity the coefficient B_e is frequently assumed to be constant regardless the parameters of roll motion (Himeno, 1981; Shin *et al.*, 2004). In the case of still water conditions and the lack of other exciting moments the right hand side of equation (2.1) is equal to zero. In such a case, the ship motion is called the free rolling and is often used in the roll amplitude decay test. If so, the rolling equation is the following

$$(I_x + A_{44})\ddot{\phi} + B_e\dot{\phi} + K(\phi) = 0 \quad (2.2)$$

The righting moment equals

$$K(\phi) = D GZ(\phi) \quad (2.3)$$

where GZ is the righting arm curve and D is ship weight.

After substitution of formula (2.3) into equation (2.1) we divide both sides by $(I_{xx} + A_{44})$ and introduce the commonly used notation. Then the roll equation becomes

$$\ddot{\phi} + 2\mu\dot{\phi} + \frac{\omega^2}{GM}GZ(\phi) = \xi_w \cos(\omega_e t) \quad (2.4)$$

where ω denotes the natural roll frequency of the ship, GM is the initial metacentric height, μ is the damping coefficient and ξ_w means the exciting moment coefficient.

Formula (2.4) is used quite often, however apart from the GZ characteristic which is valid for the full range of angles of the ship heel, it also contains the initial metacentric height and the natural roll frequency that are only related to the initial stability of the ship. Thus, the two fore mentioned variables reflecting the stiffness characteristics for small angles of heel restrict the potential applicability of equation (2.4). To avoid such restrictions and eliminate the initial stability characteristics from equation (2.4) it is transformed into a more versatile form by substituting $\omega = \sqrt{gGM}/r_x$:

— for excited rolling

$$\ddot{\phi} + 2\mu\dot{\phi} + \frac{g}{r_x^2}GZ(\phi) = \xi_w \cos(\omega_e t) \quad (2.5)$$

— for free rolling

$$\ddot{\phi} + 2\mu\dot{\phi} + \frac{g}{r_x^2}GZ(\phi) = 0 \quad (2.6)$$

where g is the gravity acceleration and r_x is the gyration radius of the ship and added masses (which is assumed to be constant for the sake of simplicity).

Formula (2.6) constitutes the mathematical model of rolling applied in the course of the conducted research. All further simulations of the ship motion are based on this equation.

The rolling equation given by formula (2.6) requires modeling the stiffness related to transverse stability of the ship. The most straightforward approach would be calculation of the righting arm based on the actual shape of the underwater part of the ship hull performed in every time step of the rolling simulation. However, such a solution is excessively time consuming and requires too much processing power for practical use. Thus, the next approach is to apply a $GZ(\phi)$ function obtained prior the start of rolling simulation for the actual loading condition of the ship. However, there is a lack of analytical formulas describing the righting arm GZ due to the fact that the shape of KN arm strictly depends on the shape of the ship hull. To address this problem, most researchers apply various approximations of the GZ curve. The choice of the GZ modeling method is a kind of trade-off decision because of the contradictory goals like accurate GZ approximation and reasonable time of each simulation.

The simplest approximation formulas like for instance $GZ(\phi) = GM\phi(1 - \phi^2)$, see Belenky *et al.* (2011), produces so rough estimation of the GZ characteristic that applied in the rolling equation they cannot achieve a sufficient accuracy of the results of rolling simulation. On the basis of the literature review, it seems that the most popular approach is the application of a polynomial power series. Many authors use the fifth to ninth order polynomials (Contento *et al.*, 1996; Surendran and Venkata Ramana Reddy, 2003; Taylan 2000) with only odd powers of the angle of heel due to a symmetrical character of the GZ curve. A limited number of authors apply higher order polynomials like seventh or ninth, and rarely even higher (Bulian, 2005).

For the purpose of this study, two approaches toward GZ approximation have been tested, e.g. the ninth-order polynomial power series with odd powers only and the trigonometric polynomial as an interesting alternative (Wawrzyński, 2015). Finally, the ninth-order polynomial power series are applied to approximate the value of the righting arm in each time-step of the performed rolling simulations. The GZ formula is the following

$$GZ(\phi) = C_1\phi + C_3\phi^3 + C_5\phi^5 + C_7\phi^7 + C_9\phi^9 \quad (2.7)$$

where C_1 to C_9 are the coefficients of odd orders obtained with the use of the least squares method.

3. Considered ships and their stability conditions

The intended scope of the study comprises researching a wide variety of ships in terms of their size, type and loading conditions. Thus, the number of significantly varying ships are selected with the length ranging from 76 m up to 320 m. The types of vessels are: motor tanker, bulk carrier, 5000 TEU Panamax container ship, 7500 TEU container ship, LNG carrier, general cargo ship and an offshore support vessel.

The stability characteristics of these vessels are also notably varying and they cover a wide range of stability options applicable in operational loading conditions. To obtain the wished-for variety of typical shapes of the GZ curve, the ships loading conditions are systematically selected. However, only loading conditions reflecting the practically applicable draft of ships and weight distributions are taken into account. The earlier work by Wawrzyński (2015) enables one to distinguish three typical shapes of the righting arm curve for loading conditions with obligatory positive GM value. The sketches of such GZ shapes are shown in Fig. 1. In the case of the pending research, stability characteristics are preselected to cover all three shapes marked A , B and C in Fig. 1.

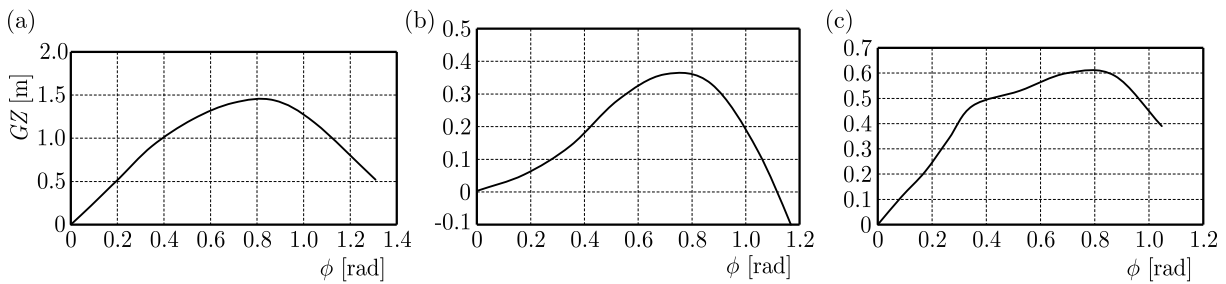


Fig. 1. Typical characteristics of the GZ curve for operational loading conditions with a positive value of GM (Wawrzyński, 2015)

To obtain a set of stability characteristics corresponding to typical cases given in Fig. 1. the initial metacentric height of considered vessels needs to significantly vary. Although some values of drafts and GM may subsist only in the ballast condition (due to location of typical ballast tanks in the ship double bottom) and others rather than in the fully loaded condition. Thus, the range of considered drafts and metacentric heights is also relatively wide. However, all the ships have a positive value of the metacentric height and not less than required by the IMO Intact Stability Code. The main particulars of the considered vessels and the variety of draft and stability of the ships are shown in Table 1. Since seven ships are studied and a couple of loading condition per each ship, the number of considered cases is pretty large.

4. Results of rolling simulations vs. GM -based IMO-recommended formula ones

The natural rolling period of the ship remains the matter of concern of many researches and practical issues. The notion of the natural rolling period is also mentioned in a number of documents issued by the International Maritime Organization, like Intact Stability Code (IMO, 2009) or MSC.1/Circ.1228 (IMO, 2007) as the second generation ship stability criteria which are under development (Umeda, 2013). The simple method for calculation of the rolling period τ is given in the Intact Stability Code and it is recommended for on-board use in absence of

Table 1. Main particulars of ships considered in the course of the research

Type of vessel	Length [m]	Breadth [m]	Considered draft T		Metacentric height GM	
			min [m]	max [m]	min [m]	max [m]
General cargo ship	140.00	22.00	6.00	9.00	0.40	1.00
5000 TEU Panamax container ship	283.20	32.20	7.50	13.50	0.50	3.00
7500 TEU container ship	285.00	45.60	7.50	12.50	2.00	5.00
Bulk carrier	156.10	25.90	6.50	10.50	1.00	3.50
Motor tanker	320.00	58.00	10.00	22.00	5.00	10.00
LNG carrier	278.80	42.60	7.50	12.00	1.00	5.00
Offshore support vessel	76.20	17.00	3.60	6.10	1.50	2.50

sufficient information. Although, the lack of reliable “sufficient information” takes place almost permanently. The formula based on the initial metacentric height of a ship is (IMO, 2009)

$$\tau = \frac{2cB}{\sqrt{GM}} \quad c = 0.373 + 0.023\frac{B}{T} - 0.043\frac{L}{100} \quad (4.1)$$

where c is the coefficient describing ships transverse gyration radius; B means ship breadth and L ship length at waterline; T denotes mean ship draft. Actually, the radius of gyration equals cB where c is the dimensionless coefficient to be multiplied by the ship breadth given in meters.

The values obtained on the basis of simple formula (4.1) are compared in the course of the study with the rolling periods calculated in a more sophisticated way. The research and further reasoning are based on the solution of the rolling equation given by formula (2.6). We consider four loading conditions per each ship except for the offshore support vessel due to exceptional variety of shapes of the GZ curve. For this OSV, six loading conditions are taken into account. Thus, the set consists of 30 cases. For each case, numerous simulations have been carried out in order to obtain the rolling characteristics, mainly the period of roll for the full range of rolling amplitudes. The consecutive by considered amplitudes vary by one degree from 1 up to 60 degrees, so the total number of executed simulations reaches 1800.

The numerical simulations have been performed with the use of two separate software tools. One was the CAS software and the Runge-Kutta build-in method was applied. The limited number of cases solved this way was used for the purpose of comparison and validation of the results obtained with the use of the main tool which was the own-developed Matlab script, prepared to run the roll simulations. The results obtained using these two tools truly converge so the Matlab script is the preferred one as a main software giving the unlimited control on the computation practice and data processing.

When the free rolling of ships is considered (the right side of equation (2.6) equals zero), the assumed initial angle of the ship heel is the cause of rolling. Generally, the idea of this research is to analyze the period of roll for a specified rolling amplitude to work out a prediction method. Thus, there is a need to keep the amplitude almost steady for at least few ship's swings. To achieve this, the value of the damping coefficient has been set relatively small. However, the damping coefficient affects mainly the rolling amplitude while the change of the rolling period may be almost neglected, so the simulations results reflect free rolling of a ship fairly enough.

The solution obtained in each separate case related to one ship, one loading condition and one rolling amplitude is just a time history of roll motion which is shown in Fig. 2. The rolling period is one of the variables obtained in the course of data post processing. The fast Fourier transform is applied to acquire this period. Gathering the values of rolling period for the full

range of amplitudes we obtain a set of data enabling comparison of numerical simulation results with the IMO formula based calculation, which is shown in Fig. 3 for one exemplary case. The description “IMO” used in the legend of the graph denotes the estimation of the rolling period according to IMO-recommended formula (4.1) based on the initial GM , and the description “num.” refers to the results of own simulation.

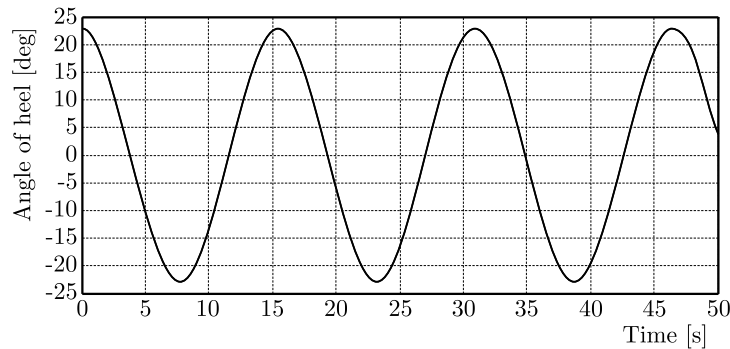


Fig. 2. Exemplary free rolling history of the general cargo ship for an considered rolling amplitude

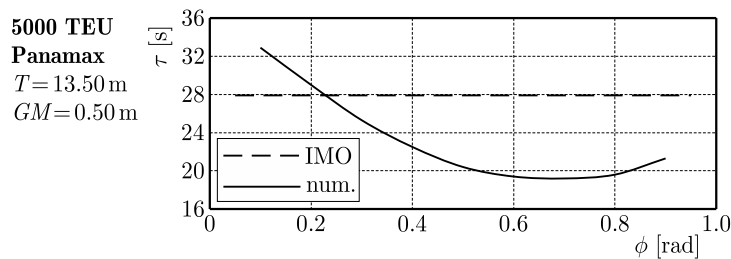


Fig. 3. Sample plot of the rolling period vs. rolling amplitude for 5000 TEU Panamax container ship

The sample plot of the rolling period vs. rolling amplitude for one selected ship (5000 TEU Panamax container ship in this case) and one loading condition (draft 13.50 m and initial metacentric height 0.50 m) clearly shows that the rolling period varies from 19 up to 33 seconds while the IMO formula returns the value close to 28 seconds. This example reveals the need for the elaboration of a new method.

5. Proposal of a simplified method for the rolling period prediction intended for practical use

To calculate the rolling period, very simple approximate formula (4.1) is recommended in the Intact Stability Code and it is used in the course of the assessment of the weather criterion of ship stability. Actually, small variations of the estimation of the rolling period influence the criterion to a limited degree as they slightly affect the angle of ships heel windward in the simplified model of rolling adopted in the weather criterion.

A much more serious matter is related to the IMO publication numbered MSC.1/Circ.1228 where simple formula (4.1) is also in use on-board. This is a *Revised guidance to the master for avoiding dangerous situations in adverse weather and sea conditions* intended to give some help to ship masters when sailing in stormy conditions. A relatively up to date publication (in comparison to dr. Rahola’s findings from 1939 being the foundation of the Intact Stability Code) contains a set of remarks and advices regarding the avoidance of following dangerous dynamical phenomena at sea like surf-riding and broaching-to; reduction of intact stability when riding

wave crest amidships; synchronous rolling motion; parametric roll motions (IMO, 2007). The recommendation expressed in the guidance is to estimate the natural roll period of the ship by observing roll motions in calm sea. Although such observations are rather difficult in many cases, so formula (4.1) is often used.

According to the IMO Circ.1228, some combinations of the wave length and wave height under certain operation conditions may lead to dangerous situations for ships complying with the IS Code (IMO, 2007). As the susceptibility of a ship to dangerous phenomena depends on the actual stability parameters, hull geometry, ship size and ship speed, the vulnerability to dangerous responses, including capsizing and its probability of occurrence in a particular sea state, may differ for each ship. Thus, the potentials for dangerous behavior of the ship shall be assessed.

One of the most important group of dangerous dynamic phenomena taken into account in IMO guidance 1228 is related to the resonance gain of rolling motion. This may occur due to nonlinearity of the ship response in resonance conditions, i.e. when the encounter wave frequency is similar to the first or second harmonic frequency of natural roll motion of a ship (Landrini, 2006). The prevention against synchronous rolling motion consists of avoiding such combinations of the ship speed and course which result in the encounter wave period T_E nearly equal to the natural rolling period of the ship τ ($T_E \approx \tau$) (IMO, 2007).

In the light of the briefly mentioned recommendations published in the *Revised guidance to the master for avoiding dangerous situations in adverse weather and sea conditions* and the degree of their importance related to safety of navigation, it seems to be fully justified to undertake the study on the rolling period prediction.

As the planned new rolling period approximation method is intended for the on-board use, it shall be well trade-off between the simplicity and the accuracy. The consequences of significant discrepancies between the predicted roll period of the ship and actual behavior at sea can be catastrophic in terms of potential involving the synchronous roll motion leading even to capsizing of the ship. Therefore, the planned method for roll period calculation should be as accurate as reasonably possible.

On the other hand, the new method cannot be too complex and complicated. Both authors of this study used to serve on-board seagoing ships and, thanks to this experience, they are aware of some limitations of practical use of any difficult formulas. Frankly, the best solution giving the greatest chance for real application in everyday sea practice is just the software realization with an easy to use interface. Thus, the proposed method of calculation should be simple enough to implement it and operate with no need for specialist knowledge of the crew, so any solver dealing with differential equations is just impractical on-board.

Keeping in mind the assumptions related to the method to be worked out, we focused our effort on the major elements governing the rolling period. On the basis of performed numerical simulations for all considered cases described in Section 3, we found two essential factors influencing variations of the rolling period. They are:

- the area under the GZ curve from the angle of heel equal to zero up to the rolling amplitude;
- the average inclination of the tangent line to the GZ curve from zero up to the rolling amplitude (such average inclination equals GZ_{φ_A}/φ_A for the amplitude of roll φ_A).

The key point is the relation of the rolling period characteristic and the appropriate GZ curve. The area under the GZ curve refers to the energy balance approach which was earlier suggested in Kruger and Kluwe (2008). The pace of change of the inclination of the GZ -tangent line describes the nonlinearity of the righting arm curve. The literature review reveals that this element was omitted in former works.

The elaborated simplified method for the rolling period prediction is based on both mentioned features which is far distinguishable from the contemporary method. On the other hand, the

proposed new method should not be found by mariners as too complicated. As deck officers are familiar with IMO formula (4.1), the new one looks very similarly

$$\tau(\phi_A) = \frac{2cB}{\sqrt{GM_{eq}(\phi_A)}} \quad (5.1)$$

where the value of c coefficient remains the same as given in formula (4.1) $GM_{eq}(\phi_A)$ denotes the equivalent value of the transverse metacentric height of the ship for a specified rolling amplitude ϕ_A .

The approach proposed in form of formula (5.2) remains as simple as the original IMO version, however it requires proper calculation of $GM_{eq}(\phi_A)$ value which strictly depends on the area under the GZ curve and the average inclination of the tangent line to GZ . It shall be emphasized that the equivalent metacentric height is a function of the rolling amplitude ϕ_A and no longer can be given by one number.

The proposed formula for the equivalent metacentric height calculation is following

$$GM_{eq}(\phi_A) = w_1 \frac{2}{\phi_A^2} \int_0^{\phi_A} GZ(\phi) d\phi + w_2 \frac{GZ_{\phi_A}}{\phi_A} \quad (5.2)$$

where w_1 and w_2 are the weights adjusting the influence of two components on the equivalent metacentric height.

The weight coefficients w_1 and w_2 can be the subject of further consideration, however their values tuned on the basis of this research equals 0.5 each. In such a case, formula (5.2) becomes

$$GM_{eq}(\phi_A) = \frac{1}{\phi_A^2} \int_0^{\phi_A} GZ(\phi) d\phi + \frac{GZ_{\phi_A}}{2\phi_A} \quad (5.3)$$

As it is mentioned earlier, the proposed method for the rolling period calculation shall be simple enough to develop undemanding software for the on-board use. Such software can be prepared simply as an amendment to the standard stability program available on many ships. The GZ curve is obtained as a routine procedure to perform the intact ship stability assessment on the basis of the stability standards issued by the classification society. This curve could be the starting point for simple calculation according to formula (5.3). The result of computation would be a curve showing the rolling period versus the rolling amplitude for a particular ship in actual loading condition. Such a graph may be helpful to the captain when sailing in adverse weather to assess the possibility of occurrence of the synchronous roll motion. As the rolling amplitude is just an observable fact, the captain is able to enquire the natural roll period of the ship relevant to the noticed situation.

The elaborated proposal of the new method of the natural roll period calculation, expressed in formula (5.3), shall be verified on the basis of the results of numerical simulations. The required verification has been done for all 30 cases considered within this study in the full range of angles of heel.

The results of comparison are given as a set of plots shown in Figs. 4 to 10. The description "IMO" in the legend denotes the estimation of the rolling period according to the IMO-recommended formula based on the initial GM. The next description "num." refers to the results of numerical simulation and "GMeq" means the rolling period calculated according to newly proposed formula (5.2) with the equivalent value of GMeq calculated according to formula (5.3). The left side of each Figs. 4 to 10 shows the graph presenting the natural rolling period versus rolling amplitude, and the right side presents the corresponding GZ curve with the metacentric triangle.

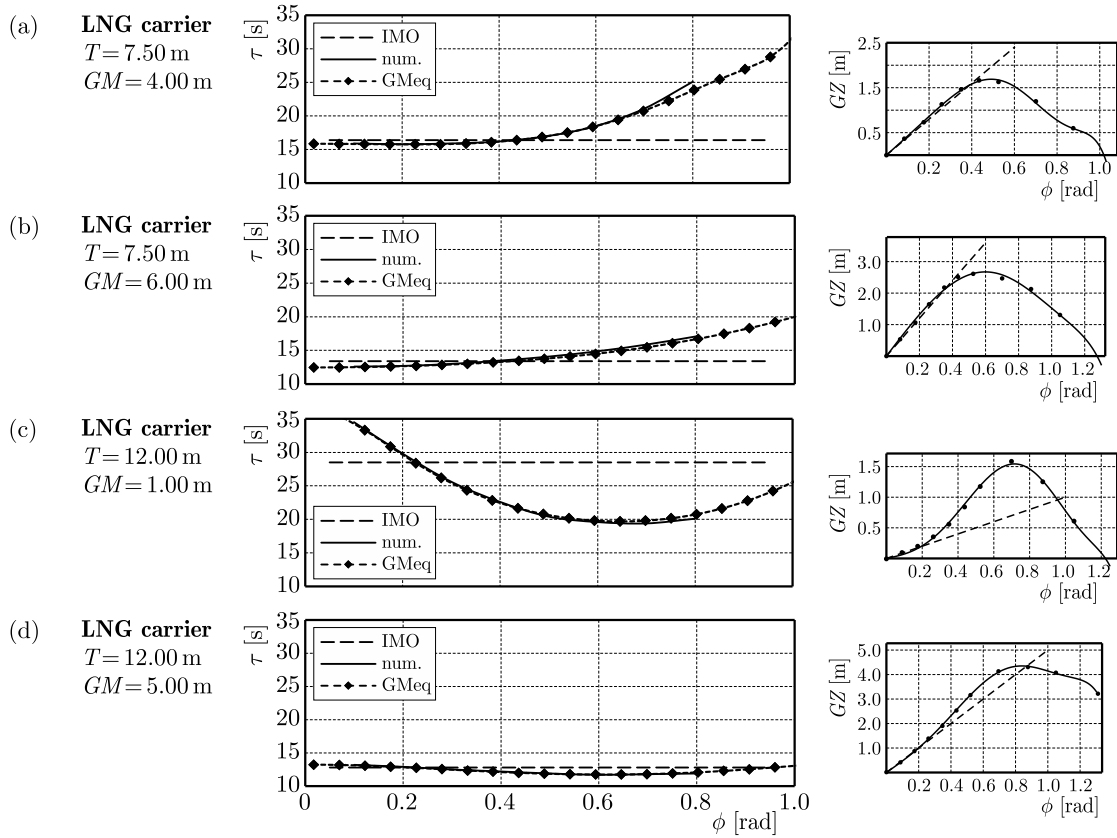


Fig. 4. Rolling period vs. rolling amplitude for the LNG carrier (left plot) and the corresponding GZ curve and the metacentric triangle (right plot)

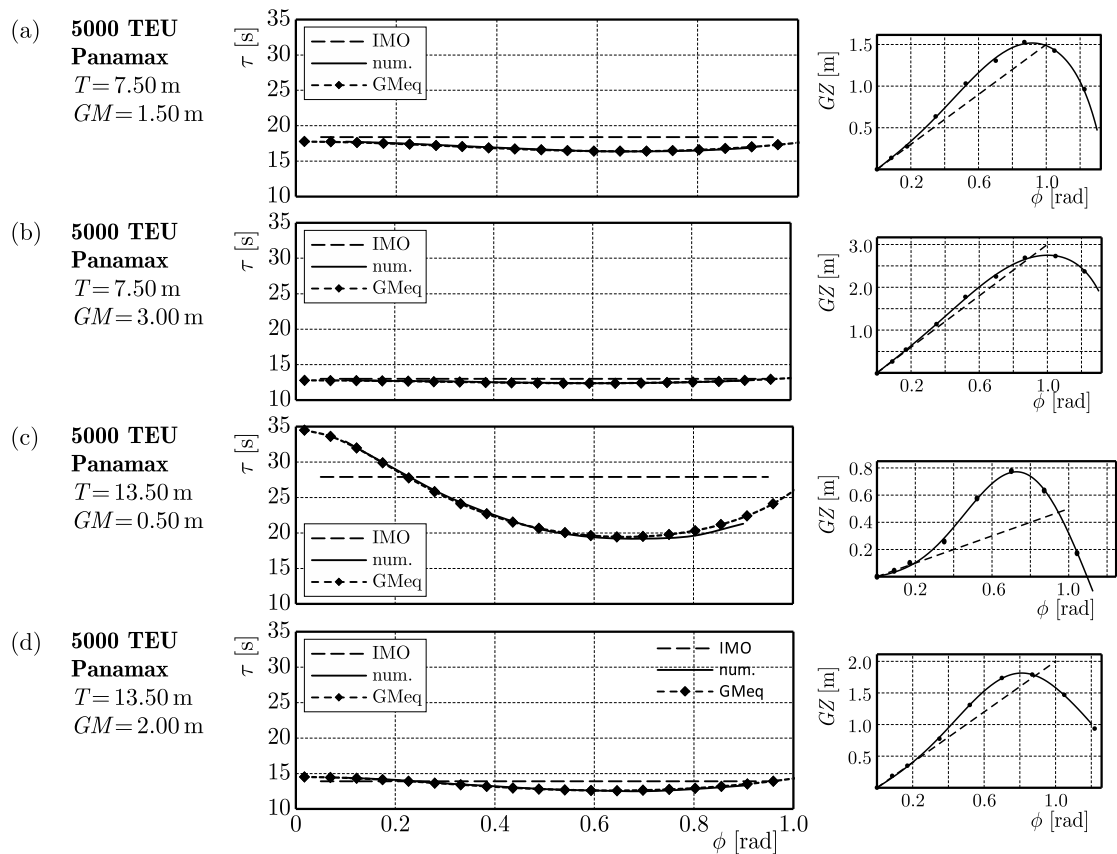


Fig. 5. Rolling period vs. rolling amplitude for the 5000 TEU Panamax container ship (left plot) and the corresponding GZ curve and the metacentric triangle (right plot)

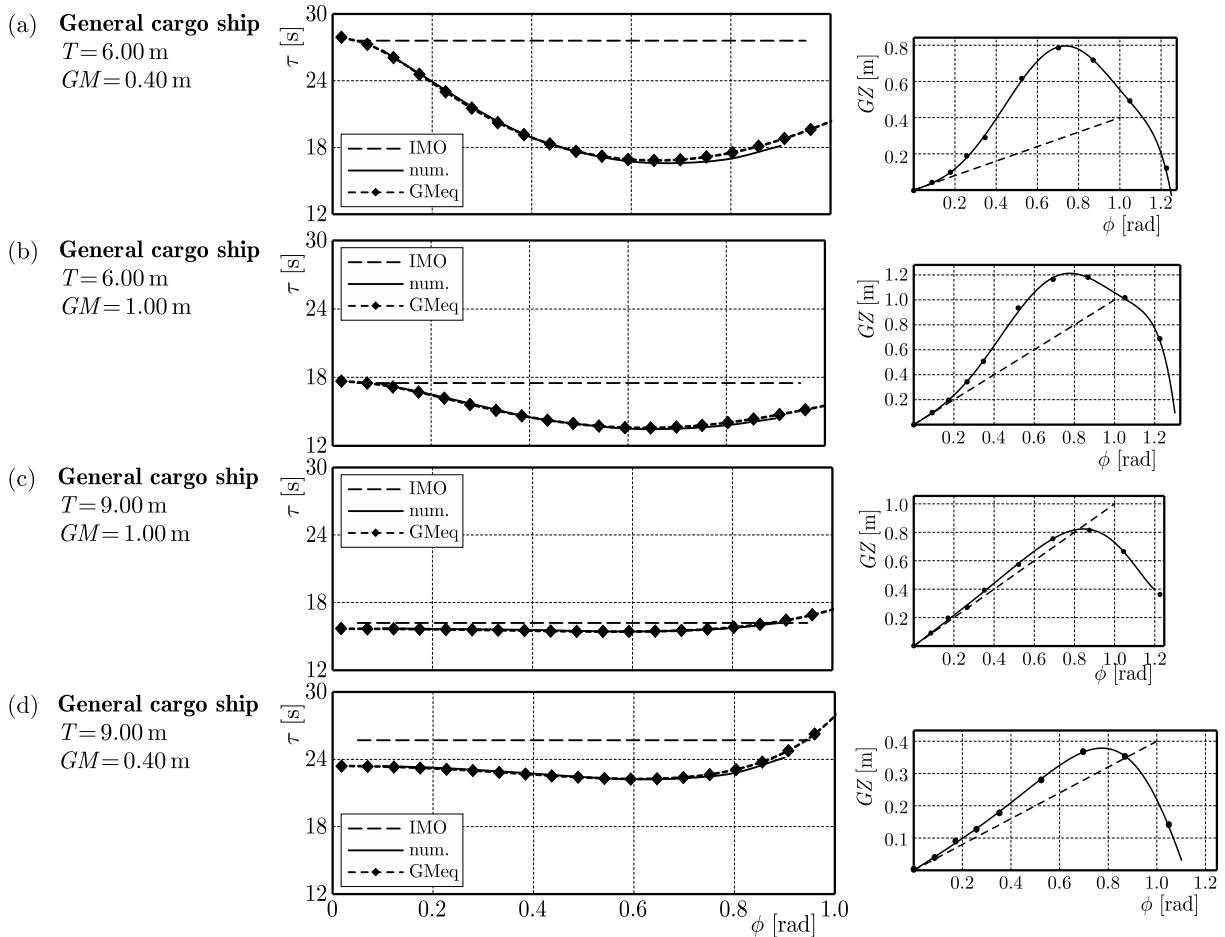


Fig. 6. Rolling period vs. rolling amplitude for the general cargo ship (left plot) and the corresponding GZ curve and the metacentric triangle (right plot)

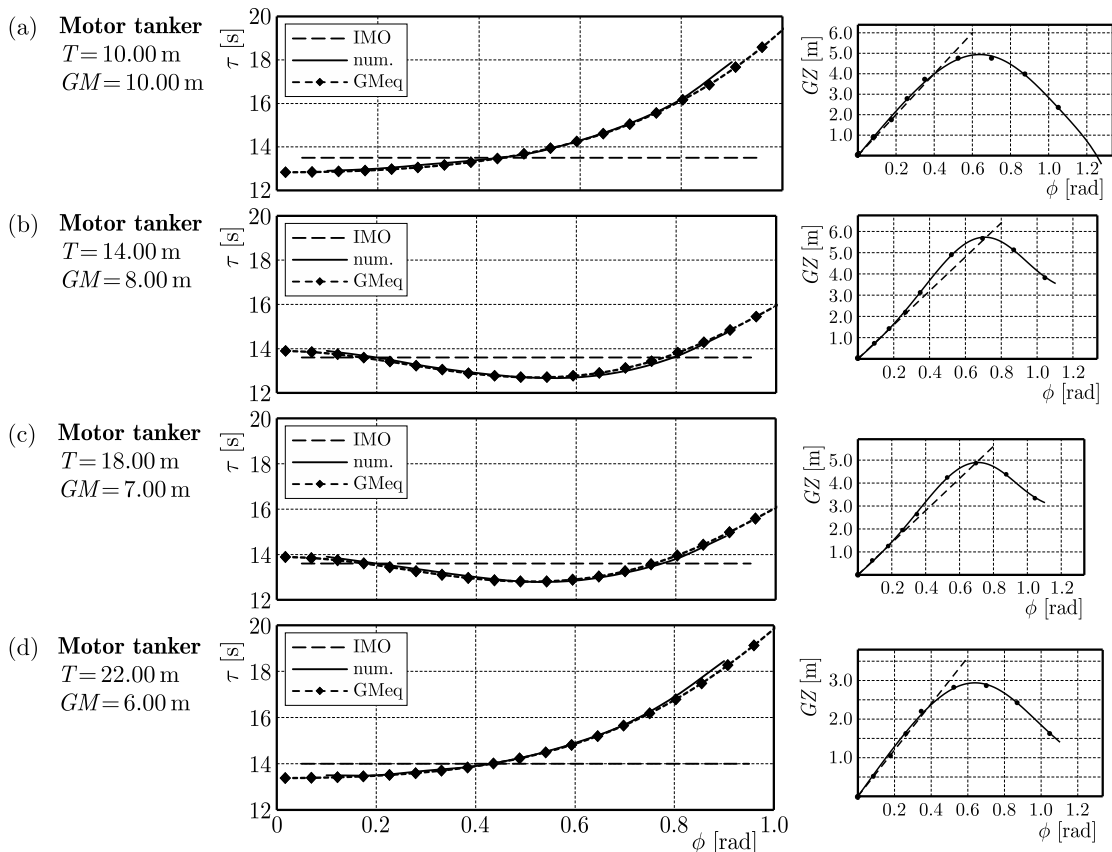


Fig. 7. Rolling period vs. rolling amplitude for the motor tanker (left plot) and the corresponding GZ curve and the metacentric triangle (right plot)

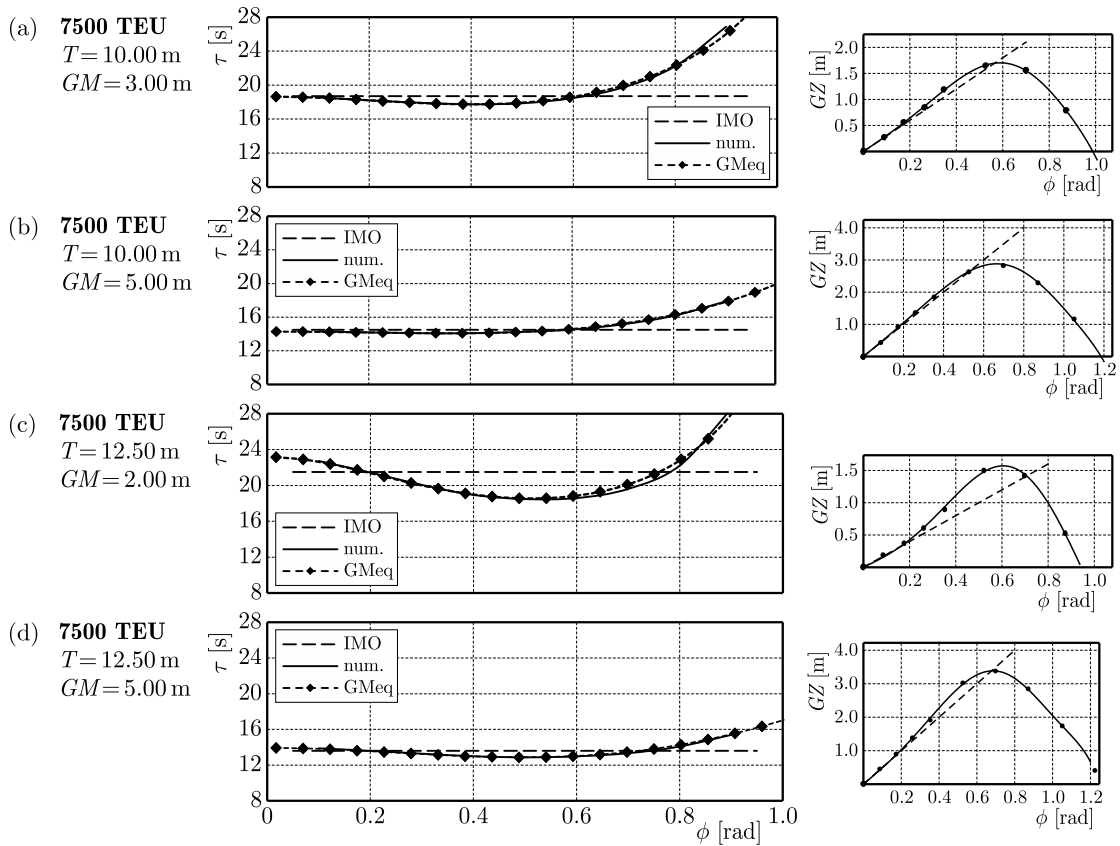


Fig. 8. Rolling period vs. rolling amplitude for the 7500 TEU container ship (left plot) and the corresponding GZ curve and the metacentric triangle (right plot)

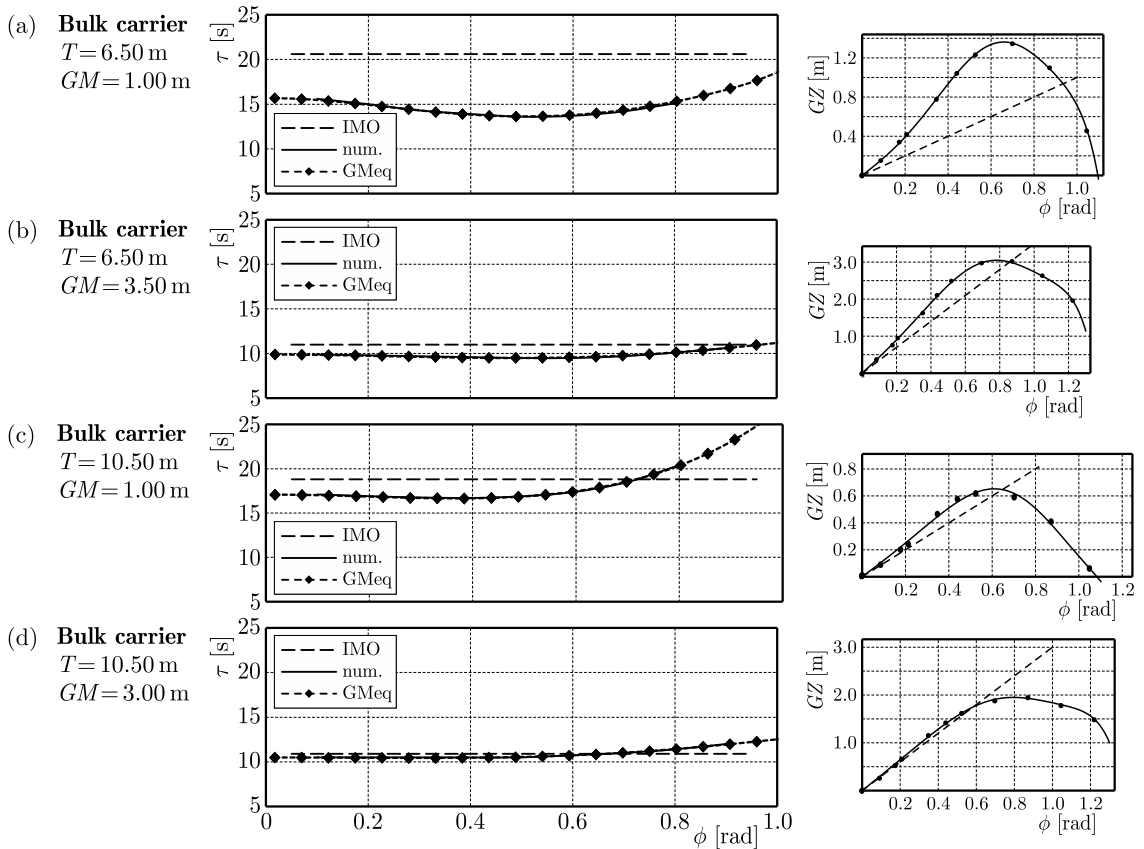


Fig. 9. Rolling period vs. rolling amplitude for the bulk carrier (left plot) and the corresponding GZ curve and the metacentric triangle (right plot)

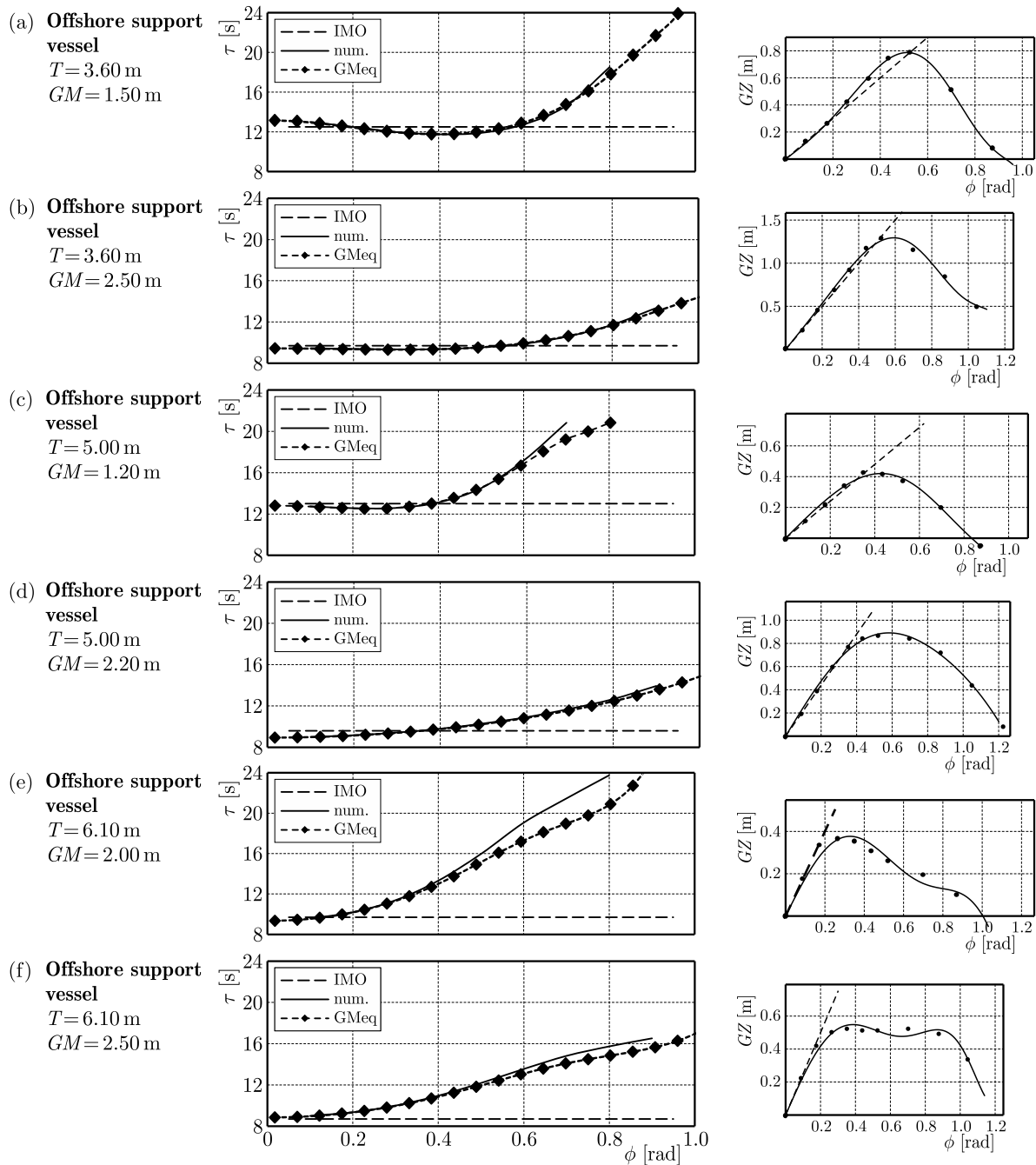


Fig. 10. Rolling period vs. rolling amplitude for the offshore support vessel (left plot) and the corresponding GZ curve and the metacentric triangle (right plot)

The verification of the proposed method of calculation of the rolling period, which is presented in Figs. 4 to 10, reveals very good consistency with to the results of numerical simulations in a wide range of angles of heel. Comparing to the IMO-recommended formula, the new one reaches the unattainable earlier level of accuracy. The most difficult and demanding cases are some loading conditions of the offshore support vessel. The results shown in Fig. 10 prove that the proposed method manages to predict the rolling period with a precision sufficient for on-board use even dealing with such complicated shapes of the righting arm curves.

Formulas (5.2) and (5.3) are rather simple in terms of practical calculations. Anyway, it is worth to consider whether the proposed method could be more simplified to enable calculation

even without any software supporting the computation. The first element $(\int_0^{\phi_A} GZ(\phi) d\phi)/\phi_A^2$ contains a definite integral $\int_0^{\phi_A} GZ(\phi) d\phi$. Its value can be easily obtained with the use of a common trapezoidal rule of numerical integration used in the same way as in the case of ship dynamical stability calculation. This approach is well known by officers on-board. The second element $GZ_{\phi_A}/(2\phi_A)$ requires no difficult computation at all. An example of such calculation is presented in Table 2.

Table 2 shows a typical pattern used for ship dynamical stability calculation (e.g. the area under the GZ curve) which is supplemented by the formula enabling calculation of the simplified equivalent metacentric height

$$GM_{eq_simple}(\phi_A) = \frac{1}{\phi_A^2} \left(S_{\phi_A} + \frac{1}{2} GZ(\phi_A) \phi_A \right) \tag{5.4}$$

where S_{ϕ_A} is the area under the GZ curve integrated from zero up to the rolling amplitude.

Table 2. Exemplary simplified calculation for the natural rolling period (5000 TEU container vessel, draft $T = 13.50$ m and metacentric height $GM = 0.5$ m) – none of the dedicated software needs to be used

ϕ_A [°]	10	20	30	40	50	60	Contemporary standard calculations
KN [m]	2.61	5.21	7.80	10.08	11.72	12.70	
GZ [m]	0.10	0.27	0.57	0.78	0.63	0.17	
$\sum GZ$	0.10	0.47	1.31	2.66	4.07	4.87	
S_{ϕ_A}	0.01	0.04	0.11	0.23	0.36	0.42	Additional calculations
ϕ_A [rad]	0.175	0.349	0.524	0.698	0.873	1.047	
GM_{eq_simple} [m]	0.61	0.71	0.94	1.03	0.82	0.46	
τ [s] (Eq. (5.1))	25.3	23.4	20.3	19.4	21.7	28.9	

$$S_{\phi_A} = [\Delta\phi_A / (2 \cdot 57.3)] \sum GZ$$

The validation of the very simplified calculation scheme presented in Table 2 is shown in Fig. 11. The results are compared to evaluate the conformity which is plotted in the graph.

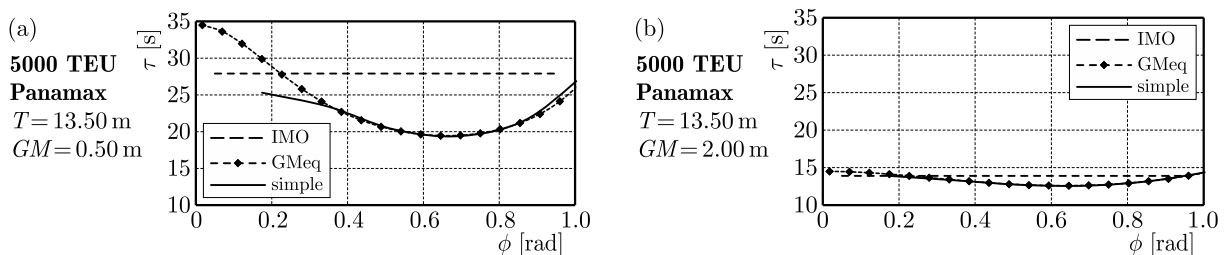


Fig. 11. Prediction of the rolling period vs. rolling amplitude for the 5000 TEU container vessel – validation of the simplified method applied according to formula (5.4) and with the use of calculation scheme presented in Table 2 (two sample loading conditions of the ship)

The graph shown in Fig. 11 reveals an astonishing conformity of the simplified method results as per the degree of the simplification used. The only range of significant discrepancies reaches from an angle of heel 0 up to about 15-20 degrees. This is due to the trapezoidal rule of numerical integration assuming a linear character of the integrated curve in every interval. However, this range of 0-15 degrees does not play an important role in terms of ship safety, especially safety against capsizing due to potential synchronous rolling motion. Basically, ships do not capsize at an angle of heel 15 or 20 degrees. The accuracy reached in the useful range of angles of heel allows one to propose the newly elaborated method instead of the IMO-recommended one.

6. Conclusions

In this paper, the problem related to the prediction of ship natural rolling period is outlined. It is revealed that rolling being a nonlinear phenomenon governed by the differential equation of ship motion can be described in terms of its period, by a relatively simple formula. Moreover, the accuracy of such an approach is outstanding as per the degree of used generalization. Both these features, e.g. simplicity and accuracy are essential in terms of practical application on-board ships. The proposed formula for the natural rolling period calculation can be implemented in fairly simple software being a decision support tool or it can even be used without any dedicated software in the course of straightforward calculation. Unlike the proposed formula, any numerical simulations of rolling cannot be performed on-board due to their complexity and high demands for crew education.

The elaborated method has been verified on the basis of the range of cases comprising seven different ships of dissimilar sizes and the number of their loading conditions covering draft and stability characteristics from the ballast condition up to the fully loaded state of a vessel. For each case and for the full range of possible rolling amplitudes, numerical simulations of rolling has been carried out. Positive verification of the new method is definitely a vital issue due to the importance of natural rolling period prediction. Generally, the greatest threat to the stability safety of a vessel is related to the resonance of rolling. The resonant motion could be predicted and avoided only in the case of quite precise prediction of the rolling period. Thus, the IMO-recommended formula ought to be rather modified and the newly proposed one could be introduced instead.

Although the proposed method has been widely verified, there is still room for further researches leading to tuning of the weight coefficients given in formula (5.1). The influence of some factors could be also assessed in the course of future researches, for instance the effects of damping, accuracy of the *GZ* curve approximation and variations of stability characteristics on waves.

References

1. BELENKY V., BASSLER C., SPYROU K., 2011, *Development of Second Generation Intact Stability Criteria*, NSWCCD-50-TR-2011/065
2. BŁOCKI W., 2000, *Stability Safety of the Ship in Resonant Conditions* (in Polish), Politechnika Gdańska, Monografie 19, Gdańsk
3. BULIAN G., 2005, Nonlinear parametric rolling in regular waves – a general procedure for the analytical approximation of the *GZ* curve and its use in time domain simulation, *Ocean Engineering*, **32**, 309-330
4. CARDO A., COPPOLA C., CONTENTO G., FRANCESCUTTO A., PENNA R., 1994, On the nonlinear ship roll damping components, *Proceedings of International Symposium NAV'94*, Roma
5. CONTENTO G., FRANCESCUTTO A., PICIULLO M., 1996, On the effectiveness of constant coefficients roll motion equation, *Ocean Engineering*, **23**, 597-618
6. FRANCESCUTTO A., CONTENTO G., 1999, Bifurcations in ship rolling: experimental results and parameter identification technique, *Ocean Engineering*, **26**, 1095-1123
7. HADDARA M., BENNETT P., 1989, A study of the angle dependence of roll damping moment, *Ocean Engineering*, **16**, 411-427
8. HIMENO Y., 1981, *Prediction of Ship Roll Damping – State of the Art*, The University of Michigan
9. HOLDEN CH., GALEAZZI R., RODRIGUEZ C., PEREZ T., FOSSEN T., BLANKE M., NEVES M., 2007, Nonlinear container ship model for the study of parametric roll resonance, *Modeling, Identification and Control*, **28**, 4

10. IMO, 2007, – Revised guidance to the master for avoiding dangerous situations in adverse weather and sea conditions, MSC.1/Circ.1228
11. IMO, 2009 – Intact Stability Code, 2008, edition 2009
12. KRUGER S., KLUWE F., 2008, *A Simplified Method for the Estimation of the Natural Roll Frequency of Ships in Heavy Weather*, Technical University Hamburg
13. LANDRINI M., 2006, Strongly nonlinear phenomena in ship hydrodynamics, *Journal of Ship Research*, **50**, 2, June
14. NEVES M., RODRIGUEZ C., 2006, On unstable ship motions resulting from strong non-linear coupling, *Ocean Engineering*, **33**
15. NEVES M., RODRIGUEZ C., 2009, A coupled non-linear mathematical model of parametric resonance of ships in head seas, *Applied Mathematical Modelling*, **33**
16. SHIN Y.S., BELENKY V.L., PAULLING J.R., WEEMS K.M., LIN W.M., 2004, Criteria for parametric roll of large containerships in longitudinal seas, *ABS Technical Papers*
17. SPANOS D., PAPANIKOLAOU A., 2009, Benchmark study on numerical simulation methods for the prediction of parametric roll of ships in waves, *Proceedings of the 10th International Conference on Stability of Ships and Ocean Vehicles*, St. Petersburg
18. SURENDRAN S., VENKATA RAMANA REDDY J., 2003, Numerical simulation of ship stability for dynamic environment, *Ocean Engineering*, **30**, 1305-1317
19. TAYLAN M., 2000, The effect of nonlinear damping and restoring in ship rolling, *Ocean Engineering*, **27**, 921-932
20. UMEDA N., 2013, Current status of second generation intact stability criteria development and some recent efforts, *Proceedings of the 13th International Ship Stability Workshop*, Brest
21. UZUNOGLU E., GUEDES SOARES C., 2015, Automated processing of free roll decay experimental data, *Ocean Engineering*, **102**, 17-26
22. WAWRZYŃSKI W., 2015, Approximation of the righting arm curve and its effect on simulations of ship rolling (in Polish), *Logistyka*, **4/CD**, 1

Manuscript received October 25, 2015; accepted for print March 7, 2016

ADAPTATION OF ENGINEERING FEA-BASED ALGORITHMS TO LCF FAILURE AND MATERIAL DATA PREDICTION IN OFFSHORE DESIGN

MAREK AUGUSTYNIAK

*Gdansk University of Technology, Faculty of Applied Physics and Mathematics, Gdańsk, Poland, and
DES ART Ltd., Gdynia, Poland; e-mail address: maugustyniak@mif.pg.gda.pl*

PIOTR GAJEWSKI

DES ART Ltd., Gdynia, Poland

KRZYSZTOF ŚWIĄTEK

Naval Academy, Gdynia, Poland

There is an ever growing industrial demand for quantitative assessment of fatigue endurance of critical structural details. Although FEA-based calculations have become a standard in engineering design, problems involving the Low-To-Medium cycle range (10^1 - 10^4) remain challenging. This paper presents an attempt to optimally choose material data, meshing density and other algorithm settings in the context of recent design of the large offshore windfarm installation vessel, VIDAR. In this study, an attempt is made to assess default FEA-based procedures in RADIOSS software by comparing an experimental test against numerical analyses. Standard slender cylindrical ("I") samples as well as originally designed "Z"-shaped samples made of A90 (S690)-grade steel have been loaded at various nominal stress ranges with or without local yielding. A good correlation has been found between FEA results and experimental cycles-to-failure in I-shaped samples, provided the software material data generator is avoided and Smith-Watson-Topper mean stress correction is used. In the case of Z-shaped samples, the calculated cycles-to-initiation of macro-crack is significantly lower (factor of 3) from the experiment. The observed discrepancy is argued to be due to stress gradient influence.

Keywords: low-cycle fatigue, Finite Element Method, high-strength steel, stress gradient influence

1. Introduction

Over the last decade, Finite Element analyses with subsequent Fatigue calculation (further referred to as "FATFEA") have become a standard practice, especially in the automotive, railway, and marine/offshore design. However, several non-trivial questions arise, whenever an engineer attempts to perform reliable fatigue life estimation, including the following:

- What are the sources of uncertainty in FATFEA procedures and how to limit them?
- What is the scatter of material data input? What is its best source? Can the axial test data be used in arbitrary 2D/3D structures?
- Can non-trivial structural details loaded in LCF/MCF range be quantitatively assessed without detailed considerations of Shakedown/Ratchetting?

The literature addressing the listed questions can be roughly divided into material-centered and structure-centered studies. In the first group, laboratory experiments on standardised samples produce data which serve to define and enhance constitutive equations for various steel brands (Basan *et al.*, 2011; Papuga *et al.*, 2012; de Jesus *et al.*, 2012). Numerical modelling is

seldom used except for studies of the notch effect (Fatemi *et al.*, 2004). The second group, i.e. structure-centered studies, range from development of novel sample shapes (as in the presented work) to the fatigue testing and validation of industrial components and assemblies. These studies lead to two types of practical results: design recommendations or development of numerical algorithms (the latter usually involving linear or non-linear Finite Element analysis). For example, Firat (2011) provided a guidance through the numerical analysis of a rear-axle assembly and correlated it with a full-scale fatigue experiment. Koh (2009) employed FEA in the case of an automotive steering link, presenting a comparison of FATFEA with experimental data. The calculated lives were moderately non-conservative by a maximum factor of three, calling for further refinement of the algorithms. The conference paper by Mercer *et al.* (2003) is one of the best previews in the field, providing evidence-based guidelines on good and best usage of fatigue numerical analysis, depending on the steel grade and loading scenario.

There is yet a group of studies which does not easily fit the proposed classification. These are the works on time-evolving phenomena of crack propagation (Biglari *et al.*, 2006) and yield zone stability (Kang, 2008). Evolution of the crack and plastic zone is a coupled material-structural phenomenon, and often requires extensions of standard FEA, like XFEM (Richardson *et al.*, 2011) or efficient shakedown predicting methods (Spiliopoulos and Panagiotou, 2012).

This paper faces both the material-related and geometrical issues. An original concept of Z-shaped samples is proposed, exhibiting non-uniform and non-uniaxial stress states while loaded with a standard uniaxial tensile testing machine.

The “MCF” regime (Middle-Cycle-Failure, from 10^3 to 10^4 cycles) is dealt with, with local yield possibly occurring at the very first cycles, but majority of the cross section working in the elastic regime. The analytic difficulty consists in insufficiency of the linear HCF approach, because the ratchetting/shakedown scenarios may develop. On the other hand, it is impossible to represent 10^3 - 10^4 cycles of engineering structure behavior in a direct step-by-step FEA analysis, so some empirical strain-life equation has to be adopted.

In this paper, a set of options is looked for, which provides stable, unbiased (or moderately conservative) fatigue life assessments regardless of the structure and loading scenario. The software has been chosen from among several products available on the market, including LIMIT, FEMFAT, FATEVAS, and DESIGNLIFE. An optimum combination of scientific soundness, flexibility, and price is looked after. RADIOSS Fatigue tools have been finally selected for their unique feature of joining underlying stress/strain calculation with subsequent fatigue analysis. The only major drawback known at the beginning of the study is the lack of Critical Plane E.S.A. (Equivalent Stress Algorithm), claimed in literature as particularly stable and unbiased in multi-axial stress states (Słowik and Łagoda, 2011; Gaier and Dannbauer, 2006). The strain-life strategy has been chosen because it covers both HCF and LCF/MCF ranges, being thus the only choice for a component experiencing at least local yield. Table 1 presents the summary of options involved in this study.

2. Experiment

2.1. Static tensile stress-strain experiment on I-shaped samples

An uniaxial material testing machine MTS of maximum load capacity of 100 kN with standard clamps was used in all the experimental activities. Full history of clamp and extensometer displacements were recorded. All I-shaped samples used in both static and fatigue experiments were dimensioned as in Fig. 1.

Static tensile tests until rupture performed on three I-shaped samples demonstrated the yield limit of 780 ± 15 MPa (see Fig. 2). This parameter exceeds by 50 MPa the nominal minimum value specified by the supplier. Young’s modulus was estimated at 209 ± 1 GPa, and Ultimate

Table 1. Fatigue analysis work-flow with analysed algorithm options

FEA software/strategy	HW Radioss Bulk/Linear Statics
FAT tool/strategy	HW Radioss Fatigue Manager/Strain-Life (E-N)
Loading type/range	Stress-controlled, pulsating tension tests; 500-800 MPa nominal average stresses in I-shaped samples; nominal stresses in Z-shaped samples not estimable
Material data source	Radioss Material Generator or Literature (de Jesus <i>et al.</i> , 2012)
Mesh type/Size	Solid (I-shaped sample), shell (Z-shaped sample), cell size from 0.5 to 1.5 mm
Mean stress correction	Smith-Watson-Topper or Morrow
Equivalent stress algorithm	Absolute max. Principal, Huber-Mises or Tresca
Surface finish	Rough or polished

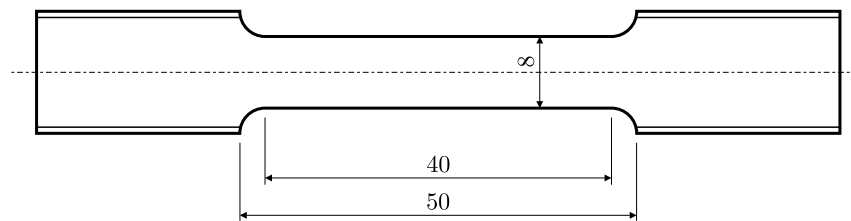


Fig. 1. Dimensioning of I-shaped samples [mm]

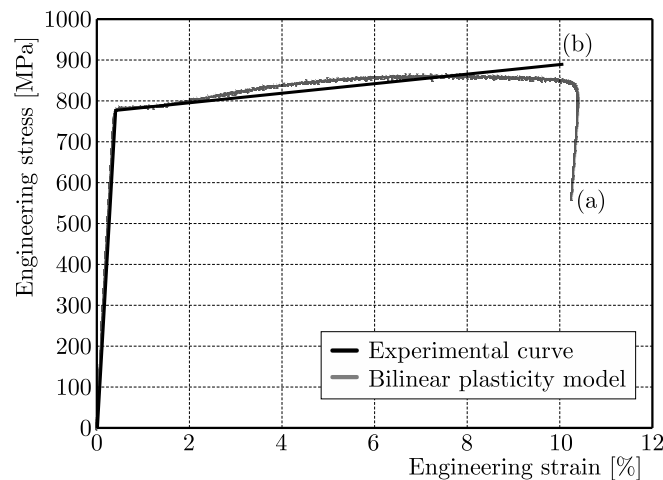


Fig. 2. Engineering stress-strain curve from static monotonic testing until failure; (exp.) – experimental curve, (mod.) – bilinear plasticity model obtained from linear regression of plastic portion of the experimental curve

Tensile Stress (UTS) at 855 ± 10 MPa. Each sample failed statically in the middle of their narrow zone.

2.2. Fatigue experiments on I-shaped samples

Stress-controlled fatigue tests were performed on a series of ten I-shaped samples. The cycles had $\sigma_{\min} = 0$ and nominal σ_{\max} ranging from 500 MPa to 800 MPa, producing failure at about 150 000 and 7000 cycles, respectively. The pulsating tensile regime was chosen in order to avoid buckling of relatively slender samples. Indeed, I-shaped samples loaded symmetrically at ± 740 MPa buckled after 24 and 29 cycles. The measured number of cycles-to-failure for

10 samples are plotted in Fig. 3. The main frequency of loading was set to 1 Hz, and the maximum frequency used was 3 Hz. Some samples were continuously observed in order to detect the instant of initiation of macrocracks, i.e. the number of Cycles-To-Crack-Initiation (CTCI). A difference between the macrocrack initiation and final failure was not observable. Contrary to the static test, the samples tested in fatigue exhibited a catastrophic crack close to the curved transition zone.

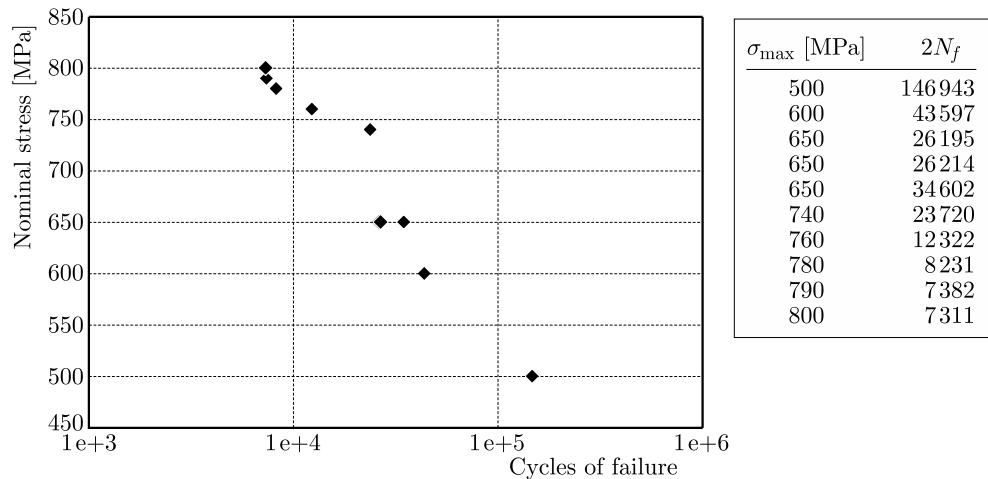


Fig. 3. Semi-log plot of cycles-to-failure obtained from uniaxial stress-controlled loading of I-shaped samples

The data points in Fig. 3 follow a fairly straight line in a log-log scale. The scatter, however, is significant, which made impossible reliable extrapolation of the curve beyond the 10^3 - 10^4 range. Reliable strain-life coefficients had thus to be obtained from other sources, cf. Section 3.2.

2.3. Fatigue experiments on Z-shaped samples

Z-shaped samples studied had dimensions as presented in Fig. 4a.

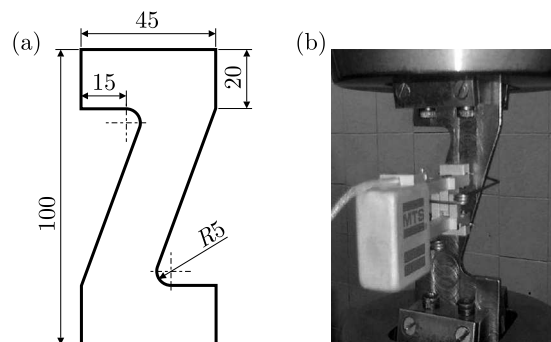


Fig. 4. (a) Dimensioning of Z-shaped samples [mm]. (b) Experimental set-up with an extensometer

Four samples of variable thickness were produced, labeled Z1, Z2, Z3 and Z4. Z4 sample had polished surfaces in order to determine crack initiation time. The samples were placed within the clamps of the tensile test machine (Fig. 4b), and an extensometer with a base set to 20 mm was installed vertically on the middle section of the sample.

The stress-controlled (constant force amplitude) pulse loading was continued until failure (see Table 2). An approximately linear relationship was found between CTF (Cycles-To-Failure) and sample thickness. During the test of Z4 sample, a movie was recorded with focus on curved regions which were prone to the earliest crack initiation. The movie allowed determination of

location and time of initiation of a macrocrack observable with a naked eye. This parameter was not determined in the remaining three samples.

Table 2. Number of Cycles-To-Failure and Cycles-To-Initiation of macrocrack in four Z-shaped samples

No.	Thickness [mm]	CTF	CTI
Z1	4.65	4487	N/A
Z2	5.35	9047	N/A
Z3	5.76	11183	N/A
Z4	6.25	14800	~ 9200

Full clamp and extensometer displacement history was recorded for all the samples. The maximum and minimum clamp displacements in each cycle (dx_{\max} and dx_{\min}) were extracted from the data, and plotted in Fig. 5.

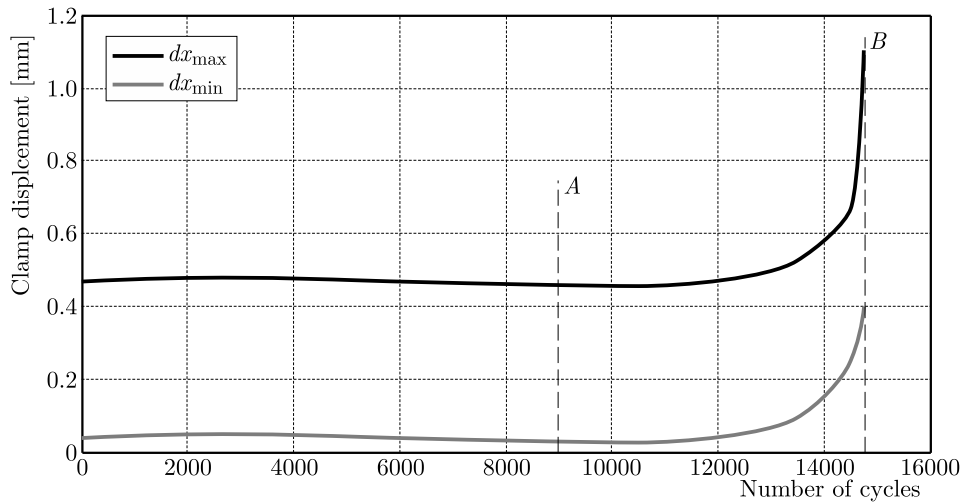


Fig. 5. Clamp displacement envelopes (min/max) [mm] in Z4 fatigue test; *A* – observed macrocrack initiation, *B* – final failure

The curve recorded for sample Z4 is fairly stable until about 90% of the total sample life. The observable macrocrack initiated at about 9200 cycles, roughly one half of the entire lifespan of “Z4” Z-shaped sample (14800 cycles). This coincides with the findings of Firat (2011), for a large scale S460 component. Other Z-shaped samples exhibited similar shapes of the displacement min/max envelope curves.

3. Modelling

3.1. Discretisation and boundary conditions

The Finite Element model of I-shaped samples was built in HyperMesh 12.0 pre-processor using hexahedral elements. Each sample was fully constrained at one end and a set of rigid connections was defined at the opposite end to simplify the application of traction force. High-quality elements of edge length of about 1.0 mm were defined in the curved transition zone. Linear-elastic analyses using a sparse direct solver were performed (Fig. 6).

The Z-shaped samples were modelled with shell elements with 1.0 mm average edge lengths. The constraints and loading method was similar to that used in the I-shaped samples. Both linear static and elasto-plastic analyses were performed and compared.

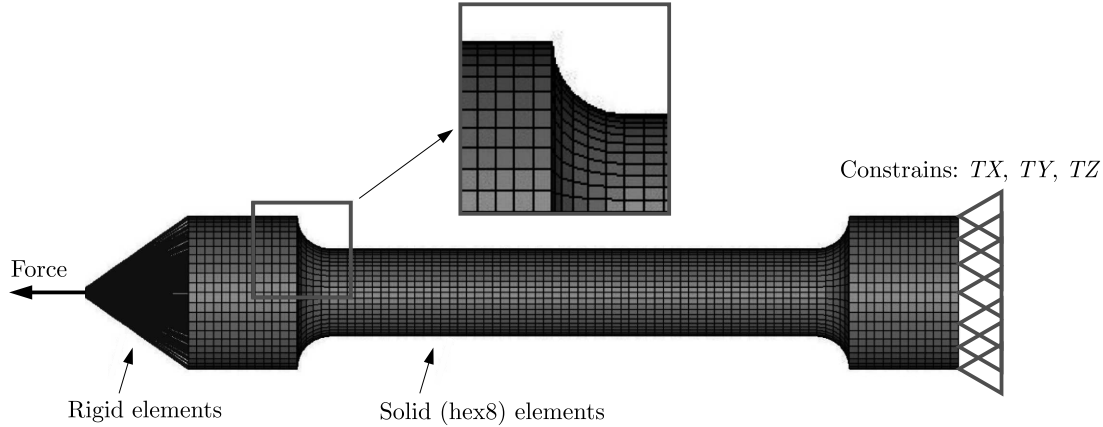


Fig. 6. I-shaped samples: meshing and boundary conditions

3.2. Material data

The strain-life fatigue assessment approach was chosen for its versatility and ability to reproduce fatigue characteristics in spots exceeding the yield limit. The required fatigue parameters of the standard Coffin-Manson strain-life equation were either produced in Radioss Material Generator or taken from a detailed study by de Jesus *et al.* (2012). The Material Generator incorporated in Radioss software required the input of Ultimate Tensile Stress, which was taken from the static tensile experiment with I-shaped samples performed in this study. Table 3 presents a comparison of six coefficients defining the E-N curves in both cases.

Table 3. Coffin-Manson parameters for S690 steel taken from literature (de Jesus *et al.*, 2012) as opposed to those extracted from a numerical Material Data Generator (Radioss software [1])

Source	K' [Mpa]	n' [-]	σ'_f [MPa]	b [-]	ϵ'_f [-]	c [-]
S690 (de Jesus <i>et al.</i> , 2012)	1283	0.09	1403	-0.09	0.74	-0.81
Radioss Material Generator	1275	0.15	1403	-0.09	0.51	-0.58

The plot of both E-N curves (Fig. 7) shows convergence in both very low and very high cycle regions. However, there is a significant discrepancy in the region of interest, namely 10^2 - 10^5 cycles. A given local strain amplitude $\Delta\epsilon/2$ may produce CTCI (Cycles-To-Crack-Initiation) estimations from the Material Generator differing by an order of magnitude from those derived from experiment (de Jesus *et al.*, 2012).

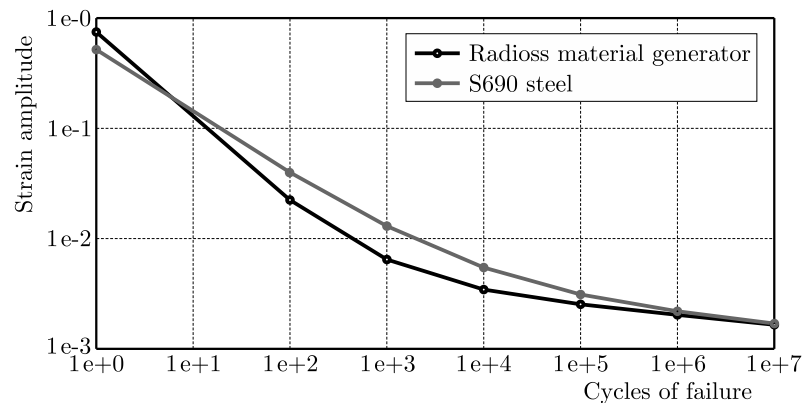


Fig. 7. Comparison of E-N curves (strain amplitude vs. number of cycles) for two sets of constitutive parameters

The sensitivity of the calculated fatigue life to the choice of E-N curve was studied by comparing FATFEA results against the experimental reference. The details are described in the following Sections.

4. Results

4.1. FEA stresses

The FATFEA calculation was performed in a standard, two-stage manner. Static stress/strain calculations were followed by application of the fatigue estimation algorithm to each model elements. Figure 8 shows the equivalent von Mises static stress on the surface and across the section cut of a I-shaped sample. The axial tensile force is applied producing the nominal stress of 500 MPa. The nominal stress is defined as the ratio of the force to the sample middle cross section area.

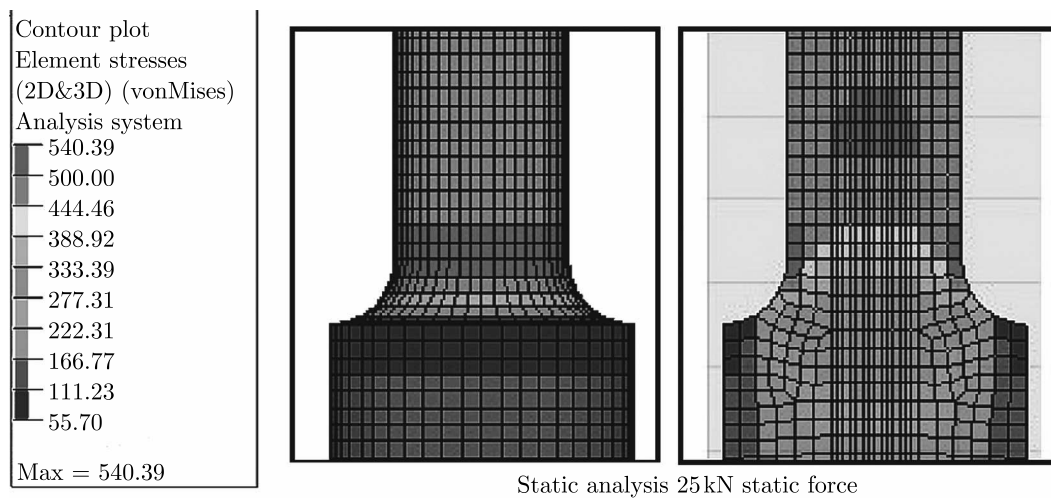


Fig. 8. Equivalent (von Mises) stress distribution on I-shaped sample surface (a) and within its cross-section (b)

As expected, the narrow section far from the transition zone exhibits uniform stresses equal to the nominal ones, as estimated from the ratio of the applied force and the cross-section area. There is a circumferential region of stress amplification at the curved surface. However, the average stress within the transition zone section is inferior to the nominal stress.

A similar static calculation was performed with Z-shaped samples (see Fig. 9a through 9d). Linear-elastic and elasto-plastic approach were compared. The symbol “max” accompanying the result type means that at each shell element its two extreme surfaces were compared and the highest stress value were plotted. For elasto-plastic analysis, a bilinear material model was prepared with the yield limit of 741 MPa and the post-yield tangent modulus of 2 GPa. As expected, elasto-plastic analysis (Fig. 9a) produced much lower stress maxima of 749 MPa, as compared against 1048 MPa in purely elastic calculation (Fig. 9b). Consequently, strain values in linear-elastic analysis were much lower compared to elasto-plastic analysis ($3.8e-03$ vs. $6.3e-03$ in Figs. 9c and 9d). The principal stress directions were not disturbed by the introduction of the bilinear elasto-plastic material characteristic.

Although the peak stresses obtained from elastic analysis are unrealistic (significantly above UTS), the area of stresses exceeding yield limit is confined to a single row of elements on the sample edge, so it is allowable to employ the Neuber procedure to deduce the actual strain/stress state in the critical region within fatigue calculation. The results are presented in the following Section.

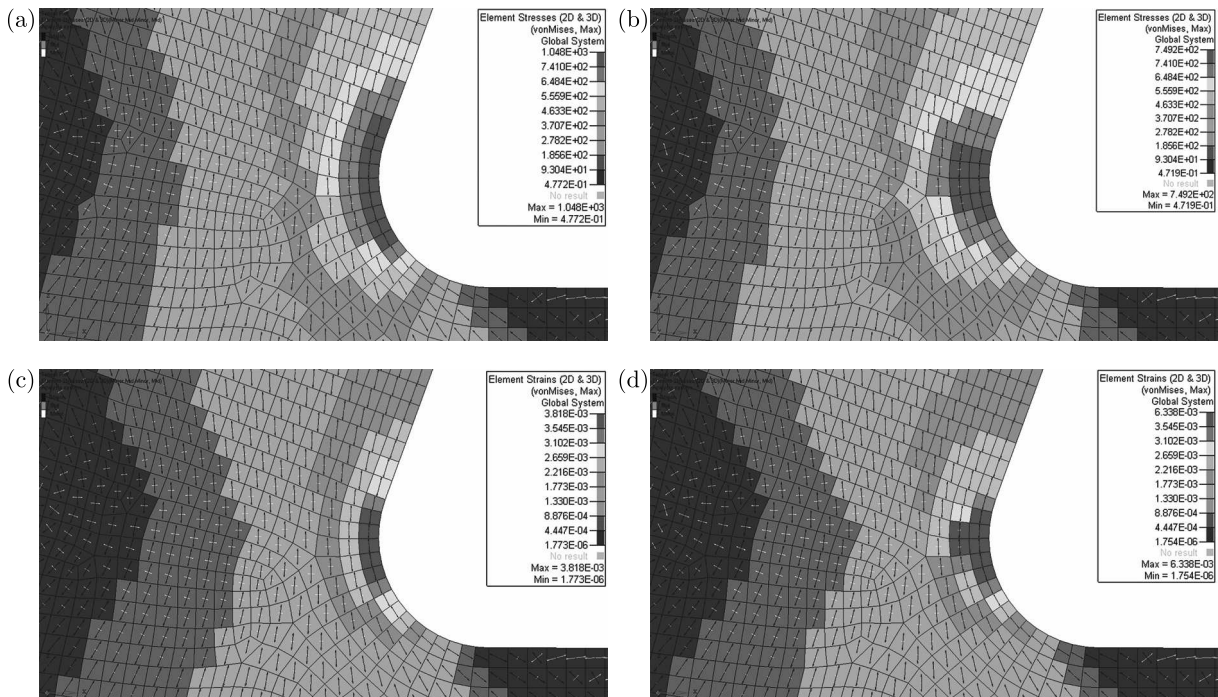


Fig. 9. (a) Linear-elastic calculation and (b) elasto-plastic calculation: contour plot of the equivalent (von Mises) stresses combined with a tensor plot of principal stresses; (c) linear-elastic calculation and (d) elasto-plastic calculation: contour plot of the equivalent (von Mises) strains

It is worth noting that a yet more accurate stress/strain distribution would be obtained if the material cyclic plasticity is modelled, e.g. using Cowper-Symond's model with the mixed isotropic-kinematic hardening. However, such an approach would require additional material parameters, which – unless carefully measured – might introduce an even more significant error. Moreover, step-by-step cyclic plasticity calculation up to hysteresis loop stabilisation is at present impossible in the context of industrial fatigue life assessment of large structures, such as floating vessels.

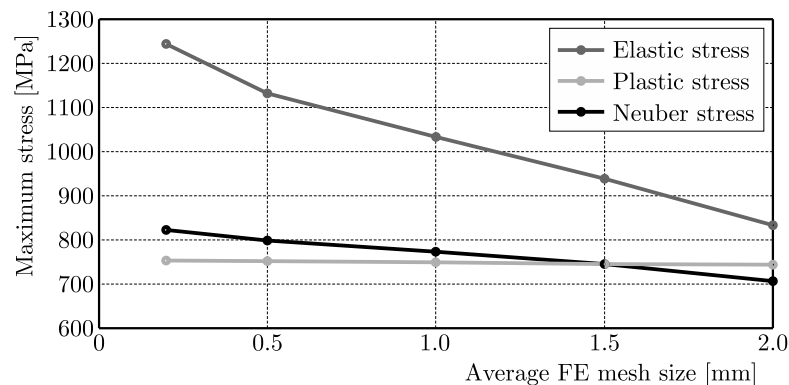


Fig. 10. Comparison of the maximum stresses in Z-shaped samples for different calculation approaches

RADIOSS software did not allow direct fatigue estimation based on elasto-plastic FEA. The widely-known Neuber correction procedure was used instead. The maximum stresses for different mesh sizes were compared (Fig. 10). The purely elastic analysis produces gross overestimation of stress, and this leads to unacceptably conservative fatigue estimates. Involving Neuber's correction leads, however, to peak stress values stably close to those from the elasto-plastic analysis. A particularly good correlation was found for the mesh sizes between 1 and 1.5 mm.

4.2. Fatigue life of I-shaped samples

The fatigue E-N analysis with the Neuber correction and different analysis options was performed referring to the static stress/strain distribution. Different algorithm options were chosen, and the obtained minimum life estimate was compared against experimental CTF (Cycles-To-Failure). The percentage of error was assessed, with positive values corresponding to non-conservative, i.e. highly unfavorable estimation. The selected analysis settings are summarised in Table 4.

Table 4. Scatter of calculated vs experimental fatigue lives in I-shaped samples

Min/Max nominal stress	Material data source	Equivalent stress algorithm	Mean stress corr.	Average mesh size [mm]	Neuber's correction	CTCI (FEA)	Experimental CTF	Relat. error [%]
0-500	Radioss	Tresca-Guest	SWT	1.0	yes	384350	146943	162
	S690	Tresca-Guest	SWT	1.0	yes	146870		0
	S690	Max. Principal	SWT	1.0	yes	164180		12
	S690	Huber-Mises	SWT	1.0	yes	227300		55
	S690	Tresca-Guest	Morrow	1.0	yes	492270		235
	S690	Tresca-Guest	SWT	1.5	yes	262580		79
	S690	Tresca-Guest	SWT	0.5	yes	103100		-30
	S690	Tresca-Guest	SWT	1.0	no	112140		-24
0-650	Radioss	Tresca-Guest	SWT	1.0	yes	80917	26204	209
	S690	Tresca-Guest	SWT	1.0	yes	23157		-12
	S690	Max. Principal	SWT	1.0	yes	25326		-3
	S690	Huber-Mises	SWT	1.0	yes	32944		26
	S690	Tresca-Guest	Morrow	1.0	yes	48776		86
	S690	Tresca-Guest	SWT	1.5	yes	37010		41
	S690	Tresca-Guest	SWT	0.5	yes	17454		-33
	S690	Tresca-Guest	SWT	1.0	no	12580		-52
0-800	Radioss	Tresca-Guest	SWT	1.0	yes	27253	7311	273
	S690	Tresca-Guest	SWT	1.0	yes	7035		-4
	S690	Max. Principal	SWT	1.0	yes	7570		4
	S690	Huber-Mises	SWT	1.0	yes	9423		29
	S690	Tresca-Guest	Morrow	1.0	yes	11990		64
	S690	Tresca-Guest	SWT	1.5	yes	10390		42
	S690	Tresca-Guest	SWT	0.5	yes	5542		-24
	S690	Tresca-Guest	SWT	1.0	no	3130		-57

The 0-500 MPa range was shown to be the most prone to the selection of algorithm options. The bar chart in Fig. 11 shows the relative error committed with wrong modelling assumptions. It is found that the best fit corresponds to the following settings: Smith-Watson-Topper mean stress correction, material data (de Jesus *et al.*, 2012), 1 mm average mesh size, Tresca Equivalent Stress Algorithm, Neuber correction included.

On the other hand, the worst correlation is associated with the material data taken from default Material Generator, Morrow mean stress correction and with using arbitrary mesh sizing without convergence test. Applying the stress-life algorithm (usually default in FATFEA software) and performing linear static analyses with local plasticity without Neuber's rule are yet more important errors. In the studied case, under most unfavourable conditions, the arithmetic sum of error contributions might reach +500%, greatly overestimating the structure safe operational life span.

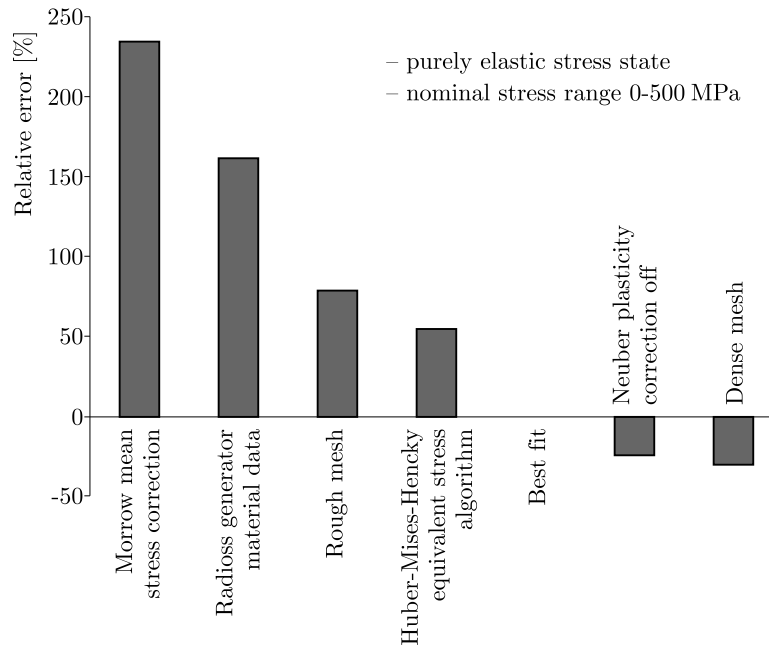


Fig. 11. I-shaped sample, elastic stress range: Discrepancy between the FATFEA result and the experiment for various algorithm settings

4.3. Fatigue life of Z-shaped samples

The sensitivity analyses of FATFEA results was subsequently performed in the case of Z-shaped samples. The results of selected computations and the experimental results are presented in Table 5.

Table 5. Z4-sample: Comparison between the FATFEA result juxtaposed with the experimental observation for various algorithm settings

Equivalent stress algorithm	Mean stress correction	Neuber's correction	CTCI
Abs. max. principal	SWT	Neuber	3323
Signed Von Mises	SWT	Neuber	3541
Signed Tresca	SWT	Neuber	2983
Signed Tresca	Morrow	Neuber	4599
Signed Tresca	SWT	none	1250
Experiment			~ 9200

It is found that the algorithm settings which gave a very good quantitative correlation in the case of I-shaped samples, behave in a significantly conservative way in Z-shaped samples. It is argued that the Neuber correction predicted overly localised concentration of stress/strain. The correlation might be better with FATFEA based on elasto-plastic stress/strain computation. Introducing the correction for the stress gradient would lead to a better agreement, too.

It is argued that in the I-shaped sample, the nearly constant stress over the sample section shortens the lifespan between the crack initiation and the final fracture. The localised nature of peak stress slows down the crack propagation. The Z-shaped sample exhibit thus an optimistic scenario of structural failure. Consequently, FATFEA calibrated on the I-shaped sample leads to conservative, shorter than observed life estimates. Fortunately, the moderate conservatism can be beneficial in the context of engineering design of safety-critical structures.

5. Conclusions and perspectives

The objective of generation of non-1D stress states with a standard 1D tensile test machine has been achieved in this study. The Z-shaped samples produced non-uniform, predominantly biaxial stresses along the crack propagation path.

It is found that the selection of best FATFEA algorithm depends on the level and distribution of the stress/strain maxima. In the case of I-shaped samples loaded below the yield limit, various algorithm settings influence significantly the fatigue estimates. It is possible to select options giving a very good quantitative correlation with the experiment. On the other hand, the scatter of calculated results is much lower in Z-shaped samples, however then the results never approach the experimental data. This observation is primarily accounted for the lack of stress gradient correction and limited applicability of Neuber's algorithm to the yield zones larger than a single row of elements. It is concluded that an analysis based on linear static solution is acceptable as long as mesh convergence tests are performed, and Neuber's algorithm should be applied with caution. It is advisable to compare linear stress/strain results with at least one non-linear, elasto-plastic calculation.

The material data generator based on UTS parameter has proven unreliable in the studied fatigue life range, producing dangerously non-conservative fatigue estimates. An acceptable Material Generator should differentiate between various steel groups (as postulated by Basan *et al.* (2011)). Unfortunately, no software known to the authors as of the end of 2015 offers such an option.

Morrow's mean stress correction strategy gives as well poor, non-conservative correlations with experiment, in both the I- and Z-shaped samples. Unlike the mean stress correction formula, the equivalent stress/strain algorithm plays a less significant role.

It has been found that the number of Cycles-To-Crack-Initiation (CTCI) and the number of Cycles-To-Failure (CTF) are equal in uniformly stressed samples, but differ in the sample exhibiting stress concentration. In the latter case, CTF could not be reliably predicted with static FEA, and would require detailed cycle-by-cycle study of crack and yield zone evolution, which remains beyond the scope of this article.

References

1. Altair Ltd: HyperWorks Users' Guide, Radioss Fatigue Manager
2. BASAN R., FRANULOVIC M., PREBIL I., CRNJARIC-ZIC N., 2011, Analysis of strain-life fatigue parameters and behaviour of different groups of metallic materials, *International Journal of Fatigue*, **33**, 484-491
3. BIGLARI F.R., REZAEINASAB A., NIKBIN K., SATTARIFAR I., 2006, Finite Element Simulation of dynamic crack propagation without remeshing, *Journal of ASTM International*, **3**, 7
4. E-Fatigue. Finite Element Model Strain-Life Technical Background, <https://www.efatigue.com/fem/background/strainlife.html>,
5. FATEMI A., ZENG Z., PLASEIED A., 2004, Fatigue behavior and life predictions of notched specimens made of QT and forged microalloyed steels, *International Journal of Fatigue*, **26**, 663-672
6. FIRAT M., 2011, A computer simulation of four-point bending fatigue of a rear axle assembly, *Engineering Failure Analysis*, **18**, 2137-2148
7. GAIER C., DANNBAUER H., 2006, An efficient critical plane method for ductile, semiductile and brittle materials, *Conference Proceedings of Fatigue Congress*, Atlanta
8. DE JESUS A.M.P., MATOS R., FONTOURA B.F.C., REBELO C., DA SILVA L.S., VELJKOVIC M., 2012, A comparison of the fatigue behavior between S355 and S690 steel grades, *Journal of Constructional Steel Research*, **79**, 140-150

9. KANG G., 2008, Ratchetting: recent progresses in phenomenon observation, constitutive modeling and application, *International Journal of Fatigue*, **30**, 1448-1472
10. KOH S.K., 2009, Fatigue analysis of an automotive steering link, *Engineering Failure Analysis*, **16**, 3,914-922
11. MERCER I., MALTON G., DRAPER J., 2003, The effect of user decisions on the accuracy of fatigue analysis from FEA, *Conference Proceedings, ABAQUS 2003 Users' Meeting*
12. PAPUGA J., VARGAS M., HRONEK M., 2012, Evaluation of uniaxial fatigue criteria applied to multiaxially loaded unnotched samples, *Engineering Mechanics*, **19**, 2/3, 99-111
13. RICHARDSON C.L., HEGEMANN J., SIFAKIS E., HELLRUNG J., TERAN J.M., 2011, An XFEM method for modelling geometrically elaborate crack propagation in brittle materials, *International Journal for Numerical Methods in Engineering*, **12**, 88(10), 1042-1065
14. SŁOWIK J., ŁAGODA T., 2011, The fatigue life estimation of elements with circumferential notch under uniaxial state of loading, *International Journal of Fatigue Volume*, **33**, 9, 1304-1312
15. SPILIOPOULOS K.V., PANAGIOTOU K.D., 2012, A direct method to predict cyclic steady states of elastoplastic structures, *Computer Methods in Applied Mechanics and Engineering*, **223/224**, 186-198

Manuscript received January 18, 2016; accepted for print March 10, 2016

NUMERICAL AND EXPERIMENTAL STUDY OF THE MECHANICAL RESPONSE OF ALUMINUM FOAMS UNDER COMPRESSIVE LOADING USING CT DATA

ALI A. MOHAMMADI NASRABADI, REZA HEDAYATI, MOJTABA SADIGHI

Mechanical Engineering Department, Amirkabir University of Technology, Tehran, Iran

e-mail: mojtaba@aut.ac.ir

Metal foams are relatively novel materials that due to excellent mechanical, thermal, and insulation properties have found wide usage in different engineering applications such as energy absorbers, bone substitute implants, sandwich structure cores, etc. In common numerical studies, the mechanical properties of foams are usually introduced to FE models by considering homogenized uniform properties in different parts of a foamy structure. However, in highly irregular foams, due to complex micro-geometry, considering a uniform mechanical property for all portions of the foam leads to inaccurate results. Modeling the micro-architecture of foams enables better following of the mechanisms acting in micro-scale which would lead to more accurate numerical predictions. In this study, static mechanical behavior of several closed-cell foam samples has been simulated and validated against experimental results. The samples were first imaged using a multi-slice CT-Scan device. Subsequently, experimental compression tests were carried out on the samples using a uniaxial compression testing machine. The CT data were then used for creating micro-scale 3D models of the samples. According to the darkness or brightness of the CT images, different densities were assigned to different parts of the micro-scale FE models of the foam samples. Depending on density of the material at a point, the elastic modulus was considered for it. Three different formulas were considered in different simulations for relating the local elastic modulus of the foam material to density of the foam material at that point. ANSYS implicit solver was used for the simulations. Finally, the results of the FE models based on the three formulas were compared to each other and to the experimental results to show the best formula for modeling the closed-cell foams.

Keywords: metal foam, image processing, compression test, Finite Element Method, CT scan

1. Introduction

Due to excellent properties such as low weight, high energy absorption capacity, exceptional acoustic and thermal properties, etc., metal foams have received much attention in the last decades. Metal foams usually have densities about 10-60% of the density of the material they are made of. Different techniques such as vapor electro-deposition on open-cell polymer foam templates, powder metallurgy, hollow sphere consolidation, solidification in open-cell mold, etc. are used for manufacturing metal foams. Metal foams are usually made of aluminum, but other metals such as steel, nickel, titanium, copper, and gold are the other prevalent materials used for making them. Density of foams is usually stated by relative density which is defined as the ratio of density of the foam to density of the material it is made of (Gibson and Ashby, 1998). Foam structures are categorized into two main groups: open-cell and closed-cell (Banhart, 2001) (Fig. 1). In closed-cell foams, the cells are separated from each other by means of thin walls. However, the open-cell foams are made of struts rather than walls and, therefore, the interior parts of the cells are connected to each other. The closed-cell foams usually have higher strength and energy absorption capacity compared to the open-cell foams.

There is a tremendous number of works on the experimental investigation of mechanical behavior of metal foams under static loading (Andrews *et al.*, 1999; Cao *et al.*, 2006; Gibson, 2000; Meguid and Xue, 2000). However, due to the fact that metal foams are usually made by different manufacturing techniques and conditions, carrying out experimental works on the mechanical behavior of these materials is still valuable.

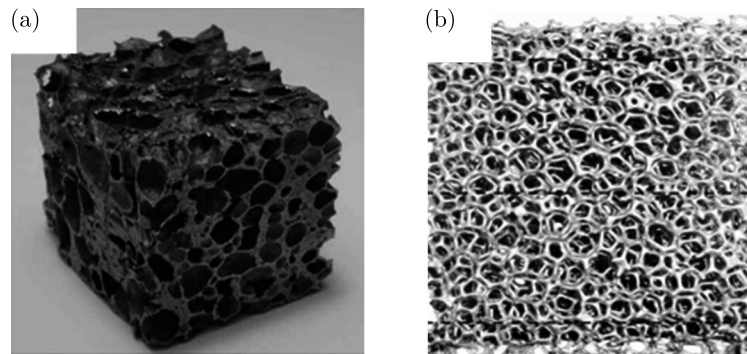


Fig. 1. 1 Different foam types: (a) closed-cell, (b) open-cell

Andrews *et al.* (1999) compared the compressive and tensile modulus and strength of several aluminum foams to each other and to pure aluminum. Cao *et al.* (2006) experimentally studied the effect of cell size on compressive properties of open-cell aluminum foams produced by an infiltrating process. They found out that the elastic modulus and compressive strength of this type of foam depends not only on relative density, but also on cell size. Gibson (2000) and Meguid and Xue (2000) also investigated the mechanical behavior of closed-cell foams under different loading conditions.

In an analytical study, Kitazono *et al.* (2003) derived elastic-plastic properties of closed-cell metal foams using a continuum micro-mechanical model. They also incorporated the effect of gas pressure inside the cells into their calculations. The model was developed to predict the response of both isotropic and anisotropic foams. Their analytical micromechanical model agreed well with the experimental elastic-plastic response of tests samples except for higher density foams. Some other analytical solutions to the mechanical properties of open-cell foams can be found in (Hedayati *et al.*, 2016a,b,c; Ko, 1965).

After the advent of efficient computers, many researchers attempted to model the micro-structure of foams by FE (Finite Element) code. There are two main methods in this regard. In the first method (Nammi *et al.*, 2010; Buffel *et al.*, 2014), simple geometrical unit cells were created by the user in such a way that the unit cell shape had the most possible resemblance to the cell shapes of the manufactured foams. Several unit cell types namely Kelvin, Weaire-Phelan, truncated cube, cube, etc. have been proposed for this type of numerical modeling. The unit cell was then repeated several times in the space to create a lattice structure. In the second method, the FE model of the foam was created based on the data obtained from CT-Scan images.

Constructing the FE model using CT data has been received much attention in the recent years and several studies have been dedicated to it. Youssef *et al.* (2005) prepared a three-dimensional (3D) model of a polyurethane foam by means of X-ray micro-tomography data. In this regard, the solid volume of the foam was meshed using tetrahedral elements. Using the constitutive equations of the bulk material, a compression test was simulated and the local deformation mechanism of the foams was predicted. Their model was able to correctly capture both the macroscopic response and local deformation mechanisms.

Jeon *et al.* (2009) fabricated two 5 mm×5 mm×5 mm Al foam specimens with completely different micro-structures, and numerically analyzed them using a microfocus X-ray CT system, 3D reconstruction program, 3D scanned data processing software, commercial mesh generation

program, and finally a FE solver. After validating the numerical results, the effects of each mechanical property of the bulk material on the compressive behavior of the foam material was analyzed. In a similar trend, Veyhl *et al.* (2011) modeled closed-cell and open-cell metal foams using the FE method and investigated the relationship between the foam density and macro-mechanical properties. Their results demonstrated a linear dependence between relative density and mechanical properties of M-Pore® and Alporas® foams. Ramirez *et al.* (2014) evaluated the elasto-plastic deformation behavior of simulated open-cell foam samples under compressive loads using experimental data. According to the results, the stress-strain distribution and magnitude in the FE model and the experimental tests matched very well. Using CT data obtained from a compact micro-CT device, Miedzińska *et al.* (2012) evaluated and described the main mechanisms that appear in the open-cell foam structures during the compression and how they influence the material energy absorbing capabilities. The most important conclusion was that the foam structures can be considered as complex beam constructions where the local instabilities decide about the energy absorbing capabilities. In a more recent study, Zhu *et al.* (2014) implemented MATLAB image processing toolbar to establish the finite element model of an aluminum foam with porosities of 56.41%, 56.71% and 58.02%. The created FE model was then analyzed using ABAQUS commercial FE code. Comparison with experiments showed the validity of the proposed method of 3D construction of the model.

In most of the previous micro-geometrical studies on the foam, the local material properties of foams have been considered uniform (and equal to the mechanical properties of the bulk material) in the walls or struts of the foam structure. This assumption is reasonable in foams fabricated by some of the foam manufacturing techniques. However, most of the foams (especially the closed-cell ones) usually do not show uniform material density (and as the result mechanical properties) in their walls or struts. Therefore, considering a uniform mechanical property for all portions of the foam leads to inaccurate results. In this study, the static mechanical behavior of several closed-cell foam samples have been simulated and validated against experimental results. The samples were first imaged using a multi-slice CT-Scan device. Subsequently, experimental compression tests were carried out on the samples using a uniaxial compression testing machine. The CT data were then used for creating 3D models of the samples. According to the darkness or brightness of the CT images, different densities were assigned to different parts of the FE models of the samples. Depending on density of the material at a point, the elastic modulus was considered for it. Three different formulas were considered in different simulations for relating the elastic modulus to density of the foam material. ANSYS implicit solver was used for carrying out the simulations. In this study, the main goal is to find out which of the three formulas can better follow the mechanical behavior of the foams manufactured by the melting method.

2. Materials and methods

2.1. Experimental technique

The foams were manufactured by adding TiH₂ powders as a foaming agent to the melted aluminum. In molten aluminum (in temperatures about 660°C), TiH₂ is decomposed into titanium and hydrogen. The gaseous hydrogen creates bubbles in the molten metal. To stabilize the bubbles, calcium particles are also added to the melted aluminum which increases the viscosity of the molten. After the formation of bubbles, the molten is cooled. Therefore, titanium and calcium materials also exist in the structure of the foam.

Using the abovementioned manufacturing procedure, a 3.2 mm thick porous plate was created, from which several 30 mm×30 mm×32 mm foam samples were obtained. The foam had some degrees of irregularity due to which the foam samples had average densities between 46-53 g/cm³, i.e. relative densities in the range of 0.17-0.21.

For carrying out the experiments, a uniaxial compression test device (Zwick 1494) was used (Fig. 2). The grip velocity was set to 3 mm/s. To apply the compressive load uniformly, two steel plates were placed under and above the test samples. The weight of the top steel plate was then taken into account in the load values. Ten samples with geometrical and material specification listed in Table 1 were tested.

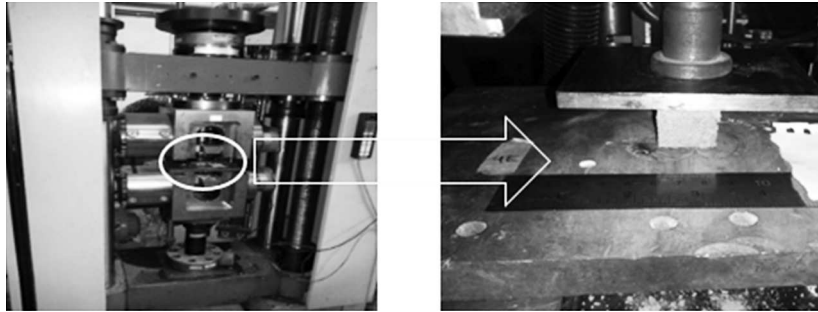


Fig. 2. A specimen in a compression test using the uniaxial compression test machine

Table 1. Geometrical and material properties of ten test samples

Specimen name	1E	2E	3E	4E	6E	3D	5D	6D	5C	6C
Mass [g]	13.59	13.21	13.52	16.22	11.40	12.69	12.24	12.31	14.53	13.80
Density [g/cm ³]	0.51	0.47	0.53	0.58	0.52	0.46	0.48	0.49	0.51	0.48
Relative density	0.19	0.17	0.19	0.21	0.19	0.17	0.18	0.17	0.19	0.18
Volume [cm ³]	26.48	28.08	25.35	28.17	21.84	27.32	25.61	25.36	28.61	28.53
Cross-sectional area [mm ²]	775	824	752	819	666	809	757	818	837	822

2.2. Numerical modeling

All the samples were imaged using Toshiba multi-slice CT scan device (Fig. 3). Four of the ten samples (1E, 2E, 3E, and 4E) were chosen for numerical modeling. Using the DICOM viewer software, the DICOM images obtained from the CT device were converted into JPEG format which is a suitable format for being read by MATLAB. Using the `imread` command, the JPEG files were imported into MATLAB. A table matrix was created each row of which consisted of the properties of each pixel including the percentage of brightness, relative density, mechanical properties, etc. Generally, in a CT image, the brighter the color of a pixel is, the denser the material at that point is. Therefore, the completely black pixels are representative of pores, while completely white pixels show that density of the foam material at the point is equal to density of the bulk material. A few examples of cross-sections of the constructed finite element models are shown and compared to the corresponding CT images in the test samples in Fig. 4. It must be noted that the arc-shaped part at the bottom of the CT images is not representative of samples, but shows the padding on the CT device bed. These arc-shaped parts were removed from the FE model in the simulations.

According to its brightness, density and elastic modulus values were assigned to each pixel. For each test sample, a 3D cubic structure meshed by cubic brick elements was created and the material properties of the pixels were assigned to the corresponding elements. An example of the 3D model for a sample is shown in Fig. 5. The constructed FE models consisted of about one million brick elements. A high number of elements promises high accuracy of consideration of the material properties gradient inside the foam model.



Fig. 3. Toshiba Multi slice 16 CT- Scan device

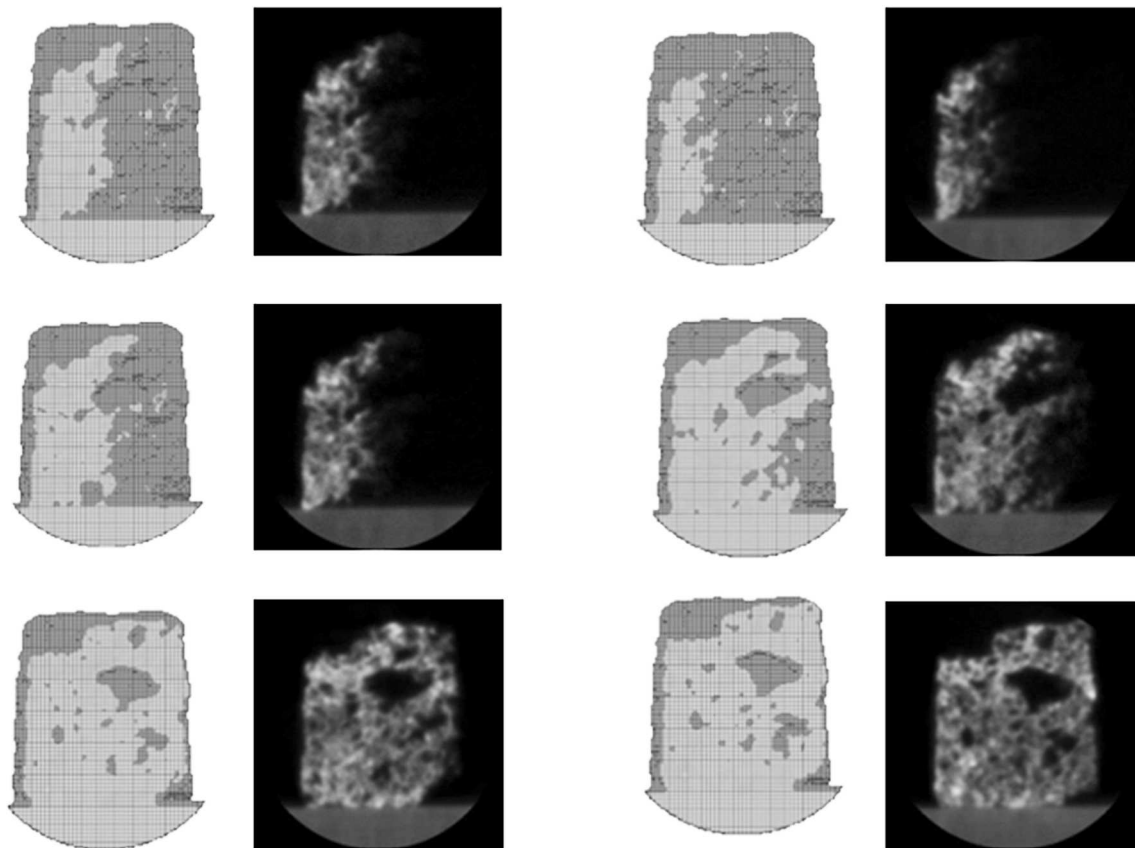


Fig. 4. Reconstructed FE models in ANSYS (left) in comparison with the corresponding CT images (right)

The colors of the CT images (and therefore material density of the foam) were categorized into eleven groups according to the degree of their brightness. The elastic modulus value assigned to each element was not linearly proportional to its density value. Three different nonlinear formulas existing in the literature were implemented for this purpose. Poisson's ratio value was set to 0.3 in all the relative densities. In the first elastic modulus formula, it is assumed that the relative elastic modulus E/E_s is proportional to the n -th exponent of relative density ρ/ρ_s , i.e.

$$\frac{E}{E_s} = \left(\frac{\rho}{\rho_s}\right)^n \tag{2.1}$$

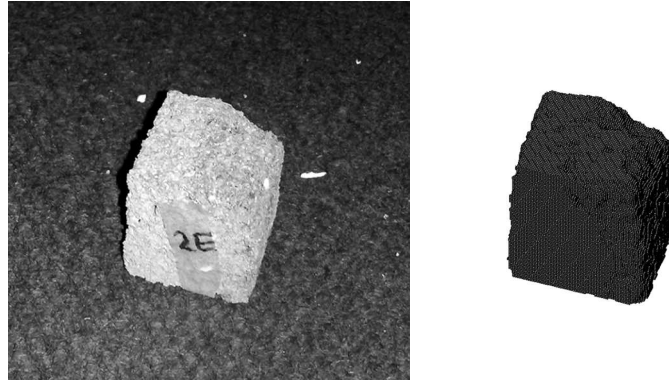


Fig. 5. 3D model of a foam (right) constructed based on the CT data of the test sample (left)

where E and E_s are respectively the elastic moduli of the foam material and the bulk material it is made of, and ρ and ρ_s are densities of the foam material and the bulk material, respectively. The constant n is obtained by fitting the elastic modulus plots of the FE model and the experiments, which shows that $n = 4.4$ gives the best results. This formula is called the n -exponential formula in the following. The second formula is based on the relationship proposed by Ashby *et al.* (2000) for open-cell foams

$$\frac{E}{E_s} = C_1 \left(\frac{\rho}{\rho_s} \right)^2 \quad (2.2)$$

where C_1 is a constant which must be determined according to experimental/numerical correlation. The best value obtained for C_1 is 0.02364. The third formula is the one proposed by Ashby *et al.* (2000) for closed-cell foams

$$\frac{E}{E_s} = C_2 \left[\frac{1}{2} \left(\frac{\rho}{\rho_s} \right)^2 + \frac{3}{10} \frac{\rho}{\rho_s} \right] \quad (2.3)$$

where $C_2 = 0.0151$ yields the best numerical/experimental correlation. The E/E_s values assigned to the eleven materials corresponding to the three noted formulations are listed in Table 2. For a black point (i.e. the locations where there is no material), the elastic modulus $E = 1$ Pa is considered which is negligible compared to the elastic moduli of the other parts of the model.

Table 2. Different elastic modulus values assigned to elements of the FE models for the three formulas

	$\frac{E_1}{E_s}$	$\frac{E_2}{E_s}$	$\frac{E_3}{E_s}$	$\frac{E_4}{E_s}$	$\frac{E_5}{E_s}$	$\frac{E_6}{E_s}$	$\frac{E_7}{E_s}$	$\frac{E_8}{E_s}$	$\frac{E_9}{E_s}$	$\frac{E_{10}}{E_s}$	$\frac{E_{11}}{E_s}$
n -exp. formula Eq. (2.1)	$1.43 \cdot 10^{-11}$	0.0000	0.0008	0.0005	0.0177	0.0474	0.1056	0.2082	0.3746	0.6290	1.0000
Open-cell formula Eq. (3.2)	$1.43 \cdot 10^{-11}$	0.0002	0.0009	0.0021	0.0038	0.0059	0.0085	0.0116	0.0151	0.0119	0.0236
Closed-cell formula Eq. (2.3)	$1.43 \cdot 10^{-11}$	0.0005	0.0012	0.0020	0.0030	0.0042	0.0054	0.0069	0.0085	0.0102	0.0121

Large and relatively small pores inside the test samples have also been considered in the constructed models by giving them a very small elastic modulus (~ 1 Pa). The hollow space in the periphery of the foam samples are also specified in the FE model in the same way. Very

small holes (with sizes smaller than the pixel size of the CT images) could not be identified in the CT images. However, these micro pores decrease the brightness of a CT image at the pixel they exist because they decrease the local density of the foam material. Their effect therefore has been incorporated in the FE model by assigning elastic moduli smaller than the elastic modulus of the bulk metal.

Similar to the conditions of the experimental tests, the FE models are constrained in the bottom side and are compressed for $\varepsilon = 2\%$ from the top side. The nodes of the lowermost elements are not allowed to move in the direction parallel to the loading direction but are allowed to move parallel to the bottom surface. To obtain the elastic modulus of each structure E^* , the total resultant force of the constrained nodes F have been measured and inserted in $E^* = FL/\delta A$, where A and L are the cross-section area and length of each sample, respectively. The dimensions of the four samples are listed in Table 3.

Table 3. Dimensions of each of the four samples considered for numerical modeling

Specimen	δ [mm]	L [mm]	A [mm ²]
1E	$0.02L$	34.10	775.671
2E	$0.02L$	34.06	824.600
3E	$0.02L$	33.67	752.920
4E	$0.02L$	34.40	819.029

3. Results and discussion

3.1. The experiments

All the test samples were compressed up to 80% strain. Knowing the cross-section area and lengths of the samples, the load-displacement curves were converted into stress-strain curves (Fig. 6). For obtaining the elastic modulus of each sample, the slope of the

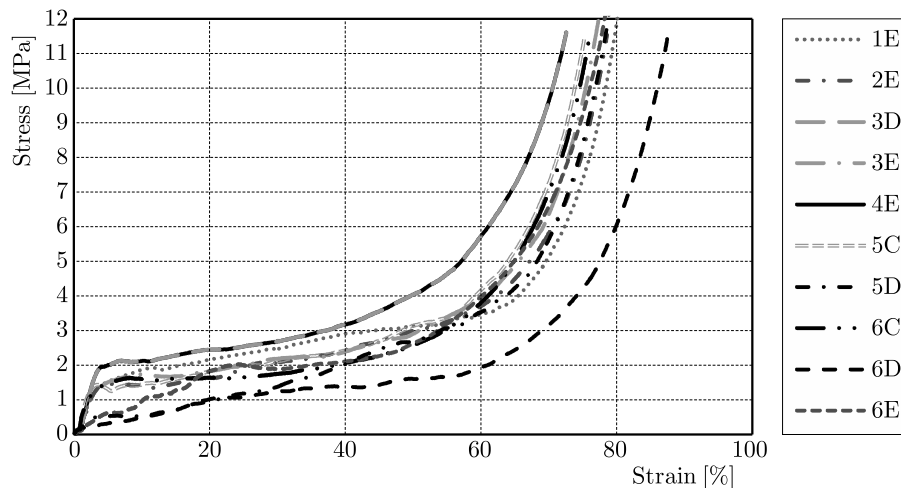


Fig. 6. Experimental stress-strain curves of different Al foam samples under compression

linear part of stress-strain curves is measured (see Fig. 7). The initial parts of the stress-strain curve are neglected in calculating the elastic modulus, because they are associated with the initial micro-plasticity of the uneven surfaces of the foam samples in contact with the grip surfaces. The obtained elastic modulus, plateau stress, densification strain, final elastic modulus and yield stress of the ten samples are listed in Table 4. Due to the presence of large holes created during manufacturing process (e.g. see the large hole in the sample shown in Fig. 8), the specimens

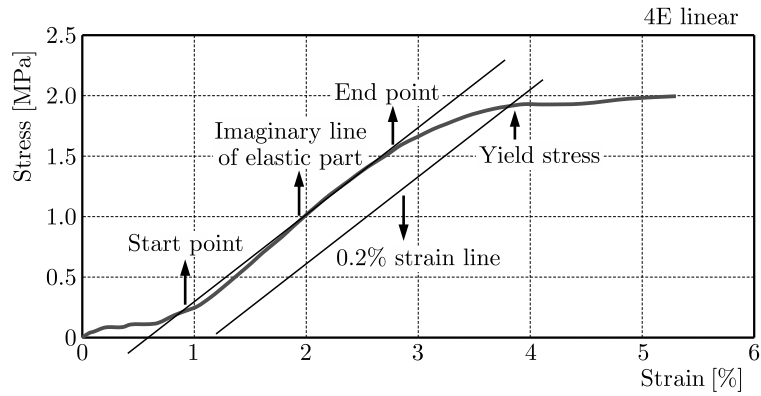


Fig. 7. Linear part of the stress-strain curve of sample 4E

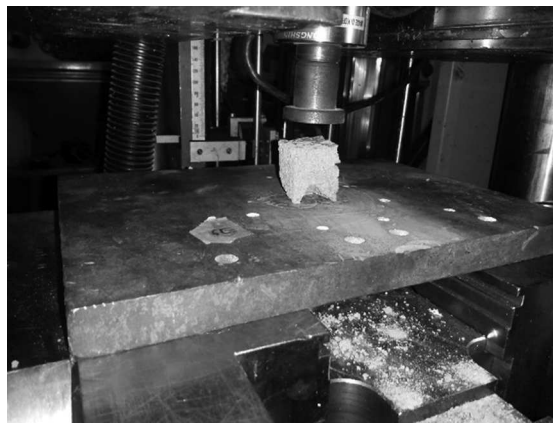


Fig. 8. A large hole in specimen 6E

Table 4. Mechanical properties obtained from compression tests for different specimens

Specimen	1E	2E	3E	4E	6E	3D	5D	6D	5C	6C
	μ									
	0.50	0.47	0.53	0.58	0.52	0.46	0.48	0.49	0.51	0.48
Elastic modulus [MPa]	65	52	77	75	–	30	16.66	–	74	39
Plateau stress [MPa]	1.7-3.5	1.43-3.5	1.5-4.01	1.93-4.02	1.07-2.9	0.6-1.8	0.53-2.98	1.0-1.77	1.24-3.14	1.56-2.35
Densification strain [%]	60	53.10	50.50	41.40	51.02	55.20	59.65	60	56.10	50
Final el. modulus [MPa]	89.2	79.12	86.29	70.17	98.22	109.11	85.21	73.60	75.30	80.30
Yield stress [MPa]	1.41	1.46	1.41	1.96	–	0.55	0.52	–	1.37	1.33

6E and 6D do not demonstrate the elastic part in their stress-strain curve and therefore the corresponding cells in Table 4 are left blank.

Table 5. Resultant forces (N) for the four samples and for different formulas

Specimen	Open-cell formula	Closed-cell formula	<i>n</i> -exponential formula
1E	1024.20	1051.97	866.58
2E	946.31	965.94	942.52
3E	1121.10	1135.25	1147.00
4E	1122.55	1045.89	1330.74

Table 6. Numerical elastic modulus values for the three formulas compared to the experimental results

Specimen	Experimental elastic modulus [MPa]	FE elastic modulus based on open-cell formula [MPa]	Differ. with exper. [%]	FE elastic modulus based on closed-cell formula [MPa]	Differ. with exper. [%]	FE elastic modulus based on <i>n</i> -expon. formula [MPa]	Differ. with exper. [%]
1E	65	66.02	1.57	67.81	4.33	55.86	-14.06
2E	52	57.38	10.36	58.57	12.63	57.15	9.90
3E	77	74.45	-3.36	75.39	-2.09	76.17	1.07
4E	75	68.53	-8.62	63.85	-14.86	111.1	45.9

As it can be seen in Table 4, the elastic moduli of different samples (with no big hole) are in the range of 16 MPa (for Sample 5D) and 77 MPa (for Sample 3E). The higher average density of the foam is, the larger is the obtained elastic modulus value. For example, samples 3E and 4E which have the highest average densities among all the samples also have the highest elastic moduli. Moreover, these two samples have the highest yield stress and lowest densification strain among all the cases.

Although in the final stages of foam compression, the relative density of the foam samples are close to unity, the elastic modulus in this part is still much smaller than the elastic modulus of the bulk material (about one thousandth), see Table 4. This is because the material particles have lost their continuity and the material layers easily slide on each other.

3.2. The FE models

The obtained resultant forces for the four samples and for the three different formulas are listed in Table 5. The obtained elastic modulus values for the three formulas and their difference with experimental results are listed in Table 6. All the numerical results have less than 15% difference with the experimental data (except the *n*-exponential formula for sample 4E which has 45.9% difference with the experiments). The good accordance of the numerical results based on the three formulas demonstrates a proper definition of loading, boundary conditions and discretization of the FE models. Moreover, the results show that the CT-based multi-material foam model, while used with an appropriate density-stiffness formula, can predict the cellular structure mechanical response as well. The results of the open-cell formula give the best numerical/experimental correlation (less than 10.5% difference), and the closed-cell formula also shows less than 15% numerical/experimental difference (Table 6).

The stress contour is demonstrated for the four samples in Fig. 9. The stress value is usually higher at locations with higher densities. This correlation between the local material density and stress level is demonstrated in Fig. 10 for cross-section of the foam sample.

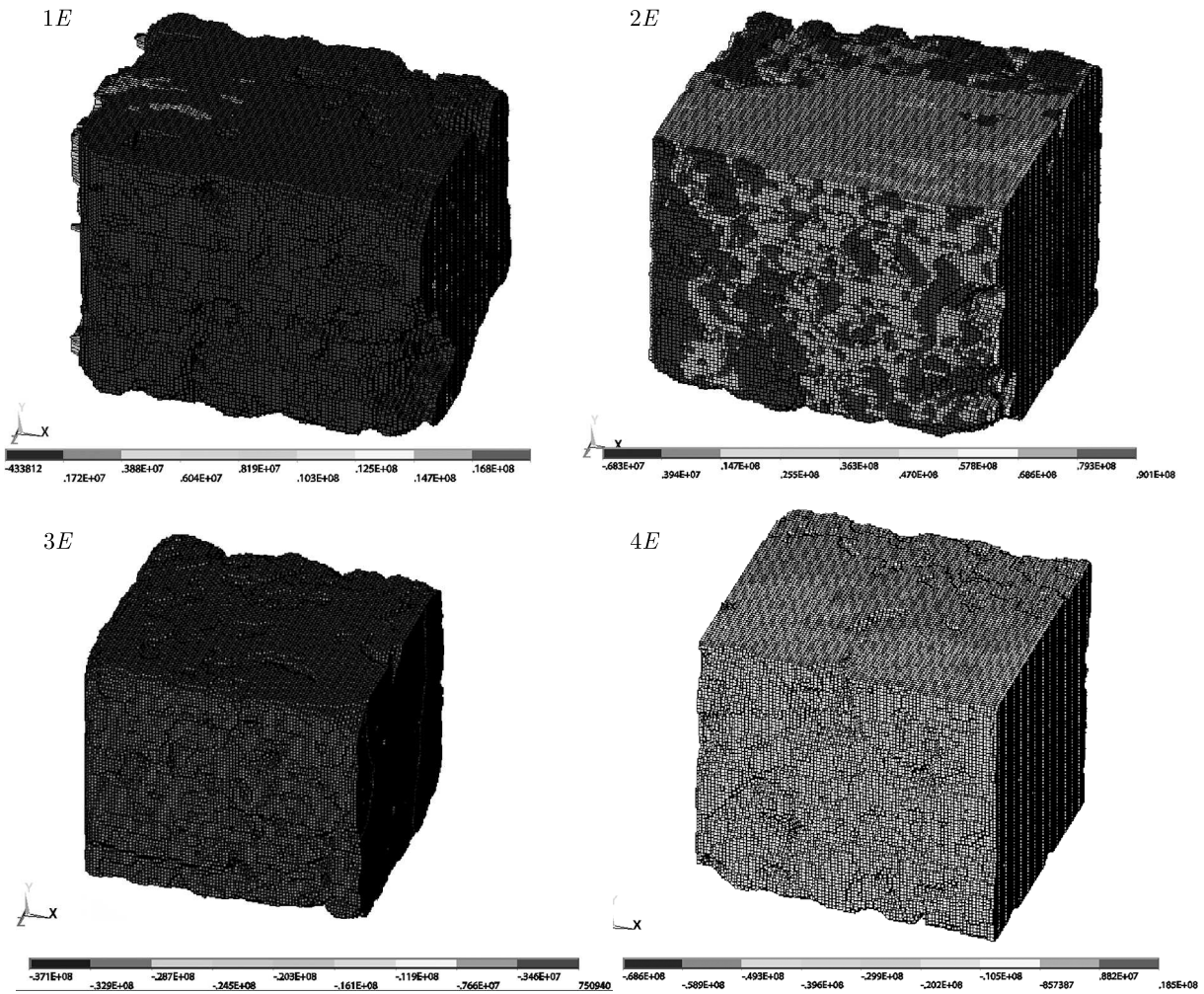


Fig. 9. Stress contour for the four samples

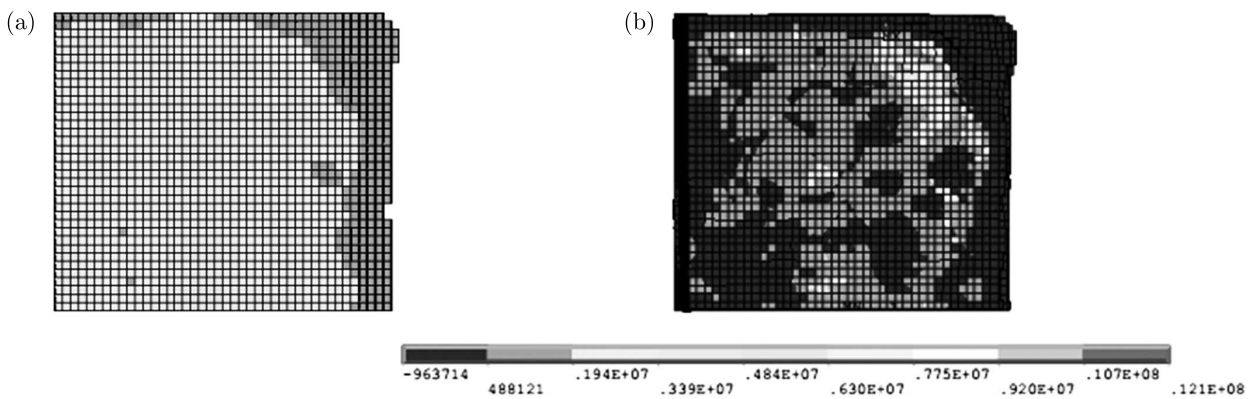


Fig. 10. Comparison of density distribution (left) and stress distribution (right) in a sample

4. Conclusions

In this study, the mechanical behavior of aluminum metal foams under compressive static loading is studied experimentally and numerically. For the experimental tests, the elastic modulus, yield stress, plateau stress, densification strain and final elastic modulus have been obtained for ten samples, two of which had large pores. For the numerical modeling, four of the ten samples used in

the experimental tests were imaged using CT-Scan device before carrying out the experimental tests. The CT data were then used for creating 3D models of the samples. According to the darkness or brightness of the CT images, different densities were assigned to different parts of the FE models of the samples. Three different formulas were considered in different simulations for relating the elastic modulus to density of the foam material. One of the formulas is first presented here (called the n -exponential formula), while the two remaining formulas are the relationships proposed by Gibson and Ashby (1998) for open-cell and closed-cell foams. Comparison of the numerical and experimental results demonstrated the superiority of the open-cell formula, in such a way that the numerical/experimental difference is less than 10.5% for all the samples. The closed-cell formula also shows less than 15% numerical/experimental difference. For the last formula (n -exponential formula), the numerical/experimental discrepancy is less than 15% except for one sample which shows an elastic modulus 45.9% higher than the experimental data. The good accordance of the numerical results based on all the three formulas demonstrates the efficiency of the proposed numerical model methodology. The image processing methodology presented in this paper can therefore be very useful in similar studies.

References

1. ANDREWS E., SANDERS W., GIBSON L.J., 1999, Compressive and tensile behaviour of aluminum foams, *Materials Science and Engineering*, **A270**, 113-124
2. ASHBY M.F., EVANS A.G., FLECK N.A., GIBSON L.J., HUTCHINSON J.W., WADLEY H.N.G., 2000, *Metal Foam: a Design Guide*, Boston, 978-0-7506-7219-1
3. BANHART J., 2001, Manufacture, characterization and application of cellular metals and metal foams, *Materials Science*, **46**, 559-632
4. BUFFEL B., DESPLENTERE F., BRACKE K., VERPOEST I., 2014, Modelling open cell-foams based on the Weaire-Phelan unit cell with a minimal, *International Journal of Solids and Structures*
5. CAO X.Q., WANG Z.H., MA H.W., ZHAO L.M., YANG G.T., 2006, Effects of cell size on compressive properties of aluminum foam, *Transactions of Nonferrous Metals Society of China*, **16**, 351-356
6. GIBSON L.J., 2000, Mechanical behavior of metallic foams, *Annual Review of Materials Science*, **30**, 191-227
7. GIBSON L.J., ASHBY M.F., 1998, *Cellular Solids, Structure and Properties*, UK, Pergamon Press
8. HEDAYATI R., SADIGHI M., MOHAMMADI-AGHDAM M., ZADPOOR A.A., 2016a, Mechanical behavior of additively manufactured porous biomaterials made from truncated cuboctahedron unit cells, *International Journal of Mechanical Sciences*, **106**, 19-38
9. HEDAYATI R., SADIGHI M., MOHAMMADI-AGHDAM M., ZADPOOR A.A., 2016b, Mechanical properties of regular porous biomaterials made from truncated cube repeating unit cells: Analytical solutions and computational models, *Materials Science and Engineering*, **C60**, 163-183
10. HEDAYATI R., SADIGHI M., MOHAMMADI-AGHDAM M., ZADPOOR A.A., 2016c, Mechanics of additively manufactured porous biomaterials based on the rhombicuboctahedron unit cell, *Journal of the Mechanical Behavior of Biomedical Materials*, **53**, 272-294
11. JEON I., KATOU K., SONODA T., ASAHINA T., KANG K.J., 2009, Cell wall mechanical properties of closed-cell Al foam, *Mechanics of Materials*, **41**
12. KITAZONO K., SATO E., KURIBAYASHI K., 2003, Application of mean-field approximation to elastic-plastic behavior for closed-cell metal foams, *Acta Materialia*, **51**, 4823-4836
13. KO W., 1965, Deformations of foamed elastomers, *Journal of Cellular Plastics*, **1**, 45-50

14. MEGUID S.A., XUE H., 2000, On the use of “SDDIS” for measuring deformation localisation in cellular materials, *Proceedings of the 3rd International Conference on Mechanics and Materials in Design*, Orlando, USA
15. MIEDZIŃSKA D., NIEZGODA T., GIELETA R., 2012, Numerical and experimental aluminum microstructure testing with the use of computed tomography, *Computational Materials Science*, **64**, 90-95
16. NAMMI S.K., MYLER P., EDWARDS G., 2010, Finite element analysis of closed-cell aluminium foam under quasi-static loading, *Materials and Design*, **31**
17. RAMIREZ J.F., CARDONA M., VELEZ J.A., MARIAKA I., ISAZA J.A., MEDOZA E., BETANCOURT S., FERNADEZ-MORALES P., 2014, Numerical modeling and simulation of uniaxial compression of aluminum foams using FEM and D-CT images, *Procedia Materials Science*, **4**, 218-222
18. VEYHL C., BELOVA I.V., MURCH G.E., FIEDLER T., 2011, Finite element analysis of the mechanical properties of cellular aluminium based on microcomputed tomography, *Materials Science and Engineering A*, **528**, 13-14
19. YOUSSEF S., MAIRE E., GAERTNER R., 2005, Finite element modelling of the actual structure of cellular materials determined by X-ray tomography, *Acta Materialia*, **53**, 719-730
20. ZHU X., AI S., FANG D., LIU B., LU X., 2014, A novel modeling approach of aluminum foam based on MATLAB image processing, *Computational Materials Science*, **82**, 451-456

Manuscript received July 4, 2015; accepted for print March 10, 2016

LIMIT LOAD OF COLD FORMED THIN-WALLED NONSTANDARD CHANNEL BEAMS

MACIEJ OBST

Poznan University of Technology, Faculty of Machines and Transportation, Poznań, Poland
e-mail: maciej.obst@put.poznan.pl

MARCIN RODAK, PIOTR PACZOS

Poznan University of Technology, Institute of Applied Mechanics, Poznań, Poland
e-mail: marcin.rodak@put.poznan.pl; piotr.paczos@put.poznan.pl

Cold-formed thin-walled beams may lose the stability in different ways. The common buckling modes which have an influence on the failure of the beam are lateral-torsional, local and distortional buckling. The strength of cold-formed members can be calculated with the Effective Width Method which is incorporated in many international and national standards. In this paper, the experimental and theoretical results calculated with the aforementioned method have been compared.

Keywords: thin walled beams, limit load, EC3

1. Introduction

Different types of loss of stability are distinguished. First one is connected with global beam buckling which is characterized by invariability of the shape of beam cross-section and long length of the half-wave of the buckling. When the wall thickness of the beam is relatively small in comparison with the width of the individual walls, then the local buckling of the beam may exist. The length of the half-wave of the buckling is small and it is comparable with the wall widths which are buckled. The beam may lose the stability in a distortional mode which was characterized by Hancock (1997) for channel sections as a rotation of the flange with its deflection in relation to the axis of connection between the flange and web. The length of the half-wave of the buckling for this type of mode of stability loss is equal to the intermediate values for the above mentioned cases. The strength of the beam can be limited by the occurrence of the above mentioned modes of stability loss. In this work, the results of experimental investigations which have been conducted in the Laboratory of the Strength of Materials at the Poznan University of Technology are applied – these ones are discussed by Pacos (2012, 2013, 2014). Similar investigations were conducted by Pastor and Roure (2008) who considered two loading conditions. Silvestre and Camotim (2010) described the mechanics of distortion in thin-walled open sections. Magnucka-Blandzi *et al.* (2012) proposed formulas which made it possible to determine the critical load of double box flange beams. They increased the strength and stability of those structural members but complicated their analysis because there were different possible buckling modes: local, distortional (rotation of a stiffened flange at a flange/web function) or global, e.g. flexural torsional buckling. The results of experimental investigations of thin-walled beams were presented by Magnucki *et al.* (2010), and Magnucka-Blandzi (2011) and SudhirSastry *et al.* (2015).

Practical calculations of the strength of the thin-walled beams which can locally lose the stability are based on the Effective Width Method (EWM). It is applied in many international and domestic standards, e.g. PN-EN 1993-1-3 (2008), PN-EN 1993-1-5 (2008) and AISI S100-2007

(2007). The effective width method has been elaborated as an approximate model of strength of long and slender plates ($L \gg b$) (Fig. 1a). Next it has been adopted to calculations of thin-walled beams. In the case of plates which are freely supported on four edges and uniformly compressed on two short edges, the distribution of normal stresses is not quite uniform after exceeding the critical compressive stresses (Fig. 1b). This state is approximated by giving the effective width of the plate b_{eff} where the uniform distribution of stresses exists, and for the other width it is assumed that the stress values are equal to zero. Moreover

$$\sigma_2 A_{eff} = \sigma_1 A \quad (1.1)$$

where $A = tb$ and $A_{eff} = tb_{eff}$.

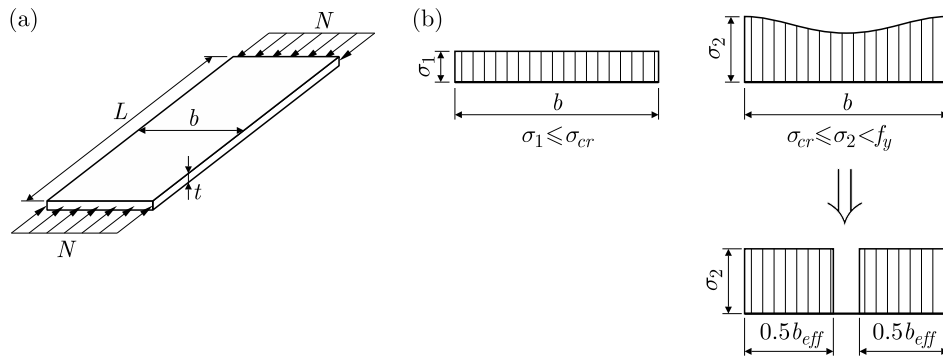


Fig. 1. (a) Plate freely supported on edges and compressed by a uniformly distributed force which is applied to the edges b , (b) distribution of normal stresses in the plate

Direct methods are other methods which are commonly applied. The most known method is the Direct Strength Method (DSM) proposed by Schafer, applied in US standards (AISI S-100-2007, 2007) and presented in many other works, e.g. Shafer (2008), Batista (2009, 2010) described the Effective Section Method (ESM).

The authors of this paper have compared strength of cold-formed thin-walled beams calculated on the basis of PN-EN 1993-1-3 (2008) with the results of the experimental investigations (Paczos, 2012). During the determination of the theoretical limiting moment the local buckling of the beam has been taken into consideration only. Freely supported and pure bending beams for the measuring length $L = 400, 500, 600$ mm (Fig. 2) have been investigated. Channel section beams with double and single boxes have been analysed (Fig. 3).

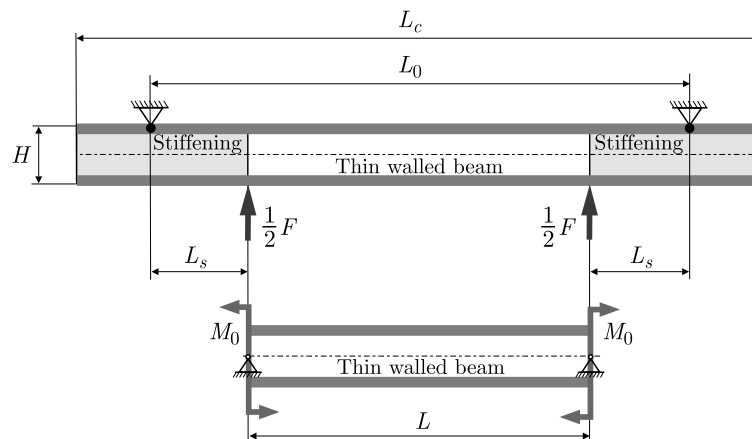


Fig. 2. Loading scheme

The presented subject is the development of researches that have been conducted in the Division of Strength of Materials and Structures of Poznan University of Technology.

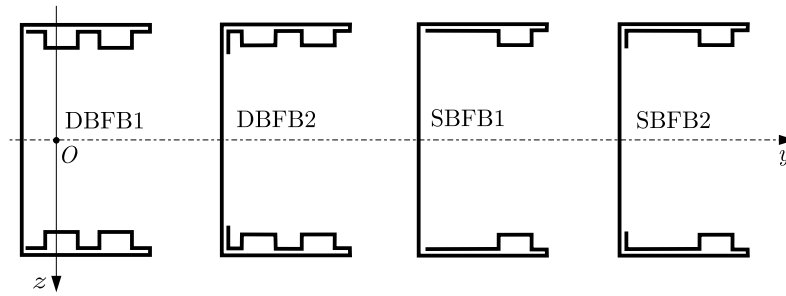


Fig. 3. Channel section beams with double boxes and with single boxes

2. Calculations

The limit value of the moment for the beam can be calculated on the basis of the following formula

$$M_{gr} = f_y W_{eff} \quad (2.1)$$

where f_y is the yield stress of the material, W_{eff} – effective section modulus for bending calculated for the local buckling of the beam walls, so the distortional mode of buckling has been omitted. The calculations have been done iteratively, because after every calculation of the effective width of the beam walls the centre of cross-section has been changed (the distribution of normal stresses is also changed in the cross-section).

The effective width of the beam wall is equal to

$$b_{eff} = \rho b_c + b_t \quad (2.2)$$

where ρ is the reduction ratio, b_c – beam width where compressive stresses exist (positive), b_t – beam width where tensile stresses exist (negative).

The calculation has been based on the assumption that cross section can be yielded only by local buckling. Therefore, it is assumed that all walls do not have any additional stiffening (see PN-EN 1993-1-3, 2008, point 5.5.2) and next the authors proceeded according to the procedure described in standard (PN-EN 1993-1-5, 2008). The load capacity of shape of the cross-section of the beam has also been determined on the assumption of elastic stress distribution in the cross-section of the beam.

Solution algorithm according to EC3

1. Calculate the bending strength indicator of cross-section W_y with the assumption that width of the supporting walls is equal to their imaginary width. Substitute $W_{y,eff}^{(i)} = W_y$, where $i = 1$.
2. Substitute $i := i + 1$.
3. For each investigated wall (beam web, upper and lower flange wall, bend) calculate elastic critical stress (plate elastic buckling)

$$\sigma_{cr} = k_\sigma \frac{\pi^2 E}{12(1 - \nu^2)} \left(\frac{t}{b_p} \right)^2 \quad (2.3)$$

where values k_σ can be found in at (PN-EN 1993-1-5, 2008, Table 4.1, 4.2), and E is Young's modulus, ν – Poisson's ratio, t – wall thickness, b_p – imaginary width of wall.

4. Slenderness plate and reduced slenderness plate for each of investigated walls are calculated with the following formulas

$$\bar{\lambda}_p = \sqrt{\frac{f_y}{\sigma_{cr}}} \quad \bar{\lambda}_{p,red} = \bar{\lambda}_p \sqrt{\frac{\sigma_1}{f_y}} \quad (2.4)$$

where f_y is yield strength, σ_1 – maximal stress in the wall (compressive stress).

5. Reduction coefficient ρ can be calculated by the following formulas (PN-EN 1993-1-5, 2008, E.1)

— for cantilevered walls

$$\rho = \frac{1 - 0.188/\lambda_{p,red}}{\bar{\lambda}_{p,red}} + 0.18 \frac{\bar{\lambda}_p - \bar{\lambda}_{p,red}}{\bar{\lambda}_p - 0.6} \quad \text{but} \quad \rho \leq 1 \quad (2.5)$$

— for span walls

$$\rho = \frac{1 - 0.053(3 + \psi)/\bar{\lambda}_{p,red}}{\bar{\lambda}_{p,red}} + 0.18 \frac{\bar{\lambda}_p - \bar{\lambda}_{p,red}}{\bar{\lambda}_p - 0.6} \quad \text{but} \quad \rho \leq 1 \quad (2.6)$$

where $\bar{\lambda}_p = \sqrt{f_y/\sigma_{cr}}$ – plate slenderness, $\bar{\lambda}_{p,red} = \bar{\lambda}_p \sqrt{\sigma_1/f_y}$ – reduced plate slenderness, $\psi = \sigma_2/\sigma_1$, σ_1 – maximum compressive stresses on one edge of the wall, σ_2 – stresses on opposite edge of the wall, σ_{cr} – critical elastic stresses for the wall.

6. Calculate effective width ((PN-EN 1993-1-5, 2008, Table 4.1, 4.2) for each investigated walls.
7. Calculate the strength indicator $W_{y,eff}^{(i)}$.
8. If $(W_{y,eff}^{(i)} - W_{y,eff}^{(i-1)})/W_{y,eff}^{(i)} < \varepsilon$ then $M_{gr} = W_{y,eff}^{(i)} f_y$ and finish. Otherwise start calculations from point 2.

The iterative procedure is rapidly convergent. To determine final values, few iterations are sufficient depending on the measure accuracy accepted for calculations (in this paper $\varepsilon = 0.001$ has been accepted). A flow chart of the procedure is presented in Fig. 4.

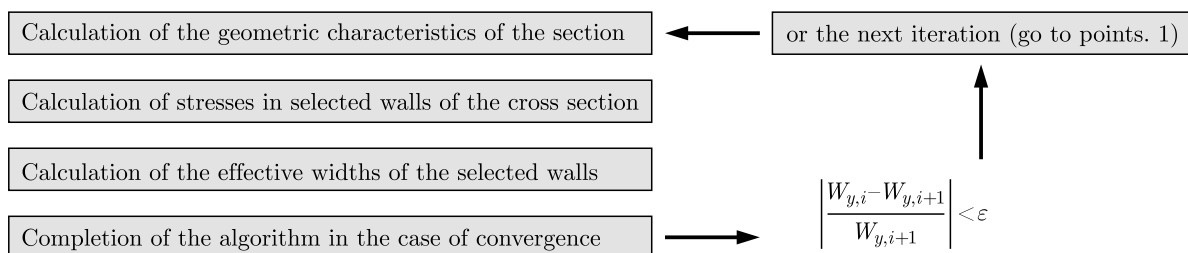


Fig. 4. Simplified block diagram of the effective cross-section calculation algorithm for pure bending

The above presented formulas can be found in standard PN-EN 1993-1-5 (2008). Figure 5 presents the examined sections and walls which are analysed for the local buckling.

The main reason for experimental investigations is the search for the optimal (strongest) shape of the cross-section of the beam. The beams are made of the same material and have the same length and wall-thickness. Two kinds of beams with double-box and single-box flange have been investigated: $L = 400, 500$ and 600 mm.

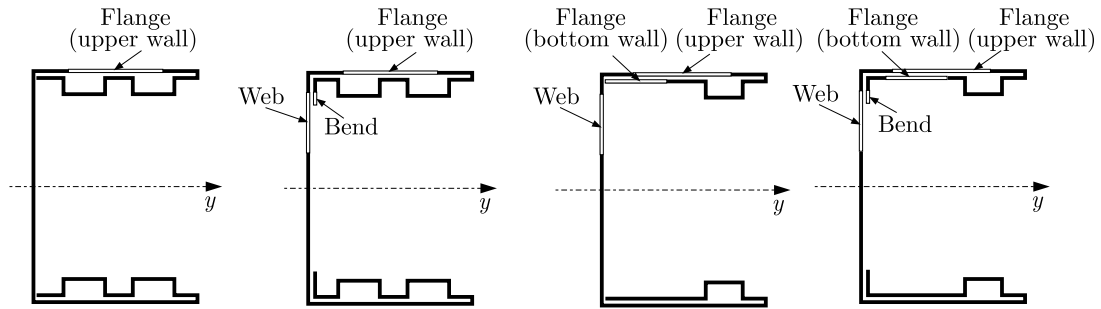


Fig. 5. Effective sections DBFB1, DBFB2 and SBFB1, SBFB2

3. Experimental investigations

The examined beams were produced by “Pruszyński Sp. z o.o.”, Sokołów, Polska and made of steel: $E = 1.81 \cdot 10^5$ MPa, $\nu = 0.3$ and $f_y = 329$ MPa. The tests have been performed with testing machine ZWICK Z100 having the range up to 100 kN. a four point bending test has been conducted for the beams where pure bending has been obtained for the measuring length L (Fig. 6).

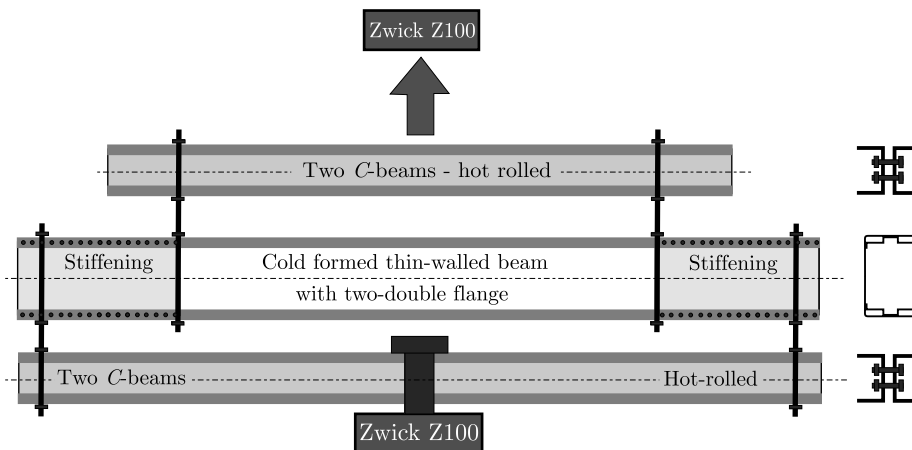


Fig. 6. Scheme of the test stand

The following equipment has been used for experimental investigations: strain gauge bridge SPAIDER, the deflection sensor 15 mm (WA15) HOTINGER, foil strain gauges HBM type 6/120LY11, gauge factor 2. They have been loaded with two moments (pure bending). Some results are presented in tables and drawings (Fig. 7 and Table 1-4). The test stand and the beam is presented in Fig. 7.

Relations between the deflection of the lower flange and the load-force within the full range of the load (maximum force) are shown in Fig. 8.

The growth of displacements of cold-formed thin-walled beams under increasing load causes local buckling that may also interact with global buckling. It is a result of the low load capacity of thin-walled beams that depends on dimensions of the beam, boundary conditions (support), load or shape of the cross-section.

The investigated beams have been made by cold-form technology of sheet steel bending using numerical CNC machines. During experimental research of beams there was no considerable aberration of the defined lateral and lengthwise dimensions. Apart from the measurement of deflection of the middle part of beam, strains have also been measured in five measuring points of the tested cross-section. Two measuring points have been placed on the beam web and

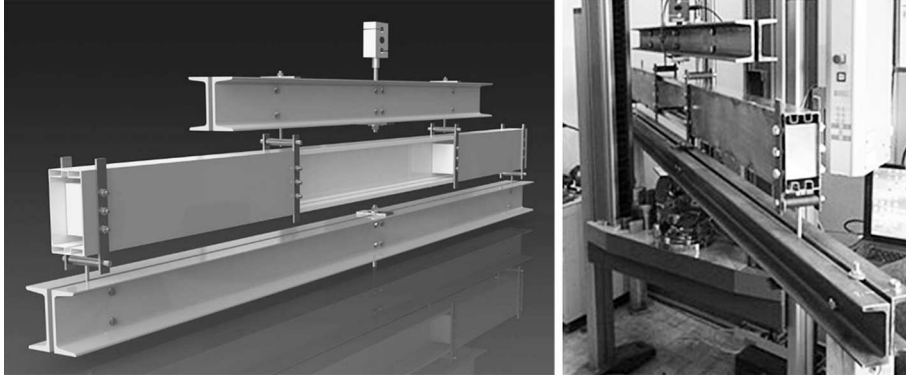


Fig. 7. Test stand (simulation of pure bending)

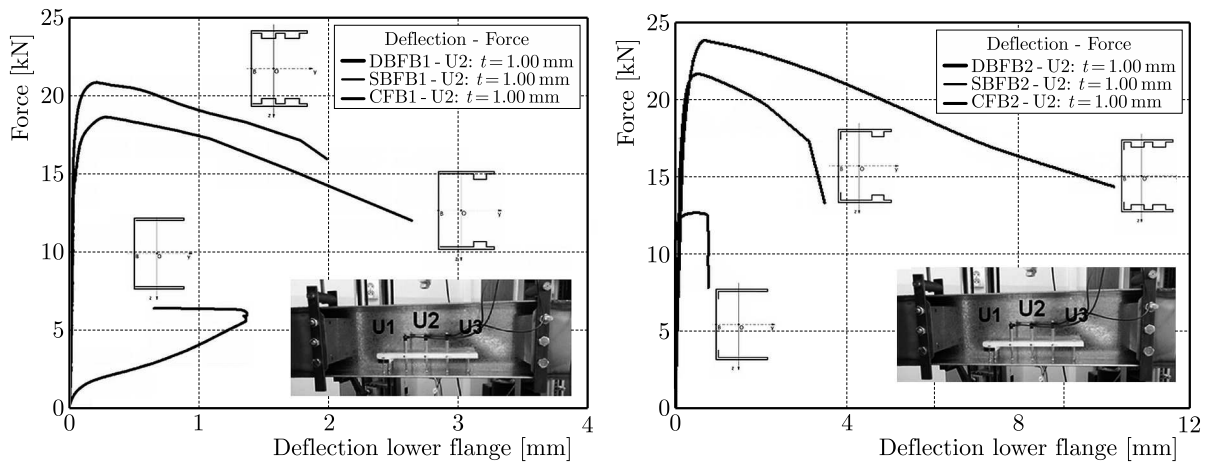


Fig. 8. Experimental relationship between forces and deflection of the lower flange for thickness $t = 1.00$ mm (beams: DBFB1, SBFB1, DBFB2, SBFB2)

three measuring points have been placed on on the press lower beam flange. On the basis of the obtained strain results and beam sheet metal material properties, stress values have been calculated. During the experimental research of beams, local buckling shapes were observed and maximum values of forces were measured which corresponded to the limit load of the beam. The participation of distortional buckling was negligible and for different cross-sections of beams it is value was in the range from 2% up to 4% of the maximal force.

4. Comparison of the results

This Section presents a comparison of strength of the beams obtained by experimental investigations and the procedure described in Standard PN-EN 1993-1-5 (2008). The dimensions of cross-sections are the following (Fig. 9): $H = 160.0$ mm – height of the beam (external dimension), $b = 80.0$ mm – width of the flange, $c = 0.0$ mm, 20.0 mm – length of the reinforcement, $d = 18.0$ mm – height of the flange, $e = 14.0$ mm, $f = 18.0$ mm, 30.0 mm, 40.0 mm, $t = 1.00$ mm and 1.25 mm – wall thickness.

Tables 1 and 2 show the comparison of the results for beams with double boxes, with and without reinforcement, correspondingly.

Tables 3 and 4 show the comparison of the results for beams with single boxes, with and without reinforcement, correspondingly.

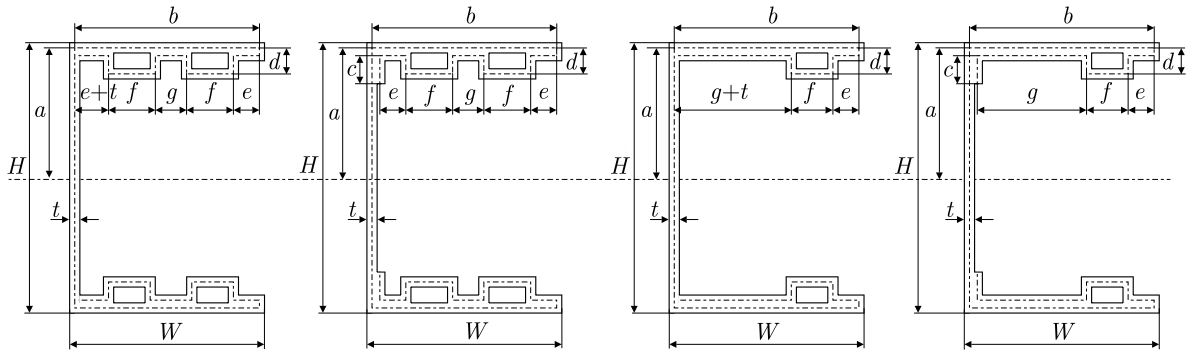


Fig. 9. Channel section beams with double boxes (without and with bend) and with single boxes (without and with bend)

Table 1. Values of limiting loads – DBFB1

t [mm]	$M_{gr}^{(EC3)}$ [kNm]	L [mm]	$M_{gr}^{(exp)}$ [kN]	$M_{gr,sr}^{(exp)}$ [kN]	\mathcal{A} [%]
1.00	9.03	400	–	7.79	–
		500	7.79		19.0
		600	–		–
1.25	12.05	400	–	10.49	–
		500	10.49		14.8
		600	–		–

$$\mathcal{A} = [(M_{gr}^{(EC3)} - M_{gr}^{(exp)}) / M_{gr}^{(exp)}] \cdot 100$$

Table 2. Values of limiting loads – DBFB2

t [mm]	$M_{gr}^{(EC3)}$ [kNm]	L [mm]	$M_{gr}^{(exp)}$ [kN]	$M_{gr,sr}^{(exp)}$ [kN]	\mathcal{A} [%]
1.00	9.70	400	8.85	8.60	9.6
		500	8.78		10.5
		600	8.18		18.5
1.25	12.87	400	12.74	12.15	1.0
		500	12.07		6.6
		600	11.63		10.6

5. Conclusions

Strength of the beams with double boxes (DBFB1, DBFB2) is higher than strength of the beams with single boxes (SBFB1, SBFB2). This result has been expected. The similar situation exists for the beams with and without reinforcement. The beams with reinforcement (DBFB2, SBFB2) have higher values of the limiting moment than the beams without reinforcement (DBFB1, SBFB2).

The analysis of the obtained results allows one to state that the strength values obtained with Standard PN-EN 1993-1-5 (2008) are higher than the experimental values. Moreover, this difference grows with an increase in the measuring length of the beam. The reason for this fact is the interaction of two forms of buckling, i.e. local and distortional one, and an increase in the percentage contribution of the second form in conjunction with an increase in the measuring length of the beam.

Table 3. Values of limiting loads – SBFB1

Dimensions [mm]	$M_{gr}^{(EC3)}$ [kNm]	L [mm]	$M_{gr}^{(exp)}$ [kN]	$M_{gr,sr}^{(exp)}$ [kN]	\mathcal{A} [%]
$t = 1.00$ $f = 30.00$	6.83	400	6.91	6.66	-1.2
		500	6.77		0.9
		600	6.31		0.8
$t = 1.00$ $f = 40.00$	7.11	400	6.81	6.81	4.5
		500	6.84		3.9
		600	6.79		4.8
$t = 1.25$ $f = 30.00$	9.42	400	–	–	–
		500	–		–
		600	–		–
$t = 1.25$ $f = 40.00$	9.75	400	–	–	–
		500	–		–
		600	–		–

Table 4. Values of limiting loads – SBFB2

Dimensions [mm]	$M_{gr}^{(EC3)}$ [kNm]	L [mm]	$M_{gr}^{(exp)}$ [kN]	$M_{gr,sr}^{(exp)}$ [kN]	\mathcal{A} [%]
$t = 1.00$ $f = 30.00$	8.30	400	7.96	7.89	4.2
		500	7.89		5.1
		600	7.82		6.1
$t = 1.00$ $f = 40.00$	8.24	400	–	–	–
		500	–		–
		600	–		–
$t = 1.25$ $f = 30.00$	11.31	400	11.47	10.93	-1.4
		500	10.98		3.0
		600	10.34		9.4
$t = 1.25$ $f = 40.00$	11.09	400	–	–	–
		500	–		–
		600	–		–

Moreover, this difference is higher for cross-sections with two boxes (DBFB1, DBFB2) than with single boxes (SBFB1, SBFB2). This results from the fact that the cross-sections with single boxes are more sensitive to local buckling, and this type of buckling has a higher percentage contribution in beam destruction than distortional buckling. Theoretical results are based on the following assumption: the beam loses local stability only – so, a better agreement between the results exists for the cross-sections with single boxes SBFB1 and SBFB2.

In the case of the cross-section with single boxes SBFB1, one can notice that the strength for $f = 30$ mm is higher than for $f = 40$ mm, and this means that $W_{eff,f=30} < W_{eff,f=40}$, but it is known that $W_{y,f=30} > W_{y,f=40}$ where $W_{eff,f=x}$ and $W_{y,f=x}$ are the bending indicators, respectively, the effective one and the indicator in the elastic range for $f = x$. This situation is caused by the following fact: during the beam flange compression the span wall has higher length for the case of $f = 30$ mm than $f = 40$ mm, and the effective widths of these span walls for both cross-sections have similar values – this leads to the above mentioned relationships.

To sum up, one should take into account the distortional buckling of the beam during calculations of the beam strength.

Acknowledgement

The presented research results executed within project No. 02/21/DSPB/3464 have been funded by the Ministry of Science and Higher Education.

References

1. AISI S100-2007, 2007, North American specification for the design of cold-formed steel members, American Iron and Steel Institute
2. BATISTA E.M., 2009, Local-global buckling interaction procedures for design of cold-formed columns: effective width and direct method integrated approach, *Thin-Walled Structures*, **47**, 1218-1231
3. BATISTA E.M., 2010, Effective section method: a general direct method for design of steel cold-formed members under local-global buckling interaction, *Thin-Walled Structures*, **48**, 345-356
4. HANCOCK G.J., 1997, Design for distortional buckling of flexural members, *Thin-Walled Structures*, **27**, 3-12
5. MAGNUCKA-BLANDZI E., 2011, Effective shaping of cold-formed thin-walled channel beams with double-box flanges in pure bending, *Thin-Walled Structures*, **49**, 121-128
6. MAGNUCKA-BLANDZI E., PACZOS P., WASILEWICZ P., 2012, Buckling study of thin-walled channel beams with double-box flanges in pure bending, *International Journal for Experimental Mechanics*, **48**, 317-325
7. MAGNUCKI K., PACZOS P., KASPRZAK J., 2010, Elastic buckling of cold-formed thin-walled channel beams with drop flanges, *ASCE: Journal of Structural Engineering*, **136**, 7, 886-896
8. PACZOS P., 2012, Stability and limit load of thin-walled cold-formed channel beams, *Proceedings of Stability of Structures XIII-th Symposium*, Zakopane 2012, Kowal-Michalska K., Mania R.J. (Edit.), 539-546
9. PACZOS P., 2013, Experimental and numerical (FSM) investigations of thin-walled beams with double-box flanges, *Journal of Theoretical and Applied Mechanics*, **51**, 2, 497-504
10. PACZOS P., 2014, Experimental investigations of thin-walled C-beams with nonstandard flanges, *Journal of Constructional Steel Research*, **93**, 77-87
11. PASTOR M.M., ROURE F., 2008, Open cross-section beams under pure bending. I Experimental investigations, *Thin-Walled Structures*, **46**, 476-483
12. PN-EN 1993-1-3, 2008, Eurokod 3, Projektowanie konstrukcji stalowych. Część 1-3: Reguły ogólne. Reguły uzupełniające dla konstrukcji z kształtowników i blach profilowanych na zimno, PKN, Warszawa 2008
13. PN-EN 1993-1-5, 2008, Eurokod 3, Projektowanie konstrukcji stalowych. Część 1-5, Blachownice. PKN, Warszawa 2008
14. SCHAFER B.W., 2008, Review: the Direct Strength Method of cold-formed steel member design, *Journal of Constructional Steel Research*, **64**, 766-778
15. SILVESTRE N., CAMOTIM D., 2010, On the mechanics of distortion in thin-walled open sections, *Thin-Walled Structures*, **48**, 469-481
16. SUDHIRSASTRY Y.B., KRISHNA Y., PATTABHI BUDARAPU R., 2015, Parametric studies on buckling of thin walled channel beams, *Computational Materials Science*, **96**, 416-424

STUDY ON DEFORMATION-INDUCED DAMAGE EVOLUTION FOR INCONEL718 SUPERALLOY WITH THE USE OF AN INNOVATIVE SINGLE-SPECIMEN METHOD

GRZEGORZ SOCHA, BARTOSZ MADEJSKI, MACIEJ MALICKI

Institute of Aviation, Warszawa, Poland

e-mail: grzegorz.socha@ilot.edu.pl; bartosz.madejski@ilot.edu.pl; maciej.malicki@ilot.edu.pl

An innovative method for investigation of deformation-induced damage of elastic-plastic materials is proposed. A static tension test, performed on a specimen with a variable cross-section gage part enabled analysis of degradation of the material structure for all stages of permanent deformation. Modified Johnson model has been used to quantify damage. Analysis of the damage of the specimen surface as well as observations of the damage induced inside the gage part of the specimen has been performed using SEM observations. Debonding at the interface between a hard inclusion and a ductile matrix has been found to be responsible for initiation of cracks on the specimen surface as well as inside the gage part of the specimen. Analysis of the subsequent void growth has been performed. Surface cracks are associated with plastic deformation resulting in an increase of the surface roughness. Variations of the specimen surface roughness have been found to be in good correlation with the damage parameter. This correlation enables the use of surface roughness as the relative damage indicator for the investigated material and deformation mode.

Keywords: damage, accumulated plastic strain, superalloy, void growth

1. Introduction

Nickel-based superalloys are often used for hot section of aircraft engines. One of the most popular among them is Inconel718. This kind of the material can be characterized by a very good resistivity to mechanical and thermal loads. Usually, hot-section aircraft engine parts are designed to work at high temperature and under high mechanical load, reaching and even exceeding the yield limit. Oversizing parts and decreasing material effort (stress) is usually not possible due to weight reduction requirements. In such service conditions, material damage progresses due to effects related to fatigue, creep and also overload. Monitoring of the damage progress is essential in this case for safety of structures. Monitoring of the progress of material damage preceding formation of detectable cracks is possible only when a proper damage indicator is used. Many damage indicators were used by researchers. A good review of such damage indicators was given by Yang and Fatemi (1998). The authors divided indicators used to quantify damage into few categories: metallurgical parameters, crack quantification, mechanical parameters and physical measures. Among metallurgical parameters related to plastic deformation that are considered in this paper, one can mention the dislocation number, dislocation cell diameter, slipband density. An attempt to measure dislocation density and its evolution was described by Petersmeier *et al.* (1998). This kind of investigation is rather difficult to perform due to the fact that determination of any of mentioned parameters requires the use of a sophisticated technique (like TEM) and determination of the average value of such a parameter for a representative volume element (RVE) of the investigated material. Since deformation leads to initiation of microcracks, parameters like the summary (or average) crack length or area are used by researchers, see Yang *et al.* (2010), Hall (1998), Zhang *et al.* (1999). For monotonic loading, like static tension reported

in this paper, microcracks evolve into voids, and the void volume fraction can be used as the damage indicator. This kind of damage indicator was used by Gurson in his well known model (Gurson, 1977). As a matter of fact, any physical quantity can be used as damage indicator if we can only prove that changes of such quantity are related to damage progress. If changes of the damage indicator with progressing damage are monotonic (either increase or decrease during the deformation process), we can quantify damage comparing actual value of such damage indicator with initial one (for virgin material). This kind of the damage indicator can be referred to as relative, and it was used successfully by many researches. One example of the successful use of the relative damage parameter is investigation of fatigue damage accumulation by observation of the local inelastic strain response to constant stress amplitude loading. Results of the investigations were published in series of papers, see Socha (2003, 2004), Socha and Dietrich (2012) together with proposition of the mathematical model for fatigue life estimation.

Another approach to quantify damage of the material is to use cumulative damage indicator. This kind of damage indicator requires integration (or simple summation) of a physical quantity during loading. Such a cumulated value of the damage indicator is then divided by the final value (corresponding to the material failure) to obtain the damage parameter (damage parameter is a normalized value of the damage indicator taking values from 0 for the virgin material to 1 for material failure). A very well known example of such a cumulative damage indicator is, in the case of fatigue loading, the number of applied load cycles. Assuming that for a constant stress amplitude every load cycle introduces the same amount of damage (Palmgren-Miner linear damage rule, see Palmgren (1924), Miner (1945)) into the material, we can define the damage parameter as the ratio of the actual to final (corresponding to failure) number of the elapsed load cycles. A discussion on relative and cumulative damage indicator parameters was given in another author's paper (Socha and Dietrich, 2016).

The most popular material damage model, introduced by Johnson (1980) and then used in almost all FEM codes defines damage as the function of accumulated equivalent plastic strain

$$D = \sum \frac{\Delta\varepsilon}{\varepsilon_f} \quad (1.1)$$

where $\Delta\varepsilon$ stands for the accumulated plastic strain and ε_f is the final value of the accumulated plastic strain corresponding to the moment of material failure (original denotation). According to this definition, one can use accumulated equivalent plastic strain as the cumulative damage indicator parameter. This approach was already followed by one of the authors of this paper in the investigation of the fatigue damage accumulation. The results were published in (Socha and Dietrich, 2014). Using the accumulated equivalent plastic strain as the damage indicator parameter has some disadvantages. First of all, the final value of this indicator is related to the stress state, or saying more precisely, is believed to be a function of three invariants of the stress state. This problem is now under intensive investigation by many researchers, see e.g. Bao and Wierzbicki (2004), Nielsen and Hutchinson (2012). Another important question is: what can be considered to be material failure and what is the damage mechanism? In the case of laboratory testing separation of two pieces of a test specimen is usually considered to be the final failure of material, but for the material of the structure in service this approach cannot be applied and the damage of such a material must be observed carefully to detect its failure. Many damage mechanisms were observed by researchers for metallic materials. Most important for elastic-plastic metal alloys are: strain localization (formation of cohesive zone) associated with big plastic deformation in the case of a ductile material, crack initiation and following propagation assisted by plastic deformation around the crack tip or finally brittle fracture in the case of a brittle material. To investigate the damage mechanism for a particular material and to detect failure (and calculate the corresponding value of ε_f) observations of structural changes

undergoing during material deformation are necessary. The aim of this paper is to propose a simple method for investigation of the damage mechanism.

2. Experimental technique

Determination of some material properties, like for example elastic constants or yield limit, requires making use of a specimen with a uniform cross-section gage part. Design of the specimen must assure uniform stress and strain distribution in the entire gage part of the specimen. To obtain a credible result of strain measurement, we have to use a technique enabling measurement on big enough volume of a uniformly stressed material (Representative Volume Element). In most cases, such kind of a specimen is used also for damage investigations (Niazi *et al.*, 2013; Ganjiani, 2013; Shen *et al.*, 2014). To investigate the effect of permanent deformation (plastic strain) on the structure of the material, such kind of the specimen is usually deformed to reach a particular level of plastic strain in the entire gage part and then unloaded to perform structural analysis. This kind of technique has some disadvantages. To perform structural analysis on the material of a deformed specimen, it must be destroyed in order to prepare metallographic samples. Due to that fact, it is necessary to perform many tests on many specimens to obtain a complete picture of damage-induced structural changes at various stages of deformation. Such analysis may be influenced by few factors like non-homogeneity of the material structure and properties, different test conditions for specimens and others.

Damage, however, is a local phenomenon. It develops at spots of stress concentration or at imperfections of the structure. Also, as it has already been mentioned, since the material is never perfectly homogeneous, there are always differences in the structure for different specimens, even if they are machined from one piece of the material. For this reason (also due to high cost of many tests), it would be beneficial to perform investigation of damage-induced structural changes on one specimen. Such a kind of the specimen proposed and by authors of this article (Socha *et al.*, 2014), is shown in Fig. 1.

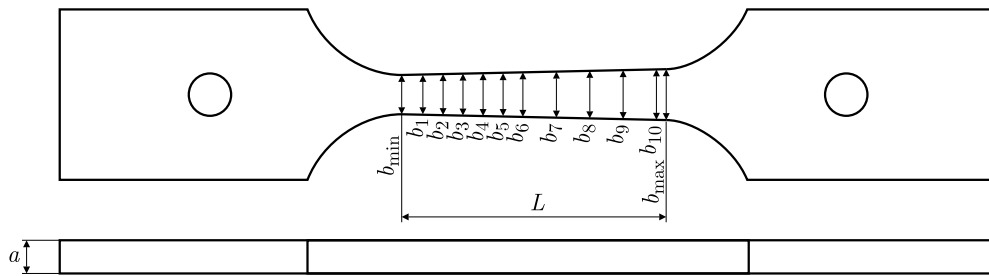


Fig. 1. Specimen for the investigation of deformation induced damage

The gage part of a flat specimen used for this investigations has variable cross-section area. Such a kind of the trapezoidal gage part design enables obtaining continuous distribution of the plastic strain after a tensile test to rupture. Assuming that the length of the gage part of the specimen is l , convergence of this trapezoidal gage part is given by formula

$$1 : \frac{\sigma_{YS}l}{(\sigma_{UTS} - \sigma_{YS})b_{min}} \quad (2.1)$$

where σ_{YS} stands for the yield limit in tension, σ_{UTS} stands for the ultimate tensile strength and b_{min} is the width of the smallest cross-section of the gage part. For a specimen with this convergence of the gage part, after strain localization and necking (formation of cohesive zone) in the narrowest section we shall obtain continuous distribution of plastic strain from the maximum value at that spot to zero at the opposite end of the gage part where the material is expected

to reach the yield limit at the instant of specimen failure. In this manner, we shall obtain a “frozen” picture of deformation induced damage of the structure for all levels of deformation from purely elastic to permanent deformation corresponding to the final failure of the material. Changes of the structure along the specimen axis reflect progress of damage with an increasing value of the above mentioned damage parameter given by Johnson (1980) that can be modified to a general form for complex stress loading along the non-linear path in the stress space

$$D = \frac{1}{\bar{\varepsilon}_f^p} \int d\bar{\varepsilon}^p \quad (2.2)$$

where the equivalent plastic strain is integrated along the path in the stress space and $\bar{\varepsilon}_f^p$ stands for its final value at the moment of material failure. In the case of presented investigations, the material is loaded along the linear path in the stress space and original definition (1.1) can be used as well.

The gage part of the specimen is marked along its axis with marks shown in Fig. 1. From the smallest cross-section, six equally distanced marks are put every 3 mm, and then four marks distanced every 5 mm are added. For these spots of the specimen, the axial plastic strain will be determined based on the incompressibility assumption using the following formula

$$\varepsilon_1 = -(\varepsilon_2 + \varepsilon_3) \quad (2.3)$$

where ε_2 and ε_3 are transversal and in-thickness direction strains. Those strains are calculated on the basis of measurements of the specimen gage part width and thickness before and after the test at selected and marked spots.

Cutting metallographic samples from marked spots along the specimen axis and performing structural observations allows analysis of the damage mechanism and sequence of events during deformation of the material.

3. Investigated alloy and design of specimens

The material under investigation is nickel-based Inco 718 alloy (AMS 5596K) in cold rolled and annealed condition. Mechanical properties of the alloy in as received state at room temperature are: 0.2% offset yield strength $\sigma_{YS} - 445$ MPa, ultimate tensile strength $\sigma_{UTS} - 855$ MPa, elongation 51%. After heat treatment, the mechanical properties at room temperature are as follows: $\sigma_{YS} - 1150$ MPa, $\sigma_{UTS} - 1350$ MPa, elongation 21%. The chemical composition of the alloy is shown in Table 1.

Table 1. Chemical composition of the alloy under investigation [% weight]

C	Mn	P	S	Si	Cr	Ni	Al
0.05	0.01	0.008	0.0002	0.10	17.98	52.30	0.60
Mo	Cu	Cb	Ta	Ti	Co	B	Fe
2.88	0.02	4.97	0.01	1.02	0.04	0.02	19.96

To verify the above-mentioned strength parameters delivered by a manufacturer, a static tension test has been performed with the use of the standard specimen with the uniform gage part.

Based on the stress-strain curve shown in Fig. 2, mechanical parameters of the alloy are found as follows: 0.2% offset yield strength $\sigma_{YS} - 450$ MPa, ultimate tensile strength $\sigma_{UTS} - 890$ MPa, elongation 58%. Taking into account the results of the static tension test and formula (2.1), the convergence of the shown in Fig. 1 specimen gage part, for the material under investigation has been found to be 1:7.6.

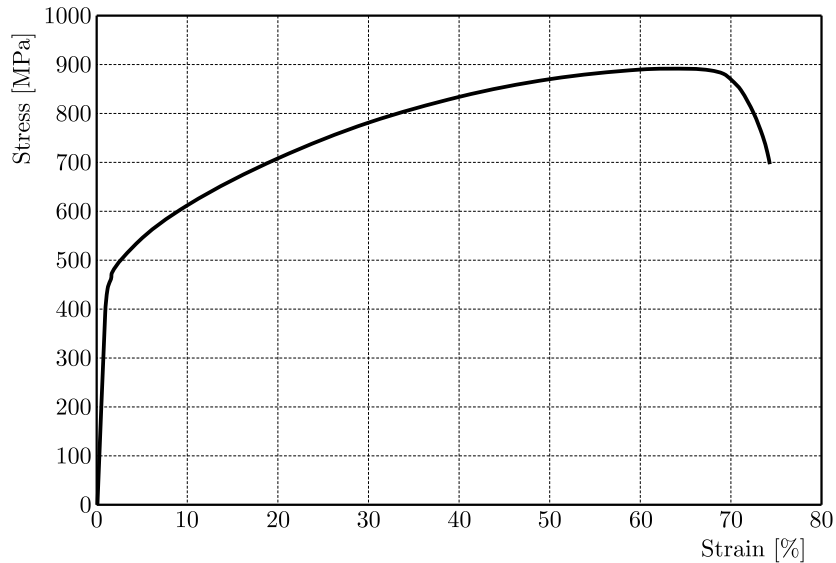


Fig. 2. Stress-strain curve for a static tension test on the standard specimen

4. Test results

A static tension test has been performed on a specimen with variable cross-section of the gage part at the room temperature. Both tests were displacement controlled with the rate 0.1 mm/min initially and, after elongation of the gage part reached 1.5%, with the rate 1.2 mm/min to rupture. A force-elongation diagram for the tests are shown in Fig. 3.

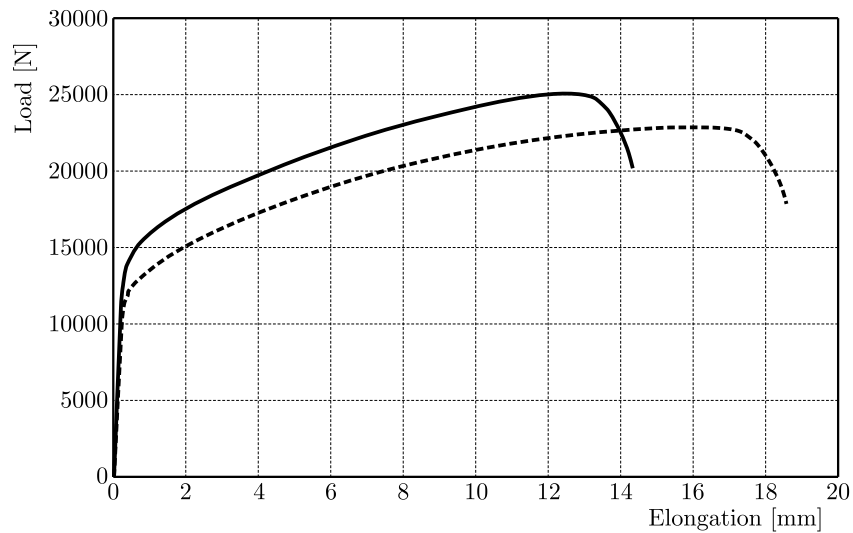


Fig. 3. Force-elongation diagram for the static tension test on a variable gage section specimen

For comparison, a force-elongation diagram for the uniform-gage part specimen (marked with a broken line) is also shown in this figure. As expected, the elongation is bigger for the specimen with the uniform-gage part. This is due to the fact that strain localization (formation of cohesive zone) is delayed for this kind of the specimen comparing to the specimen with a non-uniform cross-section.

As it has been mentioned, the specimen was marked to enable determination of the plastic strain field. The specimen with marks is shown in Fig. 1. Calculations of the axial plastic strain, using formula (2.3), are based on measurements of the specimen at marked points before and

after the test. Both width and thickness of the specimen have been measured to determine transversal strain in both directions. Distribution of axial strain along the specimen axis is shown in Fig. 4.

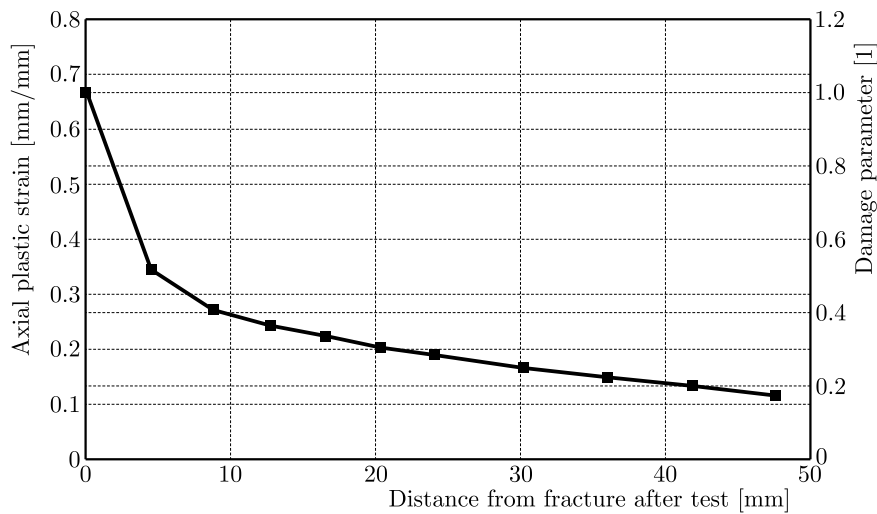


Fig. 4. Distribution of axial plastic strain for a variable gage section specimen

As it can be seen in this figure, the strain is strongly localized in the vicinity of the smallest cross section. Starting from the third mark (about 9 mm from the smallest cross-section), we can assume that the axial strain changes linearly along the specimen axis. The damage parameter has also been determined on the base of the axial plastic strain calculated for selected sections of the gage part using formula (2.3). The final value of the axial plastic strain ε_f has been calculated for the fracture surface. In Fig. 4, a plot of the damage parameter overlays the plot of the axial strain, but values of the damage parameter are shown on the right axis of the coordinate frame. As it can be seen, the axial plastic strain takes values between 0.1 and 0.68, while the damage parameter varies from 0.17 to 1 for the fractured surface.

5. Analysis of the damage mechanism

For the specimen gage part, outside the cohesive zone, the analysis of deformation-induced damage has been performed using SEM observations of the specimen surface. Figure 5 shows SEM pictures of the specimen surface. The pattern remaining after final surface finishing (grinding) is clearly visible on the specimen surface. Initially straight lines deform with progressing deformation. This deformation illustrates plastic flow of the material around the crack tip. Initially small, finally it forms bands of large plastic deformation between crack tips.

Cracking of the specimen surface occurs at an early stage of deformation ($D = 0.19$) at the interface of hard inclusions and the ductile matrix of the material. The making use of back scattering electron (BSE) technique allowed observation of hard inclusions as light grey areas (this technique is sensitive to chemical composition of the material). The chemical composition of hard inclusions was later investigated with the use of an energy-dispersive X-ray spectroscopy (EDX) technique on a polished material (see Fig. 9) cut off from the specimen gage part. The observations of the deformed surface of the material lead to the conclusion that the main mechanism of material damage in the case of the investigated alloy is the debonding at the interface of the ductile matrix and hard inclusions associated with large plastic deformation around the formed crack tips.

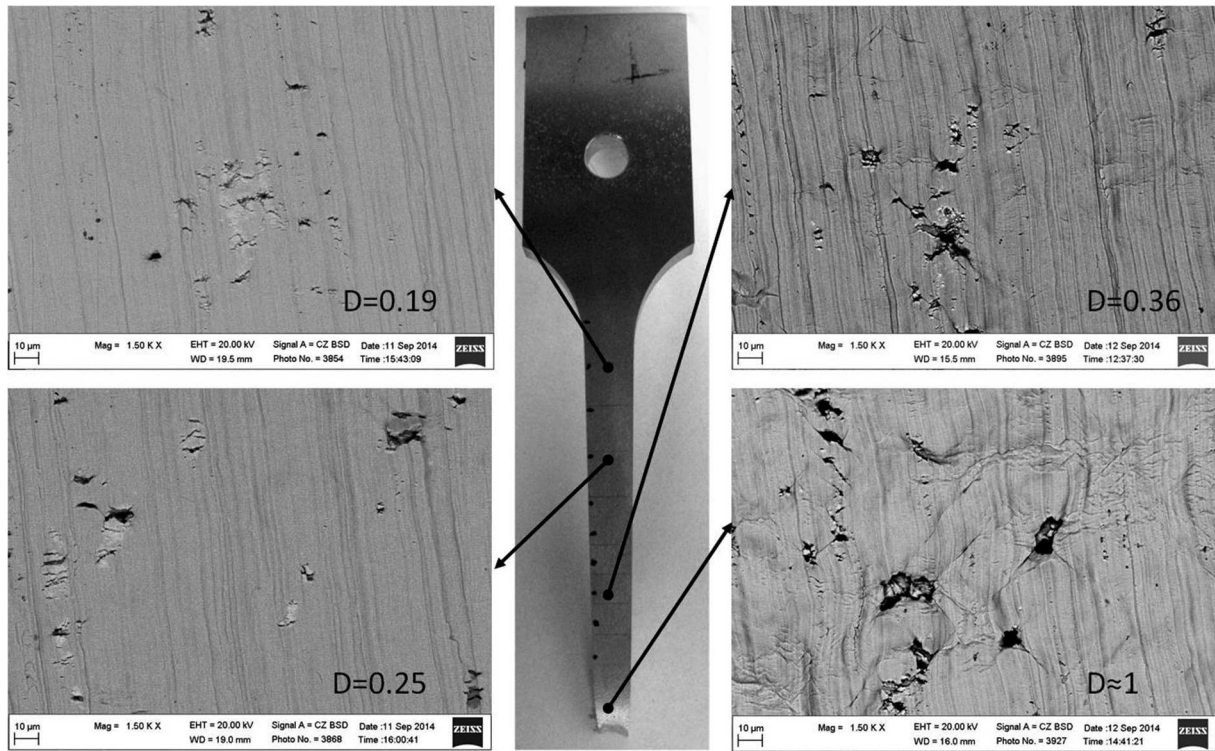


Fig. 5. SEM pictures of the specimen surface

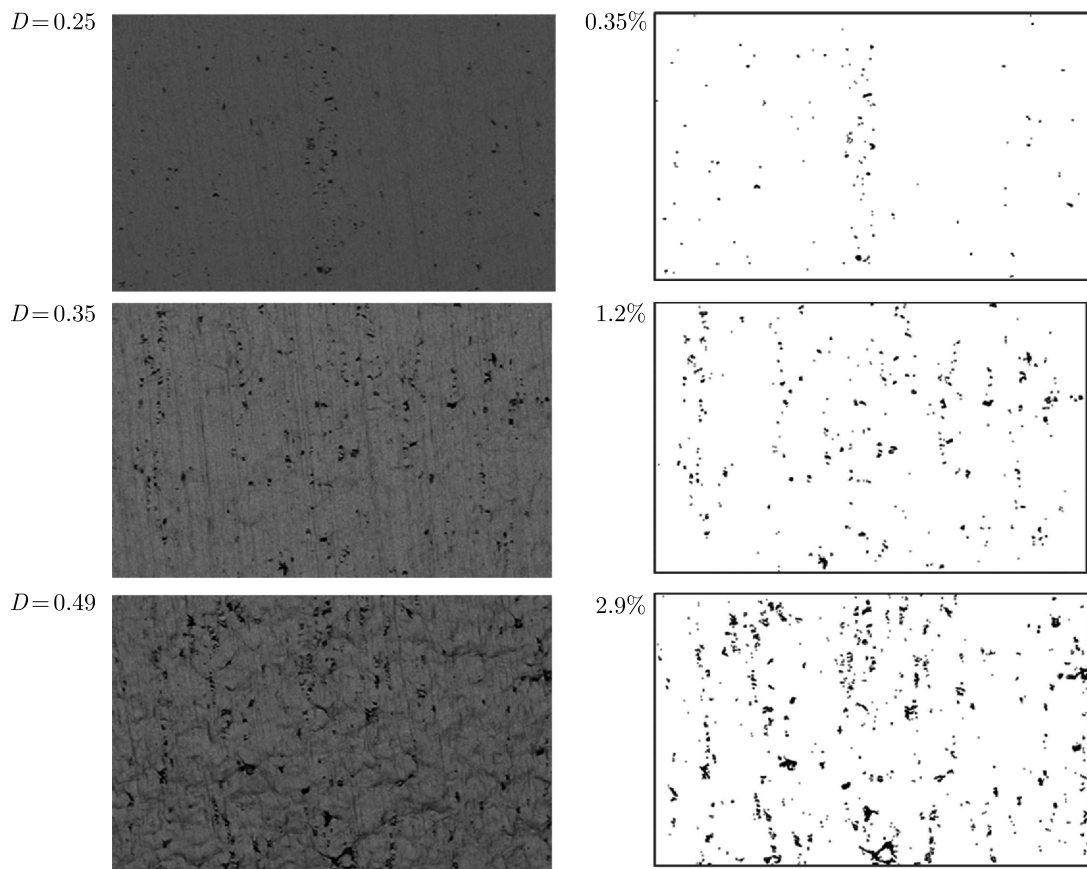


Fig. 6. Development of voids at the surface of the specimen: SEM pictures for the indicated damage degree (left side), corresponding processed pictures with voids patterns and surface void density indicated (right side)

Under the applied stress field, the debonding of the material at the phase interface develops into voids. Such voids can be seen at the surface of the specimen for consecutive phases of damage accumulation shown in Fig. 6 as dark spots.

SEM pictures taken with the use of BSE technique are shown on the left side of Fig. 6. Back Scattering Electron (BSE) technique allows reproduction of the specimen surface in the gray-scale. Lightness gray color corresponds to intensity of the back scattered electron beam making possible the detection of surface cracks and voids as dark spots. This picture is subsequently processed to obtain a black and white pattern of the material discontinuities. The first step of processing is modification of the color curve resulting in an increase in the picture contrast. Lightness and contrast of the picture is then adjusted to obtain a clear pattern of discontinuities. Finally, the picture is binarized (converted into black and white pixels) and the percentage of black pixels is calculated to obtain surface density of cracks (voids) S . The surface density of voids is used to calculate the void volume fraction assuming that the voids surface density is the same for three perpendicular planes (which is close to truth near the specimen surface) using the formula

$$f = S^{\frac{3}{2}} \quad (5.1)$$

The void volume fraction f is finally plotted as a function of the damage parameter – see Fig. 7. The power fit of data points is also shown in this figure together with the equation of the function used. This function can be used to calibrate the well known Gurson model of ductile fracture of elastic-plastic materials (Gurson, 1977).

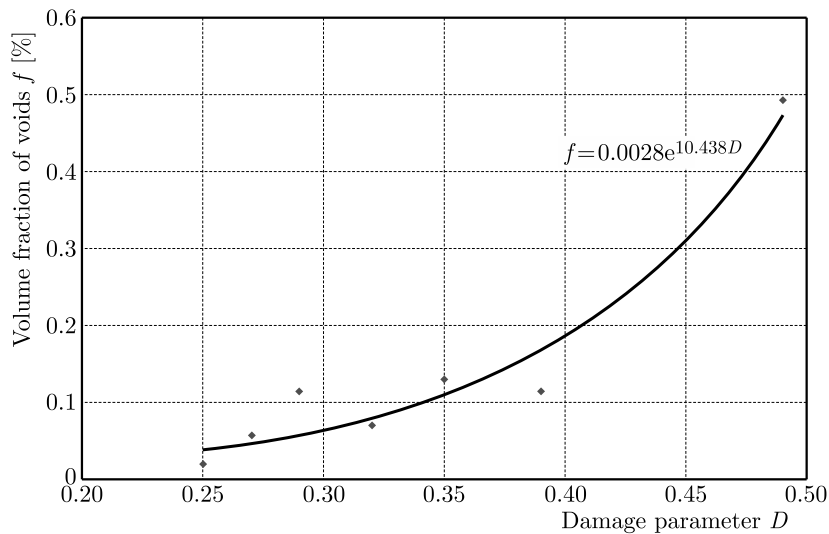


Fig. 7. Void volume fraction f at the surface of the specimen as a function of the damage parameter

The observations of the specimens surface were followed by analysis of the damage induced inside the gage part of the specimen. The specimen was cut along its axis, and metallographic samples were prepared to investigate the internal damage of the material. The samples were taken from locations close to cross sections of the gage part marked in Fig. 1 as the points of plastic strain measurements. SEM pictures of selected metallographic samples are shown in Fig. 8.

The pictures show hard inclusions in the ductile matrix at various stages of the deformation corresponding to the damage parameter indicated in the upper right corner. For a low value of the damage parameter ($D < 0.25$), no damage in form of physical discontinuities of the material exists. The debonding at the phase interface was detected at the deformation corresponding to the damage parameter 0.28. In Fig. 8, the area of debonding is surrounded by a circle. This

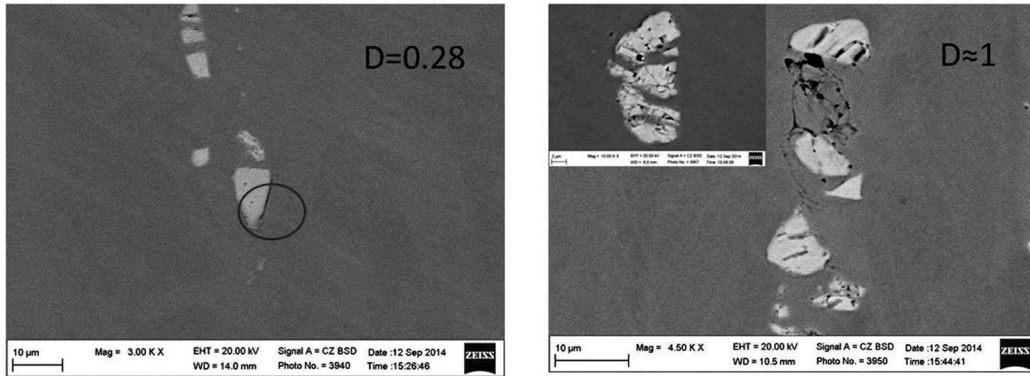


Fig. 8. SEM pictures of the metallographic samples

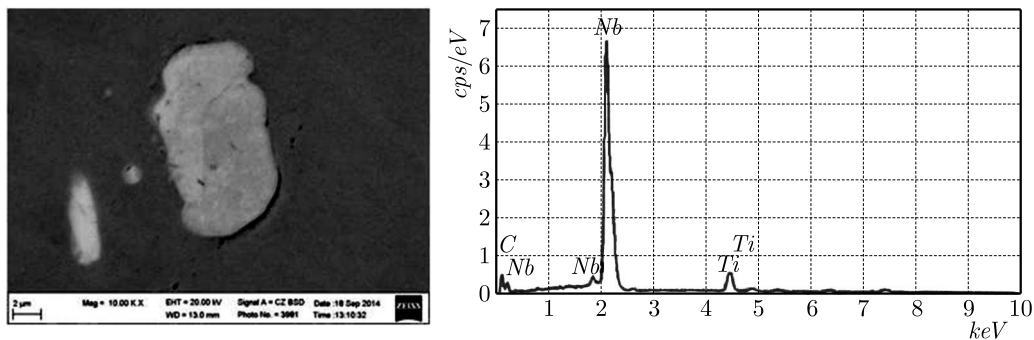


Fig. 9. Debonding of the hard inclusion and its chemical composition

process continues to the stage of advanced deformation, later associated by cracking of hard inclusions and, finally, also cracking of the ductile matrix. In Fig. 9, we can see a SEM picture corresponding to the value of 0.33 of the damage parameter with clearly visible debonding at the phase interface. On the left the chemical composition of hard inclusion can be seen. This hard inclusion can be identified as niobium carbide, and its interface with the ductile matrix seems to be the weakest point of the investigated alloy.

This observation is confirmed in Fig. 10, where the fractured surface of the specimen is shown. The analysis of chemical composition at the bottom of dimple of the fracture surface indicated the same phase, the niobium carbide hard inclusion.

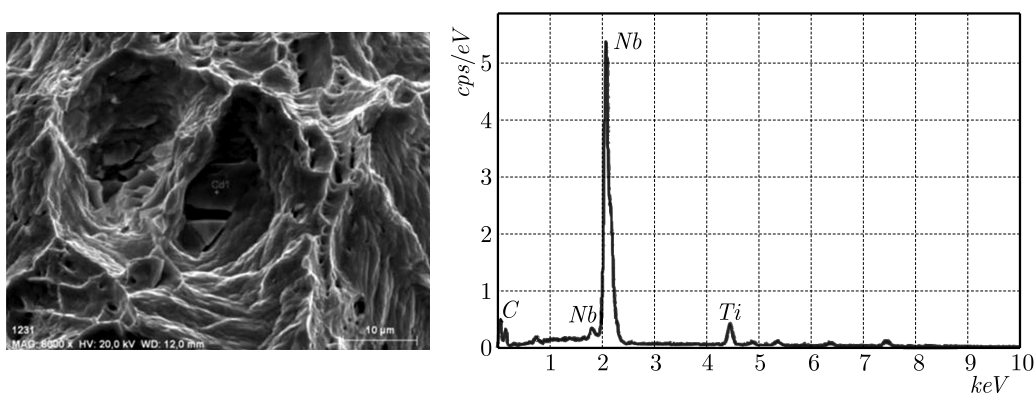


Fig. 10. Fracture surface with niobium carbide at the bottom of dimple

It has to be noticed that, in the case of internal damage analysis, the detection of damage in form of plastic deformation associating cracking on the interface between hard inclusions and the matrix is much more difficult than that on the surface. Also, the debonding can be detected

later than in the case of the surface of the specimen. Taking this fact into account, we have to notice that the detection of damage is much easier on the specimen surface than inside the material. Since the deformation around surface cracks forms a “orange skin”, the magnitude of this deformation should be in some proportion with progressing damage of the material. The easiest way to quantify such kind of deformation is to measure roughness of the specimen surface. The results of measurements are shown in Fig. 11. The correlation of the measured arithmetic average of the absolute values of the amplitude R_a and the damage parameter D can be easily seen. The linear fit of the data with the equation is also shown in this figure.

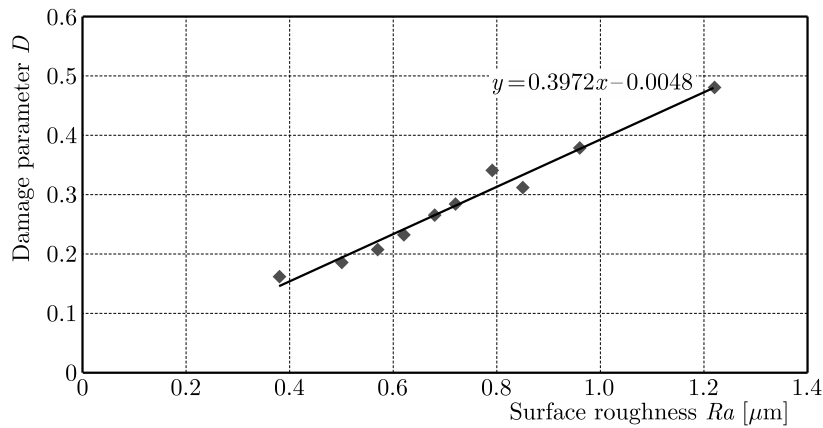


Fig. 11. Correlation between the damage parameter and surface roughness

Assuming that surface roughness increases with the progressing deformation, we can use this parameter as the relative damage indicator. The general formula for damage parameter calculation using the relative damage indicator is as follows

$$D = \frac{X - X_0}{X_f - X_0} \quad (5.2)$$

where X_0 , X and X_f stands for the initial, actual and final value of the damage indicator. To calculate the damage parameter for the deformed material, we have to measure the surface roughness R_a and use the following formula derived through linear fit of the data shown in Fig. 11

$$D = 0.4 R_a \quad (5.3)$$

It has to be stressed that this formula is valid only for the investigated material with a particular surface preparation (initial surface roughness) and for the load scheme applied (static tension). Extending this formula for other cases is not possible. Formula (5.3), however limited to the case of the deformation mode and the material used for presented investigations, is very easy to obtain using results of a simple test. The most important feature of the proposed method is the fact that using such a simple testing technique one can find correlation between damage of the material and plastic deformation, and what follows, one can identify the damage mechanism and critical deformation corresponding to the initiation of material discontinuities.

6. Conclusions

A simple experiment performed on the proposed specimen with a variable gage part allows observation of the damage mechanism of a deformed Inconel718 superalloy. Structural changes can be related to progressing deformation of the gage part of the specimen. The changes have

been observed on the surface of the specimen as well as inside of the gage part. The following conclusions can be drawn:

- The accumulated equivalent plastic strain can be used for quantifying damage of the material subject to simple and complex stress states. Using plastic deformation as the cumulative damage indicator, we can identify the critical value of the damage parameter corresponding to the most important events during deformation (e.g. initiation of material discontinuities). This task is much simplified by using the proposed in this paper investigation technique.
- The debonding of hard inclusions (niobium carbide) at their interface with the ductile matrix has been identified as the main damage mechanism for the investigated Inconel718 superalloy. This phenomenon starts early at the specimen surface, this moment corresponds to the value of the damage parameter $D = 0.2$. Inside the material, the debonding starts when the damage parameter reaches approximately 0.3.
- Cracks at the surface of the specimen are associated with large plastic deformation around their tip. This deformation is clearly visible on SEM pictures showing the specimen surface at various stages of deformation as the pattern of initially straight lines remaining after finishing (grinding).
- Observations of the specimen surface with the use of BSE technique have been used to determine the surface density of material discontinuities. Digital picture processing procedure has been used to calculate the value of this parameter. The surface density of discontinuities (voids) has been then recalculated into the void volume fraction near the specimen surface. The relationship between the void volume fraction and the damage parameter can be used to calibrate the model of material ductile fracture (Gurson, 1977).
- Deformation of the specimen surface allows measurement of the damage parameter using the surface roughness as the relative damage indicator. Derived relationship (5.2) allows estimation of the damage parameter value. This method, however, works only for a particular loading scheme (in the case of presented investigations it has been tension) and for a particular material and surface finishing.

References

1. BAO Y., WIERZBICKI T., 2004, On fracture locus in the equivalent strain and stress triaxiality space, *International Journal of Mechanical Sciences*, **46**, 81-89
2. GANJANI M., 2013, Identification of damage parameters and plastic properties of an anisotropic damage model by micro-hardness measurements, *International Journal of Damage Mechanics*, **22**, 8, 1089-1108
3. GURSON A.L., 1977, Porous rigid-plastic materials containing rigid inclusions – yield function, plastic potential, and void nucleation, *Fracture*, **2**, ICF4, Waterloo, Canada
4. HALL J.A., 1998, Fatigue crack initiation in alpha-beta titanium alloys, *International Journal of Fatigue*, **19**, Supp. **1**, S23-S37
5. JOHNSON G.R., 1980, Materials characterization for computations involving severe dynamic loading, *Proceedings of Army Symposium of Solid Mechanics*, Cape Cod, Mass., 62-67
6. MINER M.A., 1945, Cumulative damage in fatigue, *Journal of Applied Mechanics*, **67**, A159-A164
7. NIAZI M.S., WISSELINK H.H., MEINDERS V.T., VAN DEN BOOGAARD A.H., 2013, Material-induced anisotropic damage in DP600, *International Journal of Damage Mechanics*, **22**, 7, 1039-1070

8. NIELSEN K.L., HUTCHINSON J.W., 2012, Cohesive traction-separation laws for tearing of ductile metal plates, *International Journal of Impact Engineering*, **48**, 15-23
9. PALMGREN A., 1924, Die Lebensdauer von Kugellagern, *Verfahrenstechnik*, Berlin, **68**, 339-341
10. PETERSMEIER T., MARTIN U., EIFLER D., OETTEL H., 1998, Cyclic fatigue loading and characterization of dislocation evolution in the ferritic steel X22CrMoV121, *International Journal of Fatigue*, **20**, 3, 251-255
11. SHEN J., MAO J., BOILEAU J., CHOW C.L., 2014, Material damage evaluation with measured microdefects and multiresolution numerical analysis, *International Journal of Damage Mechanics*, **23**, 4, 537-566
12. SOCHA G., 2003, Experimental investigations of fatigue cracks nucleation, growth and coalescence in structural steel, *International Journal of Fatigue*, **25**, 2, 139-147
13. SOCHA G., 2004, Prediction of the fatigue life on the basis of damage progress rate curves, *International Journal of Fatigue*, **26**, 4, 339-347
14. SOCHA G., DIETRICH L., 2012, Accumulation of damage in A336 GR5 structural steel subject to complex stress loading, *Strain*, **48**, 279-285
15. SOCHA G., DIETRICH L., 2014, A fatigue damage indicator parameter for P91chromium-molybdenum alloy steel and fatigue pre-damaged P54T carbon steel, *Fatigue and Fracture of Engineering Materials and Structures*, **37**, 195-205
16. SOCHA G., DIETRICH L., 2016, Deformation based fatigue damage accumulation model, *Solid State Phenomena*, **240**, 128-133
17. SOCHA G., MADEJSKI B., KRYSZTOFIK J., CZARNEWICZ S., 2014, Test method of structural damages caused by permanent deformation of the alloy in the test sample by tensile test and the sample to test damage of the alloy structure, Patent pending no. P-409294, Urząd Patentowy RP
18. YANG B., FENG M.F., ZHAI Z.Y., 2010, Evolutionary statistical character of fatigue damage of smooth surface samples by an effective short fatigue crack criterion, *International Journal of Damage Mechanics*, **19**, 211-231
19. YANG L., FATEMI A., 1998, Cumulative fatigue damage mechanisms and quantifying parameters: a literature review, *Journal of Testing and Evaluation*, *JTEVA*, **26**, 2, 89-100
20. ZHANG M., YANG P., TAN Y., 1999, Micromechanisms of fatigue crack nucleation and short crack growth in a low carbon steel under low cycle impact fatigue loading, *International Journal of Fatigue*, **21**, 823-830

Manuscript received September 3, 2015; accepted for print March 10, 2016

COMPARISON OF NATURAL COMPLEMENT FORMULATIONS FOR MULTIBODY DYNAMICS

MARCIN PEKAL, JANUSZ FRĄCZEK

Warsaw University of Technology, Institute of Aeronautics and Applied Mechanics, Poland

e-mail: mpekal@meil.pw.edu.pl; jfraczek@meil.pw.edu.pl

The main aim of this paper is to compare the effectiveness of numerical techniques used for spatial multibody dynamics simulation by applying the natural complement method. In the paper, seven numerical schemes are considered: zero eigenvalue formulation, Pseudo Upper Triangular Decomposition, Schur decomposition, Singular Value Decomposition, QR decomposition, coordinate partitioning and Wang-Huston formulation. In order to illustrate the effectiveness of these schemes, two McPherson struts are considered. Simulations are performed with four error tolerance values and for three stabilization cases. Some suggestions on possible applications of the selected methods are formulated.

Keywords: multibody dynamics, numerical methods, spatial systems

1. Introduction

The equations of motion of multibody systems may be written using many different coordinate sets (de Jalón and Bayo, 1994; Malczyk and Frączek, 2012). However, the most frequently used are absolute, natural and relative coordinates. Absolute and natural coordinates constitute redundant sets of coordinates hence a system of equations of motion with constraints has to be considered. Such a system is the set of differential-algebraic equations (DAEs) with differential index at most equal to 3. Numerical methods used to solve DAEs are still under intensive development and the effective integration procedures are less well-known for them than for ordinary differential equations (ODEs) (Kunkel and Mehrman, 2006). Note that there exist publications about differential equations in mechanical systems, e.g. (Awrejcewicz, 2014; Eich-Soellner and Führer, 1998).

Many integration methods can be used to solve DAEs (de Jalón and Bayo, 1994; Haug, 1989). A large group of these methods transforms the equations of motion described in redundant coordinates into equations written in the minimal set of coordinates. To perform this transformation, the null space base of the constraints manifold is built and afterwards, equations of motion are expressed in this base. Null space base vectors are represented by the orthogonal complementary matrix. Finally, the set of ODEs is obtained, which can be solved efficiently. There are several methods proposed in literature to accomplish the orthogonal complement.

The main objective of this paper is to compare numerical schemes for DAEs based on or equivalent to the orthogonal complement methods using two examples. The following methods are considered: zero eigenvalue formulation, Pseudo Upper Triangular Decomposition (PUTD), Schur decomposition, Singular Value Decomposition (SVD), QR decomposition, coordinate partitioning and Wang-Huston formulation. Hereafter, spatial rigid multibody systems described with the absolute coordinates are considered. The Euler angles (consecutive rotations about the z , x and z axes) are used for the orientation description and consequently, the mass matrix is nonsingular. For the chosen coordinates set, the resulting equations of motion are in the form of differential-algebraic equations that consist of differential equations of motion and algebraic

equations of constraints. Note that there are also papers analyzing impact, e.g. (Awrejcewicz *et al.*, 2003, 2004; Awrejcewicz and Kudra, 2005) or contact, e.g. (Awrejcewicz and Kudra, 2014), but these phenomena are not examined here.

In order to compare the efficiency of the examined methods, two types of McPherson struts are analyzed. The first model of the strut has no redundant constraints, while in the second mechanism the redundancy is taken into consideration (Wojtyra and Frączek, 2013). For all the considered methods, simulations are performed with four values of the error tolerances and for three constraint stabilization approaches (with no stabilization of the constraints, with the Baumgarte stabilization and with the position constraints stabilization using the Newton-Raphson method). It is worth noting that similar comparisons were already performed by other authors (Mariti *et al.*, 2011, 2010; Pennestrì and Valentini, 2007) as well as in (Pękal, 2012). Therefore, the comparison with the previous publications (Mariti *et al.*, 2011, 2010) is also performed.

2. Spatial system dynamics

Multibody dynamics description presented in this Section is based on the absolute coordinate formulation and appears in, e.g. (Frączek and Wojtyra, 2008; de Jalón and Bayo, 1994; Haug, 1989).

The vector of the absolute generalized coordinates can be written as (Haug, 1989): $\mathbf{q}_{n \times 1} = [\mathbf{q}_1^T \ \mathbf{q}_2^T \ \cdots \ \mathbf{q}_N^T]^T = [q_1 \ q_2 \ \cdots \ q_n]^T$, where N is the number of bodies and n is the number of generalized coordinates of the multibody system. Moreover, the equation of motion has the following form (de Jalón and Bayo, 1994; Haug, 1989)

$$\mathbf{M}\ddot{\mathbf{q}} + \Phi_{\mathbf{q}}^T \boldsymbol{\lambda} = \mathbf{Q}^e \quad (2.1)$$

where \mathbf{M} is the mass matrix, $\Phi_{\mathbf{q}}$ is the Jacobian matrix of constraints (see Eq. (2.3)), $\boldsymbol{\lambda}$ is the Lagrange multipliers vector and \mathbf{Q}^e is the generalized force vector. Matrix equation (2.1) is the system of n equations with $n + m$ unknowns ($\ddot{\mathbf{q}}_{n \times 1}$ and $\boldsymbol{\lambda}_{m \times 1}$), where m is the number of Lagrange multipliers. To solve this system, the additional m constraint equations should be introduced as (de Jalón and Bayo, 1994; Haug, 1989)

$$\Phi_{m \times 1} = \Phi(\mathbf{q}, t) = \mathbf{0} \quad (2.2)$$

where t denotes time. After differentiating (2.2) over time, we obtain (Haug, 1989)

$$\dot{\Phi} = \Phi_{\mathbf{q}} \dot{\mathbf{q}} + \Phi_t = \mathbf{0} \quad (2.3)$$

Differentiation of Eq. (2.3) once again over time yields (Haug, 1989)

$$\ddot{\Phi} = \Phi_{\mathbf{q}} \ddot{\mathbf{q}} + (\Phi_{\mathbf{q}} \dot{\mathbf{q}})_{\mathbf{q}} \dot{\mathbf{q}} + 2\Phi_{\mathbf{q}t} \dot{\mathbf{q}} + \Phi_{tt} = \Phi_{\mathbf{q}} \ddot{\mathbf{q}} - \boldsymbol{\Gamma} = \mathbf{0} \Rightarrow \Phi_{\mathbf{q}} \ddot{\mathbf{q}} = \boldsymbol{\Gamma} \quad (2.4)$$

Eventually, Eqs. (2.1) and (2.4) can be written as index-1 DAEs (de Jalón and Bayo, 1994; Haug, 1989)

$$\begin{bmatrix} \mathbf{M} & \Phi_{\mathbf{q}}^T \\ \Phi_{\mathbf{q}} & \mathbf{0} \end{bmatrix} \begin{bmatrix} \ddot{\mathbf{q}} \\ \boldsymbol{\lambda} \end{bmatrix} = \begin{bmatrix} \mathbf{Q}^e \\ \boldsymbol{\Gamma} \end{bmatrix} \quad (2.5)$$

where the coefficient matrix is called the augmented matrix (Negrut *et al.*, 1997; de Jalón and Gutiérrez-López, 2013). It should be pointed out that Eqs. (2.2), (2.3) and (2.4) are analytically equivalent. However, the direct numerical solution of Eq. (2.5) does not often provide the fulfilment of position (2.2) and velocity (2.3) constraints and may cause the solution drift. Therefore,

the stabilization methods are often employed. One of the simplest is the Baumgarte stabilization method (Baumgarte, 1972). In this method, the $\mathbf{\Gamma}$ vector from acceleration constraints is replaced by the following expression: $\bar{\mathbf{\Gamma}} = \mathbf{\Gamma} - 2\hat{\alpha}\dot{\mathbf{\Phi}} - \hat{\beta}^2\mathbf{\Phi}$, where $\hat{\alpha}$, $\hat{\beta}$ are the Baumgarte stabilization parameters. The value of these parameters is often assumed as $\hat{\alpha} = \hat{\beta} \in \langle 1, 20 \rangle$ (de Jalón and Bayo, 1994).

It is also possible to stabilize the system using the well-known Newton-Raphson method (Frączek and Wojtyra, 2008; Haug, 1989). The \mathbf{q} vector is corrected when constraints norm (2.2) is greater than the assumed tolerance.

3. Orthogonal complement methods

The equations of motion of the multibody system presented previously constitute a set of DAEs. In the present Section, those equations are transformed into ODEs by means of the orthogonal complement. To perform the transformation, the projection matrix \mathbf{P} that is orthogonal to the constraint Jacobian matrix must be computed. The application of the \mathbf{P} matrix leads to direct removal of the Lagrange multipliers from the considered system (de Jalón and Bayo, 1994).

3.1. Orthogonal complement for rheonomic constraints

The following statements are derived for systems without redundant constraints and then generalized to the case of redundant multibody systems. The procedure for finding orthogonal complement matrices is presented in (de Jalón and Bayo, 1994; Mariti *et al.*, 2011, 2010; Pennestrì and Valentini, 2007; Pečkal, 2012; de Jalón and Gutiérrez-López, 2013).

Assume that the independent velocity vector $\dot{\mathbf{v}}$ can be obtained by the projection of the generalized velocity vector into the rows of the constant matrix \mathbf{B} (de Jalón and Bayo, 1994; Pennestrì and Valentini, 2007)

$$\dot{\mathbf{v}}_{s \times 1} = \mathbf{B}_{s \times n} \dot{\mathbf{q}}_{n \times 1} \quad (3.1)$$

where s is the number of independent coordinates.

Combining Eqs. (3.1) and (2.3) yields (de Jalón and Bayo, 1994; Pennestrì and Valentini, 2007)

$$\begin{bmatrix} \mathbf{\Phi}_q \\ \mathbf{B} \end{bmatrix} \dot{\mathbf{q}} = \mathbf{X} \dot{\mathbf{q}} = \begin{bmatrix} -\mathbf{\Phi}_t \\ \dot{\mathbf{v}} \end{bmatrix} \quad (3.2)$$

If \mathbf{X} is nonsingular, the inversion of this matrix exists and can be presented in the form: $\mathbf{X}^{-1} = [\mathbf{S} \ \mathbf{P}]$, where \mathbf{P} is the projection matrix and \mathbf{S} is the matrix which contains the remaining columns. Hence (de Jalón and Bayo, 1994; Pennestrì and Valentini, 2007)

$$\dot{\mathbf{q}} = \mathbf{X}^{-1} \begin{bmatrix} -\mathbf{\Phi}_t \\ \dot{\mathbf{v}} \end{bmatrix} = [\mathbf{S}_{n \times m} \ \mathbf{P}_{n \times s}] \begin{bmatrix} -\mathbf{\Phi}_t \\ \dot{\mathbf{v}} \end{bmatrix} = -\mathbf{S}\mathbf{\Phi}_t + \mathbf{P}\dot{\mathbf{v}} \quad (3.3)$$

Orthogonality of the \mathbf{X} matrix gives two orthogonality conditions in the form (de Jalón and Gutiérrez-López, 2013; Pennestrì and Valentini, 2007)

$$(\mathbf{\Phi}_q)_{m \times n} \mathbf{P}_{n \times s} = \mathbf{0}_{m \times s} \quad \mathbf{B}_{s \times n} \mathbf{P}_{n \times s} = \mathbf{I}_{s \times s} \quad (3.4)$$

The projection matrix \mathbf{P} can be used to eliminate the Lagrange multipliers.

Differentiating Eq. (3.2) and using Eq. (2.4) yields (de Jalón and Bayo, 1994; Pennestrì and Valentini, 2007)

$$\mathbf{X} \ddot{\mathbf{q}} = \begin{bmatrix} \mathbf{\Gamma} \\ \ddot{\mathbf{v}} \end{bmatrix} \Rightarrow \ddot{\mathbf{q}} = \mathbf{X}^{-1} \begin{bmatrix} \mathbf{\Gamma} \\ \ddot{\mathbf{v}} \end{bmatrix} = [\mathbf{S} \ \mathbf{P}] \begin{bmatrix} \mathbf{\Gamma} \\ \ddot{\mathbf{v}} \end{bmatrix} = \mathbf{S}\mathbf{\Gamma} + \mathbf{P}\ddot{\mathbf{v}} \quad (3.5)$$

Substituting Eq. (3.5) into Eq. (2.1) gives

$$\mathbf{M}(\mathbf{S}\boldsymbol{\Gamma} + \mathbf{P}\ddot{\mathbf{v}}) + \boldsymbol{\Phi}_{\mathbf{q}}^{\mathbf{T}}\boldsymbol{\lambda} = \mathbf{Q}^e \quad (3.6)$$

In order to eliminate the Lagrange multipliers, left-multiplication of both sides of Eq. (3.6) by $\mathbf{P}^{\mathbf{T}}$ is required. Afterwards, the use of transposition of Eq. (3.4)₁ yields (de Jalón and Bayo, 1994; de Jalón and Gutiérrez-López, 2013)

$$\mathbf{P}^{\mathbf{T}}\mathbf{M}(\mathbf{S}\boldsymbol{\Gamma} + \mathbf{P}\ddot{\mathbf{v}}) + \mathbf{0}\boldsymbol{\lambda} = \mathbf{P}^{\mathbf{T}}\mathbf{Q}^e \Leftrightarrow \mathbf{P}^{\mathbf{T}}\mathbf{M}\mathbf{P}\ddot{\mathbf{v}} = \mathbf{P}^{\mathbf{T}}\mathbf{Q}^e - \mathbf{P}^{\mathbf{T}}\mathbf{M}\mathbf{S}\boldsymbol{\Gamma} \quad (3.7)$$

Assuming $\ddot{\mathbf{v}}_{s \times 1} = \mathbf{0}$, $\mathbf{S}\boldsymbol{\Gamma}$ can be obtained from Eq. (3.5) as (de Jalón and Bayo, 1994; Pennestrì and Valentini, 2007)

$$\mathbf{S}\boldsymbol{\Gamma} = \mathbf{X}^{-1} \begin{bmatrix} \boldsymbol{\Gamma} \\ \mathbf{0} \end{bmatrix} \quad (3.8)$$

The vector $\ddot{\mathbf{v}}$ is obtained from Eq. (3.7). Substituting this vector into Eq. (3.5) yields $\ddot{\mathbf{q}}$.

In the case of redundant systems, it is convenient to use the pseudoinverse matrix \mathbf{X}^+ instead of \mathbf{X}^{-1} . Therefore, the problem becomes an optimization task, whose result has the least square norm.

3.2. Derivation of the projection matrix

Methods that directly apply the projection matrix \mathbf{P} are introduced in the following.

3.2.1. Zero eigenvalue method

The first method uses the zero eigenvalue technique (Mariti *et al.*, 2011, 2010; Pennestrì and Valentini, 2007; Pełal, 2012; Walton and Steeves, 1969) which is based on the eigenvalue problem. The eigenvalue problem can be written in the form (FreeMat v4.1; Hartfiel, 2001)

$$\mathbf{A}\boldsymbol{\Psi} = \boldsymbol{\Psi}\boldsymbol{\Lambda} \quad (3.9)$$

where the matrix \mathbf{A} is a symmetrical matrix, $\boldsymbol{\Lambda}_{n \times n} = \text{diag}(\Lambda_1, \Lambda_2, \dots, \Lambda_n)$ contains eigenvalues and $\boldsymbol{\Psi}_{n \times n} = [\boldsymbol{\Psi}_1 \ \boldsymbol{\Psi}_2 \ \dots \ \boldsymbol{\Psi}_n]$ is the orthogonal modal matrix which contains the eigenvectors.

In order to determine the projection matrix \mathbf{P} , the symmetric matrix \mathbf{A} is considered as (Walton and Steeves, 1969; Pennestrì and Valentini, 2007)

$$\mathbf{A}_{n \times n} = \boldsymbol{\Phi}_{\mathbf{q}}^{\mathbf{T}}\boldsymbol{\Phi}_{\mathbf{q}} \quad (3.10)$$

Using this matrix, the following expression is obtained (Walton and Steeves, 1969; Pennestrì and Valentini, 2007)

$$\boldsymbol{\Psi}_{n \times n}^{\mathbf{T}}(\boldsymbol{\Phi}_{\mathbf{q}}^{\mathbf{T}})_{n \times m}(\boldsymbol{\Phi}_{\mathbf{q}})_{m \times n}\boldsymbol{\Psi}_{n \times n} = \boldsymbol{\Lambda}_{n \times n} \quad (3.11)$$

where $\boldsymbol{\Lambda}$ is unique and contains non-negative eigenvalues. Assume that $\Lambda_1 \leq \Lambda_2 \leq \dots \leq \Lambda_n$, then the possible zero eigenvalues have the lowest indices. Moreover, the number of positive eigenvalues is equal to the rank r of the Jacobian matrix. Therefore, $s = n - r$ eigenvalues are equal to zero. These eigenvalues correspond to rigid body motion, so their number is equal to the number of degrees of freedom (DOFs) of the system. Consequently, the system has s independent and $r = n - s$ dependent coordinates.

Assuming (Walton and Steeves, 1969)

$$(\boldsymbol{\Phi}_{\mathbf{q}})_{m \times n}\boldsymbol{\Psi}_{n \times n} = \mathbf{D}_{m \times n} \quad (3.12)$$

Equation (3.11) can be written as (Walton and Steeves, 1969)

$$\mathbf{D}^T \mathbf{D} = \mathbf{\Lambda} \quad (3.13)$$

The order of the eigenvalues is opposite to the sequence form (Walton and Steeves, 1969), thus

$$\mathbf{D}_{m \times n} = \begin{bmatrix} \mathbf{0}_{m \times s} & \bar{\mathbf{D}}_{m \times (n-s)} \end{bmatrix} \quad (3.14)$$

hence (Pennestrì and Valentini, 2007)

$$\Phi_{\mathbf{q}_{m \times n}} \Psi_{n \times s}^1 = \mathbf{0}_{m \times s} \quad (3.15)$$

where $\Psi_{n \times s}^1$ is the matrix created from the first s columns of the modal matrix, i.e. columns which correspond to the zero eigenvalues.

Note that equation (3.15) satisfies first orthogonality condition (3.4)₁, hence: $\mathbf{P} = \Psi_{n \times s}^1$. Moreover, the modal matrix is orthogonal so condition (3.4)₂ is fulfilled for: $\mathbf{B} = \mathbf{P}^T$.

3.2.2. Schur decomposition method

The description of the Schur decomposition method can be found in (Golub and Loan, 1996; Hartfiel, 2001; Kincaid and Cheney, 2002; Mariti *et al.*, 2011, 2010; Pennestrì and Valentini, 2007; Peçkal, 2012). This decomposition is based on the fact that every square matrix \mathbf{A} can be presented in the form (Golub and Loan, 1996)

$$\mathbf{U}^H \mathbf{A} \mathbf{U} = \mathbf{T} = \mathbf{\Lambda} + \mathbf{N} \quad (3.16)$$

where \mathbf{U} is a unitary matrix, \mathbf{U}^H denotes conjugate transposition of \mathbf{U} and \mathbf{T} is a block triangular matrix, and \mathbf{N} is strictly the upper triangular matrix.

Note that the orthogonal matrix is a particular case of the unitary matrix for real numbers, thus (Golub and Loan, 1996)

$$\mathbf{U}^T \mathbf{A} \mathbf{U} = \mathbf{\Lambda} + \mathbf{N} \quad (3.17)$$

Assuming the \mathbf{A} according to Eq. (3.10) and using the fact that the \mathbf{A} is normal, it is possible to write (Golub and Loan, 1996)

$$\mathbf{U}^T \mathbf{A} \mathbf{U} = \mathbf{\Lambda} \quad (3.18)$$

Note that this is analogous to (3.11). Hence, it is possible to follow as for the zero eigenvalue method described in Section 3.2.1. Eventually, the following condition is get (Pennestrì and Valentini, 2007)

$$(\Phi_{\mathbf{q}})_{m \times n} \mathbf{U}_{n \times s}^1 = \mathbf{0}_{m \times s} \quad (3.19)$$

where \mathbf{U}^1 is the submatrix of \mathbf{U} (selected analogously to Ψ^1). Therefore, first orthogonality condition (3.4)₁ is fulfilled when: $\mathbf{P} = \mathbf{U}_{n \times s}^1$, while second orthogonality condition (3.4)₂ is satisfied for: $\mathbf{B} = \mathbf{P}^T$. Since the Schur decomposition method is equivalent to the zero eigenvalue method, these approaches are treated as one in the following.

3.2.3. PUTD method

The Pseudo Upper Triangular Decomposition method has two variants and their description can be found in (Amirouche, 2006; Ider and Amirouche, 1988; Mariti *et al.*, 2011, 2010; Ostalczyk, 2008; Pennestrì and Valentini, 2007; Pękal, 2012). The first type uses the Householder transformation and the second uses the Gauss elimination.

The transformation matrix \mathbf{H} is defined first. Using this matrix, the $\Phi_{\mathbf{q}}^T$ matrix can be transformed into the upper trapezoidal form \mathbf{Z} (in particular into the upper triangular form) as (Amirouche, 2006; Ider and Amirouche, 1988)

$$\mathbf{H}_{n \times n}^T (\Phi_{\mathbf{q}}^T)_{n \times m} = \mathbf{Z}_{n \times m} \quad (3.20)$$

where \mathbf{H} matrix can be obtained using the Householder transformation (the method denoted as PUTD-H) or the Gauss elimination (the method denoted as PUTD-G).

The matrix orthogonal to the \mathbf{Z} is found in the following step. This matrix can be computed using the Gram-Schmidt orthogonalization of the upper-triangularized Jacobian matrix, which gives an identity matrix \mathbf{D} (Amirouche, 2006). After this, the submatrix of \mathbf{D} is taken as (Pennestrì and Valentini, 2007)

$$\mathbf{D}_{2(n-r) \times n} = \begin{bmatrix} \mathbf{0}_{(n-r) \times r} & \mathbf{I}_{(n-r) \times (n-r)} \end{bmatrix} \quad (3.21)$$

thus (Pennestrì and Valentini, 2007)

$$\mathbf{D}_{2(n-r) \times n} \mathbf{H}_{n \times n}^T (\Phi_{\mathbf{q}}^T)_{n \times m} = \mathbf{0}_{(n-r) \times m} \quad (3.22)$$

which after transposing gives

$$(\mathbf{D}_2 \mathbf{H}^T \Phi_{\mathbf{q}}^T)^T = \Phi_{\mathbf{q}} (\mathbf{D}_2 \mathbf{H}^T)^T = \Phi_{\mathbf{q}} (\mathbf{H} \mathbf{D}_2^T) = \mathbf{0}_{m \times (n-r)} \quad (3.23)$$

Comparing Eqs. (3.23) and (3.4)₁ yields: $\mathbf{P} = \mathbf{H} \mathbf{D}_2^T$, while (3.4)₂ is fulfilled when: $\mathbf{B} = \mathbf{P}^T$, what is consistent with Pennestrì and Valentini (2007).

Considering the redundant systems, Eq. (3.21) is fulfilled when the redundant constraints are at the end of vector (2.2). It is not the general case. This problem can be solved by the Gauss-Jordan elimination with partial pivoting of the transposed Jacobian matrix. Using this elimination, the position of the independent constraints in the Jacobian matrix is obtained. Thus, it is possible to move dependent constraints at the end of the constraints set. Moreover, the problem of redundant constraints can be also solved by the manual setting of the constraints in Eq. (2.2) during the preprocessing stage. However, this simple approach can be used only for small systems.

In the implementation, the method based on the Gauss-Jordan elimination is used to detect redundant constraints. The choice of the independent constraints is done only once at the beginning of simulation. It should be noted that in some cases the coordinate partition must be done more frequently due to the loss of independence of the chosen coordinates.

3.2.4. SVD method

The method using singular value decomposition is described in (Mani *et al.*, 1985; Mariti *et al.*, 2011, 2010; Pennestrì and Valentini, 2007; Pękal, 2012). It uses the decomposition which can be written in the following form (Pennestrì and Valentini, 2007)

$$(\Phi_{\mathbf{q}}^T)_{n \times m} = \mathbf{W}_{n \times n} \mathbf{L}_{n \times m} \mathbf{V}_{m \times m}^T \quad (3.24)$$

where the matrices \mathbf{W} and \mathbf{V} are orthogonal, and \mathbf{L} includes singular values of the transposed Jacobian matrix on its diagonal. Assume that m is the total number of the eigenvalues of the $\Phi_{\mathbf{q}}^T$

and the rank of the Jacobian matrix r is equal to the number of nonzero eigenvalues. Thus, the decomposition can be written as (Pennestrì and Valentini, 2007)

$$(\Phi_{\mathbf{q}}^T)_{n \times m} = \begin{bmatrix} (\mathbf{W}_d)_{n \times r} & (\mathbf{W}_i)_{n \times (n-r)} \end{bmatrix} \begin{bmatrix} \Lambda_{r \times m} \\ \mathbf{0}_{(n-r) \times m} \end{bmatrix} \mathbf{V}_{m \times m}^T = \mathbf{W}_d \Lambda \mathbf{V}^T \quad (3.25)$$

Left-multiplication of Eq. (3.25) by \mathbf{W}_i^T yields (Pennestrì and Valentini, 2007)

$$\mathbf{W}_{i(n-r) \times n}^T (\Phi_{\mathbf{q}}^T)_{n \times m} = \mathbf{W}_i^T \mathbf{W}_d \Lambda \mathbf{V}^T \quad (3.26)$$

Using orthogonality of the matrix \mathbf{W} gives (Pennestrì and Valentini, 2007)

$$\mathbf{W}_i^T \mathbf{W}_d = \mathbf{0} \quad \mathbf{W}_i^T \mathbf{W}_i = \mathbf{I} \quad (3.27)$$

hence (Pennestrì and Valentini, 2007)

$$\mathbf{W}_{i(n-r) \times n}^T (\Phi_{\mathbf{q}}^T)_{n \times m} = \mathbf{0}_{(n-r) \times m} \Rightarrow \Phi_{\mathbf{q}} \mathbf{W}_i = \mathbf{0}_{m \times (n-r)} \quad (3.28)$$

Eventually, first orthogonality condition (3.4)₁ is met for (Pennestrì and Valentini, 2007): $\mathbf{P} = \mathbf{W}_i$ and second condition (3.4)₂ is fulfilled when (Pennestrì and Valentini, 2007): $\mathbf{B} = \mathbf{P}^T$.

3.2.5. QR decomposition method

The QR method is described in, e.g. (Kim and Vanderploeg, 1986; Mariti *et al.*, 2011, 2010; Pennestrì and Valentini, 2007; Peşkal, 2012). It is based on the QR decomposition described in details by Golub and Loan (1996). This decomposition takes the form (Kim and Vanderploeg, 1986)

$$\Phi_{\mathbf{q}}^T = \mathbf{Q} \mathbf{R} \quad (3.29)$$

where the matrix \mathbf{Q} is orthogonal and \mathbf{R} is upper trapezoidal or upper triangular in the particular case of the square decomposed matrix. The matrix \mathbf{R} can be written as (Pennestrì and Valentini, 2007)

$$\mathbf{R}_{n \times m} = \begin{bmatrix} (\mathbf{R}_1)_{r \times m} \\ \mathbf{0}_{(n-r) \times m} \end{bmatrix} \quad (3.30)$$

However, when the redundant systems are considered, this form of the \mathbf{R} matrix occurs only when the redundant constraints are placed at the end of constraints vector (2.2). There are several methods to achieve this, e.g. appropriate definition of the constraints vector, use of the Gauss-Jordan elimination with partial pivoting or application of the alternative version of the QR decomposition which can be written in the form (FreeMat v4.1; MATLAB®)

$$\Phi_{\mathbf{q}}^T \mathbf{E} = \mathbf{Q} \mathbf{R} \quad (3.31)$$

where \mathbf{E} is a permutation matrix, which allows the matrix \mathbf{R} to take the form from Eq. (3.30). Eventually, the QR decomposition of the transposed Jacobian matrix yields

$$(\Phi_{\mathbf{q}}^T)_{n \times m} \mathbf{E}_{m \times m} = \mathbf{Q}_{n \times n} \mathbf{R}_{n \times m} = \begin{bmatrix} \mathbf{Q}_{1_{n \times r}} & \mathbf{Q}_{2_{n \times (n-r)}} \end{bmatrix} \begin{bmatrix} \mathbf{R}_{1_{r \times m}} \\ \mathbf{0}_{(n-r) \times m} \end{bmatrix} = \mathbf{Q}_1 \mathbf{R}_1 \quad (3.32)$$

Left-multiplying Eq. (3.32) by the \mathbf{Q}_2^T gives

$$\mathbf{Q}_2^T \Phi_{\mathbf{q}}^T \mathbf{E} = \mathbf{Q}_2^T \mathbf{Q}_1 \mathbf{R}_1 \quad (3.33)$$

Using the orthogonality property of the \mathbf{Q} matrix yields (Pennestrì and Valentini, 2007)

$$\mathbf{Q}_2^T \mathbf{Q}_1 = \mathbf{0} \quad \mathbf{Q}_2^T \mathbf{Q}_2 = \mathbf{I} \quad (3.34)$$

Transposition of Eq. (3.33) using Eq. (3.34) gives

$$(\mathbf{Q}_2^T \Phi_q^T \mathbf{E})^T = \mathbf{E}^T \Phi_q \mathbf{Q}_2 = \mathbf{0} \quad (3.35)$$

Left-multiplying Eq. (3.35) by the permutation matrix yields

$$\Phi_q \mathbf{Q}_2 = \mathbf{0} \quad (3.36)$$

Thus, first orthogonality condition (3.4)₁ is fulfilled when: $\mathbf{P} = \mathbf{Q}_2$ and second orthogonality condition (3.4)₂ is met for: $\mathbf{B} = \mathbf{P}^T$.

3.3. Related methods

The following Section describes methods that do not use directly the projection matrix \mathbf{P} . Note that these methods are equivalent to the orthogonal complement methods. It was described by, e.g. de Jalón and Bayo (1994) in the case of the coordinate partitioning method and by Wang and Huston (1989) for the Wang-Huston formulation.

3.3.1. Coordinate partitioning method

The coordinate partitioning method is described in (de Jalón and Bayo, 1994; Mariti *et al.*, 2011, 2010; Pennestrì and Valentini, 2007; Pękal, 2012; Wehage and Haug, 1982).

The coordinates are partitioned into independent \mathbf{v} and dependent \mathbf{u} sets using, e.g. the Gauss-Jordan elimination with partial pivoting of the Jacobian matrix. Thus, according to the coordinate partitioning, the differential-algebraic equations of motion from Eq. (2.5) take the following form (these are dependences from Pennestrì and Valentini (2007), written in the matrix form)

$$\begin{bmatrix} \mathbf{M}^{uu} & \mathbf{M}^{uv} & \Phi_u^T \\ \mathbf{M}^{vu} & \mathbf{M}^{vv} & \Phi_v^T \\ \Phi_u & \Phi_v & \mathbf{0} \end{bmatrix} \begin{bmatrix} \ddot{\mathbf{u}} \\ \ddot{\mathbf{v}} \\ \lambda \end{bmatrix} = \begin{bmatrix} \mathbf{Q}^{eu} \\ \mathbf{Q}^{ev} \\ \Gamma \end{bmatrix} \quad (3.37)$$

giving

$$\begin{bmatrix} \ddot{\mathbf{u}} \\ \ddot{\mathbf{v}} \\ \lambda \end{bmatrix} = \begin{bmatrix} \Phi_u^{-1}(\Gamma - \Phi_v \check{\mathbf{M}}^{-1} \check{\mathbf{Q}}^e) \\ \check{\mathbf{M}}^{-1} \check{\mathbf{Q}}^e \\ (\Phi_u^{-1})^T(\mathbf{Q}^{eu} - \mathbf{M}^{uv} \check{\mathbf{M}}^{-1} \check{\mathbf{Q}}^e - \mathbf{M}^{uu} \Phi_u^{-1}(\Gamma - \Phi_v \check{\mathbf{M}}^{-1} \check{\mathbf{Q}}^e)) \end{bmatrix} \quad (3.38)$$

where (Pennestrì and Valentini, 2007)

$$\begin{aligned} \check{\mathbf{M}} &= \mathbf{M}^{vv} - \mathbf{M}^{vu} \Phi_u^{-1} \Phi_v - \Phi_v^T (\Phi_u^{-1})^T (\mathbf{M}^{uv} - \mathbf{M}^{uu} \Phi_u^{-1} \Phi_v) \\ \check{\mathbf{Q}}^e &= \mathbf{Q}^{ev} - \mathbf{M}^{vu} \Phi_u^{-1} \Gamma - \Phi_v^T (\Phi_u^{-1})^T (\mathbf{Q}^{eu} - \mathbf{M}^{uu} \Phi_u^{-1} \Gamma) \end{aligned} \quad (3.39)$$

Note that the Φ_u^{-1} should be replaced by its pseudoinverse Φ_u^+ for redundant systems. Moreover, all the generalized coordinates are integrated during the simulations in order to obtain comparable results to the outcomes from the other methods.

3.3.2. Wang-Huston formulation

The method, described by Mariti *et al.* (2011, 2010), Pekal (2012), Wang and Huston (1989) is based on pseudoinversion and is equivalent to the orthogonal complement method (Wang and Huston, 1989).

Using Eq. (2.1) yields (Mariti *et al.*, 2010; Wang and Huston, 1989)

$$\ddot{\mathbf{q}} = \mathbf{M}^{-1}(\mathbf{Q}^e - \Phi_{\mathbf{q}}^T \boldsymbol{\lambda}) \quad (3.40)$$

Substituting Eq. (3.40) into Eq. (2.4) gives (Wang and Huston, 1989)

$$\boldsymbol{\lambda} = (\Phi_{\mathbf{q}} \mathbf{M}^{-1} \Phi_{\mathbf{q}}^T)^{-1} (\Phi_{\mathbf{q}} \mathbf{M}^{-1} \mathbf{Q}^e - \boldsymbol{\Gamma}) \quad (3.41)$$

and substituting Eq. (3.41) into Eq. (3.40) leads to (Wang and Huston, 1989)

$$\ddot{\mathbf{q}} = \mathbf{M}^{-1} \Phi_{\mathbf{q}}^T (\Phi_{\mathbf{q}} \mathbf{M}^{-1} \Phi_{\mathbf{q}}^T)^{-1} \boldsymbol{\Gamma} - (\mathbf{M}^{-1} \Phi_{\mathbf{q}}^T (\Phi_{\mathbf{q}} \mathbf{M}^{-1} \Phi_{\mathbf{q}}^T)^{-1} \Phi_{\mathbf{q}} - \mathbf{I}) \mathbf{M}^{-1} \mathbf{Q}^e \quad (3.42)$$

where $\Phi_{\mathbf{q}}^T (\Phi_{\mathbf{q}} \mathbf{M}^{-1} \Phi_{\mathbf{q}}^T)^{-1}$ is the weighted pseudoinverse of the $\Phi_{\mathbf{q}}$ matrix (Wang and Huston, 1989).

For the redundant systems, the pseudoinverse matrix $(\Phi_{\mathbf{q}} \mathbf{M}^{-1} \Phi_{\mathbf{q}}^T)^+$ should be taken instead of the inverse matrix $(\Phi_{\mathbf{q}} \mathbf{M}^{-1} \Phi_{\mathbf{q}}^T)^{-1}$.

It is important to note that the Wang-Huston formulation is not suitable for multibody systems with singular mass matrices. Therefore, in the numerical examples presented below, the Euler angles are used in order to avoid this issue.

4. Numerical examples

4.1. McPherson suspensions with and without redundant constraints

The presented methods have been implemented and tested on two elementary examples of spatial mechanisms. The simplified McPherson strut without redundant constraints shown in Fig. 1a is the first example and the second one is the overconstrained McPherson strut presented in Fig. 1b. Elimination of the redundant constraints from the second example results in the simplified McPherson strut. The idea for consideration of these mechanisms is taken from (Haug, 1989). Both mechanisms consist of 5 rigid bodies (denoted below as $i = 1, 2, 3, 4, 5$) and have 4 degrees of freedom. Two of the DOFs are local mobilities (for bodies 3 and 4). Dimensions of the systems are presented in Table 1 and employ symbols presented in Figs. 1a and 1b. Moreover, origins of the local coordinate frames are located in the centers of mass of the bodies, so that certain expressions get simplified, e.g. the gravitational torques reduce to zero. It is assumed that the centers of mass are placed in the middle of the body i lengths: $|AB|$, $|CD|$, $|JK|$, $|IL|$ and $|LN|$, respectively.

The kinematics of the mechanisms is described using the absolute coordinates. The Euler angles are used for description of the orientation in order to obtain nonsingular mass matrices. Masses of all bodies are: $m_i = 1$ kg and moments of inertia are: $J_{xi} = J_{yi} = J_{zi} = 0.1$ kgm².

Table 1. Dimensions of the McPherson struts

Body	1			2						3	4	5	
Symbol	$ AB $	$ AA_a $	$ AA_b $	$ CD $	$ CE $	$ CF $	$ BC $	$ FG $	$ EH $	$ GI $	$ JK $	$ IL $	$ LN $
Dim. [m]	0.3	0.025	0.025	0.45	0.1	0.25	0.05	0.1	0.15	0.05	0.3	0.5	0.2

Both considered models are loaded in the same manner. The force of the constant value $F_z = 40$ N is applied to the center of mass of the first body in the z direction and the time

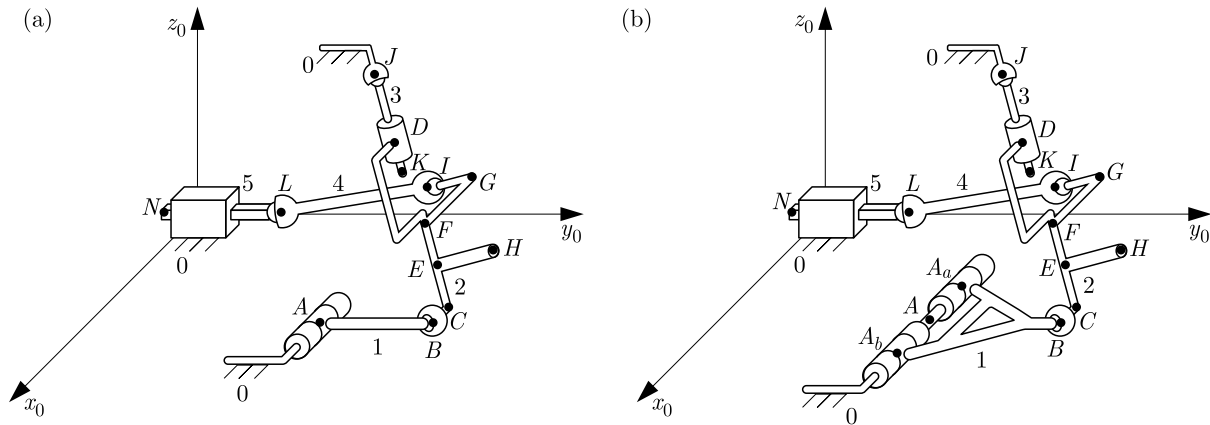


Fig. 1. (a) Simplified McPherson strut, (b) McPherson strut with redundant constraints

varying force acting in the y direction $F_y = 0.1 \sin(t)$ N is applied to body 5. Moreover, it is assumed that the gravity is acting in the negative z direction with gravity acceleration equal to $g = -9.80665$ m/s².

The analyzed methods have been implemented using MATLAB[®] R2012b. The obtained results (positions, velocities and accelerations) were compared with the outcomes of the simulations performed in Adams[™] 2013 in order to verify their correctness. To integrate the equations of motion, the ode45 method based on the Runge-Kutta scheme was used in MATLAB. Simulations were performed on the personal computer equipped with Intel[®] CORE[™] i5 CPU M520 @ 2.40 GHz 2.40 GHz processor, 4 GB of RAM and 64-bit Microsoft[®] Windows[®] 7 Home Premium operating system. Computational times were measured using *tic* and *toc* functions. Moreover, MATLAB program was run in the single thread mode in order to avoid problems with multi thread time measurements.

Each simulation was carried out for 10 s motion. Three stabilization cases were performed for each method: without constraint stabilization, with the Baumgarte stabilization (where $\hat{\alpha} = \hat{\beta} = 10$) and with the stabilization of the position constraints using the Newton-Raphson method. Moreover, four ode45 error tolerances were considered: $AbsTol = RelTol \in \{1e-10; 1e-8; 1e-6; 1e-3\}$, where *AbsTol* and *RelTol* are absolute and relative error tolerances respectively.

4.2. Numerical results – comparison

Results of the computational time versus the error tolerances are presented in Figs. 2-5. Figures 2a and 3a contain the computation time for simulations without constraint stabilization, Figs. 2b and 3b present the results for computations with the Baumgarte stabilization, and Figs. 4 and 5 depict outcomes from simulations with stabilization of the position constraints. Note that Fig. 5b shows the results presented in Fig. 5a but for clarity the Wang-Huston formulation results are excluded.

In the most examples, PUTD methods turn out to be the slowest. Note that the PUTD-H and PUTD-G give almost the same computational time in the case of the simplified McPherson strut, while for the overconstrained McPherson strut, the PUTD-G seems to be faster than the PUTD-H. It may be due to inefficient implementation of the transformation of the \mathbf{H} matrix (Eq. (3.20)). For the remaining methods, the results of most simulation cases are very close to each other. However, in the case of the redundant McPherson strut with stabilization of the position constraints, the Wang-Huston formulation is many times slower than other methods, because of the loss of accuracy of the velocity constraints. Hence, the QR decomposition can be recognized as the most reliable and efficient method though, its results are a bit slower than the outcomes from the Wang-Huston formulation in some cases.

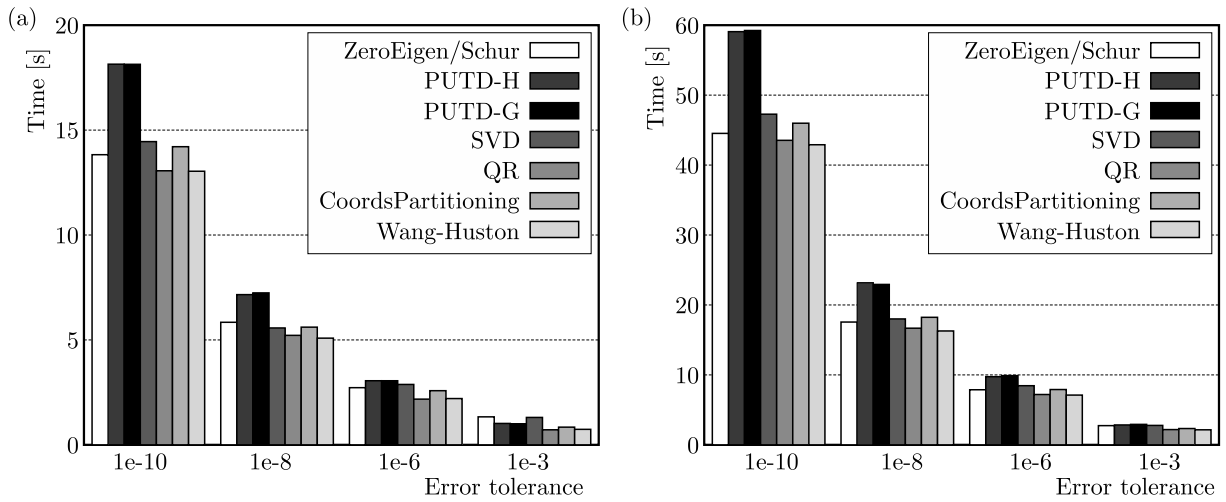


Fig. 2. Simplified McPherson strut: (a) without constraint stabilization, (b) with the Baumgarte stabilization

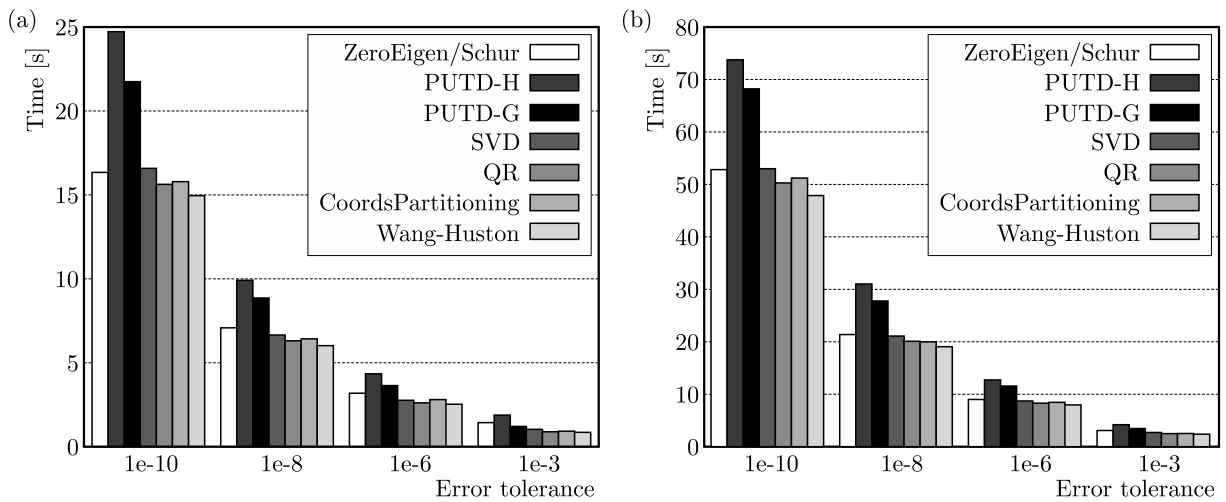


Fig. 3. Overconstrained McPherson strut: (a) without constraint stabilization, (b) with the Baumgarte stabilization

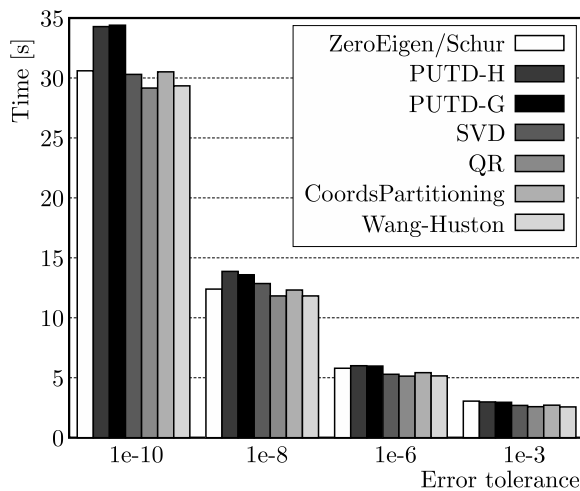


Fig. 4. Simplified McPherson strut with stabilization of the position constraints

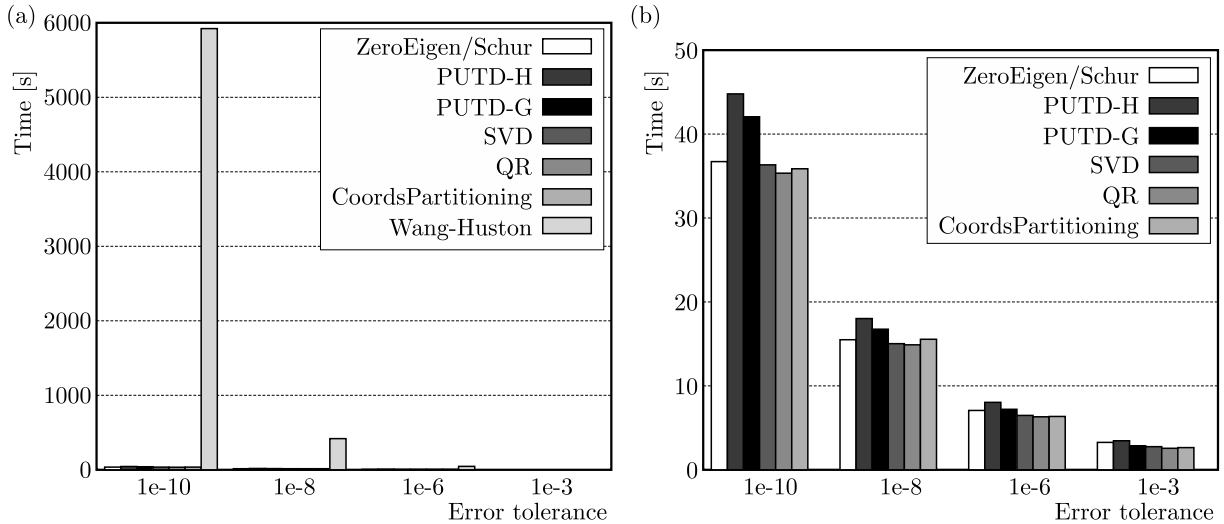


Fig. 5. Overconstrained McPherson strut with stabilization of the position constraints: (a) with and (b) without results of the Wang-Huston formulation

The simulations with stabilization of the constraints take longer than the simulations without stabilization, which should be expected due to greater computational cost.

There are other publications that compare the computation time for spatial systems, e.g. (Mariti *et al.*, 2011, 2010), where results for the Wang-Huston formulation are not presented (when the spatial systems are examined). This is because the Euler parameters were used there for description of the orientation, which resulted in the singular mass matrix and, consequently, the Wang-Huston formulation cannot be employed.

Moreover, the zero eigenvalue method and the Schur decomposition method were considered separately by Mariti *et al.* (2011, 2010), Pennestrì and Valentini (2007) but the matrix \mathbf{A} (Eq. (3.10)) is symmetric, so the Schur decomposition is equivalent to the eigenvalue problem (Golub and Loan, 1996). Therefore, these methods can be considered together as it is done in the current paper. Furthermore, only one type of the PUTD method was examined by Mariti *et al.* (2011, 2010), and in our paper 2 variants of that method are analyzed.

Comparing to Mariti *et al.* (2010), the shorter qualitative results are obtained for the coordinate partitioning method. This is due to the fact that in Mariti *et al.* (2010) coordinate partitioning was done at each time step. In our paper, only one coordinate partitioning is sufficient. In the general case, it should be monitored whether the actual partition of coordinates is still valid.

The computation time grows with the increasing accuracy of computations what is in general consistent with the intuition. This is not the case for all results presented by Mariti *et al.* (2011).

As mentioned earlier, the results of the zero eigenvalue, Schur decomposition, SVD and QR decomposition methods are close to each other. The similar conclusion was obtained by Mariti *et al.* (2010). Note also that in Mariti *et al.* (2010), the PUTD method gave results that were close to the mentioned methods. This is not the case in the present work as computations for both types of the PUTD method usually take longer than for the zero eigenvalue, Schur decomposition, SVD or QR decomposition methods. This might be caused by inefficient implementation of the \mathbf{H} matrix transformation (Eq. (3.20)).

5. Conclusions

Computational effectiveness of the simulation algorithms strongly depends on the selected method. In the current paper methods that are based on the orthogonal complement are compared:

zero eigenvalue formulation, Pseudo Upper Triangular Decomposition (PUTD), Schur decomposition, Singular Value Decomposition (SVD) and QR decomposition. Moreover, two schemes equivalent to the orthogonal complement methods are also considered: coordinate partitioning and Wang-Huston formulation. The effectiveness of these methods for two elementary mechanisms – McPherson struts with and without redundant constraints are considered. Moreover, it is worth noting that the obtained results are comparable with the outcomes from the previous publications (Mariti *et al.*, 2010; 2011). The comparison with the mentioned publications is described in details in Section 4.

The most robust and one of the most efficient formulation is the method based on the QR decomposition, although Wang-Huston formulation is faster in some cases. This is because the Wang-Huston formulation proved to be the slowest method in simulations of the redundant mechanism with stabilization of the position constraints. It is due to the loss of accuracy of the velocity constraints, which are not stabilized in that case. The other algorithms can be slower because of several reasons, e.g. they may require the solution of the eigenvalue problem, which is numerically expensive. Moreover, the computation time is shorter for simulations without stabilization than for the cases with stabilization. Despite this, there is a decrease in the constraints accuracy in the unstabilized simulations, which may cause difficulties in longer multibody motion analyses.

Acknowledgements

This work has been supported by the National Science Centre of Poland under grant No. DEC-2012/07/B/ST8/03993.

References

1. AMIROUCHE F.M.L., 2006, *Fundamentals of Multibody Dynamics, Theory and Applications*, Birkhäuser Boston
2. AWREJCEWICZ J., 2014, *Ordinary Differential Equations and Mechanical Systems*, Springer International Publishing
3. AWREJCEWICZ J., KUDRA G., 2005, Modeling, numerical analysis and application of triple physical pendulum with rigid limiters of motion, *Archive of Applied Mechanics*, **74**, 11-12, 746-753
4. AWREJCEWICZ J., KUDRA G., 2014, Mathematical modelling and simulation of the bifurcational wobblestone dynamics, *Discontinuity, Nonlinearity, and Complexity*, **3**, 2, 123-132
5. AWREJCEWICZ J., KUDRA G., LAMARQUE C.H., 2003, Dynamics investigation of three coupled rods with a horizontal barrier, *Meccanica*, **38**, 6, 687-698
6. AWREJCEWICZ J., KUDRA G., LAMARQUE C.H., 2004, Investigation of triple pendulum with impacts using fundamental solution matrices, *International Journal of Bifurcation and Chaos*, **14**, 12, 4191-4213
7. BAUMGARTE J.W., 1972, Stabilization of constraints and integrals of motion in dynamical systems, *Computer Methods in Applied Mechanics and Engineering*, **1**, 1, 1-16
8. DE JALÓN J.G., BAYO E., 1994, *Kinematic and Dynamic Simulation of Multibody Systems, The Real-Time Challenge*, Springer-Verlag, New-York
9. DE JALÓN J.G., GUTIÉRREZ-LÓPEZ M.D., 2013, Multibody dynamics with redundant constraints and singular mass matrix: existence, uniqueness, and determination of solutions for accelerations and constraint forces, *Multibody System Dynamics*, **30**, 3, 311-341
10. EICH-SOELLNER E., FÜHRER C., 1998, *Numerical Methods in Multibody Dynamics*, B.G. Teubner
11. FRĄCZEK J., WOJTYRA M., 2008, *Kinematyka układów wieloczłonowych. Metody obliczeniowe*, Wydawnictwa Naukowo-Techniczne, Warszawa

12. FreeMat v4.1, help
13. GOLUB G.H., LOAN C.F.V., 1996, *Matrix Computations*, The Johns Hopkins University Press, 3rd edition
14. HARTFIEL D.J., 2001, *Matrix Theory and Applications with MATLAB*, CRC Press
15. HAUG E.J., 1989, *Computer Aided Kinematics and Dynamics of Mechanical Systems, Vol. I: Basic Methods*, Allyn and Bacon
16. IDER S.K., AMIROUCHE F.M.L., 1988, Coordinate reduction in the dynamics of constrained multibody systems – a new approach, *ASME Journal of Applied Mechanics*, **55**, 4, 899-904
17. KIM S.S., VANDERPLOEG M.J., 1986, QR decomposition for state space representation of constrained mechanical dynamic systems, *ASME Journal of Mechanisms, Transmissions, and Automation in Design*, **108**, 2, 183-188
18. KINCAID D., CHENEY W., 2002, *Numerical Analysis: Mathematics of Scientific Computing*, Brooks/Cole, 3-rd edition
19. KUNKEL P., MEHRMAN V., 2006, *Differential-Algebraic Equations*, European Mathematical Society
20. MALCZYK P., FRĄCZEK J., 2012, A divide and conquer algorithm for constrained multibody system dynamics based on augmented Lagrangian method with projections-based error correction, *Nonlinear Dynamics*, **70**, 1, 871-889
21. MANI N.K., HAUG E.J., ATKINSON K.E., 1985, Application of singular value decomposition for analysis of mechanical system dynamics, *ASME Journal of Mechanisms, Transmissions, and Automation in Design*, **107**, 1, 82-87
22. MARITI L., BELFIORE N.P., PENNESTRÌ E., VALENTINI P.P., 2011, Comparison of solution strategies for multibody dynamics equations, *International Journal for Numerical Methods in Engineering*, **88**, 7, 637-656
23. MARITI L., PENNESTRÌ E., VALENTINI P.P., BELFIORE N.P., 2010, Review and comparison of solution strategies for multibody dynamics equations, *The 1st Joint International Conference on Multibody System Dynamics*, Lappeenranta, Finland
24. MATLAB®, help
25. NEGRUT D., SERBAN R., POTRA F.A., 1997, A topology-based approach to exploiting sparsity in multibody dynamics: joint formulation, *Mechanics of Structures and Machines*, **25**, 2, 221-241
26. OSTALCZYK P., 2008, *Wybrane zagadnienia rachunku wektorowego i macierzowego dla robotyków*, Wydawnictwo Politechniki Łódzkiej, Łódź
27. PENNESTRÌ , VALENTINI P.P., 2007, Coordinate reduction strategies in multibody dynamics: A review, *Proceedings of the Conference on Multibody System Dynamics*
28. PĘKAL M., 2012, *Porównanie metod całkowania RRA w analizie dynamiki układów wieloczłonowych* (in Polish), praca dyplomowa magisterska, Politechnika Warszawska, Warszawa
29. WALTON W.C., STEEVES E.C., 1969, A New Matrix Theorem and Its Application for Establishing Independent Coordinates for Complex Dynamical Systems with Constraints, NASA Technical Report: NASA TR R-326, NASA, Washington D. C.
30. WANG J.T., HUSTON R.L., 1989, A comparison of analysis methods of redundant multibody systems, *Mechanics Research Communications*, **16**, 3, 175-182
31. WEHAGE R.A., HAUG E.J., 1982, Generalized coordinate partitioning for dimension reduction in analysis of constrained dynamic systems, *ASME Journal of Mechanical Design*, **104**, 1, 247-255
32. WOJTYRA M., FRĄCZEK J., 2013, Comparison of selected methods of handling redundant constraints in multibody systems simulations, *Journal of Computational and Nonlinear Dynamics*, **8**, 2, 021007 (1-9)

UAV AIRCRAFT MODEL FOR CONTROL SYSTEM FAILURES ANALYSIS

MARCIN ŻUGAJ, PRZEMYSŁAW BIBIK, MARIUSZ JACEWICZ

Warsaw University of Technology, Institute of Aeronautics and Applied Mechanics, Warszawa, Poland

e-mail: zugaj@meil.pw.edu.pl; pbibik@meil.pw.edu.pl; mjacewicz@meil.pw.edu.pl

In the paper, influence of control surface failures on UAV aircraft dynamics is investigated. A method for control loads determination for a nonlinear UAV aircraft model is presented. The model has been developed to analyse the influence of various control surface failures on aircraft controllability and to form the background for developing reconfiguration methods of flight control systems. The analysis of the control system failure impact on the aircraft dynamics and the ability of the control system to reconfiguration are presented.

Keywords: UAV, flight dynamics, control, reconfiguration

1. Introduction

In the last few decades, the number of unmanned aircraft operations has increased. At the beginning UAVs were mainly used for the purposes of military forces. Today, plenty of different types of Unmanned Aircraft Vehicles (UAVs) perform missions which are too dull, dirty, or dangerous for manned aircraft also in the civil airspace. The main problems which slow down the spreading of the UAVs in the civil sector is the integration of Unmanned Aerial Systems (UAS) with the Air Traffic Management systems and safety of the UAS. For the manned aviation, there are plenty of different regulations which are forcing the manufacturers and operators to enhance safety and reliability of the aircraft. At the time, there are no such regulations for unmanned systems. Different sources show how hazardous the current unmanned systems are. Some reports show that the rate of UAV accidents is about 32 per 100 000 flight hours, which is 3 200 times more than the number for commercial liner aircraft (Defense Science Board Study, 2004). These numbers show that there is much work to do within the safety area of the unmanned systems. Various institutions around the world are now focusing on the safety aspects of the UAS usage (Loh *et al.*, 2006, 2009; Uhlig *et al.*, 2006; Lin *et al.*, 2014). The researchers try to convince manufacturers that the safety must be taken into account from the very beginning of the development process and that it does not have to increase the cost of the system very much. Especially hazardous are designs that are based on the COTS elements and subsystems. It is well known that the total safety of a complex system depends on the safety of each element. However, there are ways to assure that the failure of the single element or subsystem will not lead to an accident.

The UAV aircraft safety depends on several unpredictable factors such as, for instance, hostile actions both inside and outside the aircraft. When failures occur, the most important actions must be aimed at maintaining the aircraft controllability. The UAV aircrafts perform their flight mainly using autopilots. The automatic flight control systems are designed for normal operation and may not be able to react sufficiently efficient when an unpredicted malfunction appears. A method for assuring safety in the case of unpredictable failure is reconfiguration of the flight control system (Kozak *et al.*, 2014), which would make the control system fault tolerant and ensure aircraft controllability in the event of fault.

The process of flight control system reconfiguration is aimed to take advantage of the working part of the control system in the case of partial system failure. The reconfiguration can be performed in three levels. Level 1 performs two functions: sets control surfaces to compensate the failure effects and corrects the strategy of control surfaces handling (Burcham, 1997). In level 2, an attempt is made to rearrange the autopilot control laws to adopt to a new situation, (Bodson, 2003; Hass and Wells, 2003). In level 3, on the basis of prediction about the future situation, refinement of the flight trajectory is performed (Masui *et al.*, 2004; Suzuki *et al.*, 2004).

Typically, control surfaces such as elevators, ailerons and flaps work in pairs and are located in opposite sides of the longitudinal plane of symmetry of an aircraft (Fig. 1). This configuration is easy to handle but its redundancy is highly limited. The redundancy can be increased by splitting all paired control surfaces and control them individually. This feature of the control system property is named structural redundancy (Burcham, 1997; Żugaj and Narkiewicz, 2009) and results in increasing the flexibility of aircraft handling. The decoupled control system is more reliable for the reconfiguration process and can be supported by a broad scope of reconfiguration schemes.

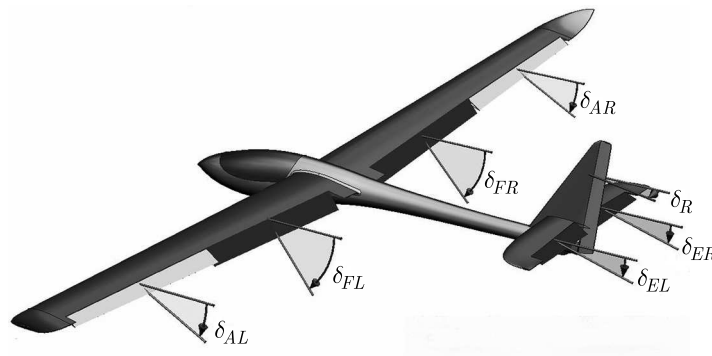


Fig. 1. Control surfaces layout

The dynamic model of UAV is needed for analysis and synthesis of the control system reconfiguration method at each level. That is why the model must assure simulation of each control surface failure and handling strategy (Żugaj and Narkiewicz, 2007, 2010). It involves complex modeling of control loads where all control surfaces are considered individually, not in pairs as usually.

The aim of the present work is to develop a UAV dynamic model for analysis of reconfiguration of the flight control system. A six degrees of freedom nonlinear model with decoupled control surfaces has been derived using the classical approach. The contributions of each control surface to aerodynamic loads are estimated based on distributions of lift and drag forces along lifting surfaces span due to the control surface deflection obtained from CFD software. The model is used for investigation of UAV aircraft performances under control surfaces failure. The analysis of decoupled control system efficiency for reconfiguration has been performed as well.

2. UAV nonlinear model

The UAV airplane considered in this study is shown in Fig. 1. The airplane is modeled as a rigid body with six degrees of freedom. The control forces and moments are produced by two ailerons and two flaps placed on the wing trailing edge, two elevators placed on the horizontal stabilizer trailing edge, and the rudder placed on the trailing edge of the fin. The aircraft is propelled by one electric motor with a constant pitch tracking propeller placed in front of the fuselage.

The elevators, ailerons and flaps work in pairs and the operation of each pair is modeled as a single control input. The modeling of the control loads of individual control surfaces is

required due to the UAV model application in analysis and validation of the control system reconfiguration. Each control surface is treated as an individual control input. So, the number of control inputs increase from four in the classical to seven in the reconfigurable configuration.

The aircraft equations of motion are derived in the body co-ordinate system $O_b x_b y_b z_b$ (Fig. 2) fixed to the airplane fuselage. The centre O_b of the system is placed at the UAV gravity centre. The $O_b x_b$ axis lies in the plane of aircraft symmetry and is directed forward. The $O_b y_b$ axis is perpendicular to the aircraft plane of symmetry and points right, the $O_b z_b$ axis points “down”.

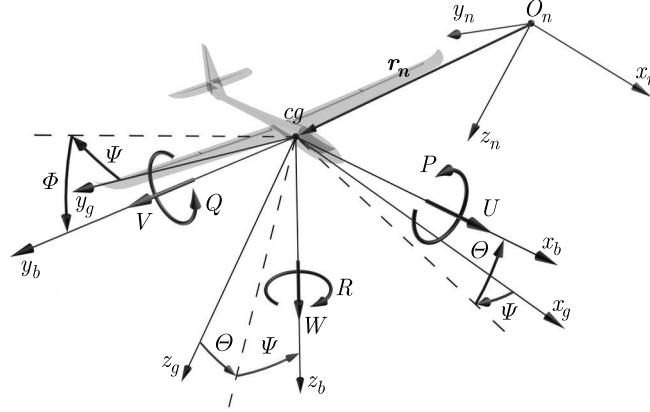


Fig. 2. Coordinate systems

The aircraft translations and attitude angles are calculated in the inertial co-ordinate system $O_n x_n y_n z_n$; the centre of this system O_n is placed at an arbitrary point on the earth surface. The $O_n z_n$ axis is along the vector of gravity acceleration, points down. The $O_n x_n z_n$ plane is horizontal, tangent to the earth surface, the $O_n x_n$ axis points to the North and $O_n y_n$ axis to the East.

The vector $\mathbf{y} = [x_n \ y_n \ z_n \ \Phi \ \Theta \ \Psi]^T$ defines position and attitude of the aircraft (Fig. 2). It is composed of the vector of the aircraft position $\mathbf{r}_n = [x_n \ y_n \ z_n]^T$ in the ground system of co-ordinates $O_n x_n y_n z_n$ and the roll Φ , pitch Θ and yaw Ψ angles describing the aircraft attitude. The airplane state vector $\mathbf{x} = [\mathbf{v} \ \boldsymbol{\omega}]^T$ is composed of linear velocity components $\mathbf{v} = [U \ V \ W]^T$ and the angular rate $\boldsymbol{\omega} = [P \ Q \ R]^T$, P, Q, R – angular velocities.

The vectors of the aircraft state, position and attitude are related by a kinematic equation

$$\dot{\mathbf{y}} = \mathbf{T}\mathbf{x} \quad (2.1)$$

The matrix \mathbf{T} is composed of two matrices: \mathbf{T}_V relating to velocities and \mathbf{T}_Ω – to rates

$$\mathbf{T} = \begin{bmatrix} \mathbf{T}_V & \mathbf{0} \\ \mathbf{0} & \mathbf{T}_\Omega \end{bmatrix} \quad (2.2)$$

where

$$\mathbf{T}_V = \begin{bmatrix} \cos \Theta \cos \Psi & \sin \Theta \sin \Phi \cos \Psi - \cos \Phi \sin \Psi & \cos \Phi \sin \Theta \cos \Psi + \sin \Phi \sin \Psi \\ \cos \Theta \sin \Psi & \sin \Theta \sin \Phi \sin \Psi + \cos \Phi \cos \Psi & \cos \Phi \sin \Theta \sin \Psi - \sin \Phi \cos \Psi \\ -\sin \Theta & \sin \Phi \cos \Theta & \cos \Phi \cos \Theta \end{bmatrix} \quad (2.3)$$

$$\mathbf{T}_\Omega = \begin{bmatrix} 1 & \sin \Phi \tan \Theta & \cos \Phi \tan \Theta \\ 0 & \cos \Phi & -\sin \Phi \\ 0 & \sin \Phi \sec \Theta & \cos \Phi \sec \Theta \end{bmatrix}$$

The airplane equations of motion have been obtained by summing up forces and moments from inertia, gravity \mathbf{f}_G , aerodynamic \mathbf{f}_A , and propulsion \mathbf{f}_T loads (Nizioł, 2005)

$$\mathbf{A}\dot{\mathbf{x}} + \mathbf{B}(\mathbf{x})\mathbf{x} = \mathbf{f}_A(\mathbf{x}, \mathbf{y}, \boldsymbol{\delta}) + \mathbf{f}_G(\mathbf{y}) + \mathbf{f}_T(\mathbf{x}, \mathbf{y}, \delta_T) \quad (2.4)$$

where \mathbf{A} is the aircraft inertia matrix, \mathbf{B} – gyroscopic matrix, $\boldsymbol{\delta}$ – vector of control surface deflections and δ_T is the position of the throttle lever

$$\boldsymbol{\delta} = \left[\delta_{AR} \quad \delta_{AL} \quad \delta_{ER} \quad \delta_{EL} \quad \delta_R \quad \delta_{FR} \quad \delta_{FL} \right]^T \quad (2.5)$$

The first letter of the subscripts A, E, F, R denotes the type of the control surface, i.e. aileron, elevator, flap and rudder, respectively. The second letter denotes the position of the control surface: L – left, R – right.

The matrix \mathbf{A} describes inertia properties of the aircraft, and the matrix $\mathbf{B}(\mathbf{x}) = \boldsymbol{\Omega}(\mathbf{x})\mathbf{A}$ results from inertia loads not depending on accelerations (Nizioł, 2005)

$$\mathbf{A} = \begin{bmatrix} m & 0 & 0 & 0 & 0 & 0 \\ 0 & m & 0 & 0 & 0 & 0 \\ 0 & 0 & m & 0 & 0 & 0 \\ 0 & 0 & 0 & I_x & 0 & -I_{xz} \\ 0 & 0 & 0 & 0 & I_y & 0 \\ 0 & 0 & 0 & -I_{xz} & 0 & I_z \end{bmatrix} \quad \boldsymbol{\Omega}(\mathbf{x}) = \begin{bmatrix} 0 & -R & Q & 0 & 0 & 0 \\ R & 0 & -P & 0 & 0 & 0 \\ -Q & P & 0 & 0 & 0 & 0 \\ 0 & -W & V & 0 & -R & Q \\ W & 0 & -U & R & 0 & -P \\ -V & U & 0 & -Q & P & 0 \end{bmatrix} \quad (2.6)$$

where m is the aircraft mass, I_x, I_y, I_z are moments of inertia, and I_{xz} is the product of inertia.

The aerodynamic loads \mathbf{f}_A may be expressed as the sum of two parts

$$\mathbf{f}_A(\mathbf{x}, \mathbf{y}, \boldsymbol{\delta}) = \mathbf{f}_{AS}(\mathbf{x}, \mathbf{y}) + \mathbf{f}_\delta(\mathbf{x}, \mathbf{y}, \boldsymbol{\delta}) \quad (2.7)$$

The part $\mathbf{f}_\delta(\mathbf{x}, \mathbf{y}, \boldsymbol{\delta})$ depends on deflections of control surfaces and the part $\mathbf{f}_{AS}(\mathbf{x}, \mathbf{y})$ does not.

Substituting Eq. (2.7) into (2.4), rearranging and multiplying by \mathbf{A}^{-1} , the nonlinear aircraft model can be written as

$$\dot{\mathbf{x}} = \mathbf{f}_1(\mathbf{x}, \mathbf{y}) + \mathbf{f}_2(\mathbf{x}, \mathbf{y}, \boldsymbol{\delta}) + \mathbf{f}_3(\mathbf{x}, \mathbf{y}, \delta_T) \quad (2.8)$$

In Eq. (2.8), the first component does not depend on aircraft control, the second one describes airplane loads increment due to deflection of the control surface, and the third one describes airplane loads due to thrust control.

The point of interest in this study is the increment of aerodynamic loads produced by deflection of asymmetric (individual) control surfaces. The control surfaces are modeled as trailing edge plain flaps (Young, 1953). The aerodynamic loads depend on the lifting surface outline and section (airfoil) geometry (Fig. 3). The flap deflection changes the lift and drag forces around the part of the lifting surface where the flap is located. The lift and drag forces as well as the pitching moment can be expressed in form (Cook, 2007)

$$L = \bar{q}SC_L \quad D = \bar{q}SC_D \quad M = \bar{q}ScC_m \quad (2.9)$$

where \bar{q} is the free stream dynamic pressure, S is the lifting surface plan form area, c is the airfoil chord C_L, C_D and C_m are lifting surface lift, drag and pitching moment coefficients, respectively. The airfoil lift increment due to plain flap deflection results from effective change of the airfoil camber and airfoil angle of attack α' (Young, 1953). The lift coefficient increment depends on the chord c_f , span b_f and deflection angle δ of the flap (Fig. 3).

The airfoil drag increment results from profile drag increment which can be analyzed in the same way as the lift coefficient increment. The profile drag does not have a significant influence on the lifting surface drag regarding to the induced drag. The lifting surface induced drag increment due to flap deflection can be estimated by (Young, 1953)

$$\Delta C_{Di} = K \frac{\Delta C_{L\delta}^2}{\pi A} \quad (2.10)$$

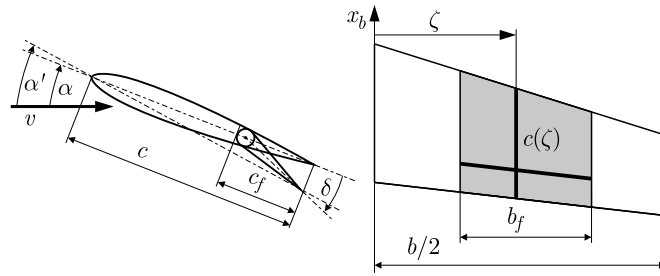


Fig. 3. Section and lifting surface parameters

where $\Delta C_{L\delta}$ is the lifting surface lift coefficient increment due to flap deflection, A is the lifting surface aspect ratio and K is an empirical constant.

The analytical methods for aerodynamic coefficients estimation allow obtaining only quantities of lift, drag and moment increments. These increment distributions along the lifting surface are also needed to calculate the influence of the flap deflection on the aircraft aerodynamics roll and yaw moments.

The numerical analysis of the lift increment distribution due to flap deflection have been done using a free software. The calculations have been performed for isolated lifting surfaces at cruise flight conditions of the UAV aircraft. An example of the wing lift coefficient increments due to aileron and trailing edge flap deflection and the horizontal tail lift coefficient increment due to elevator deflection in the body coordinate system are presented in Figs. 4-6.

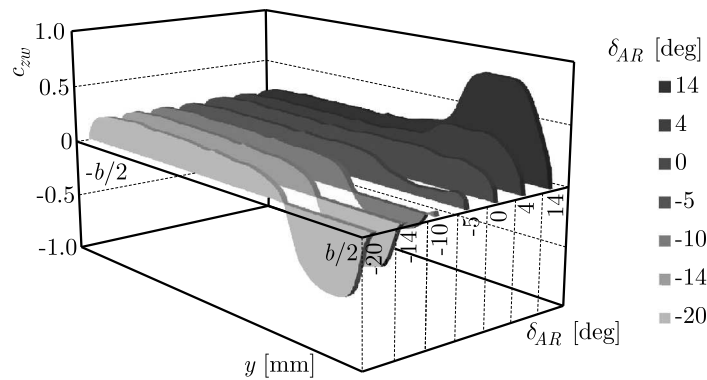


Fig. 4. Wing lift coefficient distribution due to aileron deflection

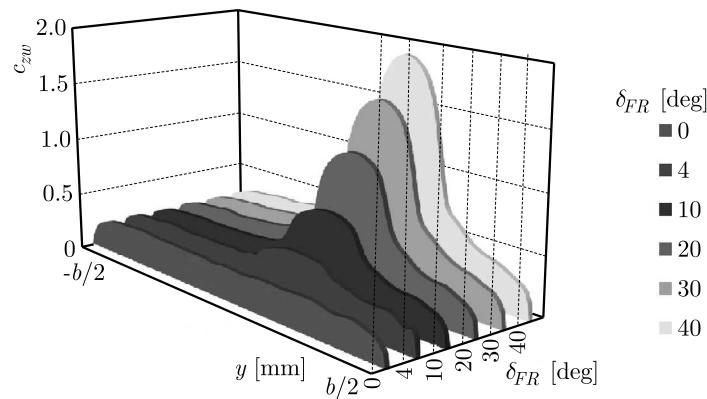


Fig. 5. Wing lift coefficient distribution due to flap deflection

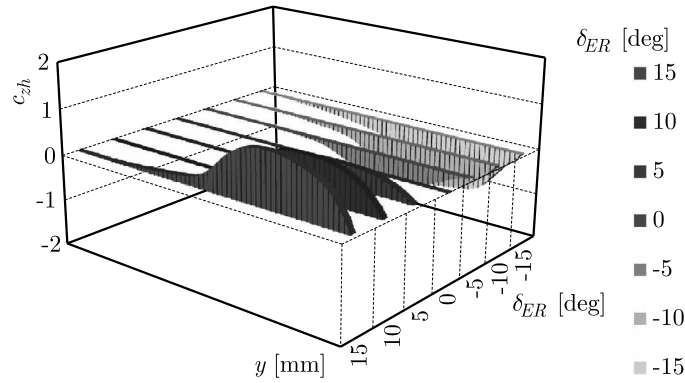


Fig. 6. Horizontal tail lift coefficient distribution due to elevator deflection

The control derivatives for each control surface have been obtained based on the lift distribution. The increment of the lift $\Delta c_{Lij}(\zeta)$, drag $\Delta c_{Dij}(\zeta)$ and pitching moment $\Delta c_{mij}(\zeta)$ coefficients distribution of the i -th control surface and j -th deflection angle along the appropriate lifting surface span have been calculated as differences of the distribution for the clear and j -th flap configuration at first. Next, the control derivatives have been obtained using analytical methods presented in Cook (2007) and Nizioł (2005) as an integral in general form

$$\Delta f_{2ij} = \bar{q} \int_0^{b/2} g(c(\zeta), \Delta c_{Lij}(\zeta), \Delta c_{Dij}(\zeta), \Delta c_{mij}(\zeta), \zeta) d\zeta \quad (2.11)$$

The i -th increment of the control loads $\Delta \mathbf{f}_{2i}(\mathbf{x}, \mathbf{y}, \delta_i)$ as functions of the flight condition parameters (angle of attack, airspeed, etc.) and the i -th control surface deflection angle have been formed by combining the control derivatives for all deflection angles of the i -th control surface. The modeled aerodynamic loads can be written in the form

$$\mathbf{f}_2(\mathbf{x}, \mathbf{y}, \boldsymbol{\delta}) = \sum_{i=1}^n \Delta \mathbf{f}_{2i}(\mathbf{x}, \mathbf{y}, \delta_i) \quad (2.12)$$

where n is the number of the control surfaces.

Figures from 7 to 9 present examples of the roll L , pitch M , and yaw N moments produced by the right aileron AR , elevator ER and flap FR at a constant angle of attack equal to 1.5 degrees. It can be seen that the single elevator has the greatest influence on the pitch moment, and the single aileron and flap produces the greatest roll moments, as expected. What is more, the elevator influence on the roll and yaw moments is very low, and the aileron and the flap produce quite significant pitch and roll moments.

3. Investigation of the control surfaces decoupling scheme

The nonlinear UAV dynamic model with decoupled control surfaces has been tested. The tests were aimed at the investigation of the influence of operation of the decoupled control surfaces on the aircraft behavior during normal smooth flight. The results show a significant changes in aircraft behavior due to asymmetric control surfaces deflection. Deflecting any single control surface causes three dimensional changes of the aircraft attitude and the trajectory which requires immediate correction using other surfaces to achieve the demanded control results. That indicates that the lock of one of the control surfaces at any arbitrary position causes an unpredicted and unexpected response of the UAV aircraft to the control inputs, what may lead to

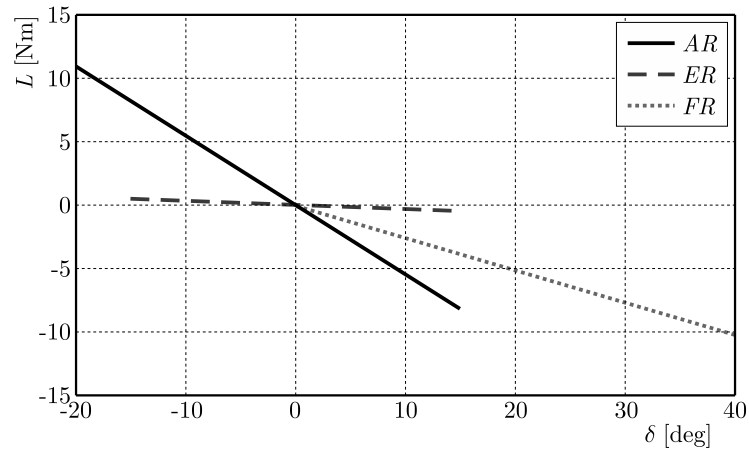


Fig. 7. Roll moment increment due to control surfaces deflection

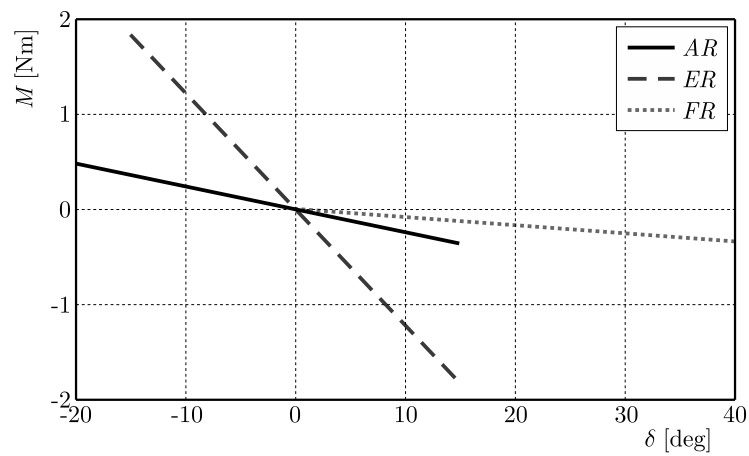


Fig. 8. Pitch moment increment due to control surfaces deflection

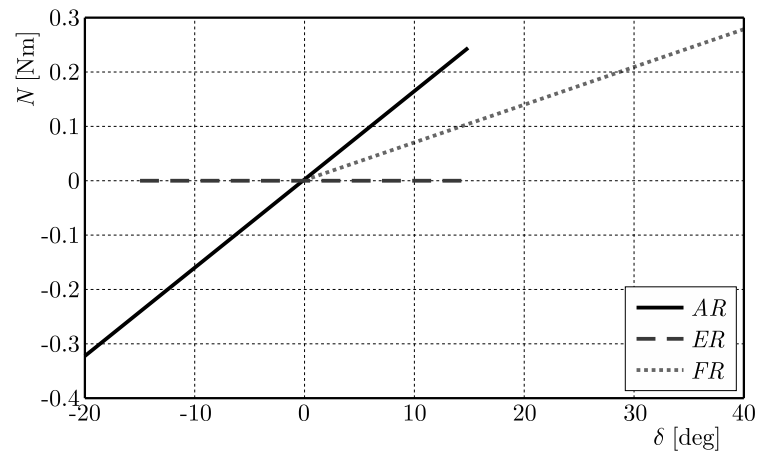


Fig. 9. Yaw moment increment due to control surfaces deflection

crash of the aircraft. What is more, if the control surface is locked in a non-neutral position (non zero deflection angle), these adverse effects will have significant influence on the equilibrium conditions of the aircraft.

Figures from 10 to 13 present a comparison of the aircraft behavior in two cases: the fault free configuration and the right elevator lock on the neutral position configuration. These tests

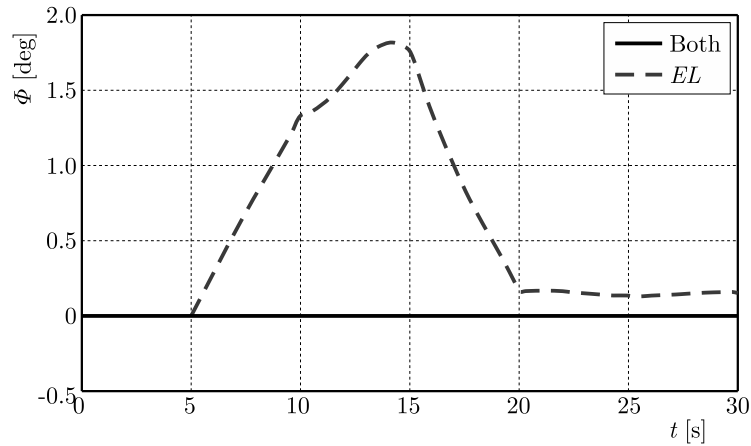


Fig. 10. Aircraft bank angle

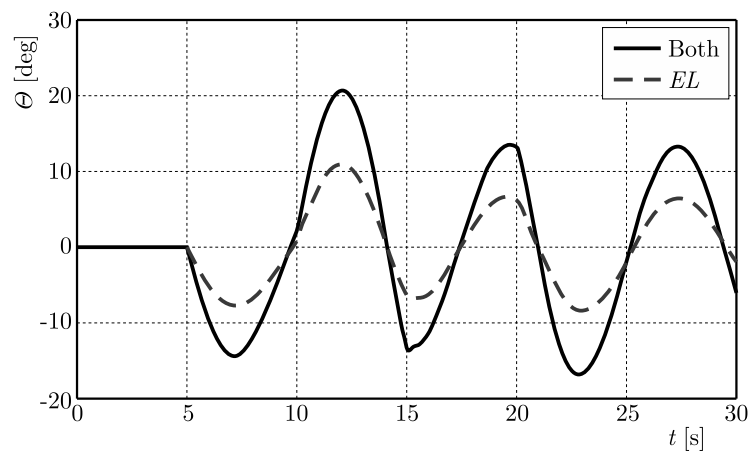


Fig. 11. Aircraft pitch angle

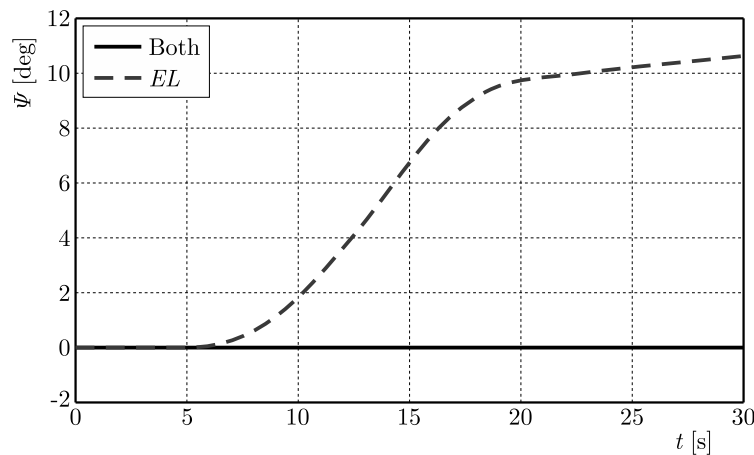


Fig. 12. Aircraft yaw angle

were performed for steady cruise conditions and the tasks were to apply a double impulse control signal to the elevators. At first, the control surfaces worked in the normal (coupled) configuration (both elevators operate), next the decoupled scheme was tested and the input signal was applied only to the left elevator. Only a phugoid oscillation was induced in the case of the normal configuration, what is typical. The phugoid oscillation had lower amplitude in the case of right elevator fault. What is more, the asymmetric elevator deflection induced disturbances to the bank and yaw angles.

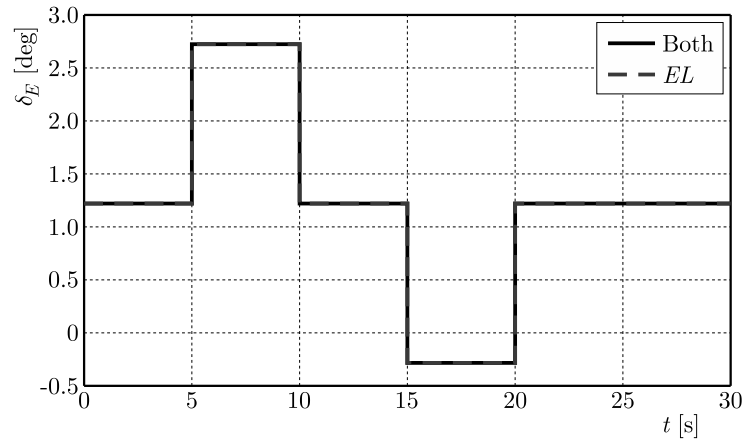


Fig. 13. Input signal

The UAV dynamic model has also been used to investigate the decoupled control system ability to reconfigure in the case of the lock of control surfaces. The main task of the control reconfiguration is at least to continue the steady flight after failure. The behavior of a damaged aircraft can be similar to the behavior of a failure-free aircraft, when the reconfigured control system is able to produce similar aerodynamic moments (Żugaj and Narkiewicz, 2010). The efficiency of the reconfiguration strongly depends on the control system redundancy.

The control system of the presented UAV aircraft consists of seven control surfaces: lefts aileron AL , elevator EL and flap FL , and rights aileron AR , elevator ER and flap FR , and the rudder R . The contribution of each control surface to the roll L , pitch M and yaw N aerodynamic moments is presented in Fig. 14. These figures present the proportion of the maximum positive and negative values of produced moments to the maximum values of moments in the normal configuration. It can be seen that the roll moment (of positive or negative value) can be generated by both ailerons and the flap. The contribution of each of these surfaces is almost equal. The pitch moment can be mainly generated by both elevators with a little contribution of both ailerons and flaps, but the flaps can produce only negative value of the pitching moment because of their handling limitations (flaps can be deflected down only). The control redundancy is very poor in the case of the yaw moment. It can be generated only by the rudder, and the contribution of other surfaces is not significant.

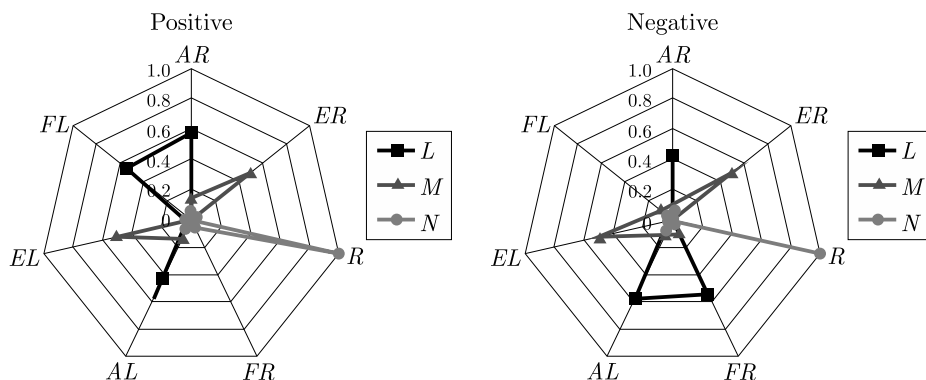


Fig. 14. Contributions of control surfaces to aerodynamic moments

Figure 15 presents the proportions (relative to the normal control configuration) of the total positive and negative values of the control moments produced by all control surfaces. It shows the advantages of the decoupled control system. The amount of the roll moment can be increased by about 60%, the pitch moment by 30% and the yaw moment by 13% through handling all

control surfaces individually. The amount of pitch moment increment could be increased by redesigning the flaps mechanization and extending their deflection range to an upper position (negative deflection angle), which could be done easily in the case of a small UAV airplane.

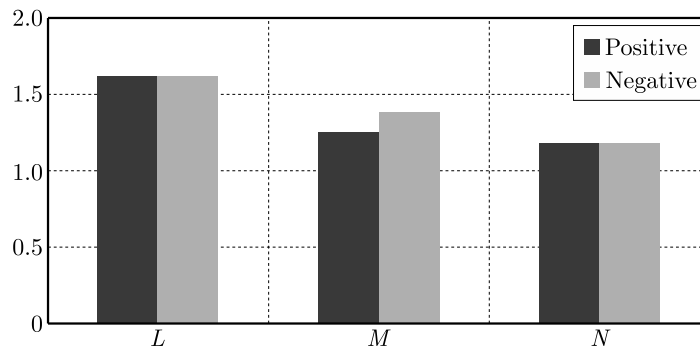


Fig. 15. Total values of aerodynamic moments produced by all control surfaces

4. Conclusions

The methodology of determination of the individual control surface aerodynamic loads is presented. A six degrees of freedom nonlinear model of the UAV aircraft with decoupled control surfaces has been developed. The influence of control surfaces failures on the UAV flight performances has been investigated using the model. The analysis of decoupled control system efficiency for reconfiguration has been performed as well.

The simulation results prove a significant influence of the control surface lock on the aircraft dynamic performances. The analysis of the decoupled control system indicates its ability to reconfigure, which could refine the aircraft reliability.

Acknowledgments

The research presented has been part of the project “Methods of synthesis of aircraft control system in emergency situations”, under grant form National Centre for Research and Development, PBS2/B6/19/2013.

References

1. BODSON M., 2003, Reconfigurable nonlinear autopilot, *Journal of Guidance Control and Dynamics*, **26**, 5, 719-727
2. BURCHAM B., 1997, Landing safely when flight controls fail, *Aerospace America*, 20-23
3. COOK M.V., 2007, *Flight Dynamics Principles*, Elsevier, Butterworth-Heinemann, Oxford
4. Defense Science Board Study on Unmanned Aerial Vehicles and Uninhabited Combat Aerial Vehicles, February 2004
5. HASS R.A., WELLS S.R., 2003, Sliding mode control applied to reconfigurable flight control design, *Journal of Guidance Control and Dynamics*, **26**, 3, 452-461
6. KOZAK V.M., SHEVCHUK D.O., VOVK V.G., LEVCHENKO M.H., 2014, Automation of aircraft control reconfiguration in flight special situations, *Proceedings of IEEE 3rd International Conference on Methods and Systems of Navigation and Motion Control*, 161-164
7. LIN X., FULTON N.L., HORN M.E.T., 2014, Quantification of high level safety criteria for civil unmanned aircraft systems, *Proceedings of Aerospace Conference, Big Sky*, 1-13

8. LOH R., BIAN Y., ROE T., 2006, Safety requirements for unmanned aerial vehicles (UAV) in future civil airspace, *Proceedings of Position, Location, and Navigation Symposium*, 1151-1163
9. LOH R., BIAN Y., ROE T., 2009, UAVs in civil airspace: safety requirements, *IEEE Aerospace and Electronic Systems Magazine*, **24**, 1, 5-17
10. MASUI K., TOMITA H., KOMATSU Y., 2004, Flight experiment on flight path optimization algorithm for aircraft in trouble, *Proceedings of 24th International Conference of the Aeronautical Science*
11. NIZIOŁ J., 2005, *Dynamics of Mechanical Systems* (in Polish), Komitet Mechaniki PAN, Instytut Podstawowych Problemów Techniki Polskiej Akademii Nauk, Warszawa
12. SUZUKI S., KAWAMURA F., MASUI K., 2004, Autonomous flight control and guidance system of accident aircraft, *Proceedings of 24th International Conference of the Aeronautical Science*
13. UHLIG D., BHAMIDIPATI K., NEOGI N., 2006, Safety and reliability within UAV construction, *Proceedings of 25th Digital Avionics Systems Conference*
14. YOUNG A.D., 1953, *The Aerodynamics Characteristics Of Flaps*, A.R.C. Technical Report No. 2622 (10766), Her Majesty's Stationery Office
15. ŻUGAJ M., NARKIEWICZ J., 2007, Impact of control system degradation on aircraft flight performance (in Polish), *Zeszyty Naukowe Politechniki Rzeszowskiej, Mechanika*, **71**, 179-186
16. ŻUGAJ M., NARKIEWICZ J., 2009, Autopilot for reconfigurable flight control system, *ASCE Journal of Aerospace Engineering*, **22**, 1, 78-84
17. ŻUGAJ M., NARKIEWICZ J., 2010, Autopilot supported by nonlinear model following reconfigurable flight control system, *ASCE Journal of Aerospace Engineering*, **22**, 1, 339-347

Manuscript received November 3, 2015; accepted for print April 14, 2016

A STRAIN ENERGY DENSITY THEORY FOR MIXED MODE CRACK PROPAGATION IN RUBBER-LIKE MATERIALS

ABDELKADER BOULENOUAR

Djillali Liabes University of Sidi Bel-Abbes, Mechanical Engineering Department, Laboratory of Materials and Reactive Systems, Larbi Ben Mhidi, Algeria; e-mail: aek_boulenouar@yahoo.fr

NOUREDDINE BENSEDDIQ

Mechanics Laboratory of Lille, CNRS UMR 8107, Ecole Polytech'Lille, University of Lille, France

MOHAMED MERZOUG, NABIL BENAMARA, MOHAMED MAZARI

Djillali Liabes University of Sidi Bel-Abbes, Mechanics and Physics of Materials Laboratory, Larbi Ben Mhidi, Algeria

In this paper, a numerical modeling of crack propagation for rubber-like materials is presented. This technique aims at simulating the crack growth under mixed-mode loading based on the strain energy density approach. At each crack increment length, the kinking angle is evaluated as a function of the minimum strain energy density (MSED) around the crack tip, using the Ansys Parametric Design Language (APDL). In this work, numerical examples are illustrated to demonstrate the effectiveness, robustness and accuracy of the computational algorithm to predict the crack propagation path. The results obtained show that the plan of crack propagation is perpendicular to the direction of the maximum principal stretch. Moreover, in the framework of linear elastic fracture mechanics (LEFM), the minimum values of the density are reached at the points corresponding to the crack propagation direction.

Keywords: strain energy density, mixed mode, hyper-elastic, crack propagation

1. Introduction

Today rubbers are used in many engineering industries. The demand for such materials and their performance is continually increasing. The performance is limited, among other factors, by the initiation of cracks. Hence, it is necessary to develop procedures that allow an exact determination of a fracture criterion of these materials. To study fracture rubbers we can use two approaches: the global approach and the local approach. The global approach of the fracture mechanics, originated from Griffith (1920, 1924), represents a good method allowing the characterisation of the materials fracture. It assumes that initiation and growth of cracks begin from pre-existing defects in the structure. In the '50s, Rivlin and Thomas (1953) generalized the Griffith's energy approach and defined the concept of tearing energy T as the energy released per unit area of crack surface growth. The parameter T can be calculated analytically from a few specimen geometries proposed by several authors (Rivlin et Thomas, 1953; Greensmith, 1963; Andrews, 1974).

The global energy approach is used qualitatively to characterize the rupture of materials under simple loading (mode I); it is not adapted for complex loadings (mode I+II). In this case, the quantitative local approach represents a good alternative which makes it possible to indicate the crack initiation and direction.

In linear elastic fracture mechanics, the various fracture criteria for cracks subjected to mixed mode loading have been introduced for the determination of the propagation direction and the critical stress such as the maximum tangential stress criterion (Erdogan and Sih, 1963; Chang, 1981; Maiti and Smith, 1983), maximum principal tangential stress criterion (Maiti et Smith,

1983), maximum strain criterion (Wu, 1974; Chang, 1981), and strain energy density criterion (Sih, 1974; Theocaris, 1984). Almost all these criteria postulate that crack initiation occurs at the crack tip and propagate towards the radial direction.

Sih's (Sih, 1973, 1974; Sih and Macdonald, 1974; Kipp and Sih, 1975) strain energy density criterion (SEDC) assumes the strain energy density to be investigated for an element around the crack tip as the starting point and the strain energy density factor as a basic parameter. It is then postulated that crack initiation will occur at the crack tip in the radial direction along which the strain energy density factor S is minimum, and the crack will begin to propagate when the factor S reaches some critical value.

The strain energy density criterion was validated experimentally and numerically on fragile materials (Theocaris, 1984; Boulenouar *et al.*, 2016, 2013a; Benouis *et al.*, 2015; Ayatollahi and Sedighiani, 2012; Pegorin *et al.*, 2012; Choi *et al.*, 2006) and ductile materials (Komori, 2005; Chow and Xu, 1985; Carpinteri, 1984). In the framework of large deformations, this criterion was used by Hamdi *et al.* (2007) on filled rubber materials to predict the initial crack orientation of a central crack.

The objective of this paper is to present the numerical modeling of the crack propagation trajectory for rubber-like materials. Using the Ansys Parametric Design Language (APDL) (2006), the crack direction is evaluated as a function of the minimum strain energy density $(dW/dV)_{min}$ around the crack tip. The numerical examples are included to illustrate the validation of the numerical approach for crack growth simulation in hyper-elastic materials.

2. The strain energy density theory

The SED fracture criterion locally focuses on the continuum element ahead of the crack and is based on the notion of weakness or severity experienced by the local material. Failure occurs when the critical amount of strain energy dW is accumulated within the element volume dV and the crack is then advanced incrementally in the corresponding direction (Sih, 1974; Sih and Barthelemy, 1980). The strain energy density function dW/dV is assumed to have the following form

$$\frac{dW}{dV} = \frac{S}{r} \quad (2.1)$$

where S is the strain energy density factor and r is the distance from the crack tip. The minimum of the strain energy density factor S_{min} around the crack tip determines the likely direction of crack propagation.

The strain energy density can be determined directly from the relationship

$$\frac{dW}{dV} = \frac{1}{2} \sigma^T \varepsilon \quad (2.2)$$

The computed discrete values for S are then fitted with an approximation function which enables simple determination of the local minimum. The strain density function has several local minima around the crack tip, where the global minimum is not necessarily the true solution, as it can be observed in Fig. 1.

The physically meaningful minimum of the strain density function S_{min} can be found numerically by incremental search for a local minimum in possible crack extension directions θ_i in the range $\pm\pi$ around the crack tip (Fajdiga *et al.*, 2007).

Fajdiga *et al.* (2007) used the position of integration points to define the corresponding angle of calculated strain energy density and strain energy density factor S around the crack tip. In this study, the minimum strain energy density $(dW/dV)_{min}$ is computed by introducing a ring of elements around the crack tip. At each crack increment, the crack direction is evaluated as a function of the angle between the centre of the element and the crack axis (Fig. 2).

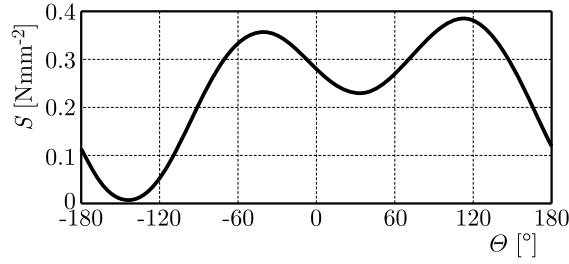


Fig. 1. Strain energy density factor S as a function of the angle θ

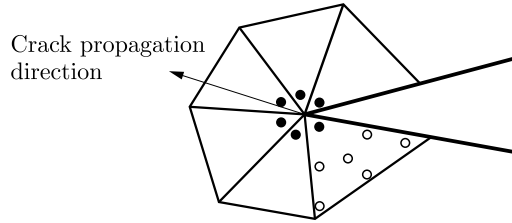


Fig. 2. Direction of propagation using the minimum strain energy density

2.1. Modeling of the hyperelasticity

The mechanical behavior of rubber materials is generally described using a hyper-elastic formalism defined by a function dW/dV called the strain energy density. The establishment of the law of this behavior is a necessary step to perform analytical and/or numerical calculations to develop or exploit multiaxial tests. These behavior laws should be specific to the strain ultimate levels and should allow description of multiaxial loadings accurately.

In this study, we based on the experimental data of Hamdi *et al.* (2006), Hamdi (2006) using four tests: uniaxial tension (UT), uniaxial compression (UC), pure shear (PS) and equibiaxial tension (ET). The tests were performed on two rubber materials: natural rubber and styrene butadiene rubber.

Based on these tests, the rubber materials are modeled by a hyperelastic potential developed for quasi-incompressible rubbers using Yeoh’s model (Yeoh, 1990), Eq. (2.3)₁, for natural rubber NR and Ogden’s model (Ogden, 1984), Eq. (2.3)₂, for Styrene Butadiene rubber SBR

$$\begin{aligned} \frac{dW}{dV} &= C_{10}(I_1 - 3) + C_{20}(I_1 - 3)^2 + C_{30}(I_1 - 3)^3 \\ \frac{dW}{dV} &= \sum_{k=1}^N \frac{\mu_k}{\alpha_k} (\lambda_1^{\alpha_k} + \lambda_2^{\alpha_k} + \lambda_3^{\alpha_k} - 3) \end{aligned} \tag{2.3}$$

where dW/dV is strain energy density, C_{10} , C_{20} , C_{30} , μ_k , α_k are material parameters to be determined, λ_1 , λ_2 and λ_3 are principal extensions.

The hyper-elastic coefficients of the studied materials are given in Table 1.

Table 1. Values of the material parameters values (Hamdi *et al.*, 2006; Hamdi, 2006)

Materials	Material parameters			
NR	C_{10} [MPa]	C_{20} [MPa]	C_{30} [MPa]	
	0.298	0.014	0.00016	
SBR	μ_1 [MPa]	α_1	μ_2 [MPa]	α_2
	0.638	3.03	-0.025	-2.35

The relevance of these material models was evaluated by Hamdi (Figs. 3a and 3b) for different loading (UT, UC, ET and PS), comparing the calculated stress-strain analytically with those obtained from the experiment.

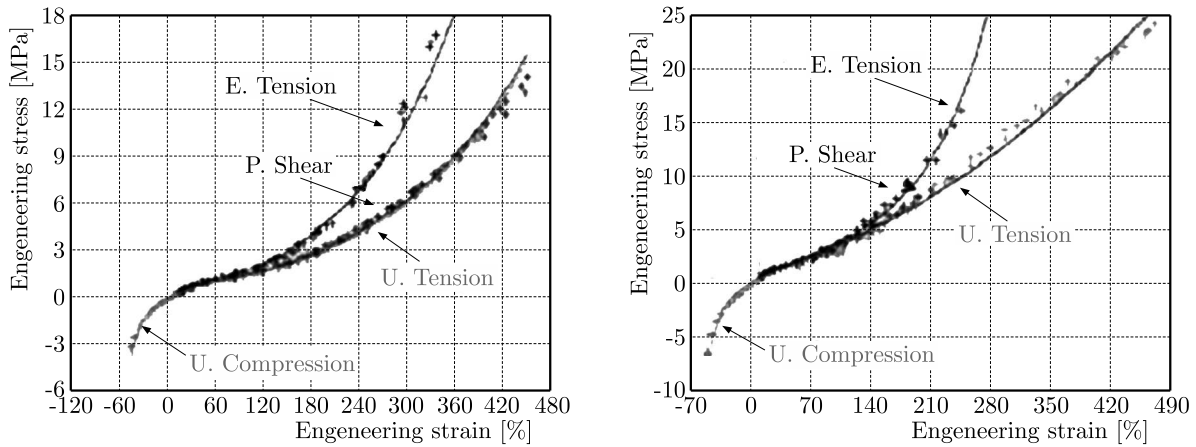


Fig. 3. Engineering stress-strain evolution for NR (left) and SBR (right) (Hamdi *et al.*, 2006; Hamdi, 2006; Boulenouar and Mazari, 2009)

2.2. Finite element modeling and crack growth algorithm

This Section presents a finite element analysis for the modeling of fracture problems in rubber-like materials using the remeshing technique. Figure 4 shows a flow-chart of the prepared

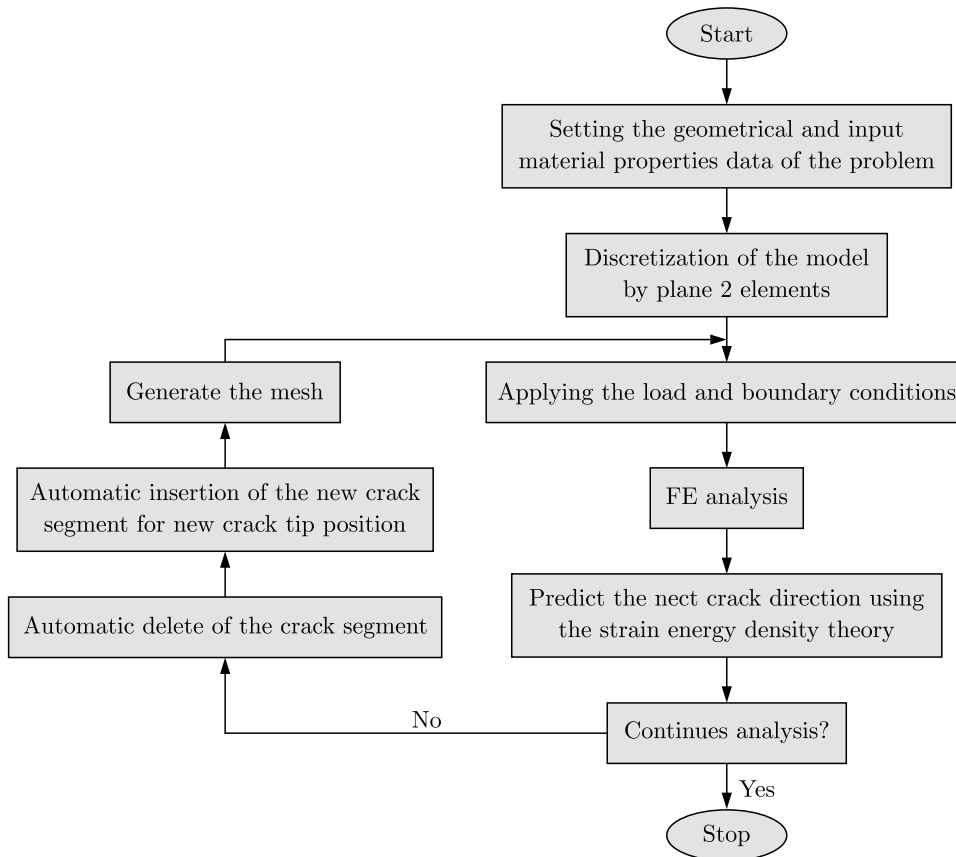


Fig. 4. Flow chart of the FEM algorithm of the problem

APDL code based on a combination of the finite element analysis and the strain energy density concept. According to the algorithm, after initial geometrical and physical modeling of the problem, the mesh pattern is generated around crack tip. In order to find a new crack tip position at each step of propagation, the Strain Energy Sih's Theory is employed to obtain the kinking angle θ_0 as a function of the minimum strain energy density $(dW/dV)_{min}$. At each increment Δa of crack propagation, the special mesh is generated around crack tip, using the quadratic six-node triangular element. It is noted that the same numeration of the nodes around the crack tip is taken during the crack propagation to evaluate automatically the new crack tip position. The algorithm is repeated until ultimate failure of the material or by using another criterion for termination of the simulation process. Figure 5 illustrates the crack propagation mechanism proposed in this study.

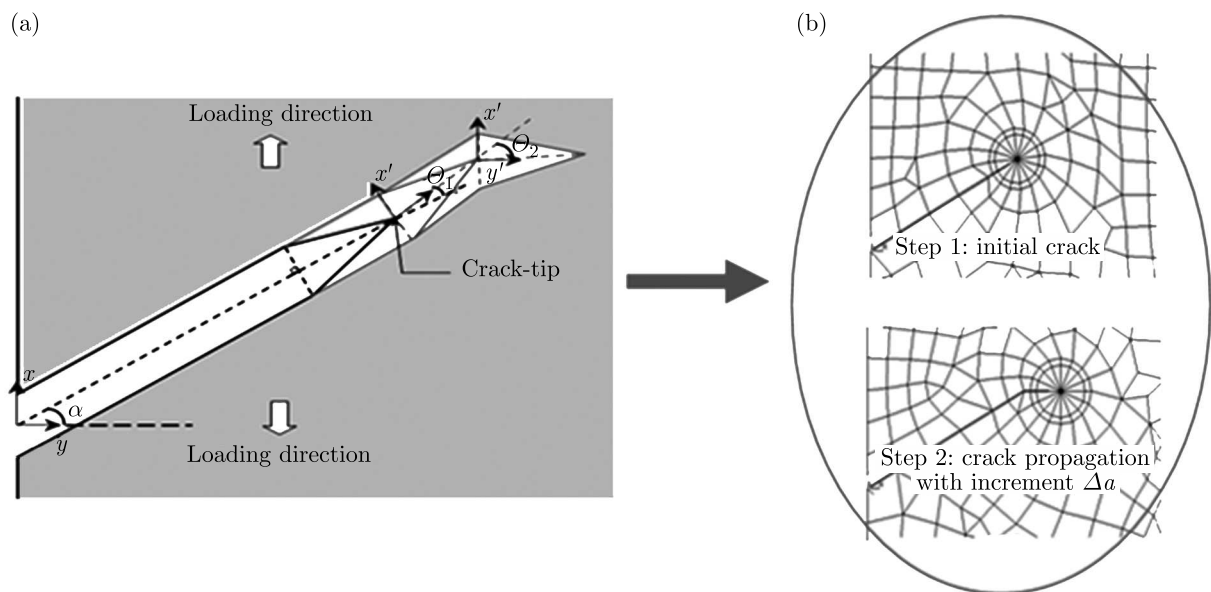


Fig. 5. (a) Crack propagation mechanism proposed in this study, (b) FE modeling for crack propagation

3. Results and discussion

3.1. Minimal strain energy density criterion

The geometry of the single edge cracked plate (100 mm \times 50 mm) with an initial crack ($a = 30$ mm) is considered for 2-dimensional finite element analysis. The pre-existing crack is inclined to the horizontal axis with the angle α (Fig. 6). The FE calculation has been achieved by gradually increasing the elongations λ_1 applied to the nodes located at the top of the plate.

For mesh generation of the cracked plate, the element type PLANE183' of ANSYS code is used, as shown in Fig. 7a. It is a higher order two dimensional, 8-node element having two degrees of freedom at each node (translations in the nodal x and y directions), quadratic displacement behavior and the capability of forming a triangular-shaped element, which is required at the crack tip areas.

Due to singular nature of the stress field in the vicinity of the crack, the singular elements, shown in Fig. 7b, are considered at each crack tip area, which is modeled with a finer mesh. Plane stress and large strains are assumed in the analysis.

The rings of the elements surrounding the tip of the crack are employed. This mesh will be used to determine the strain energy density in these elements in order to determine the kinking

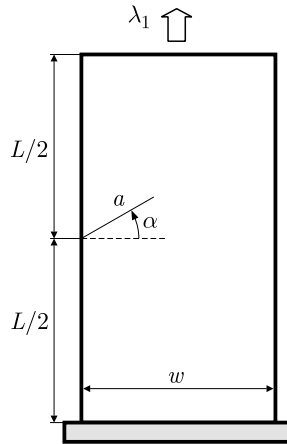


Fig. 6. Geometry of the single edge cracked plate

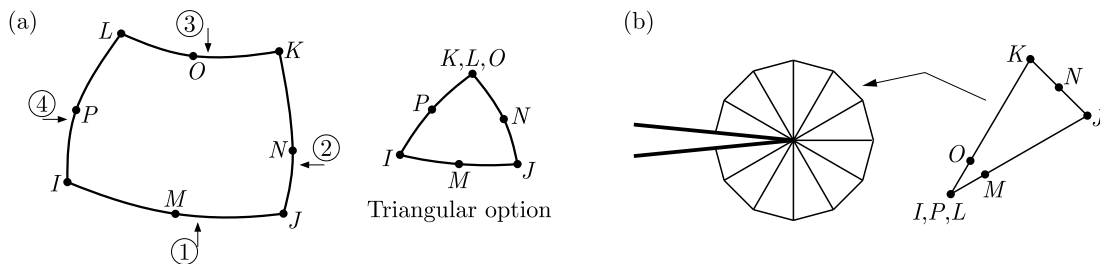


Fig. 7. (a) PLANE183 eight-node finite element and (b) singular option

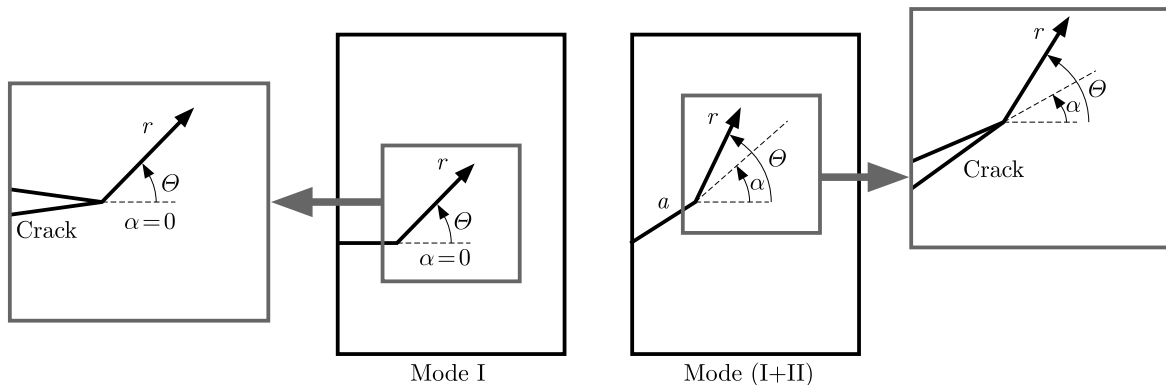


Fig. 8. Description of the parameters r , α and θ

angle θ in the direction for which this energy density is minimal $(dW/dV)_{min}$. Figure 8 illustrates description of the parameters r , α and θ , where r is the distance from the crack-tip, α is the crack inclination angle and θ is the kinking angle.

The specifications of the crack tip mesh and a close up view for the crack inclination angle $\alpha = -30^\circ$ are shown in Fig. 9. In this figure, r_i represents the distance between the crack tip and the center of the element c .

For the two materials studied NR and SBR, Figs. 10 show the evolution of the strain energy density dW/dV as a function of the angle θ . The results obtained are traced for several values of the radius r_i (1.25, 1.75, 2.5 and 3 mm) and for three orientations of the initial crack $\alpha = 30^\circ$, 0° and -30° . These figures highlights that out of the core region surrounding the crack tip (in our case $r \leq r_1$), the minimum of dW/dV is reached for a constant value independently of the distance r . The angle θ_0 corresponds to the horizontal direction perpendicular to the loading. It is noted that the observations obtained are similar to those obtained by Hamdi (2006).

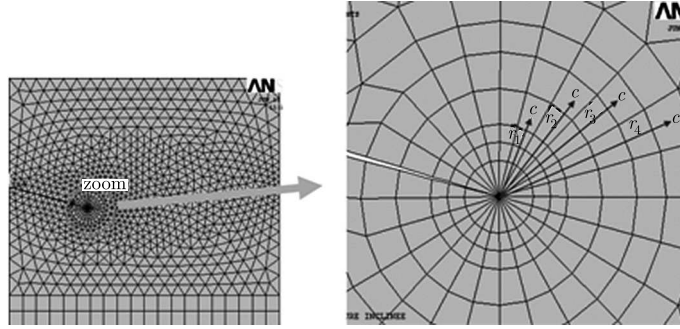


Fig. 9. The ring of elements around the crack tip

Figure 11a illustrates an example of the application of the SED approach in the case of rubbers NR and SBR under mixed-mode loading. This figure shows the evolution of the parameter S , called the strain-energy-density factor (with $S = (dW/dV)r$). The results obtained are given vs. the radius r_i and the polar angle θ for an inclination angle $\alpha = 30^\circ$. The curves plotted in Fig. 11a show that out of the core region surrounding the crack-tip, the minimum of the parameter S is reached for a constant value independently of the radius r .

The angle equalizes here to -30° , corresponding contrary to the value of the initial orientation of the crack ($-\alpha$) calculated for the reference mark $Ox'y'$ (Fig. 11b). These results show a good agreement with the results obtained by Hamdi *et al.* (2007) for other styrene butadiene rubber filled with carbon black SBR2 (Fig. 12).

3.2. Effect of the number of elements surrounding the crack tip

For the strain energy density criterion, the precision is strongly related to the number of elements surrounding crack tip zone. For this purpose, we examined the influence of the mesh size (or number of the elements) on the strain energy density variation. For that, the density dW/dV is evaluated for different numbers of elements surrounding the crack tip. In this study, the numbers of elements considered are 16, 40 and 56 (Fig. 13).

For different numbers of elements surrounding the crack tip zone and for several values of the radius r , Figs. 14 and 15 illustrate respectively for NR and SBR the evolution of the strain energy density dW/dV as a function of the initial angle of crack propagation θ (with $\alpha = 30^\circ$). The results obtained show that the precision is related to the elements size around the crack tip.

The results obtained are similar to those found in the case of a plate of rubbers (NR and SBR) containing a central crack (Hamdi, 2006) (Fig. 16). It is clear that this crack is propagated according to the horizontal direction perpendicular to the loading direction and independently of the inclination angle α . Thus, the crack propagation direction is null, according to the reference mark of calculation (Oxy).

To better show the influence of the elements size around the crack tip on the determination of the initial angle of crack propagation θ_0 , Fig. 17 illustrates the variation of the angle θ_0 as a function of $(dW/dV)_{min}$ for various numbers of elements surrounding the crack tip. The curves obtained show more elements around the crack tip make the crack direction θ_0 at each crack increment length and the final path of crack propagation more precise.

3.3. Crack propagation path

In this Section, two simple examples are proposed to validate our model of the initial crack propagation in rubber materials.

Figure 18 shows four steps for the extension of the initial crack (with $\alpha=0^\circ$). As expected, the crack propagates horizontally, depending on mode I loading. The results obtained allow us

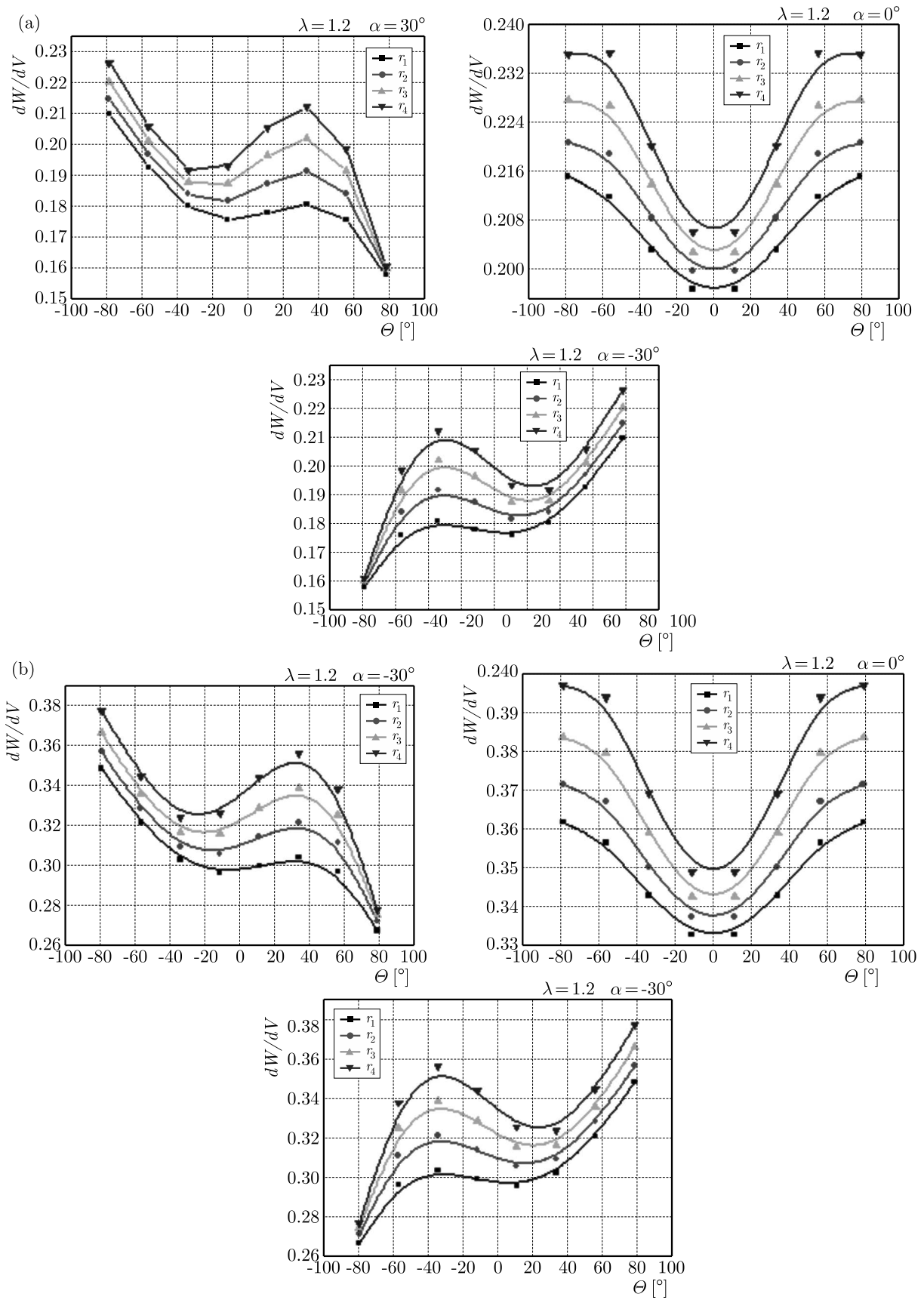


Fig. 10. Evolution of dW/dV as a function of θ for several values of the radius r (with $\alpha = 30^\circ, 0^\circ$ and -30°); (a) NR, (b) SBR

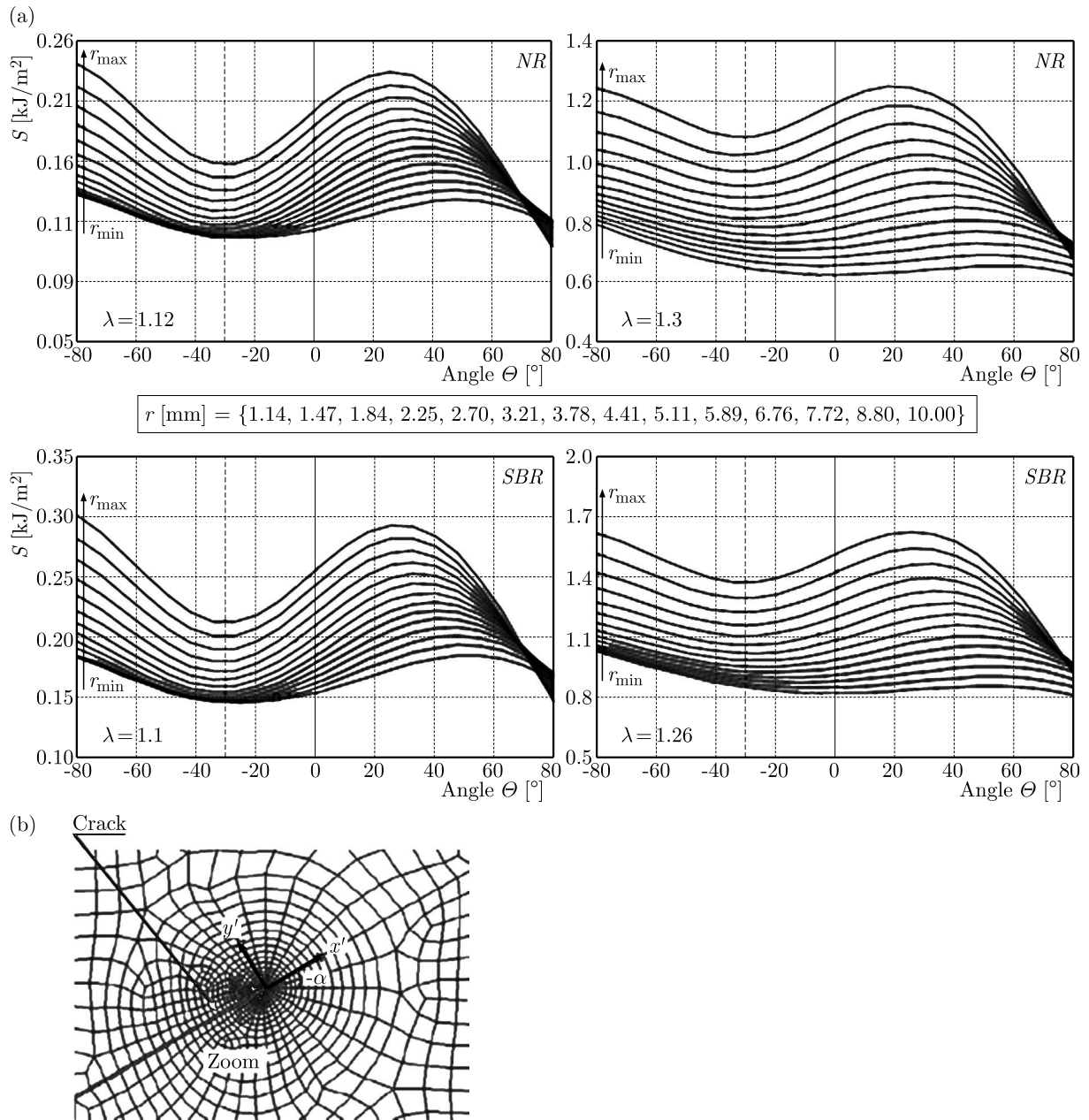


Fig. 11. (a) Evolution of S vs. θ and r for $\alpha = 30^\circ$ (for NR and SBR), (b) elements around the crack tip

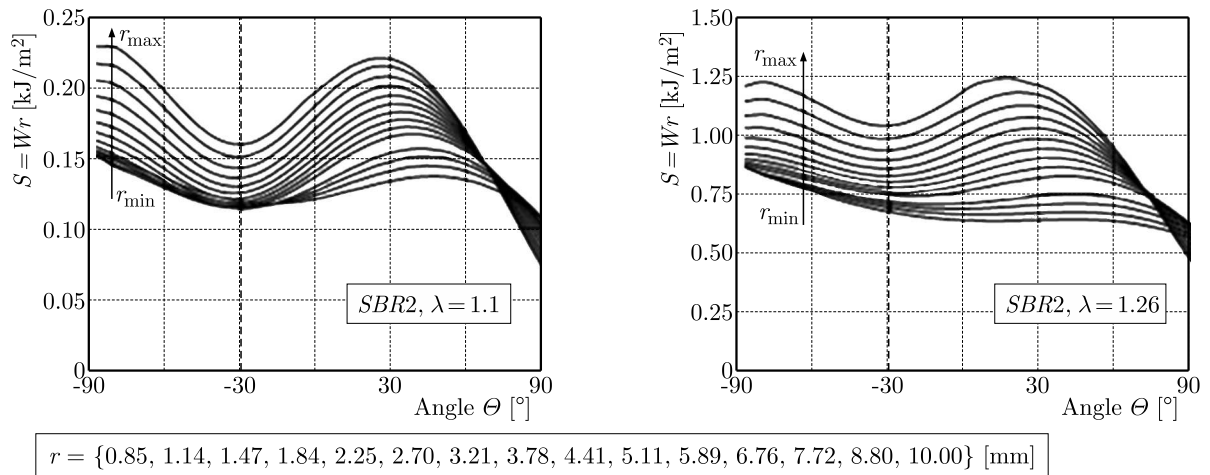


Fig. 12. Evolution of S as a function of θ for several values of the radius r and for two given stretches ($\alpha = 30^\circ$)

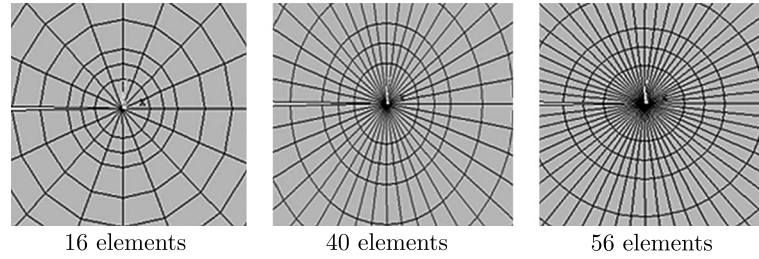
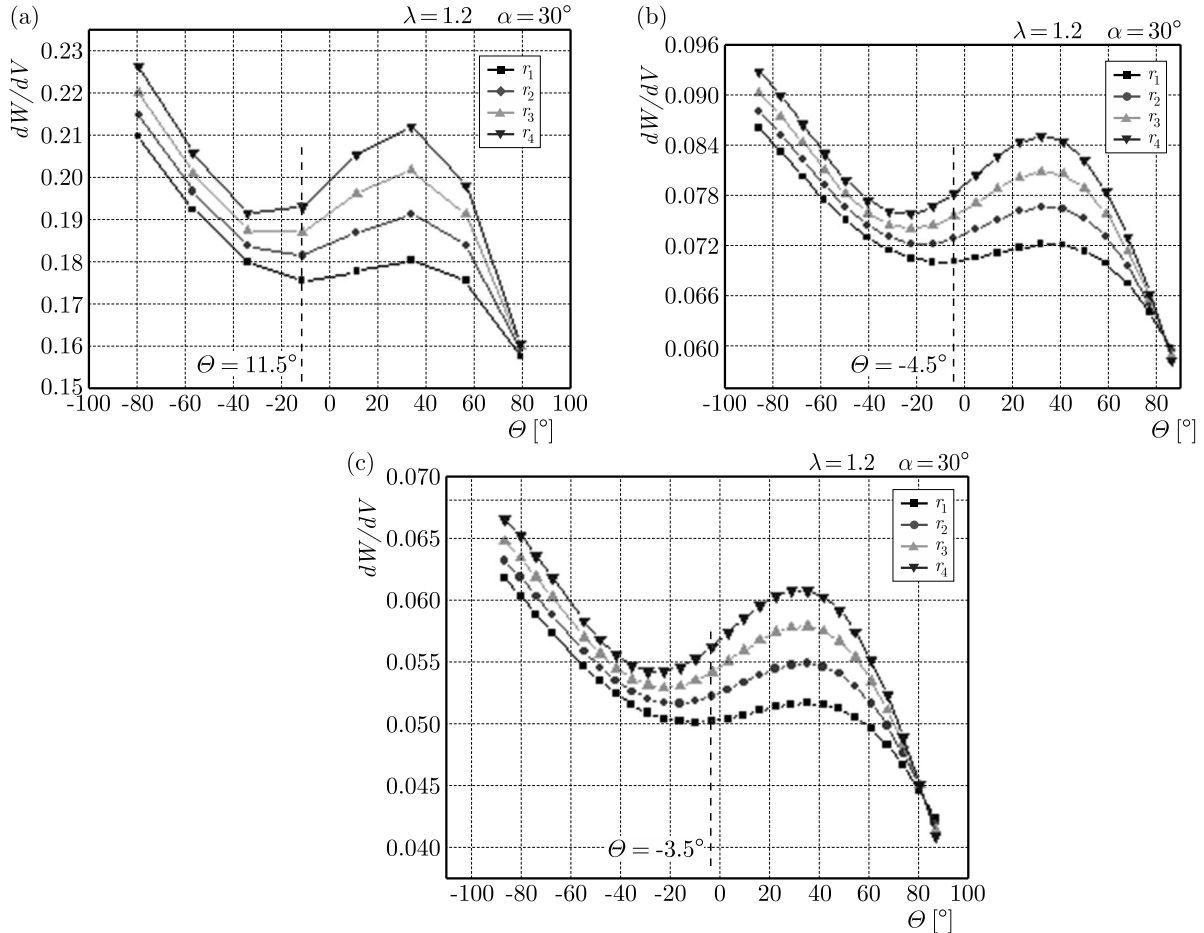


Fig. 13. Elements sizes around the crack tip

Fig. 14. Influence of the meshing on the evolution of dW/dV (NR, $\alpha = 30^\circ$); (a) 16 elements, (b) 40 elements, (c) 56 elements

to conclude that the criterion implemented gives a good crack path under mode I loading. This crack propagation trajectory is similar to the observed in the case of elastic linear materials using the strain energy density approach (Boulenouar *et al.*, 2013a, 2014) or another crack propagation criterion (Boulenouar *et al.*, 2013b; Alshoabi and Ariffin, 2006).

In what follows, we propose to study the propagation path of a crack inclined to the horizontal axis with an angle $\alpha = 30^\circ$. The kinked angle and the crack propagation are made under plane stress problems with the same loading conditions. Figure 19 presents four steps of the crack propagation path. As expected, the crack reorients towards the vertical loads and propagates horizontally until the end.

The same trajectory of crack propagation has been checked for another material elastomer presented by Hamdi *et al.* (2007), see Fig. 20. The results obtained show that this crack is pro-

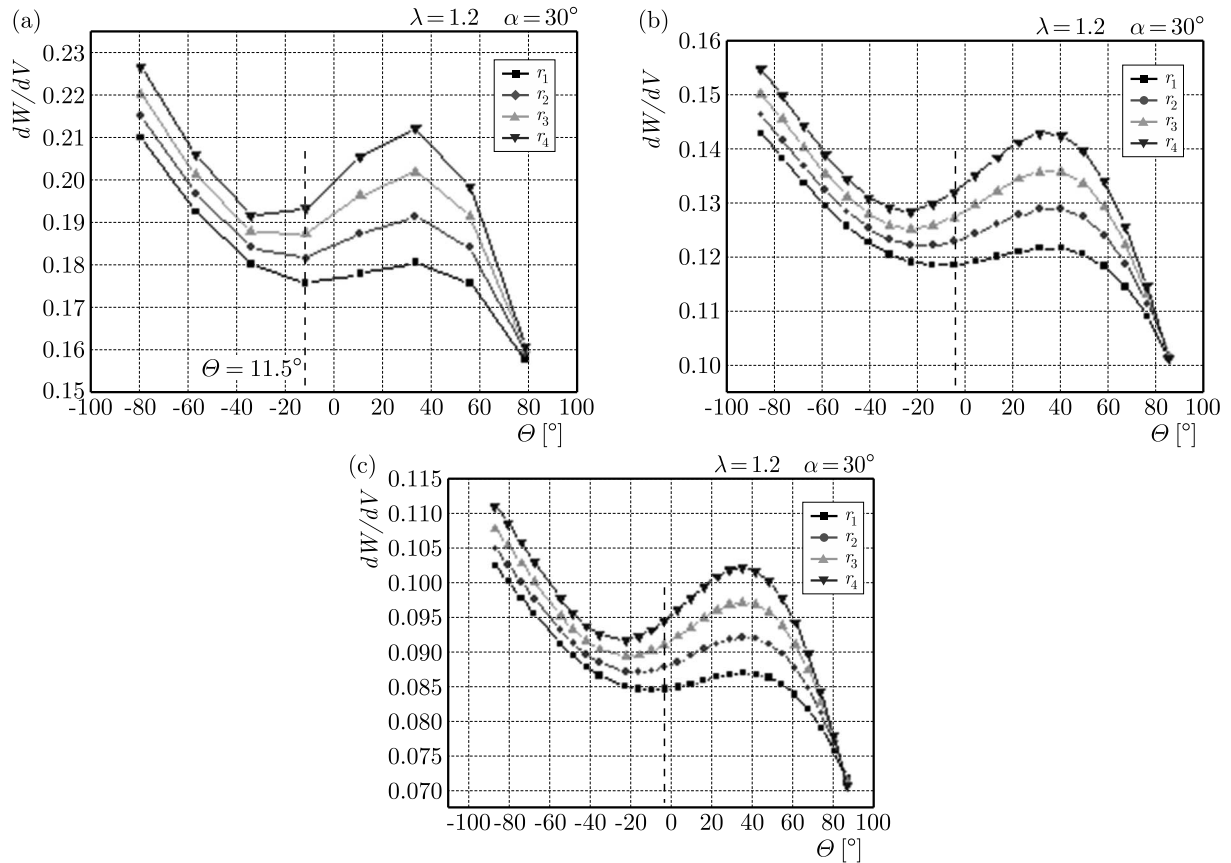


Fig. 15. Influence of the meshing on the evolution of dW/dV (SBR, $\alpha = 30^\circ$); (a) 16 elements, (b) 40 elements, (c) 56 elements

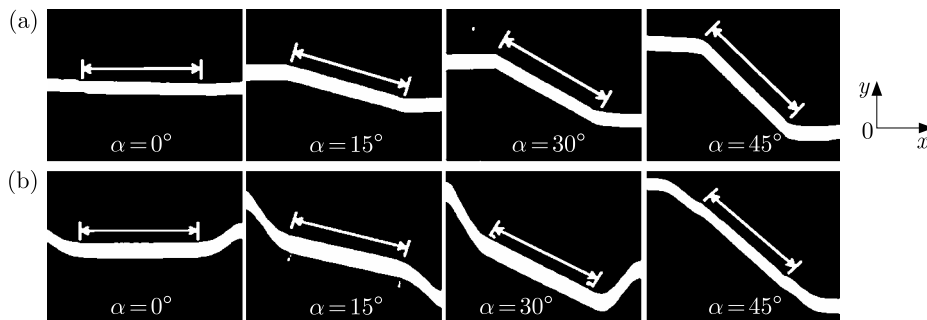


Fig. 16. Initiation and propagation of a pre-existing crack in rubbers (Hamdi, 2006)

pagated horizontally, according to mode-I (opening mode). In linear elastic fracture mechanics (LEFM), this behavior of crack propagation is similar to that observed in experiments by Bian and Taheri (2011), and numerically by Alshoaibi and Ariffin (2008).

In the last example, Legrain (2007) and Legrain *et al.* (2005) applied the X-FEM approach to large strain fracture mechanics. Figure 21 illustrates the crack propagation path estimated for a single edge cracked plate in rubber containing an inclusion. As waited, the crack is propagated horizontally, far from a defect.

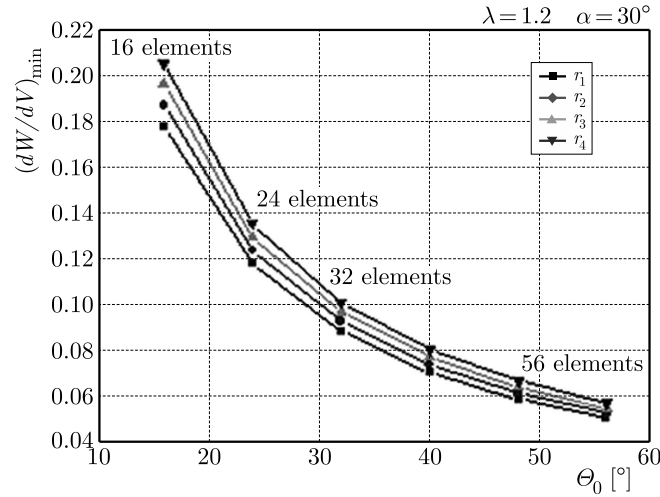


Fig. 17. Influence of the meshing on the determination of the angle θ_0 (SBR, $\alpha = 30^\circ$)

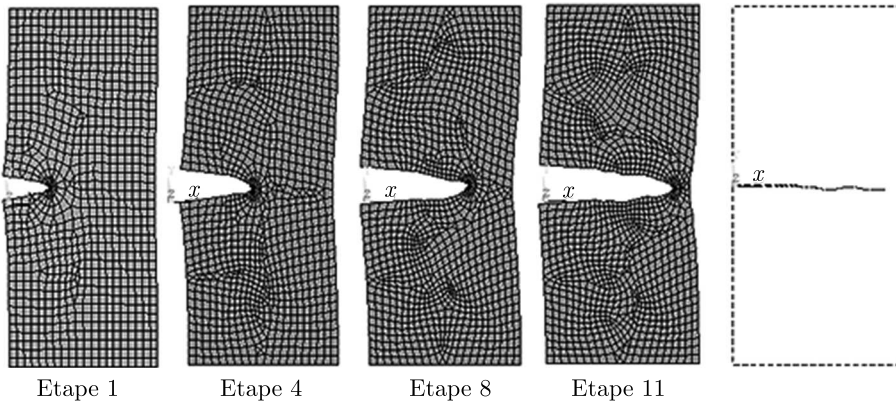


Fig. 18. Crack propagation path (NR)

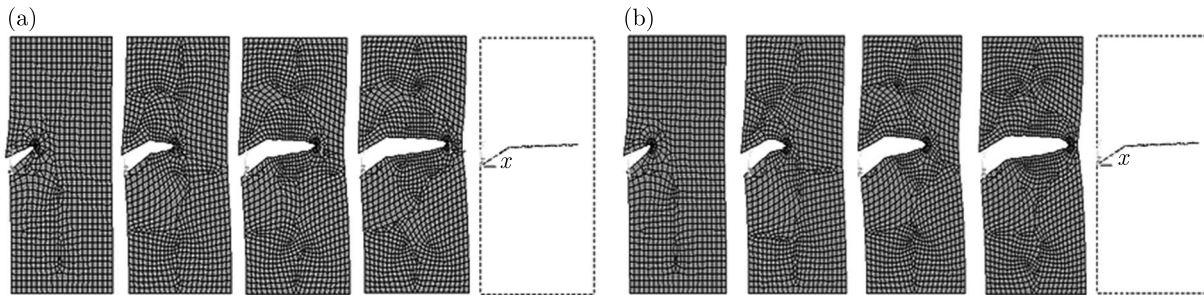


Fig. 19. Crack propagation path for an inclined crack ($\alpha = 30^\circ$); (a) NR, (b) SBR

4. Conclusion

The study has been made to analyze and simulate the crack propagation in rubber-like materials under mixed-mode loading. Using the Ansys Parametric Design Language (APDL), the strain energy density approach is investigated, at each crack increment length, the kinking angle is evaluated as a function of the Minimum Strain Energy Density (MSED) around the crack tip. The obtained results allow us to deduce the following conclusions:

- The quarter-point singular elements proposed by Barsoum (1974) are used to consider the singularity of stress and deformations fields at the crack tip.

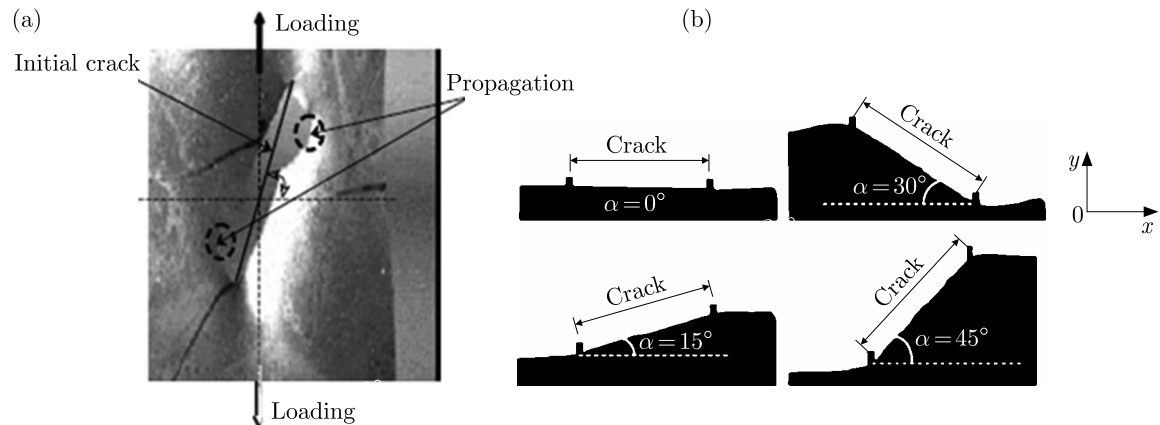


Fig. 20. Initiation and propagation of a pre-existing crack in SBR: (a) crack initiation (initial crack orientation $\alpha = 45^\circ$), (b) total breaking

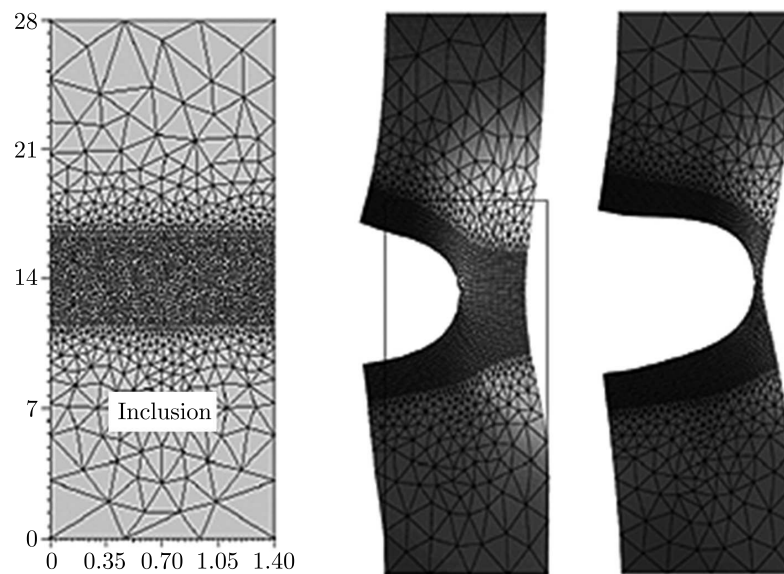


Fig. 21. Crack propagation path in the case of a rigid inclusion (Legrain, 2007)

- Out of the core region surrounding the crack tip, the minimum of SED is reached for a constant value independently of the distance r . We noted that the observations obtained are similar to those obtained in literature (Hamdi *et al.*, 2006; Hamdi, 2006).
- The minimal value of SED corresponding to the direction of crack propagation is always reached in the plane perpendicular to the loading axis, independently of the initial crack orientation.
- The values of the angle of the initial crack direction and the final path of crack propagation are related to the number of the elements surrounding the crack tip.
- Consequently, the SED approach, developed in the linear elastic fracture problems, could be extended to highly non-linear deformable materials as an indicator of the crack propagation direction.

References

1. ALSHOAIBI A., ARIFFIN A.K., 2006, Finite element simulation of stress intensity factors in elastic-plastic crack growth, *Journal of Zhejiang University – Science A*, **7**, 1336-1342

2. ALSHOAIBI A.M., ARIFFIN A.K., 2008. Fatigue life and crack path prediction in 2D structural components using an adaptive finite element strategy, *International Journal of Mechanical and Materials Engineering*, **3**, 1, 97-104
3. ANDREWS E.H., 1974, A generalised theory of fracture mechanics, *Journal of Materials Science*, **9**, 887-894
4. ANSYS, 2009, Inc. Programmer's Manual for Mechanical APDL, Release 12.1
5. AYATOLLAHI M.R., SEDIGHIANI K., 2012, Mode I fracture initiation in limestone by strain energy density criterion, *Journal of Theoretical and Applied Mechanics*, **57**, 14-18
6. BARSOUM R.S., 1974, On the use of isoparametric finite element in linear fracture mechanics, *International Journal for Numerical Methods in Engineering*, **10**, 25-37
7. BENOUIS A., BOULENOUAR A., BENSEDDIQ N., SERIER B., 2015, Numerical analysis of crack propagation in cement PMMA: application of SED approach, *Structural Engineering and Mechanics*, **55**, 93-109
8. BIAN L., TAHERI F., 2011, A proposed maximum ratio criterion applied to mixed mode fatigue crack propagation, *Materials and Design*, **32**, 2066-2072
9. BOULENOUAR A., BENOUIS A., BENSEDDIQ N., 2016, Numerical modelling of crack propagation in cement PMMA: Comparison of different criteria, *Materials Research Bulletin*, in press
10. BOULENOUAR A., BENSEDDIQ N., MAZARI M., 2013a, Strain energy density prediction of crack propagation for 2D linear elastic materials, *Journal of Theoretical and Applied Mechanics*, **67/68**, 29-37
11. BOULENOUAR A., BENSEDDIQ N., MAZARI M., 2013b, Two-dimensional numerical estimation of stress intensity factors and crack propagation in linear elastic analysis, *Engineering, Technology and Applied Science Research, ETASR*, **3**, 506-510
12. BOULENOUAR A., BENSEDDIQ N., MAZARI M., 2014, FE Model for linear-elastic mixed mode loading: estimation of SIFs and crack propagation, *Journal of Theoretical and Applied Mechanics*, **52**, 373-383
13. BOULENOUAR A., MAZARI M., 2009, Study of elastomers behavior at rupture based on the first Seth strain measures invariant, *Computational Materials Science*, **45**, 966-971
14. CARPINTERI A., 1984, Size effects in material strength due to crack growth and material non-linearity, *Journal of Theoretical and Applied Mechanics*, **2**, 39-45
15. CHANG K.J., 1981a, Further studies of the maximum stress criterion on the angled crack problem, *Engineering Fracture Mechanics*, **14**, 125
16. CHANG K.J., 1981b, On the maximum strain criterion - a new approach to the angled crack problem, *Engineering Fracture Mechanics*, **14**, 107-124
17. CHOI D.H., CHOI H.Y., LEE D., 2006, Fatigue life prediction of in-plane gusset welded joints using strain energy density factor approach, *Journal of Theoretical and Applied Mechanics*, **45**, 108-116
18. CHOW C.L., XU J., 1985, Application of the strain energy density criterion to ductile fracture, *Journal of Theoretical and Applied Mechanics*, **3**, 185-191
19. ERDOGAN F., SIH G.C., 1963, On the crack extension in plates under plane loading and transverse shear, *Journal of Basic Engineering*, **85**, 519-527
20. FAJDIGA G., REN Z., KRAMAR J., 2007, Comparison of virtual crack extension and strain energy density methods applied to contact surface crack growth, *Engineering Fracture Mechanics*, **74**, 2721-2734
21. GREENSMITH H.W., 1963, Rupture of rubber-X. The change in stored energy on making a small cut in a test piece held in simple extension, *Journal of Applied Polymer Science*, **7**, 993-1002
22. GRIFFITH A.A., 1920, The phenomenon of rupture and flow in solids, *Philosophical Transactions of the Royal Society A*, **221**, 163-198

23. GRIFFITH A.A., 1924, The theory of rupture, *Proceedings of 1st International Conference for Applied Mechanics*, Delft, 55-63
24. HAMDI A., 2006, *Critère de rupture gnralis pour les élastomères vulcanisables et thermoplastiques*, Thèse de doctorat, Universit des Sciences et Technologies de Lille
25. HAMDI A., AÏT HOCINE N., NAÏT ABDELAZIZ M., BENSEDDIQ N., 2007, Fracture of elastomers under static mixed mode: the strain-energy-density factor, *International Journal of Fracture*, **144**, 65-75
26. HAMDI A., NAÏT ABDELAZIZ M., AÏT HOCINE N., BENSEDDIQ N., HEUILLET P., 2006, Fracture criteria of rubber like-materials under plane stress conditions, *Polymer Testing*, **25**, 994-1005
27. KIPP M.E., SIH G.C., 1975, The strain energy density failure criterion applied to notched elastic solids, *International Journal of Solids and Structures*, **11**, 153-173
28. KOMORI K., 2005, Ductile fracture criteria for simulating shear by node separation method, *Journal of Theoretical and Applied Mechanic*, **43**, 101-114
29. LEGRAIN G., 2007, *Extension de l'approche X-FEM aux grandes transformations pour la fissuration des milieux hyperlastiques*, Thèse de Doctorat, Ecole Centrale Nantes, Université de Nantes, France
30. LEGRAIN G., MOES N., VERRON E., 2005, Stress analysis around crack tips in finite strain problems using the extended Finite Element Method, *International Journal for Numerical Methods in Engineering*, **63**, 2, 290-314
31. MAITI S.K., SMITH R.A., 1983, Comparison of the criteria for mixed mode brittle fracture based on the preinstability stress-strain field, *International Journal of Fracture*, **23**, 281-295
32. MATIC P., 1985, Numerically predicting ductile material behavior from tensile specimen response, *Journal of Theoretical and Applied Mechanic*, **4**, 13-28
33. OGDEN R.W., 1984, *Non Linear Elastic Deformation*, Ellis Horwood Limited Publishers
34. PEGORIN F., KOTOUSOV A., BERTO F., SWAIN M.V., SORNSUWAN T., 2012, Strain energy density approach for failure evaluation of occlusal loaded ceramic tooth crowns, *Journal of Theoretical and Applied Mechanic*, **5**, 44-50
35. RIVLIN R.S., THOMAS A.G., 1953, Rupture of rubber. I. Characteristic energy for tearing, *Journal of Polymer Science*, **10**, 291-318
36. SIH G.C., 1973, Some basic problems in fracture mechanics and new concepts, *Engineering Fracture Mechanics*, **5**, 365-377
37. SIH G.C., 1974, Strain energy-density factor applied to mixed mode crack problems, *International Journal of Fracture*, **10**, 205
38. SIH G.C., BARTHELEMY B.M., 1980, Mixed mode fatigue crack growth predictions, *Engineering Fracture Mechanics*, **13**, 439-451
39. SIH G.C., MACDONALD B., 1974, Fracture mechanics applied to engineering problems – strain energy density fracture criterion, *Engineering Fracture Mechanics*, **6**, 361-386
40. THEOCARIS P.S., 1984, A higher-order approximation for the T-criterion of fracture in biaxial fields, *Engineering Fracture Mechanics*, **19**, 975
41. WU H.C., 1974, Dual failure criterion for plane concrete, *Journal of the Engineering Mechanics Division*, **100**, 1167
42. YEOH O.H., 1990, Characterization of elastic properties of carbon black filled rubber vulcanizates, *Rubber Chemistry and Technology*, **63**, 792-805

DYNAMIC RESPONSE OF A SIMPLY SUPPORTED VISCOELASTIC BEAM OF A FRACTIONAL DERIVATIVE TYPE TO A MOVING FORCE LOAD

JAN FREUNDLICH

Warsaw University of Technology, Faculty of Automotive and Construction Machinery Engineering, Warszawa, Poland
e-mail: jfr@simr.pw.edu.pl

In the paper, the dynamic response of a simply supported viscoelastic beam of the fractional derivative type to a moving force load is studied. The Bernoulli-Euler beam with the fractional derivative viscoelastic Kelvin-Voigt material model is considered. The Riemann-Liouville fractional derivative of the order $0 < \alpha \leq 1$ is used. The forced-vibration solution of the beam is determined using the mode superposition method. A convolution integral of fractional Green's function and forcing function is used to achieve the beam response. Green's function is formulated by two terms. The first term describes damped vibrations around the drifting equilibrium position, while the second term describes the drift of the equilibrium position. The solution is obtained analytically whereas dynamic responses are calculated numerically. A comparison between the results obtained using the fractional and integer viscoelastic material models is performed. Next, the effects of the order of the fractional derivative and velocity of the moving force on the dynamic response of the beam are studied. In the analysed system, the effect of the term describing the drift of the equilibrium position on the beam deflection is negligible in comparison with the first term and therefore can be omitted. The calculated responses of the beam with the fractional material model are similar to those presented in works of other authors.

Keywords: fractional viscoelasticity, moving loads, beam vibrations, transient dynamic analysis

1. Introduction

The problem of predicting the dynamic response of a structure resulting from the passage of moving loads often occurs in engineering analysis. This problem has many applications in engineering analysis, some of these applications are vibrations that occur in bridges and railroad tracks, cranes, machine elements, weapon barrels, rails, rail and vehicle body parts. The studies show that the transversal deflection and stresses due to moving loads are considerably higher than those observed with stationary loads. The dynamic behaviour of a beam subjected to moving loads or moving masses have been studied extensively in connection with the design of railway tracks and bridges as well as machining processes. A broad overview of the analytical and numerical methods deals with these issues is provided in a book by Fryba (1972). A newer survey of these methods can be found e.g. in a book by Bajer and Dyniewicz (2012). The book also presents a comprehensive overview of the numerical methods including the finite element method (FEM) and the space-time element method (STEM). Additionally, both these books contain a broad bibliography devoted to the dynamic analysis of structures subjected to moving loads.

Furthermore, damping effects on structure dynamics are considered in many works devoted to the mentioned above subject (e.g Fryba, 1972). Therefore, selection of an appropriate viscoelastic material model is an essential element in studying the dynamical behaviour of mechanical structures. The selected model should as accurately as possible describe viscoelastic damping

over a wide interval of frequencies. A large number of engineering materials show a weak frequency dependence of their damping properties within a broad frequency range (Bagley and Torvik, 1983a,b; Caputo and Mainardi, 1971a; Clough and Penzien, 1993). This weak frequency dependence is difficult to describe using classical viscoelastic models, based on integer order rate laws. In the recent years, the fractional derivatives have been frequently utilized to describe dynamic characteristics of viscoelastic materials and damping elements (Podlubny, 1999; Mainardi, 2009; Rossikhin and Shitikova, 2010; Hedrih (Stevanović) 2014; Hedrih (Stevanović) and Machado, 2015). By introducing fractional-order derivatives instead of integer-order derivatives in the constitutive relations, the number of parameters required to accurately describe the dynamic properties can be significantly reduced (see, e.g., Caputo and Mainardi, 1971b; Bagley and Torvik, 1983b; Enelund and Olsson, 1999). A review of publications dedicated to application of fractional calculus in dynamics of solids can be found in the paper by Rossikhin and Shitikova (2010). Moreover, a fractional damping is utilized in dynamical analysis of beams under moving loads (e.g. Abu-Mallouh *et al.*, 2012; Alkhalidi *et al.*, 2013). In these papers, taken into consideration are only loads moving at a constant speed. The solutions presented in these works are obtained with the help of Mittag-Leffler functions and infinite series. In numerous studies in which fractional viscoelastic models are employed, the dynamic transient analysis is limited to the response induced by initial conditions. However, structures subjected to moving loads with a time varying velocity are often encountered in engineering practice. The number of publications considering the dynamic behaviour of a beam with a fractional viscoelastic model under moving loads is rather limited. Numerous research works related to structure vibrations described by fractional models present transient solutions expressed as series expansions (Atanackovic and Stankovic, 2002; Bagley and Torvik, 1986; Caputo, 1974; Hedrih (Stevanović) and Filipovski, 2002; Podlubny, 1999) which are not very useful for practical applications because of their slow convergence rate (Podlubny, 1999; Rossikhin and Shitikova, 2010). Thus, the aim of this work is demonstration of an approach utilizing fractional Green's function in dynamical analysis of a simply-supported beam subjected to a moving force with a constant velocity and constant acceleration. Green's function is evaluated using a closed contour of integration in conjunction with the residue theorem (Caputo and Mainardi, 1971b; Bagley and Torvik, 1983b, 1986; Rossikhin and Shitikova, 1997; Beyer and Kempfle, 1995). The proposed approach is the expansion of methods employing fractional calculus in the modelling of damping properties of dynamic systems.

2. Problem formulation

The equation of motion of the examined beam is derived on the assumption of the Bernoulli-Euler theory, neglecting rotary inertia and shear deformation. Furthermore, it is assumed that the beam is homogeneous with constant cross-section along its length, and the neutral axis of the beam bending is one of the principal axes of inertia of the normal cross section of the beam. Beam oscillations are assumed in the xy plane (Fig. 1). Moreover, it is assumed that the internal dissipation of mechanical energy in the beam material is described by a differential equation of the fractional order. Therefore, the stress-strain constitutive relation of the beam material is in the following form (e.g. Bagley and Torvik, 1983a)

$$\sigma = E\varepsilon(t) + E'_\gamma D_t^\gamma[\varepsilon(t)] = E\left(\varepsilon + \mu_\gamma \frac{d^\gamma \varepsilon(t)}{dt^\gamma}\right) \quad (2.1)$$

where: $\mu_\gamma = E'_\gamma/E$, E – Young's modulus of the beam material, E'_γ – damping coefficient, $D_t^\gamma[\cdot]$ – fractional order differential operator of the γ -th derivative with respect to time t in the following form (Miller and Ross, 1993; Podlubny, 1999)

$$D_t^\gamma f(t) \equiv \frac{d^\gamma}{dt^\gamma} f(t) \equiv \frac{1}{\Gamma(1-\gamma)} \frac{d}{dt} \int_0^t \frac{f(\tau) d\tau}{(t-\tau)^\gamma} \tag{2.2}$$

where $\Gamma(1-\gamma)$ is the Euler gamma function and $t \geq 0$ (Miller and Ross, 1993; Podlubny, 1999).

For many real materials, the fractional derivative order is commonly assumed to be in the interval $0 < \gamma < 1$ (Caputo and Mainardi, 1971a; Bagley and Torvik, 1983b; Enelund and Olsson, 1999). The constitutive relation with $\gamma = 1$ represents Kelvin-Voight material with internal linear dissipation of mechanical energy (e.g. Mainardi, 2009; Hedrih (Stevanović), 2014)

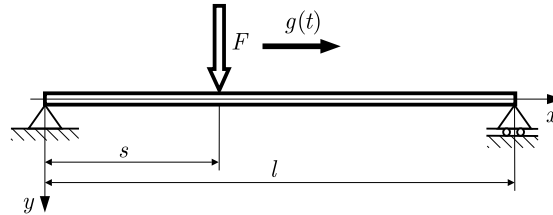


Fig. 1. Scheme of the analysed system

The beam is assumed to be subjected to a force moving with a constant velocity or acceleration from the left to the right edge of the beam, according with the sense of the x axis (Fig. 1). Based on the above assumptions, the governing equation of the analysed beam is obtained as below

$$EJ \left(\frac{\partial^4 y(x,t)}{\partial x^4} + \mu_\gamma \frac{d^\gamma}{dt^\gamma} \left(\frac{\partial^4 y(x,t)}{\partial x^4} \right) \right) + A\rho \frac{\partial^2 y(x,t)}{\partial t^2} = F\delta(x - g(t)) \tag{2.3}$$

where A is the cross-section area of the beam, J – axial moment of inertia of the beam cross-section respect to the neutral axis of the beam bending, ρ – material mass density of the beam, $y(x,t)$ – transversal displacement of the neutral beam axis (Fig. 1), t – time, x – longitudinal coordinate, F – intensity of the external moving and concentrated force, δ – Dirac delta function, $g(t)$ – function determining the force location, $g(t) = vt$ or $g(t) = \varepsilon t^2/2$ for a force moving with a constant velocity or constant acceleration, respectively. Furthermore, this function must satisfy the following condition $0 \leq g(t) \leq l$.

For the simply-supported beam, the deflection and bending moment at both beam ends have to be zero, thus the boundary conditions are as below

$$y(0,t) = 0 \quad y(l,t) = 0 \quad M_b(0,t) = 0 \quad M_b(l,t) = 0 \tag{2.4}$$

where l is the length of the beam, M_b – bending moment.

The bending moment is calculated as below

$$M_b(x,t) = \int_A \sigma y dA = \int_A \{E\varepsilon(t) + E'_\gamma D_t^\gamma [\varepsilon(t)]\} y dA = -EJ \left\{ \frac{d^2 y(x,t)}{dx^2} + \mu_\gamma D_t^\gamma \left[\frac{d^2 y(x,t)}{dx^2} \right] \right\} \tag{2.5}$$

therefore

$$\frac{d^2 y(0,t)}{dx^2} = \frac{d^2 y(l,t)}{dx^2} = 0 \quad D_t^\gamma \left[\frac{d^2 y(0,t)}{dx^2} \right] = D_t^\gamma \left[\frac{d^2 y(l,t)}{dx^2} \right] = 0 \tag{2.6}$$

Moreover, it is assumed that the beam is initially at rest and the initial bending moments are equal to 0.

The solution to Eq. (2.3) is obtained utilizing the mode superposition principle (e.g. Kaliski, 1966; Clough and Penzien, 1993; Rao, 2004). The eigenfunctions for a simply supported beam are given by

$$Y_n(x) = \sin \frac{n\pi x}{l} \quad n = 1, 2, 3, \dots \quad (2.7)$$

Then, the forced-vibration solution of a beam can be expressed as

$$y(x, t) = \sum_{n=1}^{\infty} \xi_n(t) Y_n(x) = \sum_{n=1}^{\infty} \xi_n(t) \sin \frac{n\pi x}{l} \quad (2.8)$$

and the corresponding derivatives are evaluated below

$$\frac{\partial^4 y(x, t)}{\partial x^4} = \sum_{n=1}^{\infty} Y_n^{IV}(x) \xi_n(t) \quad \frac{d^\gamma}{dt} \left(\frac{\partial^4 y(x, t)}{\partial x^4} \right) = \sum_{n=1}^{\infty} Y_n^{IV}(x) D_t^\gamma [\xi(t)] \quad (2.9)$$

where

$$D_t^\gamma [\xi_n(t)] = \frac{d^\gamma \xi(t)}{dt^\gamma} = \frac{1}{\Gamma(1-\gamma)} \frac{d}{dt} \int_0^t \frac{\xi_n(\tau) d\tau}{(t-\tau)^\gamma}$$

and

$$Y_n^{IV}(x) = \frac{d^4 Y(x)}{dx^4} \quad \frac{\partial^2 y(x, t)}{\partial t^2} = \sum_{n=1}^{\infty} Y_n(x) \ddot{\xi}_n(t) \quad (2.10)$$

where

$$\ddot{\xi}(t) = \frac{d^2 \xi(t)}{dt^2} \quad (2.11)$$

Substituting Eqs. (2.9) and (2.10) into (2.3), we get

$$\sum_{n=1}^{\infty} \left(Y_n^{IV}(x) \xi_n(t) + \mu_\gamma Y_n^{IV}(x) D_t^\gamma [\xi_n(t)] + a_b^2 Y(x) \ddot{\xi}_n(t) \right) = \frac{F}{EJ} \delta(x - g(t)) \quad (2.12)$$

Next, integrating over x from 0 to 1, and using the orthogonality property of eigenfunctions, after some mathematical transformations, the following relationships are obtained

$$\ddot{\xi}_n(t) + \mu_\gamma \omega_n^2 D_t^\gamma [\xi_n(t)] + \omega_n^2 \xi_n(t) = f_0 \sin \frac{n\pi g(t)}{l} \quad (2.13)$$

where

$$f_0 = \frac{2F}{m} \quad \omega_n = \left(\frac{\pi n}{l} \right)^2 \sqrt{\frac{EJ}{\rho A}}$$

m – mass of the beam.

Assuming zero initial conditions

$$\xi(t) \Big|_{t=0} = 0 \quad \frac{d[\xi(t)]}{dt} \Big|_{t=0} = 0 \quad \frac{d^{\gamma-1}[\xi(t)]}{dt^{\gamma-1}} \Big|_{t=0} = 0$$

the solution of equations (2.13) can be expressed as

$$\xi_n(t) = f_0 \int_0^t G_n(t-\tau) \sin \frac{n\pi g(\tau)}{l} d\tau \quad (2.14)$$

where $G_n(t)$ is Green's function corresponding to Eq. (2.13) (Miller and Ross, 1993; Podlubny, 1999; Rossikhin and Shitikova, 1997, 2010). This Green's function consists of two terms, namely

$$G_n(t) = K_{1n}(t) + K_{2n}(t) \tag{2.15}$$

The first term K_{1n} (Eq. (2.15)) represents damped vibrations around the drifting equilibrium position, while the second term K_{2n} describes the drift of the equilibrium position (Beyer and Kempfle, 1995; Rossikhin and Shitikova, 1997). The term K_{1n} could be calculated from the formula given by Beyer and Kempfle (1995)

$$K_{1n}(t) = \alpha_n e^{-\sigma_n t} \sin(\Omega_n t + \phi_n) \tag{2.16}$$

where

$$\alpha_n = \frac{2}{\sqrt{\mu_k^2 + \nu^2}} \quad \phi_n = \arctan \frac{\mu_k}{\nu} \quad \mu_k = \operatorname{Re}(W'_{(p,1,2)}) \quad \nu = \operatorname{Im}(W'_{(p,1,2)})$$

and $W(p) = p^2 + \mu_\gamma \omega_n^2 p^\gamma + \omega_n^2$ is the characteristic polynomial of equations (2.13), $W'(p) = 2p + \gamma \mu_\gamma \omega_n^2 p^{\gamma-1}$ - derivative of the characteristic polynomial with respect p , $p_{1,2} = -\sigma_n \pm i\Omega_n$ - conjugate complex roots of the characteristic polynomial $W(p)$.

The term K_{2n} could be calculated using the formula (Beyer and Kempfle, 1995)

$$K_{2n}(t) = \frac{\mu_\gamma \omega_n^2 \sin(\pi\gamma)}{\pi} \int_0^\infty \frac{r^\gamma e^{-rt} dr}{[r^2 + \mu_\gamma \omega_n^2 r^\gamma \cos(\pi\gamma) + \omega_n^2]^2 + [\mu_\gamma \omega_n^2 r^\gamma \sin(\pi\gamma)]^2} \tag{2.17}$$

In some cases of vibration analysis, K_{2n} could be neglected in comparison with K_{1n} (Kempfle *et al.*, 2002; Rossikhin and Shitikova, 1997).

In the case of a viscoelastic integer order Kelvin-Voigt material model, the governing equation of the analysed beam has the following form (Kaliski, 1966)

$$EJ \left(\frac{\partial^4 y(x,t)}{\partial x^4} + \mu \frac{\partial^5 y(x,t)}{\partial x^4 \partial t} \right) + A\rho \frac{\partial^2 y(x,t)}{\partial t^2} = F\delta(x - g(t)) \tag{2.18}$$

The solution to the equation (2.18) could be obtained using a similar approach as in the case of the equation with fractional damping. For each n -th mode, the response could be calculated as follows (Kaliski, 1966)

$$\xi_n(t) = \begin{cases} \frac{f_0}{\omega_{hn}} \int_0^t e^{-h_n(t-\tau)} \sin(\omega_{hn}(t-\tau)) \sin \frac{n\pi g(\tau)}{l} d\tau & \text{for } h_n < \omega_n \\ \frac{f_0}{\tilde{\omega}_{hn}} \int_0^t e^{-h_n(t-\tau)} \sinh(\tilde{\omega}_{hn}(t-\tau)) \sin \frac{n\pi g(\tau)}{l} d\tau & \text{for } h_n > \omega_n \end{cases} \tag{2.19}$$

where

$$h_n = \frac{1}{2} \mu \omega_n^2 \quad \omega_{hn} = \sqrt{\omega_n^2 - h_n^2} \quad \tilde{\omega}_{hn} = \sqrt{h_n^2 - \omega_n^2}$$

It should be noted that when $\gamma = 1$ (integer order derivative), the component K_{2n} of fractional Green's function (Eqs. (2.15) and (2.17)) vanishes, and it could be demonstrated that equations with a fractional and integer order derivative (Eq. (2.19)) are equivalent in the case of a subcritically damped system, i.e. $\omega_n > h_n$.

3. Calculation results and discussion

In order to demonstrate the feasibility of the described above method, exemplary calculations of a beam subjected to a moving load have been performed. Responses of the beam with the fractional viscoelastic model are computed using equations (2.13)-(2.17) whereas the responses of the beam with the integer order derivative model are computed using equation (2.19).

The dimensionless dynamic deflection of the beam y/y_0 versus the dimensionless time parameter s has been computed. The variable y_0 denotes the static deflection at the beam mid-span and can be calculated from the equation

$$y_0 = \frac{F_0 l^3}{48EI} \quad (3.1)$$

The dimensionless time parameter s is defined as

$$s = \frac{vt}{l} \quad \text{or} \quad s = \frac{\varepsilon t^2}{2l} \quad (3.2)$$

in the case of a constant force velocity or constant acceleration, respectively.

The calculations are accomplished for several values of the order of fractional derivative γ , dimensionless velocity v/v_{cr} and acceleration $\varepsilon/\varepsilon_{cr}$. Variables v_{cr} and ε_{cr} denote the critical velocity and acceleration, respectively. The critical velocity corresponds to the first natural vibration frequency of the beam and is defined as (Fryba, 1972)

$$v_{cr} = \frac{\pi}{l} \sqrt{\frac{EJ}{\rho A}} \quad (3.3)$$

whereas the critical acceleration is defined as the acceleration at which the force at the end of the beam reaches the critical velocity and is defined as

$$\varepsilon_{cr} = \frac{\pi^2 EJ}{l^3 \rho A} \quad (3.4)$$

Firstly, the dynamic response of the beam subjected to a moving force at a constant velocity calculated with the help of presented above equations are compared to the results obtained using the corresponding formula given by Fryba (1972). These comparative calculations are performed assuming a very light damping i.e. $\mu_\gamma = 1 \cdot 10^{-5} \text{ s}^\gamma$ and $\gamma = 1$ (integer order derivative). The calculations are performed for $v/v_{cr} = 0.5$ (Eq. (3.1)). The calculation results obtained using the both equations are virtually identical. Minimal differences are found in the results, which is probably caused by differences in the modelling of damping in the system. Namely, in the equations given by Fryba (1972) it is assumed that the damping coefficient is independent of vibration modes and frequency in contrast to the damping model utilized in this work (Eqs. (2.3) and (2.13)). Next, in order to illustrate the application of the presented above procedure, computational examples for the response of the beam loaded with a moving force are performed. The calculations are carried out for the beam of length 20 m, mass density 7600 kg/m³, cross-section area $2 \cdot 10^{-3} \text{ m}^2$, cross-section moment of inertia $3.953 \cdot 10^{-6} \text{ m}^4$, Young's modulus $2.1 \cdot 10^5 \text{ MPa}$, coefficient $\mu_\gamma = 3 \cdot 10^{-2} \text{ s}^\gamma$. The force value is assumed $F = 100 \text{ N}$.

From equation (2.16), it follows that the values of damping coefficients and vibration amplitudes depend on the roots of the characteristic equation and, therefore, knowledge of the roots is required for further calculations. The roots are computed for the varying fractional derivative order γ . The dependence of the roots of the characteristic equation on the fractional derivative order is shown in Fig. 2 (for the first two vibration modes). The real part of the root determines the damping coefficient whereas the imaginary part determines the vibration frequency (Eq.

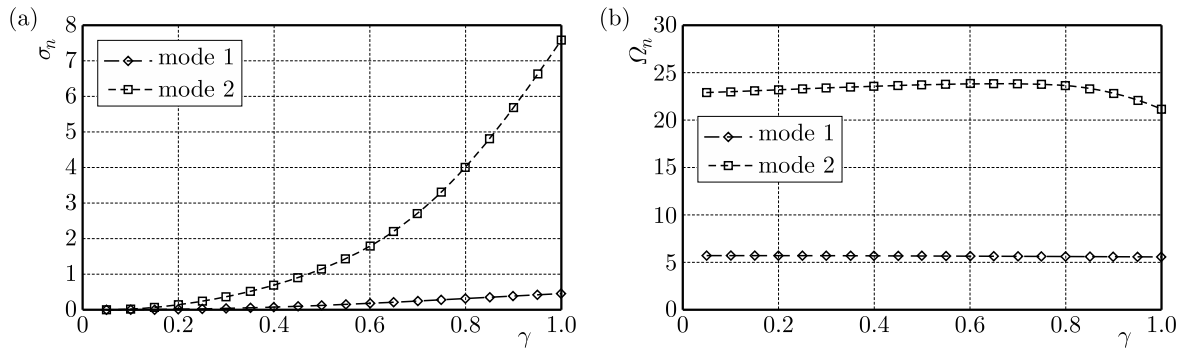


Fig. 2. Relationship between roots of the characteristic equation and the order of fractional derivative: (a) real part, (b) imaginary part

(2.16)). Performed calculations reveal that the value of the damping coefficient increases with the order of fractional derivative (Fig. 2a) but the vibration frequency is practically constant (Fig. 2b).

Moreover, the ratio of the real to the imaginary part of the roots of the characteristic equation increases with the increasing order of fractional derivative (Fig. 3a), whereas the amplitude α_n (Eq. (2.16)) is practically independent of the order of fractional derivative (Fig. 3b). It could be expected that the dynamic deflection of the beam decreases with the increasing order of fractional derivative.

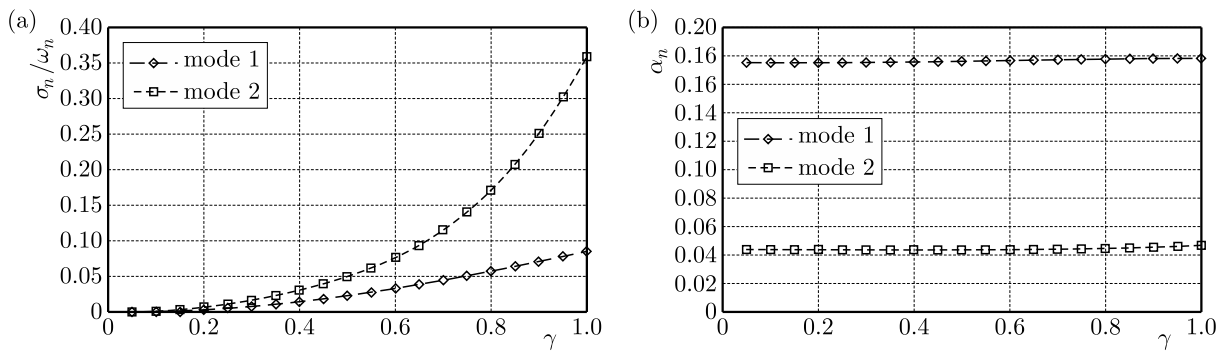


Fig. 3. (a) Ratio of the real to the imaginary part of the roots of the characteristic equation, (b) relationship between the amplitude α_n and the order of fractional derivative

The responses of the beam subjected to a force moving at a constant velocity are presented in Figs. 4-6. In Fig. 4, the dimensionless dynamic deflection of the beam at the point under the travelling force at various values of the derivative order γ is presented whereas the dynamic deflection at the mid-span of the beam is shown in Fig. 5. These results reveal that deflection of the beam under a moving force decreases with the increasing order of fractional derivative γ (Fig. 4). The maximum deflection of the beam is greater for the dimensionless velocity $v/v_{cr} = 0.5$ than $v/v_{cr} = 1.0$. In the case $v/v_{cr} = 0.5$, the dynamic deflection at the mid-span of the beam decreases with the increasing order of fractional derivative when $s < 0.775$ while increases when $0.775 < s < 1.0$ (Fig. 5a). In the case $v/v_{cr} = 1.0$, the dynamic deflection decreases with the increasing order of fractional derivative for the total duration of force action. In the case of a force moving at a constant velocity, for all computational examples, the maximum beam deflection is obtained when $\gamma = 0.25$ (Figs. 5 and 6)

A comparison between the dynamic deflections of the beam at various values of force velocity in the case of the derivative order $\gamma = 0.5$ is shown in Fig. 6. The response curves are similar to the corresponding curves computed for the integer order derivative presented in the literature (Fryba, 1972; Bajer and Dyniewicz, 2012; Abu Hilal and Zibdeh, 2000).

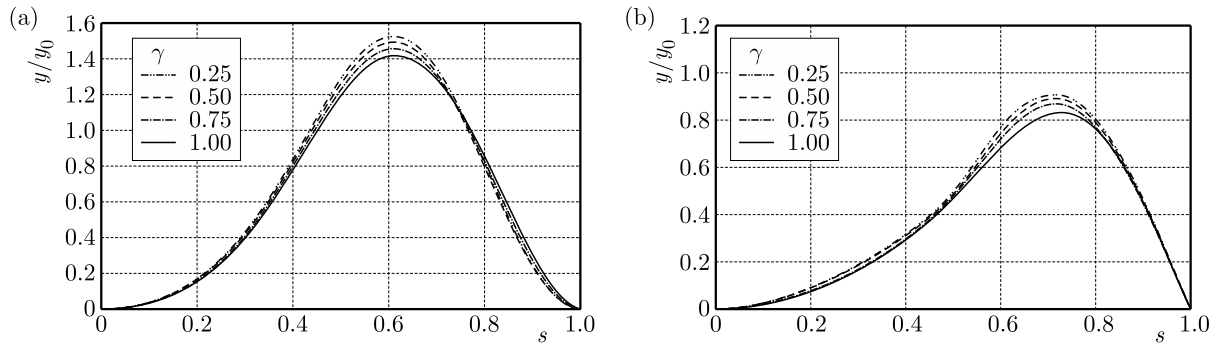


Fig. 4. Dynamic deflection of the beam under the moving force at various values of the derivative order γ , in the case of constant velocity: (a) $v/v_{cr} = 0.5$, (b) $v/v_{cr} = 1.0$

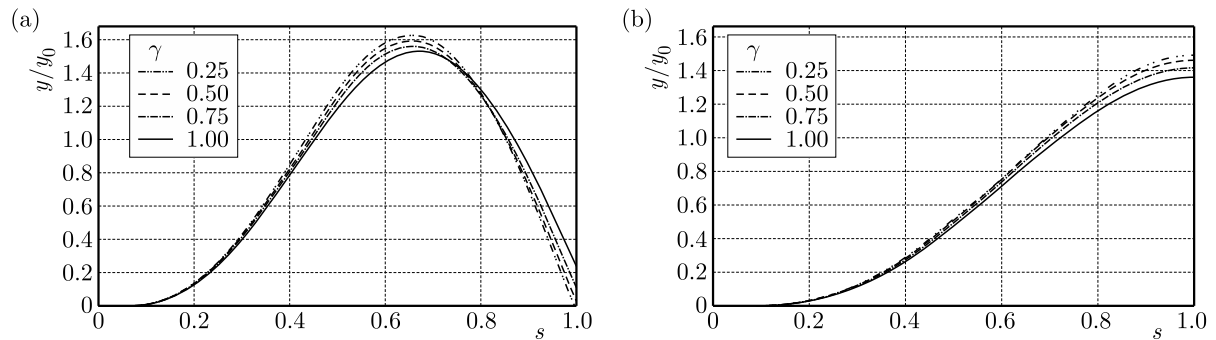


Fig. 5. Dynamic deflection at the mid-span of the beam at various values of the derivative order γ in the case of constant velocity: (a) $v/v_{cr} = 0.5$, (b) $v/v_{cr} = 1.0$

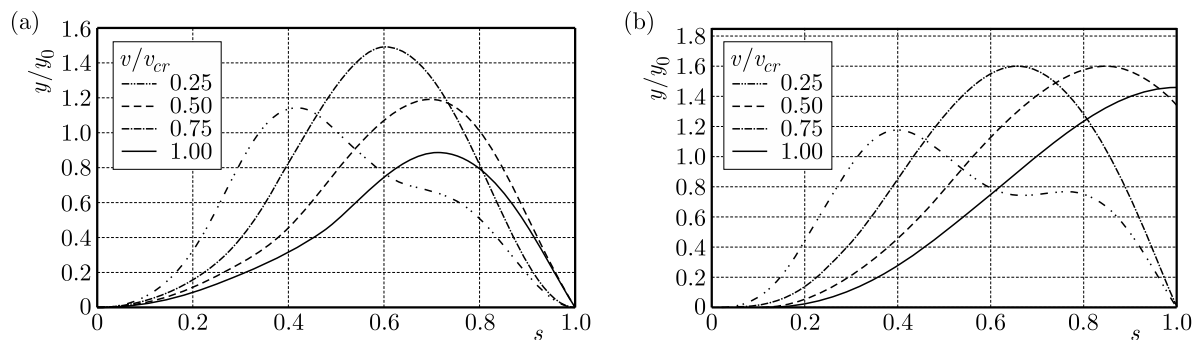


Fig. 6. A comparison between the dynamic deflection of the beam at various values of force velocity v/v_{cr} in the case of the derivative order $\gamma = 0.5$: (a) under the travelling force, (b) at the mid-span of the beam

Beam responses to the force moving at a constant acceleration are presented in Figs. 7-9. In Fig. 7, the dimensionless dynamic deflection of the beam at the point under the travelling force at various values of the derivative order γ is presented whereas the dynamic deflection at the mid-span of the beam is shown in Fig. 8. For all computational examples, the maximum beam deflection occurs in the case of $\gamma = 0.25$ (Figs. 7 and 8). In the case of $\varepsilon/\varepsilon_{cr} = 0.5$, the beam responses computed for various orders of the fractional derivatives differ slightly. The difference between curves obtained for $\varepsilon/\varepsilon_{cr} = 0.5$ are smaller than for the curves obtained for $\varepsilon/\varepsilon_{cr} = 1.0$ (Figs. 7 and 8).

In all calculation cases, the calculated values of the component K_2 of fractional Green's function are negligible in comparison to the values of the component K_1 (Eqs. (2.13)-(2.15)). Examples of K_1 and K_2 components of fractional Green's function as a function of the dimensionless time are shown in Fig. 10.

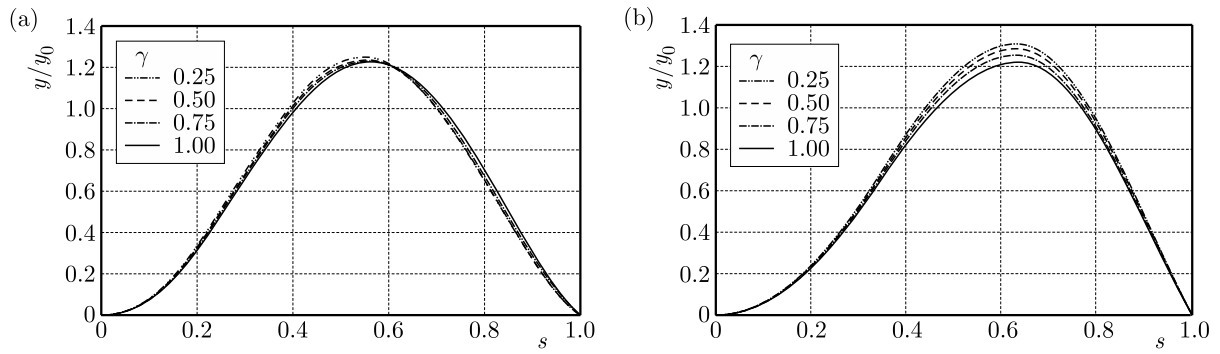


Fig. 7. Dynamic deflection of the beam under the travelling force at various values of the derivative order γ in the case of dimensionless acceleration: (a) $\epsilon/\epsilon_{cr} = 0.5$, (b) $\epsilon/\epsilon_{cr} = 1.0$

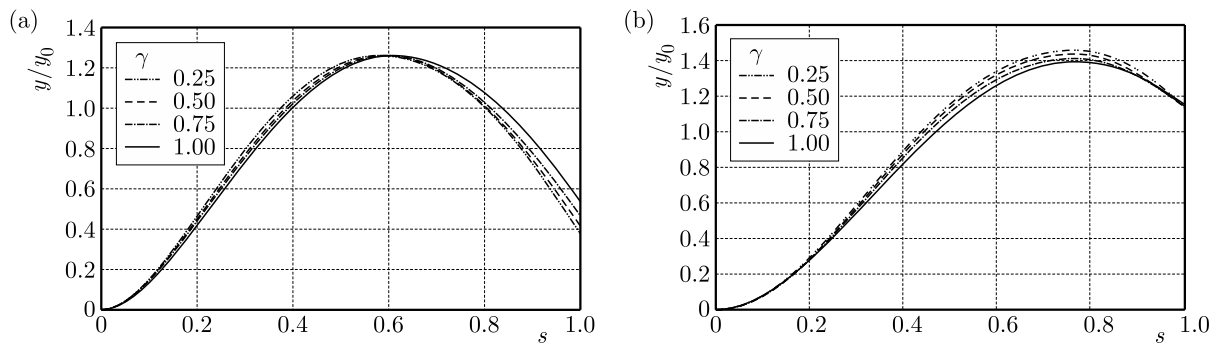


Fig. 8. Dynamic deflection at the mid-span of the beam at various values of the derivative order γ , in the case of dimensionless acceleration: (a) $\epsilon/\epsilon_{cr} = 0.5$, (b) $\epsilon/\epsilon_{cr} = 1.0$

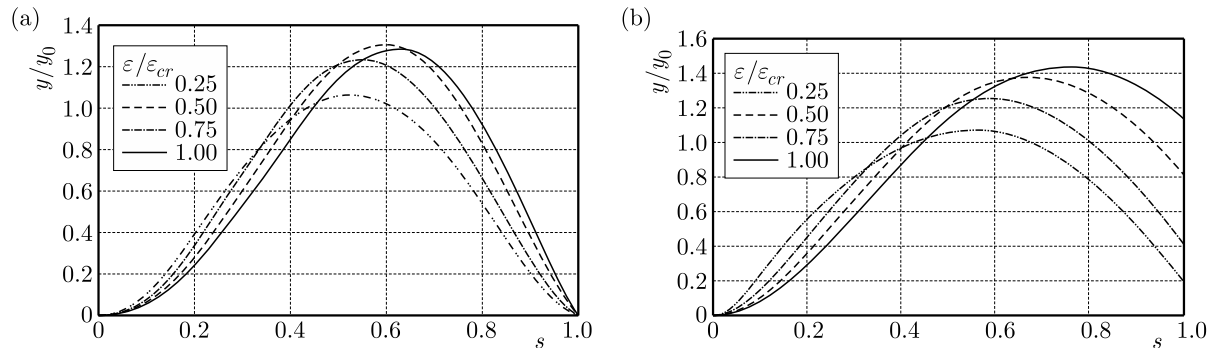


Fig. 9. A comparison between the dynamic deflection of the beam at various values of force acceleration ϵ/ϵ_{cr} in the case of the derivative order $\gamma = 0.5$: (a) under the travelling force, (b) at the mid-span of the beam

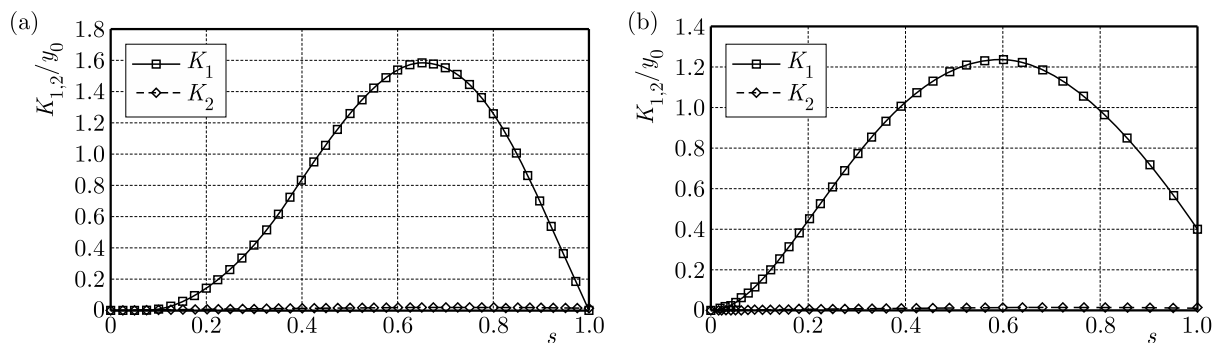


Fig. 10. Values of components K_1 and K_2 of fractional Green's function versus dimensionless time: (a) constant velocity, (b) constant acceleration

4. Conclusions

In this paper, the governing equations of dynamic behaviour of a viscoelastic beam made of a material described by the fractional derivative Kelvin-Voigt model and subjected to a force travelling with a constant acceleration are presented. The solution to the governing equations is based on the method presented by Beyer and Kempfle (1995) or by Rossikhin and Shitikova (1997). The solution is achieved with the aid of a convolution integral of fractional Green's function and the forcing function. Green's function is formulated by two terms. The first term describes damped vibrations around the drifting equilibrium position, while the second term describes the drift of the equilibrium position. In the author's opinion, the proposed method of solution of fractional differential equations has advantages over the solution with Green's function in the form of the Mittag-Leffler series, which are presented in other works (Podlubny, 1996; Abu-Mallouh *et al.*, 2012), because the mentioned series has a weak convergence rate. Furthermore, in some cases, the integral containing the second term of Green's function K_2 can be neglected (Eqs. (2.15) and (2.17)) (Rossikhin and Shitikova, 1997; Kempfle *et al.*, 2012), which significantly reduces the time of numerical calculations.

Utilizing the obtained solution to the governing equations, exemplary calculations of a beam subjected to a moving load have been performed. In the first step, responses of the examined beam subjected to the travelling force with a constant velocity have been calculated using the obtained solution and formulae given by Fryba (1972). The calculation results obtained using both equations are virtually identical. Afterwards, responses of the beam subjected to a force moving at a constant and accelerated velocity have been computed. To the best of the author's knowledge, responses of a beam whose internal dissipation of mechanical energy is described by a differential equation of a fractional order and subjected to a force moving at a constant acceleration have not been published yet.

The performed calculations reveal that in the case of a force moving at a constant velocity, the calculated maximum deflection of the beam decreases with the increasing order of fractional derivative (Figs. 4 and 5) as could be expected (see section above). In the case of a force moving at a constant velocity, the calculated beam responses are similar to those presented in the works of other authors (e.g. Fryba, 1972; Bajer and Dyniewicz, 2012; Abu Hilal and Zibdeh, 2000).

In the case of a force moving at a constant acceleration, for all computational examples, the maximum beam deflection occurs when $\gamma = 0.25$. In the case of $\varepsilon/\varepsilon_{cr} = 0.5$, the beam responses computed for various orders of the fractional derivatives differ slightly. The difference between the responses computed for various orders of the fractional derivatives are smaller for $\varepsilon/\varepsilon_{cr} = 0.5$ than for the responses obtained for $\varepsilon/\varepsilon_{cr} = 1.0$.

The proposed approach expands the methods employing fractional calculus in the analysis of transient dynamic processes.

A. Appendix

Fractional Green's function of Eq. (2.13) can be found by the inverse Laplace transform of the expression below (Bagley and Torvik, 1983b; Beyer and Kempfle, 1995; Rossikhin and Shitikova, 1997; Podlubny, 1999)

$$g(p) = \frac{1}{p^2 + \mu_\gamma p^\gamma \omega_0^2 + \omega_0^2} \quad (\text{A.1})$$

therefore

$$G(t) = L^{-1}[g(p)] = \frac{1}{2\pi i} \int_{c-i\infty}^{c+i\infty} \frac{e^{pt}}{p^2 + \mu_\gamma p^\gamma \omega_0^2 + \omega_0^2} dp \quad (\text{A.2})$$

The inverse transform integral is evaluated using Cauchy’s residue theorem (Brown and Churchill, 2003). The function $g(p)$ has only two poles lying in the left complex plane (Beyer and Kempfle, 1995; Rossikhin and Shitikova, 1997). Moreover, the function $g(p)$ has a branch point at the origin, and the branch cut follows the negative real axis, then the negative real half-axis have to be encircled by the integration contour. The contour of integration, used in conjunction with the residue theorem, is shown in Fig. 11.

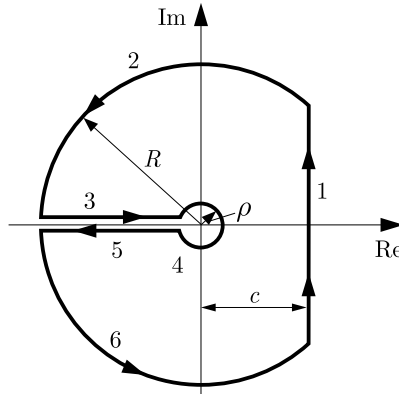


Fig. 11.

Therefore, it can be stated that

$$\oint_{L_{123456}} G(p) dp = 2\pi i \sum_{k=1}^2 rez_{p_k} g(p) \tag{A.3}$$

and

$$\begin{aligned} & \oint_{L_1} g(p) dp + \oint_{L_2} g(p) dp + \oint_{L_2} g(p) dp + \oint_{L_4} g(p) dp + \oint_{L_5} g(p) dp + \oint_{L_6} g(p) dp \\ &= 2\pi i \sum_{k=1}^n rez_{p_k} g(p) \end{aligned} \tag{A.4}$$

but

$$G(t) = \frac{1}{2\pi i} \oint_{L_1} g(p) dp \tag{A.5}$$

thus

$$\begin{aligned} \oint_{L_1} g(p) dp &= - \left(\oint_{L_2} g(p) ds + \oint_{L_3} g(p) dp + \oint_{L_4} g(p) dp + \oint_{L_5} g(p) dp + \oint_{L_6} g(p) dp \right) \\ &+ 2\pi i \sum_{k=1}^n rez_{p_k} g(p) \end{aligned} \tag{A.6}$$

It could be shown that the integrals along contours L_2, L_4, L_6 are equal to 0. The integrals along the contours L_3 and L_5 could be evaluated using substitution $p = re^{i\pi}$ and $p = re^{-i\pi}$. Noting

that $re^{i\pi} = re^{-i\pi} = r(\cos \pi \pm i \sin \pi) = -r$, $p = -r$ and $dp = -dr$, the integrals I_3 and I_5 along the contours L_3 and L_5 can be evaluated as below

$$\begin{aligned} I_3 + I_5 &= \int_{L_3} \frac{e^{pt}}{p^2 + \mu_\gamma \omega_0^2 p^\gamma + \omega_0^2} dp + \int_{L_5} \frac{e^{pt}}{p^2 + \mu_\gamma \omega_0^2 p^\gamma + \omega_0^2} dp \\ &= \int_R^0 \frac{-e^{-rt}}{r^2 e^{i2\pi} + \mu_\gamma \omega_0^2 r^\gamma e^{i\gamma\pi} + \omega_0^2} dr + \int_0^R \frac{-e^{-rt}}{r^2 e^{-i2\pi} + \mu_\gamma \omega_0^2 r^\gamma e^{-i\gamma\pi} + \omega_0^2} dr \end{aligned} \quad (\text{A.7})$$

and

$$\begin{aligned} I_3 + I_5 &= \int_R^0 \frac{-e^{-rt}}{r^2 + \mu_\gamma \omega_0^2 r^\gamma [\cos(\pi\gamma) + i \sin(\pi\gamma)] + \omega_0^2} dr \\ &+ \int_0^R \frac{-e^{-rt}}{r^2 + \mu_\gamma \omega_0^2 r^\gamma [\cos(\pi\gamma) - i \sin(\pi\gamma)] + \omega_0^2} dr = \int_R^0 \frac{-e^{-rt}(\mathcal{A} - i\mathcal{B})}{\mathcal{A}^2 + \mathcal{B}^2} dr \\ &+ \int_0^R \frac{-e^{-rt}(\mathcal{A} + i\mathcal{B})}{\mathcal{A}^2 + \mathcal{B}^2} dr = \int_0^R \frac{e^{-rt}(\mathcal{A} - i\mathcal{B})}{\mathcal{A}^2 + \mathcal{B}^2} dr + \int_0^R \frac{-e^{-rt}(\mathcal{A} + i\mathcal{B})}{\mathcal{A}^2 + \mathcal{B}^2} dr \\ &= \int_0^R \frac{-2\mu_\gamma \omega_0^2 r^\gamma e^{-rt} i \sin(\pi\gamma)}{\mathcal{A}^2 + \mathcal{B}^2} dr \end{aligned} \quad (\text{A.8})$$

where

$$\begin{aligned} \mathcal{A} &= r^2 + \mu_\gamma \omega_0^2 r^\gamma \cos(\pi\gamma) + \omega_0^2 \\ \mathcal{B} &= \mu_\gamma \omega_0^2 r^\gamma \sin(\pi\gamma) \end{aligned}$$

Denoting the sum of integrals in the RHS of Eq. (A.8) as K_2 , and for $R \rightarrow \infty$, the following relationship is obtained

$$K_2(t) = \frac{-1}{2\pi i} \int_0^\infty \frac{-2\mu_\gamma \omega_0^2 r^\gamma e^{-rt} i \sin(\pi\gamma)}{\mathcal{A}^2 + \mathcal{B}^2} dr = \frac{\mu_\gamma \omega_0^2 \sin(\pi\gamma)}{\pi} \int_0^\infty \frac{r^\gamma e^{-rt}}{\mathcal{A}^2 + \mathcal{B}^2} dr \quad (\text{A.9})$$

References

1. ABU HILAL M., ZIBDEH H.S., 2000, Vibration analysis of beams with general boundary conditions traversed by a moving force, *Journal of Sound and Vibration*, **229**, 2, 377-388
2. ABU-MALLOUH R., ABU-ALSHAIKH I., ZIBDEH H.S., RAMADAN. K., 2012, Response of fractionally damped beams with general boundary conditions subjected to moving loads, *Shock and Vibration*, **19**, 333-347
3. ALKHALDI H.S., ABU-ALSHAIKH I.M., AL-RABADI A.N., 2013, Vibration control of fractionally-damped beam subjected to a moving vehicle and attached to fractionally-damped multi-absorbers, *Advances in Mathematical Physics*, ID 232160, <http://dx.doi.org/10.1155/2013/232160>
4. ATANACKOVIC T.M., STANKOVIC B., 2002, Dynamics of a viscoelastic rod of fractional derivative type, *ZAMM*, **82**, 6, 377-386
5. BAGLEY R.L., TORVIK P.J., 1983a, A theoretical basis for the application of fractional calculus to viscoelasticity, *Journal of Rheology*, **27**, 3, 201-210

6. BAGLEY R.L., TORVIK P.J., 1983b, Fractional calculus – a different approach to the analysis of viscoelastically damped structures, *AIAA Journal*, **21**, 5, 741-748
7. BAGLEY R.L., TORVIK P.J., 1986, On the fractional calculus model of viscoelastic behavior, *Journal of Rheology*, **30**, 1, 133-155
8. BAJER C.I., DYNIEWICZ B., 2012, *Numerical Analysis of Vibrations of Structures under Moving Inertial Load*, Springer, Heidelberg
9. BEYER H., KEMPFLE S., 1995, Definition of physically consistent damping laws with fractional derivatives *ZAMM*, **75**, 8, 623-635
10. BROWN J.W., CHURCHILL R.V., 2003, *Complex Variables and Applications*, 7th ed., McGraw-Hill, Boston
11. CAPUTO M., 1974, Vibrations of an infinitive viscoelastic layer with a dissipative memory, *Journal of Acoustical Society of America*, **56**, 3, 897-904
12. CAPUTO M., MAINARDI F., 1971a, A new dissipation model based on memory mechanism, *Pure and Applied Geophysics*, **91**, 8, 134-147
13. CAPUTO M., MAINARDI F., 1971b, Linear models of dissipation in anelastic solids, *Rivista del Nuovo Cimento*, **1**, 2, 161-198
14. CLOUGH R.W., PENZIEN J., 1993, *Dynamics of Structures*, MacGraw-Hill, New York
15. ENELUND M., OLSSON P., 1999, Damping described by fading memory analysis and application to fractional derivative models, *International Journal of Solids and Structures*, **36**, 939-970
16. FRYBA L., 1972, *Vibration of Solids and Structures under Moving Loads*, Noordhoff International Publishing, Groningen, The Netherlands
17. HEDRIH (STEVANOVIĆ) K.R., 2014, Generalized functions of fractional order dissipation of energy system and extended lagrange differential equations in matrix form, *Tensor*, **75**, 1, 35-51
18. HEDRIH (STEVANOVIĆ) K.R., FILIPOVSKI A., 2002, Longitudinal creep vibrations of a fractional derivative order rheological rod with variable cross section, *Facta Universitatis, Series Mechanics, Automatic Control and Robotics*, **3**, 12, 327-349
19. HEDRIH (STEVANOVIĆ) K.R., MACHADO T.J.A., 2015, Discrete fractional order system vibrations, *International Journal of Non-Linear Mechanics*, **73**, 2-11
20. KALISKI S. (ED.), 1966, *Vibrations and Waves in Solids* (in Polish), Państwowe Wydawnictwo Naukowe, Warszawa
21. KEMPFLE S., SCHÄFER I., BEYER H., 2002, Fractional calculus via functional calculus: theory and application, *Nonlinear Dynamics*, **29**, 99-127
22. MAINARDI F., 2009, *Fractional Calculus and Waves in Linear Viscoelasticity: an Introduction to Mathematical Models*, Imperial College Press, London
23. MILLER K.S., ROSS B., 1993, *An Introduction to the Fractional Calculus and Fractional Differential Equations*, John Willey & Sons Inc., New York
24. PODLUBNY I., 1999, *Fractional Differential Equations*, Academic Press, San Diego
25. RAO S., 2004, *Mechanical Vibrations*, 4-th Ed., Prentice Hall, Upper Saddle River
26. ROSSIKHIN Y.A., SHITIKOVA M.V., 1997, Application of fractional derivatives to the analysis of damped vibrations of viscoelastic single mass systems, *Acta Mechanica*, **120**, 109-125
27. ROSSIKHIN Y.A., SHITIKOVA M.V., 2010, Application of fractional calculus for dynamic problems of solid mechanics: novel trends and recent results, *Applied Mechanics Reviews*, **63**, 1-51

INFORMATION FOR AUTHORS

Journal of Theoretical and Applied Mechanics (JTAM) is devoted to all aspects of solid mechanics, fluid mechanics, thermodynamics and applied problems of structural mechanics, mechatronics, biomechanics and robotics. Both theoretical and experimental papers as well as survey papers can be proposed.

We accept articles in English only. The text of a *JTAM* paper should not exceed **12 pages of standard format A4** (11-point type size, including abstract, figures, tables and references), short communications – **4 pages**.

The material for publication should be sent to the Editorial Office via electronic journal system: <http://www.ptmts.org.pl/jtam/index.php/jtam>

Papers are accepted for publication after the review process. Blind review model is applied, which means that the reviewers' names are kept confidential to the authors. The final decision on paper acceptance belongs to the Editorial Board.

After qualifying your paper for publication we will require L^AT_EX or T_EX or Word document file and figures.

The best preferred form of figures are files obtained by making use of editorial environments employing vector graphics:

- generated in CorelDraw (*.cdr), AutoCad and ArchiCad (*.dwg) and Adobe Illustrator (*.ai). We require original files saved in the standard format of the given program.
- generated by calculation software (e.g. Mathematica) - we need files saved in *.eps or *.pdf formats.
- made in other programs based on vector graphics - we ask for *.eps, *.wmf, *.svg, *.psfiles.

Any figures created without application of vector graphics (scans, photos, bitmaps) are strongly encouraged to be supplied in *.jpg, *.tif, *.png formats with resolution of at least 300 dpi.

Requirements for paper preparation

Contents of the manuscripts should appear in the following order:

- Title of the paper
- Authors' full name, affiliation and e-mail
- Short abstract (**maximum 100 words**) and 3-5 key words (**1 line**)
- Article text (equations should be numbered separately in each section; each reference should be cited in the text by the last name(s) of the author(s) and the publication year)
- References in alphabetical order. See the following:
 1. Achen S.C., 1989, A new boundary integral equation formulation, *Journal of Applied Mechanics*, **56**, 2, 297-303
 2. Boley B.A., Weiner J.H., 1960, *Theory of Thermal Stresses*, Wiley, New York
 3. Canon W., 1955, Vibrations of heated beams, Ph.D. Thesis, Columbia University, New York
 4. Deresiewicz H., 1958, Solution of the equations of thermoelasticity, *Proceedings of Third U.S. National Congress of Applied Mechanics*, 287-305
- Titles of references originally published not in English, should be translated into English and formulated as follows:
 5. Huber M.T., 1904, Specific work of strain as a measure of material effort (in Polish), *Czasopismo Techniczne*, **XXII**, 3, 80-81

All the data should be reported in **SI units**.

Contents

Lima J.J., Tusset A.M., Janzen F.C., Piccirillo V., Nascimento C.B., Balthazar J.M., Brasil R.M.L.R.F. — SDRE applied to position and vibration control of a robot manipulator with a flexible link	1067
Derpeński Ł., Seweryn A. — Ductile fracture criterion for specimens with notches made of aluminium alloy EN-AW 2024	1079
Domagalski Ł., Jędrzyak J. — Nonlinear vibrations of periodic beams	1095
Rosół M., Martynowicz P. — Implementation of the LQG controller for a wind turbine tower-nacelle model with an MR tuned vibration absorber	1109
Kowalczyk S., Matysiak S.J., Perkowski D.M. — On some problems of SH wave propagation in inhomogeneous elastic bodies	1125
Masmoudi A., Ben Oueddou M., Haddar M. — Mode of failure for reinforced concrete beams with GFRP bars	1137
Znaidi A., Daghfes O., Gahbiche A., Nasri R. — Identification strategy of anisotropic behavior laws: application to thin sheets of Aluminium A5	1147
Kisilowski J., Zalewski J. — Analysis of the stochastic technical stability of engineering structures on an example of a moving car	1157
Sabiniak H.G. — Load distribution in the worm meshing	1169
Baranowski L., Gadomski B., Szymonik J., Majewski P. — Comparison of explicit and implicit forms of the modified point mass trajectory model	1183
Kyzioł J., Okniński A. — Metamorphoses of resonance curves in systems of coupled oscillators	1197
Özdemir Ö. — Application of the differential transform method to the free vibration analysis of functionally graded Timoshenko beams	1205
Shahlaei-Far S., Nabarrete A., Balthazar J.M. — Homotopy analysis of a forced nonlinear beam model with quadratic and cubic nonlinearities	1219
Dumitriu M. — Numerical analysis of the influence of lateral suspension parameters on the ride quality of railway vehicles	1231
Fang C. — On the turbulent boundary layer of a dry granular avalanche down an incline. II – Closure model and numerical simulations	1245
Gonzalez M. — Analysis of a cross-channel micromixer through the dynamics of tracer gradient	1257
Seif A.E., Kabir M.Z. — The general form of the elastic stress and displacement fields of the finite cracked plate	1271
Hejčík J., Charvát P., Klimeš L., Astrouski I. — A PCM-water heat exchanger with polymeric hollow fibres for latent heat thermal energy storage: a parametric study of discharging stage	1285
Li T., Ma X., Zhang Q., Wang Z. — Band gap properties of periodic tapered beam structure using traveling wave method	1297
Pourrostami H., Viliani N.S.K. — Study of a MEMS hybrid thermo-PZT micro actuator	1309
Wang X., Schiavone P. — A mode-III crack with variable surface effects	1319
Wawrzyński W., Krata P. — Method for ship's rolling period prediction with regard to non-linearity of <i>GZ</i> curve	1329
Augustyniak M., Gajewski P., Świątek K. — Adaptation of engineering FEA-based algorithms to LCF failure and material data prediction in offshore design	1345
Mohammadi Nasrabadi A.A., Hedayati R., Sadighi M. — Numerical and experimental study of the mechanical response of aluminum foams under compressive loading using CT data	1357
Obst M., Rodak M., Paczos P. — Limit load of cold formed thin-walled nonstandard channel beams	1369
Socha G., Madejski B., Malicki M. — Study on deformation-induced damage evolution for Inconel718 superalloy with the use of an innovative single-specimen method	1379
Pękal M., Frączek J. — Comparison of natural complement formulations for multibody dynamics	1391
Żugaj M., Bibik P., Jacewicz M. — UAV aircraft model for control system failures analysis	1405
Boulououar A., Benseddiq N., Merzoug M., Benamara N., Mazari M. — A strain energy density theory for mixed mode crack propagation in rubber-like materials	1417
Freundlich J. — Dynamic response of a simply supported viscoelastic beam of a fractional derivative type to a moving force load	1433